Proceedings

International Conference on Nuclear Science and Technology

Nuclear Society Of Iran | Atomic Energy Organization of Iran | Nuclear Sciences and Technologies Research Institute

Papers on:

Nuclear Reactor
(Safe Operation, Maintenance & Engineering)

Climate Change
& the Role of Nuclear Power

*In this booklet, you will find the selected papers presented at the **First International Conference on Nuclear Science and Technology**, held from May 6-8, 2024, in Isfahan, Iran.*
We hope you find it informative and enjoyable!

ICNST 2024

Contact and Accessibility

icnst2024.com
registration@icnst2024.com


بسم الله الرحمن الرحيم

The Conference President's Message
ICNST 2024

Attendees, guests, and colleagues

I would like to warmly welcome you to the first International Conference on Nuclear Science and Technology (ICNST 2024). It has been a real honor and privilege to serve as the president of this conference. The conference this year has brought together an incredible diversity of authors and speakers from universities, government, and industry to share ideas and new perspectives on a wide range of radiation applications, nuclear reactors, particle accelerators, radiation measurements, fusion and plasma, stable and radioactive isotopes, radiation safety and security, nuclear agriculture, fuel cycle, lasers, education and training and nuclear governance.

Climate change, a new topic which has been added to this year's agenda as an important worldwide issue. a matter that has been brought up as a critical concern at the majority of IAEA conferences and nuclear scientific assemblies in recent years.

Panel discussions and exhibitions are being introduced as side activities in an attempt to keep this scientific meeting from becoming one-dimensional and increase its effectiveness.

More than 520 complete papers have been approved for this conference; when combined with the additional panels, get-togethers, and side activities, it is anticipated that over 1000 people will attend in person in the historical and touristic city of Isfahan. We look forward to welcoming participants to share their practical ideas and to enjoy an academical and cultural three days in Isfahan.

I'll close by wishing you everyone an incredible, instructive, and transformative experience during ICNST2024 and I hope that this conference can pave the route for academic materials to be used in industry and everyday life.

Prof. Javad Karimi-Sabet
President of ICNST2024
Javad Karimi-Sabet

welcome statment of scientific secretary ICNST 2024

"In the name of God, the Merciful,

Prior to giving the stage to address this distinguished forum, let me take this opportunity to express our deep gratitude, on behalf of all attendees, for His Excellency Mr. Islami's scientific, educational, and motivational remarks, as well as for his excellent organization of this conference.

I would also like to express our appreciation to His Excellency Dr. Mortazavi, Governor-General of Isfahan Province, for his constructive and useful support in enabling this meeting to take place.

This is a great pleasure and honor to extend a warm greeting to each and every one of you for the International Conference on Nuclear Science and Technology, scheduled from May 6th to May 8th, 2024, in the historic city of Isfahan, Iran.

With the aim of advancing our knowledge of nuclear science and technology, this conference is a major global convergence of experts, researchers, and practitioners. It is a platform for the sharing of creative concepts, the presentation of state-of-the-art research, and the formation of cooperative alliances.

As the scientific secretary of this prestigious event, I am particularly excited about the diverse array of participants expected to grace us with their presence. From the esteemed scientists and engineers of Russian universities and research centers to representatives from Islamic countries, friendly nations, and beyond, this conference promises to be a melting pot of perspectives, experiences, and expertise.

The extensive coverage of this conference is another aspect of its uniqueness. We have nearly 900 participants representing 22 countries around the world. Of the 900 participants, 620 are authors covering 13 major topics. There are 421 papers for oral and poster presentations, with additional documents for publication in ISC journals. There will be 3 plenary sessions, 16 panel discussions, 20 parallel oral presentation sessions, and 3 poster sessions.

Prof. Hosein Afarideh
Scientific Secretariat of ICNST2024

Organizers

Nuclear Society of Iran (NSI)

Atomic Energy Organization of Iran (AEOI)

Nuclear Science and Technology Research Institute (NSTRI)

Scientific Partnership

International Atomic Energy Agency (IAEA)

Isfahan University

Sharif University

Kurchatov Institute

Amirkabir University of Technology (Tehran Polytechnique)

Shahid Beheshti University

Isfahan University of Technology

Shiraz University

Islamic Azad University

K. N. Toosi University of Technology

Ferdowsi University of Mashhad

Kerman Graduate University of Technology

Sahand University of Technology

University of Tabriz

Islamic World Scieence Citation Center

Journal of Nuclear Science and Technology (JonSat)

Radiation Physics and Engineering journal

Nuclear Watch

Cooperative Organization

Isfahan Governorate

Isfahan Municipality

Abbasi Hotel

Iran Atomic Energy Production & Development Co.

Iran's Nuclear Raw Materials & Fuel Production Co.

Radiation Application Development Co.

Ofogh Consulting Engineers Co.

Nuclear Power Plant Safety Development & Promotion Co.

Nuclear Power Plant Engineering & Construction Co.

Engineering & Design of Industrial Simulator Co.

Energy Industry Development Engineering Co

Atomic Power Plant Pepair & support

Nuclear Reactors Fuel Co.

Iran Radioactive Waste Management Co.

Mesbah Energy Co.

Iran Gharb Industrial, Mining and Energy Co.

Pars Isotope Co.

Center for Laser Science & Technology of Iran

Centrifuge Production of Iran Co.

Plasma Technology Development Co.

Rasa Technology and Innovation Center

Behyaar Sanaat Sepahan Co.

Nuclear Data Base of Iran (NDB)

Parto think tank (strategic studies of nuclear industry development)

International Conference Alerts

Local Scientific Board

RAW	NAME	ROLE	AFFILIATION
1	**Prof. Hossein Afarideh**	**Chairman of Local Scientific Board**	**Amirkabir University of Technology (Tehran Polytechnique)(AUT)**
2	**Prof. Mohammad Ghanadi Maragheh**	**Member of The Local Scientific Board**	**Nuclear Science and Technology Research Institute of Iran (NSTRI)**
3	**Prof. Mohammad Lamei Rashti**	**Member of The Local Scientific Board**	**Nuclear Science and Technology Research Institute of Iran (NSTRI)**
4	**Prof. Mohammad Bagher Ghofrani**	**Member of The Local Scientific Board**	**Sharif University of Technology (SUT)**
5	**Prof. Hosein Faghihian**	**Member of The Local Scientific Board**	**University of Isfahan (UI)**
6	**Prof. Javad Rahighi**	**Member of The Local Scientific Board**	**Institute for Research in Fundamental Sciences (IPM)**
7	**Prof. Seyed Amirhossein Feghhi**	**Member of The Local Scientific Board**	**Shahid Beheshti University (SBU)**

Scientific Committee

RAW	NAME	ROLE	AFFILIATION
1	**Prof. Ali Akbar Salehi**	**Member of The Scientific Committe**	**Sharif University of Technology (SUT)**
2	**Prof. Seyyed Javad Ahmadi**	**Member of The Scientific Committe**	**Nuclear Science and Technology Research Institute of Iran (NSTRI)**
3	**Prof. Farhoud Ziaee**	**Member of The Scientific Committe**	**Nuclear Science and Technology Research Institute of Iran (NSTRI)**
4	**Prof. Saeed Hamidi**	**Member of The Scientific Committe**	**University of Arak**
5	**Prof. Seyedzafarollah Kalantari**	**Member of The Scientific Committe**	**Isfahan University of Technology (IUT)**
6	**Prof. Naser Bagheri Moghaddam**	**Member of The Scientific Committe**	**National Research Institute for Science Policy (NRISP)**
7	**Prof. Naser Vosoghi**	**Member of The Scientific Committe**	**Sharif University of Technology (SUT)**
8	**Prof. Seied Rabi Mahdavi**	**Member of The Scientific Committe**	**Iran University of Medical Sciences**
9	**Prof. Meisam Torab Mostaedi**	**Member of The Scientific Committe**	**Nuclear Science and Technology Research Institute of Iran (NSTRI)**
10	**Prof. Fereydoun Abbasi Davani**	**Member of The Scientific Committe**	**Shahid Beheshti University (SBU)**
11	**Prof. Seyed Farhad Masoudi**	**Member of The Scientific Committe**	**K.N.Toosi University of Technology**
12	**Prof. Rasool Ruknizadeh**	**Member of The Scientific Committe**	**University of Isfahan (UI)**
13	**Prof. Gholamreza Raeesali**	**Member of The Scientific Committe**	**Nuclear Science and Technology Research Institute of Iran (NSTRI)**
14	**Prof. Asghar Sedighzadeh**	**Member of The Scientific Committe**	

15	Prof. Hossein Kazeminejad	Member of The Scientific Committe	Nuclear Science and Technology Research Institute of Iran (NSTRI)
16	Prof. Seyyed Jaber Safdari	Member of The Scientific Committe	Nuclear Science and Technology Research Institute of Iran (NSTRI)
17	Prof. Omid Reza Kakuee	Member of The Scientific Committe	Nuclear Science and Technology Research Institute of Iran (NSTRI)
18	Prof. Alireza Keshtkar	Member of The Scientific Committe	Nuclear Science and Technology Research Institute of Iran (NSTRI)
19	Prof. Fereshte Haj esmail Beigi	Member of The Scientific Committe	Nuclear Science and Technology Research Institute of Iran (NSTRI)
20	Prof. Masoud Mahjour-shafiei	Member of The Scientific Committe	Nuclear Science and Technology Research Institute of Iran (NSTRI)
21	Prof. Mahmoud Payami Shabestar	Member of The Scientific Committe	Nuclear Science and Technology Research Institute of Iran (NSTRI)
22	Prof. Ali Bahrami Samani	Member of The Scientific Committe	Nuclear Science and Technology Research Institute of Iran (NSTRI)
23	Dr. Farhanaz Motamedi	Member of The Scientific Committe	Nuclear Science and Technology Research Institute of Iran (NSTRI)
24	Dr. Faezeh Rahmani	Member of The Scientific Committe	K.N.Toosi University of Technology
25	Dr. Ebrahim Moghiseh	Member of The Scientific Committe	Nuclear Science and Technology Research Institute of Iran (NSTRI)
26	Dr. Iraj Jabari	Member of The Scientific Committe	University of Isfahan (UI)
27	Dr. Nima Ghal-Eh	Member of The Scientific Committe	Ferdowsi University of Mashhad
28	Dr. Mitra Athari Alaf	Member of The Scientific Committe	Islamic Azad University Science and Research Branch
29	Dr. Gholamreza Etaati	Member of The Scientific Committe	
30	Dr. Amir Movafeghi	Member of The Scientific Committe	Nuclear Science and Technology Research Institute of Iran (NSTRI)

Executive Committee

RAW	NAME	ROLE
1	Dr. Farshad Ghasemi	Chairman of the Executive Committee
2	Dr. Ehsan Molazadeh	Member of The Executive Committee
3	Dr. Seyyed Ghasem Biniaz	Member of The Executive Committee
4	Mr. Aliakbar Aminidoust	Member of The Executive Committee
5	Ms. Fatemeh Zamani	Member of The Executive Committee
6	Ms. Mahya Pazoki	Member of The Executive Committee
7	Mr. Hosein Maleki	Member of The Executive Committee
8	Mr. Maziar Dalili	Member of The Executive Committee
9	Mr. Shojaei	Member of The Executive Committee
10	Ms. Fatemeh Rezaei	Member of The Executive Committee
11	Mr. Reza Rafiei	Member of The Executive Committee
12	Ms. Seyyedeh Elham Ebrahimi	Member of The Executive Committee

Nuclear Reactor (Safe operation, Maintenance and Engineering)

Neutron Flux Measurement in The Miniature Neutron Source Reactor Using Mika Nuclear Track Detector (Paper ID : 1007)....16

Thermoneutronic study of new generation TVS-2M fuel assemblies in Bushehr VVER-1000 reactor (Paper ID : 1008)....24

Modeling, comparison and analysis of fire protection system using three probabilistic safety analysis codes (Paper ID : 1013) 37

Analyzing the Impact of Internal Channel Radius of Dual-Cooled Annular Fuel on Reactor Safety Parameters in a Small Modular Nuclear Reactor (SMR): An Investigation Utilizing Artificial Neural Networks (ANN) and Gene Expression Programming (GEP) (Paper ID : 1019)....51

A Comparative Evaluation of Adaptive Robust Feedback-Linearization Control and Conventional Controllers in the Pressurized Water Nuclear Reactors During Load-Following Operation with Bounded Axial Power Distribution (Paper ID : 1022)....61

Acquiring and designing the world's most advanced nuclear reactor in line with its commercialization with unique safety and economic conditions (Paper ID : 1028)....71

Nano Materials in Pressurized Water Nuclear Reactor (Paper ID : 1038)....85

Predicting the thermal-hydraulic and natural circulation parameters in the Natural Circulation Integral Nuclear Reactor Core with dual-cooled annular fuel via CFD modeling as well as Fuel Geometry Optimization based on the ANN-GA approach (Paper ID : 1039)....96

An Artificial Neural Network Approach for Predicting the Thermal-Mechanical Parameters during the Beginning of Cycle (BOC) in NuScale Reactor Core Loaded with TVS-2M Fuel (Paper ID : 1049)..111

Assessing the Influence of Axial Power Distribution on Thermal-Mechanical Parameters in the NuScale Reactor Core Utilizing TVS-2M Fuel Assemblies (Paper ID : 1051)....119

Design and Analysis of Control Banks for NuScale Reactor Core Loaded with TVS-2M Fuel (Paper ID : 1052)....124

Development of High-Speed Neutron Noise Simulator based on High order Nodal Expansion Method for Hexagonal Geometry in Frequency Domain (Paper ID : 1067) 133

Assessment and predicting effects of Accident Tolerant Fuel (ATF) composition and geometry on the neutronic and safety parameters in the Small Modular Nuclear Reactor via Artificial Neural Network (Paper ID : 1072)....145

The Empirical Correlation for Forced Convection Heat Transfer of Homogeneous Hybrid Nanofluid TiO2/Al2O3 in a Vertical Annulus (Paper ID : 1129)....143

Simulation and analysis of fire accident in Isfahan nuclear fuel production complex and standardization of fire extinguishing system according to NFPA global standard using CFAST code (Paper ID : 1132)....150

Thermal Performance Assessment of a Small Modular Reactor's Once-Through Steam Generator Using Al2O3 Nanoparticles in the Primary Coolant System (Paper ID : 1142)....170

Feasibility study of utilizing a secondary pool for spent fuel storage in research reactor from shielding aspect (Paper ID : 1152) *181*

LQG/LTR controller design for power reference tracking molten salt reactor (Paper ID : 1182)..... *191*

The Effects of Nickel Nano-Composites on Corrosion of Pressurized Water Loop (PWL) in Nuclear Reactors (Paper ID : 1203) *202*

The control rod ejection accident in VVER-1000 using TRACE and PARCS (Paper ID : 1210) *224*

Cobalt-60 Production in Tehran Research Reactor (Paper ID : 1220) *236*

PCMI Assessment Method Using Abaqus: A Segmented Expanding Mandrel Test Approach (Paper ID : 1246) *242*

Development of transient dynamics code for a helically-coiled steam generator analysis using multi-node moving boundary model (Paper ID : 1248) *251*

Dynamic Probabilistic Safety Assessment of primary to secondary leak Accident in VVER-1000 (Paper ID : 1254) *264*

Sensitivity and Uncertainty Analysis of Halden Reactor Fuel Using SUAP Code (Paper ID : 1268).278

Investigation of the Effect of Al2O3 Nanoparticles on Thermo-hydraulic Parameters in a Mini-Loop with Natural Circulation (Paper ID : 1282) *307*

Design of molten salt reactor core power controller using MPC method (Paper ID : 1300)..... *319*

An economic evaluation of Persian Gulf desalination coupled to different energy sources (Paper ID : 1304) *328*

RELAP5 Code Investigation on Operational Characteristics of Passive siphon breaker line in Research Reactors under LOCA Conditions (Paper ID : 1330) *338*

Development of a Model for Calculation of Radial Burnup Distribution in VVER-1000 Reactor Fuel Rod Using Monte Carlo Method (Paper ID : 1354) *367*

Investigation on Delayed Neutron Grouping Effects: Numerical Solution (Paper ID : 1373) *379*

Optimal selection of the core baffle and barrel materials for a typical PWR reactor with 300MW by investigation of the reactor core neutronic parameters (Paper ID : 1374) *390*

Optimal selection of the ATF cladding for a typical PWR reactor with 300MW by investigation of the reactor core neutronic parameters (Paper ID : 1375) *398*

Investigation of the neutronic parameters of a typical PWR reactor with 300MW using different cladding coatings as ATF cladding (Paper ID : 1377) *405*

CFD Analysis of Cross-Flow in VVER-1000 Fuel Assemblies Using ANSYS-CFX (Paper ID : 1399) *414*

Simulation and investigation of neutron-induced dose distribution in the barrel of VVER 1000 Reactor (Paper ID : 1435)..... *428*

Technical and economic comparison of freshwater production by nuclear and fossil methods in Iran (Paper ID : 1437)..... *436*

The Study of breeding of 239Pu in Fusion Driven Subcritical Spent Fuel Burner Reactor (FDS-SFB) (Paper ID : 1444)....446

Neutronic Analysis of two-channel cooled Annular Fuel in the Core of the Bushehr reactor in the MCNPX (Paper ID : 1471)....467

Investigation of Temperature distribution and DNBR Safety margin in two-channel cooling Annular Fuel in VVER-1000 reactor (Paper ID : 1474)....482

The effect of radiation induced swelling on the heat transfer performance of nuclear fuel plate (Paper ID : 1499)....497

A study on the thermal properties of irradiated UO2 fuel (Paper ID : 1500)....507

Point defect effects on the phonon thermal conductivity of Zr-1%Nb single crystal by Reverse non-equilibrium Molecular dynamics (Paper ID : 1501)....520

Calculation of neutron flux along the beam line of PGNAA system of Isfahan Miniature Neutron Source Reactor Department of Physics, Isfahan University of Technology, Isfahan, Iran, 8415683111 (Paper ID : 1553)....535

Compressive properties of Zr-Nb alloy produced by multidirectional free hot forging (Paper ID : 1587)....545

Numerical analysis of a novel passive flow limiter for nuclear heating reactors (Paper ID : 1592)..557

Application of the IDON Shielding Optimization Tool (ISOT) for the Primary and Secondary Shielding of a Research Reactor (Paper ID : 1611)....565

Computational Fluid Dynamics Simulation of Siphon Breaker Performance in a Research Reactor (Paper ID : 1659)....573

Examining the nuclear reactors of Iran and the world in terms of technical knowledge, geographical location, power generation capacity, security considerations, environmental issues and economic benefits (Paper ID : 1681)....585

Climate Change & The Role of Nuclear Power....599

Innovative Carbon Dioxide Removal from the Air Utilizing Methane Dry Reforming via Plasma Technology (Paper ID : 1464)....600

Role of Nuclear Science in Addressing Environmental Challenges (Paper ID : 1600)....615

Nuclear Reactor (Safe operation, Maintenance & Engineering)

ICNST 2024 International Conference on Nuclear Science and Technology
6- 8 MAY 2024 | Isfahan, Iran

Neutron Flux Measurement in The Miniature Neutron Source Reactor Using Mika Nuclear Track Detector (Paper ID : 1007)

Zare Ganjaroodi S. Correspondent[1*], Raei N.[2], Mokhtari J.[3], Zarifi E[4]

[1]Faculty of physics and energy engineering, Amirkabir university, (Tehran Polytechnique), Hafez Ave, Tehran, Iran
[2]Faculty of Engineering Science and Research Branch, Islamic Azad university, Tehran, Iran
[3]Reactor and Nuclear Safety Research School, Nuclear Science and Technology Research Institute, AEOI, Isfahan, Iran
[4]Nuclear Science and Technology Research Institute (NSTRI), Tehran, Iran

Abstract

In the present paper, a solid-state nuclear track detector (SSNTD) is applied to measure the neutron flux in the Isfahan Miniature Neutron Source Reactor (MNSR). The 30KW MNSR is a light water cooled and moderated research reactor that runs on 900 grams of 90% highly enriched uranium (HEU) as fuel. Samples with a special arrangement consisting mica and uranium foil placed inside the polycarbonate capsules. Next, samples were sent into the irradiation channels of the reactor core to measure the neutron flux distribution indirectly. The sensitivity of the method depends on the concentration of fissile elements, while deposition of fissionable material on the mica would increase the sensitivity. Comparison of the EXPERIMENTAL data with the reactor reports shows an appropriate consistency with an acceptable error of less than three percent. fission track registration technique has been shown to be a very simple, inexpensive and accurate method for neutron flux measurements.

Keywords: MNSR, Mica nuclear track detector, Neutron flux, SSNTD.

Introduction

Research reactors have been designed as a neutrons source for a wide variety of scientific goals, including education and training in more than 50 countries around the world [1]. Common designs of the research reactors are pool-type, tank-type and tank-in-pool reactors. The Miniature Neutron Source Reactor (MNSR) is a tank-in pool type reactor that is designed and constructed by China Institute of Atomic Energy for training, education and neutron activation analysis (NAA) [2-3]. A total number of nine MNSRs have been designed and constructed around the world. Four of these reactors are located in China, one in Iran, Ghana, Syria, and Nigeria [4].

Young placed the lithium fluoride crystal next to the uranium foil and irradiated it with thermal neutrons. After a chemical etching with a suitable material, number of tracks were seen on the crystal

which the number of these tracks was proportional to the estimated number of fission fragments from uranium foil that interacted with the crystal. Seams that each track created is caused by the destruction of the crystal structure was made by fission fragments [5].

The method of solid-state nuclear track detection is based on the recording of fission fragments track on a solid-state detector. This detector is insulating solids which are usually transparent and exist naturally or artificially. Mica's nuclear track detection counting system is not online. This detection has many advantages, including economic efficiency, high durability, simplicity which it has led to extensive use in various fields [5-6].

Several reports and essays on various technical aspects of miniature neutron source reactor (MNSR) have been studied in recent years. Akaho and Nyarko studied the Characterization of neutron flux spectra in irradiation sites of MNSR reactor using the Westcott-formalism for the k_0 neutron activation analysis method in 2002 [7]. In another study, Ahmadi et al in 2018 worked on the neutronic assessment of BDBA Scenario at the end of Isfahan MNSR core life [8]. In 2018, Seyfi et al, investigated the feasibility of 198Au production in Isfahan MNSR research reactor through a multi-stage approach [9]. Mokhtari et al, studied the design the low power and LEU medical reactor for BNCT using in-tank fission converter to increase epithermal flux [10].

On the other hand, in this study, due to the importance of flux measurement in research reactors, a new high-precision method for measuring neutron flux in MNSR core has been proposed. Here, an experimental method using the Mica nuclear track detector is used to measure the neutron flux and power in the MNSR core. Finally, the results benchmarked with References to show an appropriate consistency.

Research Theories

The Miniature Neutron Source Reactor (MNSR) was designed in 1980, based on Canadian Slowpoke Reactor model, by the Atomic Energy Organization of China. The Iranian MNSR is a small, advanced research reactor of tank-in pool type with a nominal power of 30 kW have been built in 1994. The MNSR cooling system designed by natural convection mode. Light water is utilized as moderator and coolant in this reactor. Also, Beryllium is used as a reflector around the fuel to reduce neutron leakage in the core. The core diameter is about 23.1 cm and the active height is about 23 cm [11-13]. The MNSR is shown in fig 1.

The MNSR core consists of one central control rod, four tie rods, three dummy rods and 343 fuel rods with a height of 23 cm that are arranged in 10 concentric circles. The fuel is UAl_4 with an enrichment of 90.2% that is covered with an aluminum clad [12]. The MNSR design data are listed in table 1.

Table 1. MNSR design parameters.

Parameter	Value
Reactor design type	Tank-in-pool
Thermal power (KW)	30
Core shape	Cylindrical
Fuel	UAl_4
Enrichment	90.2%, HEU
Fuel density (gr/cm^3)	3.403
Diameter of fuel pellet (cm)	0.43
Fuel rod clad material	Aluminum
Diameter of fuel element (cm)	0.55
Number of fuel elements	342 - 350
Core diameter (cm)	23.1
Core active height (cm)	23.0
Number of irradiation channels	10
Inner channels	5
Reactor cooling system	Natural convection
Length of control rod (cm)	23
Control rod clad material	Stainless steel
Control rod material	Cadmium
Reflector	Beryllium metal alloy

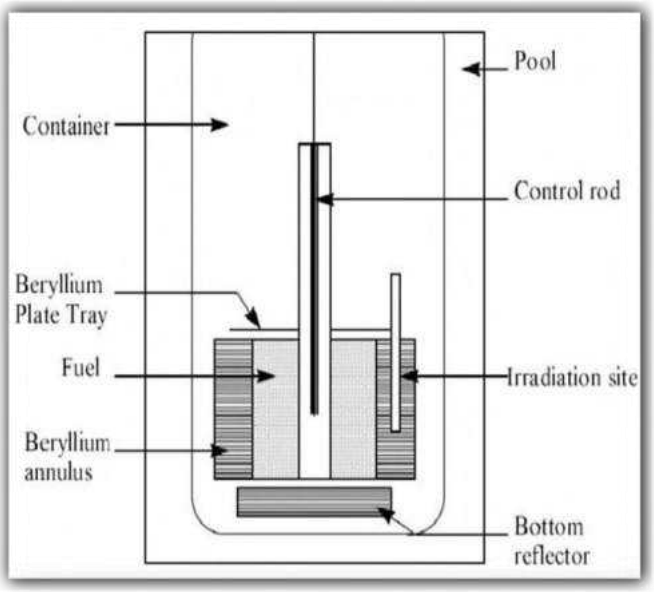

Fig.1. A schematic of the MNSR.

Experimental

In the mica detector, when a thermal neutron hits the U-235 core, it splits into two smaller atoms. If Mica's nuclear track detector is used next to the fuel, some of the fission fragments, which have enough energy will crash with Mica's foil. In this way, the effects of the collision will be visible under a microscope after the chemical etching operation. In this study, a sample containing uranium's foil and mica's foil was prepared and entered the radiation channel of the MNSRs core for irradiation process. Due to the short range of the fission fragments, the mica foil and the uranium foil must be completely fixed. During this EXPERIMENTAL test, different models of sample placement and arrangement were designed using Polycarbonate capsules. It should be noted that, the reason of using polycarbonate capsules is to prevention of mechanical stresses or sample scratches. Different types of samples layout are shown in fig 3.

Due to the created tracks of fission fragments will not be seen in the optical microscope, the irradiated foil was placed in HF acid 48% to dissolve the damaged tissue by colliding with the fission fragments. To perform the chemical etching, HF acid 48% was placed in water at a 50 C and the duration of the chemical etching is 50 minutes.

In the next step, on a piece of cardboard, create a circle equal to the diameter of the mica foil to perform sampling statistically of the entire surface of the mica's foil and to identify the location coordinates of the counted area (Fig.4). Also, a matrix design (square matrix) has been used for counting process. In this way, the square was tangent to the circle. That is, the length of the square side is equal to the diameter of the circle, and the counting of the sample surface is done with a specific step. The surface on which the sample is placed is located in both x and y directions. Therefore, the surface of the sample can be easily counted with a specific step. Here the sample surface is counted with a step of 1 mm and an average value for the track density is obtained. It should be mentioned that, among the available magnifications, the 10X magnification has been more suitable for counting tracks. A schematic of Mica sample magnification by microscope is illustrated in fig 5.

Finally, the number of tracks on the Mica foil is proportional to the number of fissions, which this proportionality ratio is equal to the detection efficiency of that foil, and thus the reactor flux can be calculated indirectly.

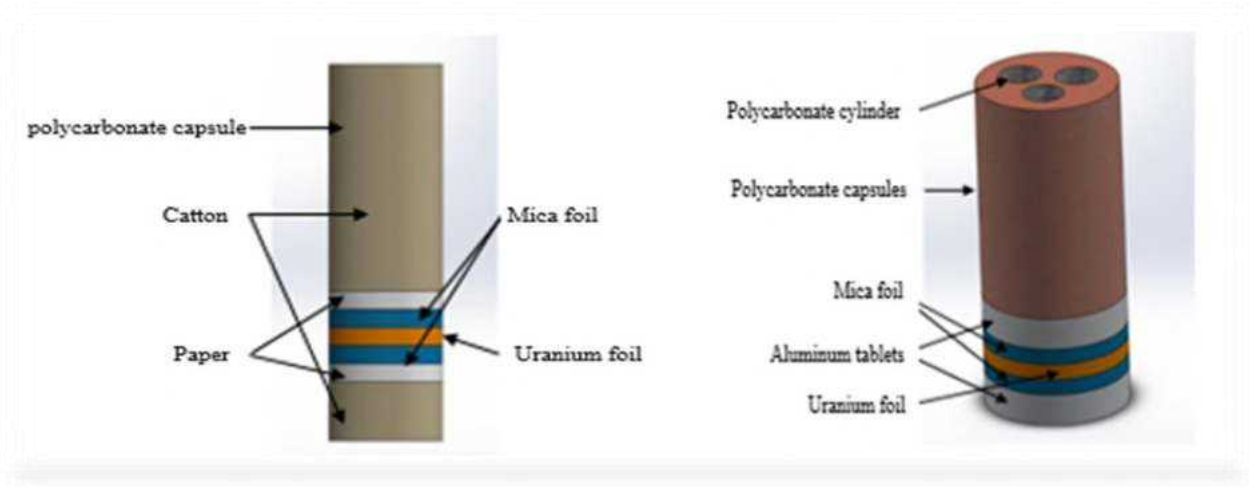

Fig. 3. Different types of samples layout.

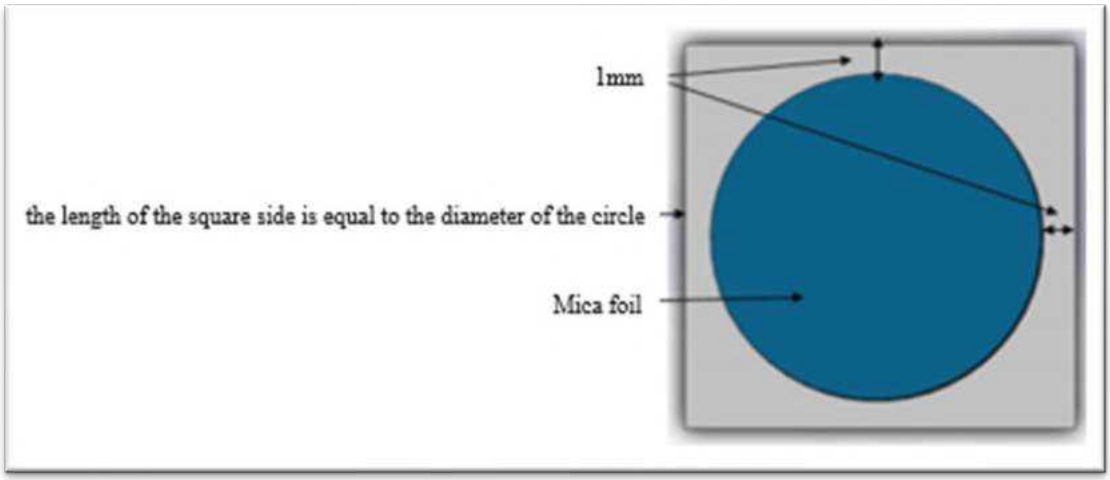

Fig. 4. Counting Mika's foil**.**

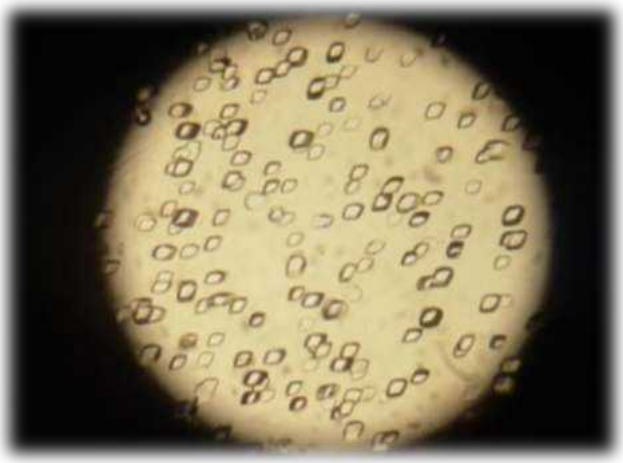

Fig. 5. Mica sample magnification by microscope.

Results and Discussion

The detector efficiency of the Mica foil nuclear track is a key factor in calculating the neutron flux by counting the Mica foil tracks. The detector efficiency is a function of the geometric shape and thickness of the uranium used. Due to the constant material and conditions during the tests, its value is constant. Mika nuclear track detector efficiency is obtained by calculating the ratio of the number of tracks in the fuel element to the number of tracks created by fission on the mica foil. Eight Mika foils with the same irradiated conditions have been performed on the chemical etching. The number of tracks counted from these eight foils is averaged, which is equal to the efficiency of the detector. It should be noted that, this value for detector efficiency can be used for experiments with the same conditions.

$$R = \sum_{i=1}^{8} R_i \,/\, 8 \qquad (1)$$

Also, the number of tracks per unit area is defined by the S symbol which is calculated as follows:

$$S = (\text{Number of tracks}) \,/\, (\text{Foil area}) \qquad (2)$$

$$R * S = N \qquad (3)$$

The number of fission fragments generated per unit volume of fuel is obtained from the following equation:

$$N = \Sigma_f \Phi_{th} t \qquad (4)$$

$$N = 0.1962\ (1 / cm) * \Phi_{th}\ (\# / cm^2.sec) * 15\ (sec)$$

$$N = 2.943\ \Phi_{th}$$

Where Σ_f is fission cross section of U-235, Φ_{th} the thermal neutron flux, and t is irradiation time. According to Table 2 and formula (3) and (4) the thermal neutron flux can be obtained as:

$\Phi_{th} = 1023369506 \backsim 1.023\ E+9$

At the same time of the measurement of the reactor thermal neutron flux at the inner irradiation tube, the measurement of power is also performed.

Power $\backsim$ 3.00 (W)

According to the safety analysis report of the MNSR the regular neutron flux in inner irradiation tubes is 1 E+12 (n / cm^2. Sec), and then the corresponding reactor power is 30 (KW) approximately. Due to the linear relationship between flux and power in the reactor core, the calculated flux and power value is quite reasonable and has good agreement with the previous studies [14].

Conclusions

The main purpose of design and construction of research reactors is to provide a neutron source for research and various applications, such as education and training. In this way, a method with high accuracy is proposed to measure the neutron flux in the core of research reactor. In this paper, the

measurement of the neutron flux in the MNSR core using the Mica nuclear track detector is discussed. The Iranian MNSR is selected as the reference research reactor for EXPERIMENTAL method calculations. In this method, a sample with a special arrangement consisting of mica foil and uranium foil was prepared and placed inside the capsules of polycarbonate. The samples were sent to the MNSR irradiation channel. After irradiation process, etching was performed on the mica foil and the neutron flux obtained by the mica track detector. Also, Comparison of the results with the reactor reports shows an acceptable error of less than three percent. Accordingly, using the Mica nuclear track detector has a high accuracy in measuring neutron flux.

References

[1] IAEA, (2016), Research Reactors: Purpose and Future**,** International Atomic Energy Agency (IAEA) Vienna International Centre.

[2] Dastjerdi, M. C., Mokhtari, J., Asgari, A., & Ghahremani, E. (2019). A neutron radiography beamline relying on the Isfahan Miniature Neutron Source Reactor. Nuclear Instruments and Methods in Physics Research Section A: Accelerators, Spectrometers, Detectors and Associated Equipment, 928, 20-25.

[3] Mokhtari, J., Faghihi, F., & Khorsandi, J. (2017). Design and optimization of the new LEU MNSR for neutron radiography using thermal column to upgrade thermal flux. Progress in Nuclear Energy, 100, 221-232.

[4] IAEA, (2018), Analyses Supporting Conversion of Research Reactors from High Enriched Uranium Fuel to Low Enriched Uranium Fuel (The Case of the Miniature Neutron Source Reactors), IAEA TECDOC Research Reactor Section International Atomic Energy Agency Vienna International Centre.

[5] S.A. DURRANI and R.K. BULL, (1987), Solid State Nuclear Track Detection Principles, Methods and Applications, Oxford; New York: Pergamon Press, ISBN 978-0-08-020605-9.

[6] Robert Louis Fleischer, Paul Buford Price, Robert M. Walker, Robert Mowbray Walker, Nuclear Tracks in Solids: Principles and Applications, University of California Press, 11, 1353 AP.

[7] Akaho, E.H., Nyarko, B.J., (2002), Characterization of neutron flux spectra in irradiation sites of MNSR reactor using the Westcott-formalism for the k0 neutron activation analysis method. Appl. Radiat. Isot. 57 (2), 265–273.

[8] M. Ahmadi, A. Pirouzmand, A. Rabiee, (2018), Neutronic Assessment of BDBA Scenario at the End of Isfahan MNSR Core Life, Nuclear Engineering and Technology.

[9] F. Seyfi, B. Soleimani, M.A. Hosseini, M. Rezvanifard, M. Ahmadi, (2018), The feasibility of 198 Au production in Isfahan MNSR research reactor through a multi-stage approach, J. Radioanal. Nucl. Chem. 316 (2) 435e441.

[10] Mokhtari, J., Faghihi, F., Khorsandi, J., & Hadad, K. (2017). Conceptual design study of the low power and LEU medical reactor for BNCT using in-tank fission converter to increase epithermal flux. Progress in Nuclear Energy, 95, 70-77.

[11] G. Jilin, (1992), General Description of Miniature Neutron Source Reactor, China Institute of Atomic Energy: internal report.

[12] G. Chengzhan, Z. Xianfa, (1992), The Iranian MNSR Safety Analysis Report (SAR), China Institute of Atomic Energy: internal report.

[13] Chengzhan, G., Yongchun, G., (1994), Safety Analysis report for miniature neutron source reactor (MNSR). China Institute of Atomic Energy Report RPT4-S-430- SIAE/SA, RC, FL, RP.

[14] IAEA, (2011), SAR, Isfahan Miniature Neutron Source Reactor (MNSR) Safety Analysis Report (SAR), AEOI- Internal Report. NSTRI, Iran.

ICNST 2024 International Conference on Nuclear Science and Technology
6- 8 MAY 2024 | Isfahan, Iran

Thermoneutronic study of new generation TVS-2M fuel assemblies in Bushehr VVER-1000 reactor (Paper ID : 1008)

Zare Ganjaroodi S.[1, 2*], Zarifi E.[3]

[1]*Energy and Physics Department, Amirkabir University of Technology, 424 Hafez Ave., Tehran, Iran*

[2]*Iran Radioactive Waste Company, Atomic Energy Organization of Iran (AEOI), Postcode: 1439955931, Tehran – Iran*

[3]*Nuclear Science and Technology Research Institute (NSTRI), Tehran, Iran*

Abstract

To increase the efficiency of VVER reactors, the Russian fuel manufacturer in collaboration with research centers has developed a new generation of fuels called TVS which has several advantages over the current standard fuel. The Porous Media Approach (PMA) is a well-known method for thermal-hydraulic analyzing of the fuel reactor core FAs. In this paper, WIMSD5 and CITATIONLDI2 codes are coupled with the PMA for the Thermoneutronic analysis of the VVER-1000 reactor core of the Bushehr Nuclear Power Plant (BNPP) in two modes of calling AFA and TVS-2M Fuel Assemblies (FAs) configurations. Results presented, the K-Factor in both AFA and TVS-2M FAs configurations are calculated at 1.01767 and 1.02652, respectively. Moreover, the maximum coolant temperature in the hottest of FAs TVS-2M and AFA arrangement reached to 328 and 331 ^{o}C. Finally, the comparison of results from AFA FAs modelling showed an appropriate consistency with previous reports and studies.

Keywords: VVER, TVS, Porous Media Approach, WIMSD5, CITATIONLDI2.

Introduction

Bushehr VVER-1000 reactor is a Russian pressurized light water reactor with thermal power of 3000 (MW) and electric power of 1000 (MW). In the first circuit of a pressurized water reactor, light water is used as the coolant by passing through the FAs which reaches a high temperature but does not boil at the applied high pressure [1-3].

To increase the efficiency of VVER reactors, the Russian fuel manufacturer (TVEL) in collaboration with research centers such as Kurchatov, has developed a new generation of fuels called TVS [4]. The new generation of TVS fuels such as TVS-2M has several advantages over the current standard fuel (AFA) such as higher physical and chemical resistance, longer fuel life, the longer active height of fuel rods, and also fissile content. It is possible to increase the core working cycle length from 10 to almost

18 months using TVS-2M fuels. Also, the use of this type of fuel in the core can ascend the electrical power level of the reactor from 1000 (MW) to 1200 (MW). [5-6].

Although several reports and papers on various technical aspects of TVS-2M fuels have been performed in recent years, the Thermoneutronic behaviors of this type of fuel have not been discussed in detail. In 2005 and 2006, Hesito and Plamen et al, examined TVSM and TVSA fuels in the VVER-1000 reactor using the ORIGEN-S code [6-8]. Faghihi proposed a new design from the VVER-1000 reactor core with $(U+Gd)O_2$ FAs based on the TVS-2M fuels [9]. Ghaemi studied the neutronic and thermohydraulic behavior of TVS-2M fuels in the VVER-1000 reactor [10]. Kosorov et al. studied the fuel cycle of VVER-1000 reactors as a result of using a new generation of TVS fuels economically and technically in an article at the 8th international conference on VVER Reactor fuels [11]. In this study, WIMSD5 and CITATIONLDI2 codes and Porous Media Approach (PMA) are coupled for the Thermoneutronic analysis of VVER-1000 reactor core in two modes of using AFA and TVS-2M arrangements.

Material and method

TVS-2M FAs contains mixed uranium gadolinium oxide with different gadolinium densities and uranium enrichments is proposed to reduce the electric energy production costs, and increase fuel cycle lengths with more intrinsic safety. In comparison with AFA fuel, the new-generation TVS-2M FAs are distinguished by higher uranium capacity, fuel burn-up, and in-pile stiffness [12-15]. The TVS-2M and AFA FAs design criteria are listed in **Table 1**.

Table 1. TVS-2M and AFA FAs design parameters.

Parameter	Value	
	AFA	TVS-2M
Core thermal power (MWth)	3000	3000
Numbers of FAs	163	163
Geometry	Hexagonal	Hexagonal
Number of fuel rods per assembly	331	331
Measuring tube	1	1
Fuel assembly overall length (mm)	4570	4570
Fuel assembly overall width (mm)	235	235
Fuel rod length (mm)	3836	3988
Active length (mm)	3530	3680
Fuel rod outside diameter (mm)	9.1	9.1
Pellet length(mm)	9-12	9-12
Pellet outside diameter (mm)	7.8	7.6
Fuel density (gr/cm^3)	10.4-10.7	10.4-10.7
Cladding material	Zircalloy-4 +1%Nb	Zircalloy-4 +1%Nb
Spacer grid material	Zircalloy-4 +1%Nb	Zircalloy-4 +1%Nb

Geometrically, the new TVS-2M FAs are almost identical to the AFA FAs except in the structure of the top and bottom of the FAs and the most important factor is the active length, which has been increased from 353 mm to 368 mm. Hence, the fissile material is increased, which ascends the fuel efficiency time and the working cycle of the core from 10 to almost 18 months. Moreover, replacing (CrB_2 + Al) with Gd_2O_3 reduces the operating cost by increasing the excess reactivity of the core. [3-6]. The VVER-1000 core configuration via the TVS-2M and the AFA FAs are demonstrated in **Fig. 1**.

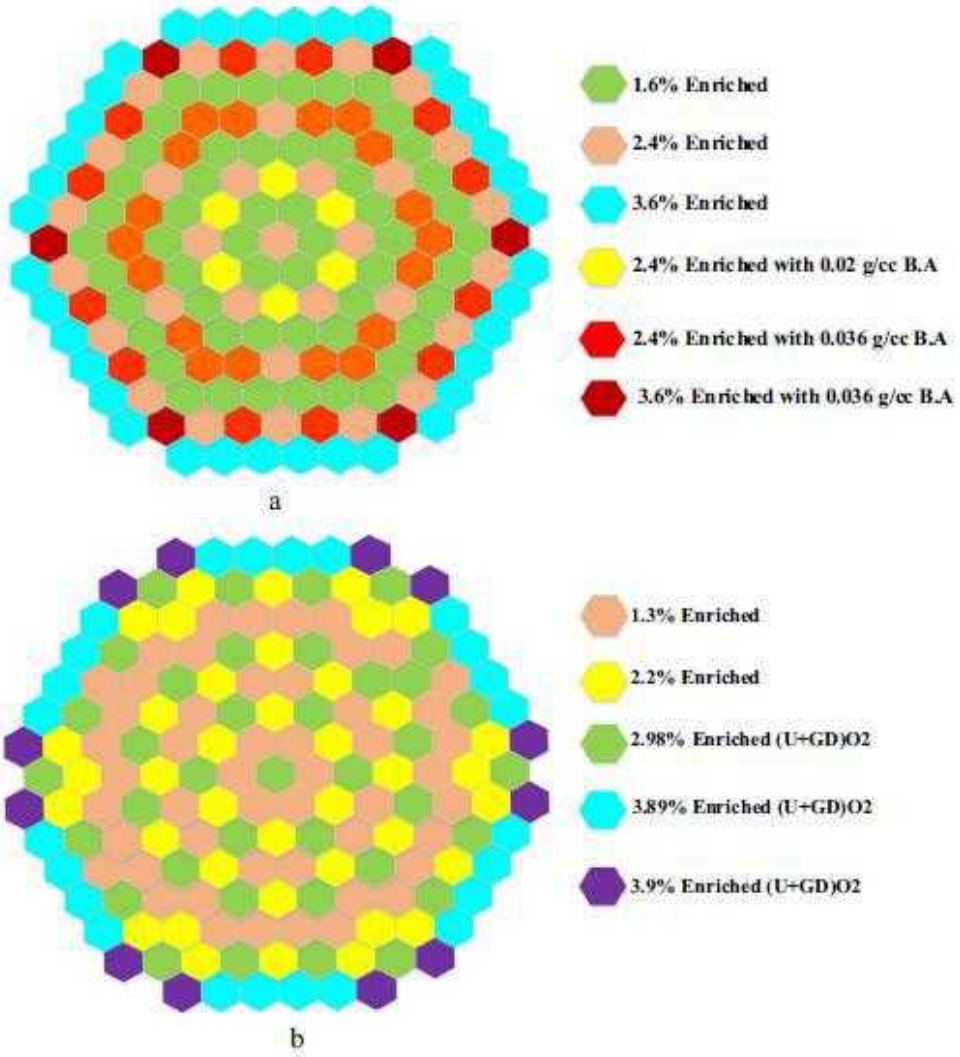

Fig. 1. A view of the AFA (a) and TVS-2M (b) FAs arrangement in the VVER-1000 reactor core.

WIMS is a general lattice cell code that uses transport theory via the deterministic method. Input data includes the structure core, and its shapes, enrichments, and dimensions. WIMS is utilized to calculate neutron flux distribution, group constants, and an effective multiplication factor. It takes as input the multi-group library of isotopic nuclear data and a description of the reactor lattice, and solves the neutron transport over a specified region of reactor lattice [16].

The finite-difference code CITATION is used to solve the neutron diffusion equation in one, two, and three dimensions. A wide range of geometries, such as one, two, and three-dimensional slab, cylinder, hexagonal and triangular geometries, can be performed by this code. CITATION code can calculate the effective multiplication factor, neutron flux and power in the core. Depletion problems may be solved and fuel managed for multi-cycle analysis. Static problems may be solved and perturbation

results obtained with microscopic data. Macroscopic data may be entered according to output results of lattice code, such as WIMS code [17].

The PMA method is a well-known approach for analyzing the FAs of the reactor core. The PMA technique is introduced to establish the conservation equations by using the porosity concept within the control volume. In such a manner, the momentum equations are solved with high accuracy for single-phase fluid. However, PMA method is not applied to evaluate the fuel temperature gradients [18].

WIMSD5 and CITATION-LDI2 codes are used to design a model for the VVER-1000 core and simulate its neutronic characteristics. These codes have jointly been used for neutronic parameters calculation. In this study, the core is divided into 588000 small meshes. The effective cross-sections and group constants obtained from WIMSD5 for various cells of the reactor core along with the core geometry and boundary condition are provided as input data to the CITATION code to calculate the neutronic parameters. The coefficients of the solved equations at each level are extracted from the calculations and therefore have a direct effect on the code results. The WIMS code library is generated from the ENDF database [12]. In this study, the power distribution and fuel rods power peaking factors were calculated by the coupling of WIMSD5 and CITATION-LDI2 codes. Finally, it was given as an input to the PMA program for the thermoneutronic analysis. The subchannel flowchart is illustrated in **Fig 2**.

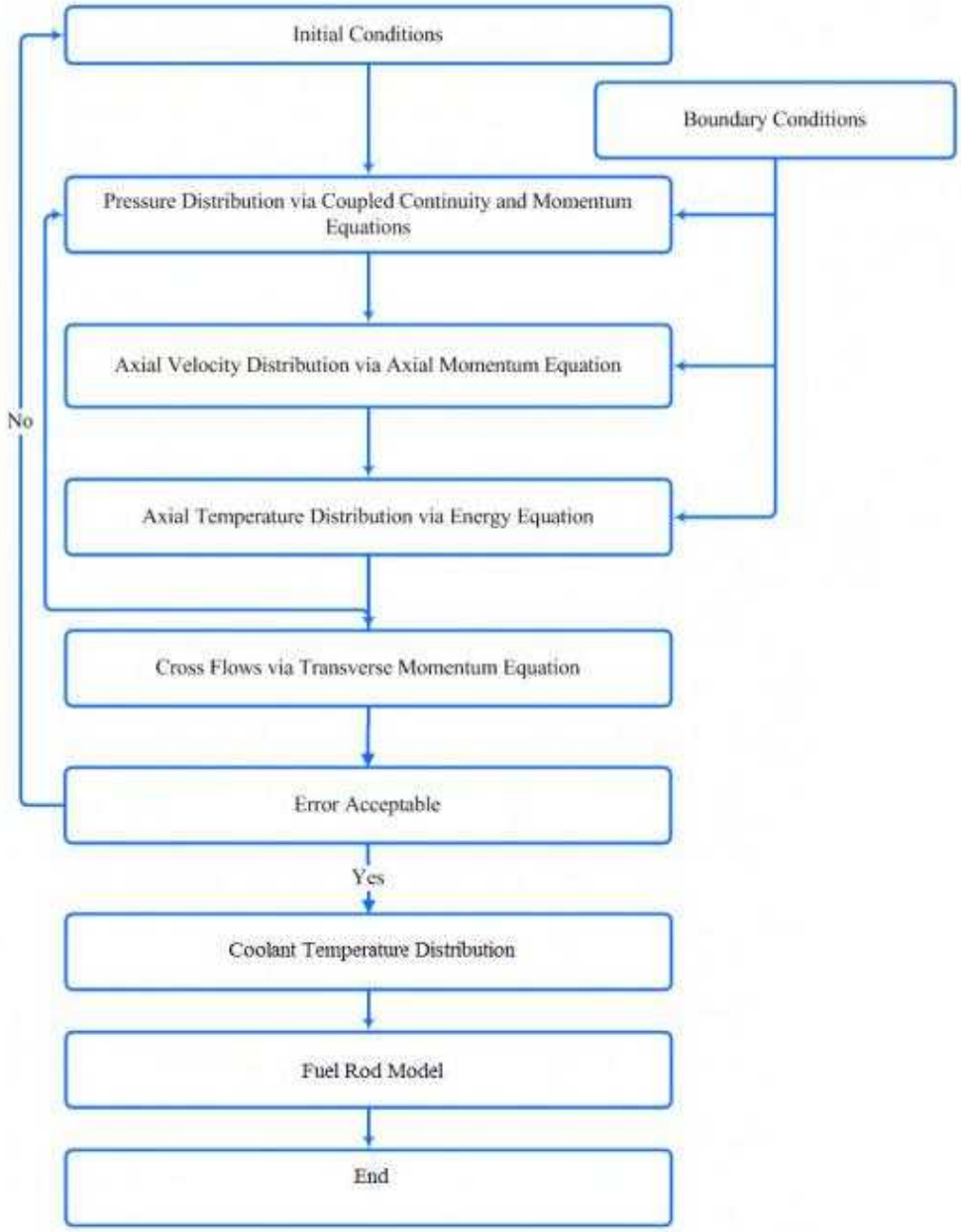

Fig. 2. The sub-cannel analysis flowchart.

Results and Discussion

The K-Factor in the TVS-2M FAs arrangement is calculated at 1.02652 using CITATION code. However, keff is calculated 1.01767 in the AFA FAs configuration in equal condition. Comparison of results shows that the values of effective multiplication factors are very close to each other in all codes.

Due to the increase of fissile materials into the core (due to 15 cm longer fuel active length and the addition of one more fuel rod in TVS-2M configuration), its effective multiplication factor is about 1% more than AFA FAs configuration. Comparison of core excess reactivity and K-factors when control rods do not enter into the core in both AFA and TVS-2M FAs' arrangements are listed in **Table 2.**

Table 2. The effective multiplication factor and excess reactivity in AFA and TVS-2M FAs.

Percentage of control rods of group 10	Keff and Excess reactivity (mK)	
	AFA FAs	TVS-2M FAs
0%	1.01767 Ex.R = 17.36	1.02652 Ex.R = 25.83
10%	1.00291 Ex.R = 2.90	1.01745 Ex.R = 17.15

The maximum thermal flux is related to about 142 cm in AFA FAs arrangement and 148 cm in TVS-2M FAs from the height of the core. The inserting of the control rods into the core can move the maximum flux height of about 40% to the end. **Figs 3 and 4** picture the radial thermal neutron flux distribution in the reactor core for both TVS-2M and AFA FAs configurations.

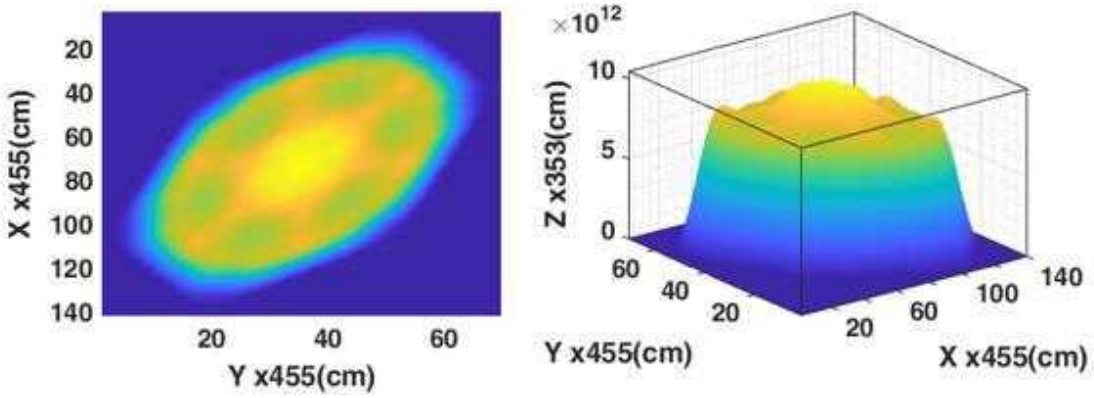

Fig. 3. The radial thermal neutron flux distribution in the reactor core in TVS-2M FAs configuration.

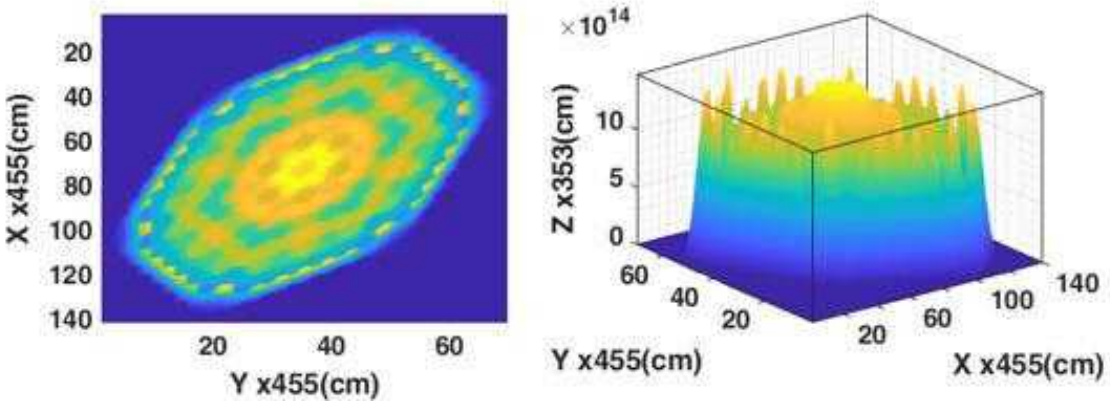

Fig. 4. The radial thermal neutron flux distribution in the reactor core in AFA FAs configuration.

In TVS-2M FAs, the peak of power density decreases in the center of the core and increases around it. Also, power density distribution tends to almost flatten mode. The reason for this phenomenon is due to the presence of Gd2O3 poisons in the central regions of the reactor core. The Axial PPF distribution for AFA and TVS-2M FAs by CITATION codes are shown in **Fig 5**.

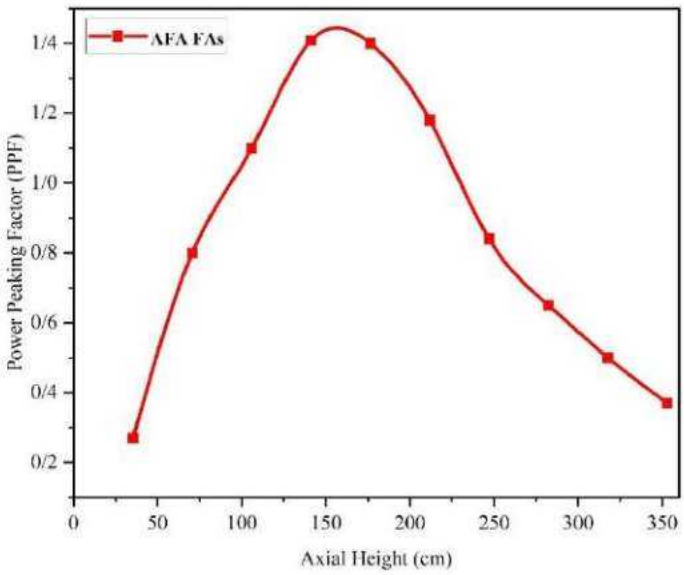

(a)

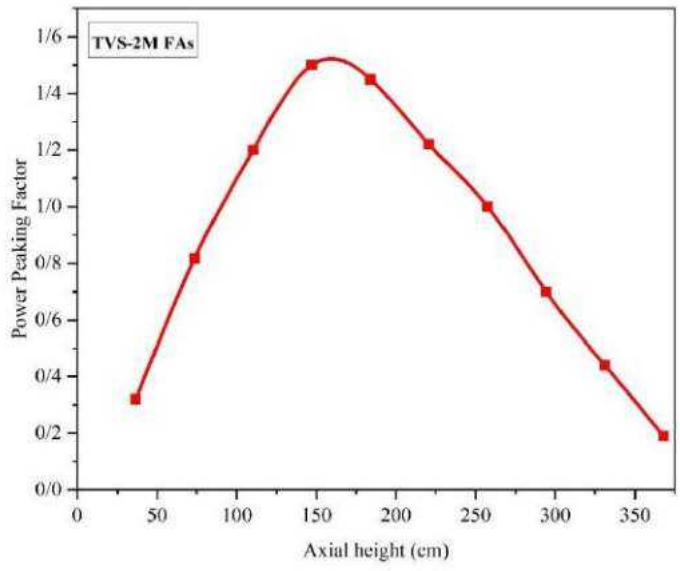

(b)

Fig. 5. Axial PPF distribution for AFA (a) and TVS-2M (b) FAs by CITATION code.

Figs 6 & 7 show the comparison of axial coolant temperature and density changes for both TVS-2M and AFA FAs. Also, Comparing the AFA fuel results of this study with previous reports show an appropriate consistency [1]. also, the axial Entalphy changes for both TVS-2M and AFA FAs is demonstrated in **Fig 8**.

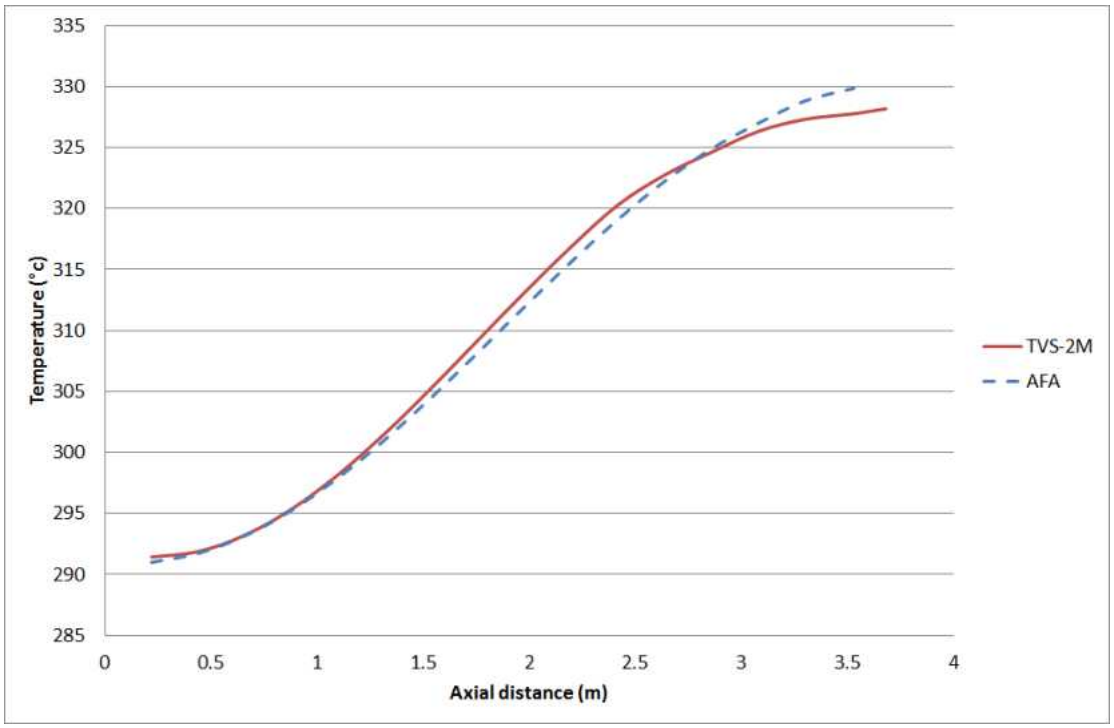

Fig. 6. Axial coolant temperature in the hottest FA.

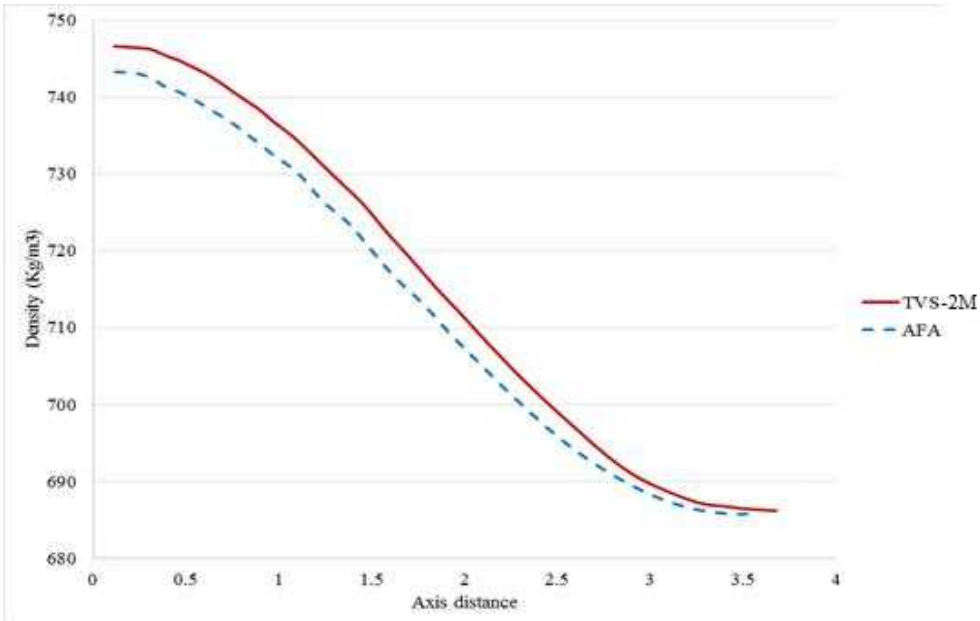

Fig. 7. Axial coolant density in the hottest FA.

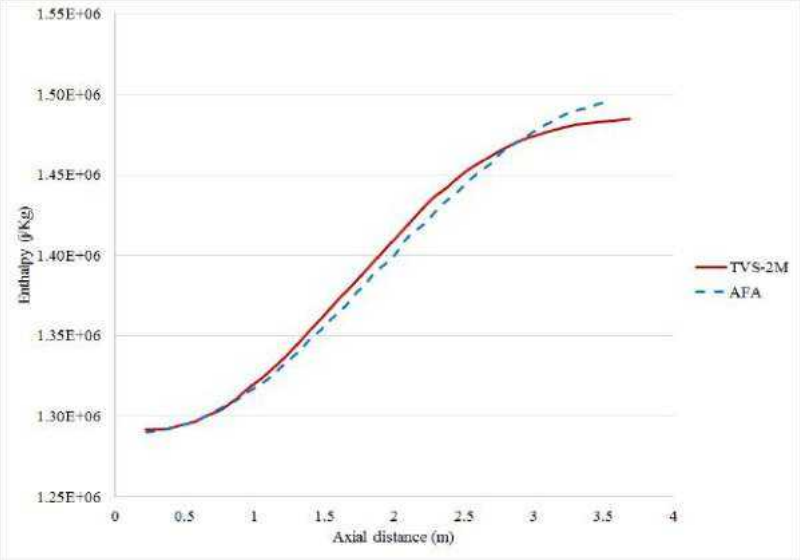

Fig. 8. Axial entalphy variations in the hottest FA.

Due to the use of Gd_2O_3 as burnable poisons in TVS-2M fuels, the power peaking factor in the middle of the core is reduced. Hence, the power distribution almost tends to be flatten. In such manner, more balanced axial temperature distribution is created in the reactor core. Consequently, the axial coolant temperature in the TVS-2M hottest FA is lower than in AFA.

According to the lack of ADF (Anti-debris filter) inlet filters and the creation of resistance to the inlet current in TVS-2M FAs, a 15 cm increase in fuel length and also a change in the number and size of the fuel spacer grids by increasing its height by 10 mm and reducing its number from 15 in AFA FAs to 13 cause the coolant pressure drop along the FA to be around 50 kPa. However, this amount is about 48 kPa in AFA FAs. **Fig 9** illustrated the axial distribution of coolant pressure variations.

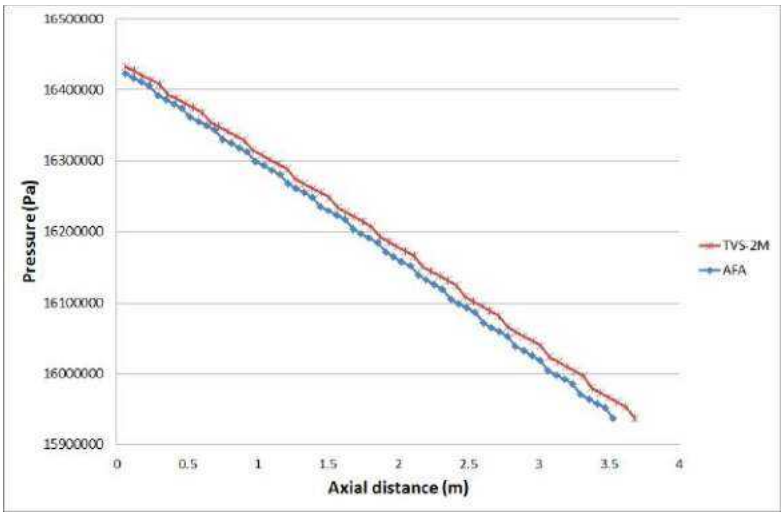

Fig. 9. Axial distribution of coolant pressure variation.

Considering that the thermal power of the hottest FA has decreased from 22.4 to 21.5 MW, the difference in coolant temperature in the hottest channel of the two types of fuels is about 2 ºC.

But this causes changes in other characteristics of the coolant such as density, so that due to the higher coolant temperature in the AFA FA, the coolant density in this type will be lower than TVS-2M. Also, considering the same flow rate in boundary conditions for both FA, the coolant velocity in TVS-2M fuel is slightly lower than AFA. **Fig 10** shows the radial temperature distribution in the center of the hottest fuel rod in the hottest FA.

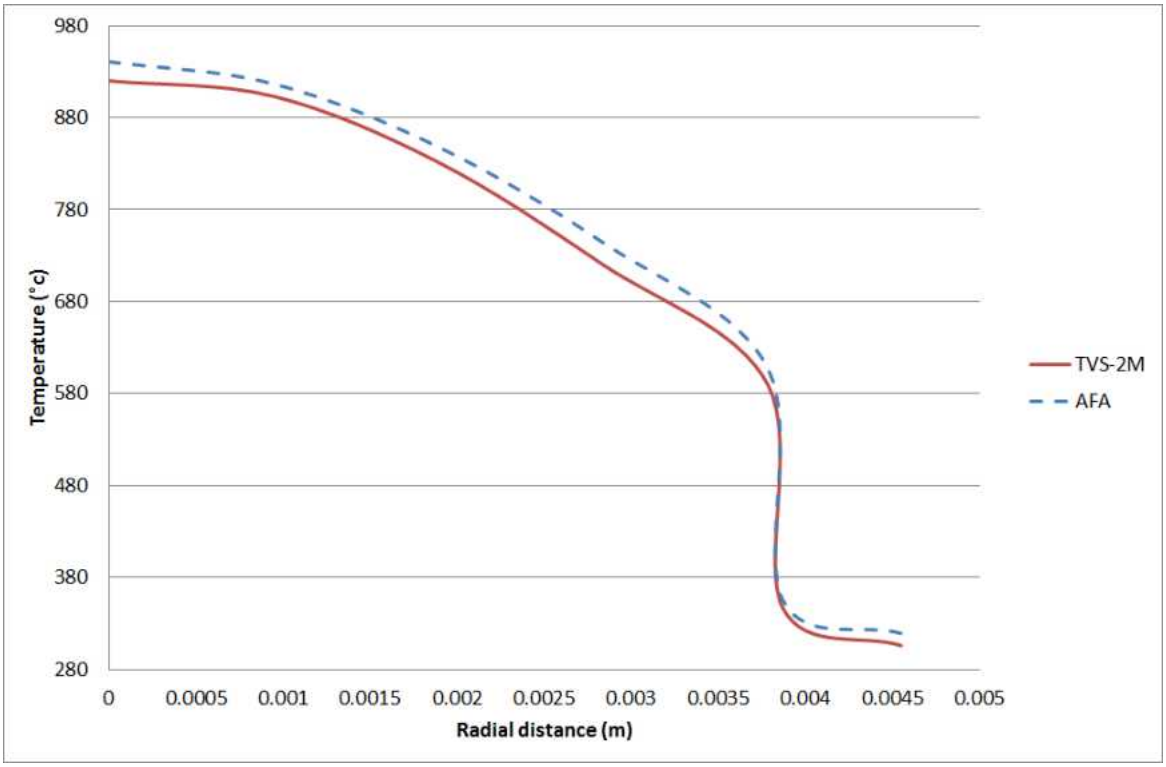

Fig. 10. Radial temperature distribution in the center of the hottest fuel rod in the hottest FA.

Conclusion

The main aim of present paper was to Thermoneutronic investigation of the VVER-1000 reactor core in both AFA and TVS-2M FAs configurations usnig WIMS, CITATION, and PMA method. The PMA method is a well-known approach for Thermal-hydraulic analyzing of the fuel reactor core FAs. The TVS fuels development is based on increasing the uranium content in the fuel rods, and also the use of effective grid spacers to ensure an increase in critical thermal neutron flux and more efficient implementation of the fuel economy cycle by increasing the power of the fuel rods in safety margins.

Results presented that, the K-Factor in both AFA and TVS-2M FAs configuration are calculated at 1.01767 and 1.02652, respectively. The maximum thermal flux is related to about 142 cm in AFA FAs arrangement and 148 cm in TVS-2M FAs from the height of the core. The inserting of the control rods into the core can move the maximum flux height of about 40% to the end. According to the calculations, using TVS-2M FAs increases the neutron flux and excess reactivity of the code to some extent compared with using AFA FAs. Finally, increased reactivity will ascend the cycle length and fuel operation time. Moreover, the maximum coolant temperature in the hottest of FAs TVS-2M and AFA arrangement reached to 328 and 331 C. Due to ADF filters, the increase of the fuel height, and the decrease of grid spacers numbers, the axial pressure loss is approximately 50 kPa. While, the axial pressure loss in the AFA FAs will be reached to 48 kPa.

References

[1]- Bushehr Nuclear Power Plant, Final Safety Analysis Report (FSAR) (2003), Technical Report, Chapter 4.

[2]- Preliminary Safety Analysis Report, (PSAR) of Nuclear Power Plant (1976), Iran 1 and 2, Vol. 1 and 2, KWU.

[3]- S.M. Dmitriev, S.S. Borodin, A.V. Varentsov, M.A. Legchanov, V.D. Sorokin, A.E. Khrobostov, (2015), **EXPERIMENTAL** study of local coolant hydrodynamics in TVS-Kvadrat PWR reactor fuel assembly using mixing spacer grids with different types of deflectors. Nuclear Energy and Technology 1 296–303.

[4]- Yu. G. Dragunov, S. B. Ryzhov, I. N. Vasil'chenko, and S. N. Kobelev, (2005), Development and adoption of TVS-2M for advanced fuel cycles. Atomic Energy, Vol. 99, No. 6.

[5]- Generation 2 fuel assembly TVS-2M. 21, Ordzhonikidze Street, 1421103 Podolosk, Moscow region, Russia Federation.

[6]- D. V. Hristov, (2005), "Preparation and verification of libraries for ORIGEN-S module in SCALE4.4a, with cross-sections for WWER-1000 TVSM fuel", 15th Symposium of AER, Znojmo, Czech Republic, 3-7 October.

[7]- D. V. Hristov, (2006), "Preparation of libraries for ORIGEN-S module in SCALE4.4a, with cross-sections for WWER-1000 TVSA fuel", 11th Meeting of AER Working Group E, Hrotovice, Czech Republic, 11-12 April.

[8]- Plamen V. Petkov∗, Danail V. Hristov, (2008), VVER-1000/V320 decay heat analysis involving TVS-M and TVSA FAs. Nuclear Engineering and Design 238 3227–3239.

[9]- F. Faghihi, F. Roosta, S. Ghaemi, S. Bagheri, (2019), Core designing of the newly proposed (U+Gd) O2 FAs in the VVERs core and comparison with current UO2 FAs, Alexandria Engineering Journal, 58, 647–658.

[10]- S. Ghaemi, F. Faghihi, (2018), Core designing of a new type of TVS-2M FAs: neutronic and thermal-hydraulics design basis limits, Front. Energy, 1-23.

[11]- Nuclear fuel for VVER reactors. TVEL JSC 49, Kashirskoye Shosse, Moscow, 115409, Russia.

[12]- Malmir, H., Maleki, N., Zahedinejad, E., (2010), Comparison between triangular and hexagonal modeling of a hexagonal-structured reactor core using box method, Ann. Nucl. Energy, 38; 2-3:371-378.

[13]- Bibilashvili Yu K, Kuleshov A V, Mikheev E N, et al. (2003), Investigation of thermal-physical and mechanical properties of uranium-gadolinium oxide fuel. In: Proceedings of IAEA Technical Committee Meeting on Improved Fuel Pellet Materials and Designs. Brussels, Belgium, 85–100.

[14]- Une K. Thermal expansions of UO2-Gd2O3 fuel pellets. Journal of Nuclear Science and Technology, 1986, 23(11): 1020–1022 3. Lysikov A V, Kouleshova V, Novikova E A, (2007), Results of thermalphysical and mechanical property investigations of modified uranium-gadolinium oxide doped fuel. In: Russian Scientific Conference Materials for Nuclear Technics. Zvenigorod, Russia, 2007, 22–44.

[15]- Nivikov V, Dolgov A, Molchanov V. (2003), In: TopFUEL Conference. Wurzburg, Germany.

[16]- NEA-1507, WIMSD-5B (98/11), (1999), Deterministic Multi-Group Reactor Lattice Calculations.

[17]- Fowler, T.B., (1999), CITATION-LDI2 Nuclear Reactor Core Analysis Code System. CCC-643, Oak Ridge National Laboratory, Oak Ridge, Tennessee.

[18]- G. Ricciardi, S. Bellizzi, B. Collard, B. Cochelin, (2008), Modelling pressurized water reactor cores in terms of porous media J. Fluid Struct., 25, pp. 112-133.

ICNST 2024 International Conference on Nuclear Science and Technology
6- 8 MAY 2024 | Isfahan, Iran

Modeling, comparison and analysis of fire protection system using three probabilistic safety analysis codes (Paper ID : 1013)

Zarnousheh Farahani A.[1,2*], Nematollahi M.[1,2], Pirouzmand A.[1]

[1] *Department of Nuclear Engineering, School of Mechanical Engineering, Shiraz University, Shiraz, Iran*

[2] *Safety Research Center, School of Mechanical Engineering, Shiraz University, Shiraz, Iran*

Abstract

Probabilistic safety assessment (PSA) is considered to be an important tool for assessing the safety of nuclear installations (and other industry) in relation to potential initiating events that can be caused by random component failure and human error, as well as internal and external hazards. In this method, two main tools, Fault Tree and Event Tree, are used. Different companies and research institutes have also provided several software for implementing PSA using Fault Tree and Event Tree tools, among the most important of which, RiskSpectrum, SAPHIRE, RISKMAN, etc. can be mentioned. With considering the required to use PSA as a key tool in order to improve the safety level and reliability of various industries, in this research, three different codes have been used for the Probabilistic safety analysis of the fire protection system, and finally, the cut sets of this system is achieved. These values of the cut-sets for fire protection systems and the probability of failure of the entire system have been compared with each other and also with the values calculated through the Boolean algorithm, which shows a good match for all three codes used.

Keywords: Risk Spectrum, SAPHIRE, IRES2.0, PSA Codes, Fire Protection

Introduction

Probabilistic Safety Analysis (PSA) is a structured method of quantitative risk assessment to navigate the design and operation of systems for achieving a certain safety or operational goal. The National Aeronautics and Space Administration [1], International Atomic Energy Agency [2], US Nuclear Regulatory Commission [3] have provided general guidelines for PSA for managers and practitioners. Recently, many research groups have performed PSA for different applications, including human health [2], airport airside safety [3], and safety in renewable power plants [4]. Mosleh [5] reported the strengths, limitations, and possible improvements of PSA.

The dynamic characteristics and behavior of a system, stochastic processes, operator response times, inspection and testing time intervals, aging of equipment or components, seasonal changes, sequential

dependencies of equipment or components, and timings of safety system operations affect system PSAs significantly [6].

Probabilistic Safety Analysis Codes

The use of computer codes in PSA developed with the experience gained on PSAs for Nuclear Power Plants (NPPs). In the 1970s and 80s about 70 PSAs have been conducted mainly to provide estimates of plant risk or on core damage frequency. Until recent years it has been generally accepted that the main benefits of performing PSAs include:

Identifying weak points in the design and/or prioritization of the corrective actions associated with them.

Evaluating the need for backfittings and/or prioritization of a backfitting program.

Evaluating the impact of design changes, test and maintenance procedural changes and the impact of new regulatory requirements.

These were the benefits pursued until the mid 80s. The computer codes used for these PSA studies were mainly fault tree codes for qualitative and quantitative analysis, importance analysis, uncertainty analysis codes and codes for drawing large fault trees. Later on, codes to treat reliability data (Bayesian analysis) were employed and in some instances codes for dependent failure analysis were included. This type of computer codes use we shall denote as "Computer Codes for Conducting PSA".

Computer codes are powerful tools to perform tasks of large complexity that manual treatment can perform only with very high economic and time penalties. Probabilistic Safety Assessment (PSA) entails several laborious tasks suitable for computer codes assistance. This section presents utilizing computer codes in the conduct of the PSA tasks and for the use of PSA results in safety management and provides information on available codes suggested or applied in performing PSA in nuclear power plants. However, no endorsement is suggested by the IAEA to any of the codes included [7].

Risk Spectrum

RiskSpectrum PSA is a creative software that you can use to edit, debug, test and deploy a fault tree and event tree model. In addition to what most standard fault tree and event tree editor provide, RiskSpectrum PSA includes tools for model completion, MCS tracing, scripting based updating, and many more features to enhance the PSA model development and maintenance process. RiskSpectrum PSA enables you to deliver every part of your PSA (Probabilistic Safety/Risk Assessment) and QRA

(Quantative Risk Assessment) model. Via its intuitive user interface, you can model everything from the basic fault tree with AND and OR gates, right through to advanced fault tree and event tree integration of sequences in linked event trees with boundary conditions and CCF events. The integrated RiskSpectrum Analysis Tool (RSAT) is specially designed for solving very large Fault Tree & Event Tree models. It offers MCS (Minimal Cut Set), BDD, sensitivity, importance, uncertainty and time-dependent analysis [7].

SAPHIRE

The Systems Analysis Programs for Hands-on Integrated Reliability Evaluations (SAPHIRE) is a software application developed for performing a complete Probabilistic Safety Analysis (PSA) using a personal computer. SAPHIRE is funded by the U.S. Nuclear Regulatory Commission (NRC) and developed by the Idaho National Laboratory (INL). The INL's primary role in this project is that of software developer. However, the INL also plays an important role in technology transfer by interfacing and supporting SAPHIRE users comprised of a wide range of PSA PSActitioners from the NRC, national laboratories, the private sector, and foreign countries. SAPHIRE can be used to model a complex system's response to initiating events, quantify associated damage outcome frequencies, and identify important contributors to this damage (Level 1 PSA) and to analyze containment performance during a severe accident and quantify radioactive releases (Level 2 PSA). It can be used for a PSA evaluating a variety of operating conditions, for example, for a nuclear reactor at full power, low power, or at shutdown conditions. Furthermore, SAPHIRE can be used to analyze both internal and external initiating events and has special features for transforming models built for internal event analysis to models for external event analysis. It can also be used in a limited manner to quantify risk in terms of release consequences to both the public and the environment (Level 3 PSA) [8].

IRES2.1

IRES2.1, which was developed as the first Iranian software in the field of probabilistic safety calculations, is an integrated software for PSA calculations, which in its evolution after the publications of RELAB-FTA, RELAB-ETA, RELAB1.3, IRES1.0 , IRES2.0 and fixing their defects, in order to achieve a commercial base version is presented[9].

This software has been developed as the first version with various capabilities to evaluate nuclear power plants and any other industrial system. In this version of the software, by changing the previous

programming, modifying the NAND, NOR, XOR, N/M gates, the ability to modify the transfer gate, modifying the way of modeling and displaying the common Cause failure (CCF), the commercial base version has been obtained[9].

IRES2.1 capable of Fault Tree Analysis, Event Tree Analysis, Common Cause Failure analysis, Human Reliability Analysis based on advanced Binary Decision Diagram), Importance & Sensitivity Analysis, Uncertainty Analysis and Logical Key Analysis (House Events) [9].

The calculation modules of this code are briefly:

ETA module for event tree analysis,

FTA module in order to analyze the fault tree,

BDD module, which is a technique to achieve minimum cutting sets in less time,

HRA module to analyze and evaluate human error.

UA module in order to calculate uncertainty in parametric levels, Significance and sensitivity analysis (SA).

Fire Protection System Description

The fire protection system shown in Figure 1 is considered for Modeling, comparison and analysis. This system is designed to extinguish all possible fires in a plant. Two physically independent water extinguishing nozzles are designed such that each is capable of controlling all types of fires in the plant. Extinguishing (fire suppression) nozzle 1 is the primary method of injection. Upon receiving a signal from the detector/alarm/actuator device, pump-1 starts automatically, drawing water from the reservoir tank and injecting it into the fire area in the plant. If this pump injection path is not actuated, plant operators can start a second injection path manually. If the second path is not available, the operators will call for help from the local fire department (fire brigade), although the detector also sends a signal directly to the fire department. However, due to the delay in the arrival of the fire brigade, the magnitude of damage would be higher than it would be if the local fire suppression nozzles were available to extinguish the fire [10].

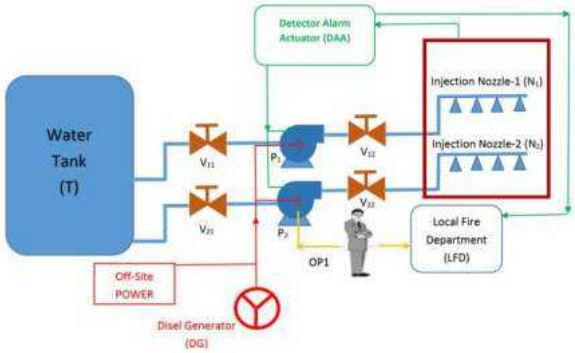

Fig. 1. A fire protection system

Fire Protection System Performance

This system is designed to extinguish all possible fires in a plant . Two physically independent water extinguishing nozzles are designed such that each is capable of controlling all types of fires in the plant. Extinguishing (fire suppression) nozzle is the primary method of injection. Upon receiving a signal from the detector/alarm/actuator device, pump-1 starts automatically, drawing water from the reservoir tank and injecting it into the fire area in the plant. If this pump injection path is not activated, plant operators can start a second injection path manually. If the second path is not available, the operators will call for help from the local fire department (fire brigade), although the detector also sends a signal directly to the fire department. However, due to the delay in the arrival of the fire brigade, the magnitude of damage would be higher than it would be if the local fire suppression nozzles were available to extinguish the fire.

Identification of Initiating Events

In step, all equipment (e.g., cables, electric and control cabinets, pumps, ventilation system) and events (e.g., transient materials and fuel subject to ignition, hot works, and human error) that could cause fire in the reactor compartment (room),must be identified.These should include equipment malfunctions, human errors, and facility conditions.The frequency of each event should be estimated.There are a number of sources of data that can be used to estimate the frequency of fire, e.g., NUREG/CR6850 (EPRI 1011989)[11]. Assuming that all events would lead to the samemagnitude of fire, the ultimate initiating eventwould be occurrence of a fire, the frequency of which is the sum of the frequencies of the individual fire-causing events. Assume in this example the frequency of fire is estimated at 1×10^{-6}

per year. Since fire is the only challenge to the plant in this example, we end up with only one initiating event. However, in more complex situations, a large set of initiating events can be identified, each posing a different challenge to the plant.

Scenario Development

In this step, we should explain the cause and effect relationship between the fire and the progression of events following the occurrence of fire. We use the event-tree method to depict this relationship. Generally, this is done inductively, and the level of detail considered in the event tree is somewhat dependent on the analyst. Two protective measures as hazard barriers have been considered in the event tree shown in Figure 2: on-site protective measures (onsite pumps, tanks, etc.), and off-site fire department measures. The selection of these protective barriers is based on the fact that availability or unavailability of the on-site or off-site measures would lead to different damage states.

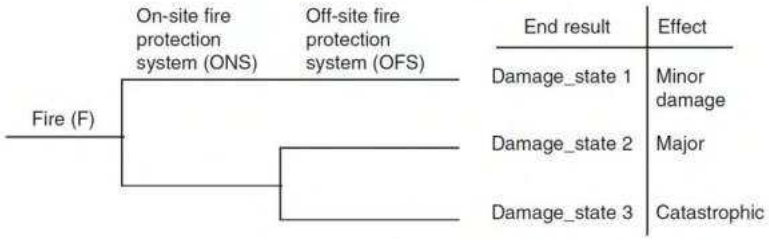

Fig. 2. Scenarios of events following a fire using the event-tree methods

Logic Modeling

This step, we should identify all failures (equipment or human) that lead to failure of the event-tree headings (on-site or off-site protective measures). For On-Site Fire Protection System(ONS) fault tree, all basic events that lead to the failure of the two independent paths are described. Note that the detector alarm actuator (DAA), the electric power to the pumps, and the water tank are shared by the two paths. Clearly these are considered as physical dependencies. This is taken into account in the quantification step of the PSA. In this tree, all external event failures and passive failures are neglected. This tree is simple because it only includes all failures not leading to an on-time response from the local fire department. Similarly, an off-site fault tree model can be developed for Off-Site Fire Protection System (OFS). Common cause failure That May Arise in Fire Protection System including the following. Most system problems, can be solved with the help of a fire protection service.In these cases, an evaluation

of the uncertainties associated with a given design problem are necessary to arrive at an adequate safety level and to inform what levels of investment in a safety scheme are justified. This can often only be achieved through probabilistic risk assessment (PRA).

CO2 Suppression Systems Do Not Extinguish the Fire

The Water Supply to the Sprinkler System Fails

Sprinkler Systems Do Not Supply Enough Water to All Fire Systems

Common cause failure between Pumps and valves

Model Description

In this research, the problem has been modeled and analyzed using the three codes introduced in the previous section. For this purpose, it is necessary to go through the following steps first. It is important at this point to calculate the probabilities of the basic failure events described in the event trees and fault trees. As indicated earlier, this can be done by using system-specific data, generic data, or expert judgment. Table 1 describes the data used and their sources. It is assumed that at least 10 hours of operation is needed for the fire to be completely under control [10].

Table 1. Sources of data and failure probabilities [10]

Failure event	Probability used
Fire initiation frequency	7.1×10^{-4}/year
Pump 1 and Pump 2 failure	1.8×10^{-2}/demand
Common cause failure between Pump 1 and Pump 2	1.8×10^{-3}/demand
Failure of isolation valves	4.2×10^{-3}/demand
Failure of nozzles	1.0×10^{-5}/demand
Diesel generator failure	5.5×10^{-2}
Loss of off-site power	1.1×10^{-4}/demand
Failure of detector alarm actuator (DAA)	7.1×10^{-4}/demand
Failure of operator to start Pump 2	7.1×10^{-2}/demand
Failure of operator to call the fire department	7.1×10^{-3}/demand
No or delayed response from fire department	7.1×10^{-4}/demand
Tank failure No such experience	7.1×10^{-5}/demand

The fire extinguishing system is modeled in the environment of all three codes. The event tree and the Fault tree in the risk spectrum code are shown in Figures 3 and 4, respectively. From the point of view of the simulation environment and space structure, the IRES code is very similar to the RISK code, but

due to the up-to-dateness of this code, it has a much more suitable graphic environment than the RISK code, and the way of working and defining the event and event trees is even easier than the RISK code. The event tree model and part of the event tree in this code are shown in Figure 5.

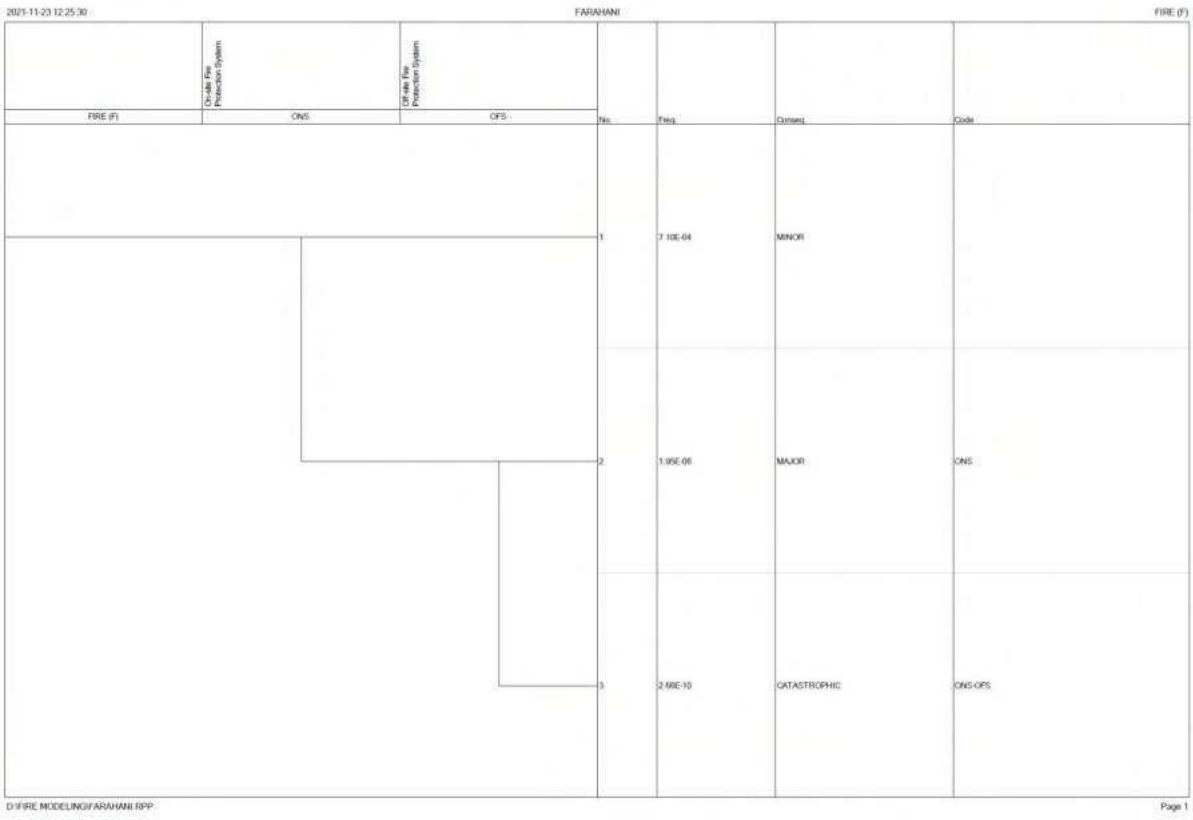

Fig. 3. Initiate Event and Top Events in Risk Spectrum Code

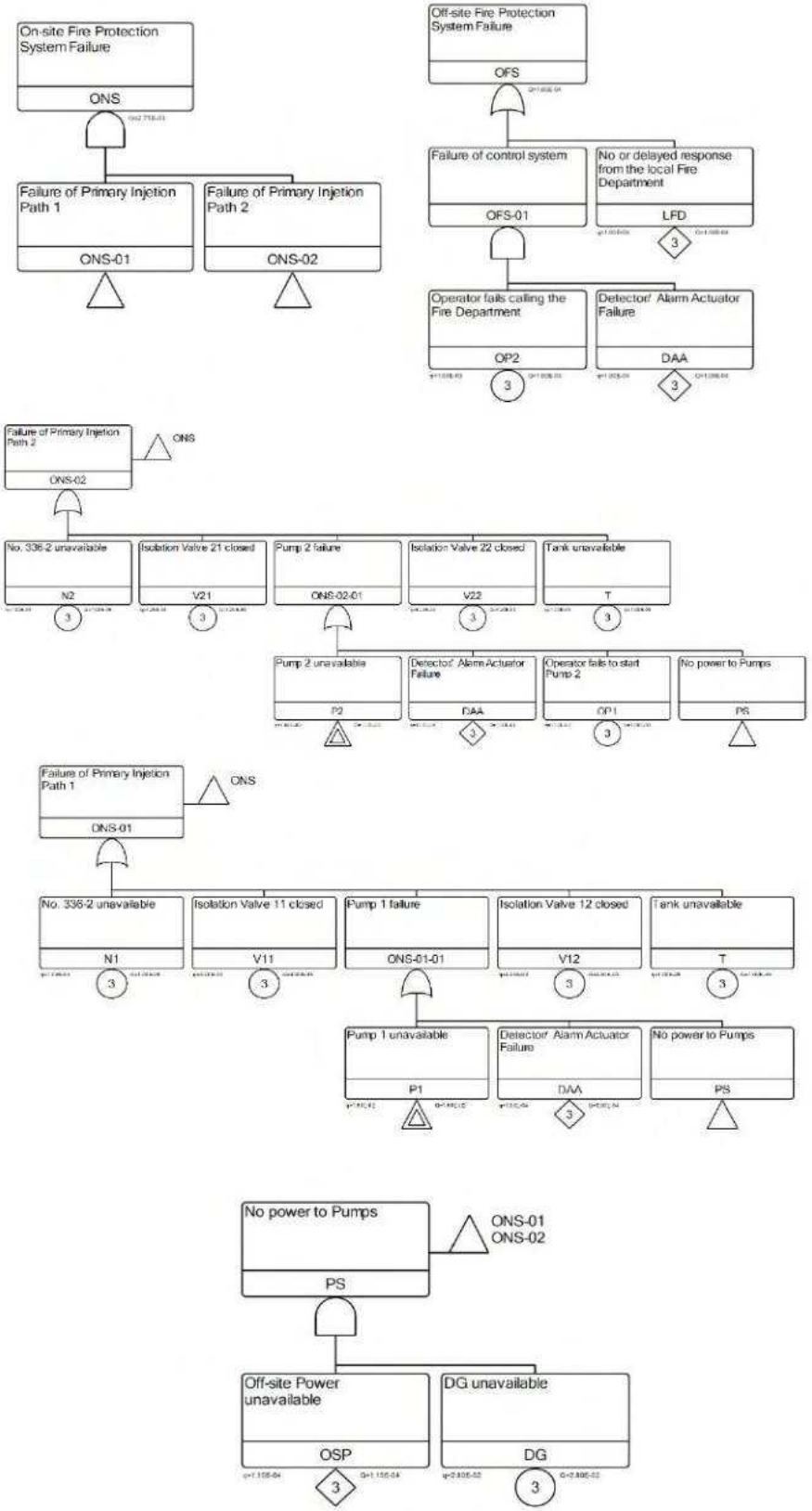

Fig. 4. Fault Tree in Risk Spectrum Code

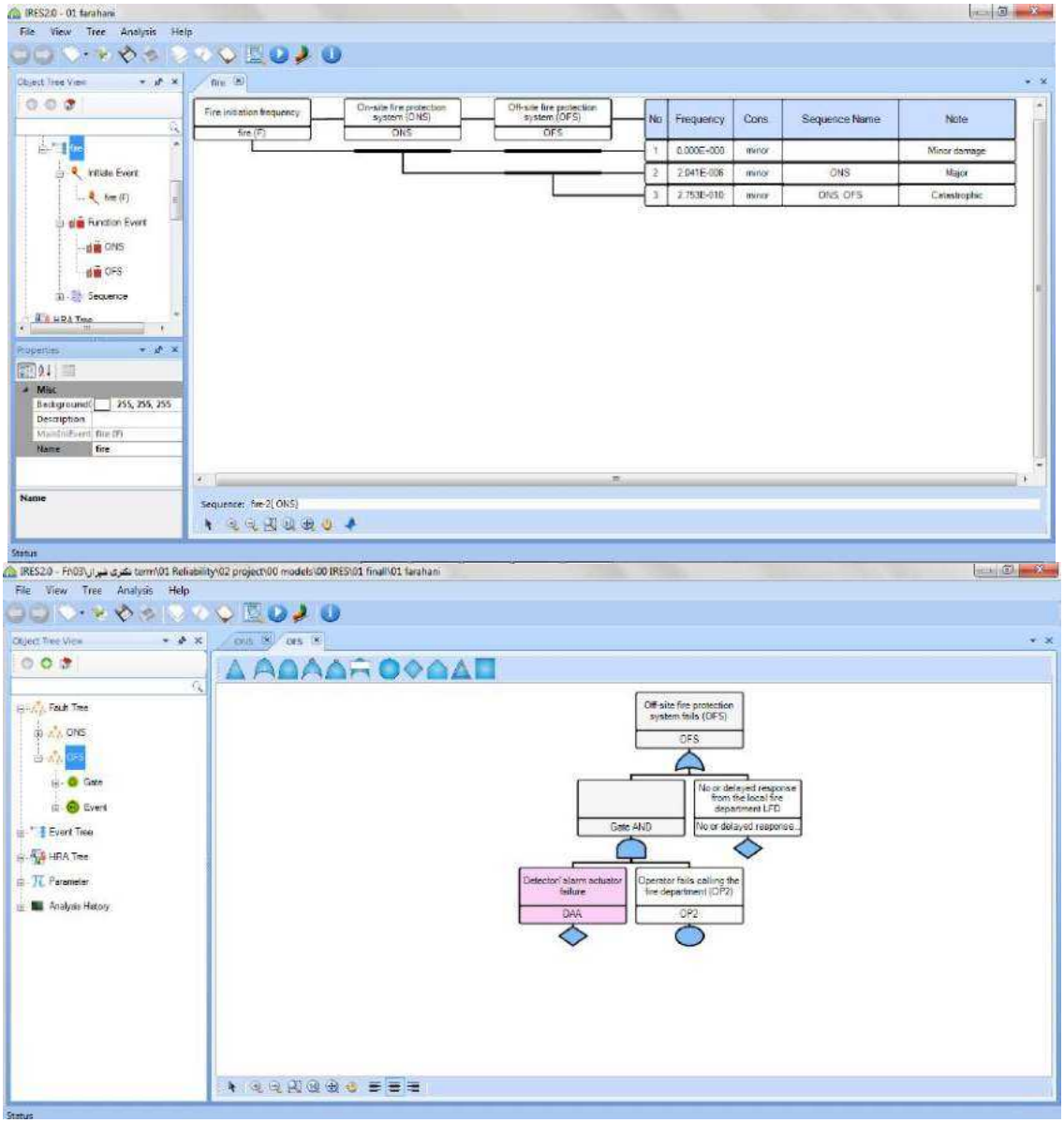

Fig. 5. Event Tree & OFS Fault Tree in IRES2.0 code

The method of modeling with SAPHIRE code is a little more difficult than the previous two codes, however, the general process of modeling is similar to the method of the previous codes described in the previous section. The event tree model and the fault tree in this code are shown in Figure 6 and Figure 7, respectively. After completing the fault tree by selecting the Solve option, for each of the cutting sets created through the code, their probability is calculated. In the next step, by going to the event tree section and selecting the Link Tree option, the event tree is connected to the event tree, and then after selecting the Edit End State option and selecting the Frequency option, the frequency value corresponding to each scenario (branch) is calculated by the code.

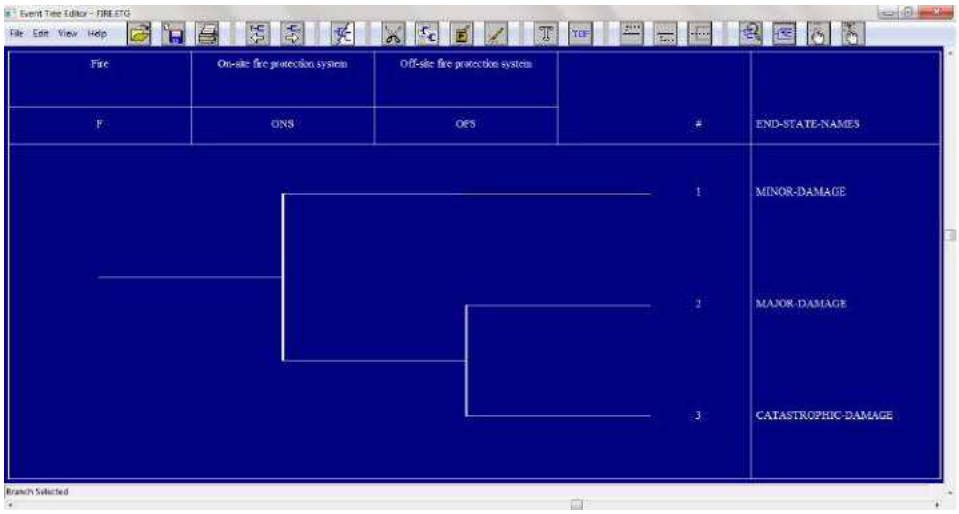

Fig.6. Event tree modeled in SAPHIRE code

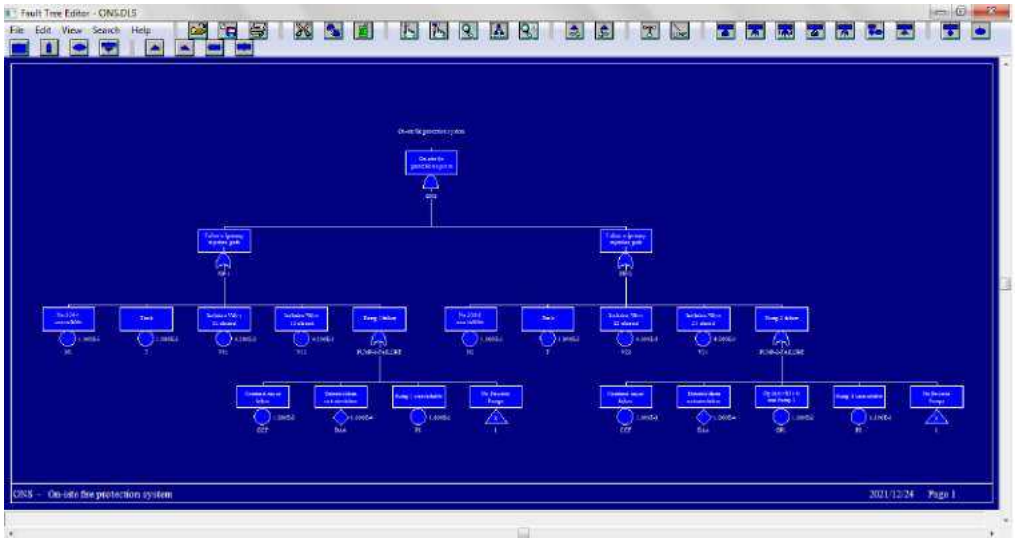

Fig.7. Fault tree of ONS system in SAPHIRE code

Results

To calculate the frequency of each scenario defined in Figure 3, we must first determine the cut-sets of the two fault trees shown in Figure 4. From this, the cut-sets of each scenario are determined, followed by calculation of the probabilities of each scenario based on the occurrence of one of its cut-sets. These steps are described below.

The cut-sets of the On-Site Fire Protection SystemFailure can be obtained by representing the fault tree of Figure 4 in terms of a Boolean equation for the top event, i.e., ONS, and then, reducing it by Boolean algebra [12]. These cut sets are listed in Table 2 for three modeling with different codes as well as the

value presented in reference [10]. Although several different types of common cause failure (e.g., among multiple valves or between the two pumps) can be considered, it is assumed that the potential for common cause failure exists only between the two pumps for simplicity.

The cut-sets of the Off-Site Fire Protection System Failure are similarly obtained and listed in Table 3. The cut-sets of the three scenarios are obtained using the following Boolean equations representing each scenario:

Scenario-1 = F · $\underline{\text{ONS}}$

Scenario-2 = F · ONS · $\underline{\text{OFS}}$

Scenario-3 = F · ONS · OFS

The **frequency** of each scenario is obtained using data listed in Table 1. These frequencies are shown in Table4.

The total frequency of each scenario is calculated using the rare event approximation. These are also shown in Table 4.

Table 2. Cut-sets of the on-site fire protection system failure

Cut Seth No.	Cut Set	Probability [10]	IRES 2.0	RISK SPECTRUM	SAPHIRE 7
1	LFD	1.0E-04	1.0E-04	1.0E-04	1.001E-04
2	OP_2.DAA	1.0E-07	1.0E-07	1.0E-07	1.0E-07
TOTAL		1.0E-04	1.0E-04	1.0E-04	1.0E-04

Table 3. Cut-sets of the off-site fire protection system

Cut Seth No.	Cut Set	Probability [10]	IRES 2.0	SAPHIRE7	RISK SPECTRUM (F* Cut Set) F=7.1E-04
1	T	1.0E-05	1.0E-05	1.0E-05	7.10E-09
2	DAA	1.0E-04	1.0E-04	1.0E-04	7.10E-08
3	OSP.DG	6.0E-06	6.05E-06	6.05E-06	2.19E-09
4	$N_2.N_1$	1.0E-10	1.0E-10	1.0E-10	7.10E-14
5	$N_2.V_{12}$	4.2E-08	4.2E-08	4.2E-08	2.98E-11
6	$N_2.P_1$	1.7E-07	1.8E-07	1.8E-07	1.15E-10
7	$N_2.V_{11}$	4.2E-08	4.2E-08	4.2E-08	2.98E-11
8	$N_1.V_{22}$	4.2E-08	4.2E-08	4.2E-08	2.98E-11
9	$V_{22}.V_{12}$	1.8E-05	1.764E-05	1.764E-05	1.25E-08
10	$V_{22}.P_1$	7.1E-05	7.56E-05	7.56E-05	4.83E-08
11	$V_{22}.V_{11}$	1.8E-05	1.764E-05	1.764E-05	1.25E-08
12	$N_1.V_{21}$	4.2E-08	4.2E-08	4.2E-08	2.98E-11
13	$V_{21}.V_{12}$	1.8E-05	1.764E-05	1.764E-05	1.25E-08
14	$V_{21}.P_1$	7.1E-05	7.56E-05	7.56E-05	4.83E-08
15	$V_{21}.V_{11}$	1.8E-05	1.764E-05	1.764E-05	1.25E-08
16	$OP_1.N_1$	1.7E-07	1.7E-07	1.7E-07	7.10E-11
17	$OP_1.V_{21}$	4.2E-05	4.2E-05	4.2E-05	2.98E-08
18	$OP_1.P_1$	1.7E-04	1.8E-04	1.8E-04	1.15E-07
19	$OP_1.V_{11}$	4.2E-05	4.2E-05	4.2E-05	2.98E-08
20	$P_2.N_1$	1.7E-07	1.8E-07	1.8E-07	1.15E-10
21	$P_2.V_{12}$	7.1E-05	7.56E-05	7.56E-05	4.83E-08
22	$P_2.P_1$	2.9E-04	3.24E-04	3.24E-04	1.86E-07
23	$P_2.V_{11}$	7.1E-05	7.56E-05	7.56E-05	4.83E-08
24	CCF	1.8E-03	1.8E-03	1.8E-03	1.28E-06
Top Event frequency F					1.951E-06

Table 4. Dominant minimal cut-sets of the scenarios

Scenario No.	Probability [10]	IRES 2.0	RISK SPECTRUM	SAPHIRE 7
1	7.1E-04	7.100E-04	7.100E-04	7.100E-04
2	2.5E-06	1.963E-06	1.951E-06	2.041E-06
3	8.6E-11	1.966E-10	2.662E-10	2.753E-10

Conclusions

The comparison of the results of three modeling with different codes shows a good match for the first and second scenarios. Differences caused by rounding and cutting off numbers and small differences in calculations are among the things to be mentioned.

References

[1]Stamatelatos M, Dezfuli H. Probabilistic Risk Assessment Procedures Guide for NASA Managers and Practitioners. Washington, DC: NASA; 2011.

[2]Barrio-Parra F, Izquierdo-Díaz M, Dominguez-Castillo A, Medina R, De Miguel E. Human-health Probabilistic Risk Assessment: The Role of Exposure Factors in An Urban Garden Scenario. Landscape and Urban Planning 2019;185:191–9.

[3]Ketabdari M, Giustozzi F, Crispino M. Sensitivity Analysis of Influencing Factors in Probabilistic Risk Assessment for Airports. Safety Science 2018;107:173–87.

[4]Habib A, Sou C, Hafeez HMuhammad, Arshad A. Evaluation of The Effect of High Penetration of Renewable Energy Sources (RES) on System Frequency Regulation using Stochastic Risk Assessment Technique (an approach based on improved cumulant). Renewable Energy 2018;127:204–12.

[5]Mosleh A. PRA: A Perspective on Strengths, Current Limitations, and Possible Improvements. Nuclear Engineering and Technology 2014;46(nr. 1):1–10.

[6]Tarannom Parhizkar, Jan Erik Vinnem, Ingrid Bouwer Utne, Ali Mosleh, Supervised Dynamic Probabilistic Risk Assessment of Complex Systems, Part 1: General Overview, Reliability Engineering & System Safety, Volume 208, 2021.

[7] RiskSpectrum Analysis Tools, Theory Manual, 2008.

[8] Smith, C., Knudsen, J., Vedros, K., Calley, M., Kvarfordt, K., & Wood, T. (2016). SAPHIRE 8 Basics An introduction to Probabilistic Risk Assessment via the Systems Analysis Program for Hands-On Integrated Reliability Evaluations (SAPHIRE) Software P-201 (No. INL/EXT-17-40988-Rev000). Idaho National Lab.(INL), Idaho Falls, ID (United States).

[9]Ingrated Reliability and Safety Assessment (IRES) Technical Manual, Release Version 2.1, 2022.

[10]Cacuci, D. G. (Ed.). (2010). Handbook of Nuclear Engineering: Vol. 3: Reactor Analysis: Chapter 15. Springer Science & Business Media.

[11]EPRI/NRC-RES Fire PRA Methodology for Nuclear Power Facilities: Detailed Methodology, Final Report, (NUREG/CR-6850, EPRI 1011989, Volume 2)

[12]Modarres, M., Kaminskiy, M.P., & Krivtsov, V. (2016). Reliability Engineering and Risk Analysis: A Practical Guide, Third Edition (3rd ed.). CRC Press.

ICNST 2024 International Conference on Nuclear Science and Technology
6- 8 MAY 2024 | Isfahan, Iran

Analyzing the Impact of Internal Channel Radius of Dual-Cooled Annular Fuel on Reactor Safety Parameters in a Small Modular Nuclear Reactor (SMR): An Investigation Utilizing Artificial Neural Networks (ANN) and Gene Expression Programming (GEP) (Paper ID : 1019)

H. Zayermohammadi Rishehri [1], G.R. Ansarifar [1*]
[1]Department of Nuclear Engineering, Faculty of Physics, University of Isfahan, Isfahan, Iran

Abstract

Investigating the influence of geometric structural characteristics of innovative dual-cooled fuel on reactor core parameters is crucial for accurate analysis of neutronics, thermohydraulic performance, and safety margins. This study examines temperature reactivity coefficients and convective heat transfer coefficient in the reactor, focusing on the increased size of dual-cooled fuel rods. Neutronics calculations using WIMS-CITATION codes are performed. Also, the Computational Fluid Dynamics (CFD) and sub-channel model method are utilized to assess the convective heat transfer coefficient for the proposed fuel rods. Findings indicate that all proposed fuel rods exhibit negative coolant and fuel temperature reactivity coefficients, with a decrease in convective heat transfer coefficient as the internal radius increases. Additionally, this study explores the potential of Artificial Neural Network (ANN) and Gene Expression Programming (GEP) models for developing an optimal, low- computational-cost methodology. The study concludes that ANN yields superior results based on statistical indicators.

Keywords: Dual-cooled fuel; Temperature reactivity coefficients; convective heat transfer coefficient; artificial neural network; Gene expression programming.

Introduction

Small Modular Reactors (SMRs) offer safe and cost-effective nuclear power. They have passive cooling and modular construction. SMRs provide flexibility for decentralized generation and can use different fuels for efficiency and waste reduction [1,2].

However, at present, most SMRs use solid cylindrical fuel. Solid fuel limits power and safety margins. Dual-cooled fuel rods have better heat transfer. Because of the reduced heat conduction resistance, the peak fuel temperature in a pellet can be decreased. The lower peak fuel temperature prevents fuel melting, and improves the thermal efficiency. Also, the Departure from Nucleate Boiling Ratio

(DNBR) margin is increased, which is very important in terms of safety, allows for a significant power uprate. Therefore, the use of Dual-cooled fuel rods increases the safety of the reactor in normal operation, accident conditions and provides the possibility of increasing the reactor power with the same amount of fuel mass [3-5].

Zaidabadi et al. (2017) and Ansarifar et al. (2016) researched using a specific fuel in a VVER-1000 reactor, finding that it reduces fuel center temperature and boosts thermal power [6,7]. They also explored using nanofluid with the Dual-cooled fuel, which increased the heat transfer coefficient and MDNBR [8]. Mehri et al. (2020) showed via the RELAP5 model that a VVER-1000 reactor with DCF is safer than one with solid fuel during a blackout [9].

This paper investigates safety parameters of an advanced SMR with dual-cooled fuels. The study analyzes the impact of fuel size using Artificial Neural Network (ANN) and Gene Expression Programming (GEP) algorithms for prediction and accuracy assessment.

Neutronics-Thermohydraulic Analysis

Neutronics-Thermohydraulic (N-Th) simulations were done on NuScale, which has a small core with 37 fuel assemblies. Each assembly has 264 fuel rods, 24 control rod guide tubes, and a central instrumentation guide tube in a 17x17 array. It uses low enriched UO2 as fuel material [10]. Fig. 1 is shown the core configuration.

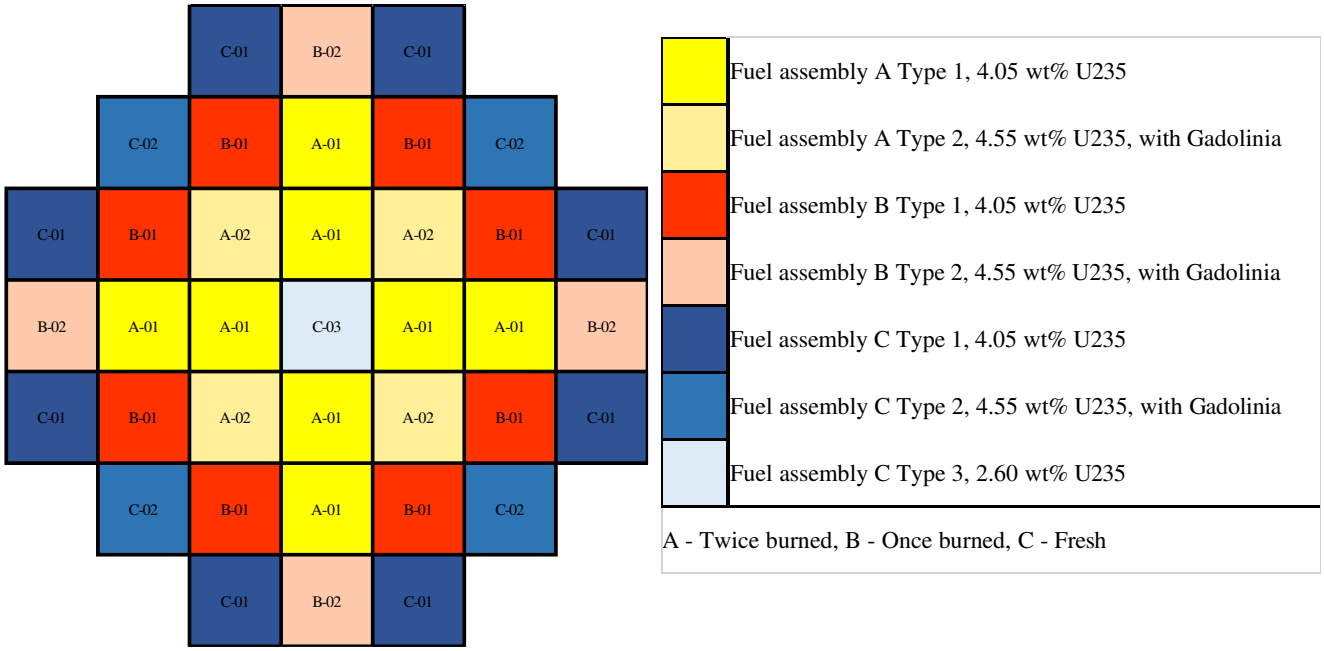

Fig. 1. Scheme of loading pattern

Analysis and simulations are divided into two phases for rods with different internal radii. Phase 1: Neutronics simulation is performed using the coupling of two codes (WIMS-CITATION) to calculate fuel and coolant reactivity feedback coefficients. Phase 2: Thermohydraulic simulation is done using Computational Fluid Dynamics (CFD) to calculate convective heat transfer coefficient. N-Th calculations are coupled to transfer power density from neutronics to CFD.

The specifications of each of the designed fuels are given in Table 1.

Table 1. Designed dual-cooled fuel rods geometrical data.

Type	Inner Radius of Inner clad	Outer Radius of Outer clad	Rod pitch	Unit
1	0.1500	0.5300	1.3600	cm
2	0.1750	0.5426	1.3853	cm
3	0.2000	0.5560	1.4120	cm
4	0.2250	0.5702	1.4405	cm
5	0.2500	0.5853	1.4701	cm
6	0.2750	0.6011	1.5022	cm
7	0.3000	0.6176	1.5352	cm
8	0.3250	0.6347	1.5694	cm
9	0.3500	0.6524	1.6048	cm
10	0.3750	0.6706	1.6412	cm
11	0.4000	0.6893	1.6786	cm
12	0.4250	0.7084	1.7168	cm
13	0.4500	0.7279	1.7558	cm
14	0.4750	0.7478	1.7956	cm
15	0.5000	0.7679	1.8359	cm

The thickness of the inner and outer claddings of the designed fuels is considered equal to 0.06 cm. Also, the distance between the cladding and the fuel pellet is considered equal to 0.008 cm as in the base reactor.

The fuel reactivity temperature coefficient (Doppler coefficient) can be calculated by varying the fuel temperature while keeping other regions constant. This allows plotting the reactivity variation based on fuel and coolant temperature. The reactivity temperature coefficient is determined by analyzing the slope of reactivity changes with temperature. Similarly, the coolant temperature coefficient is calculated by varying the temperature and density of the coolant while maintaining other parts constant (at 300 K).

In this paper, the main goal of the thermohydraulic analysis is to calculate convective heat transfer coefficient, and for this purpose, the modeling of a single channel has been used as a model of the behavior of the entire reactor core. First, the equivalent cell has been designed for different internal radii and then the equivalent channels have been analyzed by CFD simulation via Fluent software. The meaning of equivalent cell or equivalent channel of a fuel assembly is a cell that includes a fuel rod and a part of the total passing fluid of the core which represents the portion of the fluid passing through this fuel rod (according to Fig. 2.).

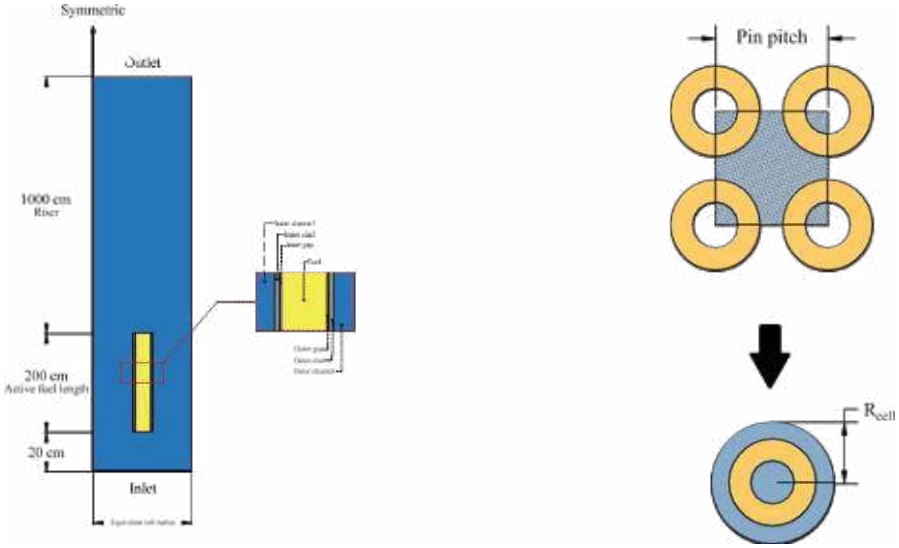

Fig. 2. The 2D equivalent cells modeling of a single channel

This paper utilizes the K-epsilon turbulence model. It is a two-equation model, that means, it includes two extra transport equations to represent the turbulent properties of the flow.

To calculate the convection heat transfer coefficient, following formula is used.

$$\bar{h} = \frac{q}{A(\Delta T)} \quad (1)$$

The q is given by:

$$q = \int_{H_e} q'' \cos\left(\frac{\pi z}{H_e}\right) A \, dz \quad (2)$$

Using CFD simulation, axial temperature distribution can be achieved and distribution of the axial convection heat transfer coefficient can be obtained using Eq. (1).

Considering the geometry of dual-cooled fuel, there is two convection heat transfer coefficients. By averaging, the axial convection heat transfer coefficient can be obtained as follows:

$$\bar{h} = \frac{h_{in}A_{in}\Delta T_{in} + h_{out}A_{out}\Delta T_{out}}{A_{in}\Delta T_{in} + A_{out}\Delta T_{out}} \quad (3)$$

Neutronics-Thermohydraulic Results

Fig. 3 shows the reactivity temperature coefficient data of fuel and coolant for different fuel rods with varying internal clad inner radius (0.15 to 0.5 cm).

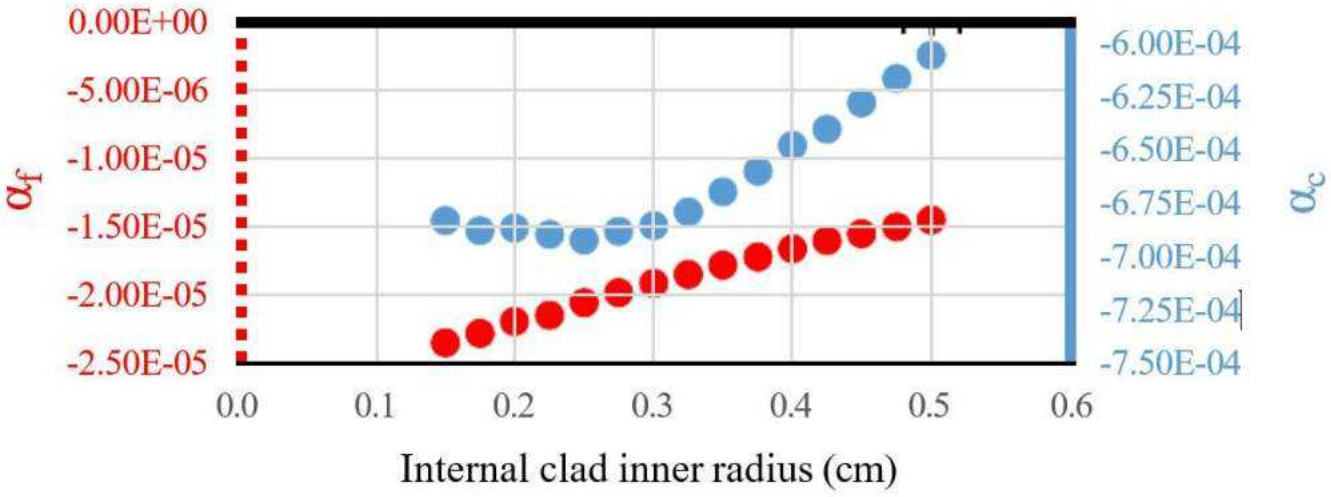

Fig. 3. Fuel and coolant reactivity temperature coefficients in term of internal radius.

The fuel reactivity temperature coefficient (Doppler coefficient) depends on fuel temperature, moderating power, and fuel geometry. Fig. 2 illustrates this behavior, showing that increasing the internal radius reduces the coefficient due to increased moderating power and resonance escape probability factor. A larger internal radius increases heterogeneity effects and the resonance escape

probability factor. The coolant temperature reactivity coefficient is crucial for reactor design and operation. A negative coefficient is desirable for safety, indicating reduced chain reaction likelihood as coolant temperature increases. Larger fuel rods have a smaller coolant temperature coefficient, indicating less responsiveness to coolant temperature changes.

Fig. 4a illustrates the convective heat transfer coefficient values in the axial direction for various designed fuel rods and the original fuel of the NuScale reactor. Additionally, Fig. 4b displays the average values of this parameter based on different radii.

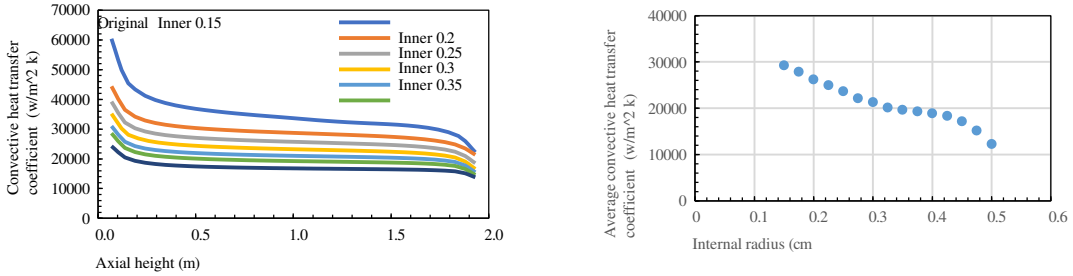

(a) (b)

Fig. 4. (a) The convective heat transfer coefficient for different fuel design, and (b) The average convective heat transfer coefficient in term of internal radius.

Simulation results indicate that the introduced annular fuels have a lower convective heat transfer coefficient compared to the original solid fuel. Additionally, the coefficient shows a decreasing trend with an increase in the internal radius of the fuel rods.

Prediction

In this study, we examined dual-cooled fuels by analyzing their neutronics and thermohydraulic properties. We calculated essential parameters like reactivity temperature coefficients and convective heat transfer coefficients for the rods. However, using the mentioned codes for these calculations can be computationally expensive. Hence, it would be beneficial to have predictive methods for estimating and evaluating these analyses. In this section, we used ANN and GEP methods to investigate the impact of the internal channel radius on important dynamic parameters of the reactor in relation to dual-cooled fuel. The calculations and analyses provided sufficient data to train both methods.

The Levenberg-Marquardt back-propagation algorithm was used for training in this network model, chosen for its fast convergence. 70% of the data in each column of the matrix were randomly selected for training. The remaining 30% was divided equally between the validation and testing sets, with each set receiving 15% of the data. The ANN structure was implemented in MATLAB. The MATLAB neural network structure displayed in Fig. 5 comprises 6 hidden layers.

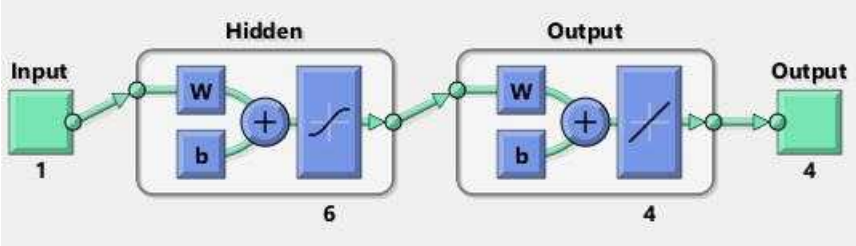

Fig. 5. Designated ANN.

Gene Expression Programming (GEP) is an advanced approach combining GA and Genetic Programming (GP). Unlike GP, GEP utilizes a tree structure to find the optimal solution [11]. GEP has several advantages, such as being less sensitive to input variables, accommodating multiple genes, and evaluating complex models with sub-models. In this study, we applied various settings before implementing the GEP model, including defining problem variables, selecting mathematical operators,

determining error criteria, setting controller parameters, establishing program end conditions, and presenting execution results. The settings used in GEP modeling are also given in Table 2.

Table 2. The used parameters in the GEP model.

Parameter	Value
Generations Numbers	15000
Mutation rate	0.014
Inversion	0.055
Insertion sequence transposition	0.055
Gene recombination rate	0.003

ANN and GEP performance and comparison

The R-squared (R2), Mean Absolute Error (MAE), and Root Mean Square Error (RMSE) are statistical indicators that used to assess ANN and GEP models for parameter estimation. Table 3 indicates strong agreement between predicted and real values.

Table 3. The values of statistical indices of ANN and GEP model.

	R^2		MAE		RMSE	
	GEP	ANN	GEP	ANN	GEP	ANN
$\frac{\delta k}{K}$ Coolant reactivity temperature coefficient,	0.9441	0.9978	4.22E-06	7.69E-07	8.04E-06	1.43E-06
$\frac{\delta k}{K}$ Fuel reactivity temperature coefficient,	0.9991	0.9992	6.31E-08	3.89E-08	9.00E-08	8.19E-08
Convective heat transfer coefficient, $\frac{w}{m^2 k}$	0.9945	0.9997	249.9083	40.2481	345.6629	85.0997

The models' predicted values were compared to simulation results in Fig. 6 ANN outperformed GEP, with R values closer to 1.

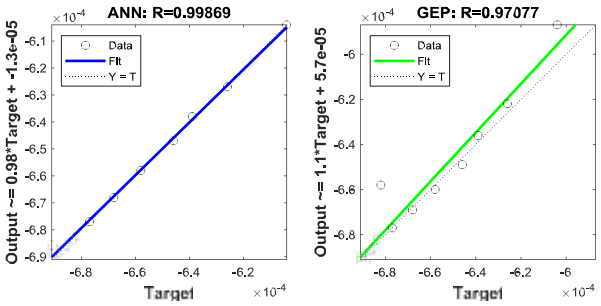

The regression chart of ANN (Left) and GEP (Right) for ca.

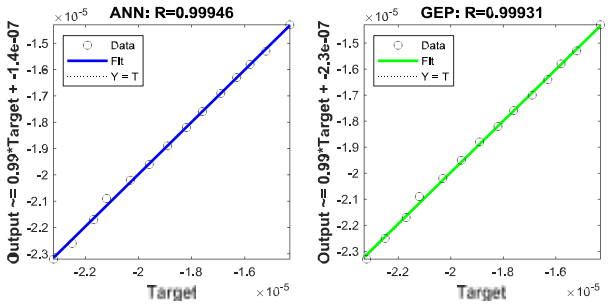

The regression chart of ANN (Left) and GEP (Right) for fa.

(a) (b)

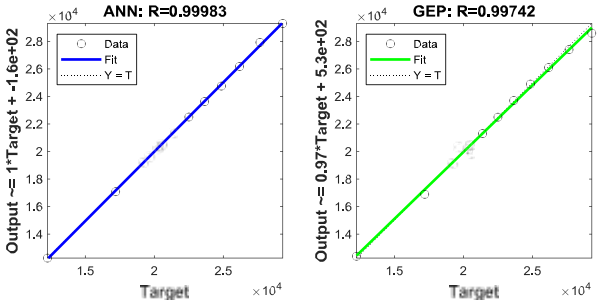

The regression chart of ANN (Left) and GEP (Right) for h.

(c)

Fig. 6. R value of ANN and GEP models.

Conclusions

The study focused on the impacts of dual-cooled fuels on reactivity feedback coefficients and heat transfer coefficient. Using WIMS-CITATION codes and Fluent, a simplified and accurate method is presented. Reactivity coefficients were calculated for all fuel designs, showing negative values. Increasing the inner radius of the fuel rod makes the coolant/moderator temperature reactivity coefficient more negative initially, but the rate decreases later. Fuel temperature reactivity becomes less negative with increased inner radius. The convective heat transfer coefficient decreases with larger internal fuel rod radius. In the second objective, ANN and GEP methods were used to predict parameters. R2, MAE, and RMSE are statistical indicators used to assess ANN and GEP models. Both methods are accurate, but ANN performs better than GEP.

This study specifically concentrated on the geometric influence (internal channel radius) of dual-cooled fuel on safety parameters. The impact of fuel composition on these parameters was acknowledged as a constraint. Subsequent research will delve deeper into this aspect, possibly considering different fuel enrichment levels and burnable poisons. Furthermore, this analysis utilized simplified models for neutronics (WIMS-CITATION) and thermalhydraulics (CFD with sub-channel model). Although these approaches offer valuable insights, integrating more advanced coupled neutronic-thermalhydraulic codes could improve the precision of forthcoming investigations.

References

[1] Lloyd, C. A., Roulstone, T., & Lyons, R. E. (2021). Transport, constructability, and economic advantages of SMR modularization. Progress in Nuclear Energy, 134, 103672.

[2] Subki, H. (2020). Advances in small modular reactor technology developments.

[3] Zayermohammadi Rishehri, H., & Zaidabadi Nejad, M. (2022). Design and Neutronic, Thermal-Hydraulic Analysis of DSCF Assembly for a SMR and Investigation of the Effect on the Thermal Power Uprate. Nuclear Technology, 1-21. https://doi.org/10.1080/00295450.2022.2120319

[4] Rishehri, H. Z., & Nejad, M. Z. (2022). Conceptual design of an innovative I&XC fuel assembly for a SMR based on Neutronics/thermal-hydraulic calculations at the BOC. Kerntechnik, 87(1), 91-103. https://doi.org/10.1515/kern-2021-1012

[5] Rishehri, H. Z. (2023). Design and optimization of dual-cooled fuel assembly in a 12× 12 configuration for NuScale SMR based on neutronic-thermohydraulic parameters using the combined ANN-GA approach. Progress in Nuclear Energy, 163, 104799.

[6] Zaidabadi, M., Ansarifar, G. R., & Esteki, M. H. (2017). Thermal hydraulic analysis of VVER-1000 nuclear reactor with dual-cooled annular fuel using K–ω SST Turbulence model. Annals of Nuclear Energy, 101, 118-127.

[7] Ansarifar, G. R., & Ebrahimian, M. (2016). Design and neutronic investigation of the Nano fluids application to VVER-1000 nuclear reactor with dual cooled annular fuel. Annals of Nuclear Energy, 87, 39-47.

[8] Ebrahimian, M., & Ansarifar, G. R. (2016). Investigation of the nano fluid effects on heat transfer characteristics in nuclear reactors with dual cooled annular fuel using CFD (Computational Fluid Dynamics) modeling. Energy, 98, 1-14.

[9] Mehri, A. M., Safarzadeh, O., & Talebi, S. (2021). The station blackout accident in a dual-cooled annular fuel of a VVER-1000 reactor with application of portable pumps for mitigating the accident. Annals of Nuclear Energy, 152, 107964.

[10] NuScale Power LLC. (2020). NuScale Standard Plant Design Certification Application. US Nuclear Regulatory Commission (NRC).

[11] Ferreira, C. (2001). Gene expression programming: a new adaptive algorithm for solving problems. arXiv preprint cs/0102027.

ICNST 2024
International Conference on Nuclear Science and Technology
6- 8 MAY 2024 | Isfahan, Iran

A Comparative Evaluation of Adaptive Robust Feedback-Linearization Control and Conventional Controllers in the Pressurized Water Nuclear Reactors During Load-Following Operation with Bounded Axial Power Distribution (Paper ID : 1022)

M. Zaidabadi nejad[1,2], G.R. Ansarifar [1*], H. Zayermohammadi Rishehri[1]

[1] *Department of Nuclear Engineering, Faculty of Physics, University of Isfahan, Isfahan, Iran*

[2] *Department of Nuclear Engineering, Faculty of Sciences and Modern Technologies, Graduate University of Advanced Technology, Kerman, Iran*

Abstract

Advanced controller design is vital for nuclear reactors. It ensures safety, efficiency, and optimization. By integrating advanced algorithms, digital technologies, and predictive modeling, we achieve real-time monitoring, precise control, and enhanced reactor performance. Continuous advancements and investments in controller design are crucial for the future of nuclear power generation, as the world seeks to meet growing energy demands while prioritizing safety and sustainability. In this paper, for the first time an Adaptive Robust Feedback-Linearization Control (ARFLC) based on the multipoint kinetics reactor model (neutronic and thermal-hydraulic) is presented. A comprehensive evaluation was conducted, comparing the performance of the newly developed controller with that of existing conventional controllers like Dynamic Sliding Mode Control (DSMC), Feedback-Linearization Control (FLC), and Sliding Mode Control (SMC). Remarkably, the evaluation unveiled a substantial enhancement in load-following capabilities for the proposed controller system, solidifying its superiority and the potential for broader implementation.

Keywords: Two-Point Kinetics reactor model; Adaptive Control; Feedback-linearization; Dynamic sliding mode

Introduction

In the ever-evolving landscape of scientific and technological advancement, nuclear reactors stand as resilient sources of clean energy, serving as the backbone of numerous power generation systems across the globe. Central to the safe and efficient operation of these monumental energy facilities are the controllers, which monitor and control critical processes within nuclear reactors. However, in an era where demands for resilience, efficiency, and enhanced safety measures are paramount, there arises an urgent need for the design and implementation of new controllers.

This article delves into the pivotal importance of developing innovative controllers for nuclear reactors, emphasizing the imperative role they play in advancing the realm of nuclear energy generation and addressing the challenges of tomorrow's energy landscape. Given the prominence of the pressurized water reactor (PWR) as the prevailing nuclear fission reactor, ensuring its efficient operation assumes paramount significance in light of the ongoing resurgence of the nuclear fission energy sector. In this regard, load-following emerges as a pivotal technique with potential to significantly influence the stability and efficacy of PWR operations. In direct comparison to conventional power-level controllers, the utilization of advanced power-level regulators confers the capability to enhance both closed-loop stability and control performance by incorporating feedback of internal state variables [1,2].

In this paper, for the first time an Adaptive Robust Feedback-Linearization Control (ARFLC) based on the multipoint kinetics reactor model (neutronic and thermal-hydraulic) is presented and compared to other conventional controllers.

Material and Methods

The applicability of point kinetics in the context of pressurized water reactors (PWRs) is rendered inadequate due to the considerable temporal variation experienced by the neutron flux shape. Consequently, explicit acknowledgement and consideration of the flux shape variation assumes requisite significance. In addressing this need, the multipoint method emerges as an efficacious and simplified approach for characterizing the space-time neutron kinetics of PWR nuclear reactors. The foundational genesis of the multipoint approach lies in the development of a neutron kinetics model for coupled reactors [3]. To employ the multipoint method, the reactor core is conceptually divided into multiple regions, wherein both the material composition and neutron flux are presumed to remain uniform. Moreover, these regions are treated as smaller cores that are interconnected via neutron diffusion, with the determination of the coupling coefficients occupying a central role within this methodology.

In order to evaluate the performance of the designed controller structure a set of simulations is performed on the VVER-1000 nuclear reactor. VVER-1000 (Russian type of PWRs) is developed on the basis of the proven performance of Pressurized Water Reactors (PWRs) with annular fuel plates that, has hexagonal configuration and 1/6 symmetric shape. The core consists of 163 FAs and each FA is comprised of 311 fuel rods and 18 guiding channels for control rods or burnable poisons. The VVER-1000 generates 3000 MWth at full power and there are six control rods with regulating function: so,

called group H10. Important physical and dynamic parameters of the VVER-1000 are given in Table 2 [4].

Table.2. Parameters of the nuclear reactor at 100% nominal power

Parameter	Value
Thermal power	3000 MW
Core height in the working state (cm)	355 cm
Core equivalent diameter (cm)	316 cm
Coolant inlet temperature (°C)	291 °C
Coolant flow rate (kg/s)	16,704 kg/s
Diffusion constant (D)	0.16 cm
Mean velocity of thermal neutron (ν)	2.2×10^5 cm/s
Microscopic absorption cross section of X	2.36×10^{-18} cm^2
Fractional fission yield of X (γ_x)	0.00228
Fractional fission yield of I (γ_I)	0.0639
Decay constant of X (λ_x)	2.08×10^{-5} s^{-1}
Decay constant of I (λ_I)	2.88×10^{-5} s^{-1}
Microscopic fission cross section	0.3358 cm^{-1}
Total delayed neutron fraction (β)	0.0065
β_1	0.0002145
β_2	0.002249
β_3	0.0040365
Effective prompt neutron life time (L)	2×10^{-5} s
Total reactivity worth of control rod (G_r)	14.5×10^{-3}

Neutronics Model

The PWR core is considered to be divided in two regions along the reactor axis as shown in Fig. 1.

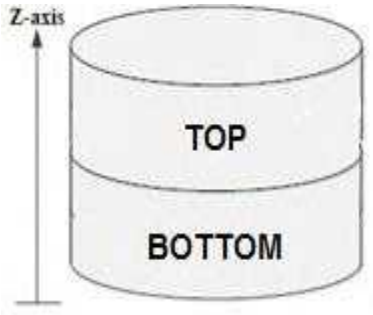

Fig. 1. Nodalizaiton of the PWR reactor core in the axial direction

To simulate the nuclear reactor core, the normalized model, with respect to an equilibrium condition, based on the multi-points kinetics equations with three delayed neutron groups are used. The used normalized neutron kinetics model is as follows [5]:

$$\frac{dn_{rt}}{dt} = \frac{\rho_t - \beta}{l} n_{rt} + \sum_{i=1}^{3} \frac{\beta_i}{l} C_{ri\,t} + \frac{\alpha}{l}(n_{rb} - n_{rt}) \quad (1)$$

$$\frac{dn_{rb}}{dt} = \frac{\rho_b - \beta}{l} n_{rb} + \sum_{i=1}^{3} \frac{\beta_i}{l} C_{ri\,b} + \frac{\alpha}{l}(n_{rt} - n_{rb}) \quad (2)$$

$$\frac{dC_{ri\,t}}{dt} = \lambda_i n_{rt} - \lambda_i C_{ri\,t} \qquad i = 1\,2\,3 \quad (3)$$

$$\frac{dC_{ri\,b}}{dt} = \lambda_i n_{rb} - \lambda_i C_{ri\,b} \qquad i = 1\,2\,3 \quad (4)$$

$$\frac{d\rho_{\mathrm{rt}}}{dt} = G_r\, Z_{r1} \quad (5)$$

$$\frac{d\rho_{\mathrm{rb}}}{dt} = G_r\, Z_{r2} \quad (6)$$

Where G_r , Z_{r1} and Z_{r2} are total reactivity worth of control rod, Control rod speed (fraction of core length per second) in top and bottom of core, respectively.

The reactor power is displayed as follows:

$$P(t) = P_0 n_r(t) \quad (7)$$

Where P_0 is the nominal power (MW) and n_r follow as:

$$n_r = \frac{n_{rt} + n_{rb}}{2} \quad (8)$$

Equations (5) and (6) demonstrate that the reactivity insertion at the bottom of the core is affected by the second control rod bank, which is assumed to travel through the bottom of the core and reactivity insertion at the top of the core is affected by the first control rod banks, which is assumed to travel through the top.

Multi-point thermal hydraulics model

In a simple case, the lumped influences of coolant and fuel temperature are taken into account for each region and for a system as illustrated the respective energy balance equations for coolant and fuel in each axial region can be defined as follows [5]:

$$\frac{dT_{ft}}{dt} = \frac{1}{\mu_{ft}}\left[f P_t - \Omega_t\left(T_{ft} - T_{ct}\right)\right] \quad (9)$$

$$\frac{dT_{fb}}{dt} = \frac{1}{\mu_{fb}}\left[fP_b - \Omega_b\left(T_{fb} - T_{cb}\right)\right] \quad (10)$$

$$\frac{dT_{ct}}{dt} = \frac{1}{\mu_{ct}}\left[(1-f)P_t + \Omega_t\left(T_{ft} - T_{ct}\right) - 2M_t\left(T_{ct} - T_{ct,in}\right)\right] \quad (11)$$

$$\frac{dT_{cb}}{dt} = \frac{1}{\mu_{cb}}\left[(1-f)P_b + \Omega_b\left(T_{fb} - T_{cb}\right) - 2M_b\left(T_{cb} - T_{cb,in}\right)\right] \quad (12)$$

Where T_c *and* T_f are average coolant and fuel temperatures, respectively and $T_{c,in}$ is coolant inlet temperature. Also, M, Ω, μ_f and μ_c are mass flow rate times heat capacity of the water, heat transfer coefficient between fuel and coolant, total heat capacity of the reactor coolant, thermal capacity of the fuel and structural material, respectively.

The following equations show the dependence of these variables on the relative power level at t = 0:

$$\mu_{ct} = \left(\frac{160}{9}n_{r0t} + 54\,022\right) MW.\ \frac{s}{^oC} \quad (13)$$

$$\Omega_t = \left(\frac{5}{3}n_{r0t} + 4\,93333)\right) MW.\ \frac{s}{^oC} \quad (14)$$

$$M_t = (28n_{r0t} + 74)\frac{MW}{^oC} \quad (15)$$

$$\mu_{cb} = \left(\frac{160}{9}n_{r0b} + 54\,022\right) MW.\ \frac{s}{^oC} \quad (16)$$

$$\Omega_b = \left(\frac{5}{3}n_{r0b} + 4\,93333)\right) MW.\ \frac{s}{^oC} \quad (17)$$

$$M_b = (28n_{r0b} + 74)\frac{MW}{^oC} \quad (18)$$

Where n_{r0} is total relative power level at t = 0 in each region.

Robust Feedback-Linearization Control

Real-world control systems often exhibit non-minimum phase characteristics, which means their unstable internal or zero dynamics pose limitations on the effectiveness of nonlinear control techniques like feedback linearization. In the case of linear SISO systems, non-minimum phase behaviour occurs when the input-output transfer function contains zeroes in the Right Half Plane (R.H.P). This can lead to instability when using bounded control inputs. To solve this problem, Shtessel (1998) proposed output tracking in nonlinear non-minimum phase systems using a dynamic sliding mode controller as follows [6]:

$$\begin{cases} \dot{x} = Ax + bu \\ y = Gx \end{cases} \quad (19)$$

Where A, b and G are constant matrices of corresponding dimensions, {A, b} is a controllable pair. First step of the dynamic sliding mode controller design, the dynamic sliding manifold can be introduced as follows:

$$\tau = u + \sigma = 0 \quad (20)$$

The function σ is a dynamic operator.

Remark 1. Existence condition of sliding mode $\tau\dot{\tau} < -\eta|\tau|$ must be satisfied in the vicinity of the sliding manifold.

Assuming that the dynamic sliding mode exists, the equation of sliding motion of the system in the dynamic sliding manifold (Eq.20) can be governed by:

$$\begin{cases} \dot{x} = A_{11}x - A_{12}\sigma \\ y = G_1 x - G_2 \sigma \end{cases} \quad (21)$$

The plant by (Eq.21) with the control input σ and the output y is a non-minimum phase system.

The function σ is a dynamic compensator for stabilizing internal dynamics. The sliding manifold is reached in a finite time $t_r = \frac{|\tau(0)|}{\eta}$ and the system's trajectory stays on the manifold thereafter where $\tau(0)$ is an initial value of a sliding manifold and $\eta > 0$. In order to satisfy the existence condition of the sliding mode on the dynamic sliding manifold, the control function u is given in the following way:

$$\dot{u} = -u + u_c \quad (22)$$

$$u_c = -[\eta sign(\tau) + \dot{\sigma} - u] \quad (23)$$

The discontinuous control law is designed in a simplified manner:

$$u_c = -U_{max} sign(\tau) \quad (24)$$

Where;

$$\begin{cases} U_{max} > (|u_{eq}| + \eta) \\ u_{eq} = \dot{\sigma} - u \end{cases} \quad (25)$$

For avoiding the control chattering, the discontinuous control is realized in a smooth form as:

$$u_c = -U_{max} tanh(\frac{\tau}{\varphi}) \quad (26)$$

Where φ is the width of the boundary layer which is introduced about the origin in the τ -space.

At the second step of controller design, the desirable two control law according feedback-linearization combine with dynamic sliding mode and a robust control law are represented as follows:

$$\tau_t = u_t + \sigma_t = 0 \Rightarrow u_t = -\sigma_t \quad (27)$$

$$\tau_b = u_b + \sigma_b = 0 \Rightarrow u_b = -\sigma_b \quad (28)$$

Then:

$$u_t = -\rho_{rt} \quad (29)$$

$$u_b = -\rho_{rb} \quad (30)$$

Also, σ_t and σ_b are defined as follows:

$$\begin{aligned}\dot{n_{rt}} = \dot{n_{rdt}} - \eta_1 e_t \Rightarrow \sigma_t \\ = \frac{l}{n_{rt}}\left[\dot{n_{rdt}} - \eta_1 e_t - \sum_{i=1}^{3}\frac{\beta_i}{l}C_{ri,t} - \frac{\alpha}{l}(n_{rb} - n_{rt})\right] - \alpha_{ft}(T_{ft} - T_{f0t}) \\ - \alpha_{ct}(T_{ct} - T_{c0t}) + \frac{\sigma_a^X(X_t - X_{0t})}{\nu\Sigma_f} - \beta\end{aligned} \quad (31)$$

$$\begin{aligned}\dot{n_{rb}} = \dot{n_{rdb}} - \eta_2 e_b \Rightarrow \sigma_b \\ = \frac{l}{n_{rb}}\left[\dot{n_{rdb}} - \eta_2 e_b - \sum_{i=1}^{3}\frac{\beta_i}{l}C_{ri,b} - \frac{\alpha}{l}(n_{rt} - n_{rb})\right] - \alpha_{fb}(T_{fb} - T_{f0b}) \\ - \alpha_{cb}(T_{cb} - T_{c0b}) + \frac{\sigma_a^X(X_b - X_{0b})}{\nu\Sigma_f} - \beta\end{aligned} \quad (32)$$

According to Eq. 22, the control rod reactivity in the reactor core (u) is related to the control rod speeds (u_c) as follows:

$$Z_{rt} = -100 * tanh(\frac{\tau_t}{\varphi}) \quad (33)$$

$$Z_{rb} = -100 * tanh(\frac{\tau_b}{\varphi}) \quad (34)$$

Results and Discussion

The results show a significant improvement in the load following, axial offset boundedness and increased ability in robustness for the proposed Adaptive robust feedback-linearization compare to the dynamic sliding mode control, sliding mode control and conventional feedback-linearization, better tracking of the desired power without chattering can be observed for the proposed Adaptive robust feedback-linearization. Desired adaptive robust controller, dynamic sliding mode control, feedback-linearization of Reactor Relative Power with uncertainty and external disturbance has been presented in Fig. 3. Also, Normalized Axial-Offset (ΔI) have been shown in Fig. 4.

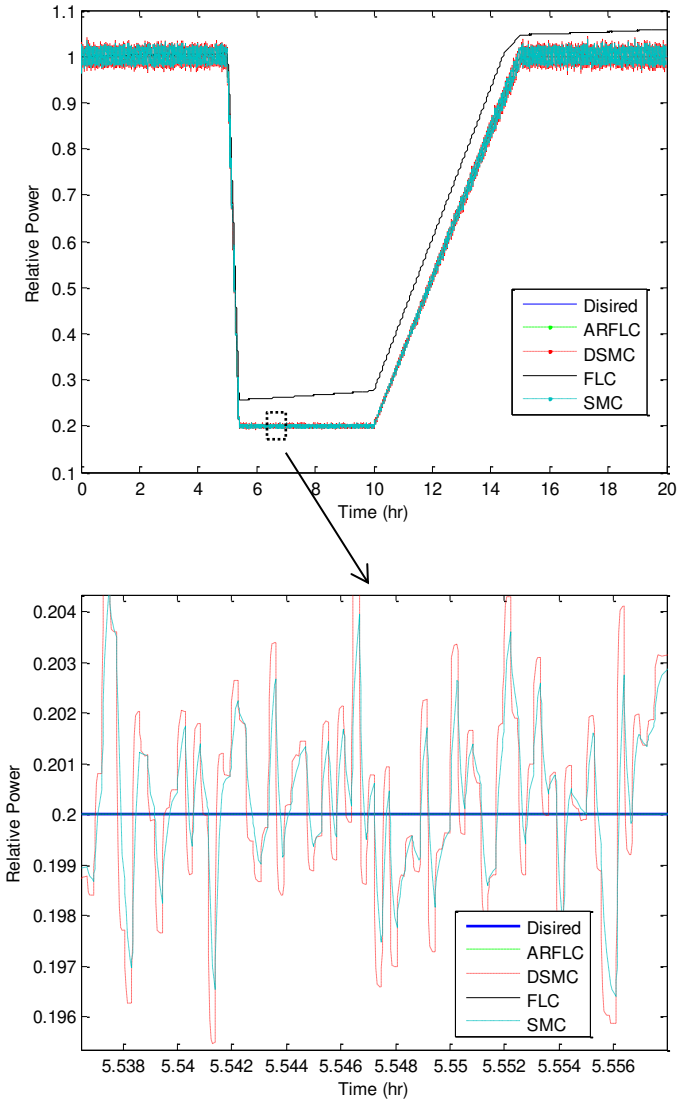

Fig. 3. Estimations of Reactor Relative Power

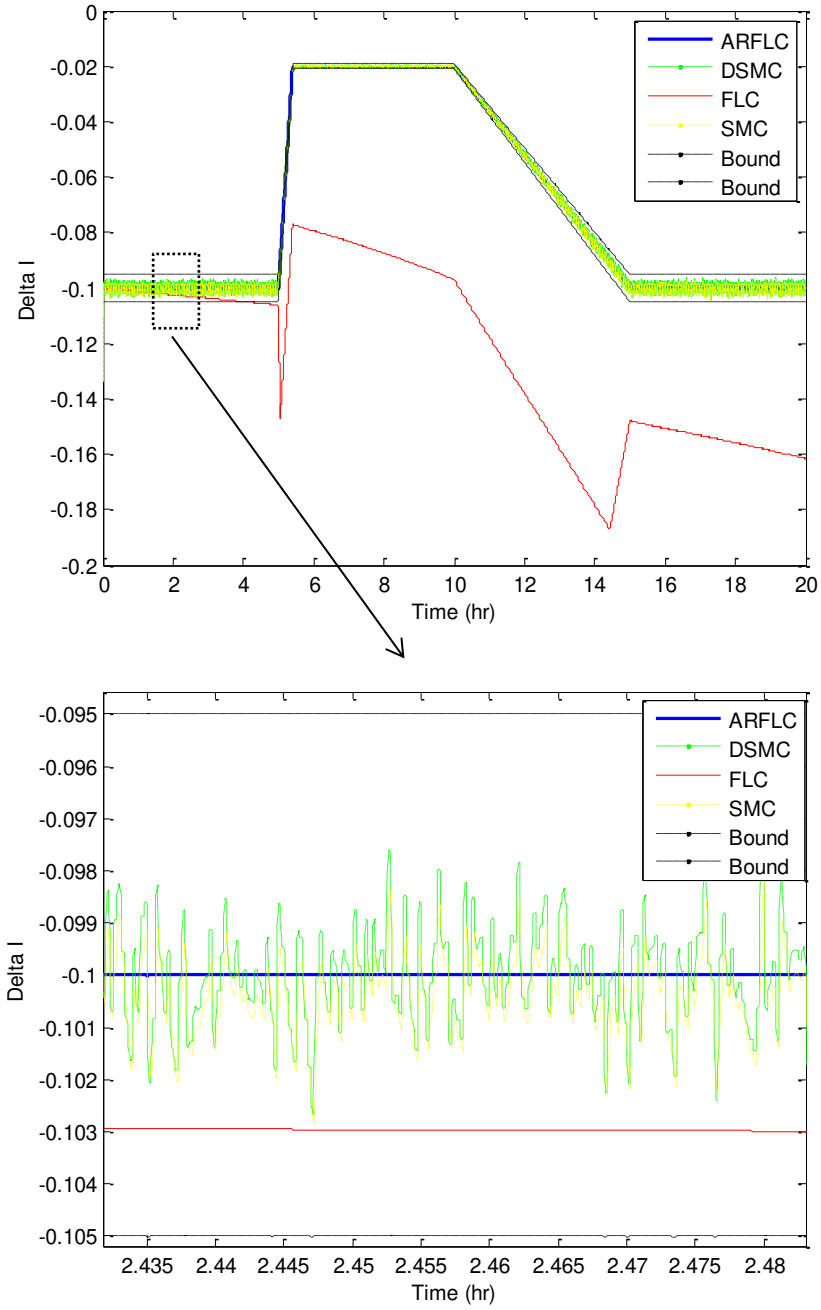

Fig. 4. Estimation of Normalized Axial-Offset (Δ I).

The results showed a significant improvement in the load following, AO boundedness and increased ability in robustness for the proposed Adaptive robust feedback-linearization compare to the dynamic sliding mode control, sliding mode control and conventional feedback-linearization, better tracking of the desired power without chattering can be observed for the proposed Adaptive robust feedback-linearization.

Conclusions

In this paper, an Adaptive Robust feedback-linearization Control based on the multipoint kinetics reactor model (neutronic and Thermal-hydraulic) has been presented for core power control of the Pressurized-Water Nuclear Reactor (PWR) to improve the load following capability.

The presented controller compared with other conventional controllers. The results presented in this paper showed that robust control with adaptive robust feedback-linearization methodologies can be used in nuclear plant systems with diverse applications including control in the presence of model uncertainties and noise.

References

[1] Park, M.G., Cho, N.Z., 1992. Design of a non-linear model-based controller with adaptive PIgains for robust control of a nuclear reactor. Prog. Nucl. Energy 27 (1), 37–49.

[2] Park, M.G., Cho, N.Z., 1993. Time-optimal control of a nuclear reactor power with adaptive proportional integral feed forward gains. IEEE Trans. Nucl. Sci. 40 (3), 266–270.

[3] Avery, R., 1958. Theory of coupled reactors. In: Proceedings of the 2nd U.N. International Conference Peaceful Uses At. Energy, vol. 12, pp. 182–191.

[4] Russia Federal Agency on Nuclear Energy (RFANE), 2005. Final Safety Assessment Report (FSAR) for BNPP. Book 1, Moscow.

[5] Zaidabadi nejad. M , Ansarifar. G.R, 2017, Adaptive robust control for axial offset in the P.W.R nuclear reactors based on the multipoint reactor model during load-following operation Ann. Nucl. Energy ,Vol 103 ,pp 251–264

[6] Shtessel .Y. B, 1998 ,Sliding mode control of the space nuclear reactor system, IEEE Trans. Aerosp. Electron. Syst., vol. 34, p. 579.

ICNST 2024
International Conference on Nuclear Science and Technology
6- 8 MAY 2024 | Isfahan, Iran

Acquiring and designing the world's most advanced nuclear reactor in line with its commercialization with unique safety and economic conditions (Paper ID : 1028)

Korosh Rahbari[1*]– Darush Masti[1] – Kamran Sepanloo[2,3]– Ehsan Zarifi[2,3]
[1] Department of Nuclear Engineering, Bushehr Branch, Islamic Azad University, Bushehr, Iran.
[2] Reactor and nuclear safety school, Nuclear Science and Technology Research Institute (NSTRI), Tehran, Iran
[3] Department of Nuclear Engineering,Science and Research Tehran Branch , Islamic Azad University, Tehran, Iran.

Abstract

The technology and structure of the advanced nuclear reactors of the new generation are the same as the fourth generation (modular) reactors. In recent years, the desire to build advanced reactors with high safety and optimal economic conditions is due to the need for production units in power networks, especially in remote areas and the sparsely populated cities are increasing. The main characteristics of these advanced reactors are high inherent safety, simplicity of equipment, longer operation time, no need for refueling for several years, higher efficiency and, lower operating cost. This and many other reasons caused many developed countries and some developing countries to present many conceptual and innovative plans in this field. In this research, according to the main structure and characteristics of the core of one of these types of advanced reactors named Alfred, using the MCNPX 2.6 code and the design stages of the core, which includes the fuel assembly, control rods, safety rods and other components, it was carried out and It is compared with sources and References and can be commercialized.

Keywords: Advanced Nuclear Reactors, Reactor Safety, Alfred Reactor, MCNPX 2.6 code.

Introduction

ALFRED, Advanced Lead Fast Reactor European Demonstrator, represents the necessary step that has emerged from a European research effort, in the frame of Lead cooled next generation nuclear power plants. The main goal behind ALFRED and Lead technology development is to maintain the nuclear energy source as an important contributor to the development of a low carbon emission European energy system.

ALFRED is one of the projects supported by the European Sustainable Nuclear Industrial Initiative (ESNII), which brings together industry and research partners in the development of so-called Generation IV Fast Neutron Reactor technology, as part of the EU's Strategic Energy Technology Plan (SET-Plan) [1].

The paper presents briefly the design status of ALFRED (Advanced Lead Fast Reactor European Demonstrator), as developed inside the LEADER (Lead European Advanced Demonstrator Reactor)

project of the 7th FWP [2], and includes an overview of the main aspects of the design concerning: system design, safety features, core design and fuel cycle as well as some highlights on safety analysis which shows the resistance of the design itself from postulated accidents. Considerations about the general behavior of the plant following a Fukushima like event are also presented.

2. Methods and materials

2.1. ALFRED design

ALFRED is a scaled down reactor compared to the industrial prototype ELFR proposed in LEADER [3], which is on its turn based on the 600 MWe ELSY reactor. ALFRED has a relatively low power (125 MWe) with a compact design to reduce the cost but maintaining its representativeness. It is cooled by pure lead. For investment protection the design is based as much as possible on simple and removable components and operates at the lowest temperatures compatible with the pure lead coolant.

The configuration of the primary system is pool-type. This concept permits containment of all the primary coolant within the Reactor Vessel RV), thus eliminating problems related to out-of vessel circulation of the primary coolant (Figure 1). The Reactor assembly presents a simple flow path of the primary coolant, with a Riser and a Downcomer. The heat source (the Core), located below the Riser, and the heat sink (the Steam Generators - SG) at the top of the Downcomer, allow for efficient natural circulation of the coolant. The primary coolant moves upward through the pump impeller to the vertical shaft, then enters the SG through the lead inlet holes, flows downwards on the shell and exits the SG. The free level of the hot pools inside the Steam Generator and Primary Pump units is higher than the free level inside the Inner Vessel (IV), the different heads depending on the pressure losses across component parts of the primary circuit. The volume between the primary coolant free levels and the reactor roof is filled by a cover gas plenum.

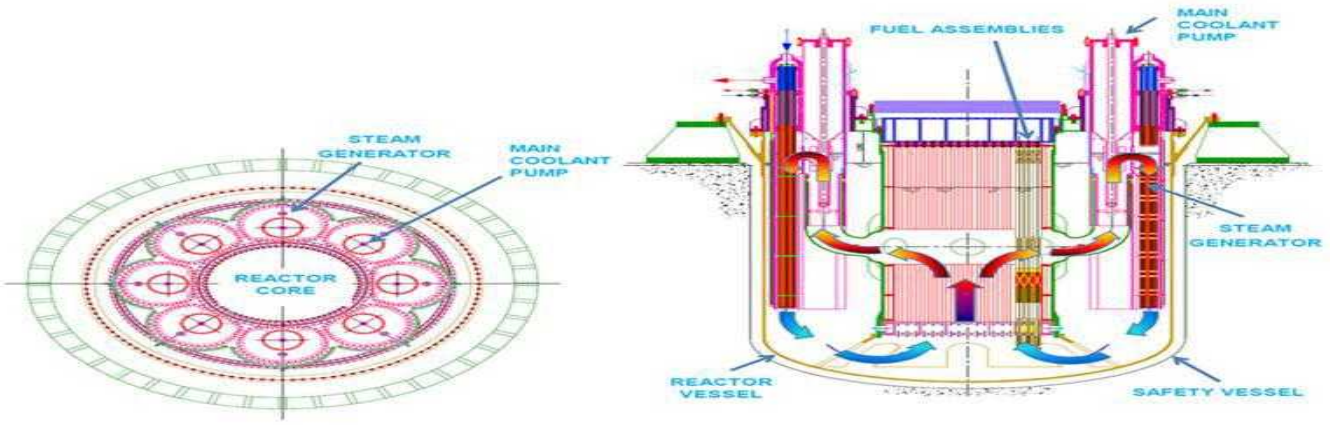

Fig. 1. Lay-out of the ALFRED primary system: vertical and horizontal sections

The Reactor Vessel is cylindrical with a Toro spherical bottom head. It is anchored to the reactor cavity from the top, by means of a vessel support. The upper part is divided in two branches by a "Y" junction: the conical skirt that supports the whole weight and the cylindrical one that supports the Reactor Cover. A cone frustum, welded to the bottom head, provides the function of bottom radial restraint of Inner Vessel. A steel layer covering the reactor pit constitutes the Safety Vessel (SV). The dimensions of the gap between the safety vessel and the reactor vessel are sufficient for the In-service Inspection tools. The SV is cooled by the same system that cools the concrete of the cavity walls. This system is inserted inside the concrete and is independent from the reactor cooling systems. This design solution mitigates the consequences of through-wall cracks with leakage of lead: any reactor vessel leakage is discharged into the Safety Vessel. The RV and the SV are arranged in such a manner that, in case of a reactor vessel leak, the resulting primary coolant always covers the SG inlet and the lead flow path is indefinitely maintained. The Inner Vessel has two main functions: Fuel Assemblies (FAs) support and separation between hot plenum and cold plenum. It is fixed to the cover by bolts and is radially restrained at the bottom. Lead flow is guided from the FAs outlet towards the PP inlet pipes by a toroidal half-ring. Moreover, the pipes that connect the hot zone with the inlet of the PP are integrated in the Inner Vessel. The cylindrical IV has a double wall shell: the outer thick wall has a structural function, while the inner thin wall follows the core section profile. The Core Lower grid is a box structure with two horizontal perforated plates connected by vertical plates. The plate holes are the housing of the FAs foots and the plate distances must be sufficient to assure the verticality of FAs. The grid is mechanically connected to the IV with pins (possible removal/replacement during reactor lifetime). The Core Upper grid is a box

structure like the lower grid but stiffer. It has the function to push down the FAs during the reactor operation. A series of preloaded disk springs press each FA on its lower housing. A hole is present for each disk to allow the passage of instrumentation (i.e., thermocouples, neutron detectors, etc.). In the following TABLE 1 the main parameters of ALFRED are briefly summarized.

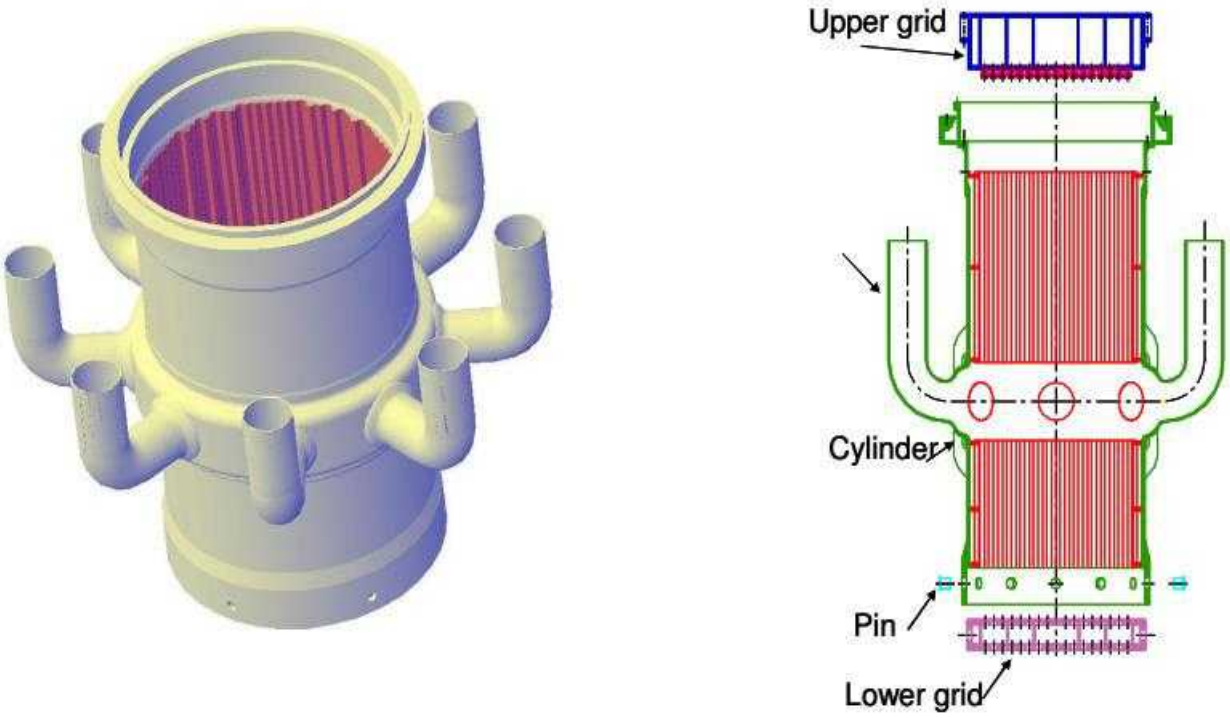

Fig. 2. Inner Vessel: 3-D sketch and axial section with FAs inside

Table 1. ALFRED – Main parameters

Parameter	Unit	Values
Thermal power	MW	300
Active height	cm	60
Pellet hollow diameter	mm	2
Pellet radius	mm	4.5
Gap thickness	mm	0.15
Cladding thickness	mm	0.6
Pin diameter	mm	10.5
Wrapper thickness	mm	4
Distance between 2 wrappers	mm	5
Coolant velocity	ms^{-1}	~1.4
Lattice pitch (hexagonal)	mm	13.86
Pins per FA	-	127
Inner vessel radius	cm	165

The adopted core configuration is constituted by wrapped Hexagonal Fuel Assemblies. It utilizes MOX as fuel and uses hollow pellets and a low active height in order to improve natural circulation. The total power is 300 MWth. The core scheme is made of 171 FAs, 12 CR (Control Rods) and 4 SR (Safety Rods), surrounded by 108 Dummy Elements (ZrO_2-Y_2O_3) shielding the Inner Vessel. Each Fuel Assembly is about 8 m long and consists of 127 fuel pins, fixed to the bottom of the wrapper and restrained sideways by grids. Tungsten deadweight (Ballast) prevents buoyancy forces in lead. Upper elastic elements (cup springs) prevent lifting induced by hydrodynamic loads and accommodate axial thermal expansions. The FAs upper end extends beyond the lead free surface in the cover gas for easy inspection and handling. In this way it is possible to achieve refueling without the need of in-vessel refueling machines. The ALFRED core is shown in **Figure 3**.

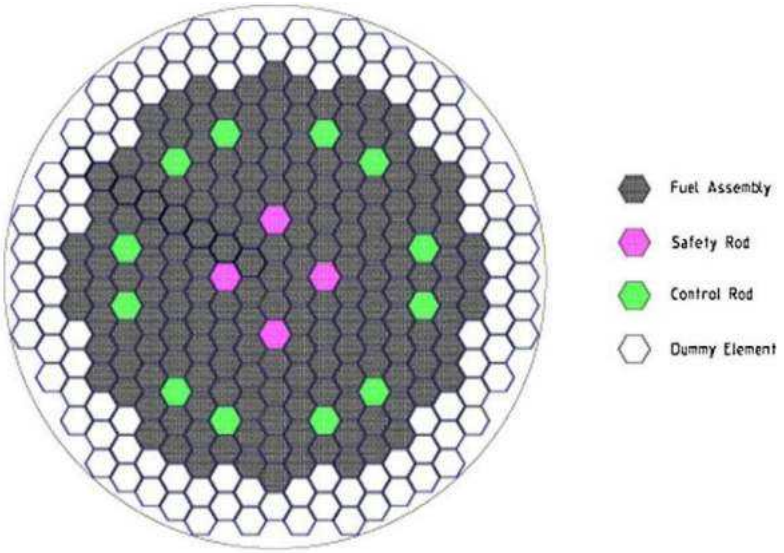

Fig. 3. ALFRED Core

ALFRED is equipped with two diverse, redundant and separate shutdown systems (adapted from that under investigation in the frame of the CDT-MYRRHA project):

(1) The CR (Control Rod) system, used for both normal control of the reactor (start-up, reactivity control during the fuel cycle, power transients and shutdown) and for SCRAM in case of emergency. The Control rods are extracted downward and rise up by buoyancy in case of SCRAM. The control mechanism pushes the assembly down with a ball screw, placed, with its motor and resolver atop the cover (at cold temperature (<70°C)), and protected from radiation by a shielding block. The actuator is

coupled to a long rod by an electromagnet. When the coupling electromagnet is switched off (in case of SCRAM), the absorber assembly and the rod are free to rise up. CRs use a 19 pins absorber bundle, cooled by the primary coolant flow. These pins are fitted with a gas plenum collecting the helium and tritium, produced by nuclear reaction of ^{10}B.

(2) The SR (Safety Rod) system, is the redundant and diversified complement to the control rods for SCRAM only. The absorber bundle stays in the primary coolant. The rod is extracted upward and is inserted downward against the buoyancy force. The absorber gets inserted by the actuation of a pneumatic system. In case of loss of this system, a tungsten ballast will force the absorber down by gravity in a slow insertion.

For both systems the materials considered are B_4C enriched in ^{10}B at 90% as the absorber, T91 for the guide tubes, 15-15 Ti for the clad and ZrO_2 (95%) - Y_2O_3 (5%) for the insulator and the reflector components. A description of ALFRED core can be found in [4], [5].

The steam generator and primary pump are integrated into a single vertical unit. Eight SG/PP units are located in the annular space between the cylindrical inner vessel and the reactor vessel wall. The primary pump is placed on the hot side of the steam generator, having its mechanical suction in the hot pool inside the inner vessel. The primary coolant moves upward through the pump impeller to the vertical shaft, then enters the SG through the lead inlet holes, flows downwards on the shell and exits the steam generator. The pump motor is located above the reactor roof. Each SG consists of a bundle of 542 bayonet tubes immersed in the lead vessel pool for 6 m of their length. The bayonet tube is a vertical tube with external safety tube and internal insulating layer, composed of 4 concentric tubes (**Figure 4**): a slave tube, an inner tube, an outer tube and an outermost tube. The internal insulating layer (delimited by the slave tube) has been introduced to ensure the production of superheated dry steam: in fact, without an insulating system, the high ΔT ($\approx$115°C) between the rising steam and the descending feed water would promote steam condensation in the upper part of the steam generator. The gap between the outermost and the outer bayonet tube is filled with pressurized helium and high thermal conductivity particles (such as synthetic diamonds) to enhance the heat exchange capability. In case of an external tube break this arrangement guarantees that the primary lead does not interact with the secondary water. Moreover, a tube break can be easily detected by monitoring the Helium gap pressure. The Primary Pump is surrounded by the SG tube bundle, and its housing is the SG casing. The Pump is fixed to the top of SG casing by a bolted joint. This allows for easy removal of the component. Primary Pump studies are in progress. Based on analyses performed during previous LFR projects (EUROTRANS, ELSY) an

axial pump has been adopted. As far as the PP impeller material is concerned, Maxthal ceramic material has been proposed, but its reliability must be still demonstrated. An alternative solution can be a SS impeller with a ceramic coating.

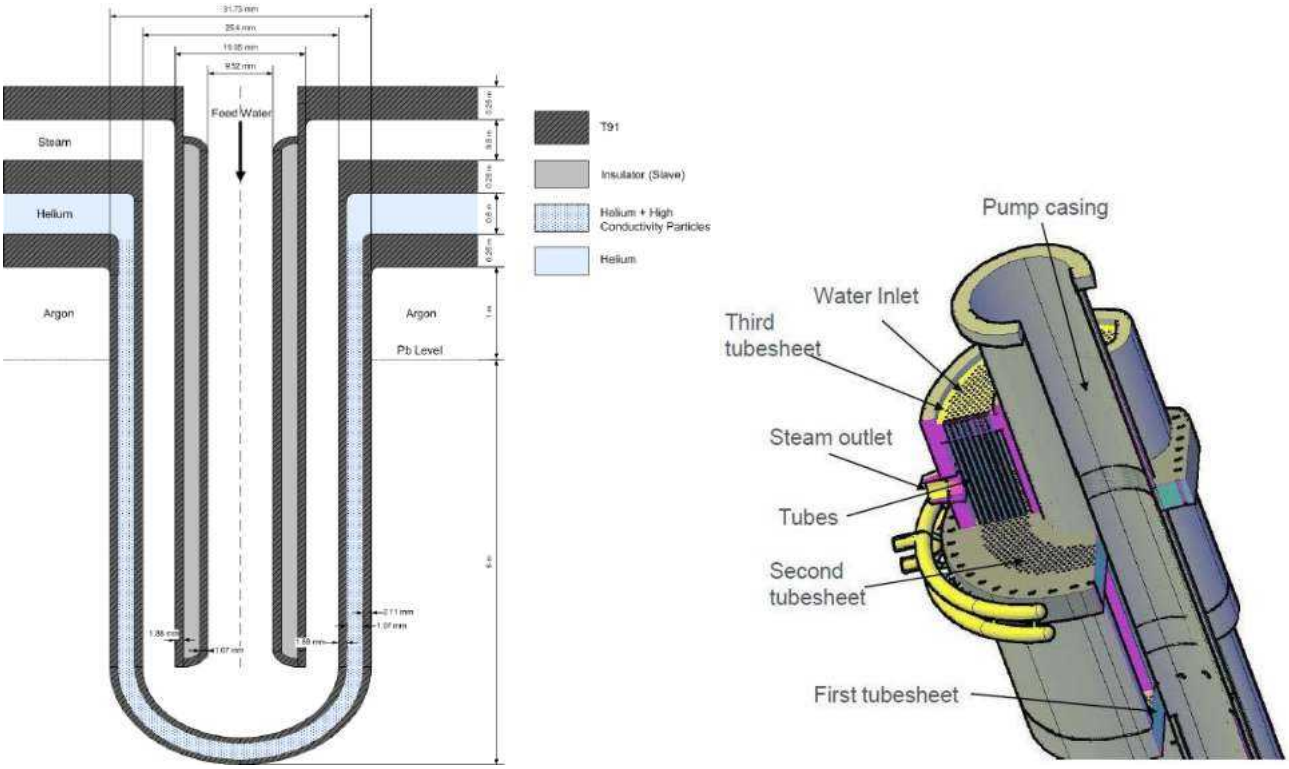

Fig. 4. Bayonet tube configuration and SG 3D scheme

The Decay Heat Removal system (DHR) consists of two passive, redundant and independent systems, DHR1 and DHR 2, both composed of four Isolation Condenser systems (ICs) connected to four SGs on the secondary side (i.e., one IC for each SG). The system design considers the single failure criterion, since three out of four ICs are sufficient to remove the decay heat power. The DHRs are dedicated safety systems, not used for normal operation. The separation is achieved through placing the two DHRs in physically different locations. A physical structural barrier or another means of protection will be placed between adjacent ICs to ensure that failure of one of them could not harm another one. The diversity requirement has been relaxed (in any case, two DHR systems will be fabricated by diverse manufacturers) due to the high redundancy and considering that the SG tube bayonet concept allows a continuous monitoring of the SG status. Both systems are completely passive, with an active actuation through valves equipped with redundant and diverse energy sources (batteries or locally stored energy). Each DHR system must be ready to operate after the reactor trip in order to remove the decay heat

power, in case of unavailability of the normal path (i.e., the by-pass to the Condenser). The actuation logic guarantees the actuation of DHR1 first, whereas the DHR2 actuates only in the case of failure of the first system. Moreover, the total number of isolation condensers called to operate can never exceed the four units, in order to avoid an excessive cooling of the primary coolant leading to fluid solidification. Each of the four independent IC sub-systems (**Figure 5**) consists of:

- One heat exchanger (isolation condenser), constituted by a vertical tube bundle with an upper and a lower horizontal header.

- One water pool, where the isolation condenser is immersed; the amount of pool water is sufficient to guarantee 3 days of decay heat removal operation.

- One condensate isolation valve (to meet the single failure criterion, this function must be performed at least by two parallel valves).

Each IC is connected to a SG: the upper header of the IC is connected to the main steam line and the lower header of the IC is connected to the main feed water line. Figure 4. Bayonet tube configuration and SG 3D scheme in normal operation, the isolation valve below the condenser is closed, the condenser is full of water and no heat exchange takes place.

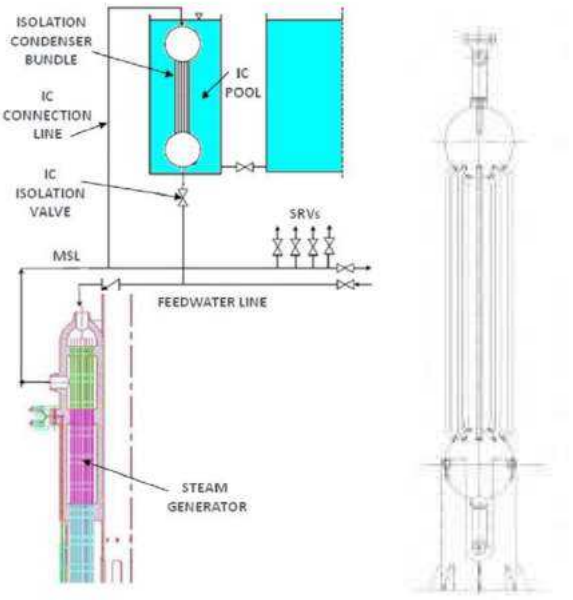

Fig. 5. ALFRED Isolation condenser scheme and IC bundle

As the IC subsystem is called to operate, the feed water line and steam line are isolated and the condensate isolation valve opens. The sub-cooled water stored into the IC tube bundle drains into the SG, due to the hydrostatic head existing between the reactor and the IC. The IC tubes and headers become empty and their internal cold surface starts to condensate the steam coming from the SG and hence to transfer heat to the cold pool water. The steam condensation causes a pressure reduction which calls other steam from the SG. The water injected into the secondary system from the IC during the draining phase, vaporizes into the SG tube bundle contributing to the secondary system pressure rise: the safety relief valves continue to operate to reject to the atmosphere the excess of steam and to guarantee a secondary side pressure of 195 bar(a). When the IC reaches its steady state condition and starts to remove the thermal power from the primary coolant, the secondary side pressure rise decreases and finally stops leading to the closure of the safety relief valves on the main steam line.

The Secondary System proposed for ALFRED is based on a dual turbine configuration with three extractions in the HP turbine and three more in the LP turbine, with an axial outlet. There will be reheating with steam from the first extraction and six preheaters supplied with steam from each turbine extraction, as well as a final heater supplied with main steam. This main steam shall be adequately throttled so that the feedwater temperature at the inlet of the steam generator (FWTC heater - feedwater temperature control) can be controlled. In addition, the de-aerator can be fed from the outlet of the HP turbine. The typical redundancy for the condensate and feedwater pumps (2x100% pumps) has also been considered. An auxiliary lead heating system is added. This system would work when the power cycle is not in operation, in order to ensure the minimum temperature of the lead by transmitting heat from the secondary system if it is needed. A 100% turbine bypass system is part of the design, to allow direct transfer from the reactor to the condenser (bypass mode).

The ALFRED development in terms of safety features follows the general guidelines of the Generation IV safety concept recommendations. Among the goals for future nuclear energy systems, improved safety and higher reliability are recognized as an essential priority in the development and operation of nuclear power plants. ALFRED has also been adopted as a significant example of LFR for the White Paper on LFR safety developed by the Reactor Safety Working Group of GIF and the GIF-LFR System Steering Committee (the paper is presently under review of the GIF Expert Group and will be published shortly on GIF Website). The fundamental safety objectives and the Defense-in-Depth (DiD) approach, as described by IAEA Safety Guides, have been preserved. The ideal outcome will be a design that optimizes both capital costs and safety by applying defense in depth where it will have the desired effect,

but not to "over-design" in a way that adds cost but provides little additional value in safety. The recommendation of the Risk and Safety Working Group (RSWG) has been taken into account, so:

• safety is to be "built-in" to the fundamental design rather than "added on";

• full implementation of the Defense-in-Depth principles in a manner that is demonstrably exhaustive, progressive, tolerant, forgiving and well-balanced (e.g., rejection of "cliff edge effects" and availability of a sufficient grace period and the possibility of repair during accidental situations);

• "risk-informed" approach - deterministic approach complemented with a probabilistic one;

• adoption of an integrated methodology that can be used to evaluate and document the safety of Gen IV nuclear systems - Integrated Safety Assessment Methodology (ISAM). In particular the Objective Provision Tree (OPT) tool is the fundamental methodology used throughout the design process. The OPT is a top-down method which, for each level of DiD and for each safety objective/function, identifies the possible challenges to the safety functions, their related mechanisms and the provisions needed to prevent, control or mitigate their consequences. A full description of the safety approach used for LFR and ALFRED in the EU can be found in [7].

Within the LEADER project all the most important DBC transient initiators were analyzed for the ALFRED reactor. The full list of the analyzed DBC transients for ALFRED is as follows:

• Spurious withdrawal of the most reactive control rod (PTOP),

• Reactivity (100 PCM) insertion due to fuel loading error,

• Spurious reactor trip,

• Turbine trip,

• Loss of AC power (PLOOP),

• Loss of one primary pump (AC power available),

• Loss of all primary pumps (PLOF),

• Protected partial flow blockage in the hottest fuel assembly,

• Reduction of FW (feed water) temperature from 335 °C to 300 °C,

• Increase of FW flowrate by 20 %, and

• Steam system piping break.

The results of the performed analysis show that ALFRED meet the DBC acceptance criteria. Calculated peak pin temperatures are not exceeding 700 °C, thus no clad failures (creep rupture) are expected, even during the loss of AC power (PLOOP) and loss of all primary pumps (PLOF) transients. This is mainly due to the large thermal inertia of the Pb-cooled primary system and the relatively high Pb natural

convection core mass flow rate observed at the initial stage of the transient. In the long-term, in case of PLOOP or PLOF transients, following reactor trip, core decay heat can be passively and safely removed indefinitely by the DHR-1 system without the need of any AC power. Large margin to clad failure (rupture) for the clad of the peak pins of the ALFRED reactor was confirmed also during the simulated peak power FA 70% flow blockage transient. Reactor safety in this case is ensured by the reactor protection system, shutting down the reactor, as well as by DHRS, efficiently removing the decay heat from the reactor primary cooling circuit. Reactor trip delay even by 10 sec does not lead to clad failure for the ALFRED reactor. During the protected FW temperature decrease to 300 ^{o}C transient, apart from an issue of Pb-freezing several hours into the transient at the outlet of the MHX for the ALFRED reactor, no safety related issues are observed. During this time period the operator has sufficient time to deactivate sub-systems of the DHR-1 system, in order to prevent Pb-coolant freezing at the outlet of the MHX. As a general conclusion, no relevant, immediate safety issues have been identified during the performance of the simulated transients aside of potential Pb-freezing several hours into the transient in case of all protected DBC transients. Reactor safety is assured by the reactor protection system, shutting down the reactor, in conjunction with a heat removal system (DHRS), removing tightly controlled amounts of decay heat from the reactor primary cooling circuit to assure prevention of freezing of the Pb-coolant at any location of the primary cooling circuit. However design modifications to the DHRs are under study in order to avoid the need of operator intervention to prevent freezing, thus warranting a very high grace time. As related to the DBC transients, all selected transients examined proved that the ALFRED plant can accommodate a rather wide range of accidental events. The ALFRED plant has also proved to be able to enter a safe shutdown phase after every DBC accident analyzed. The analysis indicated, that ALFRED is a very forgiving plant design, and there is an extended time margin (grace time) of several hours for possible manual operator intervention even under worst accidental conditions (potential of Pb-freezing in the long term, in case of uncontrolled decay heat removal by the DHRs). A comprehensive presentation of DBC transients can be found in [8].

The DEC events that are representative for the safety analysis of ALFRED have been identified by means of common safety approach adopted for liquid metal fast reactors and on the basis of engineering judgment, taking into account the specific features of the ALFRED design. These events of very low frequency are characterized either by the failure of reactor scram (so called unprotected accidents) involving:

• Unprotected reactivity insertion transient (UTOP),

• Unprotected loss of flow transient (ULOF),

• Unprotected loss of heat sinks transient (ULOHS),

• Unprotected loss of flow and heat sink transient (ULOF+ULOHS),

• Unprotected partial FA blockage,

or by the simultaneous occurrence of multiple failures in some protected transients such as:

• Loss of all secondary circuits with total unavailability of DHR system,

• Loss of all primary pumps with reduction of feedwater temperature (loss of a preheater),

• Loss of all primary pumps with increase of feedwater flowrate by 20%.

The last two protected transients have been mainly investigated to assess an important aspect for LFR systems related to the risk of lead freezing in the primary cooling circuit. This specifically concerns situations after reactor shutdown and activation of the DHR system, since, in the medium term, heat removed by the DHR system (which is almost constant in time) is expected to exceed the decreasing decay heat. The preliminary safety analysis has demonstrated that in this case the lead freezing might become an issue only after several hours, thanks to the large thermal inertia of the primary system and thus there is more than enough time for the operator to undertake appropriate corrective actions. Furthermore, the analysis of the extremely unlikely event characterized by the failure of all secondary circuits with total unavailability of any DHR system, leading to a progressive increase of the primary temperatures, has highlighted the large grace time left to the operator before reaching limiting temperatures for the core and the vessel structures. The unprotected transients are mainly investigated to obtain insights on the intrinsic safety behavior of ALFRED and thus verify the adequacy of the solutions adopted for the core and the plant design. All the unprotected transients are considered to start at full power (300 MWth) from end of cycle (EOC) conditions. Transient analyses performed for the beginning of cycle (BOC) conditions with the SIM-LFR code confirm that the general situation does not differ significantly from EOC conditions, thus similar Conclusions apply in both cases.In all simulated unprotected transients the core temperatures are maintained well below the safety limits to be considered for DEC accidental transients. In particular:

• In all simulated transients there is a very large margin to coolant boiling, since the coolant temperature is always at least 900 °C below the lead boiling point (1740 °C);

• No clad failure is predicted in any of the simulated transients, unless in case of an undetected FA blockage greater than ~85%, which might be excluded by design (there are many orifices for coolant

ingress at the FA inlet), and in case of the very unlikely ULOF+ULOHS event, when the time-to-failure reduces down to a few hours, but still leaving enough grace time for corrective operator actions;

• Fuel melting is excluded in all simulated transients except for local fuel melting (in the fuel pellet center) in the hottest FAs in case of reactivity insertion involving core compaction or core voiding due to passage of steam bubbles transported at the core inlet following the steam generator tube rupture event;

• The vessel integrity is guaranteed in the long term in all simulated transients except for the ULOHS transient, but even in this case there is enough grace time for corrective operator actions.

As a general conclusion, no relevant safety issues have been identified for ALFRED in case of representative DEC events. In particular, the ULOF transient can be accommodated without the need of corrective operator actions. Finally, the analysis of DEC transients for the lead-cooled ALFRED design has demonstrated the extremely forgiving nature of this plant when compared to other similar plant designs. A comprehensive presentation of DEC transients can be found in [9].

Results and Discussion

The technology and structure of the advanced nuclear reactors of the new generation are the same as the fourth generation (modular) reactors. In recent years, the desire to build advanced reactors with high safety and optimal economic conditions is due to the need for production units in power networks, especially in remote areas and the sparsely populated cities are increasing. The main characteristics of these advanced reactors are high inherent safety, simplicity of equipment, longer operation time, no need for refueling for several years, higher efficiency and, lower operating cost. In this research, according to the main structure and characteristics of the core of one of these types of advanced reactors named Alfred, using the MCNPX 2.6 code and the design stages of the core, which includes the fuel assembly, control rods, safety rods and other components, it was carried out and it is compared with sources and references and can be commercialized.

References

[1] SNETP Strategic Research and Innovation Agenda, February 2013

[2] LEADER project, www.leader-FP7.eu.

[3] M. Frogheri, A. Alemberti, L. Mansani, “The Lead Fast Reactor: Demonstrator (ALFRED) and ELFR Design”, International Conference on Fast Reactors and Related Fuel Cycles: Safe Technologies and Sustainable Scenarios (FR13), Paris, France (2013).

[4] G. Grasso, C. Petrovich, K. Mikityuk, D. Mattioli, F. Manni, D. Gugiu, "Demonstrating the effectiveness of the European LFR concept: the ALFRED core design", (FRl 3), Paris

[5] C. Artioli, G. Grasso, and C. Petrovich, "A new paradigm for core design aimed at the sustainability of nuclear energy: The solution of the extended equilibrium state", Ann. Nucl. En. 37(7):91 5-922 (2010).

[6] A. Alemberti, L. Mansani, G. Grasso, D. Mattioli, F. Roelofs, D. De Bruyn, "The European Lead Fast Reactor Strategy and the Roadmap for the Demonstrator ALFRED", (FRl 3), Paris

[7] E. Bubelis, M. Schikorr, M. Frogheri, L. Mansani, G. Bandini, L. Burgazzi, K. Mikityuk, Y. Zhang, R. Lo Frano, N. Forgione "LFR safety approach and main ELFR safety analysis results" (FRl 3), Paris, France (2013).

[8] E. Bubelis, M. Schikorr, L. Mansani, G. Bandini, K. Mikityuk, Y. Zhang, G. Geffraye "Safety analysis results of the DBC transients performed for the ALFRED reactor" (FRl 3), Paris

[9] G. Bandini, E. Bubelis, M. Schikorr, M.H. Stempnievicz, A. Lázaro, K. Tucek, P. Kudinov, K. Kööp, M. Jeltsov, L. Mansani "Safety Analysis Results of Representative DEC Accidental Transients for the ALFRED Reactor" (FRl 3), Paris, France (201 3).

[10] ARCADIA project, http://arcadiaproject.eu.

[11] Toshinsky, G.I., et al., 2002, "Safety Aspects of SVBR-75/1 00 Reactor", Advanced Nuclear Reactor Safety Issues and Research Needs, Proceedings of OECD/NEA Workshop, Paris, France.

[12] Adamov, E.O., 2001, "White Book of Nuclear Power", N.A. Dollezhal Research Development Institute of Power Engineering, Moscow, Russia

[13] Novikova, N., Pashkin, Y., Chekunov, V., 1999, "Some Features of Sub-Critical Blankets Cooled with Lead-Bismuth", Proceedings of ADTTA'99, Praha, Czech Republic.

[14] Wider, H., Carlsson, J., Dietze, K., Konys, J., 2003, "Heavy-Metal Cooled Reactors – Pros and Cons", Proceedings of GLOBAL'03, New Orleans, USA.

[15] Tucek, K., et al., 2004, "Coolant Void Worth in Fast Breeder Reactors and Accelerator-driven Transuranium and Minor-Actinide Burners", Annals of Nuclear Energy, Vol. 31, p. 1783

ICNST 2024 International Conference on Nuclear Science and Technology
6- 8 MAY 2024 | Isfahan, Iran

Nano Materials in Pressurized Water Nuclear Reactor (Paper ID : 1038)

Rahgoshay M. Correspondent[1*], Amanelahi Dorcheh L. Co-Author[2]

[1,2]Department of Nuclear Engineering, Science and Research Branch, Islamic Azad University, Tehran, Iran

Abstract

Nanomaterials have emerged as a promising avenue for enhancing Pressurized Water Nuclear Reactor (PWR) fuel performance and safety in the nuclear energy sector. This article provides an overview of the potential applications of nanomaterials in PWR fuel. By incorporating nanoscale particles into the fuel matrix, thermal conductivity can be improved, leading to enhanced heat dissipation and higher power densities in the coolant. Additionally, nanomaterials reinforce fuel pellet durability, preventing the migration of fission products and extending the lifespan of fuel assemblies. The use of nanomaterials also contributes to enhanced safety and accident tolerance by providing corrosion resistance in the clad and reducing hydrogen gas generation during accidents in the core. Furthermore, nanomaterials can mitigate radiation damage through radiation absorption and self-healing properties. The integration of nanomaterials into PWR fuel presents an opportunity to advance nuclear energy by optimizing power generation, improving safety margins, and increasing overall reactor efficiency. Further research and development in this field will pave the way for a sustainable and resilient nuclear energy future.

Keywords: nanomaterials- pressurized water nuclear reactor- nuclear code- nuclear fuel rod- power density- reactor efficiency

Introduction

With the rising global energy demand, the potential of nuclear energy, as a low-carbon energy resource, is becoming more and more obvious. But if nuclear energy is going to achieve its full potential, four grand challenges such as the maximization of application of available nuclear fuel uranium, the lifetime maximization of today's nuclear power plants, the resistance towards nuclear proliferation, and the minimization of nuclear waste via reasonable reprocessing and treatment must be fulfilled. New types of materials with unique behaviors and functions are considered to be central to meet all the four challenges. [1]

In its Research and Development Roadmap - Report to Congress dated April 2010, the Department of Energy (DOE) Office of Nuclear Energy clearly identified four research and development objectives, among which include, Developing technologies and other solutions that can improve the reliability,

sustain the safety, and extend the life of current nuclear reactors," Develop Improvements in the Affordability of New Reactors," and Develop Sustainable Nuclear Fuel Cycles". Scientific communities around the world are working towards achieving these objectives and demands in various ways, including via Nuclear Nano-Technology (NNT), which is an efficient tool and candidate for achieving the goal of utmost safety and performance. Nanotechnology is one of the fastest growing new areas in science and engineering. The subject arises from the convergence of electronics, physics, and chemistry, biology and material sciences to create new functional systems of nanoscale dimensions. Nanotechnology deals with science and technology associated with dimensions in the range of 0.1 to 100nm. The ability to fabricate structures with nanometric precision is of fundamental importance to any exploitation of nanotechnology. Nuclear power has evolved into a mature technology since its development in the 1950s, relying on materials that have reached near maximum performance levels. However, the challenges faced by nuclear power are deeply rooted in the limitations of these materials. Over time, the potential for significant improvements has become minimal. [1]

Pressurized Water Reactors (PWRs) are vital for the global generation of nuclear power, supplying a substantial portion of the world's electricity. To further enhance the safety and efficiency of PWRs, researchers have turned their attention to the potential applications of nanomaterials. Nanomaterials possess unique properties at the nanoscale, offering exciting opportunities for advancements in various aspects of PWR technology. Interestingly, while the benefits of nanotechnology in nuclear applications are promising, there are complexities and challenges that must be addressed. For instance, the impact of nanoparticles on the thermal-hydraulic and neutronic parameters of reactor cores is a critical area of study. Nanoparticles such as Al2O3 and ZrO2 have been shown to improve the thermal conductivity of coolants, which can lead to more efficient heat transfer and potentially affect the reactivity coefficients in reactors like the VVER-1000. However, the deposition of nanoparticles on fuel cladding could influence neutron flux and effective multiplication factors, which are essential for maintaining reactor safety. In summary, the integration of nanotechnology into nuclear reactors, specifically through Nano-enhanced fuels or coolants, offers a pathway to improve reactor performance and safety. Research indicates that nanoparticles can significantly enhance thermal properties and influence core reactivity, although the full implications on reactor dynamics and safety are still under investigation. Continued research is necessary to fully understand and harness the benefits of nanotechnology in nuclear reactors, ensuring that any advancements contribute positively to the operational and safety characteristics of

these complex systems [2]. This article delves into the role of nanomaterials in PWRs, with a particular focus on their applications in enhancing safety, performance, and overall efficiency.

Area of Nuclear Nano-technology:

NNT research focuses on various aspects of nuclear energy to enhance safety and performance. This literature review groups ongoing NNT research under the following key areas, where engineered nanoparticles, nanoscale materials, properties, or processes are used to enhance mechanical, chemical, physical, or thermos-hydraulic properties and performance in nuclear energy systems.

Nano-technology Engineered Fuels:

Nanotechnologies show promise for engineering nuclear fuels with enhanced properties by incorporating nanoparticles, which could improve radiation tolerance, fission gas retention, heat transfer, and extend fuel lifetimes and burn-up . Fuels designed or produced with nanotechnologies can enhance service lives, avoid losses during the fabrication process, and avoid the potential for failure in normal or accidental conditions, such as increased fission gas retention, plasticity, radiation tolerance, and heat transfer capability, as well as reduced fuel cladding chemical and mechanical interactions. As a result, the fuel burnup is improved and the refueling period increases. The main factors which determine the radiation resistance of structural materials for nuclear reactor are: void swelling, radiation creep, high- and low-temperature radiation embrittlement and also the radiation stability of structure and properties of material in the field of neutron irradiation. [1]

Advanced fuels designed and/or produced with nanotechnologies to enhance service lives, avoid losses during the fabrication process, and/or avoid the potential for failure in normal or accidental conditions, such as increased fission gas retention plasticity, radiation tolerance, and heat transfer capability, as well as reduced fuel cladding chemical and/or mechanical interactions. Uranium is the most common fissile material used in the nuclear reactors. Naturally-mined uranium has 99.24% U238, 0.72% U-235, and 0.0054% U-234. U-235 is a fissile isotope, which undergoes fission reaction upon absorption of slow or thermal neutrons (neutron having energy < 0.4 eV). Most common reactors are Light Water Reactors (LWR) of two types: Pressurized Water Reactors (PWR) and Boiling Water Reactors (BWR), which require U-235 content in the fuel from 0.7% to 3.5% to sustain fission reaction. However, there is some interest to take U-235 enrichment levels even closer to 20% as high-assay low enrichment uranium (HALEU) for some special reactor fuels. In order to enrich the percentage, methods like gaseous diffusion, gas centrifuge, jet nozzle/aerodynamic separation, and electromagnetic separation have been

used. In its enriched form, uranium dioxide is the major component of nuclear fuel. Wu reported the synthesis of high quality, colloidal uranium oxide nanocrystals by thermal decomposition of uranyl acetylacetonate in a mixture solution of oleic acid (OA), oleylamine (OAm), and octadecene with characteristic high reaction- yield of 75% and high reproducibility. As shown in Figure1 the X-ray diffraction (XRD) pattern confirmed that the nanocrystals were pure uranium dioxide, and the transmission electron microscopy (TEM) showed that the periodical pore structures have diameters in the nanometer scale and were available within the nanocrystals. They reported that the size of the nanoparticles and the pore size could be controlled by changing the ratio of the organic additives in the reactions and these UO3 nanocrystals could be developed as a candidate of potential Nano-fuels. The purpose of the evenly distributed pores was reported as to adsorb and accommodate the highly reactive fission products such as iodine, which can react with the clad under extreme conditions, and then mitigate fuel fuel-clad or other undesirable chemical interactions. Nanotechnologies show potential to engineer nuclear fuels with enhanced properties. Incorporating nanoparticles into fuel matrices could improve radiation tolerance, fission gas retention and heat transfer, extending fuel lifetimes and burn-up. [2]

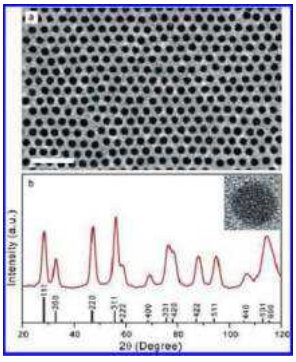

Fig1. (a) A TEM image of UO2 nanocrystals made in the typical synthesis. The scale bar is 30 nm. (b) XRD pattern of the UO2 nanocrystals. The standard diffraction peak positions and relative intensities of bulk cubic UO2 are indicated. The inset shows a HRTEM image (6.5 nm ×6.5 nm) of the nanocrystal sample. [2]

In their review paper entitled Nanomaterials and nanotechnologies in nuclear energy chemistry, discussed the research in nanomaterials and nanotechnologies for advance nuclear fuel fabrication highlighted and reported the research on uranium dioxide nanocrystals for nuclear fuel in the journal Nature Nanotechnology under the title, Uranium dioxide: Nano goes Nuclear. The research on UO2 Nano porous materials, in controlling their size and structure and its ability to adsorb fission products, are milestones of success for achieving the possibility of engineered nanomaterial in nuclear reactors.

The development of such materials as nuclear fuels will certainly enhance the thermal and radiation stability of the fuel and consequently can improve its burn-up. [2]

Nanomaterials for Fission Product Capturing:

Chemical interaction and separation methods by utilizing properties of nanoparticles and/or nonporous materials to adsorb fission product gases either from reprocessing operations or directly within a reactor fuel assembly. This avoids the potential for releases from normal or accident conditions. Reactor grade materials that could improve mechanical performance as well as radiation tolerance. Or nanoparticles dispersed coatings that could be included on the exterior or the interior of reactor core components to improve corrosion resistance, surface hardening, and clad interactions on the cladding interior. [2]

Capturing fission product either from reprocessing operations or directly within a reactor fuel assembly is of prime importance because it can prevent potential danger of material failure and thus can avoid accident. There is worldwide interest in the effective capture and storage of radioiodine, as it is both produced from nuclear fuel reprocessing and commonly released in nuclear reactor accidents. In 2012, Sava et al. [19] reported that ZIF-8 is ideal for capture and interim storage medium for volatile gaseous I2. This study can increase awareness and impact the use of Metal--Organic Framework (MOF) in the capture of related fission product gasses. In 2012, K. W. Chapman et al. [20] investigated the most effective way for capturing I2 using silver-containing Zeolites Mordenite (MOR). The capture of I2 by both silver-exchanged and reduced silver MOR was investigated. The result showed that the structure and distribution of the AgI has been correlated with the reduced silver during iodine capture. As depicted in Figure 2, the reduced Ag0 stays on the surface of the Zeolite, captures I2 to form 3nm AgI nanoparticles and then migrates to the center of the pores and in this case, mobility depends on Ag and I. for the unreduced silver-exchanged MOR, the sub nanometer AgI clusters are formed inside and confined to the pores. This may give rise to further possibility of the radioactive iodine capture for storage by using pore-blocking method. Nanomaterials may also efficiently capture radioactive fission gases released during normal operations or accidents, helping to prevent potential failures and accidental releases. [2]

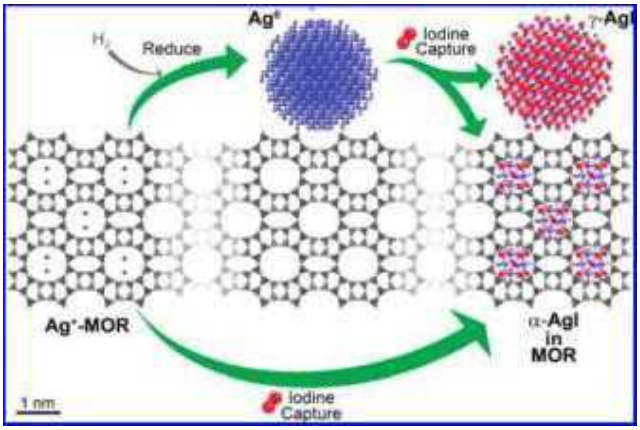

Fig2. A schematic of iodine captured by silver-containing MOR. While prereducing the silver MOR yields in a mixture of γ-AgI nanoparticles and subnanometer R-AgI, direct iodine uptake by silver-exchanged MOR produces exclusively subnanometer R-AgI. [2]

Nanotechnology Enabled Radiation Sensors, Detectors and Monitors:

Sensors, detector and/or in-service monitors developed by using nanomaterials that can directly monitor for radiation, temperature, pressure, in-situ diagnostics of material properties and mechanical response, corrosion, neutron flux, stress/strain or even chemistry with little effect on system performance with significantly reduced size and weight and increased sensitivity, performance, and functionality. Nanotechnology enabled sensors and/or in-service monitors can directly monitor the properties of a material under extreme conditions, such as radiation, temperature and pressure. Real time investigations of material properties and mechanical response along with corrosion, neutron flux, stress/strain or even chemistry with nominal effect on system performance by significant modification in shape, size, structures and morphology could be utilized for enhanced. [2]

Nuclear Waste Separation and Reprocessing Nanotechnology:

Chemical interaction and separation methods using nanoparticles and/or nonporous materials for separating the actinides and other radioactive elements from the nuclear waste for reprocessing, recycling and reusing.

Nanotechnology Aided Reactor Materials:

Oxide dispersion strengthened (ODS) alloys typically consist of a high-temperature metal matrix such as iron aluminide, iron chromium, iron-chromium-aluminum, nickel chromium or nickel aluminide - with small (5-50 nm) oxide particles of alumina (Al2O3) or Yttria (Y2O3) dispersed within it. ODS alloys exhibit ideal corrosion resistance and mechanical properties at high-temperature. They possess excellent creep resistance, which originates partly from the dispersion of oxide and other particles, and

partly from the very large elongated grain structure. ODS materials are interesting for future nuclear applications.The added advantage is, compared with the conventional ODS steels, nanostructured ODS steels have proven to show better performance in radiation resistance, corrosion resistance and tensile strength. [26-28] With all these promising properties and mechanical stability, they are more likely to be considered as serious candidates for future generation nuclear reactor high-temperature applications. Through past research, nanostructured ODS alloys have been shown to exhibit excellent creep properties, improved hardness, tensile strength, corrosion resistance, and thermal stability. These properties were excellent when compared to a V4Cr4Ti alloy that failed after 4,029 hours and 52% elongation tested at the same temperature but at a significantly lower stress of 77 MPa.[26] Y or Y-Ti Nano precipitates can reduce creep rates by six orders of magnitude at temperatures from 650 °C – 900 °C. [2]

Separation Nanotechnology and Reprocessing for Nuclear Waste:

Even though nuclear power generation is a very efficient source of energy to supply the enormous energy demands, the waste management and safe disposal of the high-level waste produced during the reprocessing of the spent fuel is a big issue to resolve for nuclear plant operation. The spent fuel contains long lived actinides such as Uranium (U), Plutonium (Pu), Americium (Am) and Curium (Cm). The reprocessing of the spent fuels comprises of the methods for the recovery of such actinides from the waste material and the recovered actinides can be reused, which diminishes hazardous radiation that could deteriorate the environment. There have been a number of techniques developed already for the nuclear fuel reprocessing such as solvent extraction, ion exchange, electro photolysis, precipitation, magnetic separation, volatilization, and molten fuel and coolant salt processing. However, the traditional methods to remove heavy metals from industrial wastewater are not cost-effective and clean technologies due to their common drawbacks such as low selectivity, high capital and energy costs, slow separation kinetics, and secondary waste generation. Nanomaterials, due to their large specific surface areas and novel physical and chemical properties, have become more attractive in wide areas of research, including nuclear waste separation and reprocessing. The drawbacks of traditional methods of removing nuclear waste can be tackled by utilizing the unique properties of the highly selective nanomaterials. In this section, we briefly review the novel emerging nanomaterials for nuclear waste separation nanotechnology: magnetic nanoparticles, carbon nanotubes, mesoporous material and magnetic composites. [3]

Challenges and limitations of applying nanomaterials:

Some points on the challenges and limitations of applying nanomaterials in each application area of nuclear technology that it could expand on include:

For Nano-engineered Fuels:

Compatibility of nanoparticles with fuel matrix and cladding materials over long periods needs testing.

Potential for nanoparticles to agglomerate or leach out of the fuel.

Uniform dispersion of nanoparticles during fuel fabrication a challenge.

For Fission Product Capture:

Materials must be able to withstand high temperatures and radiation inside reactors

Adsorption/desorption kinetics and capacity over multiple cycles needs evaluation

Eluting captured gases without damaging capture material is difficult

For Radiation Sensors/Monitors:

Sensors must be reliable in harsh reactor environments for decades

Effects of radiation on sensor response and lifetime requires study

In-situ monitoring poses integration challenges in small spaces

For Waste Processing Nanomaterials:

Adsorption selectivity between different ions/molecules should be verified

Scale-up for industrial volumes of waste presents engineering issues

Recovery of adsorbed materials post-use needs development

For Reactor Materials:

Long-term compositional and mechanical stability under irradiation

Grain growth and phase stability at high temperatures and doses

Fabrication processes may be expensive and difficult to industrialize

Providing more discussion of such technical challenges would help acknowledge research still needed before commercialization. [1]

Conclusion

The basic research progress has been highlighted in nanomaterial and nanotechnologies for advanced nuclear fuel fabrication, structural and operational material such as cladding and cooling fluid for fission and fusion reactors and Thermal Energy Storage for advanced reactor. It is clear that improvements are needed for all, from the manufacture of nuclear fuel to structural materials and other applications, and a slight improvement in each of these areas will certainly contribute to the advancement of performance

and safety in nuclear energy systems. There are many hurdles to tackle before nanoparticles can be safely and effectively used in operating power plants and other sectors of nuclear industry. Scaling up particle production to the large volumes of particles necessary for implementation in a power plant is expensive and labor intensive. New synthesis infrastructures may be necessary for large-scale production of these tiny particles. Additionally, broad adoption of this technology will not occur until significant cost savings are proven effective at a functioning plant. As a result, particles must be made available at a cost reasonable for adoption.

In addition to cost-benefit analysis, extensive testing must be performed to ensure long-term application of these particles does not threaten the operational safety of the plant. To accomplish this, smaller scale reactors (research reactors) may test these particles over the course of years to track the impacts of long-term use. Potential pitfalls include increased corrosion, system clogging, and nanoparticle leakage into wastewater. Corrosion engineers will be needed to validate the degree to which nanoparticles contribute to the overall aging of reactors in which they are used. [1]

The development of new nanomaterials and use of nanoparticles in nuclear power plant construction has the potential to increase safety, stability, durability, and reduce the need for regular inspections. However, from the point of view of current international research status, nanomaterials and nanotechnologies in the field of nuclear energy are infancy in term of technology readiness level. There are still huge key scientific issues that should be addressed. With the deepening of the further research work, the advantages of nanomaterials and nanotechnologies will be found out step by step. [1]

Indeed, the integration of nanomaterials, nanocomposites, and micro-Nano-nuclear materials into pressurized water nuclear reactors (PWRs) can bring several benefits and advancements to enhance safety, efficiency, and overall performance. These advanced materials offer unique properties and characteristics that can address various challenges faced by the nuclear power industry. Here are some key points highlighting their potential contributions:

Thermal Conductivity: Nanomaterials can enhance the thermal conductivity of materials used in PWRs. This improved heat transfer capability can lead to more efficient cooling and ultimately increase the power output of the reactor.

Fuel Durability: Nanomaterials integrated into fuel rods can enhance their mechanical strength and resistance to radiation damage. This can prevent fuel failures, reduce the risk of accidents, and extend the lifespan of fuel assemblies.

Corrosion Resistance: Nanocomposite coatings can be applied to reactor components to improve their corrosion resistance, particularly in high-temperature and high-pressure environments. This helps to ensure the integrity and longevity of the reactor system.

Radiation Absorption: Nanomaterials can be used to develop advanced radiation shielding materials that efficiently absorb and attenuate radiation. This enhances the safety of workers and reduces the environmental impact of nuclear power generation.

Safety Margins: The integration of micro-Nano-nuclear materials can enhance safety margins in PWRs. By improving fuel rod performance, preventing fuel failures, and optimizing reactor materials, the risk of accidents and fuel leaks can be minimized.

Increased Efficiency: Nanomaterials can contribute to increased reactor efficiency by optimizing fuel performance, reducing fuel consumption, and enhancing heat transfer processes. This leads to improved power generation and a more sustainable use of nuclear energy.

To fully realize the potential benefits of nanomaterials in PWRs, further research and development efforts are necessary. This includes exploring new nanomaterial compositions, evaluating their long-term behavior under extreme conditions, and ensuring their compatibility with existing reactor designs and safety regulations. By continued advancements in this field, the integration of nanomaterials can contribute to a resilient and sustainable future for nuclear energy.

References

[1] A. Z. P. R. Z. a. Seyed Kamal Mousavi Balgehshiri1*, "Review on Nanotechnology Applications," *corpuspublishers,* vol. 2, no. 2, 2022.

[2] L. Popa-Simil, "Nuclear Power Renaissance Based on Engineered Micro-Nano-Nuclear Materials," *Energy and Power Engineering,* pp. 65-74, 2021.

[3] L. R. a. S. J. A. a. Q. Y. Khanal, "Advanced nanomaterials for nuclear energy and nanotechnology," *Energy Technology,* vol. 8, p. 1901070, 2020.

[4] T.-. S. A.-. K. A. Hassan, "Functional nanocomposites and their potential applications: A review," *Journal of Polymer Research,* pp. 1-22, 2021.

[5] N.-. K. I.-. F. W. Baig, "Nanomaterials: A review of synthesis methods, properties, recent progress, and challenges," *Materials Advances,* pp. 1821-1871, 2021.

[6] M.-. T. S.-. S. D. K. Mittal, "Biopolymeric Nanocomposites for Wastewater Remediation: An Overview on Recent Progress and Challenges," *Polymers,* p. 294, 2024.

[7] M.-. A. F.-. B. P. S.-G. L. Khakbiz, "Characterization and fractal modeling of boron carbide nanoparticles synthesized by nanomilling," *Physica B: Condensed Matter,* pp. 132-140, 2019.

[8] "http://nanotechnologytoday.blogspot.com/2010/04/safer-nuclear-reactors-could-result.html," [Online].

[9] O. K.-. S. A.-. A.-A. K. Siddiqui, "A Comprehensive Review on the Use of Nanoparticles in Nuclear Power Plants," *Arabian Journal for Science and Engineering,* pp. 1-25, 2023.

[10] L.-. S. X.-. G. F.-. L. J.-. Y. C.-. S. Z.-. X. R. Wu, "Enhanced thermal transport properties of graphene/SiC heterostructures on nuclear reactor cladding material: A molecular dynamics insight," *Nanomaterials,* vol. 12, no. 6, p. 894, 2023.

[11] D. L. Chandler, "Aluminum used in nuclear reactors and other harsh environments may last longer with," https://phys.org/news/2016-03-aluminum-nuclear-reactors-harsh-environments.html#google_vignette, 2016. [Online].

[12] "https://eng.libretexts.org/Bookshelves/Materials_Science/TLP_Library_II/4%3A_Materials_for_Nuclear_Power_Generation/4.5%3A_Fuel_and_Cladding," [Online].

[13] E. a. R. A. Y. a. W. Gerber, "Insight into the structure--property relationship of UO 2 nanoparticles," *Inorganic Chemistry Frontiers,* vol. 8, pp. 1102--1110, 2021.

[14] F. Golgovici, A. Tudose, D. Diniasi, R. Nartita, M. Fulger and I. Demetrescu, "Aspects of Applied Chemistry Related to Future Goals of Safety and Efficiency in Materials Development for Nuclear Energy," *Molecules,* vol. 28, p. 874, 2023.

[15] A. a. V. a. K. a. K. a. K. a. Lytovchenko, "Nanostructural Materials in the Nuclear Engineering," *East European Journal of Physics,* 2013.

ICNST 2024 International Conference on Nuclear Science and Technology
6- 8 MAY 2024 | Isfahan, Iran

Predicting the thermal-hydraulic and natural circulation parameters in the Natural Circulation Integral Nuclear Reactor Core with dual-cooled annular fuel via CFD modeling as well as Fuel Geometry Optimization based on the ANN-GA approach (Paper ID : 1039)

S. Nasiri[1], G.R. Ansarifar[*], M.H. Esteki
[1]Department of Physics, Faculty of Nuclear Engineering, University of Isfahan, Postal Code: 81746-73441, Isfahan, Iran

Abstract

This paper studies the optimization of dual-cooled annular fuel to improve heat transfer and safety performance of the CAREM-25 as a natural circulation integral nuclear reactor with hexagonal fuel assemblies. At first, comprehensive neutronic simulation and computational fluid dynamics (CFD) are employed to design a reactor core using dual-cooled annular fuel. Indeed, the internal and external radius have been changed in such a way to maintain the reactor under-moderated. Then, thermal-hydraulic and natural circulation parameters are performed for a simulated fuel rod in the hot channel using computational fluid dynamics (CFD) simulation code. These results are compared with the conventional CAREM reactor.

Next, a developed Artificial Neural Network (ANN), utilizing the obtained data, predicts the thermal-hydraulic and natural circulation parameters of the CAREM-25 reactor core with dual-cooled annular fuel. Achieving the optimal inner and outer radius of fuel by implementing Genetic Algorithms (GA), based on the developed ANN results, is the main goal of this study.

So, the optimal geometry of fuels is determined using the neural network by implementing the genetic algorithms. Indeed, the developed Artificial Neural Network (ANN) utilizing the obtained data, predicts the thermal-hydraulic and natural circulation parameters of the CAREM reactor core with dual-cooled annular fuels. Presented optimization algorithm, which has a significant ability to attain the best solutions, also determines the optimal values of natural circulation parameters (V_{max}/V_{avg}, V_{out}-V_{in}, and pressure drops), heat transfer coefficients, and MDNBR of the reactor. Also, the designed artificial neural network and genetic algorithm has been validated using thermal-hydraulic calculations. Results indicate the potential of the proposed dual-cooled annular fuel to increase thermal and safety performance.

Keywords: Dual-cooled annular fuel, CFD, Natural circulation, thermal-hydraulic parameters, Artificial Neural Network (ANN), Genetic Algorithm (GA).

Introduction

Small integrated reactors (SMR) are reactors with a power output of less than 300 MW. The smaller and more compact design allows you to transport them by rail or truck to the site of the nuclear power plant possible. SMR is one of the advantages of lower initial investment, scalability, and flexibility of location in places where conventional large reactors can not be located. These reactors also have more safety and security [1]. Recently, there is a tendency towards smaller power generation units to be able to supply electricity to remote areas and to create systems with more energy distribution [1]. CAREM-25 is an integral type PWR based on an indirect steam cycle, with distinctive features that simplify the design and support achieving a higher safety level. Some design characteristics are integratedprimarycooling systems, in-vessel hydraulic control rod drive mechanisms, and safety systems relying on passive features. Coolant flow in the primary reactor system is done by natural circulation. And it has 61 hexagonal fuel assemblies with 127 rods. This reactor is an integrated pressurized light water reactor (IPR) based on an indirect cycle with excellent characteristics and makes it possible to achieve a higher level of safety. Also in this type of reactor, moderating and cooling with light water is performed. The primary circuit is completely located in the reactor vessel, which means that a self-pressurized reactor with 12 steam generators is inside the reactor pressure vessel, which is operated by natural circulation. This design minimizes the risk of loss of cooling events (LOCAL). The thermal power of this reactor is 100 MW (25 MW electric). The core is loaded with standard fuel elements with 1.8% to 3.1% enriched uranium in 61 hexagonal fuel assemblies, and the process of refueling is done annually.The CARE reactor pressure vessel includes the core, the steam generator, the entire primary circulate cooling system, and the mechanism for moving the absorber rods. The diameter of the pressure vessel is about 3.2 meters and its length is 11 meters. Each fuel assemblies have 108 fuel rods, 18 absorber rods,and 1 instrumentation guide tube. Its fuel is UO2 enriched. Core reactivity is controlled by neutron poison (Gd2O3) that is used in certain fuel rods. The main purpose of the reactor is to provide electricity to remote areas for research, or desalination of water [2]. Most nuclear reactors today use solid fuel rods.The work done in the field of neutron analysis of the core of this solid fuel reactor can be used, for example, by Mr. Ashlar. From Shiraz University [3], Mr. Villain from Brioche Argentina mentioned [4].

In recent years, the MIT Institute has conducted research on dual-cooled annular fuel. Also, researches have been done to investigate the neutron and thermal-hydraulic evaluation in the Nuscale reactor and also VVER-1000 reactor by Ansarifar [5 and 6], in the field of using dual-cooled annular fuel in these

reactors. It should be noted that in none of the previous researches in this type of reactor with hexagonal fuel assemblies, dual-cooled annular fuel has not been used. Studies indicate that artificial neural networks (ANNs) have the ability for the accurate prediction of complex functions [7]. ANNs have simplicity, high proceeding speed, and broad capability [8]. The results indicate an acceptable convergence between ANN and EXPERIMENTAL data. The predicted data by the ANN can be inputs to optimization algorithms for obtaining better performance of optimizing methods. Optimizing inner and outer radius in dual cooled annular fuels to attain the best design based on the selected criteria, such as maximizing power, reliability, and efficiency, is the objective of many recent researches. Based on the discussion above this study, assesses the applicability of ANN, a genetic algorithm to model and optimize the thermal-hydraulics and neutron parameters of dual-cooled annular fuels. The flux used to simulate the thermo-hydraulic core of the CAREM-25 reactor is obtained by the neutron code WIMS and CITATION, then given by User-Defined Function (UDF) it is given to Computational Fluid Dynamics (CFD) and perform thermo-hydraulic calculations for each internal radius in the appropriate fuel pitch, then define all the outputs in ANN and get the optimal internal and external radius as well as the optimal thermal-hydraulic parameters, and modeled this optimal core and compare it with the core without the dual-cooled annular fuel. The results show that the use of this type of fuel has a better heat convection coefficient, higher safety, and more natural fluid circulation, so the use of this type is efficient.

Core modeling and Thermal-hydraulic analysis

The main purpose of the reactor is to provide electricity to distant areas, research, or desalination of water. Important parameters in reactor design are given in Table 1 and Fig1 shows the reactor pressure vessel.

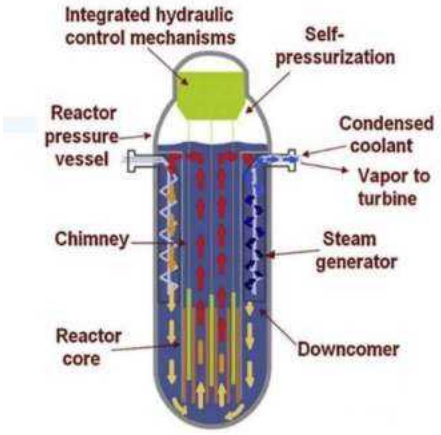

Fig.1. CAREM-25 reactor pressure vessel.

Table1. Parameters of small CAREM integrated reactor with hexagonal fuel assemblies [8].

System pressure (MPa)	12.25
RPV height (m)	11
RPV diameter (m)	3.2
Coolant temperature, Core inlet (^{0}C)	284
Coolant temperature, Core outlet (^{0}C)	326
Fuel active length (m)	1.4
Number of fuel rods in fuel assembly	108
Number of instrumentation guide tubes in F.A.	1
Number of control rod guide tube	18
The pitch of the fuel rod (mm)	13.8
The pitch of fuel assemblies (mm)	160
Number of the fuel assembly	61
The outer diameter of fuel rod (mm)	9
Clad thickness (mm)	0.625
The outer diameter of control rod (mm)	8.5
Control rod clad thickness (mm)	0.65
Control rod material	Ag – Cd – In
Number of FAs with burnable absorber	36
Number of FAs without burnable absorber	25

In this reactor, core reactivity is controlled by using Gd_2O_3 in some fuel assemblies. In some fuel assemblies, there are 12 and in some 18 burnable absorber rods. The control rods in this reactor are divided into several groups. The first group is for adjusting and controlling the reactor power, which includes 12 or 18 control rods in 19 fuel assemblies that enter the guide tubes. The second group is the rapid extension system (RES) which has been designed to apply in 6 fuel assemblies. The main role of this group of control rods is to shut down the reactor under normal or transient operating conditions. However, three other fuel assemblies remain, and additional control rods are designed for them. In this research, simulations for CAREM fuel assemblies were performed by WIMS code and a cluster fuel model was used for more accuracy. However, the code calculated the neutron transport equation for the four types of fuel assemblies used with 40 radial meshes using the DSN method.

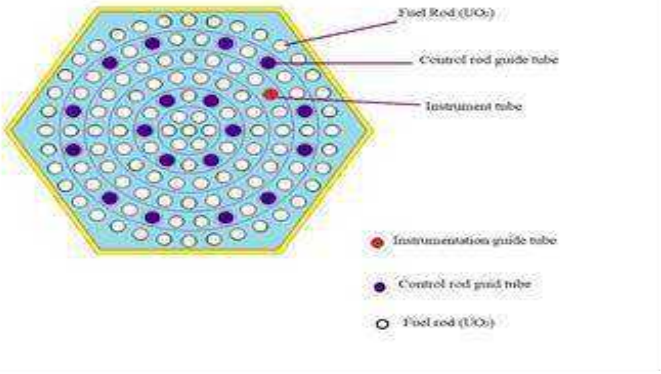

Fig.2. The FAs type pure UO2 simulated by WIMS code.

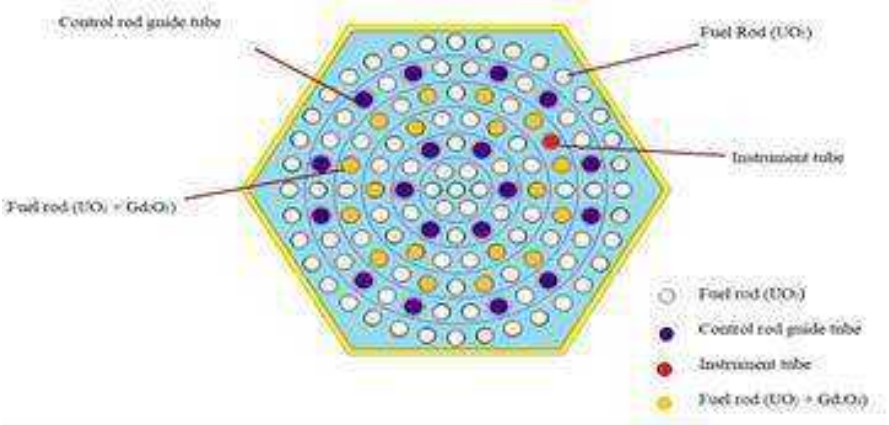

Fig.3. The FAs type UO_2+Gd_2O_3 simulated by WIMS code.

To obtain the heat flux of the CAREM reactor core, from the WIMS code, which is obtained in twogroups of fast and thermal, must be introduced the group data extracted to citation. CITATION computer code performs the reactor core simulation. The microscopic cross-sections obtained from WIMS are set as inputs to CITATION. In the citation code, full core geometry was simulated, however, each fuel assembly was divided into 7 meshes in the radial direction, and 14 regions and placed next to each other in the axial direction.

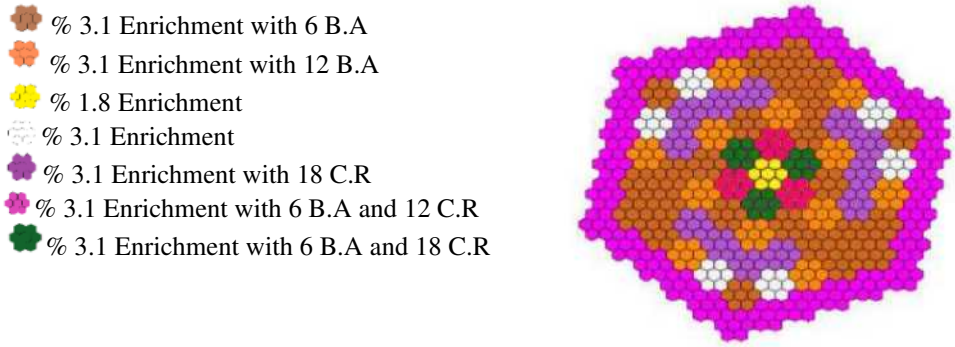

Fig 4. CAREM reactor core arrangement with solid fuel and 35% control rod entry.

As shown in Fig.4, 36 FAs of 61 FAs contain UO_2+Gd_2O_3 mixed fuel rods. Some FAs have 12 UO_2+Gd_2O_3 composite rods and some of them have 6 UO_2+Gd_2O_3 composite rods. The remaining 25 FAs have pure UO2. The FAs with UO_2+Gd_2O_3 composite rods have an 8% concentration of Gd_2O_3. The enrichment of pure UO2 fuel rods is 1.8% and 3.1%, but the enrichment of UO_2+Gd_2O_3 fuel rods is 3.1%. Also as shown in Fig.4, in 18 fuel assemblies 35% control rods are inserted, in 3 of which 12 control rods are inserted, and in the remaining 12, 18 control rods are inserted. In this study, we study the earlier stated objectives for dual-cooled annular fuel by changing the inner and outer radius using coupled WIMS-CITATION and CFD codes with keep minimize the gap-to-gap distance (2.5 mm). We acquire the maximum power density from the neutronic design in full power. The hottest channel, which has the maximum RPPF, is determined for each model. We select the hot channel of the core in the current CFD model to analyze and evaluate the performance of dual-cooled annular fuel in the thermal-hydraulic system. The next step is the hot channels' thermal-hydraulic design and analysis. For thermal-hydraulic analysis, first, the equivalent cell was designed for each internal radius and then the equivalent cells obtained by simulating the Computation Fluid Dynamic (CFD) were analyzed by thermal-hydraulic software. For Thermal-hydraulic analysis of the reactor core, neutron calculations were performed in the hot channel (where radial PPF occurred), then the equivalent cell dimensions for the desired fuel rod were obtained by its fuel pitch in the hot channel for each desired inner radius.

$$R_{cell} = P\sqrt{\frac{\sqrt{3}}{2\pi}} \qquad (1)$$

In this equation, P is the designed fuel pitch and R_{cell} is the equivalent cell radius that we obtain and use in thermal-hydraulic simulation so we simulate the equivalent cell using FLUENT as a CFD code to analyze thermal-hydraulic parameters. Therefore, according to the formula, when we find the equivalent cell diameter in our hexagonal assembly, we design the equivalent cell, which includes the coolant and the reactor core, as shown in Figure 5.

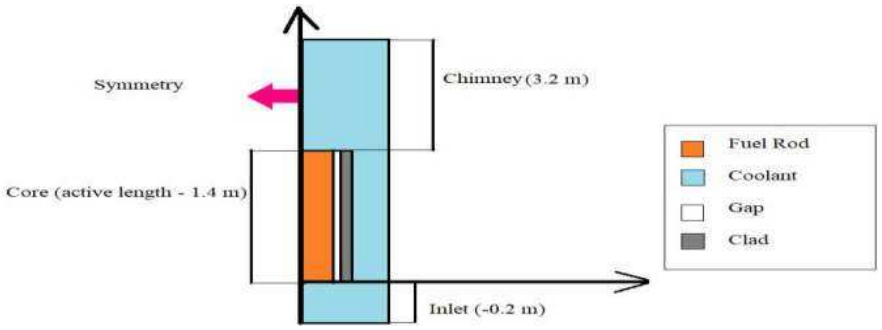

Fig 5. The simulation model of the equivalent cell in ANSYS FLUENT.

After identifying the hot channel, $q''_{max}$was obtained from the output of the citation code in that channel, and using it, the source term required for the fuel was written as the User-Defined Function (UDF) for each inner radius of the annular fuel and was given as input to the fluent software. The UDF (User-Defined Function) in the C programming language is applied to define this cosine profile in ANSYS FLUENT. By selecting the appropriate solver and considering the conditions and equations governing the problem and determining the convergence criterion, the desired problem will be solved by Fluent software. The convergence criterion for energy and all other equations is considered 10^{-6}. The solution continues until the convergence criteria are satisfied. This convergence is shown in Figure 6 section A and 2D modeling of the equivalent cell in ANSYS meshing is shown in section B.

A.

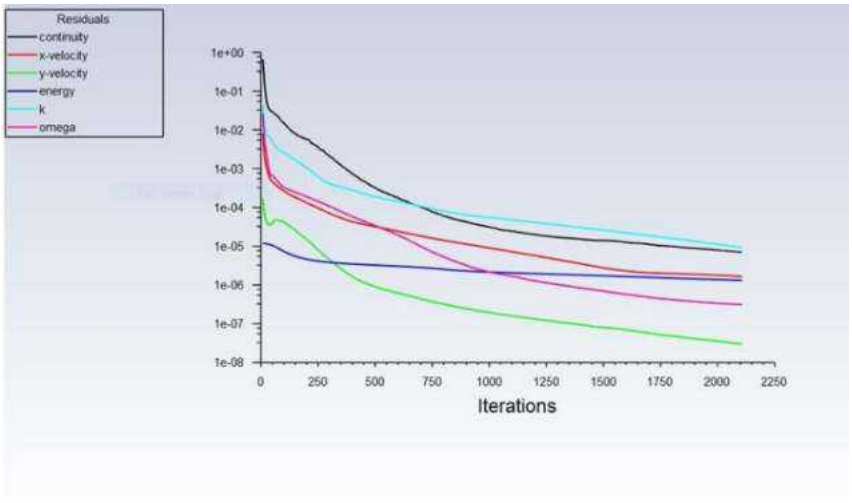

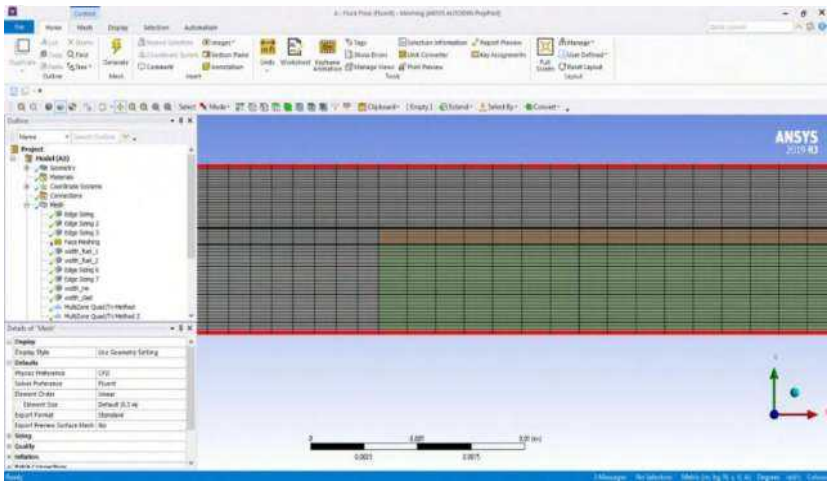

B.

Fig. 6. A. Numerical solution residues in the problem used B . Geometry simulation designed in Ansys Meshing

The inner radius of dual-cooled annular fuels is in the range of 1.5 to 5 mm and under-moderated reactors have been considered in all modeling. An example of measuring the under-moderated of one of the models is shown in Figure 7.

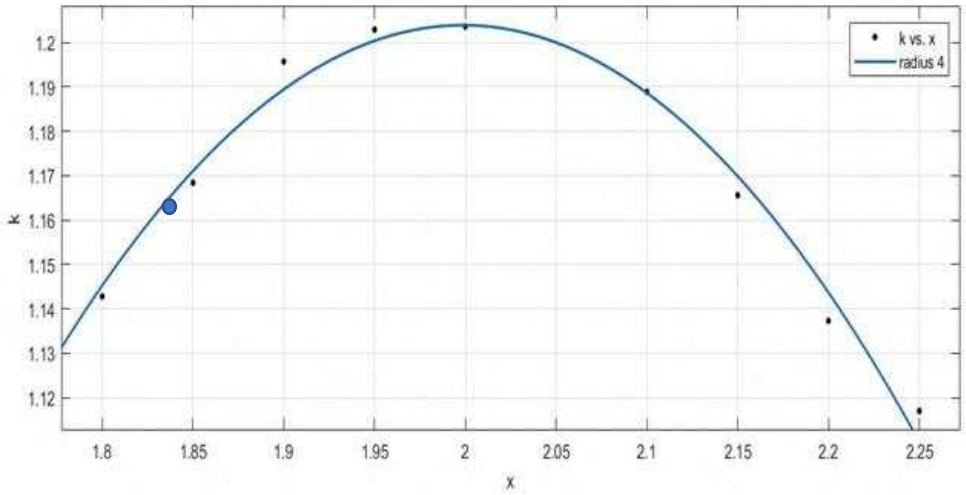

Fig. 7. Effective multiplication factor by fuel pitch with an inner radius of 4 mm.

Equation 2 is used to obtain the convection heat transfer coefficient between the fuel and the fluid, but since the fuel used in the modeling is dual-cooled annular, we use Equation 3 to model the annular fuel. The use of dual-cooled annular fuel in all modeling results in heat transfer coefficient improvement. The increment of the inner radius size can lead to an improvement in the heat transfer coefficient. This augmentation is due to the heat removal area increase, specific heat decrease, fuel temperature reduction, and coolant temperature augmentation.

$$Q = hA\Delta T \tag{2}$$

which:

Q: The heat flux that passes through the surface of the clad and is given to the fluid.

h: Heat transfer coefficient of fluid displacement.

A: Surface of heat transfer.

ΔT: The difference between the surface temperature of the clad and the fluid bulk.

$$h_{avg} = \frac{h_{in}A_{in}\Delta T_{in} + h_{out}A_{out}\Delta T_{out}}{A_{in}\Delta T_{in} + A_{out}\Delta T_{out}} \tag{3}$$

which:

h_{in} : Inner fluid heat transfer coefficient.

A_{in} : Inner clad surface in contact with internal fluid.

ΔT_{in} : The difference between the inner clad surface temperature and the inner fluid temperature.

h_{out} : Outer fluid heat transfer coefficient.

A_{out} : Outer-clad surface in contact with external fluid.

ΔT_{out} : The difference between the outer clad surface temperature and the outer fluid temperature.

DNBR is one of the most important and fundamental parameters in the safety of nuclear power plants, which limits the heat flux of the plant to prevent it from entering the film boiling zone. To calculate this important parameter, formula 4 is used [9]. In this formula, $q_c^{"}$ is the critical heat flux (CHF) to enter the boiling zone of the film and $q_{act}^{"}$ is the actual heat flux operating in the power plant. To calculate the DNBR in this study in Fluent software, we use two methods and compare each other in Fig 8 and from this comparison, we found that the methods are not much different.

$$DNBR = \frac{q_c^{"}}{q_{act}^{"}} \quad (4)$$

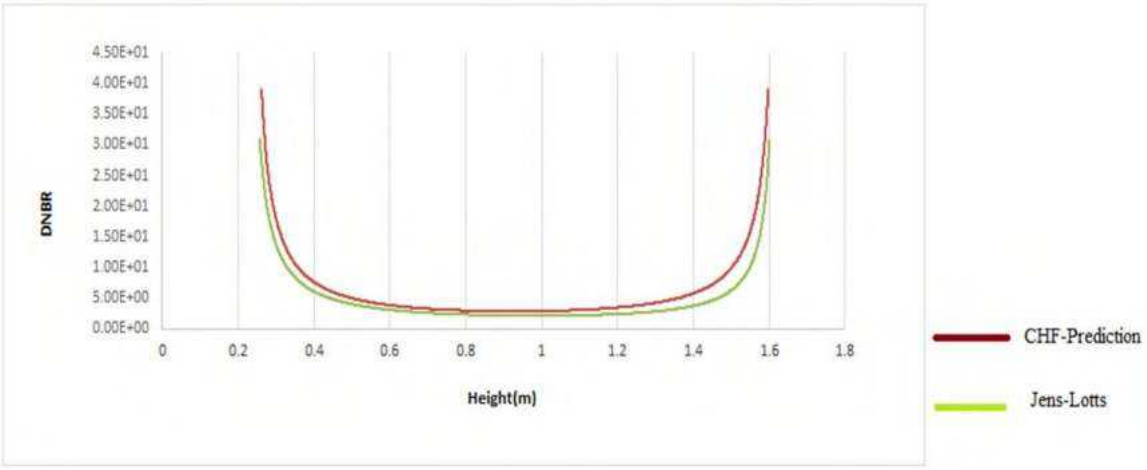

Fig. 8. Comparison of DNBR diagrams of software method and method of using Jens - Lottes experimental formula

Pressure drop increase leads to a decline in the natural circulation and heat transfer performance. The pressure drop of conventional CAREM-25 using solid fuel is less than the current design. In a pressure-light water nuclear reactor, whether in the steady state or in the transient state always designing the equipment surface in the natural circulation of the cooling flow can reduce the power required for pumping and circulating water in the steady state.

The natural circulates in a light water reactor under pressure with temperature that creates a density gradient. This temperature gradient creates a buoyancy force that rotates the slow flow. Reactors such as CAREM can continue to operate without the use of natural fluid circulation without the use of

additional power and auxiliary pumps, as this primary cooling system operates through natural rotational force, which provides good protection against melting of the reactor core, such as It will take place at the Fukushima Nuclear Power Plant in Japan in March 2011.

Results and Discussion

Table 2 shows the thermal-hydraulic parameters obtained from modeling by changing the inner and outer radius of fuel in the CAREM-25 reactor.

Table2. thermos-hydraulic parameters used to optimize internal radius and their values

$\frac{V_{max}}{V_{avg}}$	$V_{out} - V_{in}$	h	PΔ	MDNBR	Outer radius	Inner radius
1.14185	0.009748	4806.95	-39681.9	1.88	4.5	CAREM
1.063876	0.024067	12786.21	-42422.3	1.75	4.5	1.5
1.070157	0.017692	22015.45	-42822.1	2.25	4.5	1.7
1.094921	0.010855	8685.424	-43451	3	4.5	2.2
1.099397	0.00084	7721.96	-43790.5	3.8	4.5	2.5
1.111287	0.012988	7261.234	-42803.3	3.2	5.4	2.7
1.090316	0.017328	7244.441	-42393.8	2.75	6	3
1.112464	0.018736	6845.505	-42439.9	2.8	6	3.2
1.089738	0.010632	6269.897	-43213.8	3.8	6	3.5
1.106497	0.012606	6755.026	-42919.4	2.65	6	3.7
1.136463	0.039817	7846.056	-41343.8	1.77	8.7	4
1.147886	0.035303	7501.413	-41534.3	1.83	8.7	4.2
1.119601	0.032915	6830.365	-41556.7	1.84	8.7	4.5
1.132615	0.031327	6672.727	-41639.4	1.87	8.7	4.7
1.123835	0.028333	6182.22	-41782.6	1.93	8.7	5

The most important purpose of thermal-hydraulic analysis is to investigate the effect of internal radius on natural circulation parameters. Therefore, for each hot channel simulation, the distribution velocity across the hot channel is calculated with V_{out}-V_{in} and equations. For the best optimization solution, an appropriate cost function should be used.

$$\text{Cost} - \text{Function} = \frac{(\frac{V_{max}/V_{avg}}{V_{max}/V_{avg}})^2 + (\frac{\Delta P}{\Delta P})^2}{(\frac{V_{out}-V_{in}}{V_{out}-V_{in}})^2 + (\frac{MDNBR}{MDNBR})^2 + (\frac{h}{h})^2} \quad (5)$$

In order to more easily analyze the performance of the genetic algorithm, a parameter called the number of times the cost function was evaluated was considered. So with the help of this parameter, the performance of the algorithm in achieving the optimal solution can be examined. The GA algorithm code is written in MATLAB, and for ANN modeling, the Neural Network Fitting app (tool) in MATLAB is used. The cost function convergence is analyzed by changing the user-defined parameters of GA (npop (population size), selection methods, crossover, mutation). Finally, the best parameters are specified for applied algorithm. The GA is model are applied with the npop of 100 and the maximum number of iterations equal to 1000. Fig. 9 shows the performance plot. The network performance diagram indicates the performance function value versus the number of iteration and plots performances of the training, validation, and test. The training state plot represents other training variables' progress. The error histogram demonstrates the network error distribution. The regression plot expresses a regression between outputs and targets of the network for training, validation, and test sets as shows in Fig. 10.

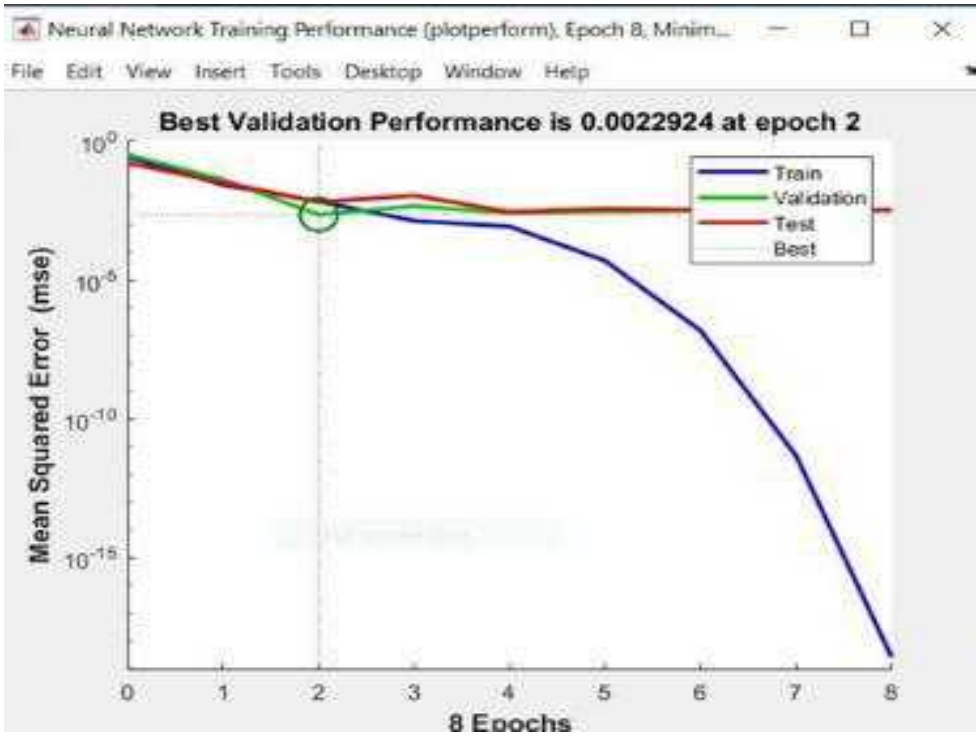

Fig.9. Neural Network Training Performance

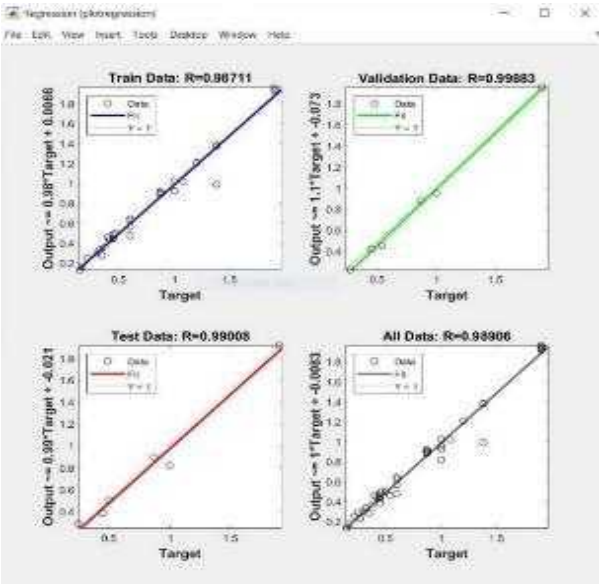

Fig.10. Neural Network Training Regression

The performance of optimization algorithms is mainly analyzed based on the Number of Function Evaluations (NFEs), which is the value of the number of function evaluations until termination & convergence criterion has been achieved. NFE shows the optimization algorithm's performance in finding the best and optimal solution Fig. 11 demonstrates the decrease in cost function value by increasing the NFE. Therefore, the results indicate the function accuracy and efficiency of the applied GA in the current paper.

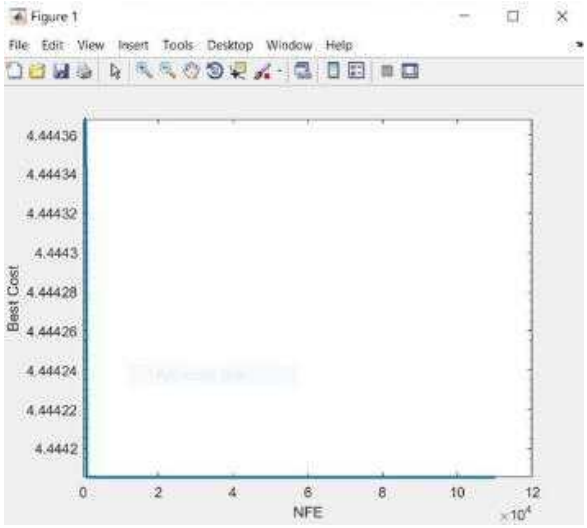

Fig.11. Variations of cost function in terms of the Number of Function Evaluation (NFEs).

By implementing the genetic algorithm, the optimal inner and outer radius for the CAREM-25 reactor core were obtained as follows (Table.3).

Table 3. Optimal inner and outer radius of fuel for CAREM-25 reactor core.

	Inner radius of fuel (cm)	Outer radius of fuel (cm)	Fuel pitch (cm)
Optimal value	0.2967	0.6963	1.6644

Then, for the validation of the artificial neural network and also the study of the reactor core with the optimal annular fuel obtained by re-modeling, the thermal-hydraulic study of the reactor core in this radius was performed. Finally, in Table 5, we compare the simulated model with the results obtained from the neural network and find that the error of all parameters is less than 10%, and this phenomenon is desirable and expresses the correctness of our work.

Table 4. Compares the reactor designed with the optimal radius with the CAREM reactor according to the calculated parameters.

V_{max}/V_{avg} (m/s)	V_{out}-V_{in} (m/s)	MDNBR	h (W/m^2.k)	ΔP (Pa)	Designed core type
1.14185	0.009748	1.88	4806.95	-39681.9	Rector core of CAREM
1.077	0.02760382	2.98	9827.198	-43260.87	Designed core with optimal radius

Table 5. Validation of modeling and artificial neural network created for optimal dual cooled annular fuel.

V_{max}/V_{avg} (m/s)	V_{out}-V_{in} (m/s)	MDNBR	h (W/m^2.k)	ΔP (Pa)	
1.085	0.026	2.82	9228	-43259.073	Network
1.077	0.02760382	2.98	9827.198	-43260.87	simulation
0.7%	5.81%	5.36%	6.09%	0.0041%	Network error

According to the presented results, we find that the use of annular fuel in CAREM reactor compared to modeling the mentioned reactor with solid fuel, in some of these inner radius with a certain fuel pitch, the power distribution becomes more uniform and the maximum radial power peaking factor decreases but in some inner radius with a certain fuel pitch, the distribution of power is concentrated towards the center of the core and the radial power peaking also increases.

Conclusions

The CAREM reactor core with optimized dual-cooled annular fuel was simulated, evaluated and compared with the conventional CAREM reactor core. It can be concluded that compared to the CAREM, presented core with optimal fuel geometry has several advantages and superiority such as

more MDNBR and heat transfer coefficient, better natural circulation parameters, lower V_{max}/V_{avg}, and larger V_{out}-V_{in} . These advantages are very important from a safety and economic point of view. Decreasing the maximum power peaking factor leads to a more uniform distribution of power and safety-improvement in the optimal core. Also, better fuel management can be achieved in the core with optimal annular fuel. Besides, considering the improvement of most safety criteria such as increasing MDNBR and decreasing the maximum temperature of fuel, the increased rated power of the presented core can be achieved.

In conclusion, the optimized CAREM core using dual-cooled annular fuel has a significant potential for thermal performance improvement. Hence, the results of this research allow an evaluation of the annular fuel's appropriateness in the CAREM reactor core.

References

[1] Rowinski M.K., White T.J., Zhao J. Small and Medium sized Reactors (SMR): a review of technology. *Renewable and Sustainable Energy Reviews*, 44, 643–656. (2015).

[2] Abu-Khader M. M. Recent advances in nuclear power:A review. *Progress in Nuclear Energy*,51, 225–235, (2009).

[3] Yang-yu O., Da-sheng W. International nuclear power application and its prospect forecast and our country nuclear electricity development. *Journal of North China Electric Power University*, 34, 1–10, (2007).

[4] Stacey W.M. Nuetron Nuclear Reactions. In: Nuclear Reactor Physics. *WILEY-VCH Verlag GmbH & Co.KGaA, Weinheim*, 10-30. (2007).

[5] Zaidabadi Nejad. M., Ansarifar. G.R., Optimal design of a Small Modular Reactor core with dual cooled annular fuel based on the neutronics and natural circulation parameters, *Nuclear Engineering and Design,* 360. (2020).

[6] Zaidabadi Nejad. M., Ansarifar. G.R., Esteki M.H. Thermal hydraulic analysis of VVER-1000 nuclear reactor with dual-cooled annular fuel using K–ω SST Turbulence model. *Annals of Nuclear Energy*,*101*,118-127, (2017).

[7] Fukami M.V., Santecchia A. "CAREM project: innovative small PWR". *Progress Nuclear Energy,* 37, 265–270. (2000).

[8] Tashakor. S., Zarif. E., Naminazari. M., Neutronic simulation of CAREM-25 small modular reactor. *Progress in Nuclear Energy,* 185-195. (20017).

[9] Chang-Hwan Shin. Tae-Hyum Chun. Dong-Seok, Oh. Wang-Kee In., Thermal hydrolic performance assessment of dual-cooled annular fuel for OPR-1000. *Nuclear Engineering and Design*, 243,291-300. (2012).

[10] Villarino, E., Hergenreder D., Matzkin, S., COMPORTAMIENTO NEUTRONICO DEL NÚCLEO DEL REACTOR CAREM 25, *Moreno 1089/ 8400 Bariloche – Argentina.*

[11] Kyu Hyun Han, Soon Heung Chang " Development of a thermal-hydraulic analysis code for annular fuel assemblies". *Nuclear Engineering and Design*, 226, 267-275, (2003). (2007).

[12] Hojjat M. Nanofluids as coolant in a shell and tube heat exchanger: ANN modeling and multi-objective optimization. Appl Math Comput 2020;365:124710.

[13] Amani M, Amani P, Kasaeian A, Mahian O, Pop I, Wongwises S. Modeling and optimization of thermal conductivity and viscosity of MnFe 2 O 4 nanofluid under magnetic field using an ANN. Sci Rep 2017;7:1–13.

[14] Erfaninia A., Hedayat A., Mirvakili S.M. "Neutronic study of new generation of the small modular pressurized water reactor using Monte-Carlo simulation". *Progress in Nuclear Energy*, 93, 218-230, (2016).

ICNST 2024
International Conference on Nuclear Science and Technology
6- 8 MAY 2024 | Isfahan, Iran

An Artificial Neural Network Approach for Predicting the Thermal-Mechanical Parameters during the Beginning of Cycle (BOC) in NuScale Reactor Core Loaded with TVS-2M Fuel (Paper ID : 1049)

Saeedi Sini S.A.[1*], Sina S.[2,1], Rakeb Z.[1], Sadeghi M.H.[1]

[1]*Department of Nuclear Engineering, School of Mechanical Engineering, Shiraz University, Shiraz, Iran*

[2]*Radiation Research Center, Shiraz University, Shiraz, Iran*

Abstract

The measurement of absorbed dose in various radiation applications, including medical and industrial applications such as radiography, CT scans, and food irradiation, is one of the most important goals of radiation protection. Dosimeters are currently used as a means of quality control in medicine and industry. Radiochromic chemical dosimeters are widely used in radiotherapy, because they often have a linear response at high doses, are low in manufacturing cost, and are easy to read. This study aimed to develop a chemical dosimeter for use at low doses by changing the proportion and composition of the Fricke-Xylenol gel.

The result was the construction of a Fricke gel dosimeter for use in low-dose and intermediate-dose measurements, using various materials, such as gelatin, distilled water, ammonium ferrous sulfate, sulfuric acid, benzoic acid, and xylenol orange. The calibration curves, fading, sensitivity to the environmental temperature, and repeatability of the dosimeter responses were investigated.

According to the results of this study, the manufactured gel dosimeter has a linear response in the dose range of 0.05 to 5 Gy. The Fricke gel dosimeter prepared in this study can be used effectively in low-dose measurements in industrial and medical applications of radiation.

Keywords: Dosimetry, Dose-response, Chemical dosimeter, Fricke dosimeter, Radiochromic

Introduction

In recent years, technological advances in radiation therapy have been significant, and as a result, the quality of radiotherapy has greatly increased. Fundamental progress with the development of external beam techniques, especially intensity-modulated radiotherapy (IMRT), has allowed the clinical implementation of highly non-convex dose distributions. This provides consistency, as shown in [1, 2]. In radiation therapy, controlling and measuring doses, along with associated parameters, is essential to ensure that the target treatment volume receives the prescribed dose. A dosimeter, such as an adequate ionization chamber, is usually used for measurements, although other types of dosimeters can also be

used [3-7]. In general, gel dosimetry using optical scanners for measuring induced attenuation has the highest rank among all dosimeters [8-10]. Ideally, commissioning and routine quality assurance of these complex therapeutic techniques (IMRT) require a dosimeter that can accurately and conveniently measure the dose distribution in three dimensions [1, 2].

There are several classes of gel dosimeters, such as radio-chromic dosimeters and polymer gels [9-13]. Gel dosimeters are unique in that they can measure the dose distribution in three dimensions and their ability to specify other characteristics such as radiation direction, energy and dose rate independence, and soft tissue equivalent. One of the disadvantages of gel dosimeters is the high uncertainty in measuring low doses, especially at doses lower than 25 cGy. Therefore, to avoid this uncertainty in the treatment evaluation, a higher dose was prescribed. For example, if the prescribed dose was 2 Gy per fraction, a dose of approximately 10 Gy was given to the gel dosimeter to evaluate the treatment, especially in the surrounding tissues that received lower doses than the target. As a result, it can be said that the effective and useful life of the linear accelerator and the time devoted to the treatment of patients will be reduced due to the delivery of a large number of monitor units (MU). As a result, it can be said that, for the reasons presented above, obtaining a gel dosimeter that is sensitive to low dose levels has a high value [14-18].

It can be said that these dosimeters rely on the oxidation caused by the radiation of Fe2+ ions to Fe3+ ions, which are dispersed in a tissue-equivalent gel matrix. Usually, these dosimeters are made of gelatin, agarose, or polyvinyl alcohol., which is connected to glutaraldehyde (PVA-GTA) as a gel matrix. Usually, to make these dosimeters, dye materials such as xylenol, nitrotetrazolium chloride, and Methylthymol blue, and activating elements such as silver nitrate, and ammonium ferros sulfate are needed [19-23]. The gel dosimeters are usually used for high-dose measurements in radiotherapy, or in blood irradiation. [24] . The purpose of this study is to develop a gel Fricke gel dosimeter for use in low-dose measurement.

Material and Methods:

In this experiment, 80 samples of gel dosimeter with different chemical compounds were made to measure low doses, and finally, we succeeded in making a Fricke gel dosimeter sensitive to low doses. The chemical materials used in the gel dosimeter structure are as follows: Gelatin (or Polyvinyl alcohol) as the gelling agent, Ferrous ammonium sulfate as the activator, Xylenol orange as the chemical dye. Water, and sulfuric acid as the solvent.

A summary of how to make gel dosimeters is:

The chemicals were inserted in 4 glasses, the first glass contained a gelling agent (gelatin or PVA) and water. The second glass contained orange xylenol, water, and sulfuric acid. The third glass contained benzoic acid and water, and the fourth glass contained ammonium ferrous ammonium sulfate and water. The first glass was heated on a heater- stirrer. For gelatin, heating continued until the temperature reached 45 degrees Celsius. For PVA, for uniform heating, the beaker was not placed directly on the heater, it was placed in a container containing oil and water, and the heating was continued until the temperature reached 85 °C to heat the PVA solution homogeneously. When the temperature of the solution reached the desired value, it was removed from the heater, and when the temperature reached about 35 degrees Celsius, the glass containing the gelatin was placed in water to cool. The contents of the second beaker were added to the first beaker whose temperature had reached ambient temperature to obtain a clear and homogeneous solution with a bright orange color. The contents of the fourth glass were added to the first glass and mixed well. The contents of the third beaker were added to the first beaker, and the final solution was mixed well. Finally, the solution was inserted into cuvettes measuring 1 x 1 x 4.5 cubic centimeters, and kept in the refrigerator until the next day.

To optimize and reach the target gel dosimeters, more than 70 dosimeters were made, and with various compositions. Finally, a gelatin-based gel dosimeter was found to have significant sensitivity to the dose in the low ranges. After preparing the dosimeters, they were kept in the refrigerator at a temperature of 5 degrees Celsius for 12 hours. Gel dosimeters were irradiated using a Cs-137 source calibrated by a standard dosimetry laboratory. The samples were placed at a distance of 60 cm from the source, where the dose rate was 2 Gy/h and the size of the irradiated field was 10 x 10 cm^2. After the irradiation, the dosimeters were placed in front of a negatoscope, and a photo was taken with a camera. The average values of red and green pixels in the images, L (1/cm), were used to obtain changes in optical absorption. In this experiment, the linearity, and the fading of the dosimeter response, energy dependence, and repeatability of the dosimeter were investigated.

Results and Discussion

As previously mentioned, one of the gelatin-based dosimeters was efficient in low-dose measurement. Table 1 shows the composition of this low-dose gel dosimeter.

Table 1: Composition of the gel dosimeter for low-dose measurement

Material	Gelatin-base dosimeter
Gelatin	124 mM
Water	100 ml
Xylenol orange	0.0416 mM
Sulfuric acid	90 mM
Ferrous ammonium sulfate	1.000 mM
Benzoic Acid	6.60 mM

The different characteristics of the dosimeter are presented in the next section.

Calibration curve of the gel dosimeter

The calibration curve of a Fricke gel dosimeter was plotted and it was observed that the response of this dosimeter is linear. This curve can be seen in Figure 1. Based on the obtained results, it was observed that the lower detection limit for this gelatin is approximately 50 mGy. The minimum detectable limit of the detector is obtained by the reading (color) of the background dosimeter. The dosimeter does not change color when exposed to a dose lower than 50mGy.

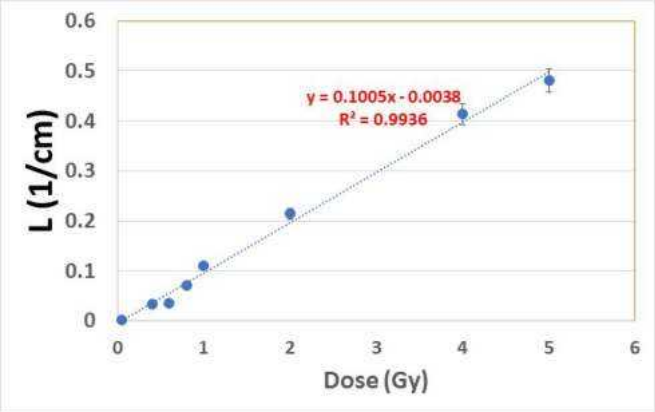

Fig. 1. Calibration curve of a gel dosimeter sample

Temperature dependency, and fading of the dosimeter response

To investigate the effect of the environmental temperature on the dosimeter response, the gelatin-based dosimeter response was obtained at room temperature, and in the refrigerator. Comparing the results shows that the responses of the gelatin-based dosimeters are temperature dependent and the stability of the samples increases by keeping the dosimeters in the refrigerator. The results show that the response of the dosimeter kept at room temperature, undergoes a 40% variation after 100 hours. However, less variation is observed in the response of the dosimeter when kept in the refrigerator.

A decrease in stability over time was observed even when the dosimeters were stored in the refrigerator. Figure 2 shows the stability of the dosimeter when exposed to doses and stored in a refrigerator. The change in gelatin-based dosimeter response was less than 0.5% at 120 hours after irradiation.

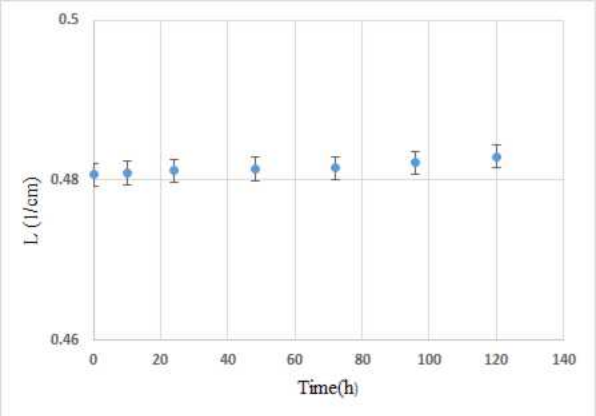

Fig. 2. Percentage changes in dosimeter response stability with time elapsed after exposure when stored at 5°C.

Repeatability of the dosimeter response

The dosimeter was prepared again, and irradiated for calibration. Figure 3 shows the reproducibility of the gel.

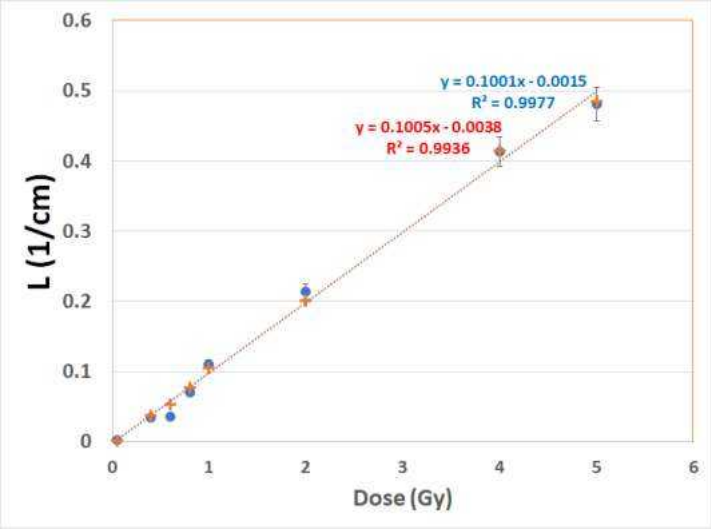

Fig. 3. Repeatability of the gelatin-based gel dosimeter sample

Energy dependency of the gel dosimeter

The dosimeter was exposed to a dose of 2Gy in 662keV gamma rays, and 70kVp X-rays. As shown in Figure 4, the obtained results show that the response of the dosimeters does not depend on the energy of the radiation rays, for the energies of 70kVp, and 662keV.

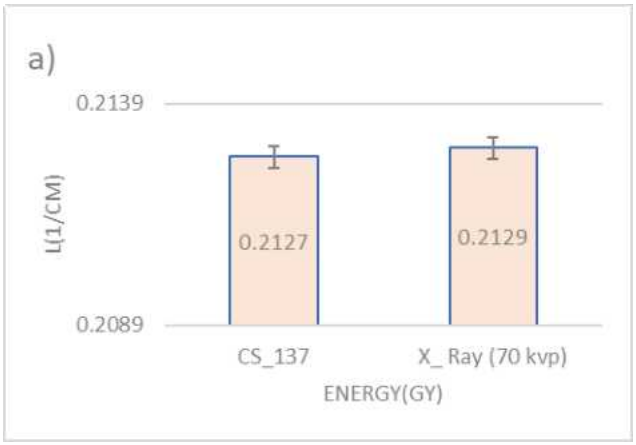

Fig. 4. Response of a gel dosimeter sample to the same dose of gamma and X

Conclusions

When a new dosimeter is established, its characteristics such as linearity of the response, repeatability, energy dependence, etc., must be investigated. In the case of gel dosimeters, when a compound with high enough sensitivity is made, further studies should be performed to investigate the linearity, stability, repeatability, and energy dependence. In this study, it was shown that a long storage time between gel preparation and irradiation may cause a noticeable decrease in dosimeter sensitivity and darkening of dosimeters, which can be seen even with the naked eye. Gel dosimeters are often used to calculate high doses, but in this study, we managed to make a Fricke gel dosimeter to measure the dose in the mGy range. It was shown that the dosimeter introduced here has a linear response in the range of 50 to 5000 mGy. The developed gelatin-based dosimeters are a promising tool for radiation detection and are potentially applicable for industrial and medical dosimetry.

Acknowledgements

We extend our gratitude to the Radiation Research Center of Shiraz University for their invaluable support.

References

[1] McAuley, K. B., & Nasr, A. T. (2013, June). Fundamentals of gel dosimeters. In Journal of Physics: Conference Series (Vol. 444, No. 1, p. 012001). IOP Publishing.

[2] Mayles, P., Nahum, A., & Rosenwald, J. C. (2007). Handbook of radiotherapy physics: theory and practice. CRC Press.

[3] Baskar, R., Lee, K. A., Yeo, R., & Yeoh, K. W. (2012). Cancer and radiation therapy: current advances and future directions. International journal of medical sciences, 9(3), 193.

[4] Attix, F. H. (2008). introduction to radiological physics and radiation dosimetry. John Wiley & Sons.

[5] F.M. Khan, "The physics of radiation therapy,"William and Wilkins, Maryland (2003).

[6] Mizukami, S., Watanabe, Y., Mizoguchi, T., Gomi, T., Hara, H., Takei, H., ... & Maeyama, T. (2021). Whole three-dimensional dosimetry of carbon ion beams with an MRI-based nanocomposite Fricke gel dosimeter using rapid T1 mapping method. Gels, 7(4), 233.

[7] Webb, S. (2001). Concepts for shuttling multileaf collimators for intensitymodulated radiation therapy. Physics in Medicine & Biology, 46(3), 637.

[8] Baldock, C., De Deene, Y., Doran, S., Ibbott, G., Jirasek, A., Lepage, M., ... & Schreiner, L. (2010). Polymer gel dosimetry. Physics in Medicine & Biology, 55(5), R1.

[9] Rabaeh, K. A., Eyadeh, M. M., Hailat, T. F., Aldweri, F. M., Alheet, S. M., & Eid, R. M. (2018). Characterization of ferrous-methylthymol blue-polyvinyl alcohol gel dosimeters using nuclear magnetic resonance and optical techniques. Radiation Physics and Chemistry, 148, 25-32.

[10] Maryanski, M. J., Gore, J. C., Kennan, R. P., & Schulz, R. J. (1993). NMR relaxation enhancement in gels polymerized and cross-linked by ionizing radiation: a new approach to 3D dosimetry by MRI. Magnetic resonance imaging, 11(2), 253-258.

[11] Noushin Bani Rezaieh, Hassan Ali Nadai, Ali Reza Shirazi, Ali Reza Zirak and Sudeh Sadat Sajjadi (2014). An overview of three-dimensional dosimeters. Razi Journal of Medical Sciences.

[12] De Deene, Y., De Wagter, C., Van Duyse, B., Derycke, S., Mersseman, B., De Gersem, W., ... & De Neve, W. (2000). Validation of MR-based polymer gel dosimetry as a preclinical three-dimensional verification tool in conformal radiotherapy. Magnetic Resonance in Medicine: An Official Journal of the International Society for Magnetic Resonance in Medicine, 43(1), 116-125.

[13] Ibbott G S. (2006). Clinical Applications of Gel Dosimeters. J Phys Conf Ser, 56:108-131.

[14] Alashrah, S., El-Ghoul, Y., & Omer, M. A. A. (2021). Synthesis and characterization of a new nanocomposite film based on polyvinyl alcohol polymer and nitro blue tetrazolium dye as a low radiation dosimeter in medical diagnostics application. Polymers, 13(11), 1815.

[15] Ranjbar, A. H., & Randle, K. (2008). Hyper pure quartz as a promising material for retrospective and radiation processing dosimetry using ESR technique. Applied Radiation and Isotopes, 66(9), 1240-1244.

[16] Kozicki, M., Berg, A., Maras, P., Jaszczak, M., & Dudek, M. (2020). Clinical radiotherapy application of N-vinylpyrrolidone-containing 3D polymer gel dosimeters with remote external MR-reading. Physica Medica, 69, 134-146.

[17] Matrosic, C. K., Culberson, W., Shepard, A., Jupitz, S., & Bednarz, B. (2021). 3D dosimetric validation of ultrasound-guided radiotherapy with a dynamically deformable abdominal phantom. Physica Medica, 84, 159-167.

[18] Babic, S., Battista, J., & Jordan, K. (2008). Three-dimensional dose verification for intensity-modulated radiation therapy in the radiological physics centre headand-neck phantom using optical computed tomography scans of ferrous xylenol–orange gel dosimeters. International Journal of Radiation Oncology Biology Physics, 70(4), 1281-1291.

[19] LJ, S. (2004). Review of Fricke gel dosimeters.

[20] Schreiner, L. J. (2015, January). True 3D chemical dosimetry (gels, plastics): Development and clinical role. In Journal of Physics: Conference Series (Vol. 573, No. 1, p. 012003). IOP Publishing.

[21] Tippayamontri, T., Guérin, B., Ouellet, R., Sarrhini, O., Rousseau, J., Lecomte, 82 R., ... & Sanche, L. (2019). Intratumoral 18F-FLT infusion in metabolic targeted radiotherapy. EJNMMI research, 9(1), 1-13.

[22] Schulz, R. J., DeGuzman, A. F., Nguyen, D. B., & Gore, J. C. (1990). Doseresponse curves for Fricke-infused agarose gels as obtained by nuclear magnetic resonance. Physics in Medicine & Biology, 35(12), 1611.

[23] Rabaeh, K. A., Eyadeh, M. M., Hailat, T. F., Aldweri, F. M., Alheet, S. M., & Eid, R. M. (2018). Characterization of ferrous-methylthymol blue-polyvinyl alcohol gel dosimeters using nuclear magnetic resonance and optical techniques. Radiation Physics and Chemistry, 148, 25-32.

[24] Farajzadeh, E., and Sina, S. (2022). Development of radiochromic dosimeter for dosimetry in blood irradiation chambers. Radiation Physics and Chemistry, 188, 109637.

ICNST 2024 International Conference on Nuclear Science and Technology
6- 8 MAY 2024 | Isfahan, Iran

Assessing the Influence of Axial Power Distribution on Thermal-Mechanical Parameters in the NuScale Reactor Core Utilizing TVS-2M Fuel Assemblies (Paper ID : 1051)

M. H. Zahedi Yeganeh[1], G.R. Ansarifar [1*], H. Zayermohammadi Rishehri [1]
[1]*Department of Nuclear Engineering, Faculty of Physics, University of Isfahan, Isfahan, Iran*

Abstract

This study focuses on analyzing the thermal-mechanical behavior of a NuScale reactor core that utilizes TVS-2M hexagonal fuel assemblies. In this paper, the FRAPCON code was employed to obtain thermal-mechanical parameters. One key aspect that can be examined during reactor control and load- following operations is the Axial Offset (AO). Consequently, this research investigates the impact of AO on the thermal-mechanical changes in fuel rod. The MCNP code, renowned for its ability to analyze neutronic physics in the nuclear field, was employed to simulate control rod inputs and collect power distribution data for various AO variations. By assessing the relationship between AO and various thermal-mechanical properties of the fuel, such as the percentage of Fuel Gas Release (FGR), cladding absorbed hydrogen, oxide layer thickness on the cladding outer surface, heat transfer coefficient across the gaps, fuel pellet outer diameter, axial stress and hoop stress of the cladding, maximum temperature of the fuel pellet, and gap thickness, it has been determined that the influence of power distribution significantly increases over time, particularly towards the end of the operational period.

Keywords: Axial offset, Thermal-mechanical analyse, Small Modular Reactor, TVS-2M fuel assemblies

Introduction

The nuclear energy industry is witnessing a surge in interest for Small Modular Reactors (SMRs). SMRs boast a compact design, generating electricity in the range of 50 to 300 megawatts electric (MWe). This makes them a more versatile solution, catering to the specific needs of smaller communities or industrial applications. Furthermore, SMRs come in a variety of designs, each with its own set of advantages and limitations. This diversity allows for tailored solutions based on specific project requirements. However, careful consideration during the design and deployment phases remains crucial to ensure optimal performance and safety [1]. One of the key strengths of SMRs lies in their inherent safety features. Unlike traditional reactors that rely on complex active safety systems, SMRs incorporate passive safety mechanisms. These features function automatically, even in the event of a power outage, significantly reducing the risk of catastrophic nuclear accidents. Additionally, the transportable nature and rapid

deployment capabilities of SMRs make them particularly well-suited for remote areas with limited access to reliable and clean energy sources [2].

SMRs have great potential for providing dependable, safe, and sustainable energy, but further research is needed to understand their implications. One of the most modern SMR reactors is the NuScale reactor. Zahedi Yeganeh and Ansarifar proposed a new NuScale SMR core using TVS-2M for improved performance. They analyzed fuel depletion during the fresh-core cycle length [3]. TVS-2M fuel design is known for its operational superiority and low failure rates, commonly used in Russian VVER reactors [4].

Further analysis is needed for successful redesign of NuScale core with TVS-2M fuel. Therefore, In this article, the effect of AO on thermal-mechanical changes in TVS-2M fuel rods is studied and discussed its implications for the design and operation of nuclear reactors.

Material and Methods

Neutronic core simulation

To start this research project, we need to perform neutronic calculations to obtain the required parameters. One way to do this is by simulating the reactor core using the MCNP code. The geometric modeling in MCNP was done realistically, considering components like fuel rods, stainless steel reflectors, bypass channels, thermal and biological shields, and the Reactor Pressure Vessel (RPV). Some simplifications were made, but they don't significantly affect the results. The simulated core's top and side views are shown in Fig. 1.

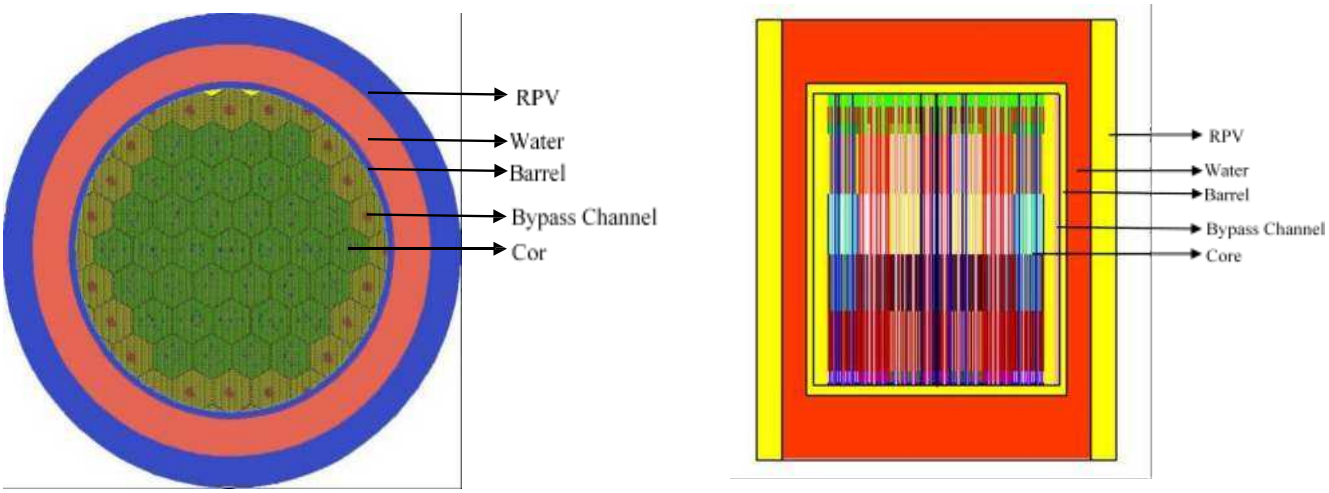

(a) (b)

Fig 1. The simulated core in MCNP, (a) Top view (b) Side view.

Thermal-Mechanical Simulation

In this paper FRAPCON is used. FRAPCON is a widely used code for modeling fuel rod behavior in light water nuclear reactors. It calculates heat transfer using a finite difference method. The code also considers Fission Gases Release (FGR), fuel reformation, and cladding deformation, all of which impact fuel rod performance.

FRAPCON code models fuel behavior in square cores, so the pitch of the hexagonal grid cannot be directly used as input. Instead, the pitch length is calculated to equalize the heating range of each rod, resulting in 1.1865 cm (hexagonal grid pitch is 1.275 cm). Due to limitations, the specific alloy used in TVS-2M cannot be modeled in FRAPCON. Therefore, Zircaloy-4 alloy is used for modeling and analysis purposes.

Results

The effect of Axial Offset on thermal-mechanical parameters

To analyze the impact of AO, a FRAPCON model was developed for the first year. The MCNP code simulated control rod inputs and obtained power distribution data for each AO deviation.

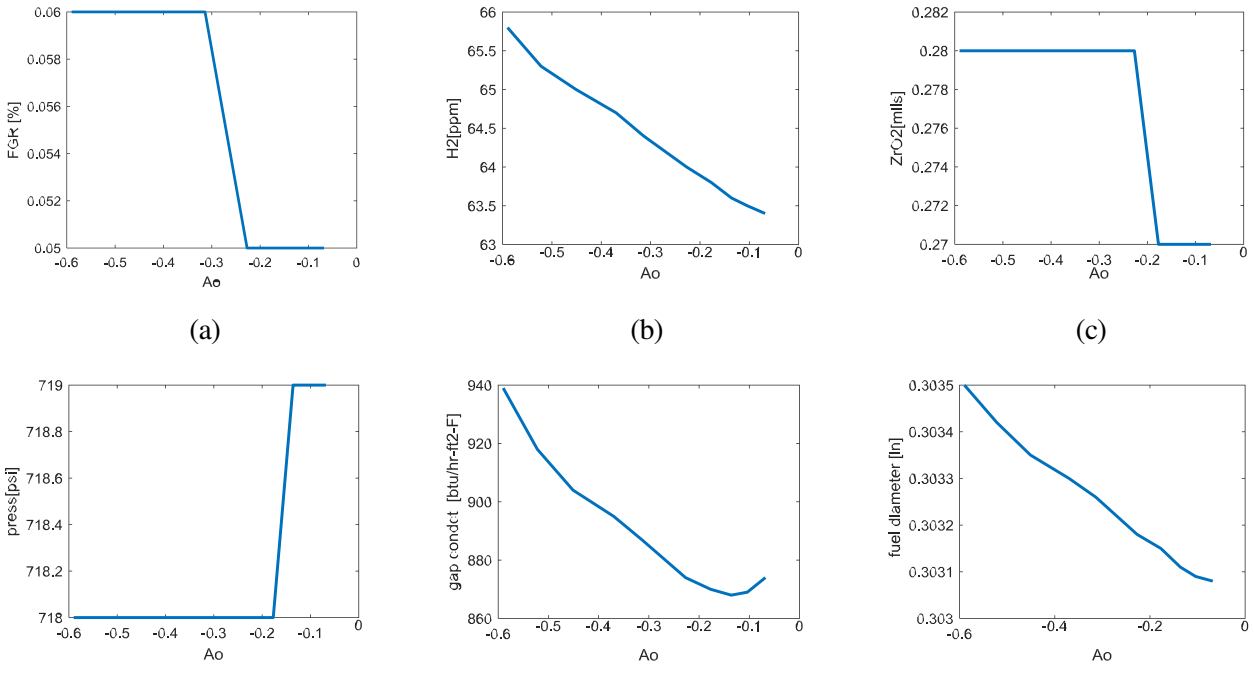

Fig. 2. The variation in thermal-mechanical parameters for different AO values. (a) FGR percentage; (b) Absorbed hydrogen of the cladding; (c) The thickness of the oxide layer on the outer surface of the cladding; (d) The internal pressure of the fuel rod; (e) The gap heat transfer coefficient; (f) The outer diameter of the fuel pellet.

Fig. 2a shows the FGR after 360 days. Gas released from fission gets trapped in the pellet to some extent, causing the step behavior in the diagram. Fig. 2b illustrates cladding hydridation. Generally, hydridation behavior is similar to oxide layer formation. Increasing AO and axial power peak intensify cladding temperature and hydridation. However, as we approach the bottom of the fuel rod, coolant temperature decreases, impacting the hydridation graph. Strain differences caused by AO also play a role. In Fig. 2c and Fig. 2d, due to FRAPCON's uncertainty in displaying values, the growth of oxide layer thickness and internal pressure are shown as steps. Decreasing AO increases FGR, which may explain the decrease in internal pressure, considering cladding deformation caused by power and expansion distribution of fuel pellets. Fig. 2e displays the heat transfer coefficient in the peak power area. Negative factors include FGR, pressure reduction, and gap thickness reduction, while positive factor is increase in heat transfer coefficient. The dominant factor for this coefficient behavior appears to be the change in gap thickness. Fig. 2f shows changes in fuel pellet diameter in the peak power area. The most influential factor for pellet expansion is the decrease in AO combined with an increase in peak power.

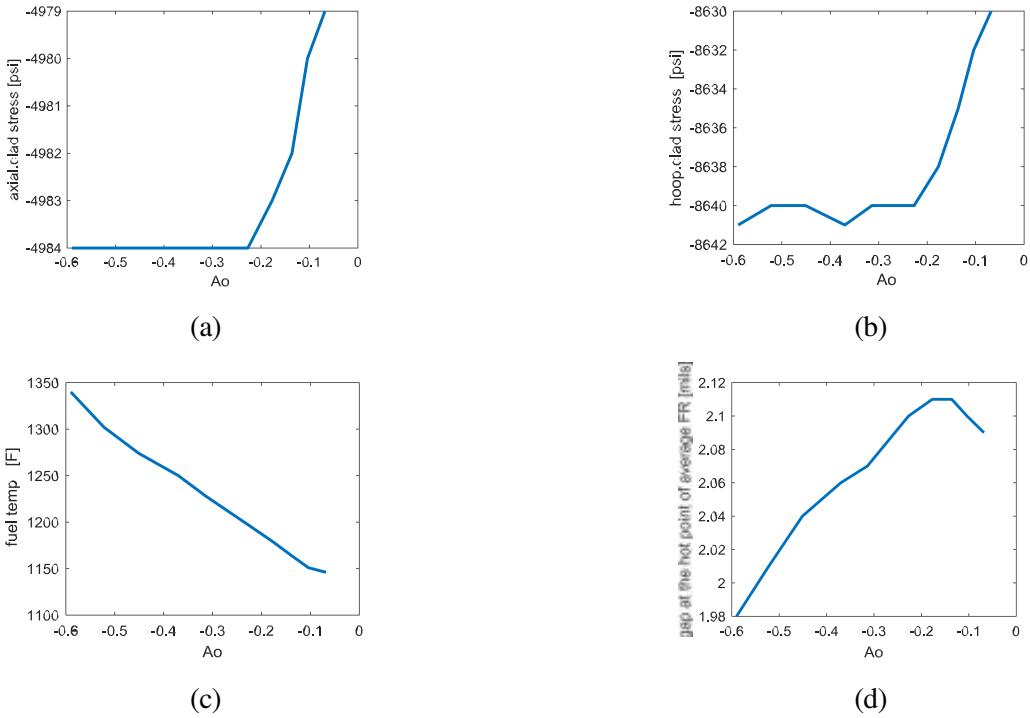

Fig. 3. The variation in thermal-mechanical parameters for different AO values. (a) The cladding axial stress; (b) The cladding hoop stress; (c) The fuel maximum temperature; (d) The gap thickness.

Fig. 3a and Fig. 3b depict cladding stress. It is influenced by temperature distribution, cladding strain, and pressure difference inside and outside. At around -20%, it exhibits a steeper slope. The temperature of the fuel pellet, shown in Fig. 3c, increases as AO decreases. Similarly, the gap thickness in the peak

power area, shown in Fig. 3d, is influenced by competition between pellet diameter increase and cladding strain and temperature changes.

Conclusions

In this research, the focus is on analyzing the thermal-mechanical properties of a NuScale reactor core that employs TVS-2M hexagonal fuel assemblies. The FRAPCON code is utilized for this purpose. The main objective is to investigate how the adjustment of axial offset (AO) affects the thermal-mechanical behavior of the fuel rods. To obtain power distribution data for different AO deviations, the MCNP code is employed to simulate control rod inputs. Through careful evaluation of the relationship between AO and the thermal-mechanical characteristics of the fuel, it has been discovered that the influence of power distribution becomes significantly more prominent as time progresses, especially towards the end of the operational period.

References

[1] Subki, H. (2020). Advances in small modular reactor technology developments.

[2] Locatelli, G., Bingham, C., & Mancini, M. (2014). Small modular reactors: A comprehensive overview of their economics and strategic aspects. Progress in Nuclear Energy, 73, 75-85.

[3] Zahedi Yeganeh, M. H., Ansarifar, G. R. (2021). Design of a new Small Modular Nuclear Reactor using TVS-2M Fuel Assemblies and Fuel Depletion analysis during the fresh-core cycle length. Nuclear Engineering and Design, 385, 111540.

[4] Hongxia, W., & Min, X. (2014). Research of core fuel management using TVS-2M fuel assemblies in VVER. Nuclear Power Engineering, 35.

ICNST 2024 International Conference on Nuclear Science and Technology
6- 8 MAY 2024 | Isfahan, Iran

Design and Analysis of Control Banks for NuScale Reactor Core Loaded with TVS-2M Fuel (Paper ID : 1052)

M. H. Zahedi Yeganeh[1], G.R. Ansarifar [1*], H. Zayermohammadi Rishehri [1]
[1]Department of Nuclear Engineering, Faculty of Physics, University of Isfahan, Isfahan, Iran

Abstract

In the ever-evolving field of nuclear energy, the design and analysis of control banks play a crucial role in ensuring the safety and efficiency of reactor cores. Initially, a detailed simulation using the widely-used MCNP code is carried out to locate the control banks within the reactor's new core. The geometric modeling in MCNP is highly realistic and accurate. In this study, the control cluster for the reactor's core is selected to resemble the hexagonal shape of the VVER-1000's control clusters. During the design phase, the ability to shut down the reactor in two scenarios is ensured. These two scenarios are chosen because they demonstrate the maximum multiplication factor of the core. In the Hot Zero Power (HZP) scenario, the MCNP simulation shows a sub-critical state with a multiplication factor of 0.94481 ± 0.00023. In the Cold Zero Power (CZP) scenario, the multiplication factor of 0.9935 ± 0.00023 confirms the effectiveness of the control assemblies. Furthermore, this study also determines the integral worth of the regulating banks.

Keywords: Control Banks, Small Modular Reactor, TVS-2M fuel assemblies, NuScale reactor, neutronic analysis

Introduction

With the continuous advancement of nuclear energy technologies, the NuScale reactor has emerged as a promising Small Modular Reactor (SMR) design for safe and efficient power generation [1-2]. Recently, various studies have been performed to improve this SMR [3-6]. Zahedi Yeganeh and Ansarifar have introduced a novel SMR core design for the NuScale, leveraging the advantages associated with TVS-2M fuel. Their study included an examination of fuel depletion over the initial cycle duration in this new core design [7]. The utilization of TVS-2M fuel assemblies is renowned for its excellent operational efficiency, high fuel burn-up rates, and minimized fuel failure incidences, characteristics commonly observed in Russian VVER reactors.

The proper design and operation of control systems within the core are essential for ensuring the reliable performance and safety of such advanced nuclear reactors, particularly when loaded with TVS- 2M fuel. The control banks play a critical role in regulating the reactor power levels, maintaining temperature distributions, and ensuring stable operation throughout the reactor's lifecycle [8].

This research aims to investigate the design and analysis of control banks specifically tailored for the NuScale reactor core fueled with TVS-2M fuel. By employing neutronics modeling and simulation, this study seeks to examines the configuration and operation of control banks to enhance the overall performance and safety of the NuScale reactor core.

Material and Methods

Reactor Core and Specifications

This study utilizes the NuScale SMR core with hexagonal fuel assemblies as the reference reactor, developed by Zahedi Yeganeh and Ansarifar. The core includes 37 FAs, each with 312 fuel rods in a hexagonal arrangement standing at 200 cm. Each FA has 18 guide tubes for control rod adjustments and one measuring tube. Important core parameters are listed in Table 1.

Table 1. Significant parameters of the NuScale core with hexagonal FAs [7].

Parameter	Value	Unit
Reactor power	160	MWt
Number of the FA	37	
FA geometry	Hexagonal	
Number of rods per assembly	331	
Number of fuel rods per assembly	312	
Overall width	23.5	cm
Fuel rod pitch	1.275	cm
Active fuel height	200	cm
Fuel rod outside diameter	9.1	mm
Pellet outside diameter	7.6	mm
Pellet hole diameter	1.2	mm
Pellet length	9-12	mm
Clad material	Zr-1%Nb	
Clad thickness	0.65	mm
Coolant type	Light Water	
Burnable absorber material	Gd_2O_3	
Fuel enrichment	<5	w/o

The core includes six types of FAs, grouped into three categories based on their fuel rod arrangements:

Category 1: 312 fuel rods, 9 with UO2 + Gd2O3 and 303 with pure UO2.

Category 2: 312 fuel rods, 12 with UO2 + Gd2O3, 234 with enrichment I, and 66 with enrichment II of uranium.

Category 3: 312 fuel rods, 252 with enrichment I and 60 with enrichment II of uranium.

Table 2 shows U-235 enrichment and Gd2O3 concentration for different FAs. The core layout with 37 FAs is depicted in Fig. 1.

Table 2. ^{235}U enrichment and Gd_2O_3 Concentration.

FA type	FA category	Blanket enrichment	U-235 enrichment in $UO_2 + Gd_2O_3$ fuel rod	Gd_2O_3 concentration in $UO_2 + Gd_2O_3$ fuel rod	U-235 enrichment I	U-235 enrichment II
A	1	1.87%	3 %	4 %	2.6 %	-
B	1	1.87%	3.2 %	6.6 %	2.8 %	-
C	1	1.87%	3.1 %	7 %	2.9 %	-
D	3	2.2%	-	-	4.8 %	4.6 %
E	1	1.87%	2.4 %	6.6 %	2.3 %	-
F	2	2.2%	4.9 %	8 %	4.95 %	4.6 %

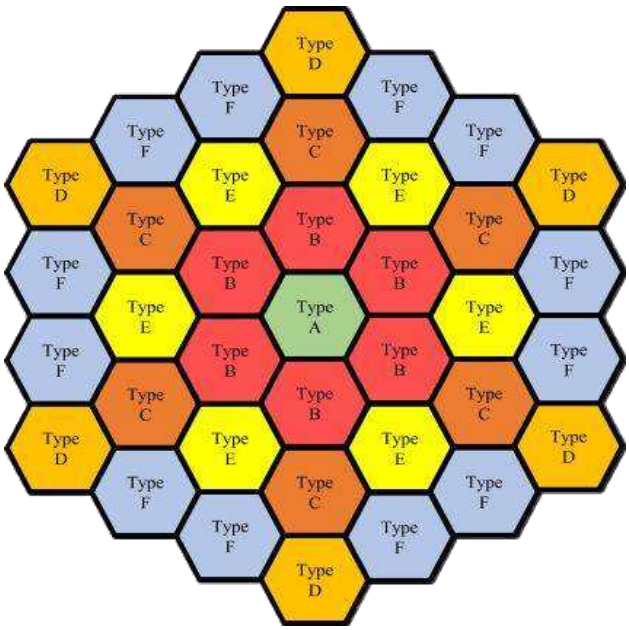

Fig 1. BOC loading pattern.

Neutronic Core Simulation

To start the research project, conducting neutronic calculations is essential. One way to do this is by using the MCNP code, which is a widely-employed radiation transport code in the nuclear industry. It utilizes the Monte Carlo method to simulate particle movement, interactions with matter, collision events, and the estimation of reaction rates and radiation dose. Managed by Los Alamos National Laboratory, MCNP is crucial for various applications in nuclear technology and safety evaluations [9].

The geometric modeling in MCNP aims for realistic accuracy. Simplifications are made without significantly impacting the output. Components like stainless steel reflectors, bypass channels for cooling, thermal shields, and the Reactor Pressure Vessel are included. The simulation also considers fuel rod details like gap area, internal hole, cladding thickness, and temperature changes. Fig. 2 display the top and side views of the simulated core in MCNP.

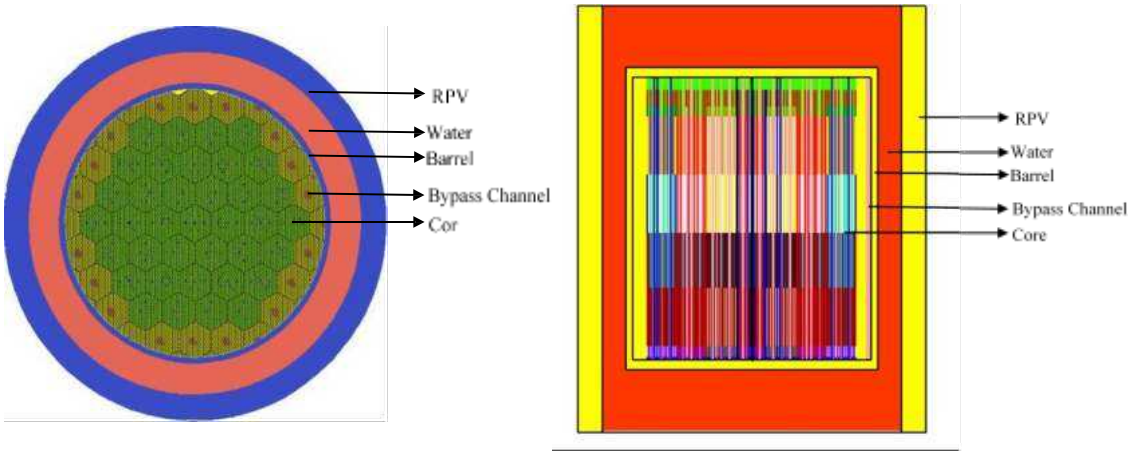

(a) (b)

Fig 2. The simulated core in MCNP, (a) Top view (b) Side view.

Design of control banks

This study requires selecting a control cluster for the reactor core that mirrors the VVER-1000's control clusters, which are hexagonal to match the Fuel Assembly (FA) shape. The VVER-1000's control clusters consist of 18 control rods primarily made of boron carbide.

The NuScale reactor originally includes 8 regulating control clusters, equivalent to a total of 200 control rods. Fig. 3 depicted the arrangement of Regulating Banks (RBs) in the NuScale reactor with hexagonal FAs. There are three banks, each with different configurations of control assemblies and FA types. Bank 1 contains a control assembly within FA type A. Bank 2 features six control assemblies within type E FA, while Bank 3 includes six control assemblies within type D FA.

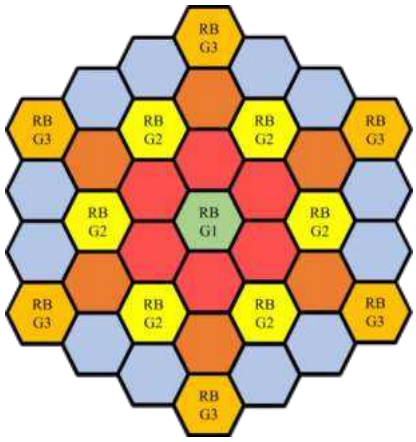

Fig 3. Regulating bank locations.

The core control rod design was inspired by the VVER-1000 control rods while being adjusted in height to meet NuScale's requirements. Fig. 4. shows a schematic control rod in the core.

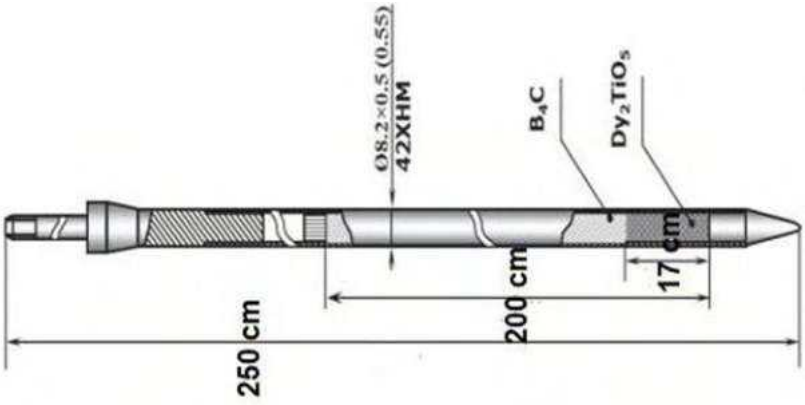

Fig 4. Designed control rod.

Dysprosium has a density of 4.9 grams per cubic centimeter, while the control rods in RBs are filled with boron carbide, which has a density of 1.7 grams per cubic centimeter. To ensure reliability, the control rods in shutdown banks have a higher density of 2.5 grams per cubic centimeter.

This study presupposes that the boron carbide concentration in the control rods of the regulating bank is 1.7 gr/cm. To precisely evaluate the shutdown margin, all control rods, both regulating and shutdown banks, need to be considered. The study assumes that the shutdown control banks share the same design as the regulating control rods and are part of all other core FAs.

Results and Discussion

Ensuring reactor shutdown in critical high multiplication factor scenarios guarantees ample safety margins in all states.

In the first scenario, known as Hot Zero Power (HZP), all control rods - except for one cluster with a high value - are inserted into the core during HZP and Beginning of Cycle (BOC) when there is no boric acid present. Considering that in HZP mode, the effect of reducing reactivity due to power generation is not taken into account, there is also no negative reactivity of boric acid. Also, on the other hand, calculations are done at the beginning of the operation period and there is no poison; Therefore, the extra reactivity of the core has not been consumed. Hence, if the core becomes subcritical under these circumstances, it can be concluded that it will also behave similarly in other situations.

In the second scenario, known as Cold Zero Power (CZP), all control rods should be fully inserted into the core while the core is at a cold temperature and without the presence of boric acid. This configuration should ensure that the core remains in a sub-critical condition, providing an additional measure of safety for the nuclear power plant.

The simulation, conducted using MCNP, yielded the multiplication factor in these scenarios as they are presented in table 3.

Table 3. The multiplication factor in these HZP and CZP scenarios.

Scenarios	Multiplication factor
HZP	0.94481 ± 0.00023
CZP	0.9935 ± 0.00023

Integral worth of entering regulating banks

In order to calculate the integral worth of regulating banks in accordance with the entry of control banks into the core, the following formula is used.

$$\rho_{w_o} = \frac{k_o - k_i}{k_i} \times k \qquad (1)$$

where, ko is the multiplication factor for the time when all the control rods are outside the core, and ki is the multiplication factor for the time when the control banks have entered the core up to a certain amount and ρw is the integral worth corresponding to the same amount of control rods entering.

The Fig. 5 shows the fitted diagram by MATLAB and the results of the reactivity value obtained from MCNP. The horizontal axis of this diagram is actually the Axial Offset (AO) proportional to the input of the control rod banks.

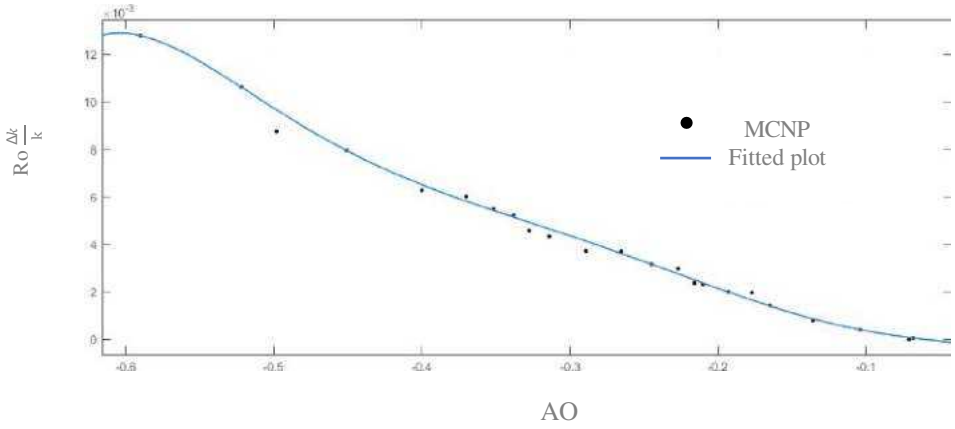

Fig. 5. The integral worth of the reactivity is proportional to the AO

Conclusions

Lately, several studies have focused on enhancing the NuScale SMR. In the most recent research endeavor, scholars introduced an innovative SMR core design for the NuScale, capitalizing on the benefits of utilizing TVS-2M fuel. The effective design and operation of control systems within the core are imperative for guaranteeing the dependable performance and safety of these advanced nuclear reactors, especially when fueled with TVS-2M fuel. The control banks play a crucial role in overseeing the reactor power levels, managing temperature distributions, and ensuring steady operation over the reactor's lifespan.

This investigation delved into tailoring the design of control banks specifically for the NuScale reactor core fueled by TVS-2M fuel, utilizing neutronics modeling and simulation through the MCNP code. Throughout the design phase, the research ensured the reactor's capability to shut down under two scenarios chosen to highlight the maximum multiplication factor of the core. In the Hot Zero Power (HZP) scenario, the MCNP simulation revealed a sub-critical state with a multiplication factor of 0.94481 ± 0.00023. Conversely, in the Cold Zero Power (CZP) scenario, the multiplication factor of 0.9935 ± 0.00023 validated the effectiveness of the control assemblies. Additionally, this study also quantified the integral worth of the regulating banks.

References

[1] Locatelli, G., Bingham, C., & Mancini, M. (2014). Small modular reactors: A comprehensive overview of their economics and strategic aspects. Progress in Nuclear Energy, 73, 75-85.

[2] Vujić, Jasmina, Ryan M. Bergmann, Radek Škoda, and Marija Miletić. "Small modular reactors: Simpler, safer, cheaper?." Energy 45, no. 1 (2012): 288-295.

[3] Fakhraei, A., Faghihi, F., Rabiee, A., & Safarinia, M. (2021). Coolant flow rate instability during extended station blackout accident in NuScale SMR: Two approaches for improving flow stability. Progress in Nuclear Energy, 131, 103602.

[4] Zayermohammadi Rishehri, H., & Zaidabadi Nejad, M. (2023). Design and Neutronic, Thermal-Hydraulic Analysis of DSCF Assembly for a SMR and Investigation of the Effect on the Thermal Power Uprate. Nuclear Technology, 209(2), 193-213.

[5] Zayermohammadi Rishehri, H., & Zaidabadi Nejad, M. (2022). Conceptual design of an innovative I&XC fuel assembly for a SMR based on neutronic/thermal-hydraulic calculations at the BOC. Kerntechnik, 87(1), 91-103.

[6] Rishehri, H. Z. (2023). Design and optimization of dual-cooled fuel assembly in a 12× 12 configuration for NuScale SMR based on neutronic-thermohydraulic parameters using the combined ANN-GA approach. Progress in Nuclear Energy, 163, 104799.

[7] Zahedi Yeganeh, M. H., & Ansarifar, G. R. (2021). Design of a new Small Modular Nuclear Reactor using TVS-2M Fuel Assemblies and Fuel Depletion analysis during the fresh-core cycle length. Nuclear Engineering and Design, 385, 111540.

[8] Oka, Y. (Ed.). (2014). Nuclear reactor design (p. 127). Springer Japan.

[9] Forster, R. A., & Godfrey, T. N. K. (2006, February). MCNP-a general Monte Carlo code for neutron and photon transport. In Monte-Carlo Methods and Applications in Neutronics, Photonics and Statistical Physics: Proceedings of the Joint Los Alamos National Laboratory-Commissariat à l'Energie

[10] Atomique Meeting Held at Cadarache Castle, Provence, France April 22–26, 1985 (pp. 33-55). Berlin, Heidelberg: Springer Berlin Heidelberg.

ICNST 2024 International Conference on Nuclear Science and Technology
6- 8 MAY 2024 | Isfahan, Iran

Development of High-Speed Neutron Noise Simulator based on High order Nodal Expansion Method for Hexagonal Geometry in Frequency Domain (Paper ID : 1067)

Kolali A.[1], Naghavi dizaji D.[1], Ghafari M.[1], Vosoughi N.[1]
[1]*Department of Energy Engineering, Sharif University of Technology, Tehran, Iran*

Abstract

Improvement of reactor safety using simulation and analysis of the power reactor noise needs to develop the neutron noise computation codes. The purpose of the current study is to develop the neutron noise simulator for hexagonal geometry reactors. Therefore in this research, the SD-HACNEM (Sharif Dynamic - High order Average Current Nodal Expansion Method) simulator is improved to solve the steady-state neutron diffusion equation and neutron noise equation in the frequency-domain for two-dimensional hexagonal geometry by the high-order nodal expansion method. Firstly, calculation is performed for the steady-state. To reduce the discretization error, the flux expansion polynomials degree is increased from 3rd to 5th by considering the nodes with the size of a fuel assembly for either ACNEM (Average Current Nodal Expansion Method) or HACNEM (High-order Average Current Nodal Expansion Method). The verification of the ACNEM and HACNEM is performed by comparing the results with valid References for the IAEA-2D benchmark problem reactor. The steady-state numerical results show that the use of HACNEM provides more accuracy compared with ACNEM, without reducing the size of the nodes. In the main part of the present study, neutron noise calculations are performed in the frequency-domain for two types of noise sources including absorber with variable strength and ILOFAIP (Inadvertent Loading and Operation of a Fuel Assembly in an Improper Position). The results are benchmarked by performing simulation at zero frequency and adjoint calculations. The numerical results show that the use of the high-order nodal expansion method is effective for the simulation of neutron noise in the hexagonal reactor.

Keywords: neutron noise, nodal expansion method, hexagonal geometry, frequency-domain

Introduction

In a nuclear reactor, fluctuations of neutronic and thermohydraulic parameters are detected even in steady-state and full-power conditions. These fluctuations are called power reactor noise and might have different sources like mechanical vibration of components, coolant boiling, temperature changes and etc. [1, 2]. By monitoring and analyzing the fluctuation, the operator might detect abnormal situations to

prevent the occurrence of an event in nuclear power plant without causing any external disturbance to the system or reducing the power plant safety [3, 4]. The fuel assembly which is not properly located in the reactor core, absorber with variable strength, very small changes in the absorption or scattering material of the reactor core, and vibration of the control rods are examples of neutron noise sources [2, 5]. The neutron noise simulation and analysis need the development of the simulators. Due to the importance of neutron noise analysis in the safety of the nuclear reactor, several studies in this field have been performed and different numerical tools have been used in recent years to develop the neutron noise simulator [6-11]. Demazière [6] used the finite difference method (box method) to discretize the 2D, 2G neutron noise equations in the frequency-domain. The developed simulator was elaborated for the reactor cores with rectangular geometries but not viable for hexagonal geometries. In 2010, Malmir [8] developed a neutron noise simulator for hexagonal geometry using the same finite difference method. In 2011, Larsson used the analytical nodal method to discretize the 2D, 2G neutron noise equations in the frequency-domain and in 2018 Hosseini used the nodal expansion method (NEM) to discretize the same equations [7, 9]. According to the research of Hosseini et al. [9], due to the use of the nodes with the size of a fuel assembly and also the use of zero-order flux expansion, the result errors should be high. Recently, many studies were conducted on the simulation and analysis of the power reactor noise using various frequency and time domain tools such as PARCS and CORE-SIM codes [1], S3K [12, 13], and DYN3D [14]. The mentioned studies demonstrate the importance of developing and improving power reactor noise simulators for noise analysis. More recently, SD-HACNEM neutron noise simulator [15] was developed to perform calculations for rectangular geometry. In this work, a new ability was added to SD-HACNEM in order to perform calculations for hexagonal geometry. In order to increase the accuracy of the results the flux expansion order was increased. In other words, the calculations were performed for hexagonal geometry with the high-order nodal expansion method. Nodal expansion method is one types of nodal methods in which average partial currents on the surfaces are used [16, 17]. The advantages of the nodal expansion method compared to finite differences and finite element methods are low-cost calculations and reduction in the execution time of the model-problems simulated [18, 19]. Also, the nodal expansion method is more convergent than analytical nodal method [20]. The high-order average current nodal expansion method has been evaluated by Putney [19] for rectangular and hexagonal geometries in detail. In the previous published paper, SD-HACNEM simulator [15] for neutron noise simulation in the rectangular geometry reactors was reported. It should be noted that in the present work,

the SD-HACNEM simulator was therefore updated to solve the steady-state neutron diffusion equation and neutron noise equation in the frequency-domain for two-dimensional hexagonal geometry by the high-order nodal expansion method.

Research theories

Steady-State Calculation

For two reasons, steady-state calculations are required. Firstly, steady-state results are used as inputs to neutron noise calculations. Secondly, one of the verification methods of neutron noise calculations is to compare the neutron noise results at zero frequency with steady-state results. Therefore in this section discretization of the neutron diffusion equation using the average current nodal expansion method is presented. In other words, fifth-degree polynomials are used in the flux expansion, and after implementing the discretization approach presented by Putney [19], the following equations are obtained.

$$\left[\frac{4}{H}C_{g5}^{m}+\Sigma_{rg}^{m}\right]\Phi_{g}^{m}=\sum_{\substack{g'=1\\g'\neq g}}^{G}\Sigma_{sg'g}^{m}\Phi_{g'}^{m}+\frac{\chi_g}{K_{eff}}\sum_{g'=1}^{G}\nu\Sigma_{fg'}^{m}\Phi_{g'}^{m}+\sum_{\substack{s=r,l\\w=x,u,v}}\frac{2}{3H}\left(1-C_{g1}^{m}-C_{g2}^{m}-2C_{g3}^{m}-2C_{g4}^{m}\right)\bar{J}_{gws}^{m} \tag{1}$$

$$\begin{bmatrix}J_{gxr}^{+m}\\J_{gxl}^{+m}\\J_{gur}^{+m}\\J_{gul}^{+m}\\J_{gvr}^{+m}\\J_{gvl}^{+m}\end{bmatrix}=\begin{bmatrix}C_{g1}^{m}&C_{g2}^{m}&C_{g4}^{m}&C_{g3}^{m}&C_{g4}^{m}&C_{g3}^{m}&C_{g5}^{m}&C_{g6}^{m}&C_{g7}^{m}&C_{g7}^{m}\\C_{g2}^{m}&C_{g1}^{m}&C_{g3}^{m}&C_{g4}^{m}&C_{g3}^{m}&C_{g4}^{m}&C_{g5}^{m}&-C_{g6}^{m}&-C_{g7}^{m}&-C_{g7}^{m}\\C_{g4}^{m}&C_{g3}^{m}&C_{g1}^{m}&C_{g2}^{m}&C_{g4}^{m}&C_{g3}^{m}&C_{g5}^{m}&C_{g7}^{m}&C_{g6}^{m}&C_{g7}^{m}\\C_{g3}^{m}&C_{g4}^{m}&C_{g2}^{m}&C_{g1}^{m}&C_{g3}^{m}&C_{g4}^{m}&C_{g5}^{m}&-C_{g7}^{m}&-C_{g6}^{m}&-C_{g7}^{m}\\C_{g4}^{m}&C_{g3}^{m}&C_{g4}^{m}&C_{g3}^{m}&C_{g1}^{m}&C_{g2}^{m}&C_{g5}^{m}&C_{g7}^{m}&C_{g7}^{m}&C_{g6}^{m}\\C_{g3}^{m}&C_{g4}^{m}&C_{g3}^{m}&C_{g4}^{m}&C_{g2}^{m}&C_{g1}^{m}&C_{g5}^{m}&-C_{g7}^{m}&-C_{g7}^{m}&-C_{g6}^{m}\end{bmatrix}\begin{bmatrix}\bar{J}_{gxr}^{m}\\\bar{J}_{gxl}^{m}\\\bar{J}_{gur}^{m}\\\bar{J}_{gul}^{m}\\\bar{J}_{gvr}^{m}\\\bar{J}_{gvl}^{m}\\\Phi_{g}^{m}\\d_{gx}^{m}\\d_{gu}^{m}\\d_{gv}^{m}\end{bmatrix} \tag{2}$$

$$d_{gx}=\frac{\left(\alpha_g^m+\beta_g^m\right)Q_{gx}^{m}-\beta_g^mQ_{gu}^{m}-\beta_g^mQ_{gv}^{m}}{\left(\alpha_g^m-\beta_g^m\right)\left(\alpha_g^m+2\beta_g^m\right)};\ d_{gu}=\frac{-\beta_g^mQ_{gx}^{m}+\left(\alpha_g^m+\beta_g^m\right)Q_{gu}^{m}-\beta_g^mQ_{gv}^{m}}{\left(\alpha_g^m-\beta_g^m\right)\left(\alpha_g^m+2\beta_g^m\right)};\quad d_{gv}=\frac{-\beta_g^mQ_{gx}^{m}-\beta_g^mQ_{gu}^{m}+\left(\alpha_g^m+\beta_g^m\right)Q_{gv}^{m}}{\left(\alpha_g^m-\beta_g^m\right)\left(\alpha_g^m+2\beta_g^m\right)} \tag{3}$$

These equations respectively are the nodal balance equation, nodal coupling equation, and the high-order coefficients equations of the flux expansion. The description of the above equations parameters can be found in Putney [19]. Reference [21] and discretization approach similar to forward equations are also used to calculate the adjoint equations.

Neutron Noise Calculation

In this section, the neutron noise equation in the frequency-domain is discretized using the high-order nodal expansion method. The general form of neutron noise equations in the two energy groups is according to **References** [2, 5]. In general, the noise source is considered as a perturbation at the macroscopic cross sections. To achieve the forward and adjoint neutron noise equations, a perturbation in the time-dependent equations macroscopic cross-sections is considered and steady-state equations are subtracted from it. As a result, leads to the neutron noise equations according to Eqs. (4-6).

$$\begin{bmatrix} \Sigma_1^m(\omega)+\frac{4}{H}C_{15}^m & -\frac{\nu\Sigma_{f,2}^{m,0}}{k_{eff}}\left(1-\frac{i\omega\beta_{eff}}{i\omega+\lambda}\right) \\ -\Sigma_{s1,2}^{m,0} & \frac{4}{H}C_{25}^m+\frac{i\omega}{v_2}+\Sigma_{a,2}^{m,0} \end{bmatrix}\begin{bmatrix}\delta\Phi_1^m(\omega)\\ \delta\Phi_2^m(\omega)\end{bmatrix}- \begin{bmatrix} \frac{2}{3H}(1-C_{11}^m-C_{12}^m-2C_{13}^m-2C_{14}^m) & 0 \\ 0 & \frac{2}{3H}(1-C_{21}^m-C_{22}^m-2C_{23}^m-2C_{24}^m)\end{bmatrix}\begin{bmatrix}\sum_{w=x,u,v}\sum_{s=r,l}\delta\bar{J}_{1w.}^m \\ \sum_{w=x,u,v}\sum_{s=r,l}\delta\bar{J}_{2w.}^m\end{bmatrix} \quad (4)$$

$$\begin{bmatrix}-\Phi_1^{m,0}\\ \Phi_1^{m,0}\end{bmatrix}\delta\Sigma_{s1,2}^m(\omega)-\begin{bmatrix}\Phi_1^{m,0} & 0\\ 0 & \Phi_2^{m,0}\end{bmatrix}\begin{bmatrix}\delta\Sigma_{a1}^m(\omega)\\ \delta\Sigma_{a2}^m(\omega)\end{bmatrix}+\left(1-\frac{i\omega\beta_{eff}}{i\omega+\lambda}\right)\begin{bmatrix}\Phi_1^{m,0} & \Phi_2^{m,0}\\ 0 & 0\end{bmatrix}\begin{bmatrix}\delta\nu\Sigma_{f,1}^m(\omega)\\ \delta\nu\Sigma_{f,2}^m(\omega)\end{bmatrix}$$

$$\begin{bmatrix}\delta j_{gxr}^{+m}(\omega)\\ \delta j_{gxl}^{+m}(\omega)\\ \delta j_{gur}^{+m}(\omega)\\ \delta j_{gul}^{+m}(\omega)\\ \delta j_{gvr}^{+m}(\omega)\\ \delta j_{gvl}^{+m}(\omega)\end{bmatrix}= \begin{bmatrix} C_{g1}^m & C_{g2}^m & C_{g4}^m & C_{g3}^m & C_{g4}^m & C_{g3}^m & C_{g5}^m & C_{g6}^m & C_{g7}^m & C_{g7}^m \\ C_{g2}^m & C_{g1}^m & C_{g3}^m & C_{g4}^m & C_{g3}^m & C_{g4}^m & C_{g5}^m & -C_{g6}^m & -C_{g7}^m & -C_{g7}^m \\ C_{g4}^m & C_{g3}^m & C_{g1}^m & C_{g2}^m & C_{g4}^m & C_{g3}^m & C_{g5}^m & C_{g7}^m & C_{g6}^m & C_{g7}^m \\ C_{g3}^m & C_{g4}^m & C_{g2}^m & C_{g1}^m & C_{g3}^m & C_{g4}^m & C_{g5}^m & -C_{g7}^m & -C_{g6}^m & -C_{g7}^m \\ C_{g4}^m & C_{g3}^m & C_{g4}^m & C_{g3}^m & C_{g1}^m & C_{g2}^m & C_{g5}^m & C_{g7}^m & C_{g7}^m & C_{g6}^m \\ C_{g3}^m & C_{g4}^m & C_{g3}^m & C_{g4}^m & C_{g2}^m & C_{g1}^m & C_{g5}^m & -C_{g7}^m & -C_{g7}^m & -C_{g6}^m \end{bmatrix} \quad (5)$$

$$\times\left[\delta\bar{J}_{gxr}^m \quad \delta\bar{J}_{gxl}^m \quad \delta\bar{J}_{gur}^m \quad \delta\bar{J}_{gul}^m \quad \delta\bar{J}_{gvr}^m \quad \delta\bar{J}_{gvl}^m \quad \delta\Phi_g^m(\omega) \quad \delta d_{gx}^m(\omega) \quad \delta d_{gu}^m(\omega) \quad \delta d_{gv}^m(\omega)\right]^T$$

$$\begin{bmatrix}\alpha_g^m & \beta_g^m & \beta_g^m\\ \beta_g^m & \alpha_g^m & \beta_g^m\\ \beta_g^m & \beta_g^m & \alpha_g^m\end{bmatrix}\begin{bmatrix}\delta d_{gx}^m\\ \delta d_{gu}^m\\ \delta d_{gv}^m\end{bmatrix}+\begin{bmatrix}d\_\alpha_g^m & d\_\beta_g^m & d\_\beta_g^m\\ d\_\beta_g^m & d\_\alpha_g^m & d\_\beta_g^m\\ d\_\beta_g^m & d\_\beta_g^m & d\_\alpha_g^m\end{bmatrix}\begin{bmatrix}d_{gx}^{m,0}\\ d_{gv}^{m,0}\\ d_{gv}^{m,0}\end{bmatrix}=\begin{bmatrix}\delta Q_{gx}^m\\ \delta Q_{gu}^m\\ \delta Q_{gv}^m\end{bmatrix} \quad (6)$$

The operator form of forward neutron noise and adjoint neutron noise equations are defined as Eq. (7). By integrating over phase space leads to Eq. (8). $d\Pi^m$ is the spatial dimension in the nodal volume. Therefore, the frequency-domain neutron noise simulator can be verified by comparing the amplitude and phase of the two sides of Eq. (8) or in other words by using adjoint calculations [6].

$$L\delta\Phi = \delta S; \quad L^\dagger\delta\phi^\dagger = \delta S^\dagger \quad (7)$$

$$\int [\delta\phi_1(r,\omega) + \delta\phi_2(r,\omega)]\, d\Pi^m = \int \left[\phi_1(r)\delta\phi_1^{\dagger}(r,\omega) + \phi_2(r)\delta\phi_2^{\dagger}(r,\omega)\right] d\Pi^m \quad (8)$$

Iaea-2d Pwr Benchmark Reeactor

The IAEA-2D reactor is used to verify the steady-state and neutron noise calculations. The core geometry is shown in

Fig. 1 in which the fuel assembly lattice pitch is 20 cm. According to references [22, 23], the Albedo boundary condition $\alpha = 0\,5$ is used for this reactor core. The IAEA-2D macroscopic cross-section values in two energy groups are also given in these **References**.

Numerical Results and Discussion

The IAEA reactor core calculations were performed using the ACNEM and HACNEM for nodes with the size of a fuel assembly. As can be seen from Table 1, the absolute value of neutron multiplication factor error (ε_k) for ACNEM and HACNEM is obtained equal to 517 *pcm* and 16 *pcm*, respectively. Also, according to Table 1, the average of relative percent error (*RPE*) of power for ACNEM and HACNEM is respectively obtained 11.36% and 3.52%. The maximum of relative percent error of power for ACNEM and HACNEM is respectively obtained 23.97% and 8.88%. Therefore, by increasing the order of flux expansion and considering fixed-size nodes, it can be concluded that the calculation accuracy is significantly improved. The *RPE* distribution using ACNEM and HACNEM for the IAEA-2D reactor is comparable in

Fig. 1. The values of reference [23, 24] are used to calculate the *RPE* in this figure.

Method	Expansion order	k_{eff}	$k_{eff}^{\dagger}$	$\varepsilon_k(pcm)$	RPE Ave.	RPE Max.	CPU-TIME (Sec)
ACNEM	3	1.00030	1.00030	-517	11.36	23.97	18
HACNEM	5	1.00534	1.00534	-16	3.52	8.88	28

Table 1. The neutron multiplication for IAEA-2D reactor
* The reference value of the effective multiplication factor is 1.00551 [23, 24].

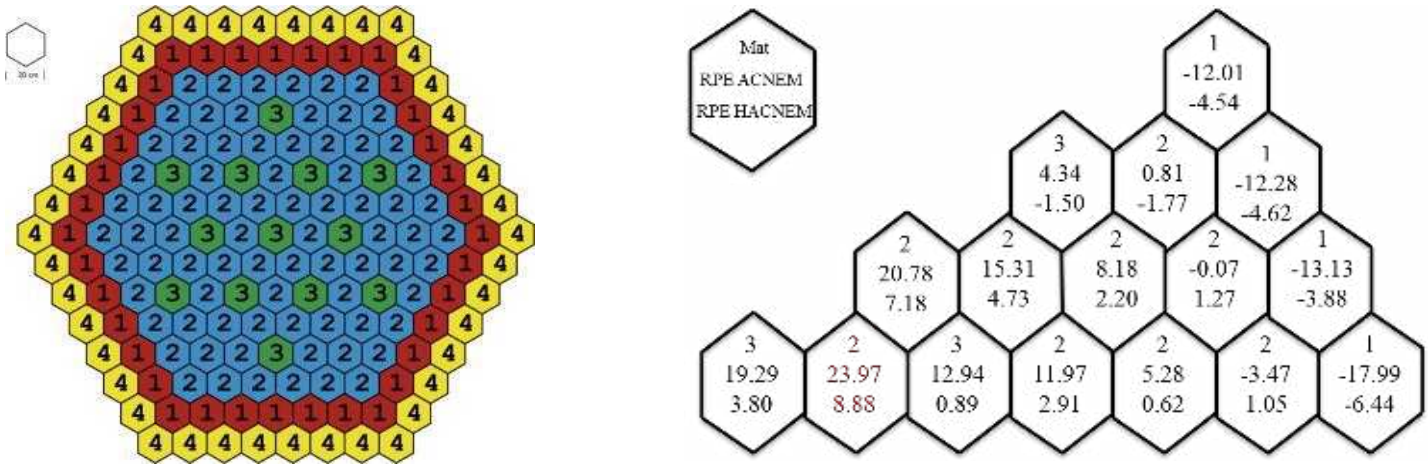

Fig. 1. IAEA-2D core arrangement and its RPE using ACNEM and HACNEM

The distribution of fast and thermal neutron fluxes for the IAEA-2D reactor computed by HACNEM are shown in Fig. 2.

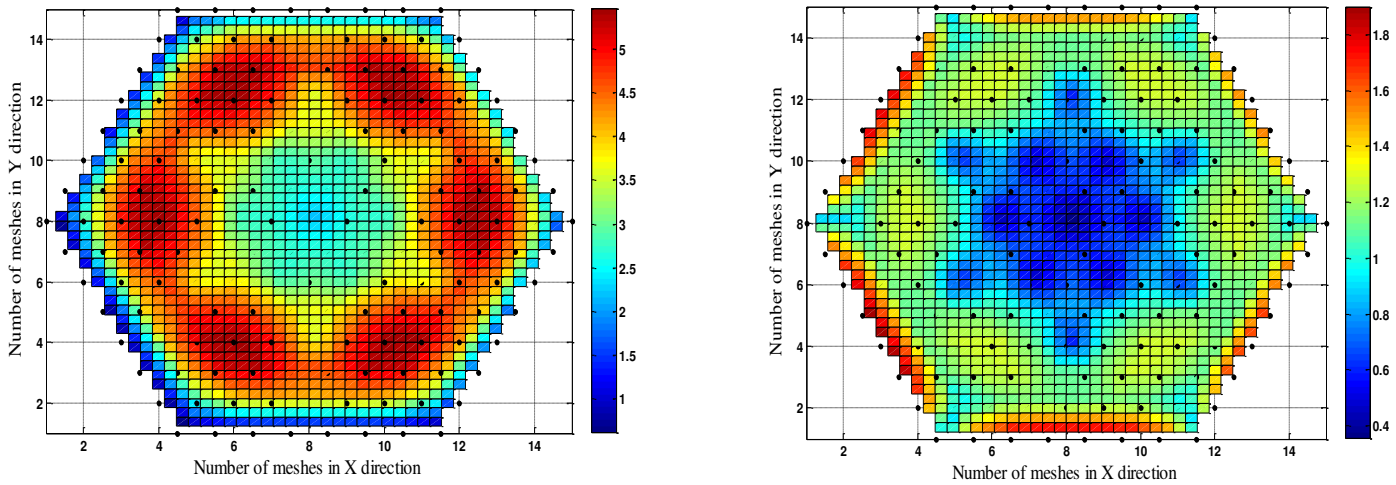

Fig. 2. Distribution of fast (left) and thermal (right) neutron flux calculated by HACNEM for IAEA-2D

In Fig. 3 are shown the thermal neutron noise distribution for a source of absorber with variable strength which calculated by developed neutron noise simulator called SD-HACNEM. In this calculation, a perturbation $0\ 0001 cm^{-1}$ at frequency 0.01 Hz has been applied to the thermal absorption cross-section of the central fuel assembly.

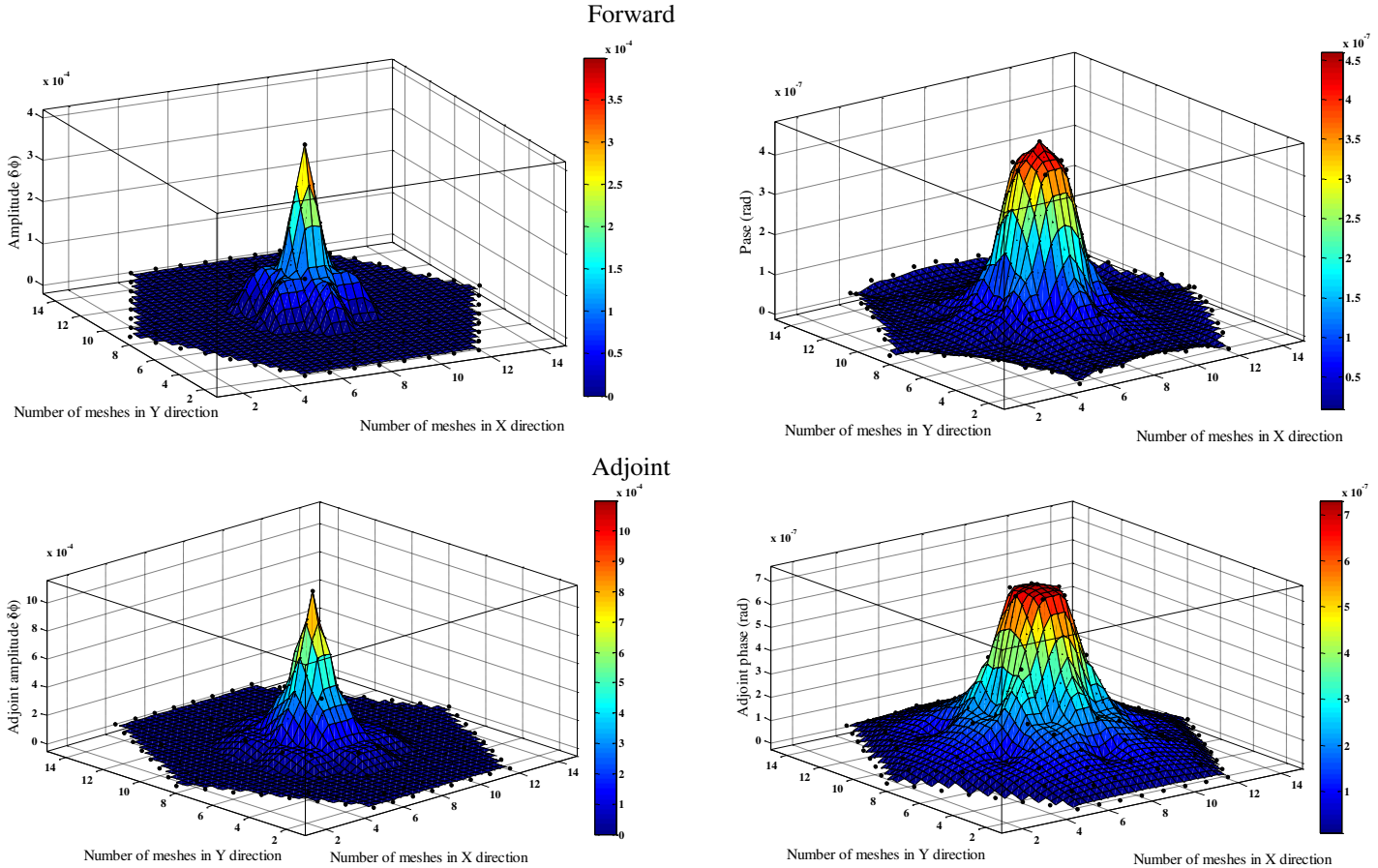

Fig. 3. Distribution of Thermal neutron noise amplitude (left) and phase (right) calculated with SD-HACNEM for IAEA-2D.

In this study, ILOFAIP neutron noise source is investigated. The ILOFAIP source is a combination of two sources of absorber with variable strength and with opposite sign. For ILOFAIP simulation, two sources of absorber with variable strength are considered within the central fuel assembly and its neighbors. The strength of this perturbation is equal to the difference in the macroscopic cross section of the two fuel assembly and the frequency of this source is 0.01 *Hz*. The distribution of the ILOFAIP neutron noise are visible in Fig. 4. Neutron noise equation is linear with respect to the perturbation and the response. The response to the combination of two sources of absorber with variable strength or ILOFAIP is, consequently, a superposition of the responses of the individual absorbers with variable strength.

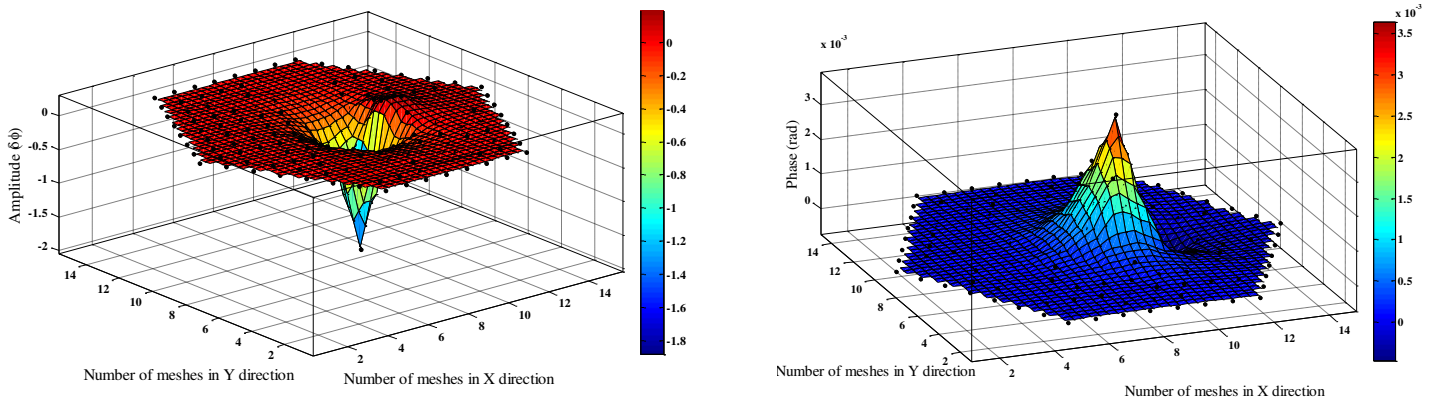

Fig. 4. Distribution of neutron noise amplitude (left) and phase (right) calculated with SD-HACNEM for ILOFAIP

The qualitative comparison of the neutron noise figures obtained using SD-HACHEM with similar previous studies confirms the high-order nodal expansion method [8, 9, 11]. Neutron noise calculation at zero frequency is another method for verification of SD-HACHEM. In other words, the neutron noise calculations at zero frequency must be equal to the results of the steady-state calculations. Fig. 5 is showing the distribution of thermal and fast neutron noise in zero frequency while this figure completely match with Fig. 2.

As previously mentioned, another method to verify the calculations was performed by using Eq. (8). Fig. 6 is showing the amplitude of the left and right hand side of Eq. (8) for a source of absorber with variable strength. Also, the phase of the left and right hand side of Eq. (8) for a source of absorber with variable strength are presented in this figure. Also, according to the same figures, acceptable equality of the results (with an average difference of 6.66 %) is consistent and since these figures show a small difference, it can be concluded that the high-order nodal expansion method is suitable for neutron noise calculations with a source in the dimension of a fuel assembly. Therefore, the verification used by qualitative

comparison with References, zero-frequency neutron noise calculations, and the use of adjoint calculations (Eq. (8)) confirms the accuracy of the neutron noise simulation with SD-HACNEM simulator.

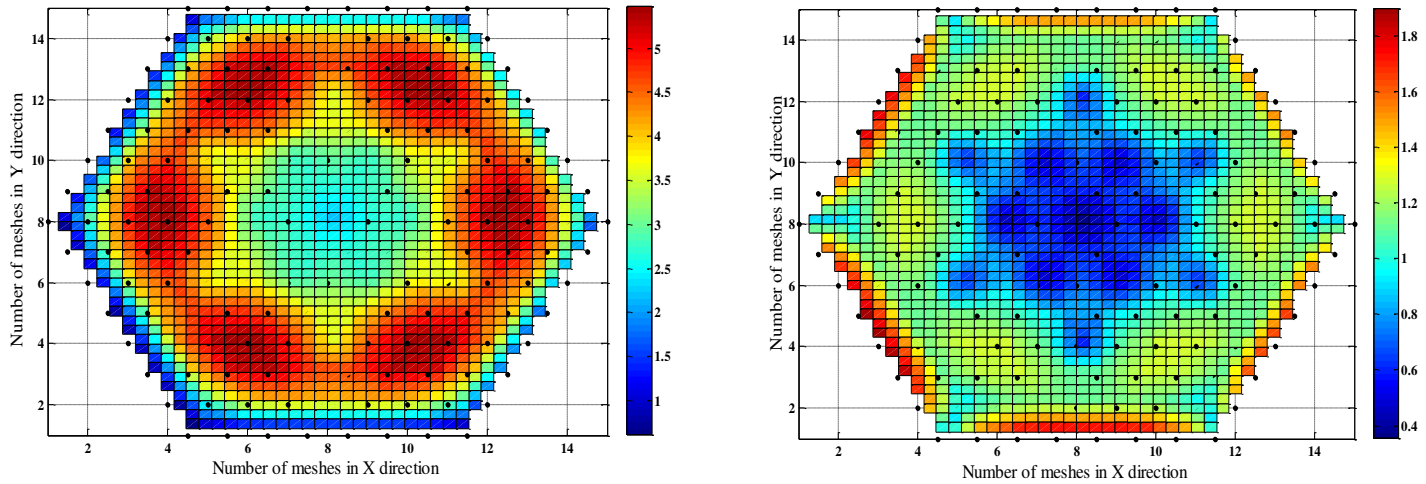

Fig. 5. Distribution of fast (left) and thermal (right) neutron noise calculated with SD-HACNEM at zero frequency

Left-hand side

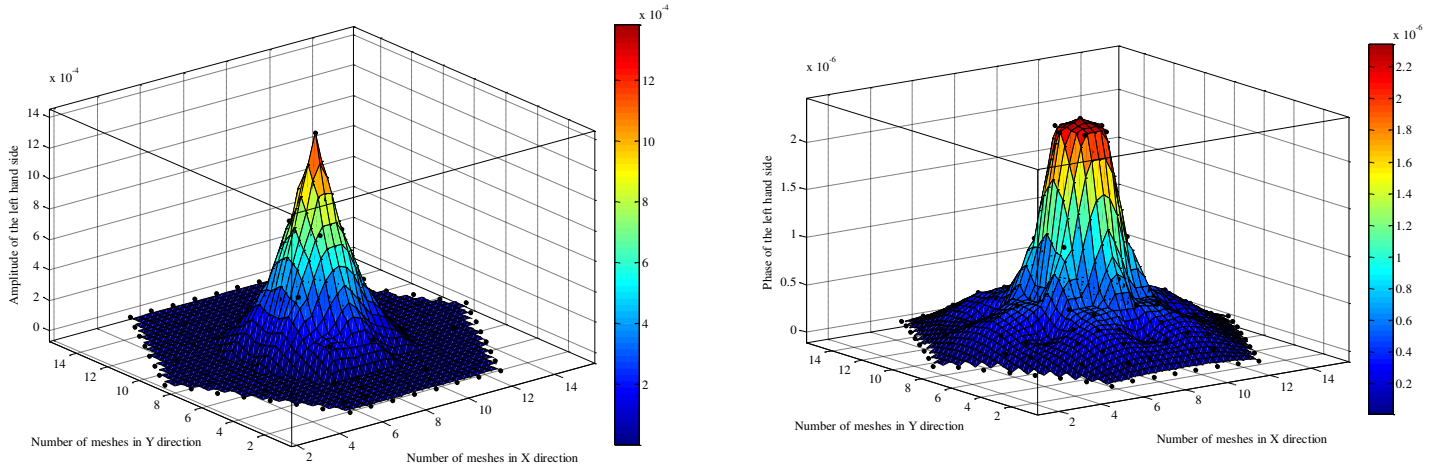

Right-hand side

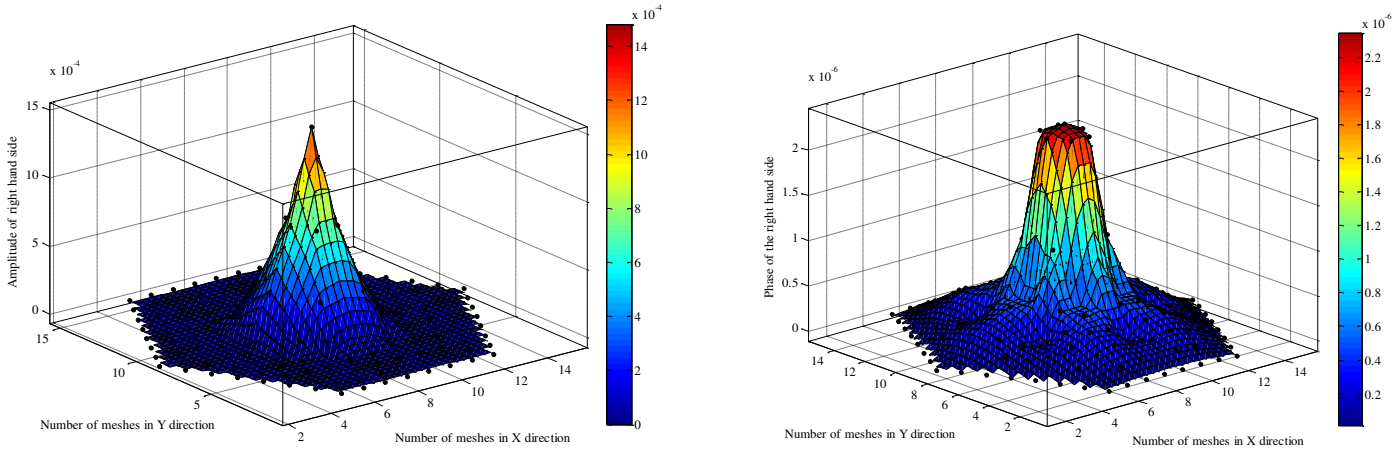

Fig. 6. The amplitude (left) and phase (right) of Eq. (8) for a source of absorber with variable strength 0.0001 cm^{-1} and frequency 0.01 Hz

Conclusions

Because the number of detectors in the reactor core is few and also to simulate the neutron noise caused by sources in the size of a fuel assembly, the average current nodal expansion method has been used to conduct neutron noise calculations. Also, the nodal expansion method calculation errors are large since their node sizes are large. Therefore, high-order expansion should be used to reduce these errors. Also, due to the use of large nodes in the nodal expansion method, the time and cost of calculations are significantly reduced. In this paper, the higher-order average current nodal expansion method was used to derive the neutron noise equations, and then SD-HACNEM hexagonal geometry core simulator was developed. To verification of steady-state calculations and neutron noise simulator, the IAEA-2D PWR reactor was used. By increasing the expansion order from the polynomials of degree three to degree five, the average relative percent error of power improved from 11.36% to 3.52%, respectively. These results show that the simulator has acceptable accuracy. Neutron noise calculations were performed with SD-HACNEM for absorber with variable strength and ILOFAIP neutron noise sources. Also, neutron noise calculations were confirmed by comparison with valid References, zero-frequency calculations, and the use of adjoint calculations. The results show that the use of the high-order nodal expansion method is effective for simulation of neutron noise in the hexagonal reactor. In general, the innovations of current research may be summarized as follows:

Usage of nodes in the dimensions of the hexagonal fuel assembly with acceptable accuracy;

Utilization of the fifth-degree polynomials in the discretization of neutron noise equations which makes HACNEM and SD-HACNEM precision considerably higher than ACNEM;

Application of the high-order flux expansion in order to simulate ILOFAIP neutron noise in the hexagonal reactor;

Improvement of the SD-HACNEM neutron noise simulator for both the rectangular and hexagonal geometry reactors;

By conducting this study, SD-HACNEM simulator is now capable to simulate the neutron noise in either rectangular or hexagonal geometries using the coarse mesh method, namely high-order nodal expansion method.

References

[1] N. Olmo-Juan, C. Demazière, T. Barrachina, R. Miró, and G. Verdú, "PARCS vs CORE SIM neutron noise simulations," *Progress in Nuclear Energy,* vol. 115, pp. 169-180, 2019.

[2] C. Demazière and I. Pázsit, "Power reactor noise, lecture notes," *Department of Nuclear Engineering, Chalmers University of Technology, Gothenburg, Sweden,* 2008.

[3] S. A. Hosseini, "High accurate three-dimensional neutron noise simulator based on GFEM with unstructured hexahedral elements," *Nuclear Engineering and Technology,* 2019.

[4] G. Petkov, "Symptom-based context quantification for dynamic accident analysis," *Safety Science,* 2018.

[5] C. Demazière and G. Andhill, "Identification and localization of absorbers of variable strength in nuclear reactors," *Annals of Nuclear Energy,* vol. 32, no. 8, pp. 812-842, 2005.

[6] C. Demazière, "Development of a 2-D 2-group neutron noise simulator," *Annals of Nuclear Energy,* vol. 31, no. 6, pp. 647-680, 2004.

[7] V. Larsson, C. Demazière, I. Pázsit, and H. N. Tran, "Neutron noise calculations using the Analytical Nodal Method and comparisons with analytical solutions," *Annals of Nuclear Energy,* vol. 38, no. 4, pp. 808-816, 2011.

[8] H. Malmir, N. Vosoughi, and E. Zahedinejad, "Development of a 2-D 2-group neutron noise simulator for hexagonal geometries," *Annals of Nuclear Energy,* vol. 37, no. 8, pp. 1089-1100, 2010.

[9] S. A. Hosseini, N. Vosoughi, and J. Vosoughi, "Neutron noise simulation using ACNEM in the hexagonal geometry," *Annals of Nuclear Energy,* vol. 113, pp. 246-255, 2018.

[10] M. Bahrami and N. Vosoughi, "SN transport method for neutronic noise calculation in nuclear reactor systems: Comparative study between transport theory and diffusion theory," *Annals of Nuclear Energy,* vol. 114, pp. 236-244, 2018.

[11] S. A. Hosseini and N. Vosoughi, "Neutron noise simulation by GFEM and unstructured triangle elements," *Nuclear Engineering and Design,* vol. 253, pp. 238-258, 2012.

[12] D. Chionis *et al.*, "SIMULATE-3K analyses of neutron noise response to fuel assembly vibrations and thermal-hydraulics parameters fluctuations," in *Int. Conf. Mathematics & Computational Methods Applied to Nuclear Science & Engineering (M&C 2017), Jeju, Korea*, 2017.

[13] L. Torres, D. Chionis, C. Montalvo, A. Dokhane, and A. García-Berrocal, "Neutron Noise Spectral Features of Simulated Mechanical and Thermal-Hydraulic Perturbations in a PWR Core," in *EPJ Web of Conferences*, 2021, vol. 247: EDP Sciences, p. 21001.

[14] M. Viebach *et al.*, "Verification of the code DYN3D for calculations of neutron flux fluctuations," *Annals of Nuclear Energy,* vol. 166, p. 108735, 2022.

[15] A. Kolali, J. Vosoughi, and N. Vosoughi, "Development of SD-HACNEM neutron noise simulator based on high order nodal expansion method for rectangular geometry," *Annals of Nuclear Energy,* vol. 162, p. 108496, 2021.

[16] R. D. Lawrence, "DIF3D nodal neutronics option for two-and three-dimensional diffusion theory calculations in hexagonal geometry.[LMFBR]," Argonne National Lab., IL (USA), 1983.

[17] H. Finnemann, F. Bennewitz, and M. Wagner, "Interface current techniques for multidimensional reactor calculations," *Atomkernenergie,* vol. 30, no. 2, pp. 123-128, 1977.

[18] T. Downar, D. Lee, Y. Xu, T. Kozlowski, and J. Staudenmier, "PARCS v2. 6 US NRC core neutronics simulator theory manual," *Purdue University, West Lafayette, IN,* 2004.

[19] J. M. Putney, "Nodal methods for solving the diffusion equation for fast reactor analysis," 1984.

[20] S. Hall, "The Development of a Nodal Method for the Analysis of PWR Cores with Advanced Fuels," 2013.

[21] G. I. Bell and S. Glasstone, "Nuclear reactor theory," US Atomic Energy Commission, Washington, DC (United States), 1970.

[22] Y. A. Chao and Y. Shatilla, "Conformal mapping and hexagonal nodal methods—II: implementation in the ANC-H code," *Nuclear Science and Engineering,* vol. 121, no. 2, pp. 210-225, 1995.

[23] U. Grundmann and F. Hollstein, "A two-dimensional intranodal flux expansion method for hexagonal geometry," *Nuclear science and engineering,* vol. 133, no. 2, pp. 201-212, 1999.

[24] A. Hebert, "A Raviart–Thomas–Schneider solution of the diffusion equation in hexagonal geometry," *Annals of Nuclear Energy,* vol. 35, no. 3, pp. 363-376, 2008.

ICNST 2024
International Conference on Nuclear Science and Technology
6- 8 MAY 2024 | Isfahan, Iran

Assessment and predicting effects of Accident Tolerant Fuel (ATF) composition and geometry on the neutronic and safety parameters in the Small Modular Nuclear Reactor via Artificial Neural Network (Paper ID : 1072)

Ansarifar G.R.[1*], Hajipour M.[2], Zahedi yeganeh M.H

[1]Department of Nuclear Engineering, University of Isfahan, Isfahan, Iran [2]Department of Nuclear Engineering, University of Isfahan, Isfahan, Iran [3]Department of Nuclear Engineering, University of Isfahan, Isfahan, Iran

Abstract

Accident Tolerant Fuels (ATF) are new nuclear fuel concepts to improve fuel performance during normal and accident conditions. In this paper, the core of the NuScale nuclear reactor as a typical Small Modular Reactor (SMR) is investigated in the equilibrium cycle to study the effect of ATF composition and geometry on the neutronic and safety parameters of the reactor core. The core is designed with UO2-FeCrAl C26M fresh and burned-up fuel assemblies. It is studied in many different compositions and geometry of fuels via neutronic simulations using MCNP. Fuel changes are applied to the gadolinium concentration, weight percentage of the cladding material, and clad thickness to study their effects on the neutronic and safety parameters, including excess reactivity, hot full power reactivity, effective delayed neutron fraction, radial power peaking factor, fuel and coolant reactivity feedback coefficients. Furthermore, an Artificial Neural Network (ANN) is designed for the predictive modeling of key neutronic and safety parameters in the NuScale small modular reactor loaded with accident-tolerant fuel based on the case studies and simulations. Indeed, a developed ANN, utilizing the obtained data, predicts the neutronic and safety parameters of the Nuscale reactor core with ATF. The presented ANN is trained in MATLAB using the observed data. The input includes gadolinium concentration, weight percentage of the cladding material, and the thickness of the cladding which is adjusted based on the outer diameter of the cladding. This results in various outputs, including excess reactivity, hot full power reactivity, effective delayed neutron fraction, radial power peaking factor, and fuel and coolant reactivity feedback coefficients. Also, the designed artificial neural network is validated using neutronic calculations.

Keywords: Accident Tolerant Fuels (ATF), Small Modular Reactor (SMR), neutronic simulations, Artificial Neural Network (ANN), excess reactivity, hot full power reactivity, effective delayed neutron fraction, radial power peaking factor, and fuel and coolant reactivity feedback coefficients

Introduction

Small modular reactors represent an exciting new direction for nuclear power, offering the potential for increased safety, cost-effectiveness, and flexibility. One of the latest and most promising types of SMRs is the NuScale reactor. NuScale reactor can generate up to 60MW of electricity and has passive safety systems suitable for remote locations. Furthermore, Accident Tolerant Fuel is a type of nuclear fuel designed to be more resistant to extreme conditions and has the potential to significantly improve the safety and economy of nuclear reactors. However, there are still many challenges that need to be addressed before it can be widely deployed. In this sense, Artificial Neural Networks are a powerful machine learning algorithms that can solve complex problems and make predictions based on large amounts of data. Zahedi and Ansarifar designed an enhanced hexagonal fuel assembly for the NuScale core with suitable neutronic and thermal-hydraulic performance [1]. Pino-Medina and François used different coating materials on ATF fuels for neutronic analysis of the NuScale core. They concluded that the NuScale equilibrium core could work with U_3Si_2 fuel of lower enrichment level without any change in the core design [2]. Pinem et al. investigated the feasibility of U_3Si_2 and various cladding materials as an ATF candidate for AP1000 Light Water Reactor, revealing the potential of SiC, FeCrAl, and AMPT claddings from the neutronic aspect [3]. Rahnama and Ansarifar used nanofluid coolant for the NuScale core. They predicted the neutronic, thermal-hydraulic, and natural circulation parameters of the core with an Artificial Neural Network and optimized algorithms [4]. Tabas et al. trained and tested ANN based on performance data of the Miniature Neutron Source Reactor and concluded the effective prediction of the reactor's behavior across all fixed power data points [5].

Rafiei and Ansarifar presented a conceptual fuel design for a space nuclear reactor and estimated the fuel mixture with an Adaptive Neuro-Fuzzy Inference System. They used various algorithms to optimize ANFIS from neutronic aspects and calculate the optimal fuel mixture and BeO thickness [6]. FeCrAls will become the next generation of nuclear fuel cladding materials, replacing Zircaloy [7]. This paper presents an equilibrium cycle of the NuScale reactor core based on a previous design by Pino-Medina and François [2] in that the cladding material is changed from Zr-4 to FeCrAl C26M. The cladding characteristics and burnable absorber concentrations in fuels are variously changed producing

different cases to evaluate the neutronic and dynamic parameters of the core. In addition, these cases are fed to an Artificial Neural Network and trained as a model to predict the effect of such changes.

Core design and Modeling

The NuScale reactor core is maintained in the reactor pressure vessel alongside the steam generator and pressurizer. In this study, the equilibrium cycle of the NuScale reactor core is developed based on a previous design by Pino-Medina and François [2]. Table 1 presents the summarized characteristics of the NuScale reactor. Figure 1 demonstrates the simulated NuScale reactor core formation. The reactor core has 37 fuel assemblies with 17 × 17 arrays. Each fuel assembly has 264 fuel rods and 25 guide tubes for control rods, spacer grids, and one measurement tube at the center. The fuel rods consist of UO_2 pellets and a homogenous Gd_2O_3 burnable absorber in specified fuel assemblies. The cladding material is changed from Zircalloy-4 to FeCrAl C26M. As an ATF material, FeCrAl is used in a wide range of high-temperature applications. The main advantage of FeCrAl compared to Zircalloy is its much slower oxidation kinetic in high temperatures. FeCrAl is also very resistant to corrosion due to forming a fine Al_2O_3 layer [8] and has superior or similar mechanical strength to Zircalloy [9]. The main disadvantage of FeCrAl is the high neutron absorption of Iron, leading to higher parasitic absorption of FeCrAl and reduction in reactivity [10,11]. The NuScale core has seven different fuel assemblies based on fuel rod specifications and burnups, as shown in figure 2. In this equilibrium core, fuel assemblies may be fresh, once or twice burned by their location. Table 2 shows the details of the fuel rods employed in each fuel assembly. In this study, other minor elements in FeCrAl such as Molybdenum are classified into the same group as Iron. Neutronic calculations in this study are simulated in both cold and clean (C&C) and hot full power (HFP) conditions. In C&C condition, the core temperature is 293.6K, without burnable absorbers or soluble boron concentrations. In HFP condition, fuel temperature is 900K, moderator temperature is 573K, burnable absorbers are utilized, and soluble boron concentration is calculated to maintain critical reactivity.

Table 1: Technical data and core design parameters [12]

Parameter	Value
Reactor thermal output Power	160 MW (th)
plant efficiency Electrical output	>30%
Coolant	45 MW(e)
Moderator	Light water Light water 2 m
Active core height Outside	2.83 m UO_2
diameter Fuel material	17 × 17
Fuel element type Cladding	FeCrAl C26M
material Fuel enrichment Burnable	<4.95 wt% Gd_2O_3
absorber	12.76 MPa
Reactor operating pressure	0.4142 cm
Cladding inside radius Cladding	0.4751 cm
outside radius Fuel pellet radius	0.406 cm
Pellet-cladding gap radius	0.0082 cm

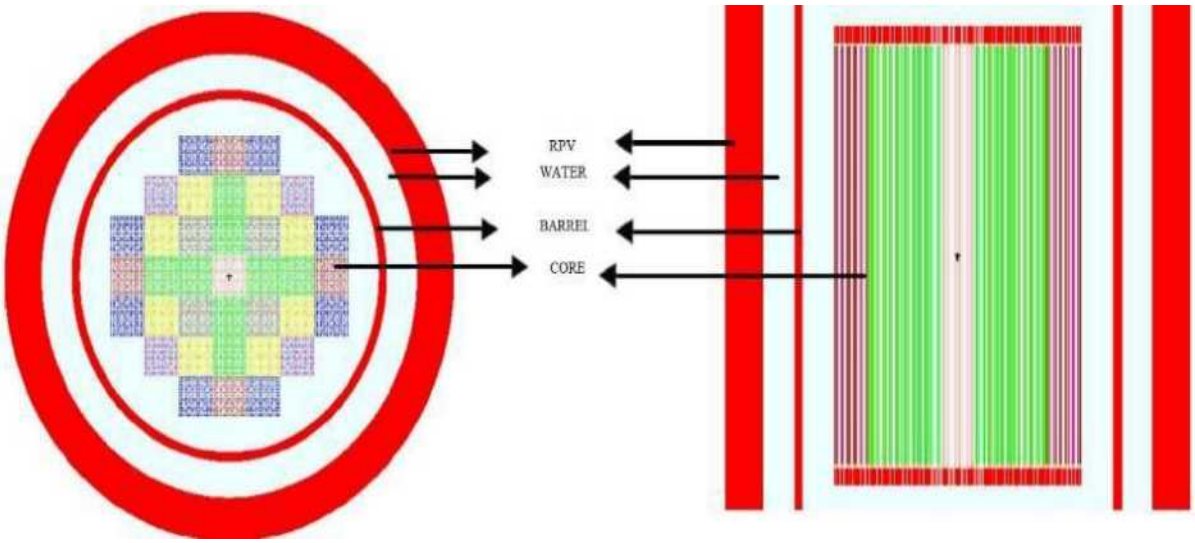

Figure 1: Top and side views of the simulated core in MCNP

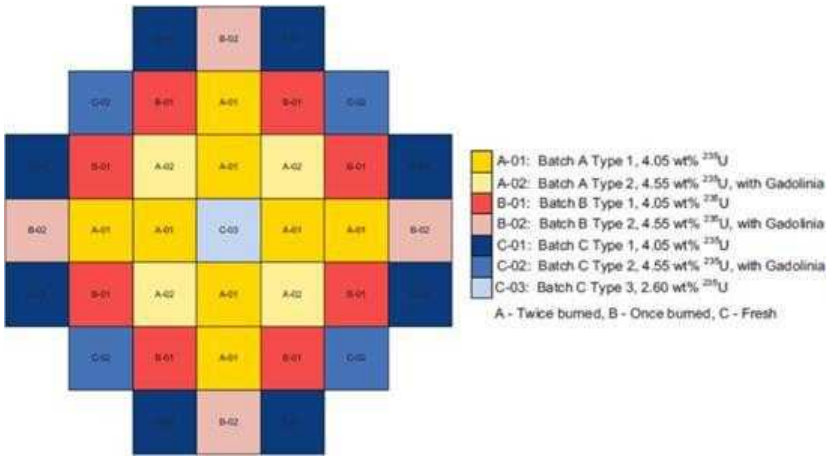

Figure 2: Loading pattern for NuScale equilibrium cycle [12]

Table 2: Fuel rod material specifications

UO_2 fuel assembly Fuel pellet specification	Type 1	Type 2	Type 3	
UO_2 density(g/cm^3)	10.5	10.5	10	
^{235}U enrichment (wt% ^{235}U /U)	2.6	4.05	4.55	
Gd_2O_3 concentration (wt%)	0	0	10	
Cladding specification Cladding material (wt%)	Fe	Cr	Al	Others
FeCrAl C26M	80	12	6	Mo, Si, and Y

All simulations are performed using MCNP6 code to achieve reactivity, power peaking factor calculations, and feedback reactivity coefficients. Cross-section data for various temperatures are obtained using MAKXSF code. For better accuracy, MCNP simulation for HFP and beta calculation was performed using 100000 particles and 900 effective cycles. In comparison, all other data were obtained from MCNP simulations with 10000 particles and 500 effective cycles ensuring proper accuracy. Table 3 illustrates the neutronic and dynamic data array for 108 cases simulated for this study. Input parameters for each case are clad thickness, clad mixture weight percentages, and Gd_2O_3

weight percentage in fuel. Also, output parameters are excess reactivity, hot full power reactivity, effective delayed neutron fraction (β), radial power peaking factor of the fuel assembly, and fuel and coolant reactivity temperature coefficients. For example, case 0 is the main core design from the previous study by [2] except for changing the cladding material from Zircaloy-4 to FeCrAl C26M and recalculating soluble boron concentration to maintain the core critical in HFP condition. Other cases have at least one change in an input parameter e.g. case 12 states a +5% change in chromium weight percentage. In certain instances, the reactivity at HFP has turned negative, implying that the core's fuel composition prevents it from attaining a critical condition. Since three major elements in the FeCrAl mixture exist, it has two degrees of freedom for applying changes. Therefore, only Chromium and aluminum weight percentages are counted as input parameters. However, their effects on each element and total weight percentage are calculated.

Table 3: Extracted data for various fuel mixture

	Input parameters (change%)				Output parameters					
Case	Clad thickness	Cr	Al	Gd_2O_3	ρ (C&C) ±0.00031	β ±0.00002	ρ (HFP) ±0.00007	Rppf(FA) ±0.012	α_f (pcm/°C) ±1.24e-6	α_c (pcm/°C) ±1.033e-05
0	0. 609 mm	12	6	10	0.1405	0.00603	0.0009	1.394	-3.0911e-5	-6.2027e-4
1	+5%				0.1371	0.00604	-0.0043	1.409	-3.0430e-5	-6.4673e-4
2	-5%				0.1457	0.00604	0.0059	1.401	-3.1064e-5	-6.3973e-4
3	+10%				0.1320	0.00606	-0.0097	1.391	-2.9924e-5	-6.3370e-4
4	-10%				0.1502	0.00602	0.0111	1.404	-2.9161e-5	-6.4458e-4
5	+15%				0.1275	0.00607	-0.0150	1.388	-3.1104e-5	-6.4965e-4
6	-15%				0.1539	0.00605	0.0160	1.421	-2.9277e-5	-6.2203e-4
7	+20%				0.1228	0.00601	-0.0201	1.378	-3.0642e-5	-6.4556e-4
8	-20%				0.1580	0.00604	0.0210	1.424	-3.0466e-5	-6.1642e-4
9	-30%				0.1661	0.00604	0.0305	1.439	-2.9551e-5	-6.0494e-4
10	-40%				0.1741	0.00599	0.0397	1.407	-2.9156e-5	-6.0871e-4
11	-50%				0.1813	0.00601	0.0489	1.463	-2.8573e-5	-6.1275e-4
12		+5%			0.1415	0.006	0.0014	1.395	-2.8889e-5	-6.3791e-4
13		-5%			0.1405	0.00606	0.0004	1.422	-2.8217e-5	-6.2575e-4
14		+10%			0.1423	0.00604	0.0020	1.395	-2.9909e-5	-6.4489e-4
15		-10%			0.1405	0.00604	-0.0001	1.403	-2.9448e-5	-6.4299e-4
16		+15%			0.1431	0.00603	0.0024	1.411	-2.8755e-5	-6.4939e-4
17		-15%			0.1395	0.00605	-0.0005	1.402	-2.9103e-5	-6.3717e-4
18		+20%			0.1431	0.00604	0.0032	1.429	-2.8797e-5	-6.2781e-4
19		-20%			0.1391	0.00604	-0.0010	1.404	-2.9983e-5	-6.4073e-4
20			+5%		0.1410	0.00603	0.0011	1.417	-2.9135e-5	-6.3972e-4
21			-5%		0.1409	0.00599	0.0007	1.395	-3.0786e-5	-6.4336e-4
22			+10%		0.1420	0.006	0.0012	1.413	-2.9038e-5	-6.3261e-4
23			-10%		0.1407	0.00605	0.0005	1.394	-3.0383e-5	-6.2608e-4
24			+15%		0.1421	0.006	0.0015	1.403	-2.9157e-5	-6.3308e-4

25			-15%		0.1402	0.00603	0.0002	1.380	-2.9056e-5	-6.2023e-4
26			+20%		0.1415	0.00604	0.0016	1.411	-2.9256e-5	-6.2892e-4
27			-20%		0.1405	0.00604	0.0002	1.406	-3.0941e-5	-6.3151e-4
28				+5%	0.1412	0.00602	0.0002	1.422	-2.8852e-5	-6.2444e-4
29				-5%	0.1410	0.00603	0.0015	1.406	-3.2418e-5	-6.2957e-4
30				+10%	0.1408	0.00602	-0.0002	1.397	-3.0691e-5	-6.1603e-4
31				-10%	0.1411	0.00604	0.0019	1.378	-2.8412e-5	-6.2740e-4
32				+15%	0.1414	0.00603	-0.0005	1.409	-2.9983e-5	-6.3220e-4
33				-15%	0.1414	0.00603	0.0026	1.387	-2.9537e-5	-6.2439e-4
34				+20%	0.1409	0.006	-0.0010	1.389	-3.1431e-5	-6.4509e-4
35				-20%	0.1411	0.00601	0.0032	1.392	-2.7473e-5	-6.2553e-4
36	+5%	+15%			0.1354	0.00601	-0.0024	1.383	-3.1844e-5	-6.3592e-4
37	+15%	-10%			0.1298	0.00605	-0.0159	1.361	-3.0168e-5	-6.4736e-4
38	-15%	+15%			0.1524	0.00601	0.0223	1.418	-3.0364e-5	-6.2655e-4
39	-50%	+20%			0.1826	0.00602	0.0502	1.453	-2.8072e-5	-6.1695e-4
40	-5%		-10%		0.1450	0.00604	0.0055	1.419	-3.0988e-5	-6.2784e-4
41	-40%		+5%		0.1739	0.00602	0.0399	1.453	-2.8447e-5	-6.0177e-4
42	-10%		+15%		0.1499	0.00602	0.0117	1.411	-3.0602e-5	-6.2581e-4
43	+20%		+20%		0.1243	0.00602	-0.0193	1.376	-3.0093e-5	-6.4312e-4
44	-50%			+5%	0.1818	0.00596	0.0485	1.441	-2.8570e-5	-6.1836e-4
45	+10%			-15%	0.1325	0.00602	-0.0079	1.359	-3.0304e-5	-6.5178e-4
46	+20%			+15%	0.1229	0.00605	-0.0221	1.375	-2.9547e-5	-6.6340e-4
47	-10%			-10%	0.1497	0.00601	0.0121	1.435	-2.9177e-5	-6.1895e-4
48		-20%	-20%		0.1379	0.00607	-0.0021	1.359	-2.8709e-5	-6.3689e-4
49		-15%	+5%		0.1395	0.00603	-0.0004	1.404	-3.0527e-5	-6.3162e-4
50		+15%	-10%		0.1423	0.00603	0.0023	1.394	-3.0140e-5	-6.4321e-4
51		+20%	+20%		0.1444	0.00608	0.0041	1.423	-2.9056e-5	-6.6571e-4
52		-20%		-20%	0.1387	0.00604	0.0013	1.396	-2.9060e-5	-6.2838e-4
53		-15%		+15%	0.1396	0.00605	-0.0020	1.434	-3.1109e-5	-6.4685e-4
54		+15%		-15%	0.1429	0.00602	0.0042	1.394	-2.7953e-5	-6.3069e-4
55		+20%		+20%	0.1428	0.00603	0.0012	1.411	-3.0200e-5	-6.3288e-4
56			-20%	-20%	0.1411	0.00602	0.0023	1.388	-2.8130e-5	-6.1795e-4
57			-15%	+5%	0.1412	0.00606	-0.0003	1.396	-3.0666e-5	-6.4436e-4
58			+10%	-15%	0.1414	0.00601	0.0029	1.401	-2.8695e-5	-6.3023e-4
59			+20%	+20%	0.1409	0.00605	-0.0003	1.429	-2.9333e-5	-6.3867e-4
60	-50%	-20%	-20%		0.1801	0.00601	0.0473	1.431	-2.8981e-5	-6.0720e-4
61	+15%	+15%	+15%		0.1312	0.00603	-0.0121	1.399	-3.0530e-5	-6.3987e-4
62	+20%	-15%	-20%		0.1201	0.00604	-0.0232	1.375	-3.0689e-5	-6.4614e-4
63	+10%	+20%	+20%		0.1351	0.00602	-0.0060	1.402	-2.9198e-5	-6.5330e-4
64	+5%	-5%	-15%		0.1357	0.00604	-0.0054	1.397	-2.9485e-5	-6.4494e-4
65	-20%	+10%	+5%		0.1591	0.00598	0.0222	1.455	-2.9265e-5	-6.2823e-4
66	-20%	-20%		-20%	0.1561	0.00604	0.0013	1.396	-2.9060e-5	-6.2838e-4
67	-15%	+10%		-15%	0.1551	0.00601	0.0183	1.401	-2.9125e-5	-6.3232e-4
68	+15%	-10%		-10%	0.1268	0.00606	-0.0150	1.388	-3.0527e-5	-6.4440e-4
69	-10%	-15%		+10%	0.1485	0.00602	0.0087	1.425	-2.9934e-5	-6.2966e-4
70	-15%	+15%		+15%	0.1549	0.00603	0.0158	1.429	-2.9896e-5	-6.2529e-4
71	+20%	+20%		+20%	0.1258	0.00603	0.0012	1.411	-3.0200e-5	-6.3288e-4
72	-20%		-20%	-20%	0.1573	0.006	0.0225	1.412	-3.0468e-5	-5.9752e-4
73	-15%		+10%	-15%	0.1542	0.00603	0.0179	1.418	-2.9196e-5	-6.1569e-4
74	+15%		-10%	-10%	0.1273	0.00605	-0.0142	1.385	-2.9883e-5	-6.3638e-4
75	-10%		-15%	+10%	0.1490	0.006	0.0095	1.436	-2.8604e-5	-6.3463e-4
76	-15%		+15%	+15%	0.1543	0.00599	0.0151	1.409	-2.8680e-5	-6.2360e-4
77	+20%		+20%	+20%	0.1242	0.00601	-0.0214	1.400	-3.0080e-5	-6.5875e-4
78		-20%	-20%	-20%	0.1377	0.00601	-0.0000	1.399	-2.7986e-5	-6.3451e-4

79		-15%	+10%	-15%	0.1399	0.00604	0.0014	1.388	-2.9958e-5	-6.3703e-4
80		+15%	-10%	-10%	0.1392	0.00602	0.0032	1.391	-2.7787e-5	-6.2089e-4
81		-10%	-10%	+10%	0.1403	0.00604	-0.0017	1.399	-3.0503e-5	-6.4853e-4
82		+15%	-15%	+15%	0.1398	0.00603	0.0005	1.404	-2.8748e-5	-6.3168e-4
83		+20%	+20%	+20%	0.1443	0.00603	0.0021	1.420	-3.0378e-5	-6.4396e-4
84	-50%	-20%	-20%	-20%	0.1799	0.00602	0.0493	1.429	-2.7370e-5	-5.9635e-4
85	+20%	-15%	+10%	-15%	0.1221	0.00602	-0.0197	1.387	-3.0556e-5	-6.5255e-4
86	-10%	+15%	-10%	-10%	0.1482	0.00605	0.0107	1.409	-2.9138e-5	-6.2479e-4
87	+10%	-10%	-10%	+10%	0.1314	0.00603	-0.0112	1.410	-3.0155e-5	-6.3045e-4
88	-15%	+15%	-15%	+15%	0.1529	0.00602	0.0139	1.419	-3.0970e-5	-6.3624e-4
89	+15%	+20%	+20%	+20%	0.1313	0.00603	-0.0131	1.385	-2.9567e-5	-6.5485e-4
90	-40%	+20%	-20%	+20%	0.1757	0.00602	0.0403	1.476	-2.8393e-5	-6.2358e-4
91	-30%	-20%	+20%	+15%	0.1648	0.00605	0.0285	1.414	-2.9844e-5	-6.3532e-4
92	-20%	+15%	+15%	+10%	0.1595	0.00601	0.0220	1.446	-3.0383e-5	-6.2666e-4
93	-15%	+15%	-15%	+5%	0.1556	0.00602	0.0171	1.436	-3.0229e-5	-6.3445e-4
94	-10%	-15%	-15%	-5%	0.1475	0.00601	0.0095	1.399	-3.0085e-5	-6.4058e-4
95	-5%	+10%	+10%	-10%	0.1443	0.00603	0.0063	1.420	-3.0330e-5	-6.4669e-4
96	+5%	-20%	-20%	-15%	0.1337	0.00604	-0.0056	1.376	-3.0978e-5	-6.3937e-4
97	+10%	-15%	+10%	-20%	0.1310	0.00605	-0.0089	1.377	-2.9102e-5	-6.5079e-4
98	+15%	+15%	-10%	+20%	0.1289	0.00603	-0.0153	1.393	-3.0207e-5	-6.5892e-4
99	+20%	-10%	-10%	-20%	0.1225	0.00604	-0.0189	1.384	-2.9524e-5	-6.3721e-4
100	-50%	+15%	-15%	+15%	0.1823	0.00603	0.0483	1.456	-2.7641e-5	-6.3145e-4
101	-40%	+20%	+20%	-15%	0.1755	0.00601	0.0434	1.420	-2.7637e-5	-6.1754e-4
102	-30%	+20%	-15%	+15%	0.1750	0.006	0.0304	1.446	-2.9501e-5	-6.3434e-4
103	+20%	+5%	-15%	+20%	0.1277	0.00601	-0.0180	1.390	-3.0718e-5	-6.5742e-4
104	-10%	-15%	+10%	+10%	0.1489	0.00601	0.0092	1.414	-2.9557e-5	-6.2871e-4
105	-10%	-10%	+20%	-20%	0.1497	0.00598	0.0133	1.425	-2.8882e-5	-6.2554e-4
106	-15%	+10%	-20%	-10%	0.1538	0.00603	0.0171	1.416	-2.8451e-5	-6.2840e-4
107	-20%	+15%	-5%	-15%	0.1592	0.00603	0.0237	1.419	-2.8161e-5	-6.3746e-4

Artificial neural network design

Artificial Neural Networks are computational models inspired by the human brain's structure and function. They consist of interconnected nodes, or neurons, organized into layers. Each neuron receives input signals, performs a computation, and generates an output signal. The connections between neurons have associated weights adjusted during training to optimize the network's performance. The input layer of an ANN receives input signals, typically numerical values representing features of the input data. The input signals are then passed through one or more hidden layers, where they are transformed by a mathematical function called an activation function. The output layer of the network generates the final output, typically a prediction or classification based on the input data. The input data is passed through the network, and the output layer generates the final prediction or classification based on the learned weights and activation functions. Figure 3 illustrates the structure of the ANN develpoed in this study a two-layer feedforward

network with sigmoid hidden neurons and linear output neurons, suitable for regression tasks. Once trained, an ANN can make predictions or classifications on new, unseen data.

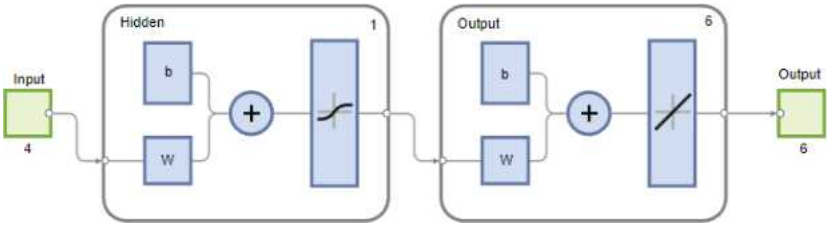

Figure 3: Artificial Neural Network structure of this study

Results and Discussion

Figure 4 illustrates the variations in reactivity under HFP conditions, with each graph representing the impact of adjusting a single input from 80% to 120%. Observations indicate that as the clad diameter and gadolinium concentration rise, reactivity declines, with the clad diameter exerting a notably stronger influence. Conversely, heightened levels of chromium and aluminum lead to an increase in reactivity, since the Iron concentration decreases, and so does the parasitic neutron absorption of Iron. Also, to predict the output data, an ANN is trained based on the Levenberg-Marquardt. There are 98 cases (0 to 97) assigned to the ANN training. To generate the ANN, the dataset is randomly divided into three sections, 40% the of data for training the ANN, 30% of the data for validation of the ANN during the training process, and 30% of the data for testing the ANN afterward. Figure 5 shows the MSE reduction in the ANN training process. To prevent the overfitting of the ANN, training stops at the least MSE value for validation to achieve the best performance in generalizing the patterns and traits of the training dataset and in the prediction of unseen or test datasets. The inputs of the ANN are the percentage of changes in clad outside diameter, Chromium weight, Aluminum weight, and Gd_2O_3 weight. The outputs are excess and hot full power reactivity, effective delayed neutron fraction (β), radial power peaking factor of the fuel assembly, and fuel and coolant temperature feedback coefficients. Efficiency of ANN and quality of predictions are evaluated by two performance indicators, namely correlation coefficient (R) and mean square error (MSE). The results of the ANN training in Table 4, Figures 5-6 describe that ANN has a high correlation and small values of mean square error.

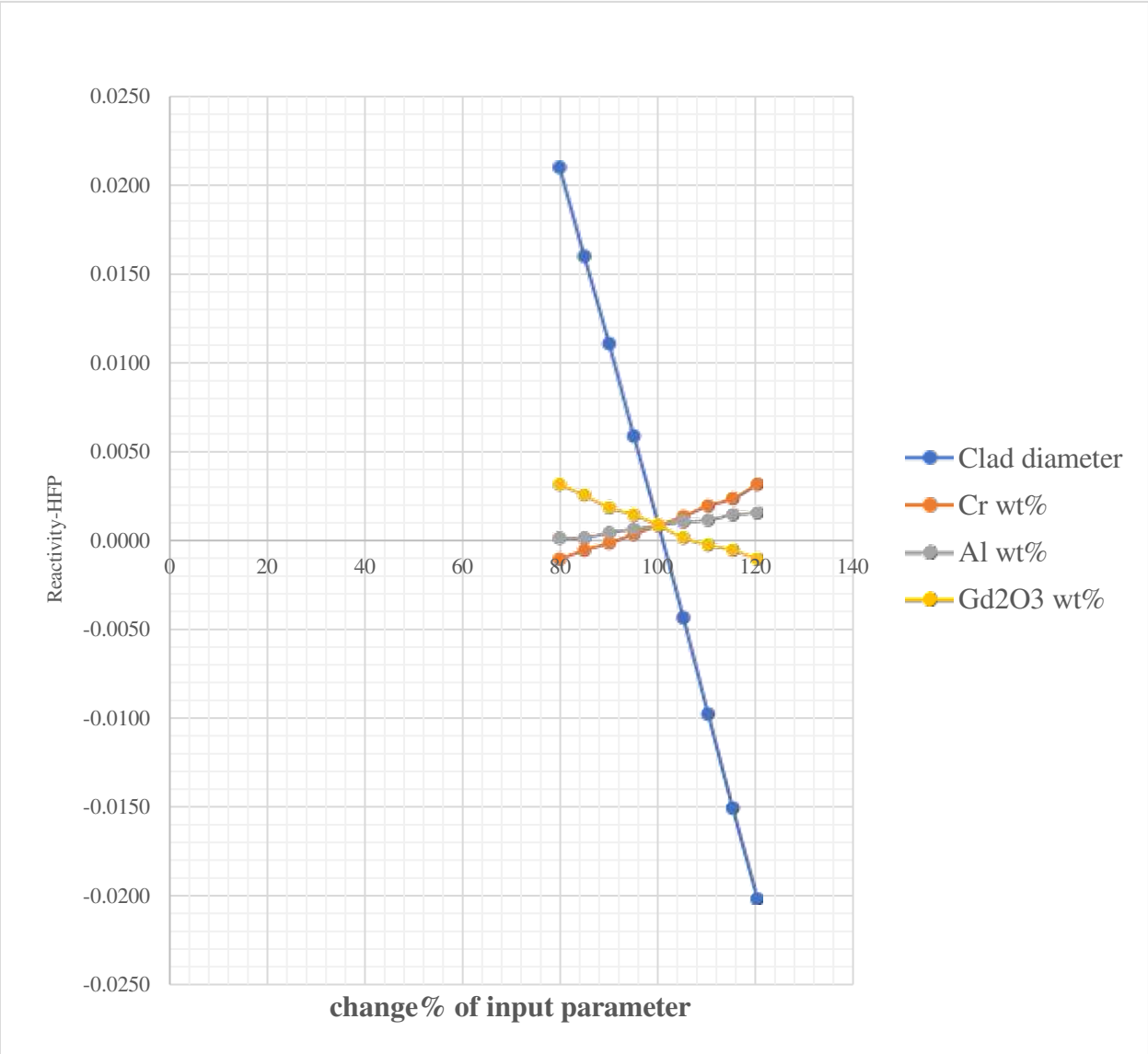

Figure 4: Variation of hot full power reactivity to the change of the input parameters

Therefore, the presented ANN has an acceptable and sufficient prediction capability. Additionally, ANN is tested by a new external dataset that was not used in the training process (cases 98 to 107). Table 4 shows the MSE of this dataset. Detailed parameter prediction of ANN is compared in Table 5. It is demonstrated that the errors all fall below the threshold of 10%, with the majority being considered negligible. Figure 7 describes the high correlation of the tested data and minor errors for each parameter. Thus, the presented ANN has a suitable performance in generalizing the data patterns and prediction of novel datasets.

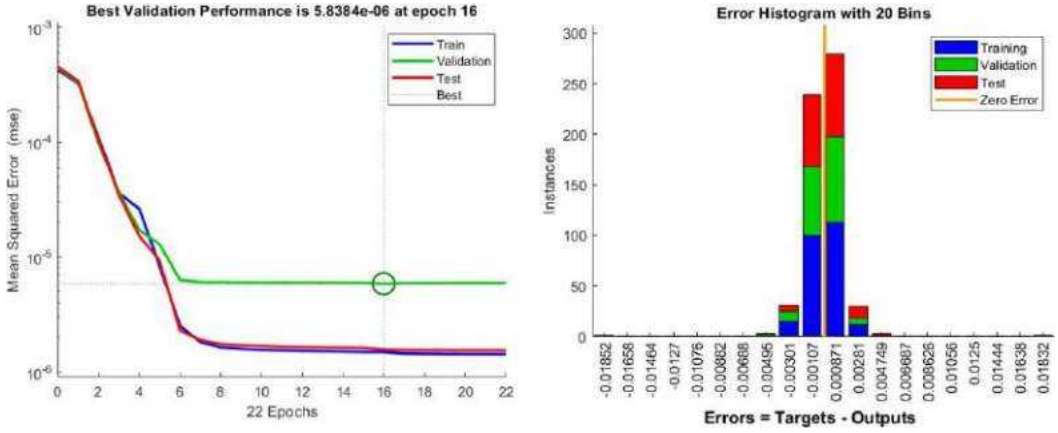

Figure 5: Mean square and error histogram of the ANN for the training, validation, and test

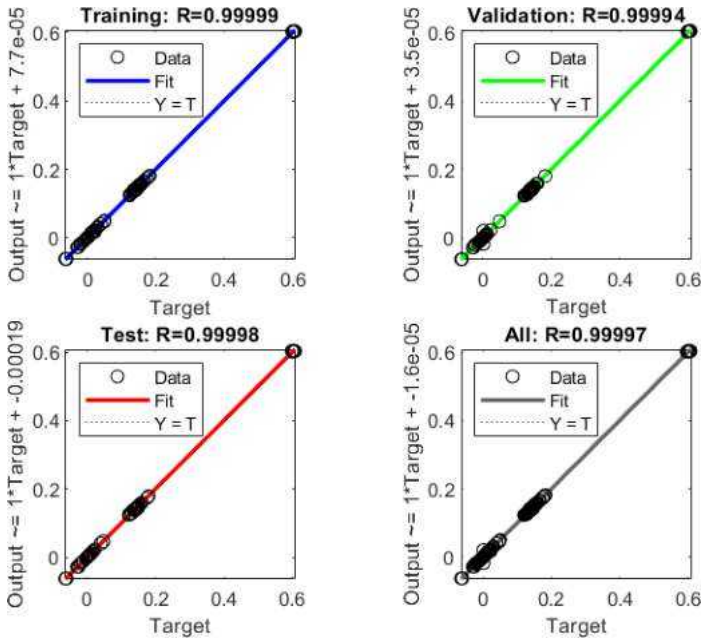

Figure 6: Regression plot for training, validation, testing and overall estimation of the ANN

Table 4: Validation of ANN for neutronic and dynamic data prediction

Internal validation	Data type	Observations	Mean Square Error
	Training	40	1.4846e-06
	Validation Test	29	5.8384e-06
		29	1.5587e-06
External validation	Data type	Observations	Mean Square Error
	Additional test data	10	2.9695e-06

Table 5: External validation for data prediction of ANN

Parameter	Data										
ρ -excess	MCNP	0.1289	0.1225	0.1823	0.1755	0.1750	0.1277	0.1489	0.1497	0.1538	0.1592
	ANN	0.1284	0.1245	0.1804	0.1760	0.1665	0.1238	0.1482	0.1503	0.1544	0.1597
	Error	0.4%	1.6%	1.04%	0.28%	4.8%	3.05%	0.47%	0.4%	0.39%	0.31%
β (*1e-3)	MCNP	6.03	6.04	6.03	6.01	6.0	6.01	6.01	5.98	6.03	6.03
	ANN	6.038	6.04	6.012	6.015	6.19	6.041	6.029	6.027	6.025	6.023
	Error	0.13%	0%	0.3%	0.08%	3%	0.5%	0.3%	0.8%	0.08%	0.1%
ρ-HFP	MCNP	-0.0153	-0.0189	0.0483	0.0434	0.0304	-0.0180	0.0092	0.0133	0.0171	0.0237
	ANN	-0.0141	-0.0188	0.0484	0.0430	0.0316	-0.0197	0.0096	0.0121	0.0171	0.0234
	Error	7.84%	0.53%	0.2%	0.93%	3.95%	9.4%	4.34%	9%	0%	1.26%
Rppf (FA)	MCNP	1.393	1.384	1.456	1.420	1.446	1.390	1.414	1.425	1.416	1.419
	ANN	1.386	1.382	1.443	1.439	1.428	1.381	1.408	1.410	1.415	1.421
	Error	0.5%	0.14%	0.9%	1.33%	1.25%	0.65%	0.43%	1.1%	0.08%	0.14%
α_f (*1e-5)	MCNP	-2.95	-2.76	-2.76	-2.95	-3.07	-2.95	-2.89	-2.84	-2.81	-2.95
	ANN	-2.79	-2.79	-2.77	-2.77	-2.78	-2.79	-2.78	-2.78	-2.78	-2.78
	Error	5.5%	0.95%	0.26%	6.1%	9.5%	5.6%	3.8%	2.3%	1.23%	5.9%
α_c (*1e-4)	MCNP	-6.37	-6.31	-6.17	-6.34	-6.57	-6.28	-6.25	-6.28	-6.37	-6.58
	ANN	-6.21	-6.21	-6.22	-6.22	-6.22	-6.22	-6.21	-6.21	-6.21	-6.22
	Error	2.55%	1.65%	0.73%	1.94%	5.4%	1.07%	0.72%	1.18%	2.58%	5.6%

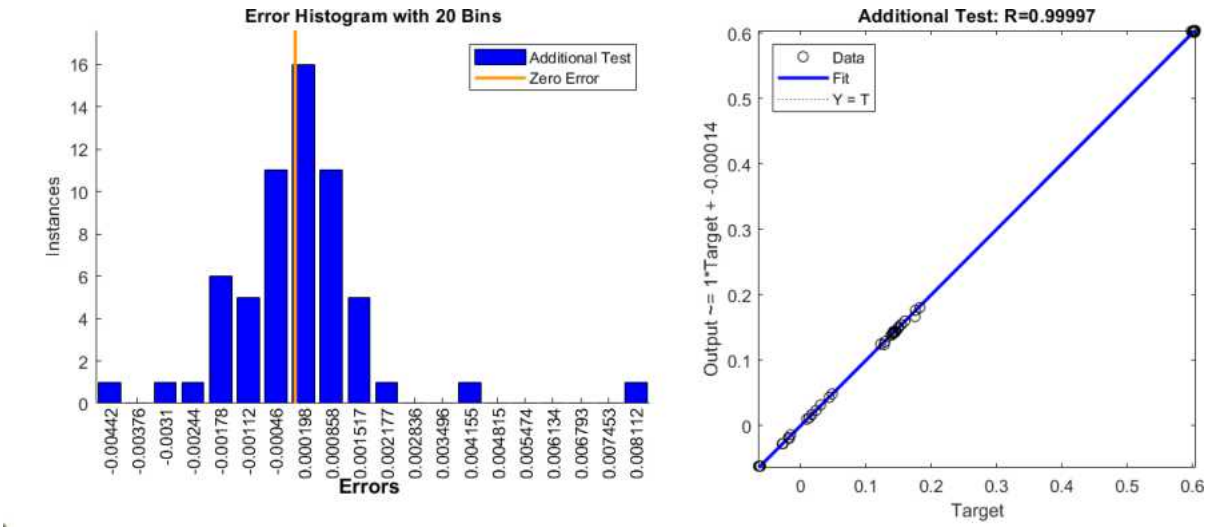

Figure 7: Results of the additional test data for the presented ANN

Conclusions

In this paper, an equilibrium core of the NuScale reactor with UO_2-FeCrAl C26M was presented and simulated. It was shown that changing the cladding material from Zr-4 affects the reactivity. It was mostly affected by the cladding diameter and then by burnable absorber concentration and cladding material concentration respectively. Moreover, according to the extracted data an ANN was trained and validated for data prediction of this equilibrium core parameters. Future works plan to employ other machine learning methods and optimizations, compare against presented ANN, and select the best model to obtain the optimally designed reactor core.

References

[1] Zahedi yeganeh, M. H. And Ansarifar, G. R. (2021). Design of a new Small Modular Nuclear Reactor using TVS-2M Fuel Assemblies and Fuel Depletion analysis during the fresh-core cycle length. Nuclear Engineering and Design, 385:111540.

[2] Pino-Medina, S., & François, J. L. (2021). Neutronic analysis of the NuScale core using accident- tolerant fuels with different coating materials. Nuclear Engineering and Design.

[3] Pinem, S., Luthfi, W., & Surbakti, T. (2024, February). Neutronic characteristics analysis of accident tolerant fuel and claddings for fuel assembly of light water reactor. In AIP Conference Proceedings (Vol. 2967, No. 1). AIP Publishing.

[4] Rahnama, Z., & Ansarifar, G. R. (2021). Predicting and optimizing the thermal-hydraulic, natural circulation, and neutronics parameters in the NuScale nuclear reactor using nanofluid as a coolant via machine learning methods through GA, PSO, and HPSOGA algorithms. Annals of Nuclear Energy, 161:108375.

[5] Tabas, E. J., Mokhtari, J., & Abbassi, Y. (2024). Application of artificial neural network for prediction of operational performance of MNSR. Nuclear Engineering and Design, 419.

[6] Rafiei, M., & Ansarifar, G. (2022). Conceptual design of a new space nuclear reactor with low- enriched uranium fuel based on the optimization of fuel composition and reflector geometry via optimized adaptive neuro-fuzzy inference system as well as investigation of fresh core cycle length. International Journal of Energy Research, 46(7): 9456-9485.

[7] Field, K. G., Yamamoto, Y., Pint, B. A., Gussev, M. N., & Terrani, K. A. (2019). Accident tolerant FeCrAl fuel cladding: current status towards commercialization. In Proceedings of the 18th International Conference on Environmental Degradation of Materials in Nuclear Power Systems–Water Reactors (pp. 1381-1389). Springer International Publishing.

[8] Brown, N. R., Todosow, M., & Cuadra, A. (2015). Screening of advanced cladding materials and UN–U3Si5 fuel. Journal of Nuclear Materials, 462: 26-42.

[9] Terrani, K. A., Pint, B. A., Kim, Y. J., Unocic, K. A., Yang, Y., Silva, C. M., ... & Rebak, R. B. (2016). Uniform corrosion of FeCrAl alloys in LWR coolant environments. Journal of Nuclear Materials, 479: 36-47.

[10] George, N. M., Terrani, K., Powers, J., Worrall, A., & Maldonado, I. (2015). Neutronic analysis of candidate accident-tolerant cladding concepts in pressurized water reactors. Annals of Nuclear Energy, 75:703-712.

[11] George, N. M., Terrani, K., Powers, J., Worrall, A., & Maldonado, I. (2015). Neutronic analysis of candidate accident-tolerant cladding concepts in pressurized water reactors. Annals of Nuclear Energy, 75: 703-712.

[12] NuScale Power LLC (2016). NuScale Standard Plant Design Certification Application, Part 2 - Tier 2.

ICNST 2024 International Conference on Nuclear Science and Technology
6- 8 MAY 2024 | Isfahan, Iran

The Empirical Correlation for Forced Convection Heat Transfer of Homogeneous Hybrid Nanofluid TiO2/Al2O3 in a Vertical Annulus (Paper ID : 1129)

Borhani Mohammad Amin.[1*], Shirani Amir Saeed[1], Talebi Mansour [2], Mokhtari Javad [2]
[1] Faculty of Engineering, Shahid Beheshti University, Tehran, Iran
[2] Nuclear Science and Technology Research Institute, AEOI, Iran

Abstract

In this research, a new empirical correlation is developed to predict the Nusselt number for nanofluid forced convection flow in a vertical annulus with cosine heat flux. The experiments investigate the heat performance of a homogeneous hybrid nanofluid composed of TiO_2 and Al_2O_3 dispersed in deionized water. Compared to other conventional fluids, nanofluid exhibits better heat transfer performance due to higher conductivity and Brownian motion, which can reduce the thermal boundary layer. Nanofluid has the potential to function as an emergency coolant in a nuclear reactor. A 25-bar test loop with a 1 m vertical test section generating cosine heat flux is used for the experiment. The tests are conducted at different Reynolds numbers and concentrations for the nanofluid. A new correlation for nanofluid heat performance is developed based on dimension analysis and multiple linear regression analysis. The obtained Nusselt number demonstrates better performance compared to existing correlations.

Keywords: hybrid nanofluid, Al_2O_3-TiO_2, empirical correlation, forced convection

Introduction

A significant challenge in improving thermal performance is the low heat transfer of conventional working fluids [1]. Nanofluids, which consist of nanoparticles (particles smaller than 100 nm) suspended in a base fluid, show better heat transfer capabilities compared to conventional fluids [2]. Heat transfer capabilities in nanofluids make them a promising option for application in emergency core cooling systems (ECCS) in nuclear reactors [3]. The pioneering work of Choi et al. [4] introduced nanofluids as working fluids in thermal systems. Recent studies have demonstrated the utilization of combined nanofluids, instead of single nanofluid applications [5].

The better thermal performance of nanofluids is attributed to various mechanisms, such as the increase in thermal conductivity, the Brownian motion of nanoparticles, and the reduction of the thermal boundary layer. Several studies have examined the specific heat capacity, thermal conductivity, viscosity, and heat transfer of nanofluids [6]. Al_2O_3 and TiO_2 nanoparticles are widely used in nanofluid research. Pak et al.[7]

Focused on the heat transfer behaviors of dispersed fluids containing submicron metallic oxide particles suspended in water. He et al. [8] conducted an experimental study to measure the heat transfer and pressure drop of water-TiO2 nanofluids in both laminar and turbulent flows. Duangthongsuk et al. [9] investigated the effects of TiO2 nanofluids in a heat exchanger and found that low nanoparticle concentrations increase pump work and also improve heat transfer.

Various methods, including dimension analysis, multivariate regression, symbolic regression with genetic algorithms, or neural networks, have been utilized to establish correlations for predicting the thermophysical properties of nanofluids [10], [11].

In this study, a high-pressure test loop with a maximum pressure of 25 bar and cosine heat flux was employed. Homogeneous mixtures of Al2O3 and TiO2 nanoparticles, dissolved in deionized water, were stabilized using an ultrasonic stirrer. The experiments were conducted at various Reynolds numbers and nanofluids. An empirical correlation for Nusselt numbers was developed to compare other correlation equations and experimental results. Dimension analysis and multiple linear regression were utilized to obtain the Nusselt number correlation. This research can be applied particularly in heat exchanger and ECCS system design.

Methodology and data analysis experimental model

The test loop in this study is a thermohydraulic loop with a maximum pressure of 25 bars. This testing facility includes various mechanical and electrical components, such as pumps, a cooling tower, a heat exchanger, a test section, and other measurement and control instruments. Figure 1 shows this facility.

Fig. 1. Experiment setup

The test section includes an annulus with a heating rod that generates a cosine heat flux of 1 kilowatt. The temperature of the rod is measured using 22 type K thermocouples attached to it, and the thermocouple data are connected to the data acquisition system. For the preparation of the nanofluid in this experiment, an ultrasonic stirrer was employed. Initially, a homogeneous mixture of TiO2 and Al2O3 nanoparticles in deionized water was added. To prevent the aggregation or clustering of nanoparticles, the ultrasonic stirrer was applied to the solution for 4 hours. The experiments were conducted at a constant inlet fluid temperature of 25°C and a pressure of 5 bars. The Nusselt numbers were determined based on the measured parameters under various operational conditions. Table 1 provides a summary of different conditions.

Table 1. Experiment conditions for different Reynolds numbers and concentrations

Volumetric concentrations	0.25%, 0.5%, 0.75%, 1%, 1.5%
Reynolds numbers	1857, 2683, 3096, 4128

Data analysis

The nanofluid exhibits Newtonian behavior at low concentrations. The volumetric concentration was employed for the calculation of density and thermal conductivity. The viscosity of the nanofluid (μnf) and thermal conductivity (knf) were calculated using empirical equations derived from previous studies. The viscosity of the nanofluid was determined using the correlation equation proposed by Wang et al. [12]. Additionally, the thermal conductivity of the nanofluid was computed using the

relationship developed by Timofeeva et al. [13]. Equations 1 and 2 represent the viscosity and thermal conductivity of the nanofluid, respectively. The volume concentration (ϕ), nanofluid (nf), and base fluid (nb) are used to represent the variables in the following equations.

$$\mu_{nf} = \mu_b(1 + 7.3\phi + 123\phi^2) \quad (1)$$

$$k_{nf} = k_{bf}(1 + 3\phi) \quad (2)$$

Nusselt number and Prandtl number values are provided in the equations. The heat transfer is calculated based on the energy equation, bulk temperature, and rod surface temperature.

$$\bar{Nu} = \frac{\bar{h}D}{k_{nf}} \quad (3)$$

$$Pr = \frac{\mu_{nf} C_{nf}}{k_{nf}} \quad (4)$$

The uncertainty analysis was conducted for all parameters in this experiment, and it was calculated based on sensor accuracy and calibration error for various parameters. The uncertainty for the Nusselt number in this experiment is approximately 4.3%.

Correlation Development

Correlation can be achieved through the use of dimensional analysis to simplify the problem and express it in a more straightforward physical relationship. A dimensionless group is needed to calculate the amount of heat for different states. The equation can be written as:

$$h = f(\rho, \mu, cp, K, V, D, \phi) \quad (5)$$

For the nanofluid, the thermal properties are calculated at bulk temperature. The equation is modified using Dimensional Analysis and Buckingham's Pi method into the following format:

$$Nu = f(Re, Pr, \phi) \quad (6)$$

The general form of the correlation, based on previous studies and the design of the experiments, can be written as:

$$Nu = aRe^b Pr^c (1 + \phi)^d \quad (7)$$

The coefficients of a, b, c, and d were calculated using the multiple linear regression analysis method based on the data obtained from the EXPERIMENTAL test using Python. This method is used to

investigate the relationship between a dependent variable and two or more independent variables. The coefficients and the value of R2 (coefficient of determination) are presented in Table 2

Table 2. Calculated coefficients and R^2

a	b	c	d	R^2
0.42	0.32	0.7	0.95	0.92

Results and Discussion

The Nusselt numbers for nanofluids were determined using the equations presented in the data analysis section. Figure 2 illustrates experimental Nusselt numbers for various Reynolds numbers and nanoparticle concentrations. The graph shows a noticeable increase in the Nusselt number with higher Reynolds numbers or nanoparticle concentrations. For the 1% nanofluid, the Nusselt number at high Reynolds numbers increases by approximately 35% compared to pure water.

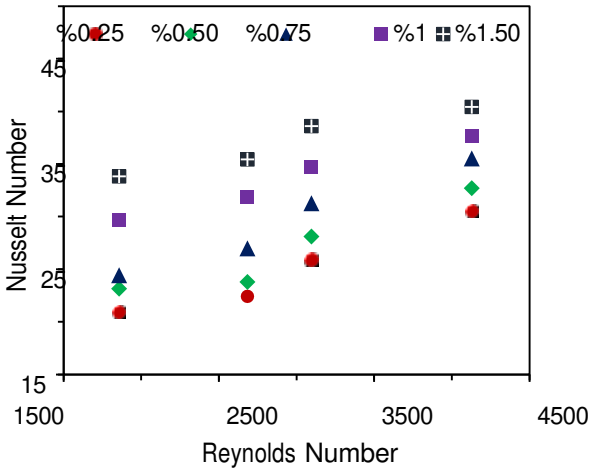

Fig. 2. Experiment Nusselt numbers

Figure 2 demonstrates the comparison between predicted Nusselt numbers from developed correlation and experimental Nusselt numbers. It shows that correlation can predict Nusselt number accurately. The Correlation developed by Pak et al [7] and Duangthongsuk et al. [9] have R2 of 0.70 and 0.75. This number for the developed correlation is 0.92.

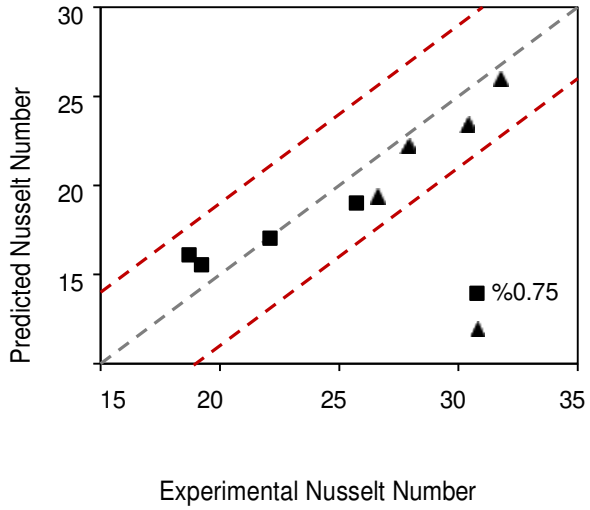

Fig. 3. Predicted Nusselt number vs experimental Nusselt number

Conclusions

In this study, the thermal performance of a homogeneous nanofluid composed of suspended Al2O3 and TiO2 nanoparticles in deionized water was investigated. experimental analysis was conducted using a high-pressure test loop with a test section generating a cosine-shaped heat flux. The experiment examined the influence of nanoparticle volume fraction and Reynolds numbers on the Nusselt number. Based on the conducted experiment, a Nusselt number correlation was developed using multiple linear regression, which showed an accurate performance with an R2 value of 0.92.

References

[1] M. A. Borhani, A. S. Shirani, M. Talebi, and J. Mokhtari, "Comparative investigation of nanofluid heat transfer in vertical annular channel with cosine heat flux by experimental and numerical methods," *J. Solid Fluid Mech.*, vol. 13, no. 4, pp. 147–158, Sep. 2023, doi: 10.22044/jsfm.2023.13065.3736.

[2] M. Talebi, M. A. Borhani, S. M. M. Zadeh, and G. R. Ansarifar, "experimental analysis of forced convection heat transfer of Hybrid Nanofluids in a vertical annulus with cosine heat flux," Prog. Nucl. Energy, vol. 153, p. 104438, Nov. 2022, doi: 10.1016/j.pnucene.2022.104438.

[3] S. Chinchole, A. Dasgupta, P. P. Kulkarni, D. K. Chandraker, and A. K. Nayak, "Exploring the Use of Alumina Nanofluid as Emergency Coolant for Nuclear Fuel Bundle," J. Therm. Sci. Eng. Appl., vol. 11, no. 021007, Nov. 2018, doi: 10.1115/1.4041441.

[4] S. U. Choi and J. A. Eastman, "Enhancing thermal conductivity of fluids with nanoparticles," Argonne National Lab. (ANL), Argonne, IL (United States), 1995. Accessed: Jan. 03, 2024.

[5] Available: https://www.osti.gov/biblio/196525

[6] J. Pérez Vallejo, J. I. Iglesias Prado, and L. Lugo Latas, "Hybrid or mono nanofluids for convective heat transfer applications. A critical review of EXPERIMENTAL research," Appl. Therm. Eng., 2022, Accessed: Jan. 03, 2024. [Online].

[7] M. U. Sajid and H. M. Ali, "Recent advances in application of nanofluids in heat transfer devices: a critical review," Renew. Sustain. Energy Rev., vol. 103, pp. 556–592, 2019.

[8] C. Pak and Y. I. Cho, "HYDRODYNAMIC AND HEAT TRANSFER STUDY OF DISPERSED FLUIDS WITH SUBMICRON METALLIC OXIDE PARTICLES," Exp. Heat Transf., vol. 11, no. 2, pp. 151–170, Apr. 1998, doi: 10.1080/08916159808946559.

[9] Y. He, Y. Jin, H. Chen, Y. Ding, D. Cang, and H. Lu, "Heat transfer and flow behaviour of aqueous suspensions of TiO2 nanoparticles (nanofluids) flowing upward through a vertical pipe," Int. J. Heat Mass Transf., vol. 50, no. 11–12, pp. 2272–2281, 2007.

[10] W. Duangthongsuk and S. Wongwises, "Heat transfer enhancement and pressure drop characteristics of TiO2–water nanofluid in a double-tube counter flow heat exchanger," Int. J. Heat Mass Transf., vol. 52, no. 7–8, pp. 2059–2067, 2009.

[11] Y. Xuan and W. Roetzel, "Conceptions for heat transfer correlation of nanofluids," Int. J. Heat Mass Transf., vol. 43, no. 19, pp. 3701–3707, 2000.

[12] Sánchez-Escalona, Y. Camaraza-Medina, E. Góngora-Leyva, and Y. Retirado Mediaceja, "New Approach to Obtain the Mean Heat Transfer Coefficients for Single-Phase Fluid Flow Inside Tubes by Simulating Evolution of Nusselt Equation (I).," Int. J. Heat Technol., vol. 40, no. 1, 2022, Accessed: Jan. 22, 2024.

[13] X. Wang, X. Xu, and S. U. S. Choi, "Thermal Conductivity of Nanoparticle - Fluid Mixture," J. Thermophys. Heat Transf., vol. 13, no. 4, pp. 474–480, Oct. 1999.

[14] E. V. Timofeeva et al., "Thermal conductivity and particle agglomeration in alumina nanofluids: Experiment and theory," Phys. Rev. E, vol. 76, no. 6, p. 061203, Dec. 2007.

ICNST 2024
International Conference on Nuclear Science and Technology
6- 8 MAY 2024 | Isfahan, Iran

Simulation and analysis of fire accident in Isfahan nuclear fuel production complex and standardization of fire extinguishing system according to NFPA global standard using CFAST code (Paper ID : 1132)

H.R Momtaz[1], M.R Nematollahi[2]

1-Master's degree in Nuclear Engineering, Reactor Specialization, Faculty of Mechanical Engineering, Shiraz University

2- Faculty of Nuclear Engineering Department - Faculty of Mechanical Engineering - Shiraz University

Abstract

Fire accident has always been considered as the most dangerous accident. Due to the importance of the issue of fire accident in Isfahan nuclear fuel production complex, in this article, simulation of fire accident using CFAST code, which is one of the safety analysis tools with accident certainty methods, is used. In this research, building 505 of nuclear fuel production complex in Isfahan was investigated and simulated. All the information needed to carry out this project is from the safety analysis reports and documents of the Isfahan nuclear fuel production complex, as well as the international standard NUREG-6850 and NFPA. Also, two events were investigated in this research. The first event is the absence of fire alarm and extinguishing systems and the second event is the presence of a standard fire alarm and extinguishing system according to the NFPA global standard. In the two mentioned events, the amount of heat release as well as the protection temperature and oxygen concentration were discussed and investigated. The smoke emission method in the protector is also presented schematically. The maximum amount of heat emission in the first case (absence of the fire alarm and extinguishing system) is 1000000 $^{W}/_{S}$ and in the second case (the presence of the standard fire alarm and extinguishing system) it is 580000 $^{W}/_{S}$. Also, the maximum temperature of the upper layer in compartment number 3, which is the place where the fire started, is 180 degrees Celsius if there is no standard fire extinguishing system and 120 degrees Celsius if there is a standard fire extinguishing system.

Keywords: Fire, Nuclear Site, Isfahan Nuclear Fuel Production Complex, CFAST, NFPA

1- Introduction

In nuclear sites, due to the sensitivity of materials and facilities, a fire incident can cause irreparable damage. According to the characteristics of the design and operation of a nuclear site, fire has the ability to be one of the most important risks that a nuclear site faces. The experience of fire incidents in such plants as Browns Ferry in 1975 in the United States, ARMEXIA in 1982 in Armenia, VANDELLOS in 1989 in Spain and NARORA in 1993 in India shows that fire is very important in terms of safety and It can be the source of very serious damage to the nuclear site [1].One of the tools of safety analysis with certainty methods of fire incidents is the CFAST1 code. CFAST is a two-zone fire model used to calculate the developing smoke, fire gases, and temperatures in parts of a building during a fire. One of the basic parameters that can be calculated in CFAST is the heat release rate. The amount of heat release is a function of viscosity, density, calorific value, latent heat of fuel, fuel burning rate and combustion temperature. The rate of heat release includes premixed combustion, controlled combustion and late combustion. Heat release rate is not simply a variable used to characterize fire. In fact, this is the only important variable in defining phenomena such as fire risk. The speed of heat release is the driving force in terms of fire. Therefore, the production of adverse effects of fire and its products also increases with the increase of Heat release rate. This means that toxic gases, smoke and other types of fire hazards increase in parallel with the rate of heat release. One of the basic solutions in reducing the amount of heat emission is the standardization of the fire alarm and extinguishing system. A timely and effective fire extinguishing system can reduce many damages, including financial, human and environmental damages [2]. In an article, Safai Arashi and his colleagues evaluated and investigated the safety of the Tehran research reactor building against potential fire hazards by coupling CFAST certainty code and SAPHIRE probabilistic code. In carrying out this project, CFAST software was used to simulate fire scenarios and SAPHIRE software was used to calculate the frequency of heart damage due to fire. Since all the fire protection programs used in the Tehran reactor have been based on a deterministic process, this project is a probabilistic evaluation of the effectiveness of these protection programs in reducing the total frequency of damage to the heart of the Tehran research reactor due to presents the incident of fire [3]. Gallucci et al evaluated and investigated the statistical characteristics of the heat emission rate caused by fire in electrical enclosures for nuclear power plants. The results show that a simplified approach to develop

[1] Consolidated Model of Fire and Smoke Transport

true or representative peak heat release rate distributions for fires in electrical enclosures is currently available and requires only a reasonable approximation. The fact that only two distributions are now required for the peak heat release rate per fuel mass can simplify the amount of analysis required to support the assessment of potential fire risks [4]. Day et al presented a conceptual framework to increase the quality of fire protection in nuclear power plants by using probabilistic methods of risk analysis based on the dynamic model of fire effects and proved that this method is cost-effective compared to deterministic methods that have been used in the past. It is more economic and also has a more complete assessment of fire risk and is able to determine the things that have the most and least effect on the risk [5]. Kim and his colleagues have used a comparison of probabilistic fire safety estimations of Korean pressurized water nuclear power plants and WOLSONG Unit 1, a heavy water power plant, to determine the significant problems from a risk perspective. In addition, these two units are different in terms of design, and another difference is that KSNP cables comply with the IEEE-383 standard, while this is not the case with WOLSONG. The entire fire scenarios in the fire safety probabilistic estimation were re-examined to investigate the effect of standardization of cables on WOLSONG, and it was concluded that standardization of cables increases safety by 70% [6]. In a research, McGrattan and colleagues have validated the models used for nuclear power plant fire safety. For each model and each value of interest, there are two accuracy measures. The first criterion shows how much the model tends to over- or under-predict the given quantity. The latter is a relative standard deviation that indicates the degree of scatter in the predicted quantity compared to EXPERIMENTAL measurements. While this study is motivated by nuclear power plant safety, the general method and results are suitable for most industrial applications [7].

2- Research Theories

We divide the desired area into two control volumes, a relatively warm upper layer and a relatively cold lower layer according to Figure 1. The gas in each layer has characteristics such as mass, internal energy, density, temperature, and volume, which are represented by m_i, E_i, ρ_i, T_i and V_i respectively, where L is for the lower layer and U is for the upper layer.

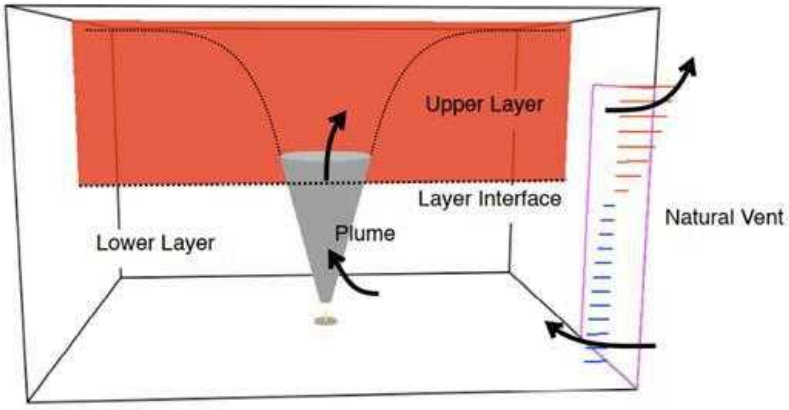

Figure 1: Control volumes in the two-layer model [8]

$$\rho_i = \frac{m_i}{V_i} \quad (1)$$

$$E_i = c_v m_i T_i \quad (2)$$

$$P = R\rho_i T_i \quad (3)$$

$$V = V_L + V_v \quad (4)$$

Equations (1), (2), (3) and (4) express density, internal energy, ideal gas law and total volume, respectively.

Specific heat is C_v at constant volume and C_p at constant pressure. The global constant of gases is R, $\gamma = \frac{C_p}{C_v}$ and $R = C_p - C_v$. At normal temperature, $C_p \approx 1\frac{KJ}{Kg}$ and $\gamma = 1\,4$. For the mass in each of the layers, the differential equations can be expressed as (5) and (6):

$$\frac{dm_L}{dt} = \dot{m_L} \quad (5)$$

$$\frac{dm_U}{dt} = \dot{m_U} \quad (6)$$

According to Newton's first law, the rate of increase in internal energy plus the rate in the layer that does work by expansion is equal to the amount of enthalpy added to the gas, in other words:

$$\frac{dE_i}{dt} + P\,\frac{dV_i}{dt} = \dot{h_i} \quad (7)$$

In relation (7), $\frac{dE_i}{dt}$ represents internal energy, $P\,\frac{dV_i}{dt}$ represents work and $\dot{h_i}$ represents enthalpy. In enthalpy, C_p is considered constant,

$$\dot{h} = C_p \dot{m_U} T_U + \dot{E_U} + C_p \dot{m_L} T_L + \dot{E_L} \quad (8)$$

The pressure differential equation can be obtained according to equation (7), taking into account that $\frac{dV_U}{dt} = -\frac{dV_L}{dt}$ and also:

$$\frac{dE_i}{dt} = \frac{d(C_v m_i T_i)}{dt} = \frac{C_v}{R}\frac{d(PV_i)}{dt} \quad (9)$$

To obtain

$$\frac{dP}{dt} = \frac{\gamma - 1}{V}(\dot{h_l} + \dot{h_U}) \quad (10)$$

Using equation (11), differential equations for layers can be calculated:

$$\frac{dV_i}{dt} = \frac{1}{p\gamma}\left((\gamma - 1)\dot{h_i} - V_i\frac{dP}{dt}\right) \quad (11)$$

To remove $\frac{dV}{dt}$, equation (7) can be rewritten as equation (11):

$$\frac{dE_i}{dt} = \frac{1}{\gamma}\left(\dot{h_i} + V\frac{dP}{dt}\right) \quad (12)$$

By using the used law of $\frac{d\rho_i}{dt} = -\frac{d}{dt}(\frac{m_i}{V_i})$ and equation number (11), the differential equation for density can be rewritten:

$$\frac{d\rho_i}{dt} = \frac{-1}{C_p T_i V_i}\left(\left(\dot{h_i} - C_p\dot{m_i}T_i\right) - \frac{V_i}{\gamma - 1}\frac{dP}{dT}\right) \quad (13)$$

The differential equations of temperature can be obtained from the equation of state using $\frac{dT}{dt} = \frac{d}{dt}(\frac{P}{R\rho_i})$ and using equation (13):

$$\frac{dT_i}{dt} = \frac{1}{C_p\rho_i V_i}\left(\left(\dot{h_i} - C_p\dot{m_i}T_i\right) + V_i\frac{dP}{dt}\right) \quad (14)$$

2-1- Heat Release Rate

By consuming fuel and oxygen, heat is released and various combustion products are formed. Also, heat is released in the form of radiation and convection heat:

$$\dot{Q_r} = X_r\dot{Q} \quad (15)$$

$$\dot{Q_c} = (1 - X_r)\,\dot{Q} \quad (16)$$

where $\dot{Q}$ is the heat released by the fire. The parameters $\dot{Q_r}$ and $\dot{Q_c}$ are the heat released by radiation and convection, respectively, and X_r is the fraction of the fire's heat release rate emitted as radiation. The user specifies the heat release rate as the actual heat released, accounting for combustion efficiency, along with a characteristic base diameter which is used in the plume temperature and mass entrainment correlations. The combustion efficiency, ca, is the fraction of the theoretical energy that is actually released during combustion [9]. X_a is a function of fuel type, scale, and vitiation. For small fires, Tewarson provides measured values for specific fuels. Within CFAST, the user also specifies a radiative fraction which takes a default value of 0.35; i.e., 35 % of the fire's energy is released via

radiation. For specific fuels, the work of Tewarson [10], McCaffrey [11], or Koseki [12] is available for reference. The typical range for the radiative fraction is from about 0.05 to 0.4. The assumed and constant values for the combustion efficiency and radiative fraction may add uncertainty to the calculated results, so the heat release rate and radiative fraction should be chosen carefully to best model the scenario of interest. Using the specified heat release rate of the fire, $\dot{Q}$, and a user-specified the heat of combustion, ΔH, the model calculates the pyrolysis rate of fuel, $\dot{m}_f$:

$$\dot{m}_f = \frac{\dot{Q}}{\Delta H} \quad (17)$$

In the event that the heat release rate is constrained by the availability of oxygen, it is assumed that the pyrolysis rate does not change. However, only part of the pyrolyzed fuel burns and the heat release rate becomes:

$$\dot{Q} = \mathrm{MIN}(\dot{m}_f \Delta H,\ \dot{m}_e Y_{O_2} C_{LOL} \Delta H_{O_2}) \quad (18)$$

Where $\dot{m}_e$ is the entrainment rate, Y_{O_2} is the mass fraction of oxygen in the layer containing the fire, ΔH_{O_2} is the heat of combustion based on oxygen consumption1, and C_{LOL} (Lower Oxygen Limit) is the smoothing function ranging from 0 to 1:

$$C_{LOL} \approx \frac{\mathrm{TANH}\left(800\left(Y_{O_2,1}\right) - 4\right) + 1}{2} \quad (19)$$

The limiting oxygen mass fraction, $(Y_{O_2,1})$ is 0.15, by default. This value is not a function of temperature.

2-2- Sprinkler & Smoke Detector

The temperature of the sensing element (or "link") of an automatic fire sprinkler is estimated from the differential equation put forth by Heskestad and Bill [13], with the addition of a term to account for the cooling of the link by water droplets in the gas stream from previously activated sprinklers:

$$\frac{dT_l}{dt} = \frac{\sqrt{u}}{RTI}\left(T_g - T_l\right) - \frac{C}{RTI}\left(T_l - T_m\right) - \frac{C_2}{RTI}\beta\sqrt{u} \quad (20)$$

where u is the gas velocity, RTI is the response time index, T_l is the link temperature, T_g is the gas temperature in the neighborhood of the link, T_m is the temperature of the sprinkler mount (assumed ambient), and β is the volume fraction of (liquid) water in the gas stream. The sensitivity of the sprinkler link is characterized by its RTI value. The amount of heat conducted away from the link by the mount is

indicated by the "C-Factor", *C*. The RTI and C-Factor are determined experimental. The constant C_2 has been empirically determined by DiMarzo and co-workers [14], [15], [16] to be $6 \times 10^6 \ {}^{K}/_{({}^{m}/_{s})^2}$, and its value is relatively constant for different types of sprinklers.

Consider the simple idealization of a "spot-type" smoke detector. A disk-shaped cover lined with a fine mesh screen forms the external housing of the device, which is usually mounted on the ceiling. Somewhere within the device is a relatively small sensing chamber where the smoke is actually detected in some way. A simple model of this device has been proposed by Heskestad [17]. He suggested that the mass fraction of smoke in the sensing chamber of the detector Y_c lags behind the mass fraction in the external free stream Y_e by a time period $\delta t = {}^{L}/_{u}$, where u is the free stream velocity and *L* is a length characteristic of the detector geometry. The change in the mass fraction of smoke in the sensing chamber can be found by solving the following equation:

$$\frac{dY_c}{dt} = \frac{Y_e(t) - Y_c(t)}{{}^{L}/_{u}} \qquad (21)$$

The detector activates when Y_c rises above a detector-specific threshold.

An analytical solution for Eq. (35) can be found, but it is more convenient to simply integrate it numerically as is done for sprinklers and heat detectors. Then, the predicted mass fraction of smoke in the sensing chamber $Y_c(t)$ can be converted into an expression for the percent obscuration per unit length by computing:

$$OBSCURATION = (1 - e^{-K_m \rho Y_c}) \times 100\ \%\ PER\ LENGTH\ l \qquad (22)$$

where K_m is the mass extinction coefficient, ρ is the density of the external gases in the ceiling jet, and l is the unit of length over which the light is attenuated. For most flaming fuels, a suggested value for K_m is $8700 \ {}^{m^2}/_{Kg} \pm 1100 \ {}^{m^2}/_{Kg}$ at a wavelength of 633 nm [18].

3- Results and Discussion

Fire simulation has been done in building 505 of nuclear fuel production complex with CFAST code. The CFAST code is such that it examines a two-zone model. In these models, the intended environment is classified into two different aspects, including the lower or colder layer and the upper or hotter layer. The basic characteristics of these types of models are that the top layer represents the mass of smoke under the roof. The temperature is uniform in each layer and there is a common horizontal surface between the lower and upper layers. In the first stage, basic information must be

collected, including weather characteristics, environmental characteristics, location of sensors and characteristics of equipment inside the nuclear site. After the first stage, the precise definition of the desired area for the fire should be done. For this purpose, the area in question should be defined in such a way as to prevent the fire from spreading to other areas. In general, the target area becomes a closed environment whose boundaries are made of non-flammable materials. At the boundaries of this area there may be doors, hatches and stairways, which should be designed to prevent the spread of fire from them to other areas. In addition, to define the desired area accurately, the proximity of fire sources and flammable materials to doors, hatches, and stairways should be checked to ensure that the spread of fire to other areas from these routes is not possible. In this research, the worst case is that the ventilation doors are closed, as well as mechanical ventilation systems, so that according to the global NFPA[2] standard, the fire alarm and extinguishing system are placed inside the enclosure. In this research, one of the most basic parameters is the rate of heat emission. The amount of heat released in this incident was investigated in two situations: the presence of a fire extinguishing system according to the NFPA standard and the absence of a fire extinguishing system. The sample nuclear fuel production complex is divided into six buildings according to Figure 2. The building under study is building 505, which produces nuclear fuel in this building.

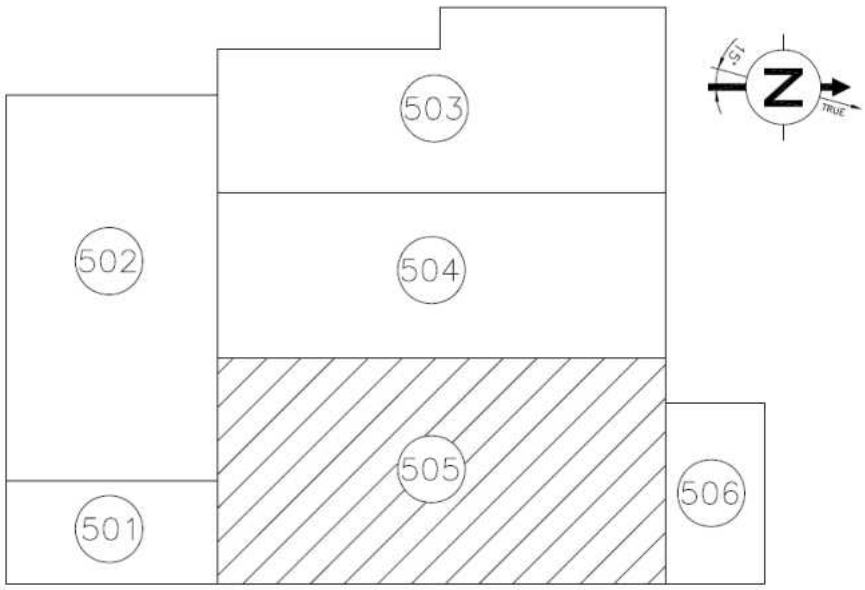

Figure 2: The location of the buildings of the nuclear fuel production complex

[2] National Fire Protection Association

Building 505 is divided into four compartments according to Figure 3 for simulation and calculations:

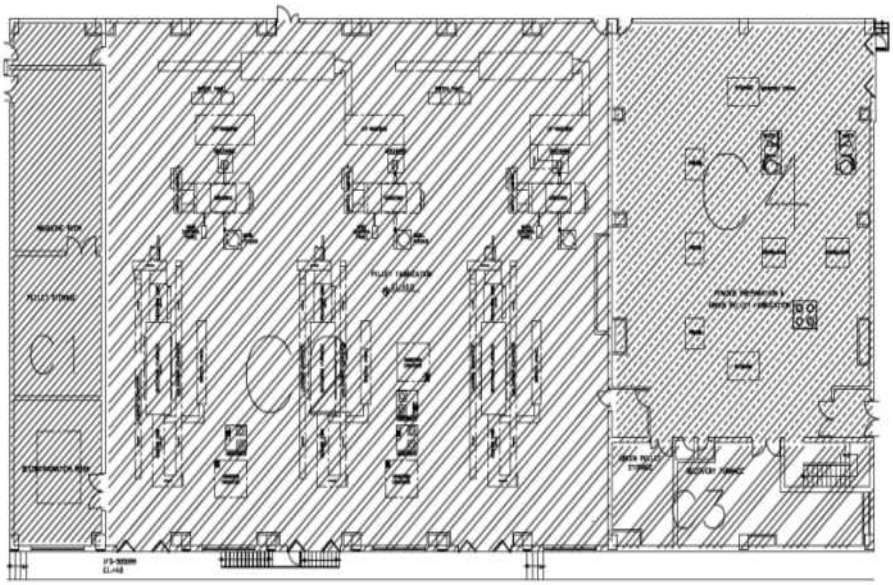

Figure 3: General plan of building 505

Information is given to the CFAST code to perform the simulation. This information includes the simulation time, temperature and pressure inside and outside the simulation environment, the dimensions and material of the shield, the fire source and its related features, and the fire alarm and extinguishing system. The information mentioned in Table 1 can be seen.

Table 1: Simulation information

PARAMETER	VALUE
SIMULATION TIME	1800 SEC
TEMPERATURE INSIDE THE COMPARTMENT	25 ℃
TEMPERATURE OUTSIDE THE COMPARTMENT	23 ℃
THE HUMIDITY OF THE INNER COMPARTMENT	50 %
PRESSURE	101325 Pa
MATERIAL OF FLOOR, ROOF AND PROTECTIVE WALLS	CONCRETE AND GYPSUM
FIRE SOURCE	ELECTRICAL CABLE WITH XLPE INSULATION

MASS PER UNIT LENGTH	0.508 $^{Kg}/_{m}$
HEAT OF COMBUSTION	46000 $^{kJ}/_{Kg}$
SPRINKLERS ACTIVATION TEMPERATURE	79 ℃
SMOKE DETECTOR ACTIVATION OBSCURATION	23.93 %
RTI OF SPRINKLERS	404 $(m\ s)^{0.5}$
RADIATIVE FRACTION	0.33
SPRINKLER FLOW RATE	180 $^{Lit}/_{min}$
C_FACTOR	0.3
DISTANCE BETWEEN TWO SPRINKLER	1.8 m
DISTANCE BETWEEN TWO SMOKE DETECTOR	9.1 m

First of all, the investigation of the fire accident, how the rate of heat, temperature and oxygen release changes without the presence of a fire extinguishing system is discussed.

3-1- Simulation of fire in the building in two states of presence and absence of fire alarm and extinguishing system

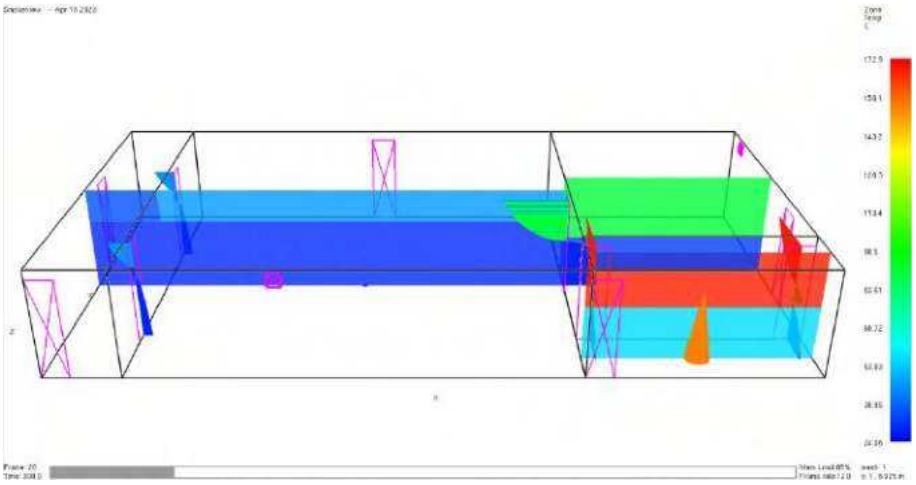

Figure 4: Simulating a fire in a building in the absence of a standard fire alarm and extinguishing system

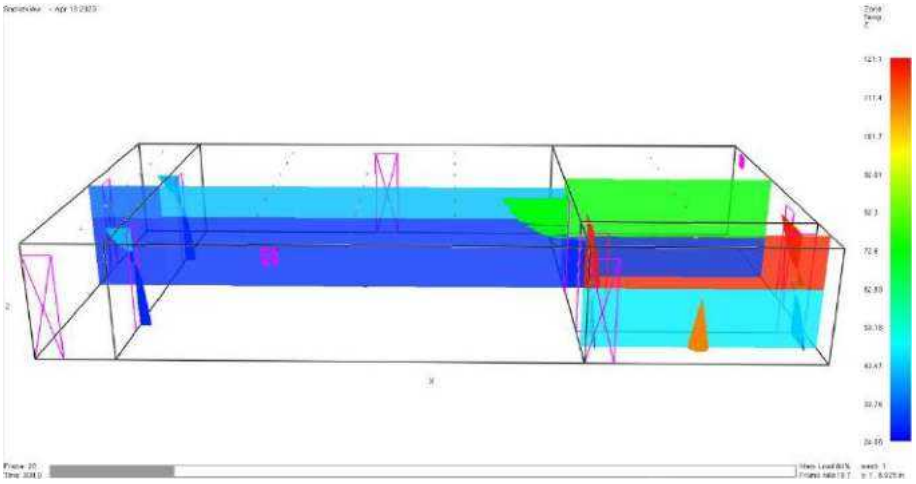

Figure 5: Simulating a fire in a building in the presence of an standard fire alarm and extinguishing system

The point that can be seen in Figure 3 and 4 is that in cases where there is no standard fire extinguishing system, the temperature in compartment 3 increases to 180 degrees Celsius, but in the case where there is a standard fire extinguishing system, the temperature is 120 degrees Celsius. Also, the proper functioning of the standard fire extinguishing system in chamber No. 3 prevents the temperature from rising in other compartments as well

3-2- Heat release rate in the presence and absence of the standard fire alarm and extinguishing system

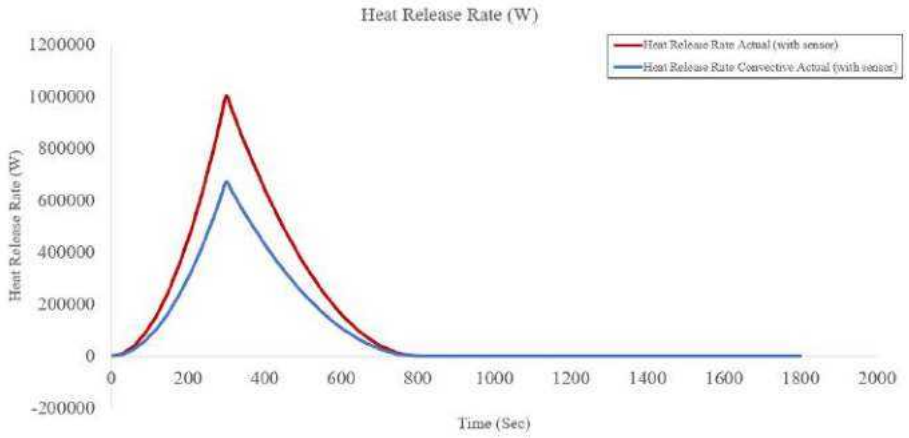

Figure 5: Heat release rate in the state without fire alarm and extinguishing system

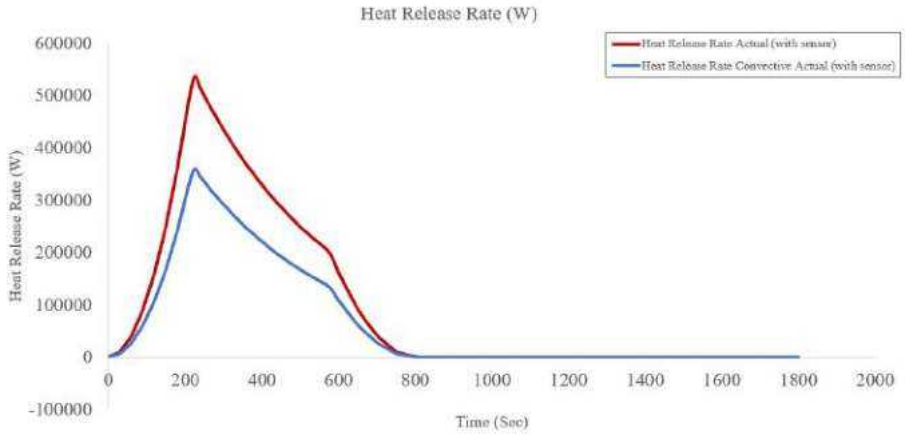

Figure 6: Heat release rate in the presence of an standard fire alarm and extinguishing system

According to figures 5 and 6, the impact of the standard fire extinguishing system can be well seen. When the building does not have a standard fire extinguishing system, it is observed that the heat emission rate is 1000000 $^{W}/_{S}$ during a fire incident. But when there is a fire extinguishing system in the building according to the NFPA international standard, it can be seen that the maximum heat emission rate is reduced and reaches 580000 $^{W}/_{S}$, compared to when there is no standard fire extinguishing system. This issue also causes a decrease in the temperature in the compartments, and the results related to the temperature will be examined in the next sections.

3-3- Temperature changes in the compartments in the presence and absence of the standard fire alarm and extinguishing system

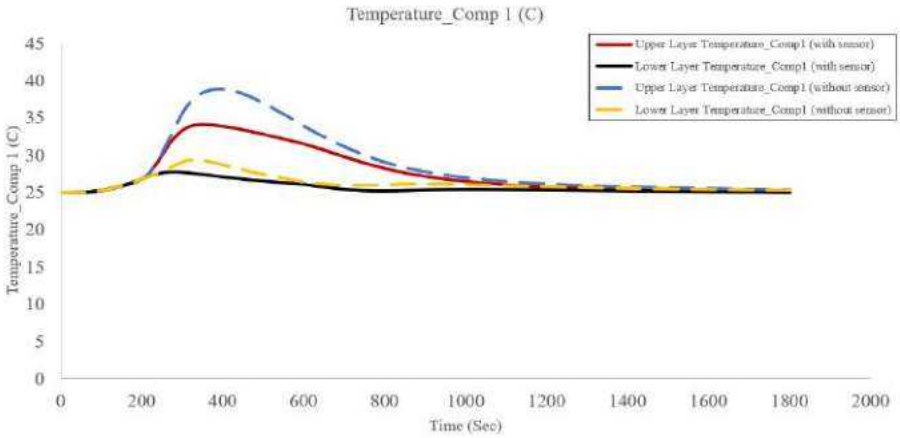

Figure 7: Temperature changes in compartment 1 in the presence and absence of the standard fire alarm and extinguishing system

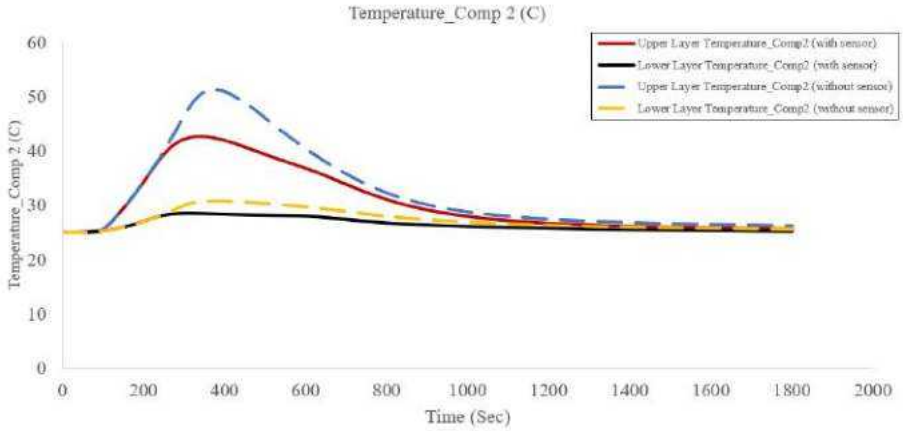

Figure 8: Temperature changes in compartment 2 in the presence and absence of the standard fire alarm and extinguishing system

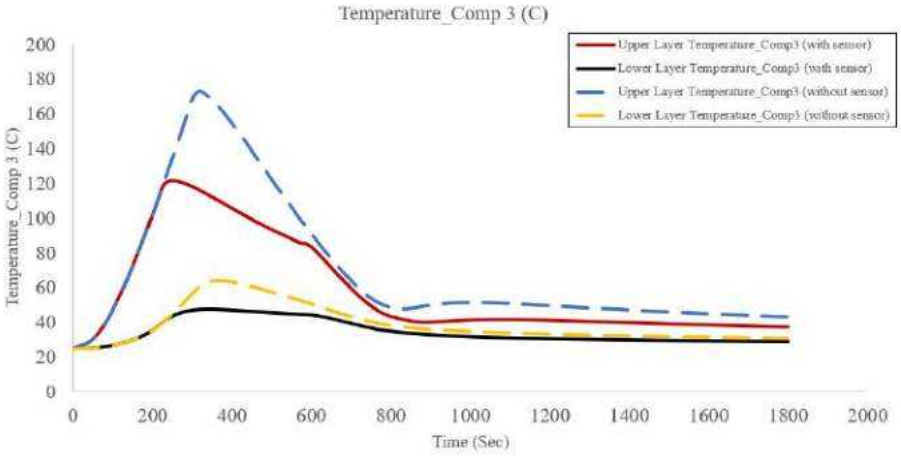

Figure 9: Temperature changes in compartment 3 in the presence and absence of the standard fire alarm and extinguishing system

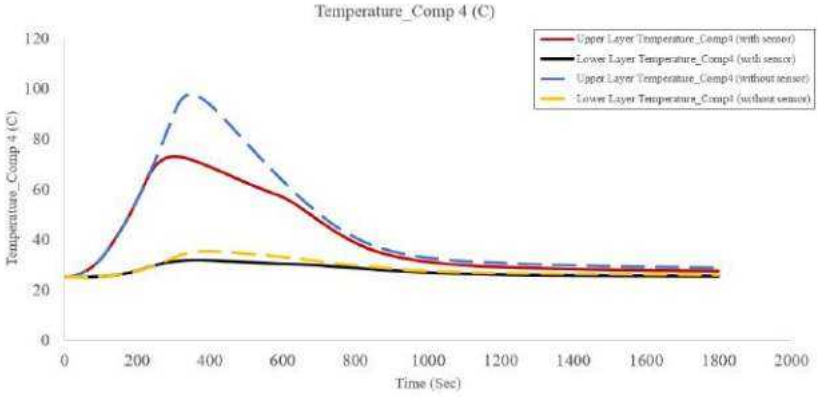

Figure 10: Temperature changes in compartment 4 in the presence and absence of the standard fire alarm and extinguishing system

The above graphs show the amount of temperature changes in the presence and absence of the standard fire extinguishing system. The temperature of room number 3, where there is a source of fire in this chamber, shows how effective the existence of a standard fire extinguishing system can be in stopping the fire in time and reducing the speed of heat release and thus reducing the temperature. The maximum temperature in compartment number 3 is 120°C if there is a standard fire extinguishing system, while in the absence of a standard fire extinguishing system, the temperature rises to 180°C and does not decrease until the fuel supply is exhausted. Also, the timely and correct operation of the fire extinguishing system in this compartment is very important because as it was said in the compartment where there is a source of fire, if the fire extinguishing system in this compartment works well and the fire is fully controlled, It prevents the increase in temperature in other chambers, especially compartment number 2, where nuclear fuel production takes place in this chamber. This can be seen in the graphs above.

3-4- Oxygen changes in the compartments in the presence and absence of the standard fire alarm and extinguishing system

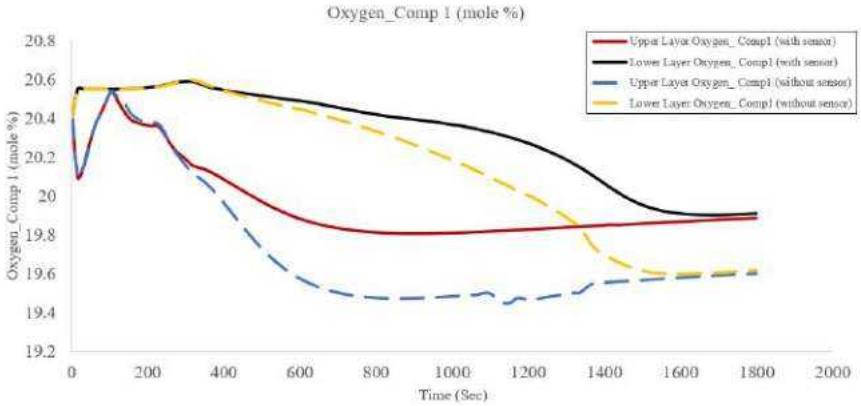

Figure 11: Oxygen changes in compartment 1 in the presence and absence of the standard fire alarm and extinguishing system

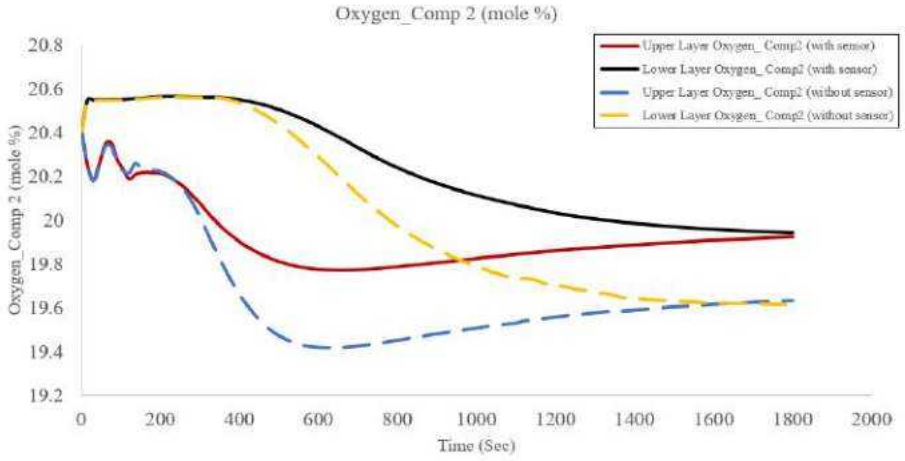

Figure 12: Oxygen changes in compartment 2 in the presence and absence of the standard fire alarm and extinguishing system

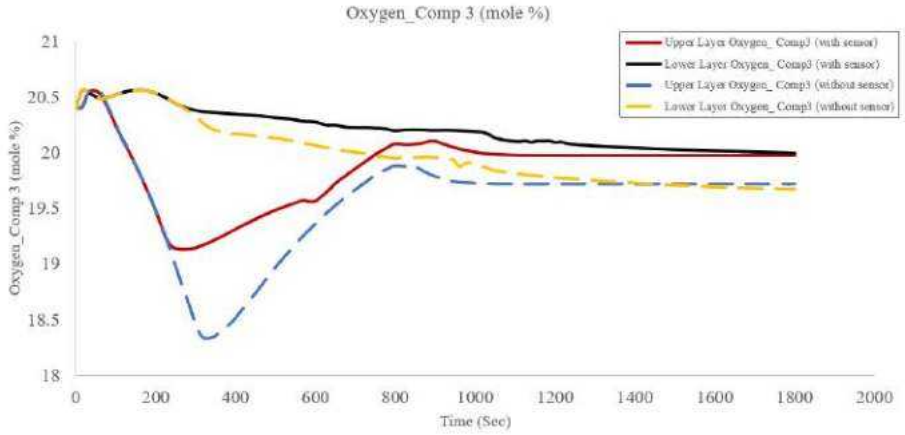

Figure 13: Oxygen changes in compartment 3 in the presence and absence of the standard fire alarm and extinguishing system

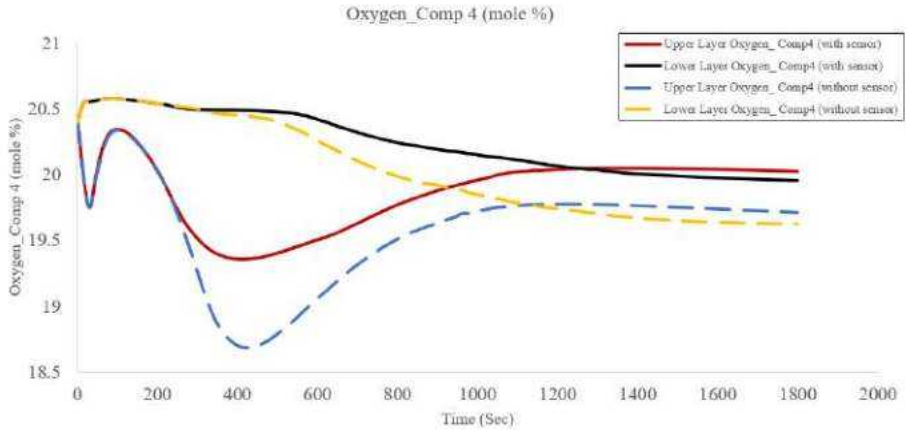

Figure 14: Oxygen changes in compartment 4 in the presence and absence of the standard fire alarm and extinguishing system

One of the main goals of fire extinguishing systems is to reduce oxygen and suppress the fire by this means. At first, it can be seen that oxygen is reduced by the standard fire extinguishing system to contain the fire well, and after the fire is contained, some chemicals produced by the fire can help reduce oxygen. Carbon monoxide, hydrogen cyanide, and hydrogen sulfide can do this. The water fire extinguishing system is able to prevent excessive concentration of smoke by regularly spraying water on the smoke and reduce toxic and harmful smoke particles that reduce oxygen. This can be clearly seen in the figures above.

Conclusions

In this research, fire behavior in the compartments of the -1 floor of building 505 of the nuclear fuel production complex was investigated in the presence and absence of a standard fire alarm and extinguishing system. The most important compartment for us in this research is compartment number 3 because the source of the fire is located in this compartment and if the fire in this compartment is well controlled it will prevent the spread of fire and increase in temperature and pressure in other compartments and finally the amount of damage The input to the facility is reduced. When there is no standard fire extinguishing system, the heat release rate increases up to 1,000,000 W/S and then begins to decrease as the fuel source is exhausted. But when there is a standard fire extinguishing system, it is observed that the maximum amount of heat release is 580,000 W/S and immediately after reaching its maximum value, due to the proper functioning of the standard fire extinguishing system, it decreases and finally It reaches zero in 800 seconds. Regarding the temperature, it can be said that in compartment number 3, where there is a fuel source in this compartment, if it has a standard fire extinguishing system, it prevents the temperature from increasing too much. If there is a standard fire extinguishing system, the maximum temperature increase in the upper layer is 120 degrees and in the lower layer is 45 degrees Celsius. But if there is no standard fire extinguishing system and the fire control is not formed well, the temperature in the upper layer will rise up to 180 degrees Celsius and in the lower layer up to 70 degrees Celsius. Also, the temperature in other compartments increases a lot and causes damage to the facilities of other parts. Regarding oxygen, we also checked that the standard fire extinguishing system can be effective even in increasing oxygen. The effective operation of the standard fire extinguishing system first reduces the supply of oxygen and suppresses the fire,

and after the fire is extinguished by regularly spraying water on the smoke, it prevents excessive concentration of smoke and thus increases oxygen.

NUREG/CR-7010 has been used for validation of the research. This edition of NUREG discusses electric cable heat release, ignition and fire spread. In this important reference, it can be well understood that the maximum heat release rate of electrical cable with XLPE clad is about 1 $\boldsymbol{MW}$ or 1000000 $\boldsymbol{W}$ [19].

Acknowledgements

I would like to express my gratitude to Prof. Mohammad Reza Nematollahi, faculty member of nuclear engineering department of Shiraz University, who helped and supported me in this research.

Supplementary information

Table 1: Simulation information

PARAMETER	VALUE
SIMULATION TIME	1800 SEC
TEXT OUTPUT INTERVAL	50 Sec
BINARY OUTPUT	0 Sec
SPREADSHEET OUTPUT INTERVAL	10 Sec
SMOKEVIEW OUTPUT INTERVAL	10 Sec
SCALE HEIGHT	10 m
POWER LOW	10 m

Table 2: Size and location of compartment 1

PARAMETER	VALUE
WIDTH	2.8 m
DEPTH	13.85 m
HEIGHT	4.2 m
X POSITION	0.0 m
Y POSITION	0.0 m
Z POSITION	0.0 m

Table 3: Size and location of compartment 2

PARAMETER	VALUE
WIDTH	16.1 m
DEPTH	13.85 m
HEIGHT	4.2 m
X POSITION	2.8 m
Y POSITION	0.0 m
Z POSITION	0.0 m

Table 4: Size and location of compartment 3

PARAMETER	VALUE
WIDTH	8.3 m
DEPTH	2.65 m
HEIGHT	4.2 m
X POSITION	18.9 m
Y POSITION	0.0 m
Z POSITION	0.0 m

Table 5: Size and location of compartment 4

PARAMETER	VALUE
WIDTH	8.3 m
DEPTH	11.2 m
HEIGHT	4.2 m
X POSITION	18.9 m
Y POSITION	2.65 m
Z POSITION	0.0 m

References

[1] IAEA, "IAEA-TECDOC-1421 Experience gained from fires in nuclear power plants. Lessons learned.," *IAEA-Tecdoc 1421*, no. November, 2004.

[2] R. D. Peacock, P. A. Reneke, and G. P. Forney, "NIST Technical Note 1889v2 CFAST – Consolidated Model of Fire Growth and Smoke Transport (Version 7) Volume 2 : User ' s Guide," vol. 2, no. Version 7.

[3] S. Safaei Arshi, M. Nematollahi, and K. Sepanloo, "Coupling CFAST fire modeling and SAPHIRE probabilistic assessment software for internal fire safety evaluation of a typical TRIGA research reactor," *Reliab. Eng. Syst. Saf.*, vol. 95, no. 3, pp. 166–172, Mar. 2010, doi: 10.1016/J.RESS.2009.09.006.

[4] R. H. V. Gallucci and B. Metzger, "Statistical Characterization of Heat Release Rates from Electrical Enclosure Fires for Nuclear Power Plant Applications," *Fire Technol.*, vol. 53, no. 3, pp. 1249–1271, May 2016, doi: 10.1007/S10694-016-0633-Z.

[5] R. H. V. Gallucci and B. Metzger, "M. K. Dey, 'A conceptual framework for formulating a focused and cost-effective fire protection program based on analyses of risk and the dynamics of fire effects,' Nuclear Engineering and Design, vol. 193, no. 1–2, pp. 185–196, Sep. 1999, doi: 10.1016/S0," *Int. Top. Meet. Probabilistic Saf. Assess. Anal. PSA 2017*, vol. 1, pp. 231–240, 2017, doi: 10.1007/s10694-017-0650-6.

[6] S. Kim, B.-H. Jeong, S.-K. Kang, Y.-K. Jeong, P. Kim, and B. Cho, "Lessons Learned from Internal Fire PSAs on Candu Reactors and PWRs in Korea," 2004.

[7] K. McGrattan, R. Peacock, and K. Overholt, "Validation of Fire Models Applied to Nuclear Power Plant Safety," *Fire Technol.*, vol. 52, no. 1, pp. 5–24, Jan. 2016, doi: 10.1007/S10694-014-0436-Z/METRICS.

[8] W. W. Jones, R. D. Peacock, G. P. Forney, and P. A. Reneke, "CFAST: Consolidated Model of Fire Growth and Smoke Transport (Version 6). Technical Reference Guide." 2009. Accessed: Dec.

29, 2023. [Online]. Available: https://www.nist.gov/publications/cfast-consolidated-model-fire-growth-and-smoke-transport-version-6-technical-reference

[9] A. Hamins, K. Konishi, P. Borthwick, and T. Kashiwagi, "Global properties of gaseous pool fires," *Symp. Combust.*, vol. 26, no. 1, pp. 1429–1436, Jan. 1996, doi: 10.1016/S0082-0784(96)80363-8.

[10] A. Tewarson, "Generation of Heat and Chemical Compounds in Fires," 2002.

[11] B. J. Mccaffrey and G. Cox, "Entrainment and Heat Flux of Buoyant Diffusion Flames. Final Report." 1982. Accessed: Dec. 31, 2023. [Online]. Available: https://www.nist.gov/publications/entrainment-and-heat-flux-buoyant-diffusion-flames-final-report

[12] H. Koseki, "Combustion properties of large liquid pool fires," *Fire Technol.*, vol. 25, no. 3, pp. 241–255, Aug. 1989, doi: 10.1007/BF01039781/METRICS.

[13] P. Ruffino and M. Dimarzo, "The Effect of Evaporative Cooling on the Activation Time of Fire Sprinklers," pp. 481–492.

[14] F. Gavelli, P. Ruffino, G. Anderson, and M. Di Marzo, "THE EFFECT OF MINUTE WATER DROPLETS ON A SIMULATED SPRINKLER LINK THERMAL RESPONSE".

[15] M. J. Hurley *et al.*, "SFPE handbook of fire protection engineering, fifth edition," *SFPE Handb. Fire Prot. Eng. Fifth Ed.*, pp. 1–3493, Jan. 2016, doi: 10.1007/978-1-4939-2565-0/COVER.

[16] T. Cleary, A. Chernovsky, W. Grosshandler, and M. Anderson, "Particulate entry lag in spot-type smoke detectors," *Fire Safety Science*. pp. 779–790, 2000. doi: 10.3801/IAFSS.FSS.6-779.

[17] K. Mcgrattan, S. Hostikka, J. Floyd, H. Baum, and R. Rehm, "Fire Dynamics Simulator (Version 5) Technical Reference Guide," *Nist Spec. Publ.*, vol. 1, no. Version 5, p. 86, 2007.

[18] "Specific extiction coefficient of flame generated smoke | Request PDF." Accessed: Apr. 24, 2024. [Online]. Available: https://www.researchgate.net/publication/247958071_Specific_extiction_coefficient_of_flame_generated_smoke

[19] "Cable Heat Release , Ignition , and Spread in Tray Installations During Fire (CHRISTIFIRE) Phase 1 : Horizontal Trays," vol. 1.

ICNST 2024
International Conference on Nuclear Science and Technology
6- 8 MAY 2024 | Isfahan, Iran

Thermal Performance Assessment of a Small Modular Reactor's Once-Through Steam Generator Using Al2O3 Nanoparticles in the Primary Coolant System (Paper ID : 1142)

Ghazanfari V.*, Mansourzadeh F., Amini Y., Shadman M.M.

Nuclear Fuel Cycle Research School, Nuclear Science and Technology Research Institute, Tehran, Iran

Abstract

This study investigated the impact of Al_2O_3 nanoparticles on the primary coolant system of a Small Modular Reactor (SMR) associated with NuScale reactors. A 3-D simulation using the finite volume method in Fluent software was conducted. The effect of a 10% volume fraction of Al_2O_3 nanoparticles was examined at flow rates of 0.5, 1, and 2 kg/s. The analysis revealed a 20% improvement in the heat transfer performance with the use of nanoparticles. This improvement is attributed to increased surface area and altered fluid dynamics. The findings highlight the potential benefits of incorporating nanoparticles in SMRs for enhanced thermal performance.

Keywords: Nanoparticles, primary coolant, SMR, Thermal performance, NuScale

Introduction

The NuScale reactor module is a compact and modular small modular reactor (SMR) technology that offers clean and reliable nuclear power generation [1]. It integrates multiple components into a single assembly, including the reactor core, steam generators, and containment structure. This design allows for standardized fabrication, simplified construction processes, and potential cost advantages. The core design optimizes heat transfer and safety with advanced fuel assemblies, control rod arrangements, and engineered coolant channels. Passive safety features ensure safe shutdown and cooling, relying on natural phenomena rather than active systems. The module also offers operational flexibility for load-following and responsive power output, enhancing grid stability and integration with renewable energy sources [2]. The Multi-Application Small Light Water Reactor (MASLWR) Test Facility serves as a proof of concept for reactors utilizing natural circulation. In the MASLWR concept design, the primary coolant is circulated around the outside of the steam generator (SG) tubes [3]. The test loop tube bundle is a helical coil consisting of fourteen tubes. This SG is a once-through heat exchanger and is located within the pressure vessel in the annular space between the riser and the inner surface of the reactor pressure vessel. There are three separate parallel sections (coils) of

stainless steel tubes. The outer and middle coils are composed of five tubes each, whereas the inner coil comprises four tubes. Each coil is separated from others but joined at a common inlet header to ensure pressure equilibrium within the coil, as shown in Fig. 1 and Fig. 2.

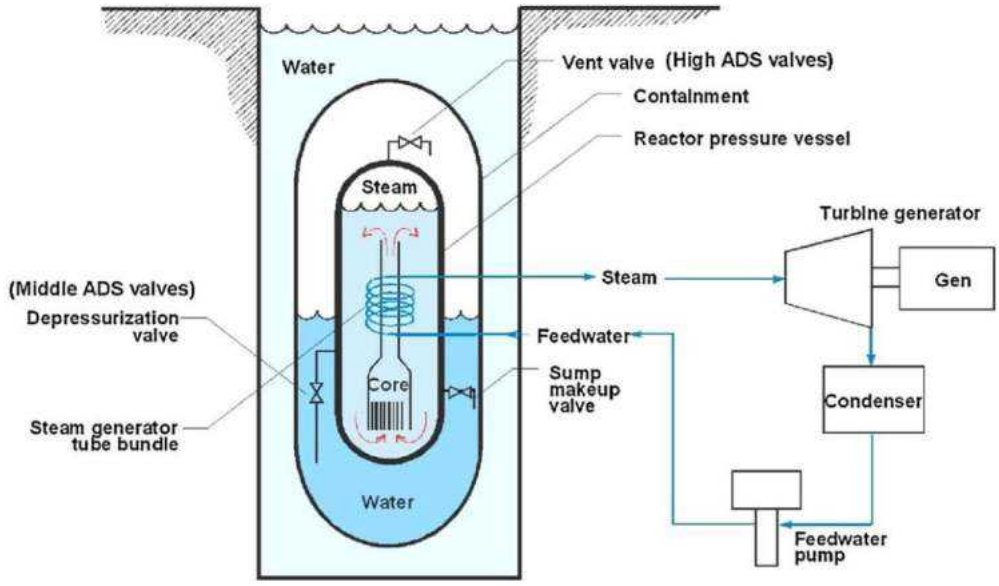

Fig. 1. MASLWR conceptual design layout [4]

Fig. 2. Photographs of SG coil bundle arrangement [3]

Thermo-fluid-dynamic analysis is a crucial tool for the design, operation, and safety assessment of small modular reactors (SMRs). This analysis allows engineers to evaluate coolant flow, heat transfer, and pressure distribution to identify safety hazards and optimize system performance. It also helps in heat transfer and cooling analysis to ensure efficient cooling of the reactor core. Thermo-fluid-dynamic analysis provides insights into the system's dynamic behavior, aiding in operational

flexibility and compliance with regulatory requirements. Previous studies on helical steam generators have focused on their thermo-fluid-dynamic behavior, utilizing experimental investigations and computational modeling to understand flow patterns, pressure drops, and heat transfer performance. These studies have contributed to advancing helical steam generator design and optimization in the nuclear industry.

In recent years, the application of nanofluids has shown significant advancements in enhancing heat transfer performance across various industries [5, 6, 7, 8]. Nanoparticles, when dispersed in base fluids, form nanofluids that exhibit improved thermal conductivity and enhanced heat transfer characteristics [9]. Nanoparticles have gained significant prominence in the fields of science and engineering. Within this context, nanofluids have emerged as a notable area of interest. Nanofluids are colloidal dispersions that contain nanometer-sized materials, including stable metals, metal oxides, oxide ceramics, and metal carbides. These nanofluids have attracted considerable attention due to their unique properties and potential applications [10]. In particular, nanofluids containing Al2O3 nanoparticles have been extensively studied due to their desirable thermal properties, high efficiency, and stability. Understanding the thermophysical characteristics of Al_2O_3 is crucial for investigating how the addition of Al_2O_3 nanoparticles modifies the heat transfer properties of nanofluids [11]. Kumar et al. conducted research on the thermal conductivity of Al_2O_3 nanofluids at different temperatures (30°C, 40°C, and 50°C) and observed that the thermal conductivity improved as the volume fraction of nanoparticles in water increased from 0.01 to 0.08 vol.%, with a more pronounced effect at higher temperatures [12]. Gkountas et al. investigated heat transfer in printed-circuit heat exchangers of a supercritical CO_2 Brayton cycle using Al_2O_3 nanofluid. Their study showed that incorporating a maximum volume fraction of 5% nanoparticles resulted in a 10% improvement in the heat transfer coefficient compared to using pure water as the working fluid. This improvement led to a 0.9% reduction in the total length of the heat exchanger and a pressure drop reduction of up to 14% [13]. Sharma et al. examined the impact of combining protruded ribs with twisted tape inserts and Al_2O_3 nanofluid on the performance of heat exchanger tubes. CFD simulations demonstrated significantly improved friction factor (2.51 times) and heat transfer (68 times) when using twisted tape inserts combined with nanofluid and protruded ribs [14].

Our study focused primarily on the thermal performance assessment of the helical coil heat exchanger by adding Al_2O_3 nanoparticles. However, we acknowledge the broader challenges that can hinder the

practical deployment of nanoparticles in various applications. Compatibility and stability issues are crucial considerations when incorporating nanoparticles into the system. The interaction between nanoparticles and the base fluid, as well as the materials used in the heat exchanger, may affect the overall stability and performance of the nanofluid. Safety and radiological considerations are also important factors to address. The potential release of nanoparticles during operation and their impact on personnel and the environment should be carefully evaluated and mitigated. Regulatory approval and licensing processes play a significant role in the practical implementation of nanofluid-based systems. Compliance with regulations and obtaining necessary approvals are essential steps to ensure such technologies' safe and reliable deployment.

Furthermore, neutron absorption and fuel performance considerations are particularly relevant in nuclear applications. The influence of nanoparticles on neutron absorption and their potential impact on fuel performance should be thoroughly investigated. Lastly, achieving a uniform distribution of nanoparticles in the fluid is a challenge that can affect the overall performance of the nanofluid. Non-uniform distribution may lead to variations in heat transfer characteristics and hinder the desired enhancement.

This study aimed to analyze the heat transfer between the primary and secondary loops of the MASLWR test loop. The focus was on investigating the cooling of the core through a simulated helical coil steam generator. The study assumed a constant temperature for the tube wall in the steam generator. Additionally, the impact of Al_2O_3 nanoparticles on thermal performance was examined.

Research Theories

The governing equations of the nanofluid for the conservation of mass, momentum, and energy in a steady state are written as [15, 16]:

$$\nabla.\left(\rho_{nf}V\right) = 0 \tag{1}$$

$$\nabla.\left(\rho_{nf}VV\right) = -\nabla p + \nabla.\,\tau \tag{2}$$

$$\nabla.\left(\rho_{nf}Ve\right) = -\nabla.\left(k_{nf}\nabla T\right) - \nabla.\,(pV) + \nabla.\,(\tau\, V) \tag{3}$$

Where ρ is the density of the nanofluid, p is the pressure, V is the velocity vector, τ is the stress tensor, T is the temperature, and e is the specific total energy. k_{nf} is the conductivity of the nanofluid.

This study employs Al_2O_3 particles as nanofluids in the primary coolant system of the MASLWR test loop. Table 1 illustrates the thermo-physical properties of this nanoparticle and base fluid.

Table 1. Thermo-physical properties of nanoparticles and base fluids [17]

Property	C (J/kg K)	ρ(kg/m^3)	k (W/mK)	α(m^2/s)
Al_2O_3	765	3970	40	1317
water	4179	997.1	0.605	1.47

The correlations for density (ρ_{nf}), specific heat (Cp_{nf}), viscosity (μ_{nf}), and thermal conductivity (k_{nf}) of the nanofluid can be calculated [15, 17]:

$$\rho_{nf} = (1-\varphi)\rho_{bf} + \varphi\rho_{np} \quad (4)$$

$$Cp_{nf} = (1-\varphi)Cp_{bf} + \varphi Cp_{np} \quad (5)$$

$$\mu_{nf}/\mu_{bf} = 123\varphi^2 + 7.3\varphi + 1 \quad (6)$$

$$k_{nf}/k_{bf} = 4.97\varphi^2 + 2.72\varphi + 1 \quad (7)$$

In this study, φ is the volume fraction of nanofluid considered 10. The subscript " *bf* " signifies the base fluid, and the subscript " *np* " denotes the nanoparticle (Al_2O_3), as well as the subscript " nf " signifies the final nanofluid.

The present solution uses a coupled pressure-based procedure to solve the pressure-based continuity and momentum equations simultaneously employing Fluent software. Fluent is a fluid simulation program renowned for its advanced physics modeling and accuracy in CFD.

The geometric parameters for the helical coil steam generator of the Multi-Application Small Light Water Reactor are presented in Table 2 and Table 3.

Table 2. MASLWR steam generator section dimensions [4]

Parameter	Value
RPV Outer Diameter (mm)	355
RPV Shell Thickness (mm)	32
Chimney Outer Diameter (mm)	114
SG Section Height (mm)	1251

Table 3. Steam tube dimensions [4]

Parameter	Inner	Middle	Outer
Direction	CW	CCW	CW
Number of tubes	4	5	5

Tube length (mm)	6205	6299	6364
Coil diameter (mm)	146	203	260
Rotations	13	9.5	7.5
Pitch (mm)	19.8	21	26.1
Rise/rotation (mm)	80	105	130
Total coil rise (mm)	1028	1003	978
Lead length (mm)	15.8	15.8	15.8

Fig. 3 demonstrates the geometry and mesh of the helical coil steam generator. The high-temperature primary coolant, originating from the reactor core, enters the heat exchanger through the inlet chimney. Subsequently, it ascends through the chimney channel and is distributed over the helical coil tubes, enabling heat transfer between the coolant and the coils. Under these conditions, heat is exchanged between the coolant and the helical coil tubes, reducing the coolant's temperature. Finally, the coolant is reintroduced into the core through the outlet shell.

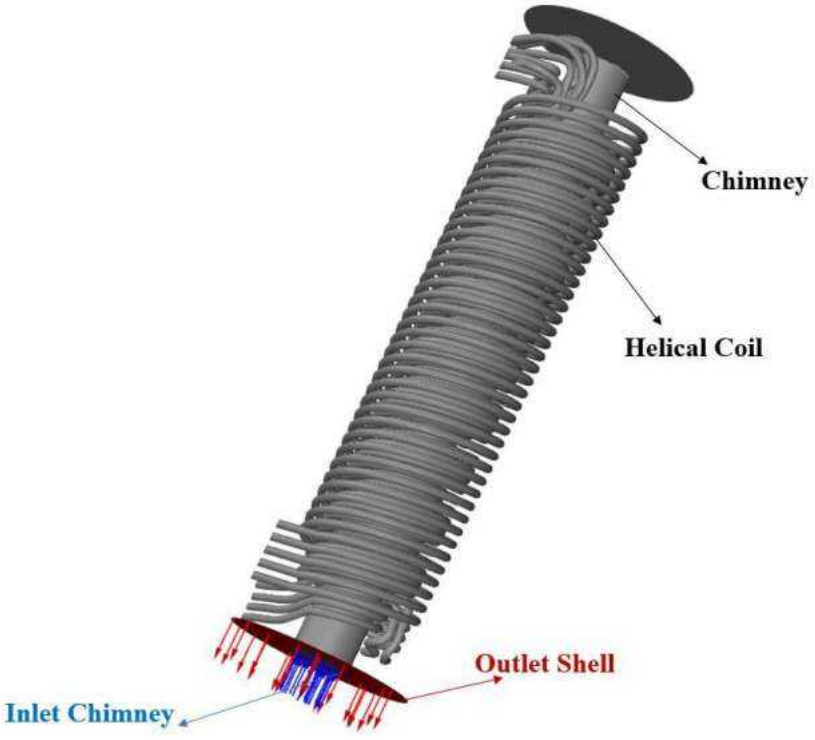

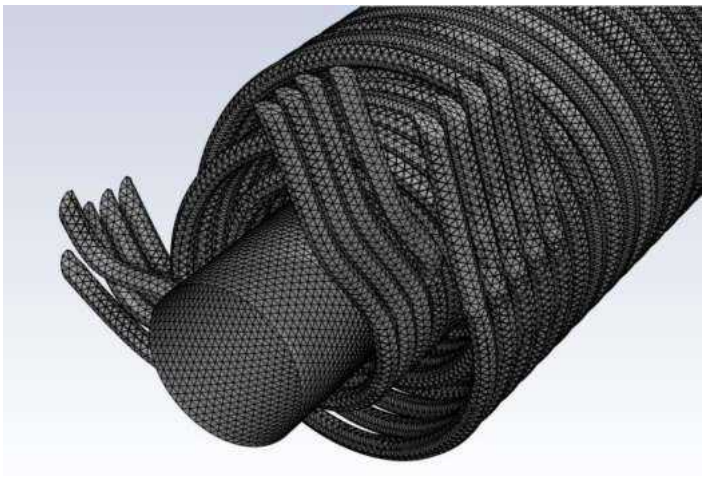

Fig. 3. The geometry and mesh of the helical coil steam generator

In this study, an inlet temperature of 545 K is considered for the coolant entering the inlet chimney at three different flow rates: 0.5, 1, and 2 kg/s.

Results and discussion

Fig .4 shows the results obtained from the computational fluid dynamics (CFD) analysis, where the Navier-Stokes equations were solved. The simulations were conducted to investigate the heat transfer characteristics in the system. Two scenarios were considered: pure water and a nanofluid containing a 10% volume fraction of Al_2O_3 nanoparticles. The contour plots in Fig. 4 display the temperature distribution for pure water. The colors used in the visualization represent different temperature levels, with warmer temperatures depicted by warmer colors and cooler temperatures represented by cooler colors. The contour plots are generated for three flow rates: 0.5, 1, and 2 kg/s. These visual representations provide valuable insights into the system's thermal behavior and allow for a comprehensive analysis of the heat transfer process

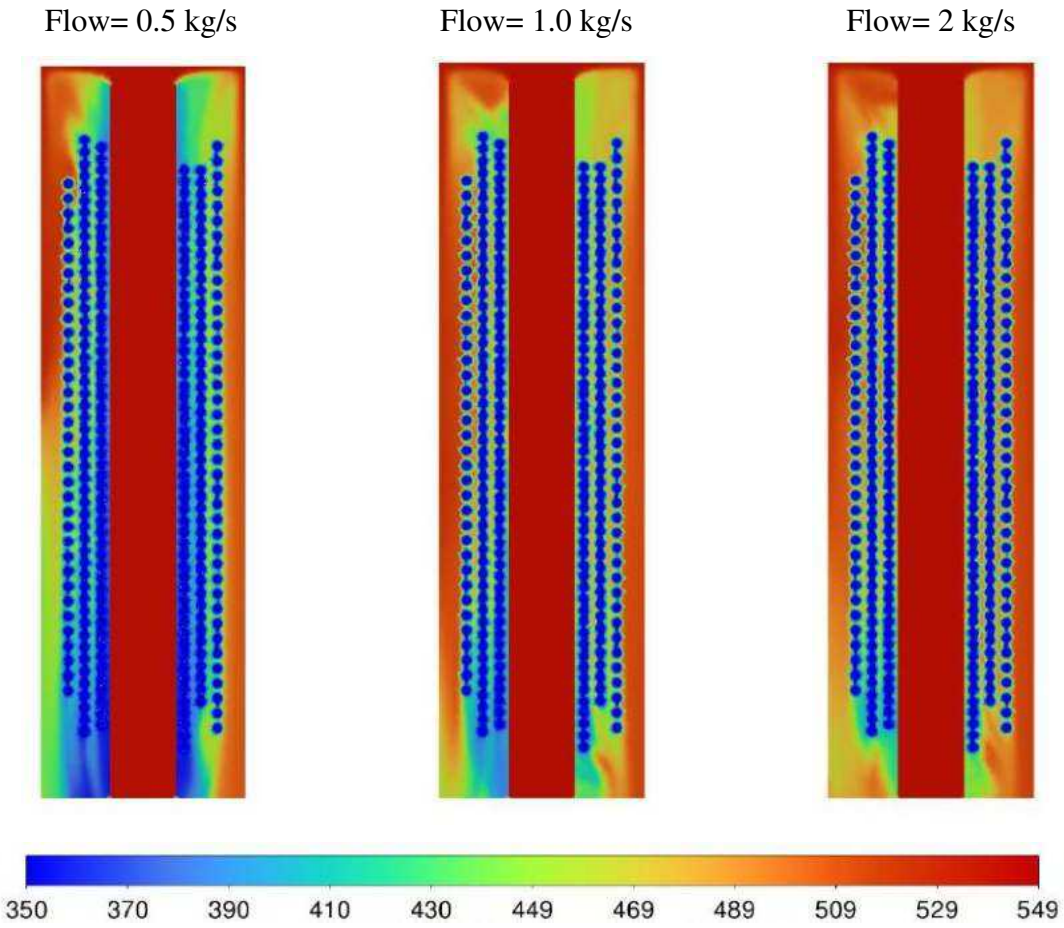

Fig. 4. The temperature distribution in the middle cross-section

As observed, the tube wall temperature of the helical coil heat exchanger is assumed to be maintained at 300 K. When the coolant, with a temperature of 545 K, passes through this tube walls, heat transfer occurs between the coolant and the helical coil tubes, resulting in a decrease in the coolant temperature at the outlet.

Fig. 5 illustrates the variations of temperature, pressure drop, and total heat transfer for pure water and a nanofluid (10% Al_2O_3) at different flow rates. The plot's temperature value refers to the outlet shell's average temperature. It can be observed that increasing the flow rate results in higher outlet temperatures. Additionally, as the flow rate increases, the pressure drops and total heat transfer increases. Utilizing the nanofluid, which enhances heat transfer, decreases the outlet temperature compared to pure water. Specifically, at flow rates of 0.5, 1, and 1.5 kg/s, the outlet temperatures for pure water are 447 K, 474 K, and 489 K, respectively. However, these values are reduced to 439 K, 465 K, and 482 K for the nanofluid, respectively.

Furthermore, the difference in total heat transfer between pure water and the nanofluid is quantified as 15%, 16%, and 20% for flow rates of 0.5, 1, and 2 kg/s, respectively.

In addition, it should be noted that despite the increase in heat transfer with the use of the nanofluid, there is also an increase in pressure drop. In this case, the pressure drop has increased by approximately 14%.

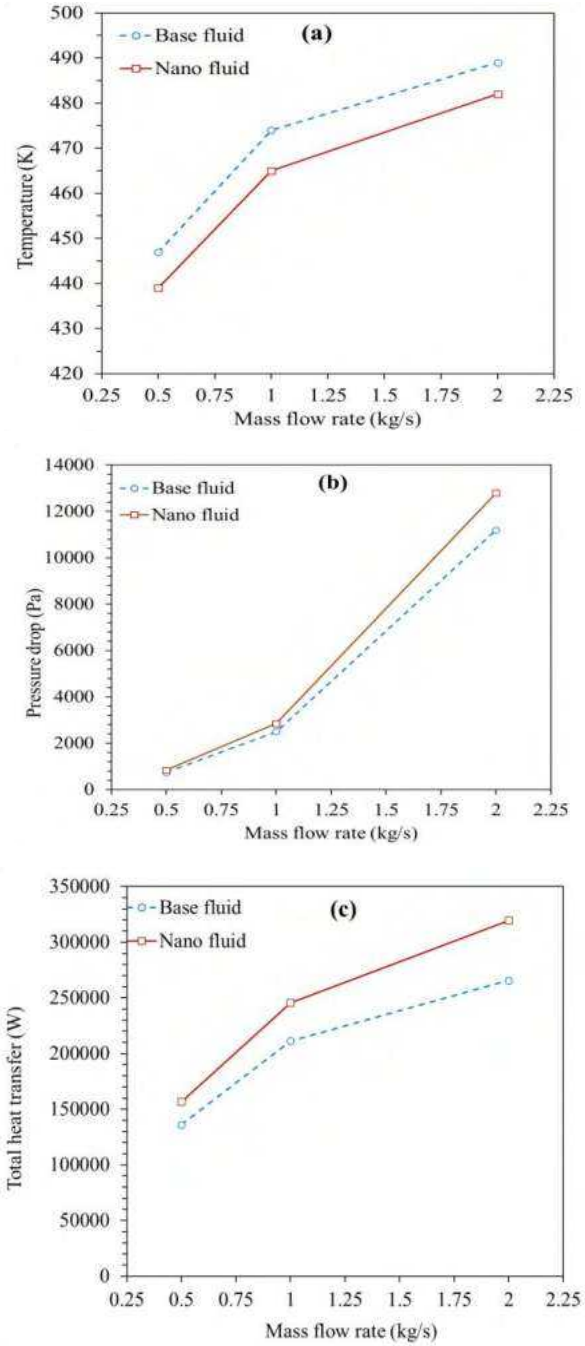

Fig. 5. Comparison of the outlet temperature (a), pressure drop (b), and total heat transfer (c).

Conclusions

In this study, computational fluid dynamics (CFD) analysis was employed to investigate the heat transfer characteristics of a helical coil heat exchanger. Two scenarios were considered: pure water and a nanofluid containing a 10% volume fraction of Al_2O_3 nanoparticles. The temperature distribution in the middle cross-section was visualized using contour plots, providing valuable insights into the system's thermal behavior. The results showed that increasing the flow rate led to higher outlet temperatures, increased pressure drop, and total heat transfer. The utilization of the nanofluid resulted in decreased outlet temperatures compared to pure water, indicating enhanced heat transfer performance. The difference in total heat transfer between pure water and the nanofluid was found to be 15%, 16%, and 20% for flow rates of 0.5, 1, and 2 kg/s, respectively. However, it is important to note that using the nanofluid also increased pressure drop, which rose by approximately 14%. This trade-off between heat transfer enhancement and increased pressure drop should be carefully considered in practical applications.

Overall, the findings demonstrate the potential of utilizing nanofluids in helical coil heat exchangers to improve heat transfer performance. Further research and optimization are recommended to explore the optimal operating conditions and nanofluid concentrations for achieving the desired balance between heat transfer efficiency and pressure drop. While our study demonstrated the improvement in heat transfer due to the higher thermal conductivity of the nanofluid, we acknowledge that there are broader considerations that deserve investigation. The comparison of different nanoparticles, their corrosion effects, and finding solutions to reduce pressure drop are important aspects warrant further research.

References

[1] Kakaei, P. and Zangian, M. (2023). Multi-physics core analysis and verification of NuScale reactor with coupling PARCS/RELAP. Annals of Nuclear Energy, 193(1):110021.

[2] Sanchez-Torrijos, J. and Zhang, K. (2023). Multiscale analysis of the boron dilution sequence in the NuScale reactor using TRACE and SUBCHANFLOW. Nuclear Engineering and Design, 415:112708.

[3] Mascari, F. and Vella, G. (2012). Analyses of the OSU-MASLWR **EXPERIMENTAL** Test Facility. Science and Technology of Nuclear Installations, 1:1-19.

[4] Mascari, F. and Vella, G. (2011). Sensitivity analysis of the MASLWR helical coil steam generator using TRACE. Nuclear Engineering and Design, 241:1137–1144.

[5] Rahnama, Z. and Ansarifar, G. (2021). Nanofluid application for heat transfer, safety, and natural circulation enhancement in the NuScale nuclear reactor as a small modular reactor using computational fluid dynamic (CFD) modeling via neutronic and thermal-hydraulics coupling. Progress in Nuclear Energy, 138: 103796.

[6] Al-Farhany, K. and Abdulsahi, A. D. (2021). Study of mixed convection in two layers of saturated porous medium and nanofluid with rotating circular cylinder. Progress in Nuclear Energy, 135:103723.

[7] Ghorbanali, Z. and Talebi, S. (2020). Investigation of a nanofluid-based natural circulation loop. Progress in Nuclear Energy, 129:103494.

[8] Husain, S. and AhmadKhan, S. (2021). Wall boiling of Al2O3-water nanofluid: Effect of nanoparticle concentration. Progress in Nuclear Energy, 133:103614.

[9] Wang, Z. and Wu, Z. (2018). **EXPERIMENTAL** comparative evaluation of a graphene nanofluid coolant in miniature plate heat exchanger. International Journal of Thermal Sciences, 130:148-156.

[10] JinKim, H. and Lee, S.H. (2015). Effect of particle shape on suspension stability and thermal conductivities of water-based bohemite alumina nanofluids. Energy, 90:290-1297.

[11] Das, P. K. and Islam, N. (2017). **EXPERIMENTAL** investigation of thermophysical properties of Al2O3–water nanofluid: Role of surfactants. Journal of Molecular Liquids, 237:304-312.

[12] Kumar, N. and Sonawane, S. S. (2018). **EXPERIMENTAL** study of thermal conductivity, heat transfer and friction factor of Al2O3 based nanofluid. International Communications in Heat and Mass Transfer, 90:1-10.

[13] Gkountas, A. A. and Benos, L. T. (2020). Heat transfer improvement by an Al2O3-water nanofluid coolant in printed-circuit heat exchangers of supercritical CO2 Brayton cycle. Thermal Science and Engineering Progress, 20:100694.

[14] Sharma, S. and Kumar, A. (2022). Influence of twisted tape with collective protruded rib parameters of thermal–hydraulic performance of Al2O3-H2O nanofluid flow in heat exchanger tube, Materials Today: Proceedings, 50:1129-1133.

[15] Ghazanfari, V. and Talebi, M. (2016). Effects of water based Al2O3, TiO2, and CuO nanofluids as the coolant as the coolant. Progress in Nuclear Energy, 91:285-294.

[16] Ozden, E. and Tari, I. (2010). Shell side CFD analysis of a small shell-and-tube heat exchanger. Energy Conversion and Management, 51:1004-1014.

[17] Ghazanfari, V. and Talebi, M. (2016). Thermalehydraulic modeling of water/Al2O3 nanofluid as the coolant in annular fuels for a typical VVER-1000 core. Progress in Nuclear Energy, 87:67-73.

ICNST 2024
International Conference on Nuclear Science and Technology
6- 8 MAY 2024 | Isfahan, Iran

Feasibility study of utilizing a secondary pool for spent fuel storage in research reactor from shielding aspect (Paper ID : 1152)

Ehsan Boustani[3], Mostafa Hasanzadeh

Reactor and nuclear safety school, Nuclear Science and Technology Research Institute (NSTRI), Tehran, Iran

Abstract

Designing a spent fuel pool requires considering various aspects of calculations such as neutronic, thermohydraulic and shielding. Due to empty spaces in pool of some research reactors, the shielding calculations for feasibility study of using a second pool of a typical research reactor as a spent fuel storage have been performed in this research. The first step is the source term calculation for fuels with 60% burnup as the most pessimistic case. The distance between spent fuels (grid pitch) should meets the safety criterion of K_{eff} being less than 0.95. Racks arrangement, spent fuels numbers, water height and concrete pool wall thickness are the other parameters that investigated. The results show that it is possible to use of the second pool as a spent fuel pool with a capacity of 100 fuels, where the dose rate is less than criteria of 1 and 10 μSv/h behind the wall and above the water level, respectively.

Keywords: Shielding calculations, Design criteria, Research reactor, Spent fuel storage, Second pool.

Introduction

Spent fuel management in research reactors includes safe storage of spent fuel from discharge to final disposal. The spent fuel pool must provide safe, stable and reliable storage of spent fuel before reprocessing it or transfer to final disposal. The spent fuel pool must have features that can be used for the safe storage and recovery of spent fuel during the entire lifetime of the facility and in normal and emergency conditions. Relevant features include:

- Maintaining sub-criticality,
- Removing residual heat of spent fuel,
- Providing protection against radiation,

[3] Eboustani@aeoi.org.ir

• Maintaining isolation of radioactive materials from the environment.

With increasing fuel burnup, the neutron dose rate and temperature increase with a higher gradient than the gamma dose rate. This means that the gamma dose rate is the governing factor for fuel storage at lower burnups while for higher burnups, heat removal becomes the primary design criterion, and as burnup increases so more, the neutron dose rate is the determining factor in the storage of spent fuel in the spent fuel pool.

The spent fuel pool has a stainless-steel lining and a water purification system, and its capacity is considered for several years. The spent fuel pool must be equipped with an independent cooling and water purification system. Electrical conductivity, water temperature and pH, along with the area radiation are among the quantities that must be continuously and regularly monitored.

Different designs have been considered for the spent fuel pool in other reactors. In Argentina, the number of 608 spent fuels in 2 rows, each row containing 19 racks with a storage capacity of 32 spent fuels is stored in a pool with a depth of 16 meters, and the racks are designed in such a way that each one is placed on top of the other. Pool No. 2 in Australia's OPAL reactor, as given in **Fig. 7**, is designed as a spent fuel pool to store 330 spent fuels. According to the annual consumption of 30 fuels, this is designed to store 10 years of reactor spent fuels. There are empty spaces in some other research reactors such as second pool of the Pakistan's Research Reactor No. 1 (PARR-1), which could be used as spent fuel pool.

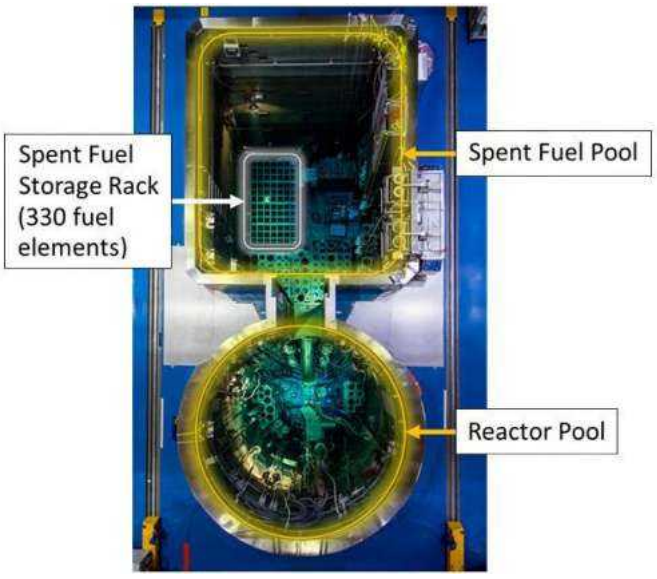

Fig. 7. Pool No. 2 as a spent fuel pool in the OPAL reactor.

The purpose of this article is the shielding calculations for the feasibility of using the second pool of a typical research reactor as a spent fuel pool. Pool type reactors are of the most common types of research reactors. The dose criteria used in the design include doses less than 1 μSv/h and 10 μSv/h behind the pool wall and above the water surface.

The required information for this research is from the safety analysis report and some documents available in other reactors. Criticality calculations to determine the arrangement of spent fuels are performed using MCNP code where calculation of source term, which is an important part of the shielding design program, have been done using ORIGEN code. The MCNP Monte Carlo code is used to define gamma and neutron sources and also the dose rate calculations.

Materials and Method

The ORIGEN 2.1 is a volatile and versatile point burn up and decay tool that solves decay and growth equations for numerous isotopes for arbitrary coupling. This code uses the matrix exponential method and first-order, linear, and coupled ordinary differential equations with the constant coefficient for solving large systems. The general nature of the exponential method allows for the investigation of complex decay and transmutation schemes. An extensive library of nuclear information has been collected. This code is used to calculate the compositions and radioactivity of fission products, cladding materials, and fuel materials in some types of reactors. The output of the ORIGEN code is used as the MCNP6 code input to compute the under-containment dose rate. The MCNP6 is a Monte Carlo transport code for tracking numerous particles in extensive energy and complicated geometries. The ENDF/B-IV and MCPLIB libraries are used for neutron and photon computations, respectively. The DFn card is used for conversion coefficient from flux to dose rate.

The spent fuel pool is used for long-term storage of spent fuel for even more than 50 years before sending for reprocessing or final disposal. In some documents, up to 100 years have been mentioned for storage in the spent fuel pool.

The spent fuel pool is equipped with racks for storing spent fuel. Deep pool creates a safety margin to protect the personnel and allows the spent fuel to be stored without special measures. Radioactive equipment and samples, defective fuels, graphite reflectors, and other devices used in operation are the equipment and devices stored in the second pool of a research reactor.

The spent fuels are U3O8-AL with 20% enrichment and maximum burnup of 60%. The racks are made of Al- 6061 and has a capacity of 100 fuels. Fig. 8 shows the suggested location of the spent fuel storage rack and its position relative to the location of the core in pool No. 1 and No. 2. Please note that all measurements are in centimeters.

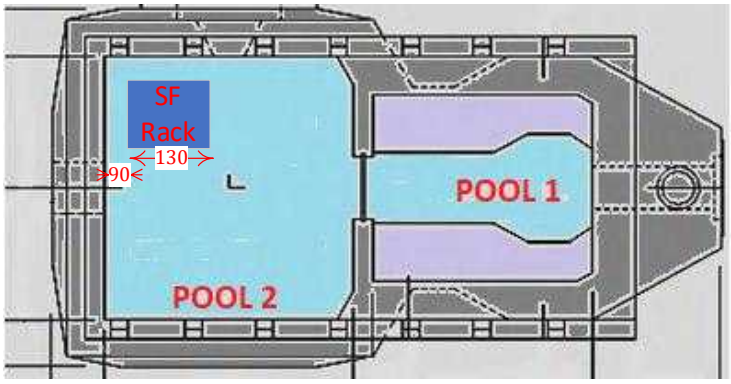

Fig. 8. Reactor pool and proposed location for spent fuel rack [**Error! Bookmark not defined.**].

Since in the case of continuous operation of the reactor, one fuel is removed from the core every month, the designed rack has the capacity of 100 spent fuels for continuous operation of the reactor for 8 years.

Due to the necessity of considering a sufficient distance between the location of the core in pool No. 2 and the spent fuel storage rack for the safe operation of the core in case of transferring the core to Pool No. 2, the location of the racks was done in such a way that its distance from the core is approximately 75 cm.

CALCULATIONS AND RESULTS

The distance between the spent fuel storage rack and the core in pool number 2 is about 75 cm. Considering the maximum range of neutrons in water, this distance is sufficient in terms of safety criteria to prevent the effect of the spent fuels on the core.

In order to calculate the values of neutron and gamma dose rates, and the necessary shielding thickness, several other essential effective factors including criticality calculations, fuel burnup, cooling time and reactor operation time should be studied.

According to references, the distance between the spent fuels supposing fresh ones should be such that the effective multiplication factor (Keff) has a safety margin of 5% or less after taking into account all the uncertainties in the calculations and data.

In order to obtain the initial plan and to predict the storage capacity of the spent fuels, the changes of the Keff with the distance between 100 fuels in 10 x10 arrays, supposing fresh fuels are calculated using the Kcode card in MCNP code and shown in Fig. 9. In this research, 106 histories are considered, and the relative error of all results is less than 10%.

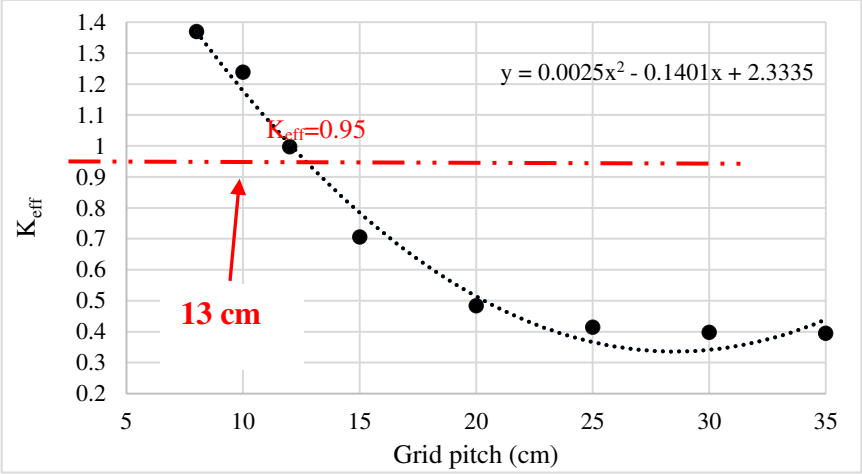

Fig. 9. Variations of K_{eff} for different distances between spent fuels.

According to the results presented in Fig. 9, the minimum distance between the fuels to have the sub-criticality condition is 13 cm.

The burnup value affects the spectrum and intensity of emitted photons. In order to better understand the effect of this factor, the spectrum of flux and intensity of photons for fuels with minimum and maximum burnup of 5 and 50%, respectively calculated and shown in Fig. 10. Results for the end of irradiation conducted using ORIGEN code for less than 2.5 MeV energy range.

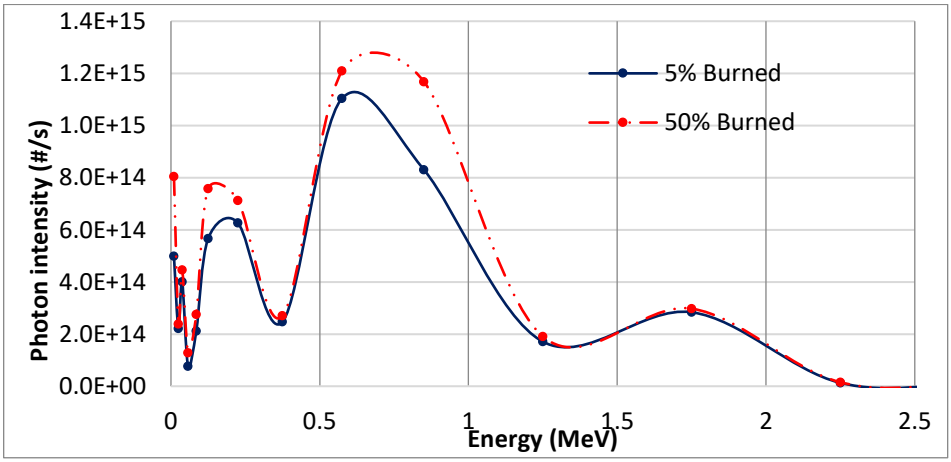

Fig. 10. The spectrum of photons from 5 and 50% burned fuels after the end of irradiation.

Since the spectrum values for higher energies are very close together, the photon spectrum for the energy range 2.5 to 9.5 MeV is given in Fig. 11 for better illustration.

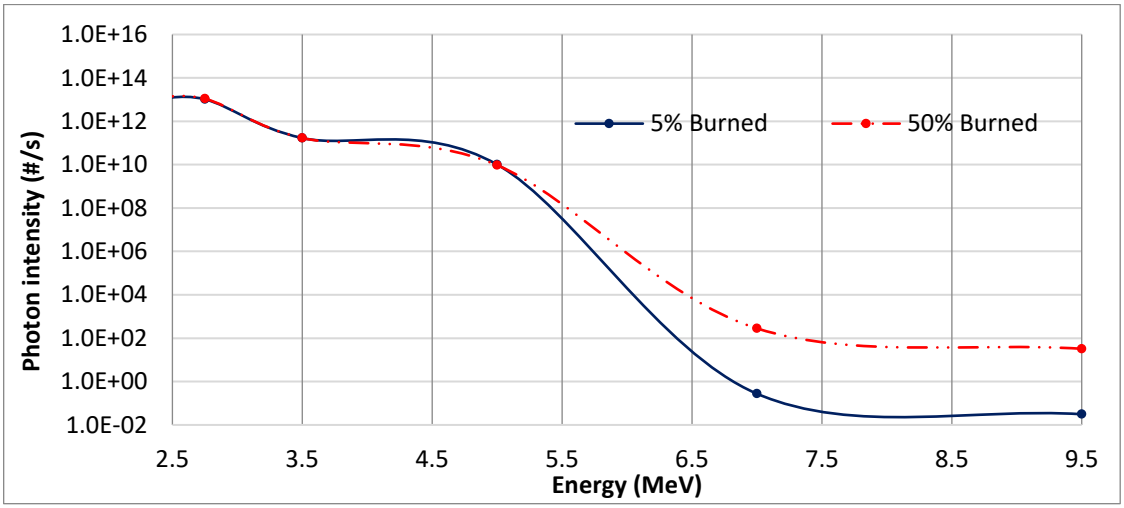

Fig. 11. Spectrum of photons from 5 and 50% burned fuels after the end of irradiation for upper 2.5 MeV.

As could be seen from Fig. 11, the photon intensity for fuel with 50% burnup is on average 20% higher than fuel with 5% burnup.

The cooling time is a duration of removing fuel from the core which affects the intensity of the gamma irradiation from the fuel. To investigation of this factor, the photon intensities for a fuel with maximum burnup of 60% immediately after the end of irradiation (cooling time is zero) and with 2 different cooling times of 30 days and 1 year are shown in Fig. 12.

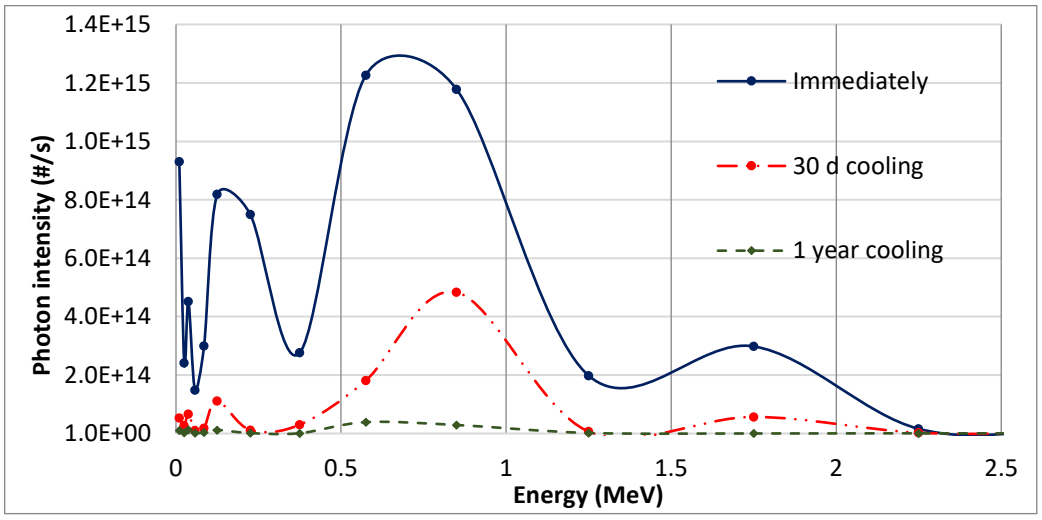

Fig. 12. Photons intensities for different cooling times.

As can be seen from the results presented in Fig. 12, cooling has a significant effect in reducing photon intensities. According to these results, the spectrum of emitted photons decreases by 84% after 30 days and by 98% after 1 year.

To calculate the dose rate, pool number 2 along with the used fuel storage rack is simulated using MCNP code as schematically is shown in Figure 7. Red, blue and green colors in this figure are water, concrete and air, respectively.

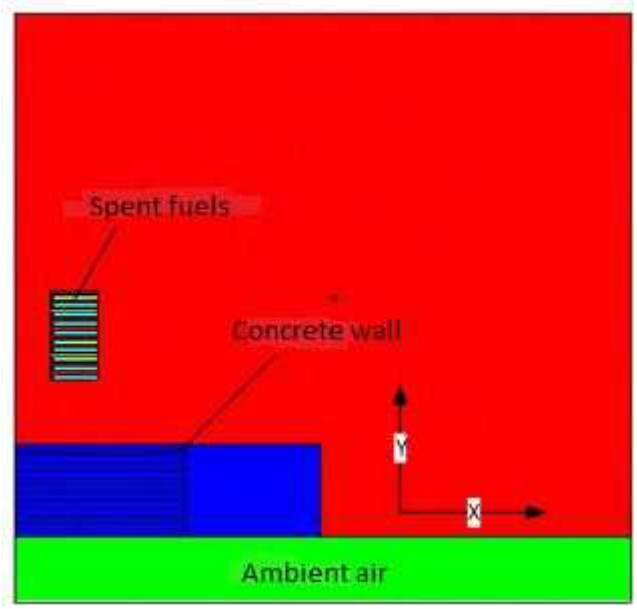

Fig. 13. Top view of simulation using MCNP code.

Measurement of underwater gamma dose rates of spent fuel in Pool No. 2 of the TRR is done periodically by International Atomic Energy Agency. The results of simulation and measurement at a distance of 30 cm from the two spent fuels with 7% and 43% burnup and 0 and 73 days cooling are shown in Table 2.

Table 2. results of experiment and calculation for two spent fuels.

Fuel number	Dose rate (mSv/h)		Relative difference (%)
	Measurement	Calculation	
Fuel 1	6.10E+6	5.41E+6	-11
Fuel 2	1.64E+4	2.02E+4	+23

According to Table 2, taking into account the significant effect of some factors such as the distance of the detector from the fuel, which is approximate, the relative difference of up to 20% can be acceptable and indicates the confirmation of the correctness of the simulation.

The axial and radial gamma dose rates in pool number 2 are calculated and presented in Fig. 14 and Fig. 15. The height given in these figures are the axial distance from the top of the spent fuels as the radial distance is the pool No. 2 concrete wall thickness.

In this research, the variance reduction method based on statistical population control was used based on multiplication methods and Russian Roulette with spatial meshing as well as energy cutting methods to reduce results errors and execution times.

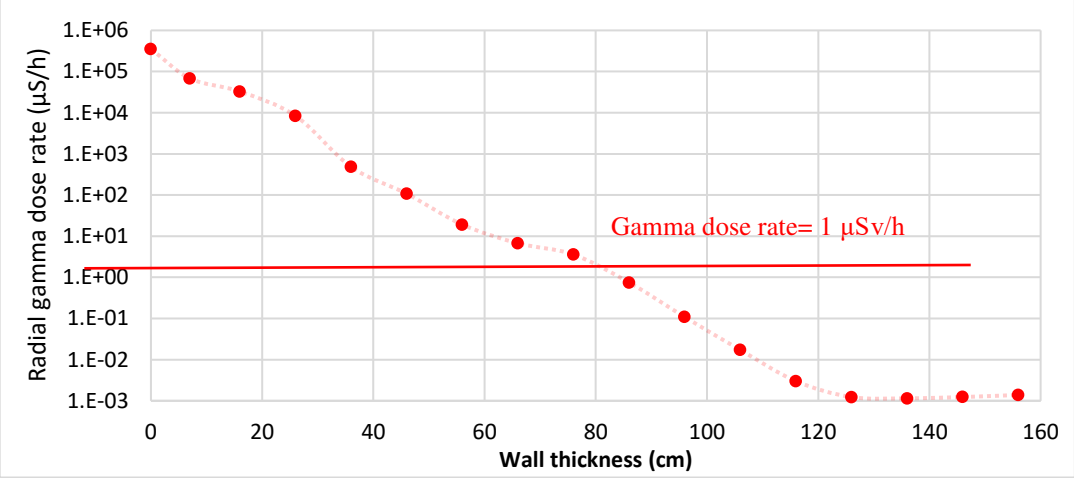

Fig. 14. Radial gamma dose rates in pool No. 2.

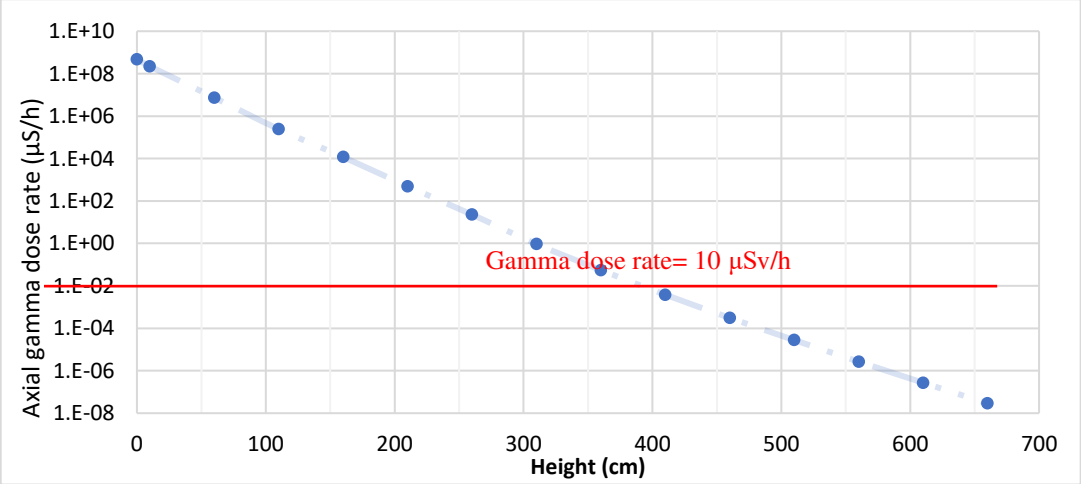

Fig. 15. Axial gamma dose rates in pool No. 2.

As can be seen from **Fig. 14** and **Fig. 15**, the required water height to reduce the gamma dose to less than the safety criterion of 10 μSv/h is about 300 cm as the required concrete thickness to reduce the gamma dose to less than the safety criterion of 1 μSv/h is approximately 85 cm. On the other hand, the gamma dose rate from the spent fuels to the inner edge of the wall has decreased by 3 times. Due to the considerable thickness and density of the concrete wall and after running program up to 500 million particles, the dose rate has decreased by 6 times from the beginning to the middle of the pool wall.

The neutron sources resulting from the alpha-neutron reaction and spontaneous fission for 100 spent fuels in pool No. 2 were calculated with the ORIGEN code. The total neutron source intensity is 3.81 E06 which is approximately 10^9 times lower than the gamma source intensity. The thickness of the water layer between the spent fuels and the concrete wall is 90 cm.

The macroscopic cross section of neutron transport and dispersion can be extracted from different references for arbitrary elements to calculate the mean free path according to the equation (1).

$$\lambda_{tr} = \frac{1}{\Sigma_{tr}} = \frac{1}{\Sigma_s(1-\bar{\mu})}, \bar{\mu} = \frac{2}{3A} \qquad (1)$$

Where λ_{tr}, Σ_{tr}, Σ_s, $\bar{\mu}$ and A are the transport mean free path, macroscopic transport cross section, macroscopic scattering cross section, average cosine of neutron scattering and mass number of the desired material, respectively. According to equation (1), the possibility of the existence of neutrons beyond 90 cm water is very small. Therefore, it does not cause a problem from radiation shielding aspect.

Conclusions

Spent fuels are radioactive for many years, so they need to be storage. For this reason, these spent fuels are kept inside the spent fuel pool up to some decades so that the resulting gamma and neutron dose rates outside the pool are reduced to less than the pre-set criteria. Shielding calculations are performed for the spent fuel pool of a typical pool reactor. Calculations show that the thickness of 85 cm for the concrete wall and the height of 300 cm for the water column above the designed rack with the grid pitch of 13 cm and the capacity of 100 spent fuel in pool No. 2 are sufficient to meet the dose criteria. Therefore, pool No. 2 in research reactors, which always has bigger than 85 cm wall thickness and 300 cm water column, respectively is a very suitable option to be considered as a spent fuel pool from radiation shielding point.

It could be concluded that the design of a spent fuel storage is possible according to the shielding design criteria. But it should be emphasized that the design of a spent fuel pool requires consideration of the other design criteria such as thermal-hydraulic, safety, and etc. which should be considered.

References

[1] IAEA safety standards (2011), Radiation Protection Aspects of Design for Nuclear Power Plants. Safety guide No. NS-G-1.13. International Atomic Energy Agency, Vienna.

[2] Lebrun A, Bignan G. (2016), Nondestructive assay of nuclear low-enriched uranium spent fuels for burnup credit application.

[3] Robert K. (2011), Criticality Safety in the Waste Management of Spent Fuel from NPPs.

[4] Arndt B, Klaus R, Wasinger K. (2003), Advanced spent fuel storage pools, Storage of spent fuel from power reactors. Vienna. IAEA. 130-141.

[5] Perschmann WD, Fuchs HP, Banck J. (2002), Impact of Extended Burnup of Spent Fuel on Backend of Fuel Cycle. German Perspective. IAEA. Vienna.

[6] IAEA-Nuclear Energy Series. No. NF-T-3.9. (2021), Research Reactor Spent fuel management Options and Support to Decision Making. VIENNA.

[7] IAEA-TECDOC-1508. (2006), Spent fuel management options for research reactors in Latin America. VIENNA.

[8] Benz JM, Smartt HA. (2006), Maintaining Continuity of Knowledge of Spent Fuel Pools Tool Survey. the U.S. Department of Energy.

[9] IAEA-Tecdoc-233. (1980), Research Reactor Core Conversion from The Use of Highly Enriched Uranium to The Use of Low Enriched Uranium Fuels Guidebook.

[0] AEOI (2018), Safety Analysis Report for Tehran Research Reactor.

[1] ANSTO (2004), Safety Analysis Report for Australian Nuclear Science and Technology Organization.

[2] Pelowitz DB. (2013), MCNP6TM User's Manual. Version 1.0, Los Alamos National Laboratory report LA-CP-13-00634.

[3] Crofft AG. (2000), A User's Manual for the ORIGEN 2.1 Computer Code. Rep. ORNL/TM-7175Oak Ridge National Laboratory.

[4] Harold Feiveson, Zia Mian, M.V. Ramana and Frank von Hippel (2011), Managing Spent Fuel from Nuclear Power Reactors, Experience and Lessons from Around the World, International Panel on Fissile Materials.

[5] US NRC (2010), Standard Review Plan for Spent Fuel Dry Storage Systems at a General License Facility, NUREG-1536, Revision 1.

[6] IAEA (2012), Safety Standards, Storage of Spent Nuclear Fuel, Specific Safety Guide, No. SSG-15.

[7] Lamarsh, J.R. (1975), INTRODUCTION to Nuclear Engineering. Addision- Wesely Publishing Company.

ICNST 2024
International Conference on Nuclear Science and Technology
6- 8 MAY 2024 | Isfahan, Iran

LQG/LTR controller design for power reference tracking molten salt reactor (Paper ID : 1182)

Hemmatzadeh M., Safarzadeh O.*
Faculty of Engineering, Shahed University, Tehran, Iran

Abstract

Molten salt reactor (MSR) has been identified as one of the six advanced reactor designs for the next generation reactors in the Gen-IV international forum due to its advantages in safety and efficiency. This reactor is the most promising type because of its key features such as high boiling point, low vapor pressure, large heat capacity, and great insensitivity to radiation. Considering the complexities of nuclear reactors, the issue of their control is important. The LQG/LTR method is one of the optimal control methods that shows useful properties of stability and good robustness in system control, and if there is measurement and input noise, this method is usually used to design the controller. In this paper, an LQG/LTR controller design method is used to power control the molten salt reactor. The designed controller is simulated using MATLAB/SIMULINK. The simulation results show that the proposed controller has low overshoot and fluctuations, and also has a fast system response time to power transients and load changes.

Keywords: Molten Salt Reactor – LQG/LTR controller – Reactor core power

Introduction

The quest for sustainable sources of energy has brought nuclear power into reconsideration as a potential candidate to meet the durability and environment-friendly paradigms. As such, a resurgence of interest is developed under Generation IV of nuclear energy for certain pioneer designs of nuclear reactors. The Molten Salt Reactor (MSR) technology originated in 1940–1950 through the American Aircraft Reactor Experiment (ARE) and was further exploited from 1950 to 1970. The project has nevertheless been abandoned afterward due to technical and economic issues. The MSR design employs a fluid fuel mixture of Uranium-thorium dissolved in fluoride salts (LiF/BeF2) and accordingly merits remarkable features in terms of safety and reliability. The development of efficient dynamic models for the MSR has long been the subject of several studies and the current need for load following and power control in nuclear reactors highlights this need [1]. Control of nuclear

reactors has been a challenging problem that attracts the attention of researchers worldwide. Several control strategies are reported in this domain. The design of a conventional controller for reactor control demands a precise mathematical model of the reactor. However, several critical parameters of the reactor system undergo wide variations during the operating lifespan of the reactor. Hence, a controller designed using a given reactor model under a given operating condition may not yield a satisfactory response under a different operating condition. Nevertheless, reactor systems are also seldom susceptible to operational disturbances. In this scenario, controllers that adapt themselves to such parametric uncertainties and disturbances form better candidates for reactor control [2]. Several approaches, from classical control techniques to artificial intelligence-based techniques, have been reported for power control of NPPs. Many of these controllers are designed around a reactor equilibrium operating point, which limits their satisfactory tracking performance over a wide range of throughput levels [3-5]. In the recent past, the design of controllers that handle parameter uncertainties and disturbances has gained considerable attention. Neural network-based controllers [6], fuzzy controllers [7], some of the robust techniques like sliding mode controller [8], Linear Matrix Inequalities (LMI) controller [9], model predictive controller [10], etc. have been proposed to control NPPs. In this paper, after introducing the reactor equations and its state space model, we will examine and present the design method of the LQG/LTR controller. In the end, we will see the results of the simulation and implementation of this controller on the system.

In 1960, Kalman introduced the optimal system controller in the form of an equation for the linear second-order regulator (LQR). The LQR method is considered an ideal method, but it is difficult to use it due to not having all the state variables. Therefore, to solve this problem, the solution of using the Kalman filter estimator was presented. By estimating the output state variables by the estimator, the state variables in the LQR control law can be replaced with these state variables, and with this change in the LQR control algorithm, the optimal LQG controller was created [11]. LQG is a controller that gives the best optimal response to system noises. Loop Transfer Recovery (LTR) is a methodology to recover LQG robustness properties (in terms of open-loop gain and phase margins) to approach the LQR [12] and restore the dynamic characteristics of a closed loop to improve the performance of the controller [13].

The Linear quadratic Gaussian with loop transfer recovery (LQG/LTR) design method is based on the optimal control theory, the most important theory used is the LQG problem. This method allows the designer to shape the fundamental gains of the rate of return at the input or output of the system to achieve the required performance or robustness characteristics. The stability of this method is guaranteed automatically. LQG/LTR is a kind of linear robust optimal control based on state observer, which can deal with a series of linear control problems such as disturbance noise and state variables that can't be measured directly [14]. The LQG/LTR control is utilized to design controllers of linear SISO and MIMO models of the core. The major advantages of the LQG/LTR controller are that it possesses strong robustness and can be designed for single-variable or multi-variable plants. The strategy has been developed from the Linear Quadratic Gaussian (LQG) control, which is an integrated design way based on the linear quadratic regulator (LQR) and a state observer. However, the Introduction of a state observer in designing an LQG controller weakens the robustness of stability and performances of LQR that usually has an infinite gain margin and a phase margin from [60°, ∞). To improve the robustness of an LQG control system, Athans, 1986, Stein and Athans, 1987, Doyle and Stein, 1981 have proposed and developed the LTR technology based on LQG. The method can recover the robustness of an LQG/LTR control system of a model in light of the robustness of the Target Feedback Loop (TFL) of the model. Therefore, this robust control is suitable for designing control systems of nonlinear plants such as the core by using the controller based on the linearized core model to control the nonlinear core model [15].

Table 1. Parameter definitions and nominal data [1]

P	Reactor power (MWth)	2250
ρ_0	Initial balancing reactivity ($\delta k/k$)	130×10^{-5}
Λ	Prompt neutron lifetime (s)	$3\,6 \times 10^{-4}$
β	Effective delayed neutron fraction	240×10^{-5}
λ	Effective delayed neutron decay constant (s^{-1})	5×10^{-2}
τ_C	Core transit time (s)	4
τ_L	Loop transit time (s)	6
α_f	Fuel temperature coefficient of reactivity ($°C^{-1}$)	$-3\,22 \times 10^{-5}$
α_g	Graphite temperature coefficient of reactivity ($°C^{-1}$)	$2\,35 \times 10^{-5}$
γ_f	Fraction of heat generated within the fuel	0 97
γ_g	Fraction of heat generated within the graphite	0 03
$\dot{m}_f$	Core inlet rate of the fuel salt (kg, s^{-1})	$1\,2 \times 10^4$

m_f	Mass of the fuel salt in the core (kg)	$5\,42 \times 10^4$
m_g	Mass of the graphite in the core (kg)	$1\,22 \times 10^6$
m_h	Mass of the fuel salt in the heat exchanger (kg)	$5\,38 \times 10^3$
$c_{p,\,f}$	Specific heat capacity of the fuel ($Jkg^{-1}℃^{-1}$)	1357
$c_{p,\,g}$	Specific heat capacity of the graphite ($Jkg^{-1}℃^{-1}$)	1760
$k_{f,\,g}$	Fuel to graphite heat transfer coefficient ($W℃^{-1}$)	$2\,48 \times 10^7$
$k_{h,\,s}$	Heat exchanger heat transfer coefficient ($W℃^{-1}$)	$2\,32 \times 10^7$
T_s	Heat sink temperature (℃)	450
T_{f1}	Average fuel temperature (˚C)	616
T_{f2}	Average fuel temperature (˚C)	686
T_g	Average graphite temperature (˚C)	619
T_h	Average temperature of the heat exchanger fuel salt (˚C)	547

Molten salt reactor model

The underlying point kinetics equations for the circulating fuel reactor developed based on the conservation of neutron density are given in Eqs. (1) and (2) respectively. The model accounts for both abrupt neutrons generated within the fission process and those retarded neutrons generated by the precursors some seconds later inside the core (Eq. (2)). The ex-core delayed fissions as an outcome of the circulating fuel are moreover incorporated by the term $C(t-\tau_L)$. The plant is thus an instance of a nonlinear time-delay system. The nonlinear model is presented as follows [1]:

$$\frac{dP}{dt} = \frac{\rho_{net} + \rho_0 - \beta}{\Lambda} P + \lambda C \tag{1}$$

$$\frac{dC}{dt} = \frac{\beta}{\Lambda} P - \lambda C - \frac{1}{\tau_c} C + \frac{1}{\tau_c} e^{-\lambda \tau_L} C(t-\tau_L) \tag{2}$$

$$\rho_{net} = \rho_{ext} + \rho_{th} \tag{3}$$

$$\frac{m_f c_{p,\,f}}{2} \frac{dT_{f1}}{dt} = \frac{\gamma_f}{2} P + \dot{m}_f c_{p,\,f} (T_h - T_{f1}) - \frac{k_{f,\,g}}{2} (T_{f1} - T_g) \tag{4}$$

$$\frac{m_f c_{p,\,f}}{2} \frac{dT_{f2}}{dt} = \frac{\gamma_f}{2} P + \dot{m}_f c_{p,\,f} (T_{f1} - T_{f2}) - \frac{k_{f,\,g}}{2} (T_{f1} - T_g) \tag{5}$$

$$m_g c_{p,\,g} \frac{dT_g}{dt} = \gamma_g P - k_{f,\,g}(T_g - T_{f1}) \tag{6}$$

$$m_h c_{p,\,f} \frac{dT_h}{dt} = \dot{m}_f c_{p,\,f}(T_{f2} - T_h) - k_{h,s}(T_h - T_s) \tag{7}$$

ρ_{net} is the resultant reactivity exerted on the core with the inherent thermal feedback effects ρ_{th} incorporated (Eq. (3)).

The above equations are nonlinear. A locally linearized version of the described model is developed employing the following first-order Taylor approximation routine.

$$\dot{x} = f(x) + g(x)u \rightarrow \delta\dot{x} = \left(\frac{\partial f}{\partial x} + \frac{\partial g}{\partial x}u\right)\Big|_{x_0}\delta x + g(x_0)\delta u = A\delta x + B\delta u \tag{8}$$

The state space equations of the reactor are given in Eq. (9):

$$\begin{aligned} \dot{X} &= AX + BU \\ Y &= CX \end{aligned} \tag{9}$$

In the following, how to design the controller according to the above state space equations is presented.

LQG/LTR method

LQG is based on optimal control. In this method, we use linear plants with known dynamics. Kalman filter is an optimal estimator that can estimate the system output and its state if the estimation error becomes a minimum value to maintain its optimal effect. Then, feedback for the optimal mode was designed to reach the optimal output feedback by applying the output estimation. Consider the following plant in state-space form:

$$\begin{aligned} \dot{x} &= Ax + Bu + \Gamma w \\ y &= Cx + v \end{aligned} \tag{10}$$

where w and v are 'white noises' namely zero-mean Gaussian stochastic processes which uncorrelated in time, having covariances:

$$E\{ww^T\} = W \geq 0$$
$$E\{vv^T\} = V \geq 0 \quad (11)$$
$$E\{wv^T\} = 0$$

The LQG control problem is to find the optimal control $u(t)$ which minimizes:

$$J = \lim_{T\to\infty} E\left\{\int_0^T (x^T Q x + u^T R u)\, dt\right\} \quad (12)$$

where Q and R are appropriately chosen constant weighting matrices (design parameters) such that:

$$Q = Q^T \geq 0$$
$$R = R^T \geq 0 \quad (13)$$

The solution is prescribed by the separation principle, which states that the optimal result is achieved by:

1. Obtain an optimal estimate $\hat{x}$ of the state x, optimal in the sense that $E\{(x-\hat{x})^T(x-\hat{x})\}$ is minimized.
2. Use $\hat{x}$ as if it were an exact measurement of the state to solve the deterministic linear quadratic control problem (LQR).

The solution of the first problem is presented by Kalman-filter as shown in Fig. 1.

The second problem is to find the control signal u as a linear function of the states that minimize the following cost $\int_0^\infty (x^T Q x + u^T R u)dt$ on the assumption that: $\dot{x} = Ax + Bu,\ u = -K_c x$.

So the final structure of the series connection is a Kalman filter with a state feedback matrix, shown by a block diagram in Fig. 2.

According to Fig. 2, we would like to have the return ratio at point 2 because the error dynamics of the filter are not excited by the control input u - they are uncontrollable from u. In general, the return ratios at points 1 and 2 are quite different. The LTR procedure forces the return ratio at point 1 to approach that at point 2.

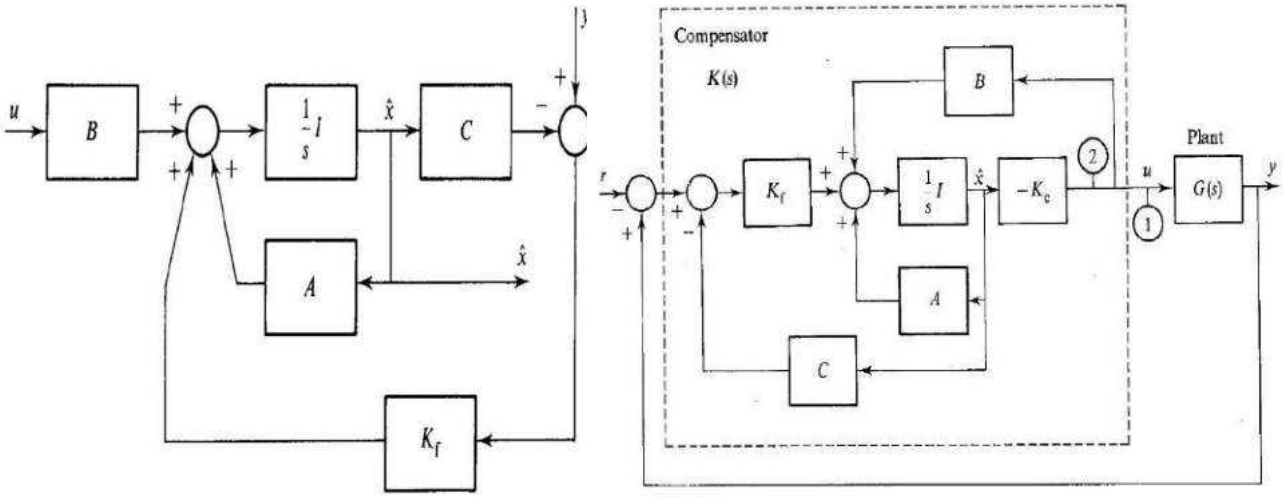

The purpose of this design is to estimate system state variables based on measurements of noise and disturbance. Then, the estimated states are used to control the optimal feedback of the system. Hence, we need to add a set of dynamics to the system and our first choice for such dynamics is $V = I$ and $W = I$ (it is necessary to note that here I refers to an identity matrix). In this step, we consider $G = B$, W, and V for the system. In this way, the Kalman filter is designed using Kf_1. The matrix B is considered equal to Kf_1 and the output is depicted with single values. Fig. 3 shows that there is no slope at low frequencies and gains are different because of variety in singular values. They need to be closed, and also the bandwidth needs to be improved. Now, to bring these two diagrams together, we need to multiply the real part of v by 10. Therefore, to achieve proper gain at lower frequencies and

reduce the steady-state error, we need to add an integrator to the system, the results of which are shown in Fig. 4.

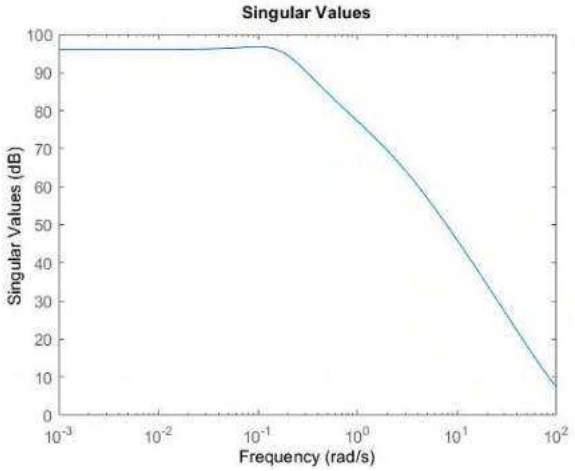

Fig. 3. Singular values

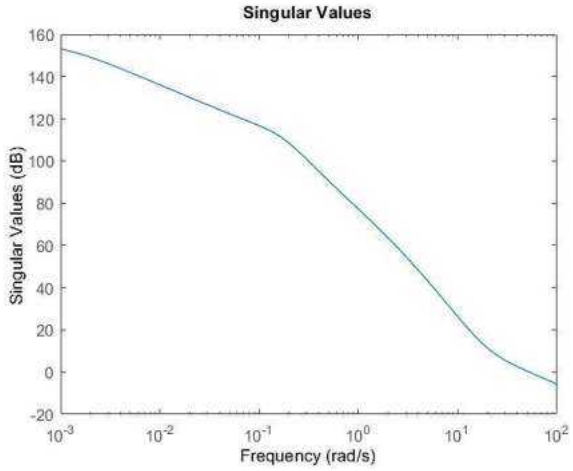

Fig. 4. Singular values after applying the integrator

Also, to speed up the removal of the steady state error, we try to increase the smaller gain value at low frequencies to about the larger gain value. For this purpose, we take help from singular value decomposition (SVD) and Eqs. (14) and (15).

$$G_f(j\omega_1)W^{\frac{1}{2}} = U\Sigma V^H = \sum_{i=1}^{m} u_i \sigma_i v_i^H \tag{14}$$

$$G_f(j\omega_1)W^{\frac{1}{2}}(1 + \alpha v_j v_j^H) = \sum_{i \neq j} u_i \sigma_i v_i^H + (1 + \alpha) u_j v_j^H \tag{15}$$

where σ_i is the basic gain and u_j and v_i are the basic input and output paths. Therefore, due to the large gains, we use open-loop gain instead of closed-loop gain.

Finally, after reaching the appropriate return rate in the Kalman filter, we design an optimal regulator using the lqr function. Now the output of the system has reached a stable state and has a good response time.

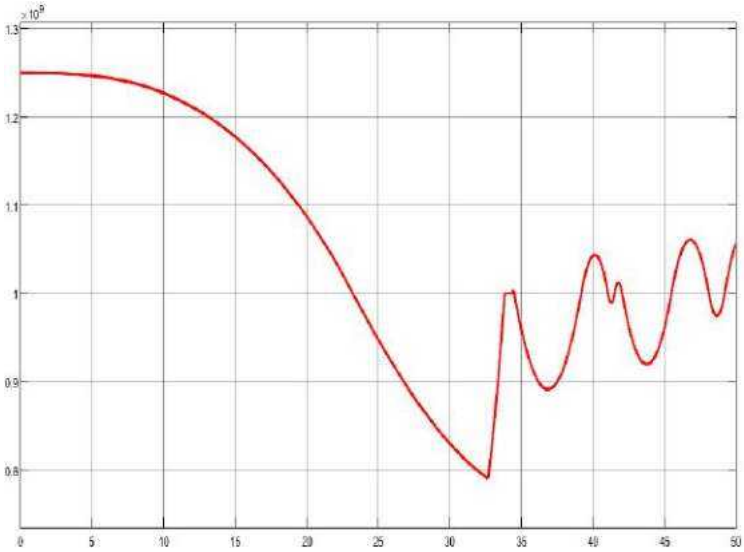

Fig. 5. MSR power change without controller

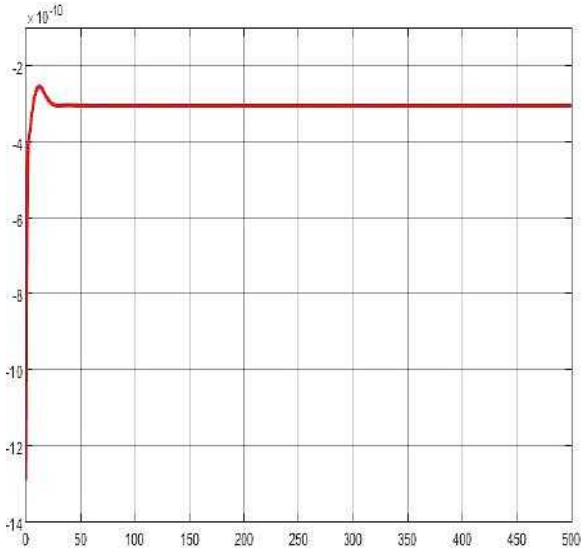

Fig. 6. control signal curve

Results and Discussion

As shown in Fig. 5, the MSR power change without a controller has an unstable behavior. But, after applying the controller, the system has become stable. The control signal curve is shown in Fig. 6.

A PID controller is applied as shown in Fig. 7. The gain of the optimized PID is as K_p=2, 9184 × 10^{-18}, K_i=1, 2568 × 10^{-6}, K_d=5, 2629 × 10^{-9}. Overshoot in PID controller is 24% but in LQG/LTR controller is 9%. The sitting time and overshoot in the LQG/LTR controller are less than that of the PID controller. The proposed method has a faster step response than other controllers.

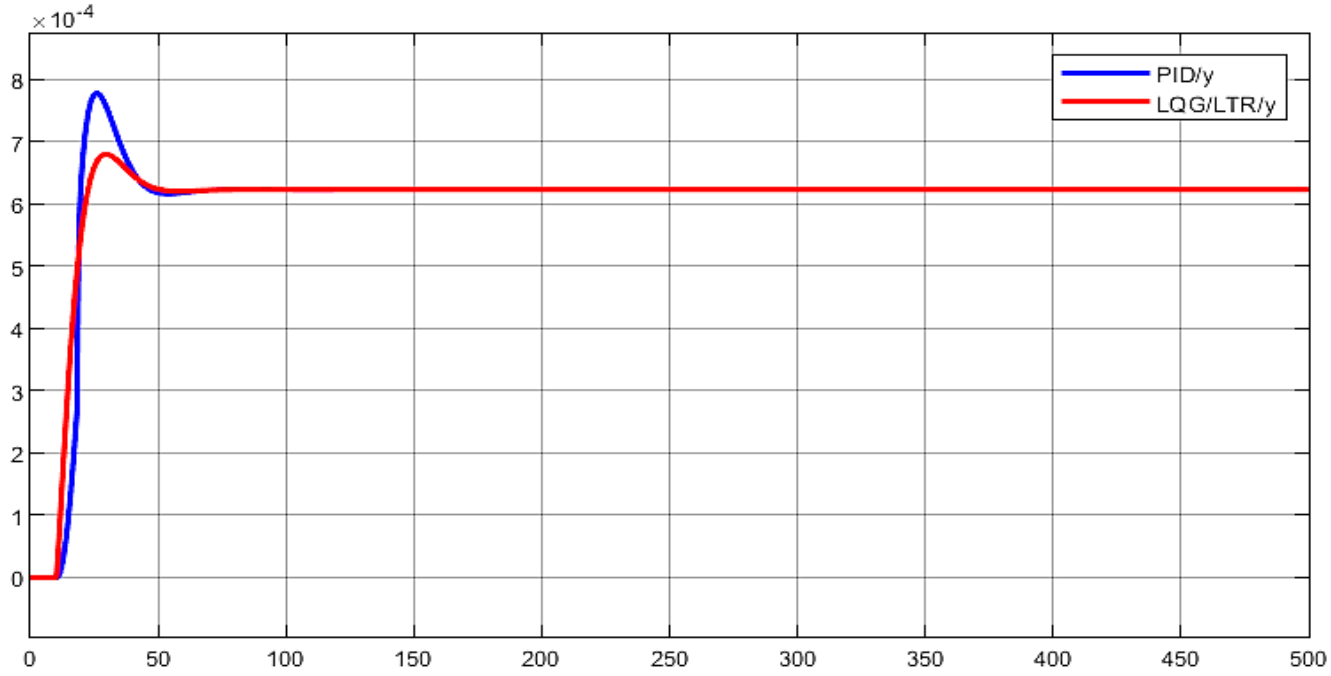

Fig. 7. MSR power tracking by controller (comparison of LQG/LTR and PID)

Conclusions

Molten salt nuclear reactors benefit quite promising features in terms of inherent safety and long-term sustainability which comply with the paradigms for future energy resources. The LQG/LTR controller has a simple and systematic design procedure so it can be applied to many Multi-Input Multi-Output plants. The power system model can considered for thermal power plants, and also the LQG/LTR procedure can often be applied to a non-minimum phase plant or it can be applied to a hydropower plant without difficulty. LQG/LTR has robustness properties. The analysis of the step response of the controlled system using the LQG/LTR controller shows that after applying the controller, the system becomes stable and the performance of the system becomes optimal. The damping of the system is adjusted and the persistent error of the system is reduced. Also, the overshoot in the LQG/LTR controller is 0 0098% less than that of the PID controller. In this way, the designed controller makes the system have an acceptable and suitable performance. Also, this controller can be used to control the desired outputs at the same time. In this paper, it was shown that the design of the controller in the LQG/LTR method gave us an acceptable answer. Reducing the overshoot or increasing the settling time will help improve the performance of the controller. Therefore, it is expected that the use of an H-infinity controller will give better results. [16].

References

[1] M. Zarei, "Nonlinear dynamics and control in molten salt reactors," *Nuclear Engineering and Design,* vol. 332, pp. 289-296, 2018.

[2] P. M. Reddy, S. Shimjith, A. Tiwari, and S. Kar, "Output feedback Model Reference Adaptive Control of nuclear reactor," *Nuclear Engineering and Design,* vol. 407, p. 112276, 2023.

[3] R. M. Edwards, K. Y. Lee, and M. Schultz, "State feedback assisted classical control: an incremental approach to control modernization of existing and future nuclear reactors and power plants," *Nuclear technology,* vol. 92, no. 2, pp. 167-185, 1990.

[4] R. M. Edwards, K. Y. Lee, and A. Ray, "Robust optimal control of nuclear reactors and power plants," *Nuclear Technology,* vol. 98, no. 2, pp. 137-148, 1992.

[5] R. M. Edwards, C. K. Weng, and R. W. Lindsay, "**EXPERIMENTAL** development of power reactor advanced controllers," Argonne National Lab., 1992.

[6] C.-C. Ku and K. Y. Lee, "Diagonal recurrent neural networks for dynamic systems control," *IEEE transactions on neural networks,* vol. 6, no. 1, pp. 144-156, 1995.

[7] P. Ramaswamy, R. M. Edwards, and K. Y. Lee, "An automatic tuning method of a fuzzy logic controller for nuclear reactors," *IEEE Transactions on Nuclear Science,* vol. 40, no. 4, pp. 1253-1262,

[8] P. V. Surjagade, S. Shimjith, and A. Tiwari, "Second order integral sliding mode observer and controller for a nuclear reactor," *Nuclear Engineering and Technology,* vol. 52, no. 3, pp. 552-559.

[9] S. Qaiser, A. Bhatti, M. Iqbal, and J. Qadir, "LMI-based robust control system design for a Research Reactor," in *6th International Bhurban Conference on Applied Sciences & Technology*, 2009: IEEE, pp. 207-211.

[10] G. Wang, J. Wu, B. Zeng, Z. Xu, W. Wu, and X. Ma, "Design of a model predictive control method for load tracking in nuclear power plants," *Progress in Nuclear Energy,* vol. 101, pp. 260.

[11] L. Chrif and Z. M. Kadda, "Aircraft control system using LQG and LQR controller with optimal estimation-Kalman filter design," *Procedia Engineering,* vol. 80, pp. 245-257, 2014.

[12] A. Kozáková and M. Hypiusová, "LQG/LTR based reference tracking for a modular servo," *Journal of Electrical Systems and Information Technology,* vol. 2, no. 3, pp. 347-357, 2015.

[13] S. Tang, D. Tian, M. Huang, B. Li, and L. Tao, "Load control optimization method for offshore wind turbine based on LTR," *Energy Reports,* vol. 7, pp. 4288-4297, 2021.

[14] W. Zeng, J. Li, T. Hui, J. Xie, and T. Yu, "LQG/LTR controller with simulated annealing algorithm for CIADS core power control," *Annals of Nuclear Energy,* vol. 142, p. 107422, 2020.

[15] G. Li, "Modeling and LQG/LTR control for power and axial power difference of load-follow PWR core," *Annals of Nuclear Energy,* vol. 68, pp. 193-203, 2014.

[16] G. Lee, K. You, T. Kang, K. J. Yoon, J. O. Lee, and J. K. Park, "Modeling and design of H-Infinity controller for piezoelectric actuator LIPCA," *Journal of Bionic Engineering,* vol. 7, no. 2, pp. 168-174, 2010.

ICNST 2024
International Conference on Nuclear Science and Technology
6- 8 MAY 2024 | Isfahan, Iran

The Effects of Nickel Nano-Composites on Corrosion of Pressurized Water Loop (PWL) in Nuclear Reactors (Paper ID : 1203)

S. H. Tohidi [1.a] M. Tallebi[2], S. Gholamzadeh[3]

[1)] *Physics & Accelerators Research School, NSTI, Karaj, Iran.*

[2)] *Nuclear Reactors Research School, NSTI, Isfahan, Iran.*

[3)] *Information Technology Division, Amir Kabir University, Tehran, Iran.*

Abstract

In this investigation, mechanical corrosion of metal parts was studied for corrosion in metal pipelines in water supply system in pressurized water loop (PWL) system of nuclear reactors. For controlling or reducing corrosion of metal parts in corrosion area were noticed using nickel nano-composites and carbon-nickel nanotubes. Resistance behaviors to corrosion of nano-particles layers and nanotubes in this part were analyzed. Appearance review of PWL system presents that system have mechanical corrosion such as; uniform, groove, pitted, inter granular, selective separation, abrasion, corrosion with stress that have similar aspects. Also, this investigation was studied for controlling or reducing of mechanical corrosion with using nanotubes in PWL system. These results have presented that the nano-composites have an important role in increasing resistance to mechanical corrosion. In this investigation, corrosion velocity can be compared between uncoated surface, pure nickel alloy coated and carbon-nickel nanotubes coated on the surface in PWL system of nuclear reactors.

Keywords: Corrosion, Nickel Nano-Composites, PWL System, Nuclear Reactors.

[1a] htouhidi@yahoo.com

Introduction

Today, one of the most important problems in pressurized water loop (PWL) system is the corrosion of metallic parts that were refereed to mechanical corrosion of steel pipelines in water supply system. The new method is important for reducing of corrosion, using of nano-composites in nuclear industries [1]. Substitution and examination of these parts are expensive and be long time. The method of reinforced these parts with nano-composite materials were presented the best method for prevention of growing and breaking [2]. The individual properties of nano-composites are from nano-scale structures. Mechanical properties, structure, thermo-mechanic and measurements of anti-corrosion effect of nano-composites are important for covering and understanding mechanism of anti-corrosion of these materials [3]. The main goal of fabrication of pressurized loops is studying for thermal and hydro-dynamic behavior of flow in nuclear fuel of reactors, also studying of dangerous related to nuclear reactors. The study of thermal and hydro-dynamic behavior of flow in nuclear fuel of reactors is very important. The importance of the pressurized loops is that researchers can be perform without of nuclear emission, the first reactors circulation confirm and examine.

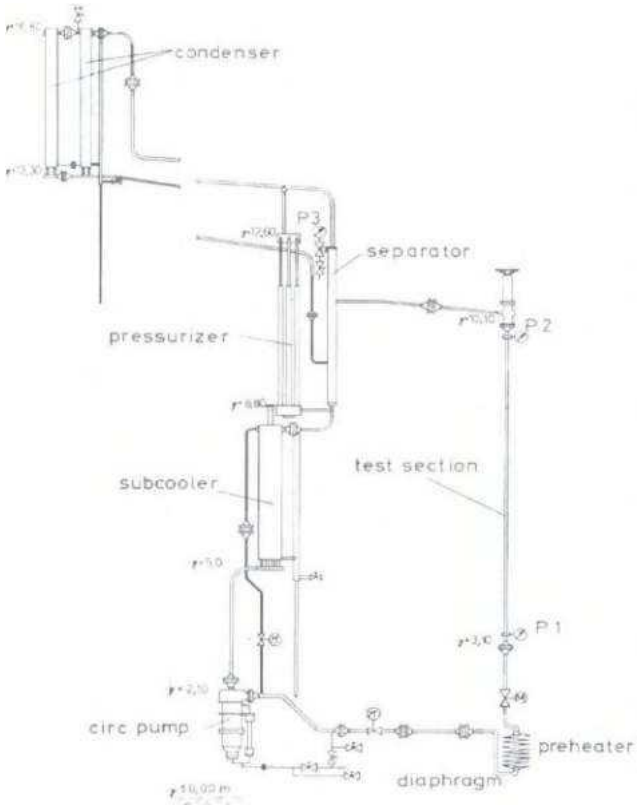

Fig. 1. Isomeric schematic of PWL system

Therefore, investigations on the pressurized loop on the surface technology of countries is related to mechanic, electronic, control and IT subject at different pressure and various designing of fuel conditions can be planned [4]. For example; from pressurized loops can be refereed to pressurized water loop (PWL) in nuclear center in IRAN country.

This loop is with max pressure 20 bar and 170°C temperature. The Fig. 1 is related to isometric schematic of pressurized loop in a nuclear center. In the Fig. 1, has been presented PWL of nuclear center in IRAN country. The main parts of PWL system are; experimental container, the pumps, invertor, pressurizer and cooler tower. The PWL system consist two separate circulators, the first related to main flow due to transmission fluid from experimental container, and second circulation related to invertor and cooling tower and in first part, we have a close circulation. The outer cool flows arrive to pump and pass-through valve, arrive to experimental zone and warmed. The flow out of experimental container arrive to invertor and miss the thermal to second fluid in cooled invertor and repeat this circulation. For setup of pressure in this system, nitrogen gas has been used.

Experimental Section

Appearance review of PWL system presents that system have mechanical corrosion such as; uniform, groove, pitted, inter granular, selective separation, abrasion, corrosion with stress that have similar aspects. Sometimes interfere about appearance form, but hydrogen corrosion cannot be seen in PWL system. Also, after identification all of types corrosion, coping and reduction methods were investigated and studied. Macroscopic studies of faucets, flinches, flakes, connections, pumps and so on in PWL system confirm the above corrosion. For prevention of further corrosion, a method of prevention corrosion is using nickel nano-composites such as; nano-tubes must be applied. With using of nickel nanotubes, carbon-nickel nano-tubes for covering surface of the above equipment were applied and compared with pure carbon nano-tubes, in this matter corrosion velocity compare with time pass.

Results and Discussion

Mechanical Corrosion in Pressurized water Loop (PWL)

Mechanical corrosion is a type of demolished metal in contact to the surroundings that causes the high cost and log in metal to the pressurized water loop (PWL) system. Resistance to corrosion of pipes under pressurized systems depends to properties of pipes and so chemical quality of water. Sedimentation of water can be caused the corrosion, and finally, lead to reduction of the pipes surface and reduction of pressure of system, and reduction of flow in direction of system. One of the best methods for controlling

of mechanical corrosion in PWL of nuclear reactors is using of nickel nano-composites material led to economic efficiency and controlling, reduction of corrosion in water supply system of PWL in nuclear reactors [5].

Using of Nickel Nano-Composites Material in PWL

Using of nano-materials for prevent of corrosion in PWL system can be form to polymeric nano-composites covers and addition nano-composites into epoxy, silicon polymers and organic (inorganic) hybrid polymers. Nano-composite materials with polymeric matrix can be cured the intrinsic properties of composite materials to polymeric matrix material such as; waterproof and elasticity properties, also produce more mechanical properties; hardness, resistance to scratch, impermeability. For example, in used composites, optimal values of carbon-nickel nano-tubes can be added [6].

Effects of using Nickel Nano-composites on the Corrosion of PWL

For protection of systems from corrosion conditions, cathode protection and surface isolation can be applied. But, sometimes have been occurred that structure corrosion is very high and surface thickness is very low and these protections are not useful. In this time, corrosion section separates, and replace with healthy parts. In attention to problems, using of better method is necessary. The method of strengthen the structure with nickel nano-composite materials is the best and cheapest method. In this method, the costs of separation and removal of activity were removed and using this method can be increased of resistance to corrosion. Increasing this nano-material can be lead that the path of penetration of water molecules and oxygen is longer and resulted to increasing of barrier nano-composite properties. Their properties are such as rigidity, high thermal stability, low permeability against the gases, low flammability is mechanical corrosion effects. Ability to network and high adhesion effect of epoxy are the reason of high resistance in contact corrosion. These materials act very powerful against oxidation, which creates an anti-oxide layer with high adhesion property on the surface. One of these nano-materials is carbon-nickel nano-tubes that are the most usable and the most effective in corrosion studies [7]. Carbon-nickel nano-tubes are one of the most important nano-fillers that have optimal thermal-mechanical properties. These materials are used as amplifier in polymeric matrices [7]. Carbon-nickel nano-tubes are direct tubes with diameter about nanometer that have properties near to carbon fibers; nano-tubes can be formed one or semi layers. The presences of nano-composites in coating of PWL system led to increasing nuclearization and reducing of seed growths. Thus, rigidity of nano-composite coating is very high. The presence nano-composites are

obstacle against deformation of matrix change. Table. 1 presents mechanical properties of nickel nano-composites on the steel surface of PWL system.

Table 1. The properties of components of nano-composites on metallic surface of PWL system

Carbon-Ni Nano- tube	**Carbon Fiber**	**Matrix**	**properties**
MWCNT	T-300	ML-506	
1000	230	3.13	Yang Modulus(GPa)
-1	-0.41	62.45	Thermal expansion coefficient
1.65	1.76	1.11	Density(g/cm^3)

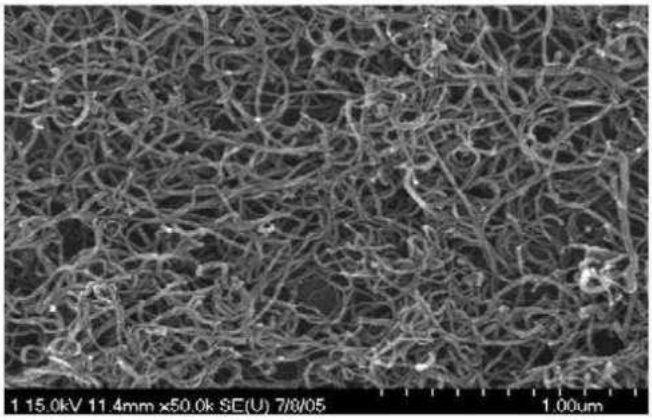

Fig. 2. The TEM of carbon-nickel nano-tubes in polymeric matrix in PWL system

But this is necessary that addition the amounts of nano-materials are not allowed and has accurate calculations. In nickel nano-composites, increasing of nano-materials concentrations can be led to particles agglomerations. Decreasing of particles lead to increasing of rigidity, and agglomeration can be caused to decreasing of rigidity; therefore, the size of particles in coating and uniformity distribution effect on the rigidity. In PWL system, nickel nano-composite coating has more uniform and condense surface. That means nano-particles were distributed in surface and nano-materials were affected in matrix, and show higher mechanical properties and higher resistance to corrosion. In nano-composite materials, it is important the ratio of length to width of filler is more, although with increasing this ratio, matrix is more stable. If concentrations of filler are low, this led to cheaper and lighter products, which is optimal for other researches.

Figure. 2 presents transmission electron microscopy (TEM) of carbon-nickel nano-tubes in polymeric matrix. In PWL system, using of polymeric nano-composites contain carbon-nickel nano-tubes on corrosion surface can be cured thermal-mechanical properties. At first, a suitable condition can be formed between nano-tubes and matrix, second step is distribution of nano-tubes in polymeric matrix can be formed, optimally. The method of nano-tubes distribution in polymeric matrix is the most important parameters for stability of composites, because an intense wonder-vale attraction can be occurred between nano-tubes and, this led to nano-tubes aggregation in matrices.

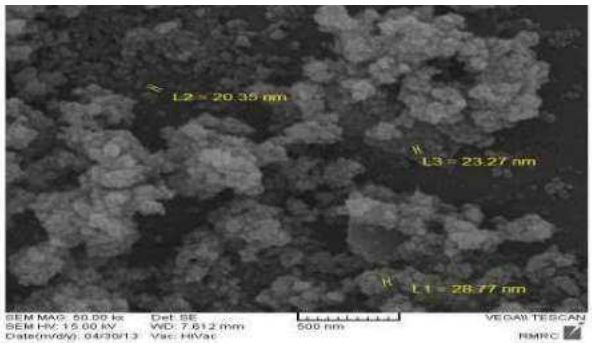

Fig 3. SEM image of Ni nano-particles after calcination

The results indicate that particles are in spherical shape and nano-clusters due to agglomeration process. The average size of the Ni nanoparticles observed from SEM images is 24 nm. The one of others parameters on mechanical properties of nickel nano-composites is the ratio of length to diameter that effected on modulus of elasticity. In metallic surface of PWL, nano-materials in polymeric matrices can be increased modulus in reason of increasing of surface even in low concentration. The longitudinal of modulus depend on nano-tubes rigidity and transverse modulus depends on matrix rigidity, too. Increasing of carbon-nickel nano-tubes can be reinforced the matrix and increased transverse modulus, considerably. The resulted of table 1 presents the using of nano-particles to polymeric matrix for metallic coating used in PWL system. Also, this table presents, in PWL system using of this nano-material till 1% weight led to decreasing of residual stresses.

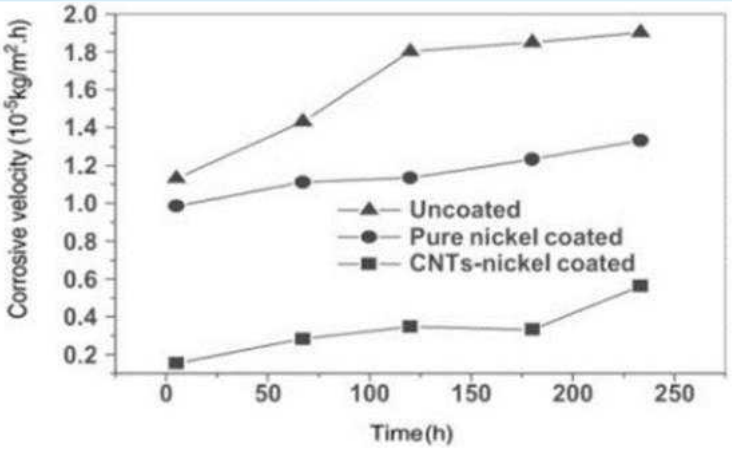

Fig. 4. Variation of corrosion velocity to corrosion time (nickel coating)

A metallic structure in PWL, need to paint, corrosion protection, welding and high cost of repair and maintenance. This mechanical corrosion metallic structure can be reinforced with nano-composite coating that it cannot need to painting, in return, it has lower weight with higher stability. Using of nickel nano-composite coating for deal with effects of impact, moisture absorption, corrosion and decay of water supply system in PWL system [8]. Vang, et.al have presented polymeric matrices nano-composite coating, can be reinforced surface rigidity and resistance to humidity [9,10]. Also, these materials can increase the other properties such as water proofing, hardness and resistance to high scratch. Other nano- materials such as Poly-Thiophen and Poly-Pyrrole have been used as surface coating, increase the resistance of corrosion. These nano-materials perform anti-corrosion role in reason of prevent infiltrate electrolyte to common level metal and coating [11]. In PWL system, at first studying on the metallic surface coated were done with using carbon-nickel nano-tubes and were studied corrosion effect to time pass. Figure. 4 presents comparison two states, without coating and coating with pure nickel were performed. This figure presents that corrosion velocity in starting 100 hours increase, and then will be constant till about 200 hours. Then, corrosion velocity can be compared pure nickel alloy without addition of nano-materials, resulted that corrosion rates revealing in very large amounts.

The Effective of Nickel Nano-Composite Materials in Surrounding Environment of PWL

In PWL system, some new materials were presented to case less destruction in the environment in the zone of PWL system and ability to recycle parts effect on the commercialization of material. Nanotechnology has high ability for reducing of carbon emission, toxic gases and destruction of environment. In production of nano-composites on metallic surface, there are two thermoset and thermo- plat resins. Thermo-plat resins have ability of recycling after cooking and there is reproducibility property in these materials. Also, this is

possible that nano-coats with phosphate or chromate have dangerous properties for their hexagonal structure that this problem removes with using phosphor-cobalt nan- materials. Of-course, most of nano-materials such as carbon-nickel nano-tubes are valid and no dangerous for environment and toxic gases emission. In PWL system, nano-materials are good for repairing of water pipes and act very effective with reducing the costs. It is proposed, instead of replacing water pipes, nano- composite materials were used as repair agent. Figure. 5 presents using of nickel nano-composite coating in water transmission pipes in PWL system.

Fig 5. Using of nickel nano-composite coating in water supply system in PWL system

Conclusions

The mechanical corrosion of water supply system in PWL of nuclear reactors is one of the most problems in this industry. One of the methods for controlling of corrosion is using of nano-composites such as nickel nano-particles in this system. These materials were selected for controlling corrosion of metallic surface as selection materials. These materials have very optimal properties as anti-oxidant property and high impermeability. Addition nickel nano-composites such as nickel nanoparticles and carbon-nickel nanotubes to matrices and coating in corrosion places can be caused decreasing of corrosion, corrosion costs and prolongation corrosion time. The addition of carbon-nickel nano-tubes till 1 volume percent can be cured polymeric properties in the best conditions. There are not any bad aspects on environment and reducing of carbon gas emission. Using and application of nano-composite materials are very easy, and there are not any problems related the replacement of parts and economic losses.

References

Ilna, News Reporter Website, Economic Section., (2012).

Ghasemi, A. R., Mohammadi, M. M.,Journal of Polymer Science and Technology., (2014), 27(3), 213-230.

Affdl, J. C., & Kardos, J. L., Polymer Engineering & Science,(1997), 16(5), 344-352.

Komarneni., S., Journal of Materials Chemistry, (1992), 2(12), 1219-1230.

Koutsky., J. Kocik, J., "Radiation Damage of Structural Materials". Elsevier (London)., (1994).

Harrison, N. F., AECl's., **EXPERIMENTAL** Fuel and Material Test Loops in NRU, International Atomic Energy Agency, Vienna, (2013).

Rezvani-Nouri, M., "Effect of Singel-Walled Carbon Nanotubes on Non-Isothermal Crystallization Kinetics of Poly-propylene"(2011).

Praveen, B. M., Naik, Y. A., Surface and Coating Technology, (2007), 201(12), 5836- 5842.

Kim, B. G., Sohn, J. M., Choo., K. N., Nuclear Engineering and Technology, (2009),42(2), 420.

Saji, V. S., & Thomas J., Current Science., (2007), 92(1), 51-55.

Wang, Y., Lim, S., Lou, J., Wear., (2006), 260(9), 976-983.

ICNST 2024 International Conference on Nuclear Science and Technology
6- 8 MAY 2024 | Isfahan, Iran

Experimental investigation of onset of flooding in a hot leg of VVER-1000 (Paper ID : 1209)

Rahimian A[1*], Amin Mozafari M.[1]

Nuclear Science and Technology Research Institute (NSTRI), Tehran, Iran

Abstract

In a scaled VVER-1000 hot-leg, flooding or countercurrent flow limitation (CCFL) has been experimentally investigated. The reactor vessel (RV), steam generator (SG), and hot-leg pipe are the components of the planned test facility. Its construction and design were based on the power to volume scaling technique, keeping the hot leg's Froud number constant. The scaling ratio was considered 1/19 of the Bushehr NPP (VVER-1000) geometry. The designed facility's hot leg offers clear optical observation of the gas/liquid interface. A side view is also proposed for optical observation on the SG simulator. experimental results were captured at atmospheric pressure with air/water as fluid. CCFL was obtained by analyzing the pressure differences between RV and SG simulators.

This CCFL data were compared with empirical data and correlations available in the literature. With increasing liquid superficial velocity, the gas superficial velocity curve is continuously decreased, which is consistent with Navarro's results. In this study, an experimental correlation is proposed and compared to other correlations. It was very close to the Navarro and Richter correlations.

Keywords: Countercurrent flow limitation, Onset of flooding, Flooding, Hot-leg, air/water, VVER-1000

Introduction

Countercurrent flow limitation refers to a phenomenon that can occur in certain types of heat exchangers or fluid systems where the flow of two fluids is in opposite directions. In such systems, there is a limit to the effectiveness of heat transfer due to the countercurrent flow arrangement. CCFL, or flooding, is a class of gravity-based hydrodynamic processes that create a restriction on the performance of gas–liquid systems [1].

The safety aspects, including the LOCA (Loss of Coolant Accident), must be considered in designing a nuclear reactor. At the end of LOCA scenario when CCFL occur, the level of primary water decrease and the vapor attempts to rise from the overheated reactor core and the condensate coolant from SG attempts to return to the core by gravity [2, 3]. In PWRs, the CCFL can occur in the pressurizer surg line and hot-legs during LOCAs or SB-LOCA without operation of residual heat removal system [4]. As mentioned, for accident condition analyses of a PWR (or VVER), the CCFL must be considered appropriately, which

it is determined with the relationship between superficial velocity of gas and returning liquid. This falling liquid compensate the water mass in the reactor core and prevent the fuel rods melting. Al Issa and Macian [4] provided a complete review article of almost all of the studies in CCFL phenomenon. They reported that CCFL is caused by periodic plugging at the riser mechanisms, instable wave growth at a hydraulic jump, and active liquid entrainment.

Al Issa and Macian [4] indicated that a smooth stratified condition, in hot-leg geometry, created at low superficial velocities of air and liquid. With increasing air velocity, at interface, the instabilities start to appear and then initiating and growing of the small waves begin. Wave growing, Instabilities, hydraulic jump, chaotic interface movement, droplets entrainment, and appearance and development leads to occurrence of the CCFL [4]. Siddiqui, Banerjee [5] considered various horizontal-to-vertical angle of pipes experiments in and investigated the effect of bend curvature radius, pipe diameter, entrance geometry, length and inclination of horizontal part on the CCFL phenomenon. They determined that CCFL forms near bend with formation of unstable wave at the hydraulic jump. Ardron and Banerjee [6] developed an analytical model to predict the onset of CCFL in horizontal to vertical geometry. They showed that the flooding occurs near the bend where the thickness of liquid is highest. Ghiaasiaan, Turk [7] reports that, in the near-horizontal and horizontal channels, the mechanism of flooding is the result of slug formation on the thick interfacial of the wave. Wongwises [8] shown that the water superficial velocity is the mechanism of flooding. They suggested that the mechanism of CCFL for moderate to high liquid flow rates in vertically downward sloping pipes is the breaking of a turbulent jet-like liquid flow near the knee and the transfer of droplets by the countercurrent gas flow to the upper tank. They also noted that, at low superficial velocity of water ($J_L^{*0.5}$ < 0.7), gas flow rates have been decreased with increasing superficial velocity of water. Reflux condensation conditions for CCFL investigation are obtained by Kang, Chu [9]. Similar to Wongwises [8], they introduced a three-zone division based on superficial fluid velocity as a flood mechanism. They found that the water flow rate causes the onset of flooding, but the end point of the flooding, i.e., the zero penetration of the coolant, is independent of the coolant flow rate. Navarro [3] considered three zones for onset of flooding. In general, they proposed a similar mechanism for onset of flooding as Wongwises [8], Kang, Chu [9]. In his facility, two zone have been covered. First region is Low and coolant superficial velocity in the region $J_L^{*0.5}$ < 0.35 m/s of liquid superficial velocities studied by Wongwises [8]. Second zone is the 3rd zone proposed by Kang's ($J_L^{*0.5}$ > 0.4 m/s).

In the present study, the CCFL phenomenon in the hot leg of a typical VVER-1000 reactor is studied. In this type of reactor, there is a 90-degree elbow in the hot leg. The hot leg scaled 1/19 rather than hot leg

of VVER-1000 reactor. The CCFL phenomenon in VVERs has been less studied and investigated compared to western PWRs. The measured experimental results have been compared with the results of other researchers.

Test Facility and Procedure

An isometric view of the facility has been demonstrated in Figure 1. This facility consists of the visible hot leg, a compressor, a pump, a SG simulator a, RPV simulator, several instrument (including Pressure gage, DP, Level meter, gas and liquid flowmeters), and a data acquisition system. The scaling ratio was considered 1/19 of the Bushehr NPP (VVER-1000) geometry. Piping and structural part of this facility were made od stainless steel, but the test section was equipped with plexiglass to be visible. The horizontal length of the test section is 100 cm long. A 90° bend has been used as a connection of the horizontal and the vertical pipe. Reactor pressure vessel simulator was connected to the horizontal pipe while the SG simulator was connected to the upper end of the vertical pipe. In this test section, the fluids are water and air. Water was pumped from the reservoir while air was pumped from a compressor. A gas and water flowmeters were used for measuring the air and water flow rate, respectively. To measure the pressure difference between to tanks (the RPV simulator and SG simulator), a differential pressure transducer was installed. The excess water in steam generator simulator was disposed through the drain.

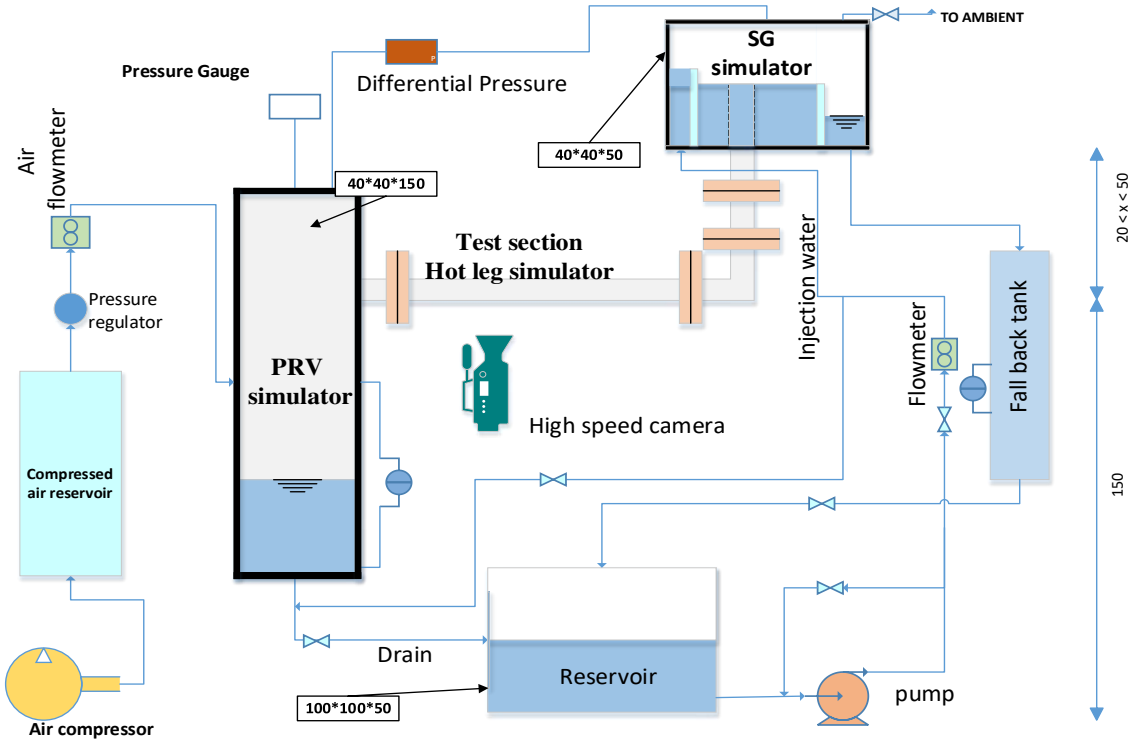

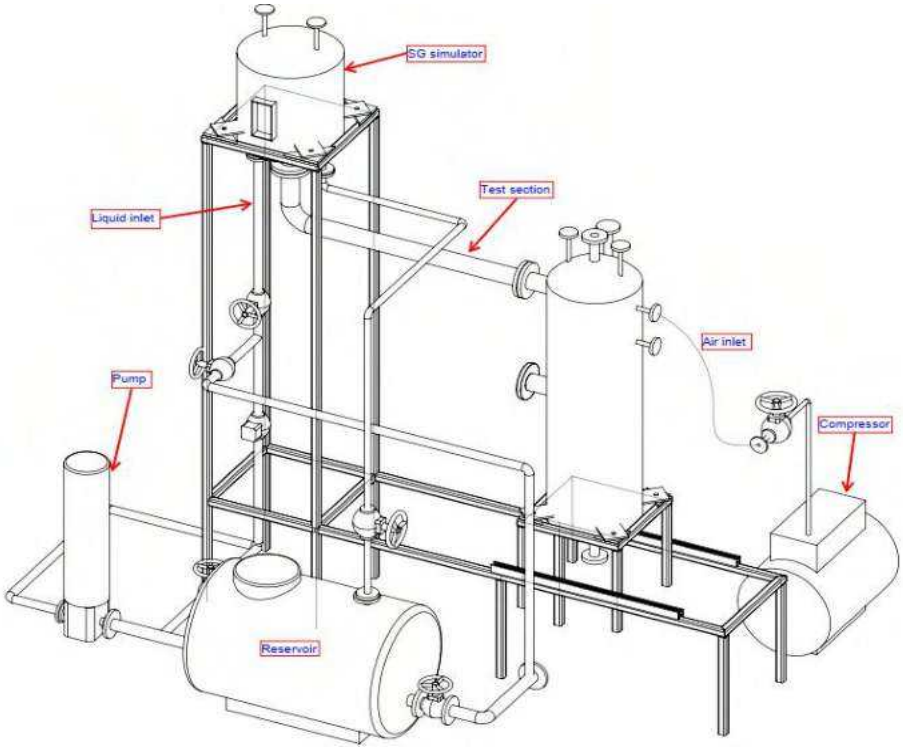

(a)

Figure 16: Isometric view of CCFL test facility

The experimental apparatus is shown in Figure 17. A compressor system makes it possible to increase the air pressure in the loop up to 5 bar.

The compressor injects the air into the RPV simulator and then air flowed through the test section (hot leg) to the SG simulator, from which it was released to atmosphere. The coolant is pumped into the SG simulator and after that it counter-currently to the air enters the test section and finally the reactor simulator tank by gravity. The onset of CCFL was measured by a stepwise increment of the air flow rate with a small increasing (2–30 m3/h), under a constant water flow rate.

Figure 17: CCFL test facility

The limiting point of stability of the counter-current flow was defined as the onset of flooding, indicated by the maximum air mass flow rate at which the decreasing water flow rate is equal to the inlet water flow rate. The working range of each equipment is as follows (

Table 3):

Table 3 Measuring devices

Water flow rate (m^3/h)	Gas flow rate (m^3/h)	Level meter (m)	Pressure gage (bar)	Pressure regulator (bar)	Pressure difference transmitter (mbar)
0.6-6.0	0-50	0-1.5	0-10	0-10	Accuracy 0.1

Results and discussion

Flow behavior at low water flow rate (Superficial velocity = 0.11 m/s)

Figure 18 shows the pressure difference between the RPV simulator and the steam generator simulator, as well as the superficial velocity of the injected air. During the test, water was injected with a superficial velocity of 0.11 m/s. The stepwise increasing of gas superficial velocity is continued until the starting point of the CCFL. At this point, a sudden drop in gas pressure will occur in the flow path. The starting point of CCFL occurs with a liquid superficial velocity of 0.11 m/s and a gas velocity of 1.44 m/s.

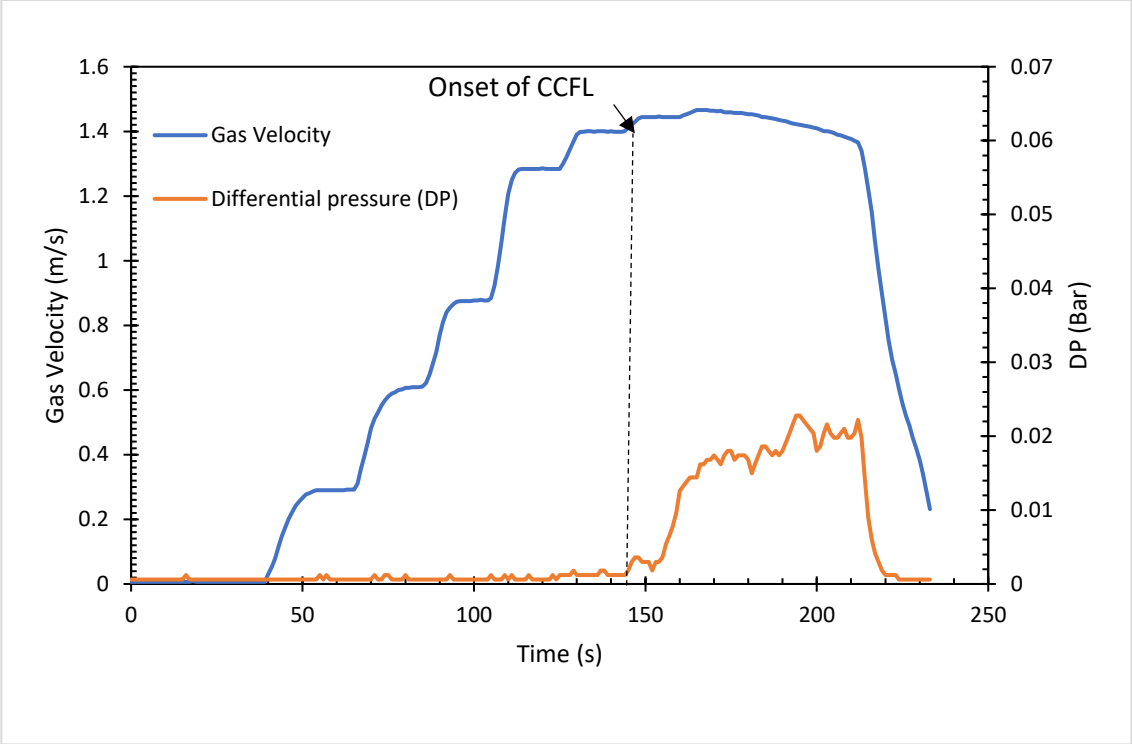

Figure 18: Pressure difference between RPV and SG (red curve) and gas superficial velocity (blue curve) with superficial water velocity of 0.11 m/s during flooding test

The different flow patterns observed in the experiment are shown in Figure 19. In the studies related to the vertical steam generator used in PWR reactors, because the horizontal part of the hot base is connected to the riser at an angle of about 50 degrees, the return flow from the steam generator descends with less disturbance. But in VVER reactors, this angle is 90 degrees, and in the horizontal part of the hot base, which is close to the steam generator, the return flow has more disturbances due to passing through the 90-degree bend.

Without air injection

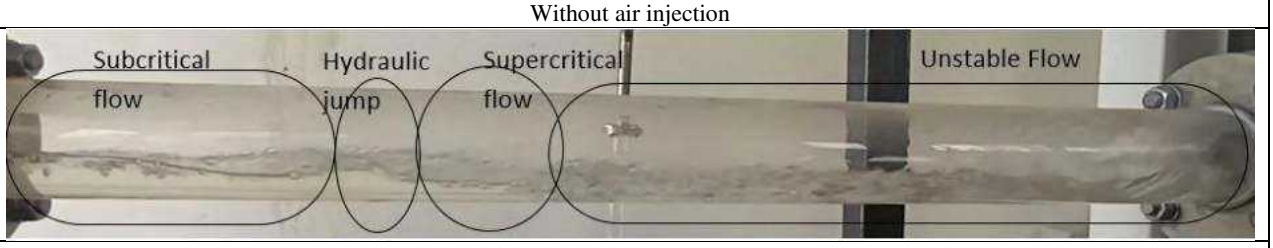

Gas superficial velocity = 0.29

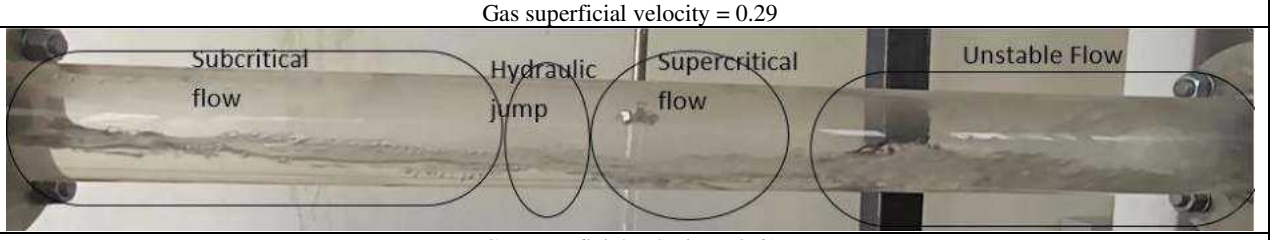

Gas superficial velocity = 0.61

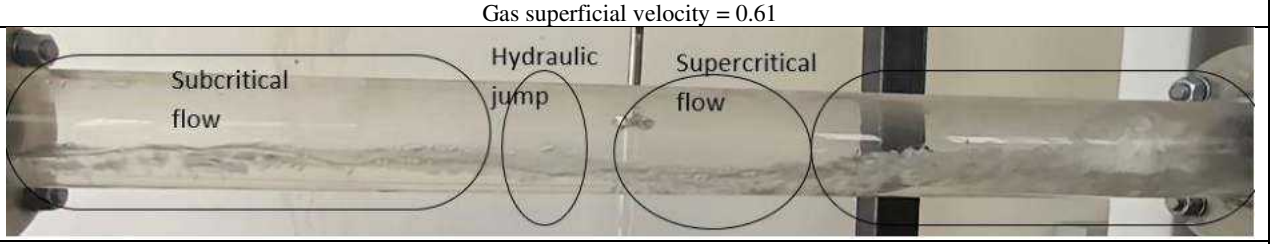

Gas superficial velocity = 0.88

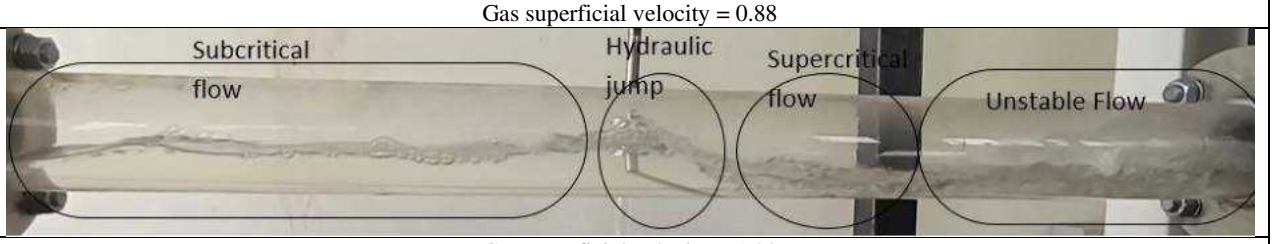

Gas superficial velocity = 1.28

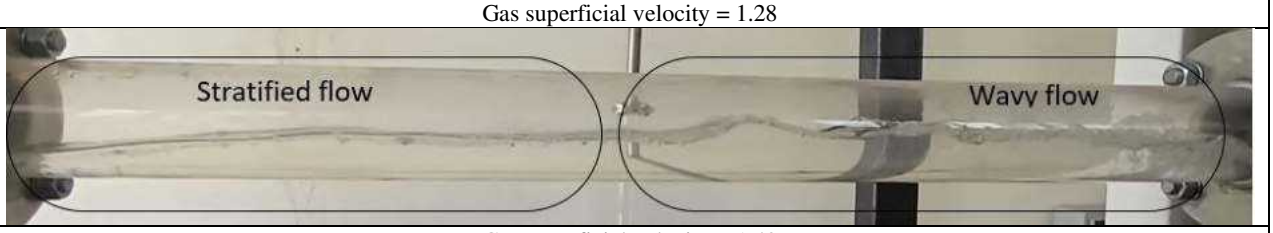

Gas superficial velocity = 1.40

Gas superficial velocity = 1.44

Figure 19: Flow behavior along the horizontal length of the pipe with superficial water velocity of 0.11 m/s
Flow behavior at low water flow rate (Superficial velocity = 0.25 m/s)

At this speed of the liquid, the patterns will be slightly different and the other four patterns that were created at low air flow rates will not be created, and a wavy flow pattern will be created from the beginning. Finally, the blocking and starting of CCFL will be occurred. The results of this liquid superficial velocity are shown in Figure 20 and Figure 21.

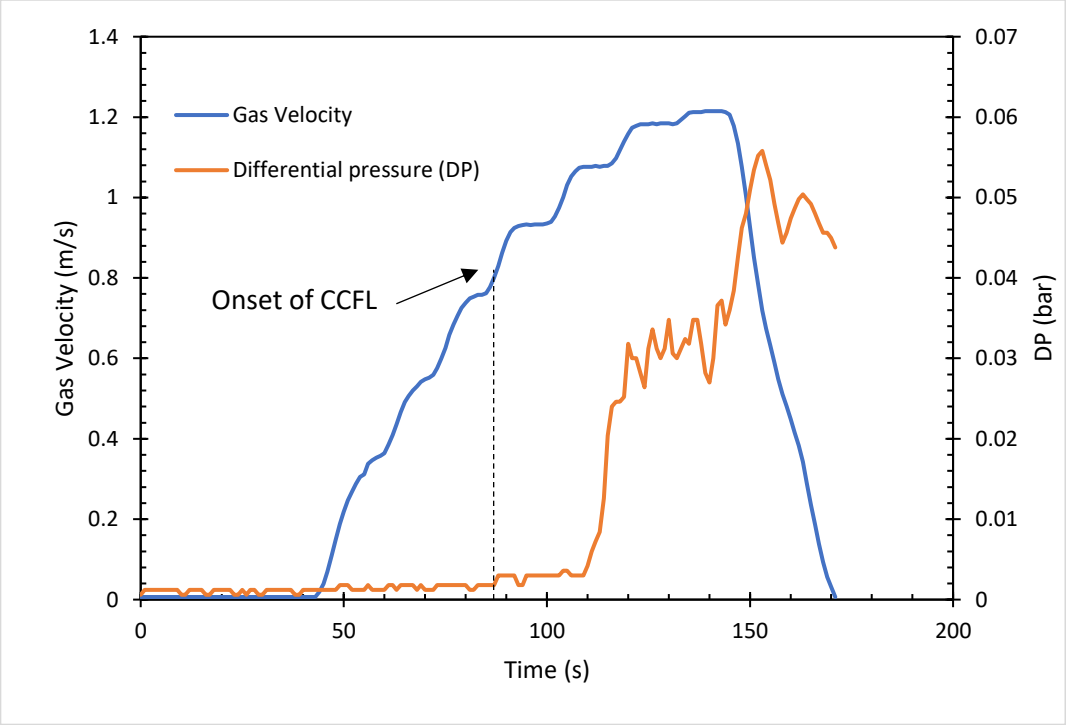

Figure 20: Pressure difference between RPV and SG (red curve) and gas superficial velocity (blue curve) with superficial water velocity of 0.25 m/s during flooding test

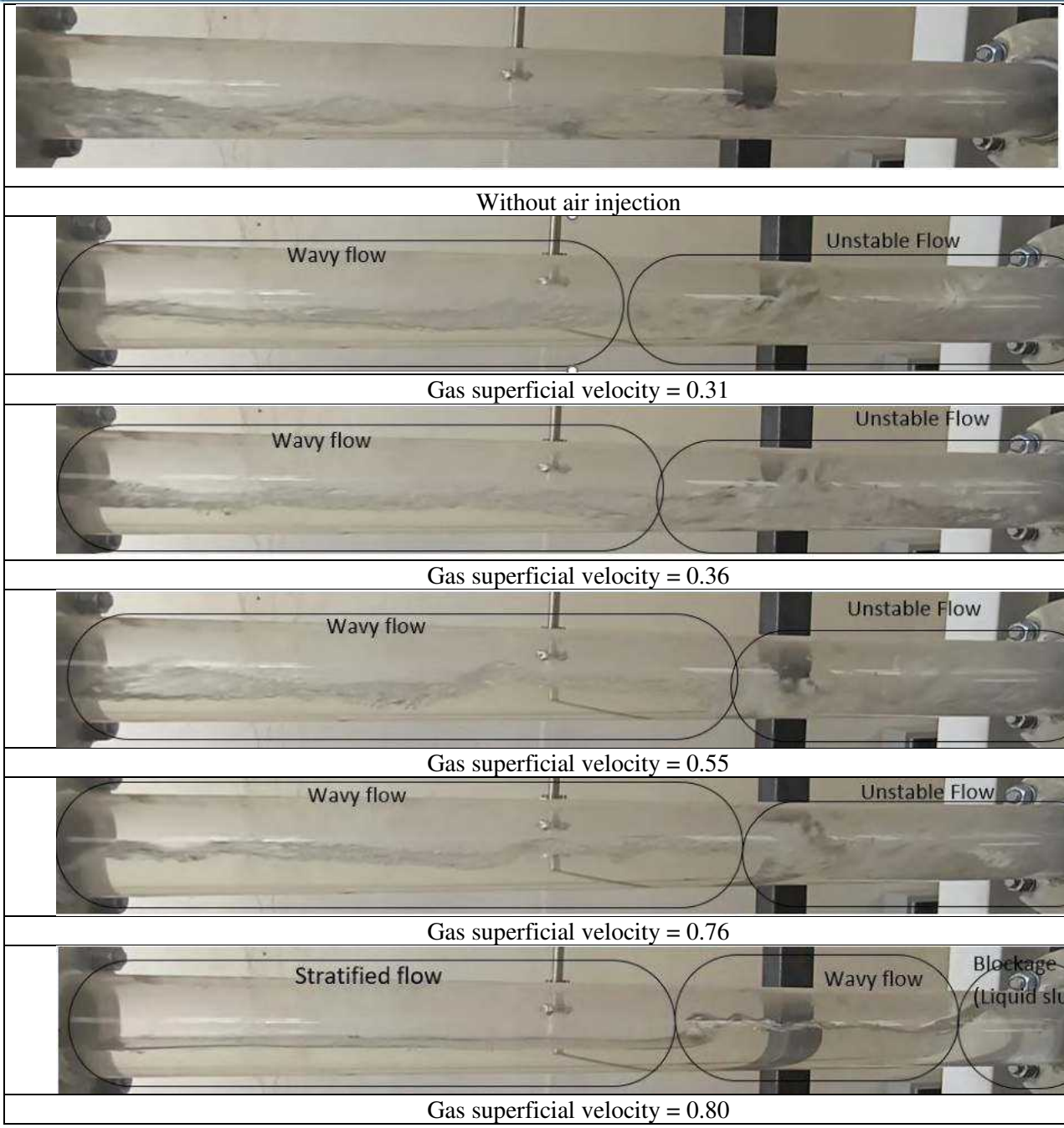

Figure 21: Flow behavior along the horizontal length of the pipe with superficial water velocity of 0.25 m/s

Comparison with the Previous Data

Most of the studies conducted on CCFL are PWRs, and there are fewer studies on VVERs (90-degree bend). The results of this study have been compared with two cases with 90-degree inclined angle.

Wongwises [8] proposed three regions to explain their CCFL curve. Each zone has its own CCFL mechanism and depends on the superficial velocity of the liquid. For JL*0.5< 0.2 (region 1), the air superficial velocity decreases at the onset of the CCFL while the superficial water velocity increases. For

0.2 < JL*0.5< 0.35 (second region), the superficial air velocity for flood initiation increases with the increasing of the superficial liquid velocity. For JL*0.5> 0.35, the onset of CCFL decreases with increasing superficial liquid velocity.

Navarro [3], however, reported a different result, in which the three regions cannot be easily distinguished because in his curve the gas superficial velocity decreases monotonically with increasing liquid superficial velocity.

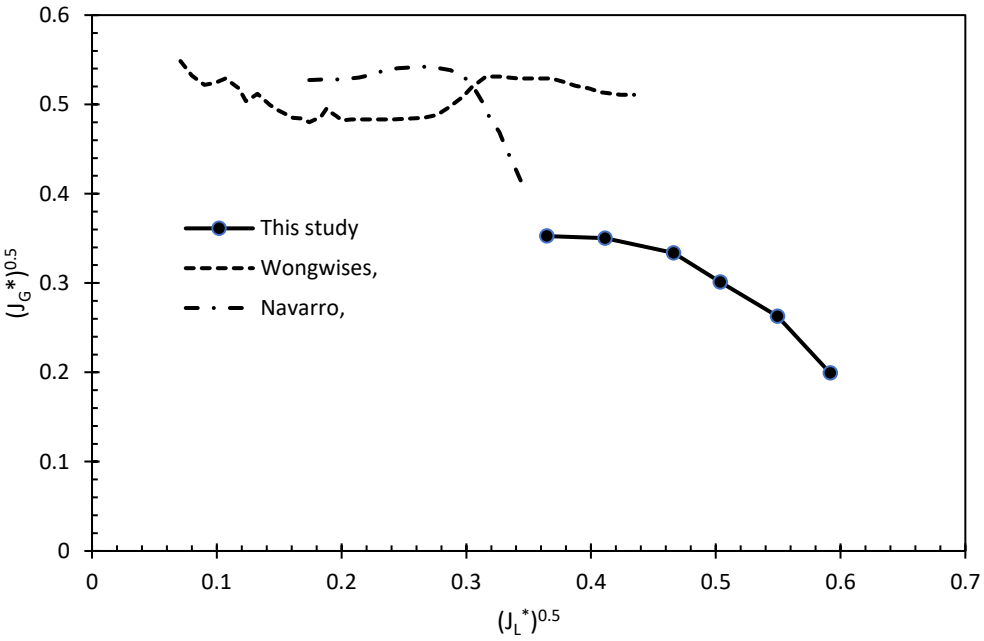

Figure 22: Comparison of the experimental data of this study with Wongwises [8] and Navarro [3] results

As shown in Figure 22, the results of this study are closer to Navarro's experimental results. In this way, the gas velocity curve decreases with the increasing of liquid superficial velocity.

Comparison with correlations obtained for the hot leg geometry

In studies on CCFL, a number of researchers studied the CCFL in typical hot leg geometries consisting of a horizontal section attached to an inclined riser. In their papers they presented certain correlations for such geometries, which should be compared with our experimental data.

Richter, Wallis [10] performed an air/water experiments to investigate CCFL in a hot leg of the PWR. The length and the inner pipe diameter of the horizontal part were 0.914 and 0.203 m, respectively. In their experiment, the highest possible flow rate of air or lowest flow rate of water have been investigated. The following correlation were obtained from their experimental results:

$$J_L^{*1/2} + J_G^{*1/2} = 0\ 7$$

Ohnuki [11] carried out an EXPERIMENTAL investigation on the flooding in a horizontal pipe connected to an inclined riser. He also proposed an empirical correlation to predict the onset of CCFL by using the Wallis [12] parameter. In this correlation in which the effect of the length of the inclined riser and length to diameter of the horizontal pipe are considered. The correlation can be found in Table 4. Next, de Bertodano [13] also proposed a correlation (Table 4) by using the Wallis parameter, based on the formation of slug flow at flooding conditions.

Navarro [3] performed a small-scale hot leg experiments with air and water. Several parameters including; the effect of geometrical parameters on flooding, such as the inner pipe diameter, the ratio of length to diameter, the length as well as the inclination of the riser. According to these results, a correlation was developed.

Some of these correlations listed in Table 4.

Table 4 experimental flooding data for CCFL in hot leg typical geometries

Reference	**Inner pipe diameter(m) / Length of horizontal part(m) / Inclination angle of riser (°)**	**Proposed correlation**
Wallis [14]	-	$J_L^{*1/2} + J_G^{*1/2} = 1\,0$
Weiss, Emmerling [15]	0.750 / 7.197 / 50	$J_L^{*1/2} + J_G^{*1/2} = 0\,7$
Richter, Wallis [10]	0.203 / 0.914 / 45	$J_L^{*1/2} + J_G^{*1/2} = 0\,7$
Ohnuki [11]	0.026, 0.076 / 0.4 / 45	$0\,75\ J_L^{*1/2} + J_G^{*1/2} = ln\left\{\left(\frac{L_H}{D}\right).\left(\frac{1}{I}\right)\right\}^{-0\,066} + 0\,88$
de Bertodano [13]	0.026, 0.076 / 0.4 / 50	$0\,798\ J_L^{*1/2} + J_G^{*1/2} = 0\,619$
Kang, Chu [9]	0.04, 0.08 / 0.7-3.39 / 35	$0\,397\ J_L^{*1/2} + J_G^{*1/2} = 0\,603 - 0\,00234\frac{L_H}{D}$
Navarro [3]	0.36-0.054 / 0.1-0.8 / 30-90	$0\,2452\ J_L^{*1/2} + J_G^{*1/2} = 0\,5963 - 1\,17\ J_L^{*}$

The experimental relationship resulting from the results of this study is obtained as follows:

$0\,659\ J_L^{*1/2} + J_G^{*1/2} = 0\,617$

The comparison between the current studies and other studied correlations is shown in Figure 23. This figure shows that the proposed correlation is very close to the correlation of Richter, Wallis [10] and Navarro [3].

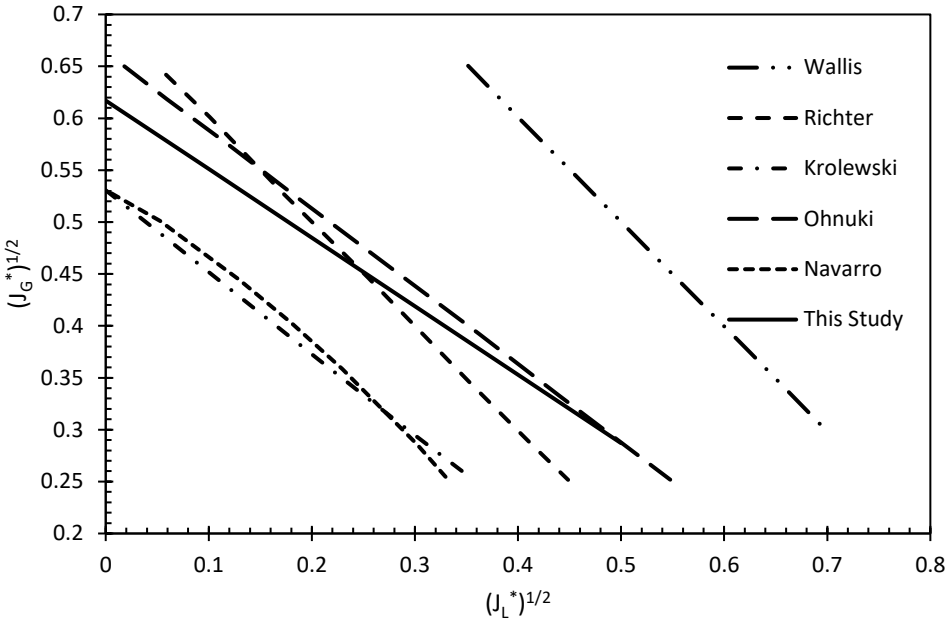

Figure 23: Comparison of CCFL empirical correlations for 10 < L/D < 25

Conclusion

In this study, an experimental investigation of the CCFL phenomenon was performed. The reference reactor was considered the Bushehr NPP which is a VVER-1000 reactor; test section of the test facility was down-scaled to the 1/9 actual hot leg size. At low liquid superficial velocities, four regions including unsteady, supercritical flow, hydraulic jump and subcritical flow were observed and by increasing of gas superficial velocity, wavy flow region and finally blockage occurred in low liquid velocities. At high superficial velocities of liquid, only wavy flow was formed at lower velocities of air at the beginning of CCFL. The gas superficial velocity curve has been continuously decreased with increasing liquid superficial velocity, which is consistent with Navarro's results. Furthermore, in this study, an experimental correlation $0.659\,J_L^{*1/2} + J_G^{*1/2} = 0.617$ was proposed and compared to other correlations. It was found that current experimental data were close to the results of Navarro and Richter correlations. In other words, the CCFL experimental results showed good agreement with the available experimental data of other researchers.

References

1. Ghiaasiaan, S.M., Two-phase flow, boiling, and condensation: in conventional and miniature systems. 2007: Cambridge University Press.

2. Wintterle, T., et al., **EXPERIMENTAL** and numerical investigation of counter-current stratified flows in horizontal channels. Nuclear engineering and design, 2008. 238(3): p. 627-636.

3. Navarro, M.A., Study of countercurrent flow limitation in a horizontal pipe connected to an inclined one. Nuclear Engineering and Design, 2005. 235(10-12): p. 1139-1148.

4. Al Issa, S. and R. Macian, A review of CCFL phenomenon. Annals of Nuclear Energy, 2011. 38(9): p. 1795-1819.

5. Siddiqui, H., S. Banerjee, and K. Ardron, Flooding in an elbow between a vertical and a horizontal or near-horizontal pipe: Part I: Experiments. International journal of multiphase flow, 1986. 12(4): p. 531-541.

6. Ardron, K. and S. Banerjee, Flooding in an elbow between a vertical and a horizontal or near-horizontal pipe: Part II: Theory. International journal of multiphase flow, 1986. 12(4): p. 543-558.

7. Ghiaasiaan, S., R. Turk, and S. Abdel-Khalik, Countercurrent flow limitation in inclined channels with bends. Nuclear engineering and design, 1994. 152(1-3): p. 379-388.

8. Wongwises, S., Two-phase countercurrent flow in a model of a pressurized water reactor hot leg. Nuclear Engineering and Design, 1996. 166(2): p. 121-133.

9. Kang, S.-K., et al., Air-Water Countercurrent Flow Limitation in a Horizontal Pipe. Journal of the Korean Nuclear Society, 1999. 31(6): p. 548-560.

10. Richter, H., et al., Deentrainment and Countercurrent Air-water Flow in a Model PWR Hot-leg. US Nuclear Regulatory Commission Report NRC-0193-9, 1978.

11. Ohnuki, A., **EXPERIMENTAL** study of counter-current two-phase flow in horizontal tube connected to inclined riser. Journal of Nuclear Science and Technology, 1986. 23(3): p. 219-232.

12. Wallis, G.B., Flooding velocities for air and water in vertical tubes. 1961, United Kingdom Atomic Energy Authority. Reactor Group. Atomic Energy ….

13. de Bertodano, M.L., Countercurrent gas-liquid flow in a pressurized water reactor hot leg. Nuclear Science and Engineering, 1994. 117(2): p. 126-133.

14. Wallis, G., 1969, One Dimensional Two-Phase Flow, McGraw-Hill, New York. 1969.

15. Weiss, P., et al. Two-phase flow experiments in full-scale to extend knowledge of PWR LOCA thermal–hydraulics. in ANS Proceedings of the National Heat Transfer Conference. 1992.

ICNST 2024 International Conference on Nuclear Science and Technology
6- 8 MAY 2024 | Isfahan, Iran

The control rod ejection accident in VVER-1000 using TRACE and PARCS (Paper ID : 1210)

Safarzadeh O.[1*], Abaszadeh A.[2], Dadashzadeh S.[3]
[1]*Faculy of Engineering, Shahed University, Tehran, Iran*
[2]*NPPs Safety Development & Improvement, TAVANA, Tehran, Iran*
[3]*Faculy of Engineering, Shahied Beheshti University, Tehran, Iran*

Abstract

To fully control the reactor systems, it is essential to fully understand the behavior of the reactor, which requires a thorough examination of the neutronic and thermohydraulic aspects. By using neutronic and thermohydraulic codes, the behavior of the reactor can be simulated and analyzed in normal operation, transient states and in accidents. In order to better understand the behavior of the reactor, especially at the time of the accident, the interactions between the neutronic and thermohydraulic aspects should be considered simultaneously, which is done by the coupling of the neutronic and thermohydraulic codes. Therefore, in order to simulate Design Basis Accident (DBA), including the control rod ejection accident, we also need to use the codes and their coupling. The rod ejection is a DBA in accordance with Final Safety Analysis Report (FSAR) and is usually studied using point kinetics. In this paper, a 3D kinetic model PARCS is prepared and coupled with a thermal hydraulic system code TRACE for simulating this accident scenario in a VVER-1000 reactor.

Keywords: Rod Ejection Accident, Bushehr NPP, TRACE, PARCS

Introduction

The criticality of a reactor is usually regulated using control rods or chemical controls. Control rods are parts of neutron-absorbing materials whose movement has an effect on the core reactivity coefficient. Therefore, if a control rod is withdrawn from the core, it become supercritical, while if the rod is inserted into the core, it becomes subcritical. In chemical control, regulation is achieved by altering the concentration of neutron absorbers, usually using boric acid (H3BO3) in the moderator. In the BNPP, there are 85 cluster control rod assemblies divided into 10 different groups. Fig. 1, illustrates the positions of these groups in the core. The main groups used for power adjustment are groups 8, 9, and 10. Each of these groups has specific constraints on the minimum and maximum entry into the core at different power levels. At nominal power, only group 10 in the core. This group is the most commonly used for control rod manipulation [1] [2].

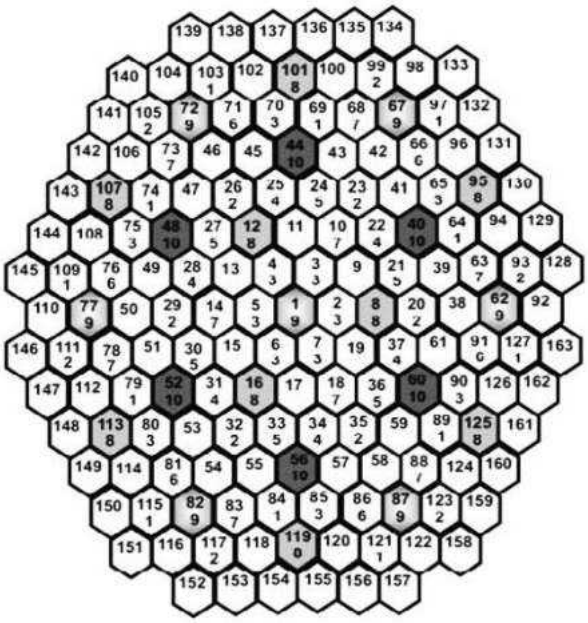

Fig. 1. Arragement of a bank of control rods in the core [2]

Since the incident of the control rod being released is one of the most important incidents, we are going to investigate the incidents that have occurred in the world. The SL-1 was a small, low-power nuclear reactor. In January 1961, this reactor, exploded, resulting in the deaths of three working engineers. The cause of the accident was that during repairs of control rod, the central control rod rises to a height of 20 inches in 0.5 second. The withdrawal of the control rods caused the reactor to go into a supercritical state within 4 milliseconds. As a result, the core power reached nearly 20,000 megawatts, which is 6,000 times greater than the reactor's output power, leading to a destructive explosion that rendered the facility completely destroyed and irreparable [1]. In another accident, The NRX was a Canadian heavy-water research reactor. In December 1952, during a shutdown at a power level of 17 megawatts, some control rods failed to insert into the core due to a malfunction. At the same time, the coolant flow had decreased, causing the melting of some fuel rods [2].

The purpose of this paper is to modeled the BNPP at the beginning of the first cycle of the core with of a couple of thermohydrualic (TRACE) and notronic (PARCS) codes to simulation and investigate the sudden ejection of the control rod accident.

Research Theories

Trace Model

The TRACE code is designed to be able to perform best estimate analysis of accident and transient. The nodal discretization used for the core model in this paper includes 22 axial segments, 3 radial regions, and 6 angular sectors.

The primary side model begins with the VESSEL component, representing the Reactor Pressure Vessel (RPV). The main circuit is simply formed using relevant TRACE components, including fill break and pipe. As mentioned, the break and fill components are used to model boundary conditions. The PIPE components represent the coolant inlet and outlet connections. The schematic structure of the initial circuit modeling is illustrated in Fig. 2.

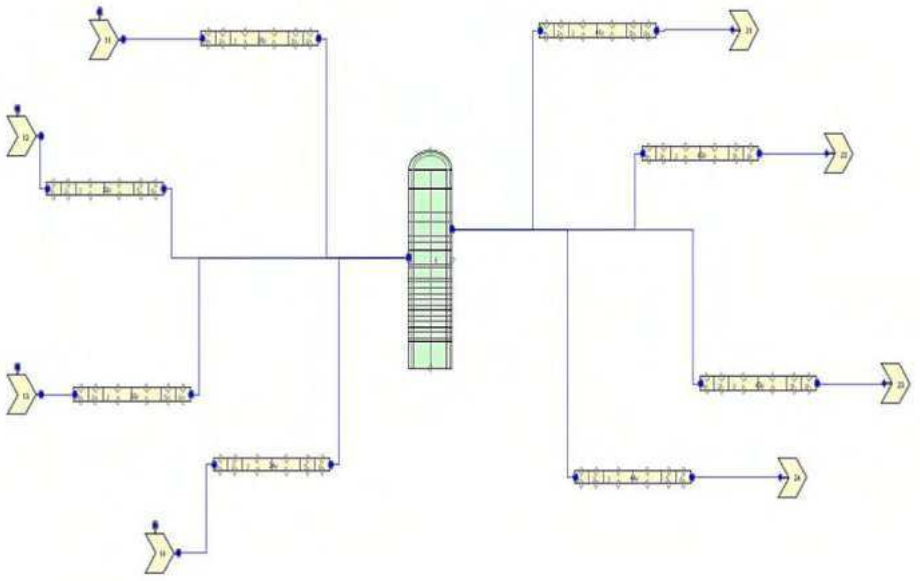

Fig. 2. Nodalization of TRACE

Parcs Model

PARCS is a three-dimensional reactor core simulation that solves low-order, time-dependent neutron diffusion and transport equation for multi-group neutrons in both orthogonal and non-orthogonal geometries. It can be directly coupled with the TRACE thermal-hydrualic system code, providing tempeature and flow field information to PARCS through multi-group cross-section data [2]. This coupling enhances the simulation capabilities by integrating neutronics and thermal-hydrualics aspects of reactor behavior.

The neutronic model of the VVER-1000 in the PARCS code is relatively simple and concise compared to system codes or Monte Carlo codes such as SERPENT or MCNP. PARCS is composed of various cards such as CNTL (control), XSEC (cross-sections), and more [8].

Coupling of Trace Whit Parcs

To describe the feedback effects between neutronics and thermal-hydraulics, reasonable data exchange between PARCS and TRACE needs to be achieved through an appropriate coupling. To accomplish this, the two programs are coupled to each other using the PVM software [10]. in this study, an internal coupling method has been employed to couple two models (TRACE and PARCS). The TRACE model is utilized for calculating thermohydrualic behavior and heat transfer, while the PARCS model is responsible for neutron kinetics. This approch enables the exchange of information between the two codes. The values of coolant and fuel temperatures are determined based on thermodynamic conditions and flow, and then transforred to the PARCS code to calculate neutron flux. These value and subsequently send to the TRACE code, where new thermohydraulic related value s are computed.

Experimental

The accident of control rod ejection, considered as a Design Basis Accident (DBA), holds significant importance, and simulating this scenario is unavoidable for the design of pressurized reactors. This event is defined as a mechanical failure of the pressure vessel of the control rod bank, leading to the ejection of Rod Cluster Control Assembly (RCCA) and its drive mechanism. This rapidly results in the injection of positive reactivity accompanied by an uneven power distribution within the reactor core.

Accident scenario

According to the final safety analysis report of Bushehr nuclear power plant (BNPP), the accident of sudden ejection of control rods occurs at the beginning of the cycle. The initial event triggering this accident, as mentioned before, is a disruption in the control rod drive system due to a pressure difference in the moving parts of the system, leading to the ejection of control rods. The disruption results in a fracture equivalent to a diameter of 58 millimeters, with coolant flowing inside it.

Table 5.sequence of events in the withdrawal of control rod from the nominal power level of 104% [4]

Time, sec	Event sequence
0,0	A break in the CPS housing occurs and sudden ejection of one set CPS CR. - Power loss leads to a trip for all RCPs. - Closure of Turbine safety valves. - Trip of main and auxiliary feed water pumps. - Disconnection of PRZ systems. - Shutdown of boron control system.
0,1	-CPS CR completely ejected from the core - Neutron flux increase to 107% nominal. - The reactor run-away period is less than 10 seconds. - Generate of scram signal
0,2	The maximum relative reactor power is 1,72 times the initial value
0,9	Increase DNB for the hot fuel rod.
1,0	Initiation of the CPS AR movement into the core.
3,5	Initiation of the BRU-A valves in the SG 1-4.
4,2	Complete entry of CPS into the core.
11,0	Initiation of opening SG PSD.
22,0	Initiation of closing SG PSD.
127,0	Appearance of coolant boiling in RCC
910,0	Initiation of injecting boron solution through pumps.
2512,0-2518,0	Complete closure of BRU-A valves.
2930,0	Initiation of ECCS operation.
5500,0	Increase of the water level in RCC to the nominal value.
7000,0	End of calculation.

It is evident that the risk-inducing factors for the core, which may lead to fuel rod damage or even core meltdown, all occur at the beginning of the accident. Among these factors, the maximum relative power crossing the critical point and the maximum fuel temperature are noteworthy. it is clear that the transition to hazardous states, such as the sudden ejection of control rods from the core, occurs within a very short time after the onset of the accident. Therefore, simulating the early moments is of utmost importance compared to other times. Simulations in the first 20 seconds are conducted in this paper.

Results and Discussion

Result of the Steady-State

To obtain results in a steady-state condition, initial conditions for the power plant, including temperature, pressure, coolant velocity, and flow rate in the initial circuit, are approximately set to conditions close to the operational state of the power plant in the TRACE input file. The code is then run for an extended

period. Subsequently, the output values are used as the initial conditions for a new input file. After a few seconds, the new input file converges to steady-state conditions. The resulting plots from the analysis show that there is no significant change in the thermal-hydraulic parameters after a few seconds, hence accepting these values as steady-state values. The most important thermal-hydraulic parameters after a few seconds are presented as steady-state values in Table 6, which can be compared with the values reported in the final safety analysis report of the power plant.

Table 6. Steady state parameters [6] [7]

Parameter	TRACE	FSAR
Reactor power, MW	3000,0	3000,0
Coolant inlet to core temperature, °C	291,0	290,95
Coolant outlet to core temperature, °C	321±5	321,43
Pressure in the reactor, MPa	15,7+0.3	15,7
Pressure drops between inlet and outlet, MPa	0,44	0,2484
Maximum fuel rod temperature, °C	1883,0	1579,35
Maximum fuel cladding temperature, °C	352,0	335,04

Result of the Transient

In this section, we will simulate the control rod ejection accident using two methods, first using the TRACE code based on the information provided in previous section. Following that, we will examine the results by coupling the TRACE and PARCS codes.

Simulation Results Whit Trace

Considering that the initial circuit model in this simulation is not complete, a simplified model is used for simulating the accident with the TRACE code, and the necessary graphs are plotted. In this section, we will examine the results obtained from the TRACE code and compare them with the results in the final safety analysis report of Bushehr. Fig. 3-6 compare the results obtained by the TRACE code with the values in the FSAR. In the given figure, the maximum relative power is approximately 1.7, accuring around 0.258 seconds. The noticeable trend in graph is that before the onset of the emergency shutdown, power value start to decline. this indicates the significance of temperature feedback and moderator feedback mitigating events. Furthermor, it illustrates the effective simulation of density, doppler and temperature feedback effects [6].

At zero second, the RCPs and PRZ systems are disconnected from the reactor, so the pressure drop is not compensated by the cooling pumps. Additionally, pressure regulation by the pressure controller is unavailiable. At 0.1 second, the reactor abruptly shutdown, causing in increase in pressure in the main

circuit before tis moment. In the subsequent seconds, no power is generated in the reactor, and the heat absorbed by the steam generator, transerring the produced steam to the atmosphere. This leads to a decerase in pressure in the main loops. However, considering the primary inertia of the circuit pumps, this pressure decrease does not occure suddenly.

The coolant temperature in the cold leg of the primary circuit initially decrease due to the sudden reactor shutdown. However, in the subsequent seconds, it begins to increase, potentially attributed to the heat removal performance in the steam generators as a result of the closure of PSD valves. Meanwhile, the coolant temperature in the hot leg of the primary circuit start to rise, driven by the increase in the reactor power. This increase is not observed in the FSAR, possibly due to the extensive time simulation, sampling rate, and data acquistion from the FSAR plots.

The fuel temperature difference can be caused by a minor calculation error, a minor error in the input data, especially the geometric dimensions and fluid volume values, or the inaccuracy of the model presented for some components of the first circuit. In general, according to the obtained results, the presented model is very close to reality and can be used to investigate the thermohydraulic behavior of the reactor in normal and accident conditions.

According to the Fig. 4, it can be seen that the maximum temperature of the fuel is located in about 1.6 seconds, while the power reaches its maximum value in less than one second. This difference is due to the adiabatic behavior of ceramic fuel heat conduction, which causes a gentle increase in temperature. The temperature and pressure increased in the initial moment of the accident, but due to the rapid loss of reactor power, it decreases.

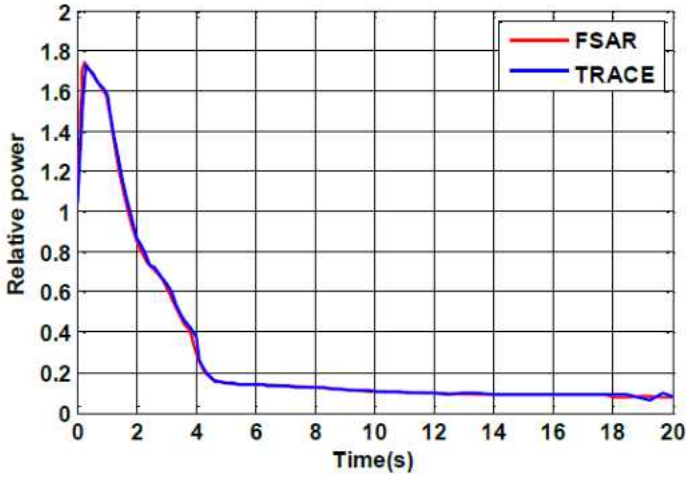

Fig. 3. Relative power of the core.

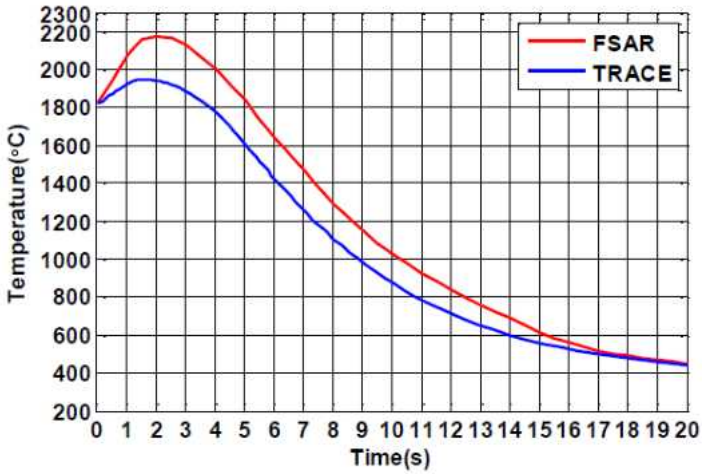

Fig. 4. The hot rod maximum fuel temperature.

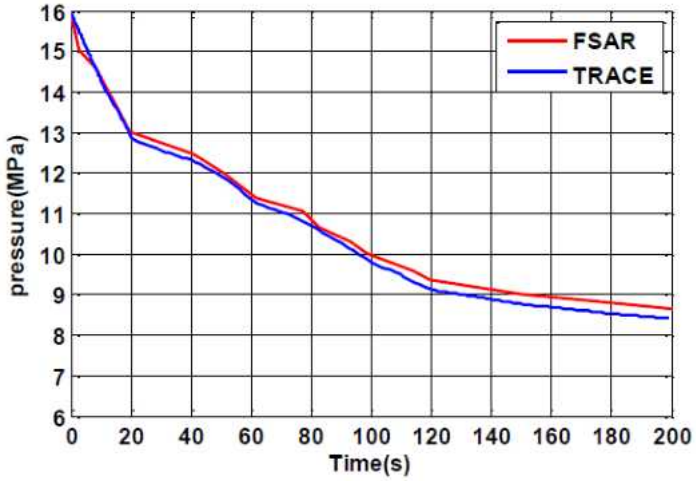

Fig. 5. Coolant pressure in the core

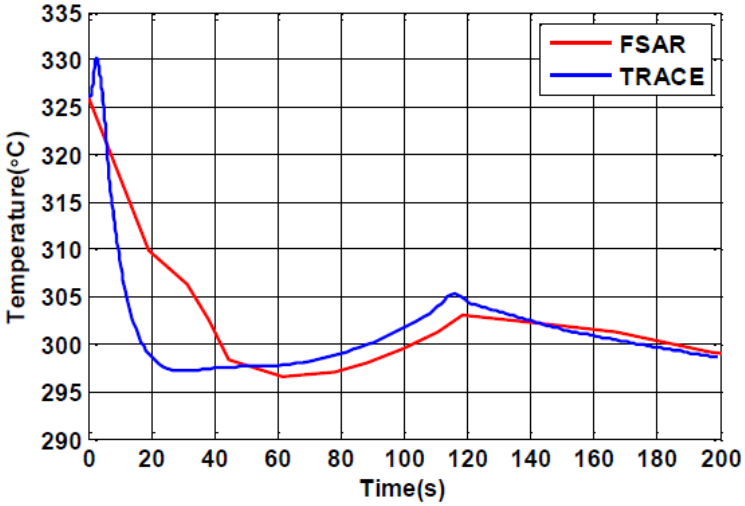

Fig. 6. Temperature of the hot leg 1-4

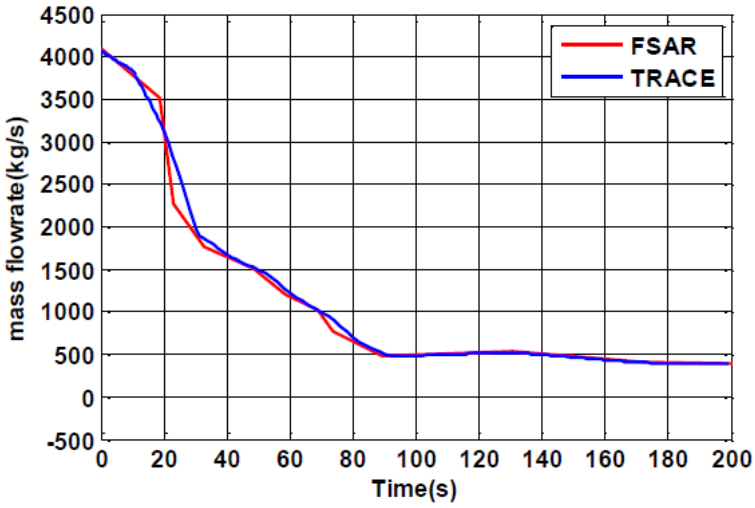

Fig. 7. The mass flow rate of loop-1

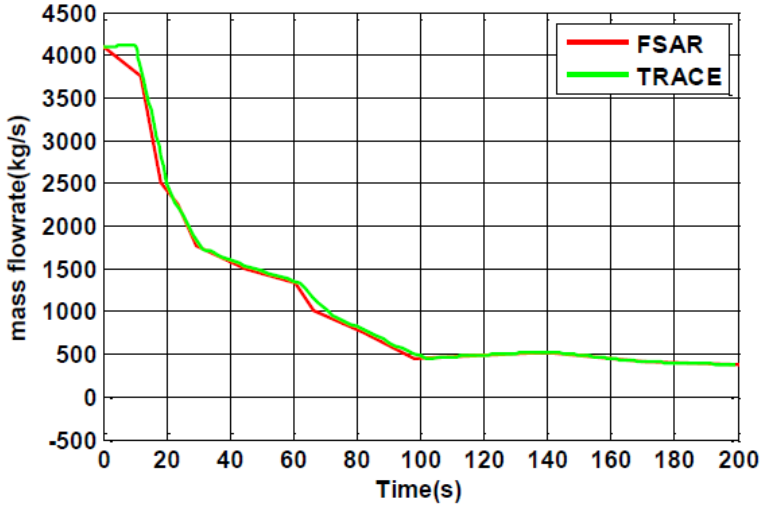

Fig. 8. The mass flow rate of loop-2

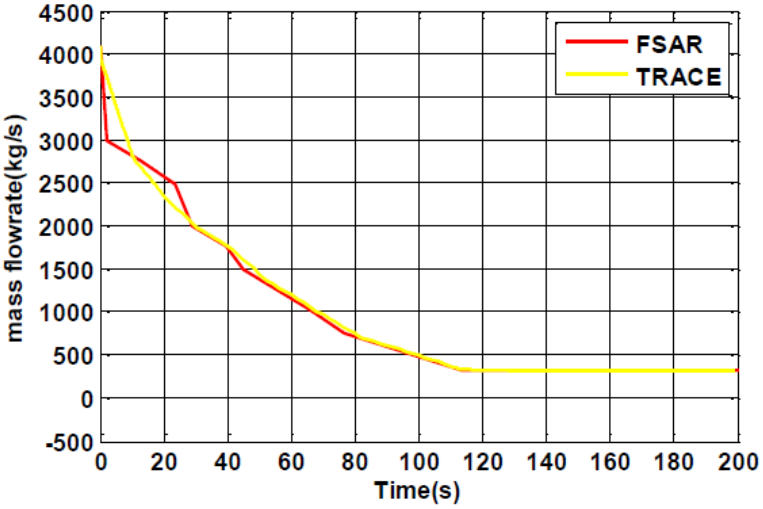

Fig. 9. The mass flow rate of loop-3

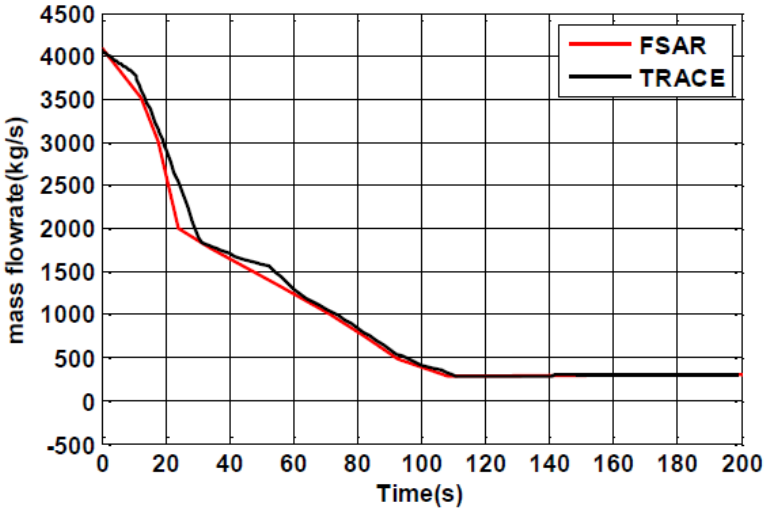

Fig. 10. The mass flow rate of loop-4

Coupling Results of Trace And Parcs Code

In the previous section, the results of simulating the sudden ejection of control rods using the TRACE code were analyzed. In this section, we will investigate the same accident using the coupling of TRACE and PARCS codes. After conducting simulations for the first scenario of control rod sudden ejection, various parameter plots over time are presented in Fig. 11-14. as evident from the Fig. 13, group 10, initially positioned at aproximately 247.206 cm (above 70% of the core height), begins to exit the core at zero second and completely leaves the core around 0.1 second, reaching a location of 353 cm. Groups 1 to 9, which are fully outside the core at 353 cm until 0.1 seconds, start moving back into te core upon receiving the scram signal at 0.1 second. By approximately 1 second, they initiate inward motion and reach a position of 0 cm (completely inside) around 4.2 seconds.

According to Fig. 12, it can be seen that the obtained temperature is actually the average temperature of the fuel rods and the hot rod is not simulated. And the observed difference is for this reason.

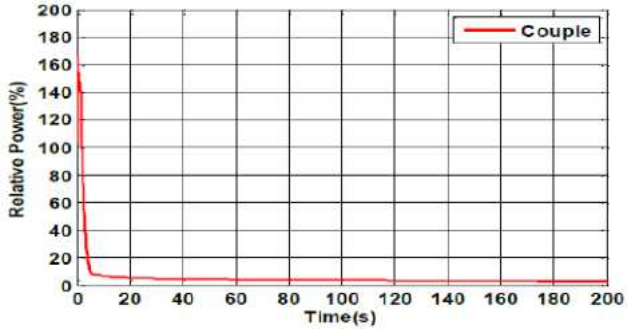

Fig. 11. Relative power of the core, obtained from coupling.

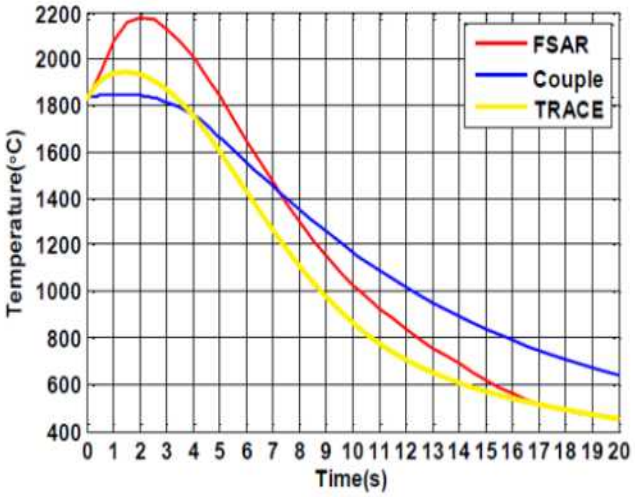

Fig. 12. The hot rod maximum fuel temperature.

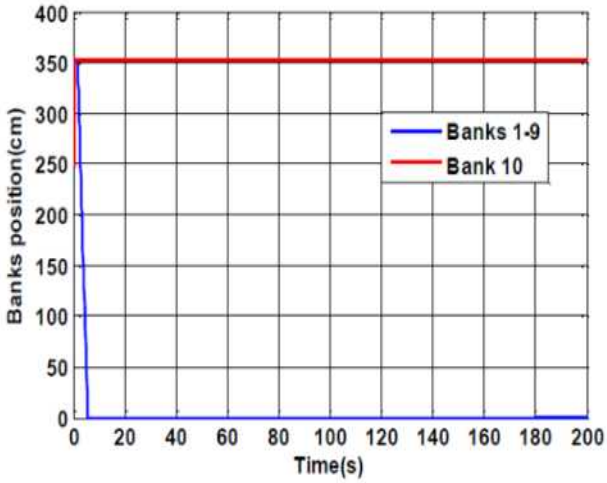

Fig. 13. Relocation of control rods, obtained from coupling.

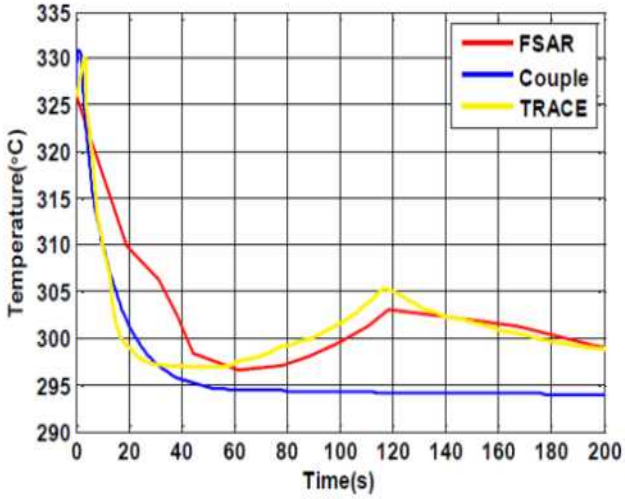

Fig. 14. Temperature of the hot leg 1-4.

Conclusion

Since the control rod ejection accident falls into the category of design basis accidents, most studies aim to find reactor parameters' responses to control rod ejections using various methods and codes. In fact, simulating this accident is a standard practice in the design of any reactor worldwide. This paper also attempts to simulate and analyze this accident, examining and comparing all results, including steady-state and transient states, with similar parameters in the FSAR report.

References

[1] Jayhuni. A., simulationg the accident of the sudden ejection of control rod in Bushehr Nuclear Power Plant using PARCS and WIMS codes, Master thesis of Shahid Beheshti University, 2013.

[2] Assesment of Defence in Depth for Nuclear Power Plants, IAEA Safety Reports Series No. 46, Vienna, 2005..

[4] Amlashi, S., Investigation the accident of large break of the coolaning water in the pressurized light wter reactor using the couple of TRACE/PARCS and evaluating the uncertainty and sensitivity of the main parameters, Master thesis of Shahid Beheshti University, 2018.

[5] Final Safety Analysis Report (FSAR), Chapter 15, Atomic Energy Organization of IRAN, 2005..

[6] Final Safety Analysis Report (FSAR), Chapter 4, Atomic Energy Organization of IRAN, 2007..

[7] Final Safety Analysis Report (FSAR), Chapter 5, Atomic Energy Organization of IRAN, 2007..

[8] Lamarsh, J. R., & Baratta, A. J. (2001). INTRODUCTION to nuclear engineering (Vol. 3). Upper Saddle River, NJ: Prentice Hall.

ICNST 2024 International Conference on Nuclear Science and Technology
6- 8 MAY 2024 | Isfahan, Iran

Cobalt-60 Production in Tehran Research Reactor (Paper ID : 1220)

Mazhari. F.[1], Rezaey Uchbelagh D.[1], Arkani M.[2*], Mirvakili M.[2]

1- Department of Energy Engineering & Physics, Amirkabir University of Technology (Tehran Polytechnic), Tehran, Iran.
2- Nuclear Science & Technology Research Institute (NSRTI), Tehran, Iran.

Abstract

One of vitally important and widely applicable radioactive sources in industry, agriculture, medicine and in nuclear research applications is Cobalt-60 radioisotope. Its production depends on the neutron flux characteristics such as neutron flux energy distribution and absolute neutron flux level. Generally, the neutron flux level depends on the neutronic power of the reactor core. While, neutron flux energy distribution depends on material composition and the reactor core design specifications. In this work, Tehran research reactor is evaluated as a great neutron source for Cobalt-60 production. One of important and influential components in the production efficiency of Cobalt-60 in Tehran research reactor, is the location of the irradiation, the arrangement, and the diameter of Cobalt-59 pencils loaded in the reactor core. In order to achieve the maximum specific activity of the product, pencils with diameter of 0.7 cm and height of 61.58 cm with the assumption of full power operation of the reactor, are simulated utilizing MCNPX calculational code. Moreover, self-shielding effects as well as production efficiency with different arrangements of Cobalt-59 pencils at different positions are investigated.

Keywords Tehran Research Reactor, MCNPX, Cobalt-60, Nuclear Reactor Core, Irradiation, Neutron Activation.

Introduction

In nuclear reactors, Cobalt-60 is produced by the activation of the stable and natural Cobalt-59 isotope through neutron bombardment and absorption of a neutron [1]. Considering the Cobalt-59 neutron absorption cross-section is 37.2 barn, thermal neutrons are the main activation source for production of Cobalt-60. There are 29 known isotopes, but only Cobalt-59 has a density of approximately 8.89 $\frac{gr}{cm^3}$ is found naturally which is stable. The other isotopes are radioactive, and among them, Cobalt-60 with a half-life of 1925 days is the most popular one. By emitting beta and gamma rays, Cobalt-60 has extensive applications such as in medical, industry [2], and food irradiation [3].

In a study conducted by Khalafi and Gharib in 2005 [4], the impact of increasing the diameter of cobalt-59 pencils on the reduction of neutron flux was investigated. In this research, a cluster of cobalt-59 pencils with a diameter of 0.7 cm and a height of 10 cm was simulated in the central irradiation positions of the

Tehran Research Reactor (TRR). The results of this study demonstrate the possibility of producing 50 kCi of cobalt-60 within a one-year irradiation period in the irradiation position at the core center of the TRR.

In 2024, Gholamzadeh and Rokrok [5] demonstrated through calculations using the MCNPX code that optimizing the dimensions of the assembly is crucial for increasing production efficiency, reducing negative reactivity of the core during irradiation, and minimizing self-absorption effects. In the TRR, if possible, utilizing the central channel of the core and irradiating a 26-rod assembly in a 27 element arrangement would allow for the maximum production of approximately 40 kCi of cobalt-60 after 3 years of irradiation. This value is derived assuming the reactor operates for 255 days per year. The use of beryllium in the vicinity of a cobalt complex can help mitigate its negative reactivity to some extent [6].

In this study, the feasibility of producing Cobalt-60 in TRR is investigated using MCNP simulation code [7]. One of the crucial and influential factors in the efficiency of Cobalt-60 production in the TRR core is the irradiation position, arrangement method, and diameter of Cobalt-59 pencils. The study aims to optimize the production of Cobalt-60 sources by examining the effects related to self-shielding and the efficiency of Cobalt-60 production and irradiation of Cobalt-59 pencils in the central region of the reactor core.

Simulation Methodology and Results

Neutron Self-Shielding and Irradiation Efficiency

The production of radioisotopes through neutron irradiation depends on neutron spectrum and neutron flux in the irradiation position. The total neutron flux is mainly dependent on the reactor power, while the spectrum is influenced by the core materials and the geometry surrounding the radiation positions.

In this section, the impact of self-shielding effects of Cobalt-59 pencils with different arrangements on the yield of Cobalt-60is investigated. The production of Cobalt-60 involves the use of a Cobalt-59 pencil assembly. Initially, a number of Cobalt-59 pencils with specified diameters and initial heights are selected for the study.

The reactor core configuration of TRR, investigated in the current study to examine the self-shielding effects, is presented in Figure (1). This figure illustrates a simulated view of the research reactor core geometry designed for a maximum power of 5 megawatts using the MCNPX code. Each standard fuel element consists of 19 fuel plates, while it is 14 for any control fuel element. The chemical composition of the fuel is U_3O_8Al with a fuel enrichment of 20%. Around the reactor core, there are 12 graphite boxes (GR BOXs) and 12 irradiation boxes (IR BOXs). Radiation positions are located in sections D5 and A7 within the reactor core.

Assuming the operational power of TRR equal to its nominal level, the maximum available neutron flux is presumed. In the initial stage, in the central channel of the reactor core located in D5 irradiation position, the thermal neutron flux at the nominal power, is approximately $1.01\times 10^{14}\ \frac{\#}{\mathrm{cm}^2\ s}$ simulated by the MCNPX code. In the A7 irradiation position of the reactor core, this value is about $4.49\times 10^{13}\ \frac{\#}{\mathrm{cm}^2\ s}$. Showing that the central region (D5 position) provides higher thermal neutron flux in comparison with the reactor core periphery (D7 position).

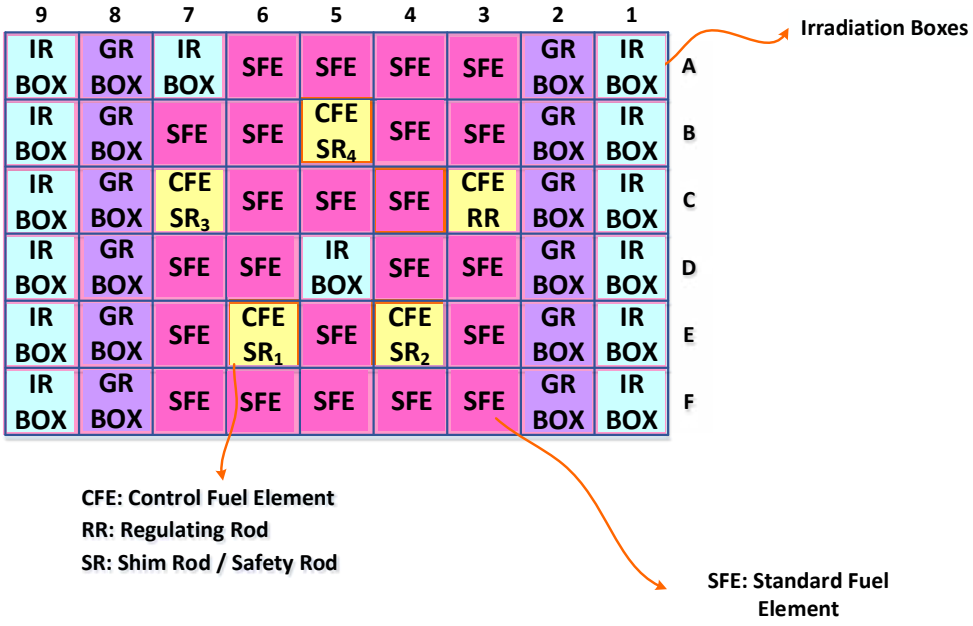

Fig. 1. TRR core configuration simulated in MCNPX code.

One of important effects which must be taken into account is the self-shielding effect. As neutrons penetrate to the internal regions of the pencils from moderator (outside of the pencils), outer layers are exposed to higher neutron flux values. In other words, neutrons are absorbed by the outer layers of the pencils, therefore there is a drop in neutron flux in the central regions of the pencils. In Figure (2), this effect is clearly seen. It is obvious that, pencils with bigger diameters, have deeper drop in the radial neutron flux distribution and the radiation efficiency, when loading cobalt-59 pencils at the center of the radiation position D5, decreases with an increase in the diameter of the cobalt-59 pencils. The results shown in this figure, is calculated by MCNPX code simulation. Actually, the neutron flux is disturbed by the presence of the Cobalt-60 pencils. Note that the top curve belongs to the zero-diameter pencil (it means without any pencil). In this work, the diameter of the pencils is chosen equal to 7 mm.

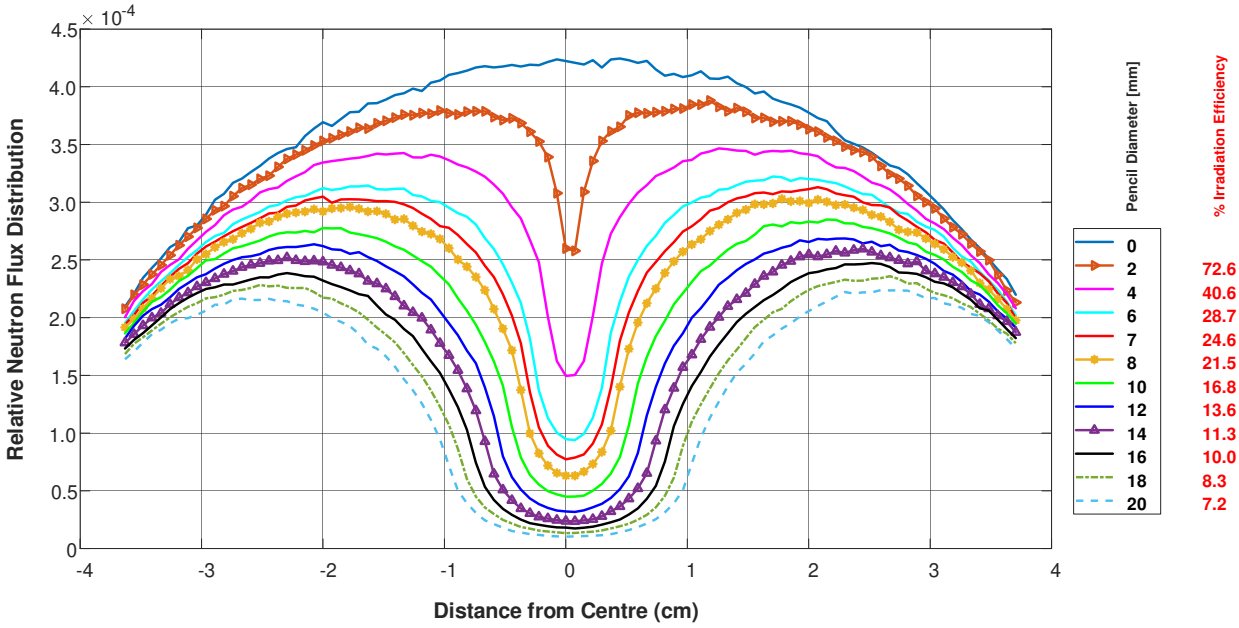

Fig. 2 Relative thermal neutron flux distribution for different diameters of Cobalt-59 pencils in D5 irradiation position.

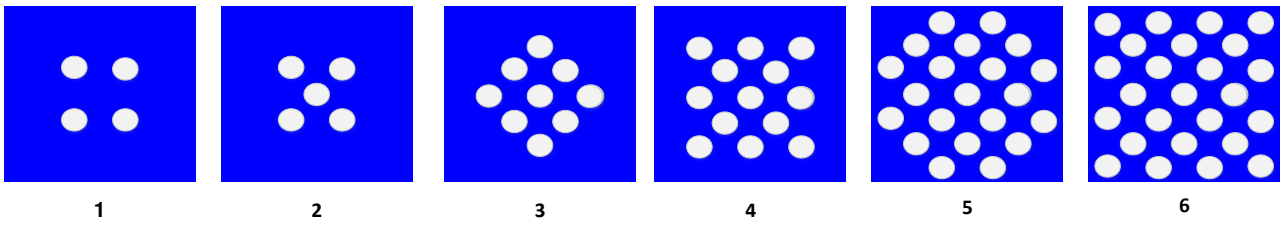

Fig.3 . A representation of the simulated clusters in D5 and A7 irradiation positions of TRR core simulated in MCNPX code.

Different Arrangements of Cobalt-59 Clusters

In this section, different clusters of Cobalt-59 pencils are evaluated. In Figure (3), six different clusters for Cobalt-59 irradiation in TRR IR BOXs (D5 and A7 positions as explained above) are shown. These clusters include 4, 5, 9, 13, 21, and 25 pencils. In Figure (4), the activity of the product at different irradiation times for these clusters are depicted. It is obvious that more loadings of the pencils in a cluster, results in more activities of the results. If the activities are normalized in unit mass of the Cobalt-59 loaded in the reactor core, the specific activity is easily calculated. Specific activity is a really important feature of Cobalt-60 gamma source in some special applications like medical implementations. In Figure (5), it is obvious that

clusters with smaller number of Cobalt-59 loading pencils, result in higher levels of specific activity of the product. This is due to the shadowing effect of the neighbouring pencils in a cluster. Therefore, depending on the aim of the applications of the Cobalt-60 as a product, a justification between specific activity and the total activity of the product is necessary.

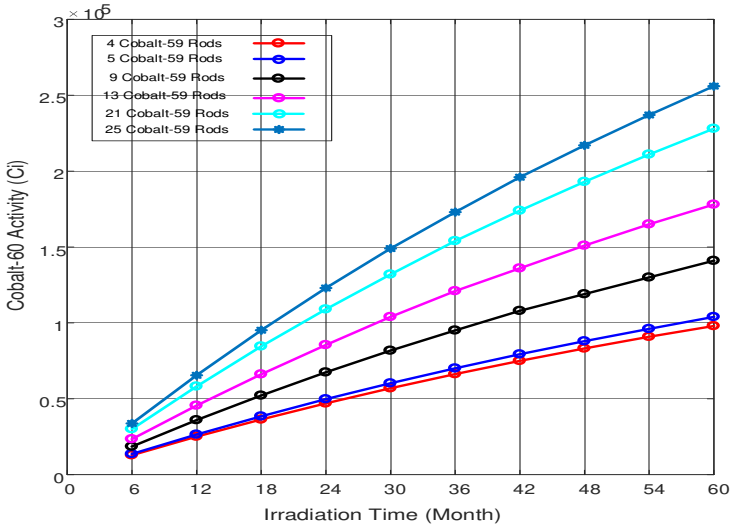

Fig. 4. Growth of Cobalt-60 activities for different cluster types.

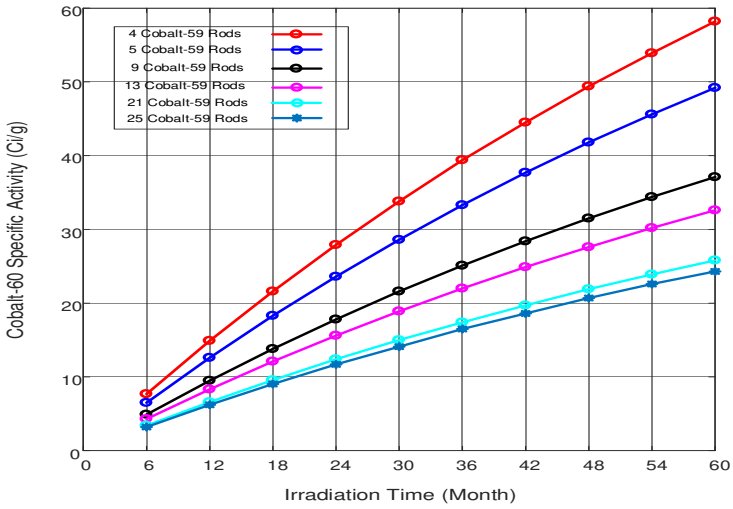

Fig. 5. Growth of Cobalt-60 specific activities for different cluster types.

Conclusions

TRR is an important neutron source facility for radioisotope production. An important probable application of the reactor is production of Cobalt-60 gamma sources. The practicability of this application is studied in this research. For this purpose, two in-core irradiation positions of the reactor are evaluated using MCNPX simulation code system. The radius of Cobalt-59 pencils as well as different arrangements of them in clusters, are properly assessed. The thicker radius means more self-shielding of the pencils, and, the greater number of pencils in cluster result in a more powerful shadowing effect of the irradiation samples. The Cobalt-60 as a product of the irradiation work in TRR has two important features as: the total activity and the specific activity. These features have an inverse relationship to each other which must be justified depending on the later applications of the product as a gamma source.

References

[1] .Malkoske GR, Slack J, Norton JL. Cobalt-60 Production in Candu Power Reactors. Can Nucl Soc Bull. 2002;23(3):1-6.

[2] *Manual for reactor produced radioisotopes*, (IAEA-TECDOC-1340, 2003) http://www.isotopes.gov/outreach/reports/Reactor_Isotopes.pdf

[3] AR Ghahremani et al., Utilization of 4 MW Tehran research reactor by production of industrial and medicine radioisotope. International Atomic Energy Agency (IAEA) IAEA-CN--100, 2003

[4] H. Khalafi, et al. Optimization of 60Co production using neutron flux trap in the Tehran research reactor, Annals of Nuclear Energy , Volume 32, Issue 3, February 2005, Pages 331-341

[5] Zohreh Gholamzadeh et al. simulation of the possibility of cobalt-60 production in Tehran research reactor, Journal of Nuclear Science and Tehnology, Volume:45 Issue: 3, 2024

[6] Zohreh Gholamzadeh et al. Computational investigation of 1 up to 3 kCi Co-60 source production at external irradiation boxes of TRR core using MCNPX code, Radiation Physics and Engineering 2024; 5(1):1–9

[7] D.B. Pelowitz, *Users' manual versión of MCNPX2.6.0*, (LANL, LA-CP-07-1473, 2008).

ICNST 2024 International Conference on Nuclear Science and Technology
6- 8 MAY 2024 | Isfahan, Iran

PCMI Assessment Method Using Abaqus: A Segmented Expanding Mandrel Test Approach (Paper ID : 1246)

Zeinab Mohammadi[1], Navid Ayoobian[1*], Hamed Khodadadi[1], Mohammad Javad Ashrafi[2]
[1]Department of Nuclear Engineering, University of Isfahan, Isfahan, Iran
[2]School of Mechanical Engineering, Iran University of Science & Technology, Tehran, Iran

Abstract

Pellet and Cladding Mechanical Interaction (PCMI) plays a substantial role in nuclear reactor fuel safety and performance analysis. PCMI test involves exposing the fuel cladding to harsh thermal, mechanical, and radiation conditions similar to those that may happen during fast transient and accidental conditions inside the power reactor cores. One of the reliable experimental analysis methods that fuel designers and testing institutes frequently use is the Segmented Expanding Mandrel Test (SEMT). In this research, a reliable two-dimensional Abaqus model of the SEMT is developed. This study also investigates the effect of the friction coefficient between segment and cladding contact surfaces and the number of segments on the hoop strain of Zircaloy-4 (Zry-4) cladding tubes. Moreover, the impact of temperature and hydrogen content on the equivalent plastic strain (PEEQ) amount is analyzed. These parameters were selected strategically due to their significant influence on the Zry-4 cladding response. The predictable effect of the friction coefficient and number of segments on the hoop strain value on both sides of the cladding confirms the model's validity. Results show that the model can properly exhibit temperature-induced ductility and hydrogen-induced embrittlement by utilizing an acceptable approximation for damage criteria.

Keywords: Pellet and Cladding Mechanical Interaction (PCMI), Segmented Expanding Mandrel Test (SEMT), Abaqus, Zircaloy-4 (Zr-4), Ultimate Tensile Strength (UTS), Yield Stress (YS), plastic equivalent strain (PEEQ)

Introduction

Nuclear energy is a widely highlighted element of sustainable power production and a reliable way to supply electricity to reduce climate change[1]. Starting the fission process triggers pellets and cladding thermal expansion, pellet swelling, and fragmentation. Furthermore, coolant pressure leads to cladding creep. These factors can cause the pellets and cladding to mechanically interact by closing the initial gap between them. The term used to describe this situation is Pellet and Cladding Mechanical Interaction (PCMI)[2]. In abnormal conditions, such as an unexpected power increase united with the presence of the hydrides in the zircaloy cladding structure, PCMI can induce a high-stress level, leading to deformation, cracking, damage, and failure of the clad. Fuel rods serve as both the initial and secondary barriers against

releasing radioactive fission products into the environment. Thus, the design must ensure the integrity of the cladding during both normal and abnormal operational conditions[3].

For this reason, researchers have sought to enhance cladding performance over the decades and mitigate potential issues connected to the PCMI. To this purpose, integral tests and separated effects tests have been developed. Although the integral tests contribute to the comprehensive insight into PCMI phenomena, the preparation and post-irradiation examination issues, such as hot-cell requirements and safety protocols, make it impracticable for each circumstance. The separated effects tests include standard mechanical methods applicable to irradiated or unirradiated cladding materials. In these tests, parameters like hydrogen content, temperature, and loading pattern are assessable[4]. Among several techniques, the Segmented Expanding Mandrel Test (SEMT), shown in is one of the promising methods for analyzing PCMI [5]. The main parts of this set-up consist of the mandrel segments, the cladding tube specimen, and the axially-movable shaft. The segments aim to emulate pellet fragments. The shaft's axial movement leads to radial expansion of the segments inside the cladding, representing fuel fragments' expansion and swelling. This process exerts a load on the inner surface of the tube. Simplicity, uncomplicated sample preparation, controllable load-displacement procedure, and manageable experimental conditions can be considered the other advantages of the SEMT [6]. However, it is worth mentioning that the stress-strain curves obtained from SEMT depend on friction between the different parts[7].

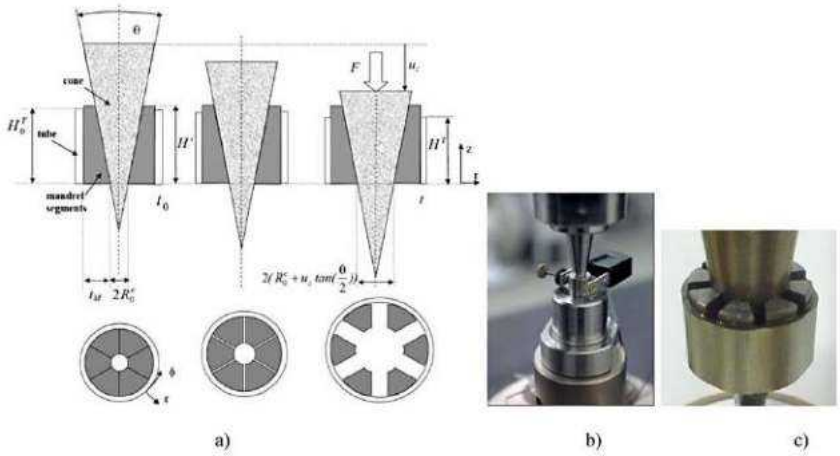

Fig. 1. Mandrel Expanding Test Instrument[7]

Research Method

Using the SEMT, the present study investigates Zr-4 cladding behavior during PCMI. The research is systematically structured in two sections. The first section involves selecting specific cases, serving as

input data for the Pacific Northwest National Laboratory (PNNL) stress-strain correlation. Simultaneously, a suitable damage criterion will be chosen, facilitating an exploration of the damage mechanisms. Outputs function as material properties input data for Abaqus software[8]. The subsequent step entails the creation of a two-dimensional Abaqus model to assess the cladding behavior within the SEMT set-up.

PNNL Stress-Strain Model

Table 7 outlines the case studies objectively elected as PNNL input data. Cases 1 to 3 are the representers for assessing the impact of the elevated temperature and hydrogen content. Additionally, case 4 signifies the temperature and hydrogen content of a typical VVER nuclear fuel rod after 1200 days of operating in normal conditions. The philosophy for studying temperature and hydrogen is their inherent ability to impact Zircaloy cladding mechanical properties such as ductility and hardness.

Table 7: Case Studies on Hydrogen and Temperature Effects

	Temperature (K)	Hydrogen Content (ppm)
Case 1	300	0
Case 2	300	2000
Case 3	600	0
Case 4	556.4	54.8

The PNNL correlation uses two different models describing Zircaloy's stress-strain behavior in both elastic and plastic zones. The relations specific to this research have been exhibited in ***Table* 8**. It is essential to highlight that to concentrate on the influences of temperature and hydrogen content, the impact on neutron flux is omitted, and all cases are assumed to be unirradiated.

Table 8: PNNL model material correlation

Material properties	Correlations
Elastic Modulus	E
Elastic deformation before yield	$\sigma = \varepsilon\ E$
Plastic deformation after yield	$\sigma = K\ \varepsilon^n \left(\frac{\dot{\varepsilon}}{10^{-3}}\right)^m$
Yield Stress	$\sigma_y = \left[\frac{K}{E^n}\left(\frac{\dot{\varepsilon}}{10^{-3}}\right)^m\right]$
Strength coefficient	$K = K(T)\ (1 + K(CW))$

K(T)	$T < 750K$	$K(T) = 1\,176282 \times 10^{9} + 4\,54859 \times 10^{5}\mathrm{T} - 3\,28185 \times 10^{3}\,\mathrm{T}^{2} + 1\,72752 \times T^{3}$
K(CW)	CW = 0.5	$K(CW) = 0\,546\ CW$
Strain hardening exponent	$T < 419\,4K$	$n = 0\,11405$
	$419\,4 < T < 1099\,0772K$	$n = -9\,49 \times 10^{-2} + 1\,165 \times 10^{-3}T - 1\,992 \times 10^{-6}T^{2} + 9\,588 \times 10^{-10}T^{3}$
Strain rate exponent	$T < 750K$	$m = 0\,15$

In these equations, ε, $\dot{\varepsilon}$, σ, T are the symbols for strain, strain rate, stress, and temperature respectively. ***Fig. 2(a)*** presents the PNNL model applied to the three temperatures up to UTS. It illustrates that temperature increment diminishes the UTS, reducing the material's ability to withstand high-stress levels before failure. Moreover, the YS has also decreased, making the material more susceptible to plastic deformation.

In the PNNL model, hydrogen slightly decreases the fracture strain, but this model provides no exact information regarding its hydrogen influence on YS and UTS. Reviewing the available literature, hydrogen is not only capable of changing fracture strain but also affects YS and UTS [6], [9], [10]. Another approach has been used to apply these effects on the Yield curve. More details can be found in [6]. The following equation demonstrates the relationship between the hydrogen content and the Yield curve.

$$(\sigma,\ \varepsilon) \rightarrow \left(n\sigma,\ \frac{\varepsilon^{n}}{n}\right)$$

$$for\ H = 54\,8\ ppm \rightarrow n \approx 1\,01$$
$$for\ H = 2000\ ppm \rightarrow n \approx 1\,5$$

Results of the modified model have been shown in ***Fig. 2 (b)***, displaying an elevated hydrogen content effect on the Yield curve. Hydrogen can cause a reduction in the cladding ductility, by decreasing the total elongation. The ultimate outcomes of these modifications augment the probability of failure under loading conditions.

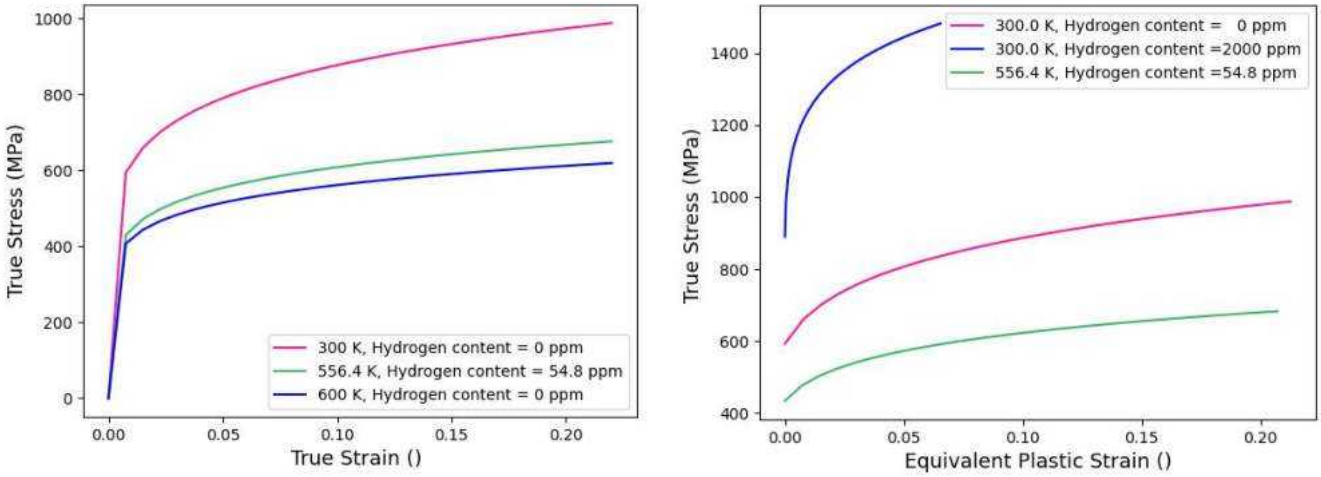

(a) (b)

***Fig. 2**. Visualization of **(a)** application of the PNNL model for different temperatures, **(b)** Hydrogen content effect on Yield curve*

Abaqus Simulation

In the second and final step, a 2D SEMT model in Abaqus was developed. In order to reduce the computational cost and regarding the symmetries, only half of one segment was modeled. This approach allowed us to achieve the desired results more efficiently while sustaining the accuracy of the simulations. ***Fig. 3*** depicts a schematic of the 2-D model in Abaqus.

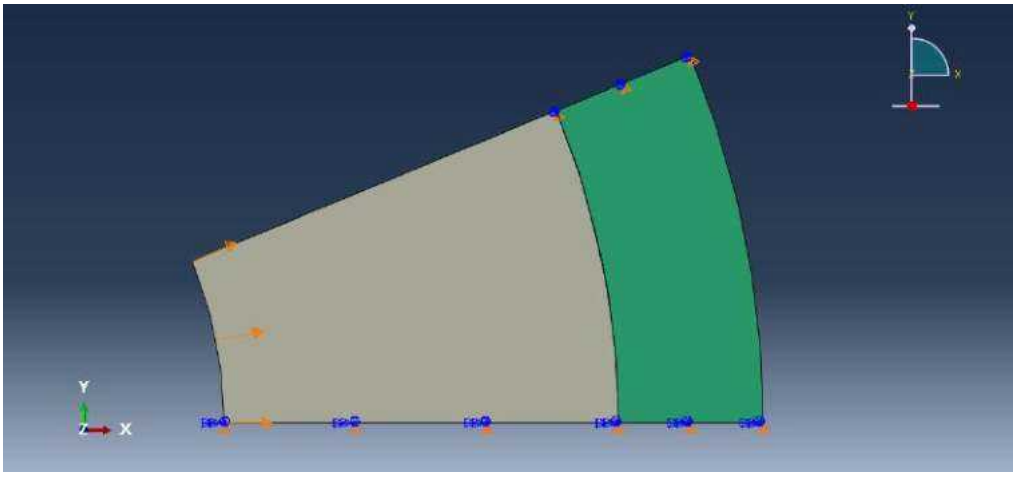

Fig. 3. Schematic representation of the 2-D model in Abaqus

Ultimately, it was assumed that the cladding rupture starts at the necking point initiation (UTS) and would have 10% higher displacements after this point. Cladding elements would reach the complete fracture/elimination situation at a stress level equal to 1% of its UTS.

In the Abaqus ductile damage model, the damage parameter (D) signifies the degree of material degradation or loss of structural integrity due to plastic deformation, ranging from 0 (undamaged) to 1 (fully damaged

or failed). The evolution of D is governed by considering factors like stress, strain, strain rate, and material properties. *Error! Reference source not found.* depicts the evolution of the damage parameter as a function of p lastic displacement after the UTS point for different cases.

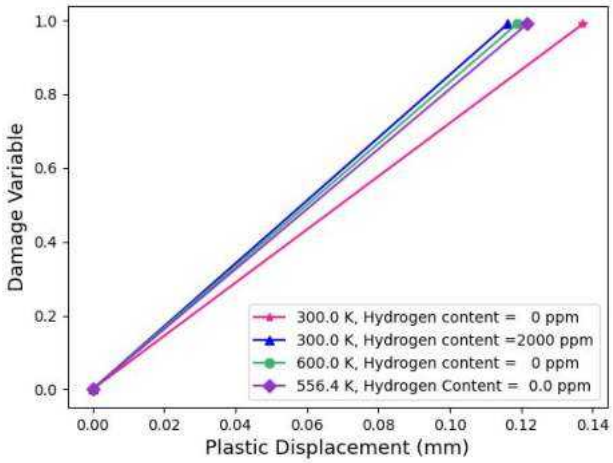

Fig. 4. Correlation between the damage variable and plastic displacement

Results and discussion

Fig. 5 demonstrates that the maximum hoop strain across the inner and outer surface of the cladding is located at the contact area with the segment's edge. Notably, the overall maximum hoop strain increases significantly with the friction coefficient. The reason is evident because a higher friction coefficient reduces sliding freedom between segments and the clad. This observation emphasizes friction's influence on cladding's mechanical responses during an SEMT.

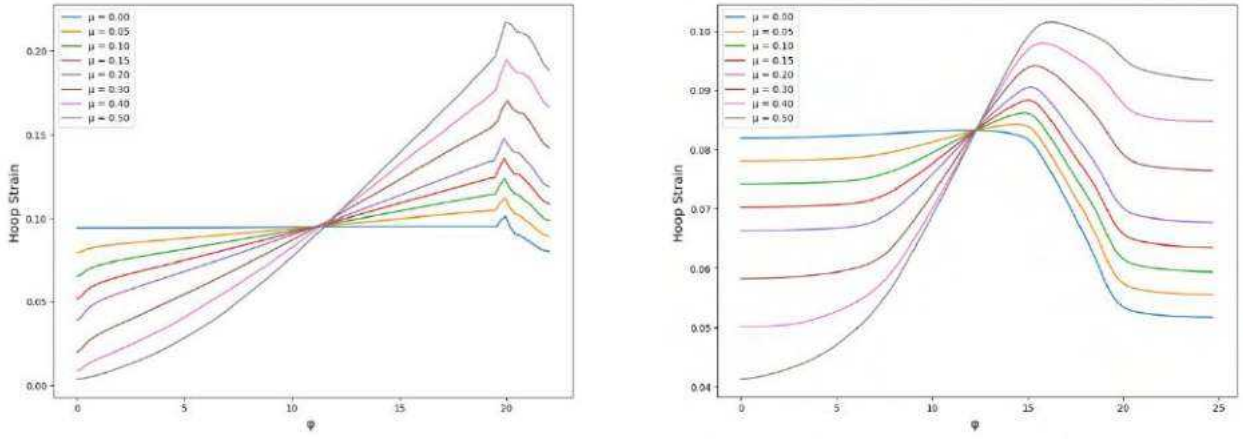

(a) (b)

Fig. 5*. a: Hoop Strain along the cladding inner surface for different friction coefficients. b: Hoop Strain along the cladding outer surface for different friction coefficients*

Fig. 6(a) and ***(b)*** provide an inclusive understanding of the influence of segment numbers on the maximum hoop strain and its distribution. In this figure, two cases with 1% (***Fig. 6.a***) and 10% (***Fig. 6.b***) relative displacement of segments are compared. As depicted, a clear correlation emerges, in which an increase in the number of segments corresponds to a more uniform strain distribution along the inner and outer cladding surfaces.

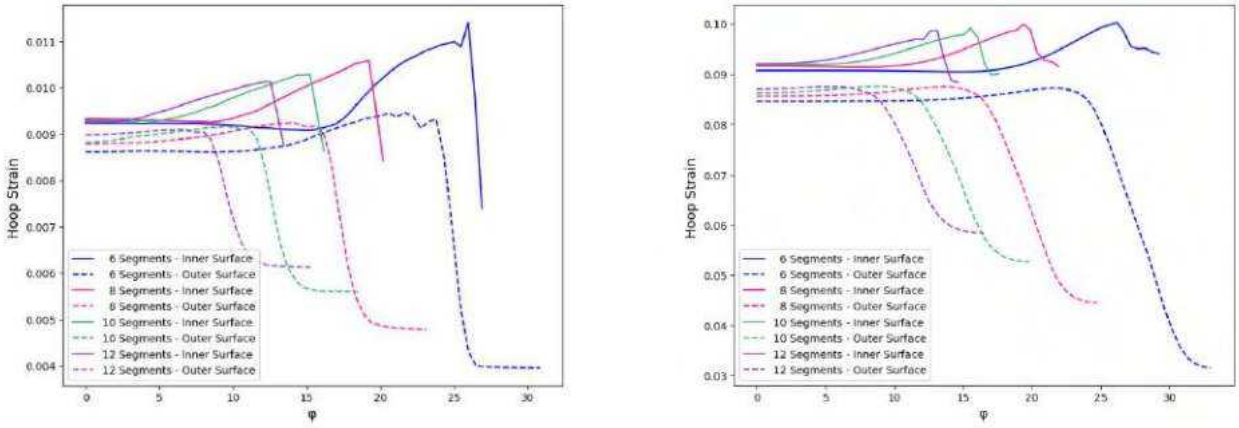

(a): (u/r_0=1%) (b): (u/r_0=10%)

Fig. 6. *Hoop Strain along the inner(solid-lines) and outer cladding surface (dash-lines) for 6,8,10,12 numbers of segments, (In this case, u is displacement, and r_0 is the cladding initial inner radius.)*

In Abaqus software, plastic equivalent strain (PEEQ) measures the accumulated plastic strain in the material. It is commonly used to evaluate plastic deformation in materials subjected to mechanical loading. ***Fig. 7*** displays the contour of PEEQ in the cladding for four distinct cases (***Table 7***) at u/r_0 = *15%* for an SEMT with eight segments. Considering ***Fig. 2 (a)***, for a zero-hydrogen content at different temperatures, *Error! Reference source not found.* ***(a) and (d)*** signifies an increased level of plastic deformation within the m aterial. The rupture in ***Fig. 7 (b)*** is evidence of hydrogen's effect on the sample's ductility.

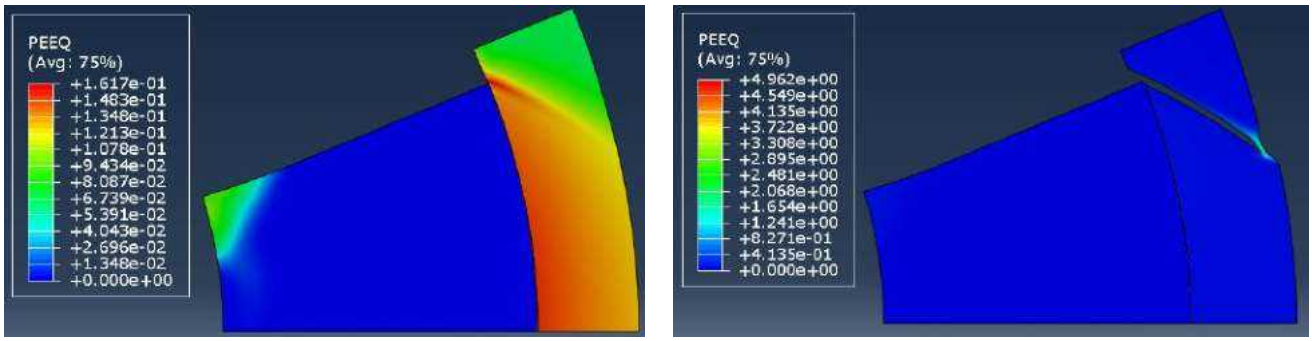

a: Temperature = 300 and Hydrogen content = 0 ppm b: Temperature = 300 and Hydrogen content= 2000 ppm

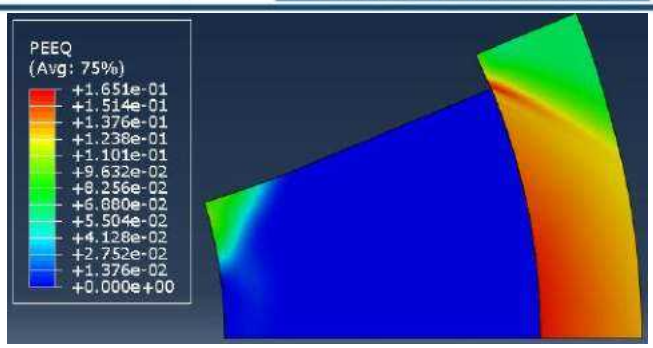

c: Temperature = 556.2 and Hydrogen content=54.8

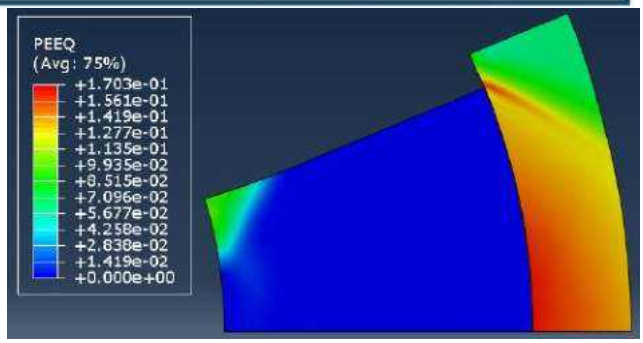

d: Temperature = 600 and Hydrogen content=0 ppm

Fig. 7. *Equivalent Plastic Strain (PEEQ) considering ductile damage*

Conclusions

In conclusion, this paper has provided a primitive study on developing a reliable Abaqus SEMT model to assess Zry-4 cladding response during PCMI. To attain a comprehensive modeling approach, the elastic and plastic behavior of the cladding within the Abaqus material input was enhanced with correlations related to temperature and hydrogen effects. The following key findings affirm the model's reliability and validity:

The proportional increase in maximum hoop strain with friction coefficient between the segment and cladding surface highlights the sensitivity of the SEMT on friction.

The correlation between segment numbers and the peak value of the hoop strain emphasizes the role of SEMT configuration.

Higher PEEQ in elevated temperatures even in low hydrogen contents shows the Zry-4 cladding ductility increment.

The occurrence of rupture in the elevated hydrogen content specimen substantiates the credibility of the applied damage criteria, affirming the hydrogen embrittlement of the sample.

Collectively, these findings promote our understanding of the factors shaping cladding behavior during a simulated PCMI via SEMT, which is the foundation for refining the set-up design and analysis of nuclear fuel systems.

References

[1] "Understanding the interface interaction between U3Si2 fuel and SiC cladding | Nature Communications." Accessed: Oct. 24, 2023. [Online]. Available: https://www.nature.com/articles/s41467-020-16435-x

[2] F. Qi *et al.*, "Pellet-cladding mechanical interaction analysis of Cr-coated Zircaloy cladding," *Nucl. Eng. Des.*, vol. 367, p. 110792, Oct. 2020, doi: 10.1016/j.nucengdes.2020.110792.

[3] G. Pastore, P. Botazzoli, V. Di Marcello, and L. Luzzi, "Assessment of the prediction capability of the TRANSURANUS fuel performance code on the basis of power ramp tested LWR fuel rods," presented at the 8 international conference on WWER fuel performance, modelling and **EXPERIMENTAL** support, Bulgaria, 2009.

[4] J. Desquines, D. A. Koss, A. T. Motta, B. Cazalis, and M. Petit, "The issue of stress state during mechanical tests to assess cladding performance during a reactivity-initiated accident (RIA)," *J. Nucl. Mater.*, vol. 412, no. 2, pp. 250–267, May 2011, doi: 10.1016/j.jnucmat.2011.03.015.

[5] D. S. Tomalin, R. B. Adamson, and R. P. Gangloff>, "Performance of Irradiated Copper and Zirconium Barrier-Modified Zircaloy Cladding Under Simulated Pellet-Cladding Interaction Conditions," in *Zirconium in the Nuclear Industry*, ASTM International, pp. 122–144. doi: 10.1520/STP36676S.

[6] R. Nagy, M. Király, D. M. Antók, L. Tatár, and Z. Hózer, "Dynamic finite element analysis of segmented mandrel tests of hydrogenated E110 fuel cladding tubes," *Mater. Today Commun.*, vol. 24, p. 101005, Sep. 2020, doi: 10.1016/j.mtcomm.2020.101005.

[7] K.-F. Nilsson, O. Martin, C. Chenel-Ramos, and J. Mendes, "The segmented expanding cone-mandrel test revisited as material characterization and component test for fuel claddings," *Nucl. Eng. Des.*, vol. 241, no. 2, pp. 445–458, Feb. 2011, doi: 10.1016/j.nucengdes.2010.10.026.

[8] K. J. Geelhood, C. E. Beyer, and W. G. Luscher, "PNNL Stress/Strain Correlation for Zircaloy," PNNL-17700, 969740, Jul. 2008. doi: 10.2172/969740.

[9] H. Lee, K. Kim, J.-S. Kim, and Y.-S. Kim, "Effects of hydride precipitation on the mechanical property of cold worked zirconium alloys in fully recrystallized condition," *Nucl. Eng. Technol.*, vol. 52, no. 2, pp. 352–359, Feb. 2020, doi: 10.1016/j.net.2019.07.032.

[10] Y. Zhang, L. You, X. Li, J. Zhou, and X. Song, "*In-situ* investigation of the fatigue crack initiation and propagation behavior of Zircaloy-4 with different hydrogen contents at RT and 300 °C," *J. Nucl. Mater.*, vol. 532, p. 152065, Apr. 2020, doi: 10.1016/j.jnucmat.2020.152065.

ICNST 2024 International Conference on Nuclear Science and Technology
6- 8 MAY 2024 | Isfahan, Iran

Development of transient dynamics code for a helically-coiled steam generator analysis using multi-node moving boundary model (Paper ID : 1248)

Fakhraei A.[1*], Faghihi F.[1]
[1]*School of Mechanical Eng., Shiraz University, Shiraz, Iran*

Abstract

Due to its compact design, higher heat transfer, and capability of superheated steam production, helical coil steam generators (HCSG) have become a popular option for usage in small modular reactors. In this research a multi-node moving boundary model is developed for transient calculation of these steam generators. The secondary side of HCSG is comprised of subcooled, two-phase, and superheated regions. The developed model is able to track boundary of the phases and allocate their proportional heat transfer coefficient accordingly. Also, each region is divided to multiple nodes for more accuracy. This approach obviates the need for fine nodes and phase detection in each node in each time step which significantly reduce the computational cost for calculation of steam generator behavior. Furthermore, in this research a RELAP5 model for HCSG is developed. The results calculated by the developed code are benchmarked against RELAP5 calculated parameters. Multiple scenarios for change in properties of feedwater and primary flow to the steam generator are modeled. Simulated scenarios shows that both codes are calculating same trends for variation of the parameters. The methodology presented in this study is applicable for modeling HCSG dynamics in future studies.

Keywords: Small Modular Reactors, Helical Coil Steam Generator, Multi-node Moving Boundary Model, steam generator dynamical simulation

Introduction

It has been attractive for nuclear engineers to integrate steam generators and pressurizer enclosed within an RPV in order to eliminate external piping and its relevant accidents such as LOCA since first nuclear era. Nowadays some SMR designs such as NuScale, IRIS and CAREM-25 have been successful in utilizing this idea. To do so the best choice for heat transport from the primary to the secondary is helical coil steam generators. There are several advantages in using HCSGs compared to current steam generators in the commercial PWRs such as compact design, higher heat transfer and capability of producing superheated steam.

In order to develop control system and transient analysis, a robust dynamic model is needed to evaluate response of the system to different scenarios and design a well-tuned controller. However, presence of three phase in the secondary side and different properties of the fluid in each region make dynamic simulation of this equipment complex.

HCSGs can be modeled dynamically using two approaches. The first approach utilizes finite volume method with fixed boundaries. This method requires a large number of fine nodes to track boundary of each phase correctly and use its characteristics. The second approach propose moving boundary model and coarse nodes. This method tracks boundary of phases with its special formulation so the necessity for using fine nodes obviates.

Using a movable boundary model for steam generator is computationally more efficient for these types of systems. Kerlin, Secker and Gilbert developed HTGR steam generator model based on nine nodes in the HTGR OTSG [1, 2]. In these simplified models, secondary side is comprised of three nodes. One node for each region.

Tzanos devised a movable boundary model for LMFBR [3, 4]. In this work, a computer code named STEGA was written which was able to simulate LMFBR OTSG behavior. This model utilized different heat transfer models for nucleate boiling and film boiling regions. The set of equations solved with semi-analytic method for the steady-state condition. The Gear method implemented in LSODE package for stiff differential equations was used for integration of differential equations for transient solution. Also, the proposed approach benchmarked in transient condition with numerical experiment ETEC shutdown experiment that was carried out with PSM-W numerical code [5].

Jensen and Tummescheit developed a 7th order model for system and controller design of multi-phase heat exchanger. This model utilized slip ratio to calculate mean average void fraction in the two-phase section. Also, Leibnitz's rule was applied for converting governing PDE equations to set of ODEs [6].

The main objective of this article is to present results obtained from developed model for simulation of the NuScale HCSG transient conditions with its set of ODEs with RELAP5 calculated data. The developed model takes advantage for both moving boundary model and fine mesh approaches through detecting boundary of the phases and also the capability to having each region divided into several computational nodes.

Research Theories

Steam generator is divided into three regions as shown in Fig. 1. Each region can be divided into several nodes, with the node lengths in the primary system and tube metals varying according to their corresponding secondary nodes. The mathematical formulation for the secondary side is based on mass and energy balance equations, while only energy balance equations are required for the tube metal section and primary side. The following assumptions have been made:

- Uniform secondary pressure,
- One-dimensional flow,
- Negligible axial heat conductivity,
- No phase-change in the primary side,
- One equivalent helically-coiled tube in the SG.

It shows the schematic diagram of the implemented model for HCSG. The subcooled boundary extends from the secondary feedwater inlet to the point that fluid reaches the saturated enthalpy $(h \leq h_f)$ while two-phase boundaries placed between the steam quality of $(0 < x < 1)$ and superheat section $(h > h_g)$. Each region consists of numbers of nodes with the same lengths.

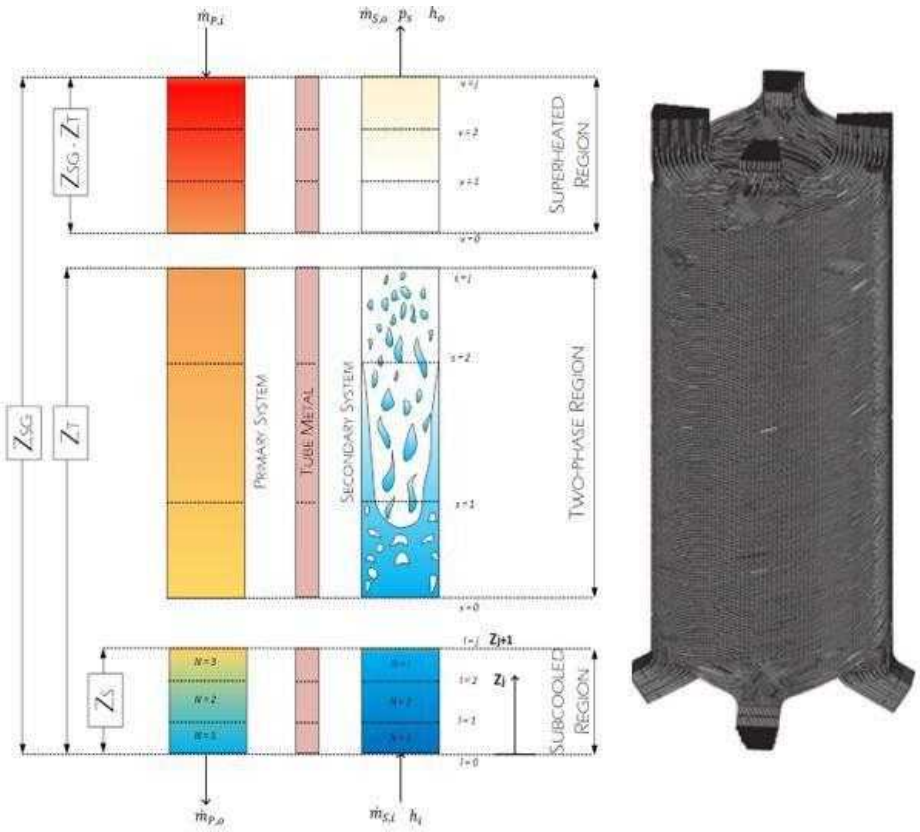

Fig. 1. HCSG model schematic.

The energy balance equation for the primary circut can be formulated as follows:

$$\rho C_p A_{pr}\left[(Z_{j+1}-Z_j)\frac{d\bar{T}_i}{dt}+(\bar{T}_i-\bar{T}_{i+1})\frac{dZ_{j+1}}{dt}\right]=n\pi D_o\alpha_o L_i(\bar{T}_{wi}-\bar{T}_{pi})+\dot{m}_p C_p(\bar{T}_{i+1}-\bar{T}_i)$$

Using this formula, a system of equations can be achieved for the primary system temperatures in each node. Upwind approximation is used for discretization of this equation. Table 1 shows the system of equations for primary system.

Table 1. System of equations for primary system.

Vol	Equation
1	$T_{p1}=(f_{p1}-a_{p1,2}\dot{Z_S})/a_{p1,1}$
2	$T_{p2}=(f_{p2}-a_{p2,2}\dot{Z_S})/a_{p2,1}$
3	$T_{p3}=(f_{p3}-a_{p3,2}\dot{Z_S})/a_{p3,1}$
4	$T_{p4}=(f_{p4}-a_{p4,2}\dot{Z_S}-a_{p4,3}\dot{Z_T})/a_{p4,1}$
5	$T_{p5}=(f_{p5}-a_{p5,2}\dot{Z_S}-a_{p5,3}\dot{Z_T})/a_{p5,1}$
6	$T_{p6}=(f_{p6}-a_{p6,2}\dot{Z_T})/a_{p6,1}$
7	$T_{p7}=(f_{p7}-a_{p7,2}\dot{Z_T})/a_{p7,1}$
8	$T_{p8}=(f_{p8}-a_{p8,2}\dot{Z_T})/a_{p8,1}$
9	$T_{p9}=(f_{p9})/a_{p9,1}$

Metal heat transport is modeled using energy balance equations. These equations are written for each node. The characteristics of the tube metal are represented through:

$$C_w\rho_w A_w\left[(Z_{j+1}-Z_j)\frac{d\bar{T}_{w(i)}}{dt}+\frac{(\bar{T}_{w(i)}-\bar{T}_{w(i+1)})}{2}\frac{dZ_{j+1}}{dt}+\frac{(\bar{T}_{w(i-1)}-\bar{T}_{w(i)})}{2}\frac{dZ_j}{dt}\right]$$
$$=n\pi\alpha_i D_i(Z_{j+1}-Z_j)(\bar{T}_{s(i)}-\bar{T}_{w(i)})+n\pi\alpha_o D_o(Z_{j+1}-Z_j)(\bar{T}_{p(i)}-\bar{T}_{w(i)})$$

Writing this equation for nodes lead to system of equations represented in Table 2.

Table 2. System of equations for metal temperature.

Vol	Equation
1	$T_{w1}=(1/a_{w1,1})*(f_{w1}-a_{w1,2}\dot{Z_S})$
2	$T_{w2}=(1/a_{w2,1})*(f_{w2}-a_{w2,2}\dot{Z_S})$
3	$T_{w3}=(1/a_{w3,1})*(f_{w3}-a_{w3,2}\dot{Z_S})$
4	$T_{w4}=(1/a_{w4,1})*(f_{w4}-a_{w4,2}\dot{Z_S}-a_{w4,3}\dot{Z_T})$
5	$T_{w5}=(1/a_{w5,1})*(f_{w5}-a_{w5,2}\dot{Z_S}-a_{w5,3}\dot{Z_T})$
6	$T_{w6}=(1/a_{w6,1})*(f_{w6}-a_{w6,2}\dot{Z_S}-a_{w6,3}\dot{Z_T})$
7	$T_{w7}=(1/a_{w7,1})*(f_{w7}-a_{w7,2}\dot{Z_T})$
8	$T_{w8}=(1/a_{w8,1})*(f_{w8}-a_{w8,2}\dot{Z_T})$
9	$T_{w9}=(1/a_{w9,1})*(f_{w9}-a_{w9,2}\dot{Z_T})$

Mass and energy balance equations should be solved to simulate the secondary system performance. The mass balance for secondary can be expressed as:

$$A_s\left[(Z_{j+1}-Z_j)\frac{d\bar{\rho}_i}{dt}+(\bar{\rho}_{i-1}-\bar{\rho}_i)\frac{dZ_j}{dt}\right]=\dot{m}_{Z_j}-\dot{m}_{Z_{j+1}} \quad 3$$

The number of unknowns will match the number of equations if density correlates with pressure and temperature in both the subcooled and superheated regions, and with void fraction in the two-phase section.

$$\begin{cases}\frac{d\bar{\rho}_i}{dt}=\frac{\partial\rho_i}{\partial P_s}|_h\frac{dP_s}{dt}+\frac{\partial\rho_i}{\partial h_i}|_{P_s}\frac{dh_i}{dt} & \text{for subcooled and superheat section}\\ \frac{d\bar{\rho}_i}{dt}=\left(\frac{\partial\rho_f}{\partial P_s}+\frac{\partial\rho_f}{\partial h_f}\frac{\partial h_f}{\partial P_s}\right)\frac{dP_s}{dt} & \text{for saturated node}\\ \frac{d\bar{\rho}_i}{dt}=\rho_{fg}\frac{d\alpha_i}{dt}+\left(\alpha_i\frac{d\rho_{fg}}{dP_s}+\frac{d\rho_f}{dP_s}\right)\frac{dP_s}{dt} & \text{for two-phase section}\end{cases} \quad 4$$

Vol	Equation
1	$a_{1\,1}\dot{P}_s+a_{1\,2}\dot{h_1}=f_{m1}$
2	$a_{2\,1}\dot{P}_s+a_{2\,2}\dot{h_2}+a_{2\,3}\dot{Z}_s=f_{m2}$
3	$a_{3\,1}\dot{P}_s+a_{3\,2}\dot{Z}_s=f_{m3}$
4	$a_{4\,1}\dot{P}_s+a_{4\,2}\dot{\alpha}_1+a_{4\,3}\dot{Z}_S=f_{m4}$
5	$a_{5\,1}\dot{P}_s+a_{5\,4}\dot{\alpha}_2+a_{5\,3}\dot{Z}_S+a_{5\,4}\dot{Z_T}=f_{m5}$
6	$a_{6\,1}\dot{P}_s+a_{6\,2}\dot{Z}_S+a_{6\,3}\dot{Z_T}=f_{m6}$
7	$a_{7\,1}\dot{P}_s+a_{7\,2}\dot{h_7}+a_{7\,3}\dot{Z_T}=f_{m7}$
8	$a_{8\,1}\dot{P}_s+a_{8\,2}\dot{h_8}+a_{8\,3}\dot{Z_T}=f_{m8}$
9	$a_{9\,1}\dot{P}_s+a_{9\,2}\dot{h_9}+a_{9\,3}\dot{Z_T}=f_{m9}$

Furthermore, secondary system energy balance is:

$$A_s\left[(Z_{j+1}-Z_j)h_i\frac{d\bar{\rho}_i}{dt}+(Z_{j+1}-Z_j)\rho_i\frac{dh_i}{dt}-(Z_{j+1}-Z_j)\frac{dP_i}{dt}+(\rho_{i-1}h_{i-1}-\rho_ih_i)\frac{dZ_j}{dt}\right] \quad 5$$
$$=\dot{m}_{i-1}h_{i-1}-\dot{m}_ih_i+n\pi D_i\alpha_i(Z_{j+1}-Z_j)(\bar{T}_{w(i)}-\bar{T}_{s(i)})$$

In the two-phase section, the heat transfer coefficient value significantly decreases in the post-dry-out regime compared to other areas within the same section. To address this, the Levitan and Borevskiy correlation has been utilized to identify nodes positioned in the post-dry-out regio

Table 4. Energy balance equations for secondary system.

Vol	Equation
1	$b_{1\,1}\dot{P}_s + b_{1\,2}\dot{h_1} = f_{e1}$
2	$b_{2\,1}\dot{P}_s + b_{2\,2}\dot{h_2} + b_{2\,3}\dot{Z}_s = f_{e2}$
3	$b_{3\,1}\dot{P}_s + b_{3\,2}\dot{Z}_s = f_{e3}$
4	$b_{4\,1}\dot{P}_s + b_{4\,2}\dot{\alpha_1} + b_{4\,3}\dot{Z}_S = f_{e4}$
5	$b_{5\,1}\dot{P}_s + b_{5\,4}\dot{\alpha_2} + b_{5\,3}\dot{Z}_S + b_{5\,4}\dot{Z_T} = f_{e5}$
6	$b_{6\,1}\dot{P}_s + b_{6\,2}\dot{Z}_S + b_{6\,3}\dot{Z_T} = f_{e6}$
7	$b_{7\,1}\dot{P}_s + b_{7\,2}\dot{h_7} + b_{7\,3}\dot{Z_T} = f_{e7}$
8	$b_{8\,1}\dot{P}_s + b_{8\,2}\dot{h_8} + b_{8\,3}\dot{Z_T} = f_{e8}$
9	$b_{9\,1}\dot{P}_s + b_{9\,2}\dot{h_9} + b_{9\,3}\dot{Z_T} = f_{e9}$

$$x_{ad} = 2.7 \left(\frac{\rho_f}{G^2 d}\right)^{1/3} \left(\frac{\sigma}{\rho}\right)^{1/4} \left(\frac{g}{\rho}\right) \quad (6)$$

For nodes with steam quality of more than x_{ad} Chen and Chen's formula is used to calculate the heat transfer coefficient. Steam mass flow rate that flows toward the turbine is obtained from

$$\dot{m}_{turbine} = K_c \sqrt{P_{SG} - P_{turbine}} \quad (7)$$

The detail of mathematical model and its derivation process is elaborated in with detail in [7].

HCSG Relap5 Model

RELAP5 code is employed to evaluate performance of the developed model. This model uses the fixed node approach. For this reason, the helical part of steam generator is divided into 30 nodes as shown in Fig. 2. The shell part of the HCSG is modeled using an annulus component comprised of 32 nodes. Vertical bundle with crossflow is the closest heat transfer model which can be used for this component. For this reason, this model is enabled for primary flow. Boundary condition of the HCSG is modeled using a set of time-dependent volumes, time-dependent junctions and single junction components. Tube side of steam generators which is comprising 1380 tubes is modeled using series of pipes with equivalent inclination angle, length and flow area. A brief specification of the steam generator is brought in Table 5.

Table 5. Specification of the NuScale reactor steam generator.

Parameter	value	Unit
Number of steam generators per NPM	2	
Number of helical tubes per steam generator	690	
Outer diameter of tubes	1.59	cm
Tube wall thickness	0.127	cm
Average length of tubes	24.2	m
Feedwater temperature	421.87	K
Main steam temperature range at nominal power	574.8-580.4	K
Outlet pressure	3.45	MPa

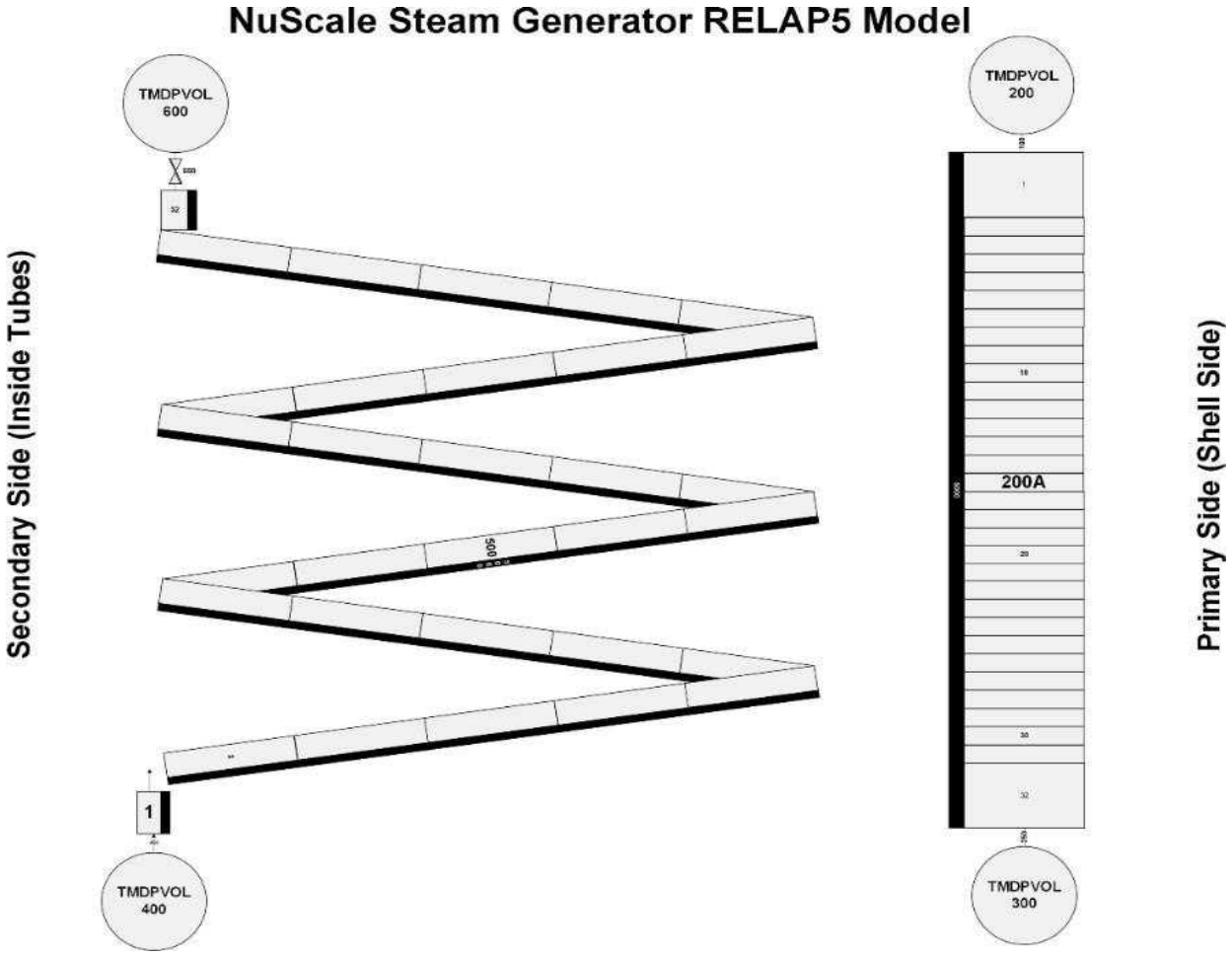

Fig. 2. RELAP5 model of HCSG.

Results and Discussion

Steady-state results calculated from RELAP5 and developed model is demonstrated in Table 6. Results shows a good agreement for the models and design data of the reactor. Furthermore, temperature profile in steady-state condition calculated by the mathematical model is illustrated in Fig. 3. It can be seen that this model calculates the temperature profile in each phase with more accuracy compared to previous works [8].

Table 6. Steady-State performance of the models.

	Design data	RELAP5	Current model
Core outlet Temperature (K)	585.9	585.9	585.9
Core inlet Temperature (K)	533.7	535.16	533.9
Feedwater inlet Temperature (K)	421.9	421.9	421.87
Steam outlet temperature (K)	575 - 580	579.83	579.73
Steam pressure (MPa)	3.45	3.45	3.45

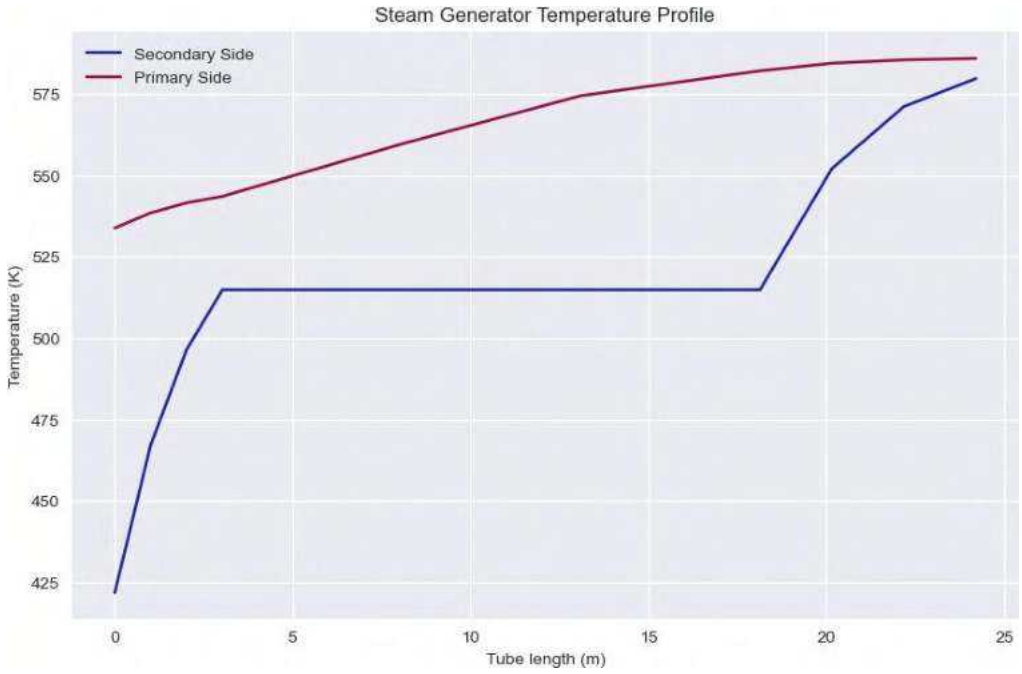

Fig. 3. HCSG temperature profile for primary and secondary side based on developed model.

In this study, two scenario is considered to evaluate model performance during transient conditions. The detail of these scenarios is brought in the following sections.

Ramp Changes of the Feedwater Flow Rate

In this scenario, as depicted in Figure 4 (a), it is assumed that a gradual decrease in the feedwater flow rate begins at 100 seconds. Over a span of 300 seconds, the feedwater is reduced by 5%. Subsequently, the feedwater value remains constant for 10 minutes, after which it gradually increases over a duration of 1 minute to its nominal value. The results from the two codes are compared in Figure 4, which reveals a similar trend of changes for both codes.

The pressure of the secondary system is directly related to the feedwater flow rate, meaning that as the feedwater flow increases, the pressure in the steam generator also increases. This relationship is demonstrated in Figure 4 (c), which displays the pressure variation during the transient and highlights its proportional correlation with the feedwater flow. It is worth noting that both codes calculated the same value for the pressure decrease in the given scenario.

Accurately calculating the primary side outlet temperature is crucial because its fluctuations can impact the core inlet temperature. Figure 4 (b) depicts the response of the primary side outlet temperature to the transient in feedwater. The results indicate that both RELAP5 and the developed code accurately calculate the same temperature decrease during the transient for the core inlet temperature.

Figure 4 (d) demonstrates the impact of a 5% ramp decrease and subsequent increase in feedwater flow rate on the steam temperature. It reveals that the steam temperature rises accordingly, aligning with the expected behavior. While both methods employed exhibit a consistent trend in steam temperature, there are slight differences of approximately 1 degree in the final values. This can be attributed to the significantly lower specific heat capacity of the superheat section and its sensitivity in the case study SG compared to the primary and other SG sections. As a result, even minor disparities between the heat transfer models and the length of the superheat section can lead to temperature variations between RELAP5 and the mathematical model.

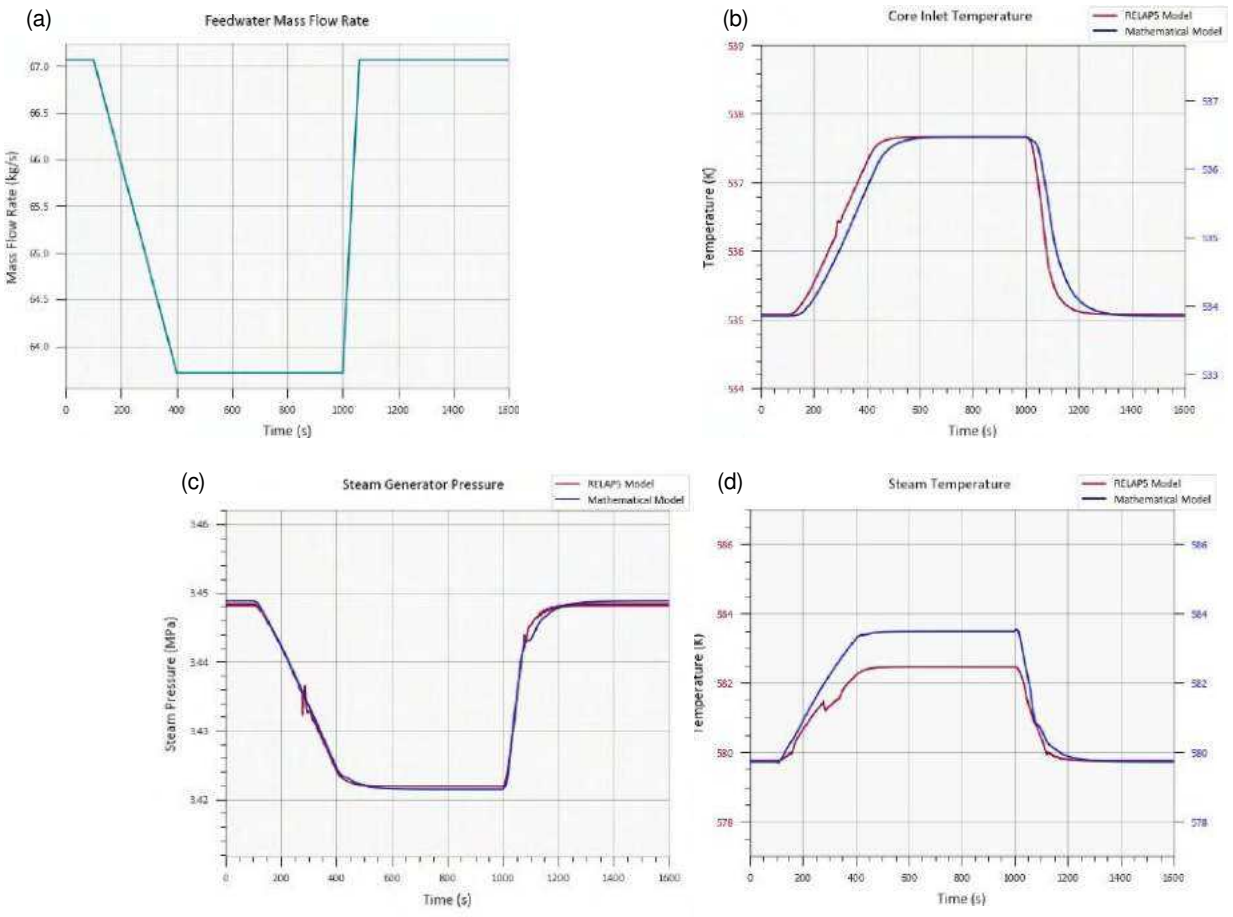

Fig. 4. System response to the 5% ramps in feedwater flow rate.

Ramp Changes of The Feedwater Flow Rate

The primary system's temperatures and flow are interconnected in the NuScale reactor's primary loop, which operates through natural circulation. This means that any power transient in the core leads to fluctuations in both the primary flow and temperatures. Figure 5 (a, b) demonstrate the changes in the primary system parameters resulting from the application of ramp reactivities to the reactor core. The response depicted in the figure is calculated using a RELAP5 model of the reactor that was developed in previous research [9].

In this particular scenario, both the mass flow rate and inlet temperature of the primary circuit undergo changes over time. The results indicate that an increase in the inlet temperature of the SG leads to a corresponding rise in the steam outlet temperature, as illustrated in Figure 5 (f).

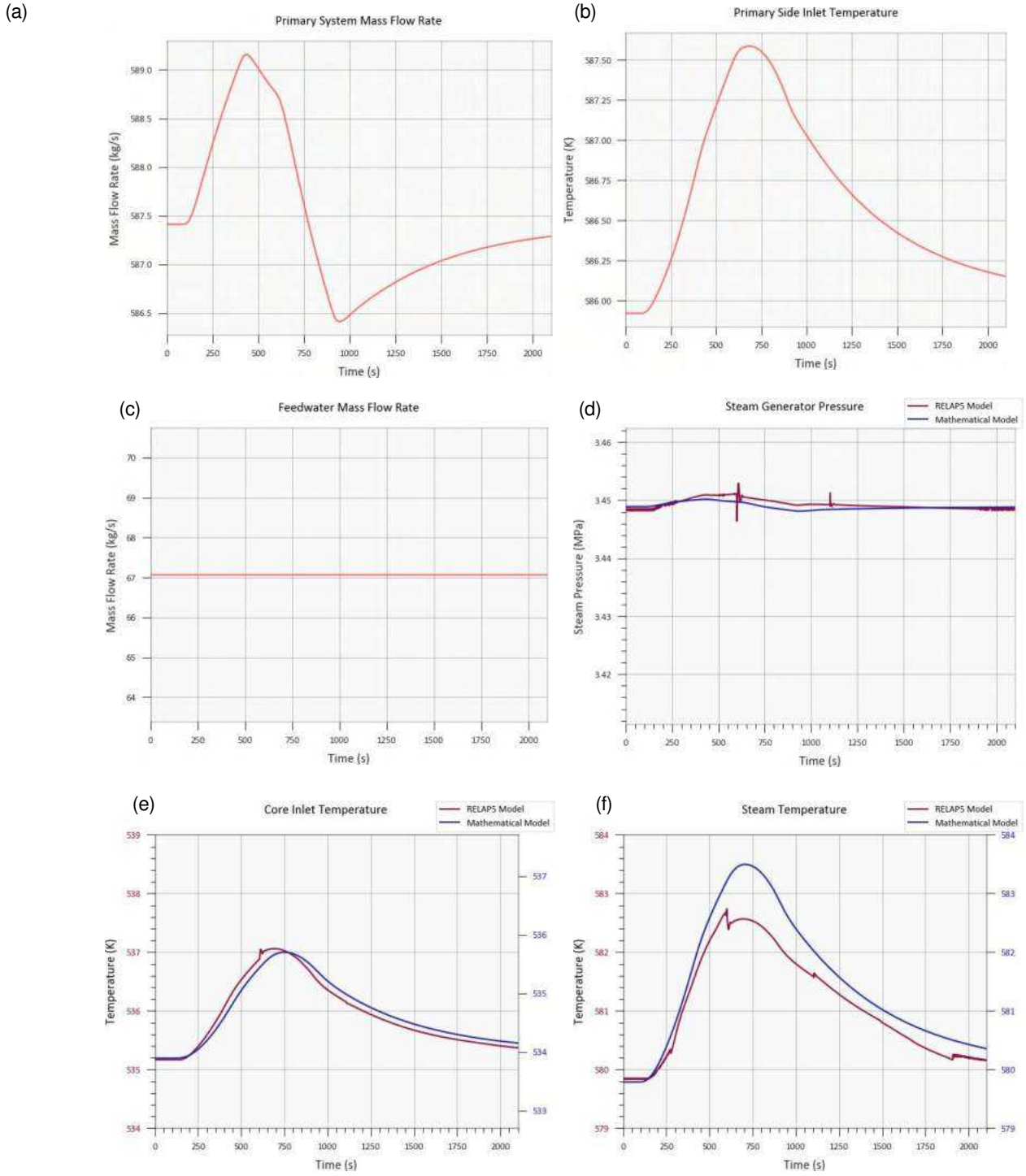

Fig. 5. System response to transients in primary parameters.

Additionally, the variation in the primary mass flow rate has an impact on the secondary pressure, as shown in Figure 5 (d).

In this scenario, an increase in the primary inlet temperature causes an elevation in the steam temperature. However, the secondary side of the system is unable to effectively remove all the generated power from the primary. Consequently, the primary exit temperature experiences an increase, as depicted in Figure 5 (e).

The results demonstrate that both codes produce similar trends. However, there are instances where the RELAP5 results exhibit discontinuities, such as at 600 seconds in Figure 5 (f). To assign accurate heat transfer coefficients to each volume, codes with fixed nodes are required to determine the flow regime at each time step. Consequently, during points of flow regime changes in certain nodes, it is noticeable that some discontinuities emerge in the results when using the moving boundary model. This model, however, is capable of calculating the results with greater precision because there is no physical phenomenon that corresponds to these discontinuities.

Conclusions

In this research, performance of the multi-node moveable boundary model is evaluated and compared with RELAP5 code. The secondary side of SG is divided into three regions and linked with primary and tube metal equations. Each region has its own formulation and heat transfer coefficients. Calculated results show a good agreement between the design data of the reactor and simulations. Also, a RELAP5 model of SG is developed. The model's response to several transients in the model's inputs is calculated and compared with the RELAP5 code. It is observed that the trend of transient responses was similar in all cases. The change in final values for pressure and primary outlet temperature was in good agreement between the developed model and RELAP5. Due to the different nature of equations and solving methods of the two codes, there was a slight difference between the results for steam temperature. However, the overall behaviors were identical.

References

[1] Secker, P. and J. Gilbert, Status of CHAP: composite HTGR analysis program. 1975, Los Alamos Scientific Lab.

[2] Kerlin, T., HTGR steam generator modeling. 1976, Oak Ridge National Lab.

[3] Tzanos, C.P., A semianalytic method for the solution of the steady-state steam generator equations. Nuclear Technology, 1988. 80(3): p. 380-391.

[4] Tzanos, C.P., A movable boundary model for once-through steam generator analysis. Nuclear Technology, 1988. 82(1): p. 5-17.

[5] Berry, G., Model of a once-through steam generator with moving boundaries and a variable number of nodes. 1983, Argonne National Lab., IL (USA).

[6] Jensen, J.M. and H. Tummescheit. Moving boundary models for dynamic simulations of two-phase flows. in Proc. of the 2nd int. modelica conference. 2002. Oberpfaffhenhofen Germary.

[7] Fakhraei, A., et al., DYSN: Dynamics simulator for the NuScale SMR-A mathematical framework for transient analysis. Progress in Nuclear Energy, 2024. **170**: p. 105128.

[8] Arda, S.E. and K.E. Holbert, Nonlinear dynamic modeling and simulation of a passively cooled small modular reactor. Progress in Nuclear Energy, 2016. **91**: p. 116-131.

[9] Fakhraei, A., et al., Safety analysis of an advanced passively-cooled small modular reactor during station blackout scenarios and normal operation with RELAP5/SCDAP. Annals of Nuclear Energy, 2020. **143**: p. 107470.

ICNST 2024 International Conference on Nuclear Science and Technology
6- 8 MAY 2024 | Isfahan, Iran

Dynamic Probabilistic Safety Assessment of primary to secondary leak Accident in VVER-1000 (Paper ID : 1254)

Kordalivand S. Correspondent[1*], Abaszadeh A[1]., Varchandi A[1].

[1]NPPs Safety Development & Improvement, TAVANA, Tehran, Iran

Abstract

Probabilistic safety assessment (PSA) based on event trees and fault trees has been widely used in the safety assessment of nuclear power plants. Integrated Deterministic and probabilistic safety assessment (IDPSA) is a complementary methodology that considers dynamic scenarios between the system and human operations by interfacing physical simulation with thermohydraulic models for safety assessment. This paper proposes to apply IDPSA for assessing the primary-to-secondary leak accident in a WWER-1000 nuclear power plant. This accident has been modeled using the thermohydraulic code RELAP5. In this accident, the BRU-A valve was critical role in removing heat from the primary side. Therefore, the opening time of the BRU-A valves, which allows them to open without causing Core Damage (CD) is examined. This calculated duration, referred to as Time Window (TW) in the reliability model of BRU-A valves, is compared with CD frequency resulting from this accident, and is analyzed against the normal TW (24) in the PSA level 1.

Keywords: IDPSA, RELAP5, WWER-1000

Introduction

Nuclear power plants (NPPs) are vital role in addressing the increasing global energy needs. However, their operation comes with inherent complexities and potential risks. Prioritizing the safety and reliability of NPPs is paramount, requiring the utilization of advanced methodologies for thorough risk assessment [1]. Probabilistic Safety Assessment (PSA) emerges as a systematic and quantitative approach, providing a comprehensive understanding of the risks associated with different components and systems within an NPP [2]. In this paper, after simulating different scenarios using the RELAP5 code, the Core Damage Frequency (CDF) has been calculated by PSA level 1. IDPSA is conceived as a way analyze the evolution of accident scenarios in complex dynamic systems, like nuclear, aerospace and process ones, accounting for the mutual interactions between the failure and recovery of system components, the control and operator actions, the software and firmware [3].

RELAP5 model

The RELAP5 model of the WWER-1000 was developed to analyze operational occurrences, abnormal events and design basis scenarios, providing significant analytical capability for WWER-1000 safety specialists. This paper utilizes the RELAP5/MOD3.3 code to analyze transient states and simulate events for light water reactor using best estimate methods. One of the key principles in preparing the thermo-hydraulic model involves considering horizontal and vertical dimensions, equipment placement angles, and channels. Figure 1 illustrates the thermal-hydraulic model of the WWER-1000 reactor [3]. In order to evaluate the qualification of the nodalized model of WWER-1000, calculated hydrodynamic volumes, heat transfer areas in critical region, piping length and mass of metal structures are compared with corresponding reference values which are presented in last revision of the FSAR, technical and manufacturing reports (Table 1). To confirm the validity of the simulations, some critical parameters are obtained by RELAP5, in steady-state, and compared with the Final Safety Analysis Report (FSAR) of WWER-1000 reactor. The results indicate the accuracy and benchmarking of the input model in a steady-state case (Table 2). The calculation considers an accident scenario with a break in the steam generator cold collector. The analysis focuses on the most conservative version of damage, an instantaneous break with an equivalent diameter of 100 mm in the area of the lower row of heat-exchanging tubes in the steam generator.

Table 1.Comparison between the model parameters and corresponding reference value

COMPONENT	CALCULATED VALUE	REF. VALUE (FSAR)	ERROR OF CALCULATION, %	REFERENCE
		HYDRODYNAMIC VOLUME [M³]		
REACTOR (WITH NOZZLES)	111.944	111	0.851	[4]
SG (PRIMARY SIDE)	21.169	21	0.807	[5] [6]
SG (SECONDARY SIDE)	128.176	125	2.540	[5] [6]
MAIN COOLANT PIPELINES (WITHOUT NOZZLES)-4 LOOPS	93.817	93	0.878	[5] [6]
PRESSURIZER	79.032	79	0.040	
REACTOR COOLANT PUMP (WITH NOZZLES)	5.986	3	-	[5] [6]
PRIMARY COOLANT SYSTEM	394.826	391.6	0.817	[5] [6]
		HEAT TRANSFER AREA [M²]		
REACTOR CORE	5144.789	5144	0.015	[4]
SG TUBES	6034.587	6036	0.023	[5] [6]

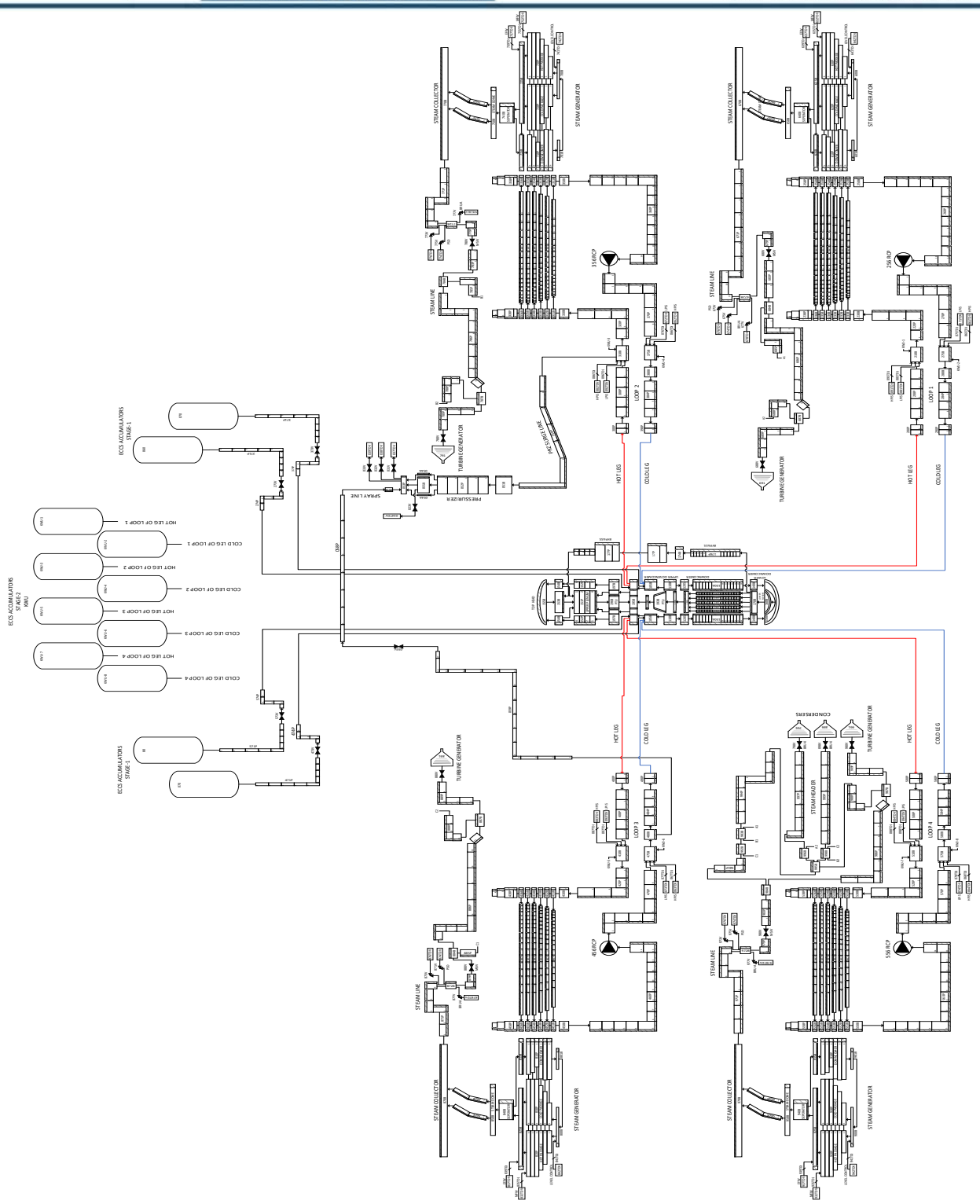

Fig. 15. WWER-1000 reactor nodalization [3]

Table 2. Validation of RELAP5 and FSAR code results in the steady-state.

parameters	relap5 value	wwer-1000 (fsar)
nominal heat power of the core (mw)	3000	3000
the flow rate through the cold leg with the operation of four loops (m^3/h)	21,288	21200 ± 1200
fraction of coolant leaks bypassing the core	4.0	4.0
coolant pressure at the core outlet (mpa)	15.733	15.7 ± 0.3
coolant temperature at the core inlet (^oc)	292.311	291 ± 5
coolant temperature at the core outlet (^oc)	323.411	321 ± 5
steam pressure in the sg header (mpa)	6.24	6.27 ± 0.1

A primary-to-secondary leak can result in a long-term loss of coolant beyond the boundaries of the containment, leading to the release of radioactive into the atmosphere and potentially causing a loss of reactor core cooling [4]. To prevent or significantly decrease the release of radioactive coolant through the steam dump devices of the affected steam generator, a unique automatic algorithm for accident management is introduced at the initial state of the accident. This algorithm consists of a sequence of action involving various systems.

In this paper, three REPLAP5 scenarios are simulated. The first scenario involves simulating the primary-to-secondary leakage accident and comparing its results with the FSAR. The event sequence of the second scenario is similar to the first scenario. but it assumes that with the increase in pressure in the SGs, the BRU-A valve does not open, eventually the fuel clad temperature reaching Core Damage Criteria (CDC) in PSA calculations. In the third scenario, the time needed to open the BRU-A valve has been calculated, provided that the reactor core is not damaged and coolant and clad temperature decrease.

Result of Relap5

Scenario 1: The automatic algorithm within the framework is aimed at maintaining pressure in the RP primary system at a level that prevents the safety valve of the affected SG from opening. This involves injecting boron solution into the PRZ using pumps from the additional boron injection system and accelerating the RP cooldown through BRU-A of intact SGs. The following sequence of automatic actions of the system and equipment is assumed in performing calculations for accident management:

Closing of BRU-A on the affected SG steam line at a primary pressure decrease down to 8,0 MPa or an increase in the collapsed level in the affected SG of over 3,0 m from the lower SG generatrix.

Start-up of the additional boron injection system for injection into the PRZ involves transferring the pumps of the system into operating condition via recirculation line when the PRZ level increases above

the nominal value. Boron solution injection resumes when the PRZ level decreases below the nominal value.

The following actions are taken as part of the automatic algorithm for accident management:

Closing of the MSIV and cut-off motor-operated gate valve on the steam line of the affected SG

Cooldown of the primary system through BRU-A of operable SGs with automatic maintenance of a cooldown rate of 60 ^{o}C/h.

Closing of the gate valves on the lines of feedwater supply and blowdown of the affected SG.

Disconnection with prohibition for all THE groups in PRZ to be connected

All MSIV and cut-off gate valves closed in response to a signal of pressure decrease in the steam line of the SG down to 4,9 MPa under an increase in the difference between saturation temperature of the primary and secondary side above 75 ^{o}C

Closing of valves on the line of the main and auxiliary feedwater in response to a signal of pressure decrease in the steam line down to 4,4 MPa under an increase in the difference between saturation temperature of the primary and secondary side over 75 ^{o}C and coolant temperature of the primary system over 150 ^{o}C.

Table 3 .Event sequence of scenario 1 [4]

Time moment, s (FSAR)	Time moment, s (RELAP5)	Event	Interlock, setpoint for actuation or other reason
0,0	0,0	Break of SG 2 cold collector	Initiating event
9,75	9,75	RCP set trip of affected loop	By the fact of increase in affected SG collapsed level by 200 mm from the nominal value
10,0	10,0	Signal generation due to increase in gamma - activity in the steam line of affected SG 2	Reaching of setpoint of radiation signal
10,8	10,8	Trip of primary makeup-blowdown system Trip of the main and auxiliary feedwater of the secondary side BRU-K disconnection Trip of all RCP sets Loss-of-power supply to pressurizing system of the primary coolant (injection and PRZ heaters)	Loss-of-power supply to the power unit auxiliaries
11,2	11,7	Scram signal generation	Due to pressure decrease above the core to 14,7 MPa at reactor power over 75 % Nnom
11,4	12,0	Closing of TG stop valves	Loss-of-power supply to the power unit auxiliaries

11,75	12,1	Generation of signal "Primary–to-secondary leak" and start-up of automatic algorithm: - start-up of two pumps of additional boron injection for injection into PRZ; - prohibition against connection of all PRZ TEH groups; - isolation of affected SG 2 by feedwater and blowdown; - MSIV and cut-off motor–operated gate valve closing on the steam line of affected SG 2; - BRU-A opening of operable SG and their transition into cooldown condition at the rate of 60 °C/h	By the fact of coincidence of the following signals: - increase in gamma - activity in steam line of affected SG 2; - level in affected SG 2 over H nom + 300 mm
12,5	13,0	Beginning of control rod motion	Action of emergency protection
12,8	12,8	Start-up of diesel-generators and their loading by the program of stepwise start-up	Loss-of-power supply to the power unit auxiliaries
13,5	13,0	SG 2 BRU-A opening	Setpoint for BRU-A opening - 7,154 MPa is reached
41,75	41,75	Beginning of injection into PRZ from additional boron injection system pumps	Action of automatic algorithm
130,0	130,0	Closing of BRU-A on the steam line of affected SG 2 by the fact of pressure decrease above the core below 8,0 MPa	Signal from automatic algorithm
1295,0	2129,0	Signal for emergency feedwater supply to SG 3, 4	By the fact of collapsed level lowering in operable SGs Hnom - 900 mm from nominal level
1800,0	1800,0	Opening of the valves on the line of system of emergency gas removal from the reactor	Actions of the operative personnel
2200,0	2200,0	Closing of valves on the line of system of emergency gas removal from the reactor	Actions of the operative personnel
2320,0	3000,0	Filling of operable SGs 3, 4 to the nominal boiler water level – 2,4 m	-

Due to a break in the SG 2 collector with an equivalent diameter of 100 mm, there is a coolant leak from the primary system into the affected SG. This leak caused the water level in the affected SG to increase from the nominal value. Consequently, the RCP set of loop 2 was tripped at 9,75 seconds. The loss of coolant in the primary system resulted in a decrease in pressure, reaching the set point for reactor scram at 11,2 seconds into the transient. The closing of the TG stop valves led to a sudden rise in secondary coolant pressure, and the BRU-A opened on the affected SG 2 steam line at 13,0 seconds. Due to the primary-to-secondary coolant leak, the operation of steam dump devices on the secondary side, and the reactor scram, the BRU-A on the steam line SG 2 closed at 130,0 seconds due to pressure decrease above the core, which dropped below 8,0 MPa. As a result, the steam-water mixture continued to flow through BRU-A until this time. The emergency feedwater supplied from the AFWP into SG 3 and 4 caused the coolant in the pressure chamber to cool down. This, combined with the operation of the additional boron injection system for injection into the pressurizer, led to a decrease in primary pressure to the level of restoring supply from the emergency boron injection pumps for leak compensation. This action prevented the repeat of control of the SG.

The opening of valves on the line for emergency gas removal from the reactor top head at 1800,0 seconds, along with the operation of the additional boron injection system for injection into the PRZ, further decreased the primary pressure and dropped the level in the emergency SG. After 2200,0 seconds from the onset of the transient, the pressure in the primary circuit and the emergency SG increased and stabilized at 7,4 MPa by 3000,0 seconds.

Figures 2-7 show the results obtained from RELAP5 and their comparison with FSAR.

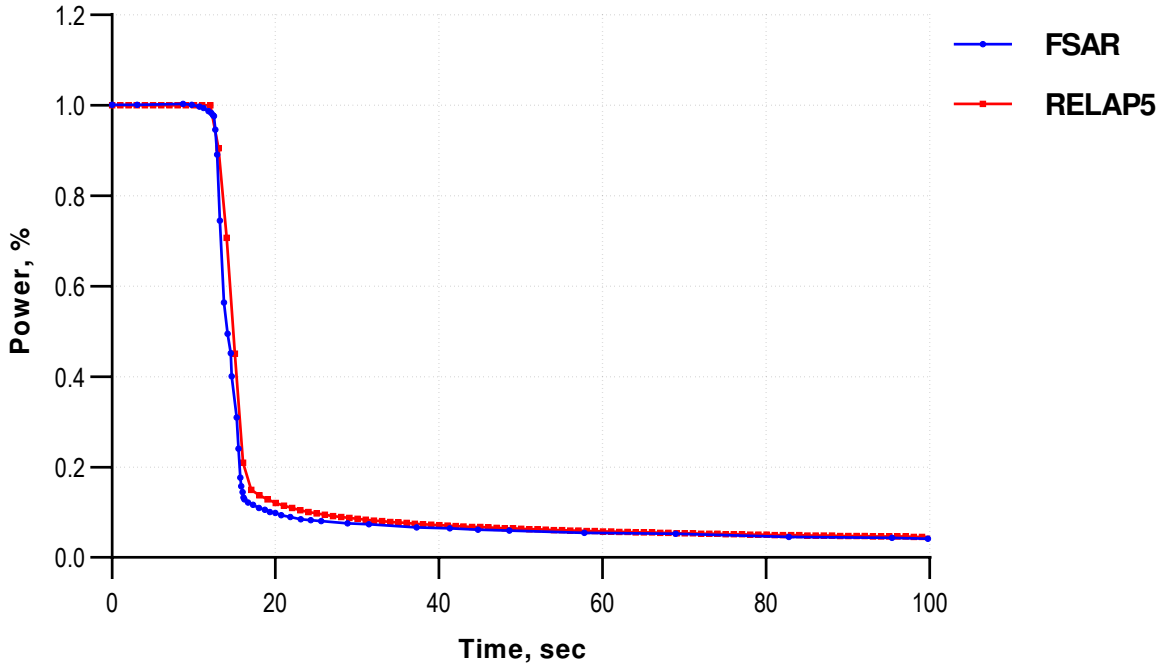

Fig. 16. Core relative power (Scenario 1)

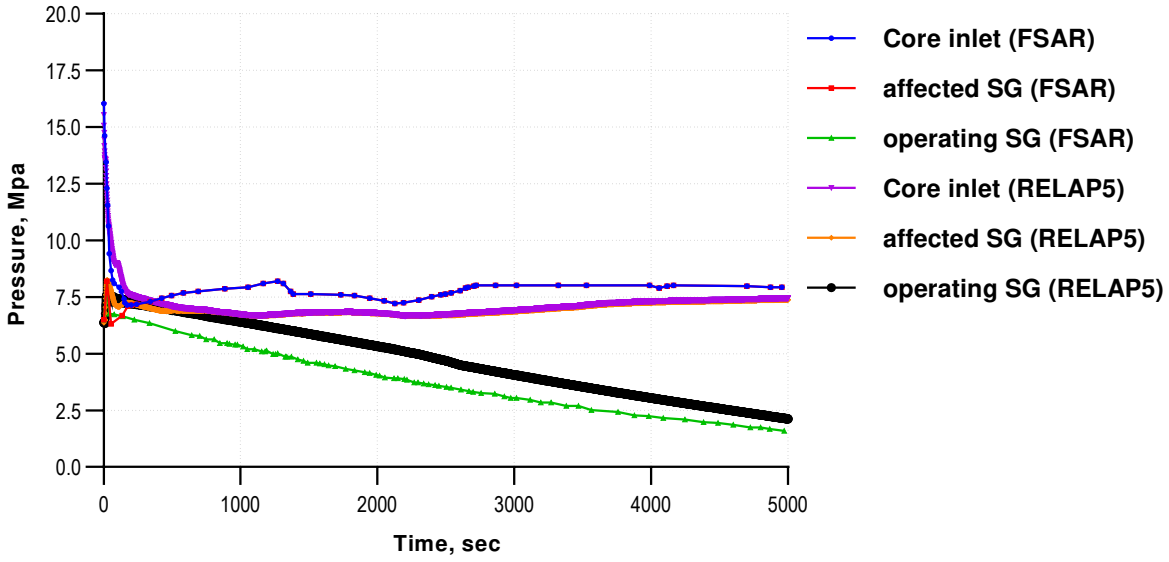

Fig. 3. Pressure at the core inlet and operating and affected SGs (Scenario 1)

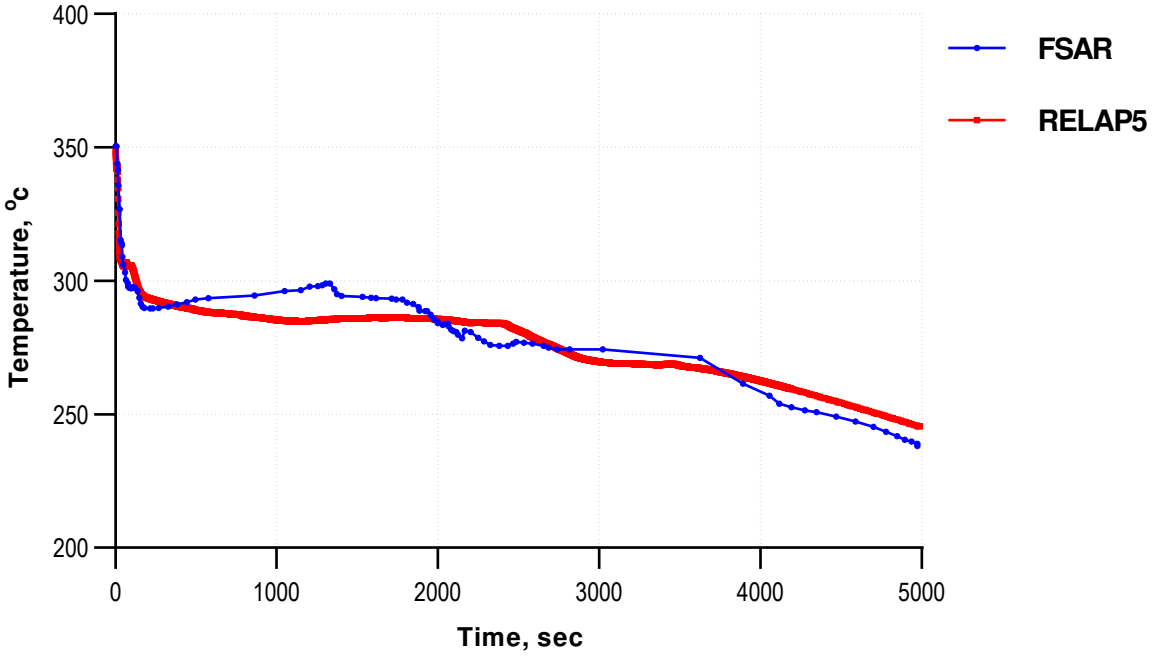

Fig. 4. Maximum fuel rod cladding temperature (Scenario 1)

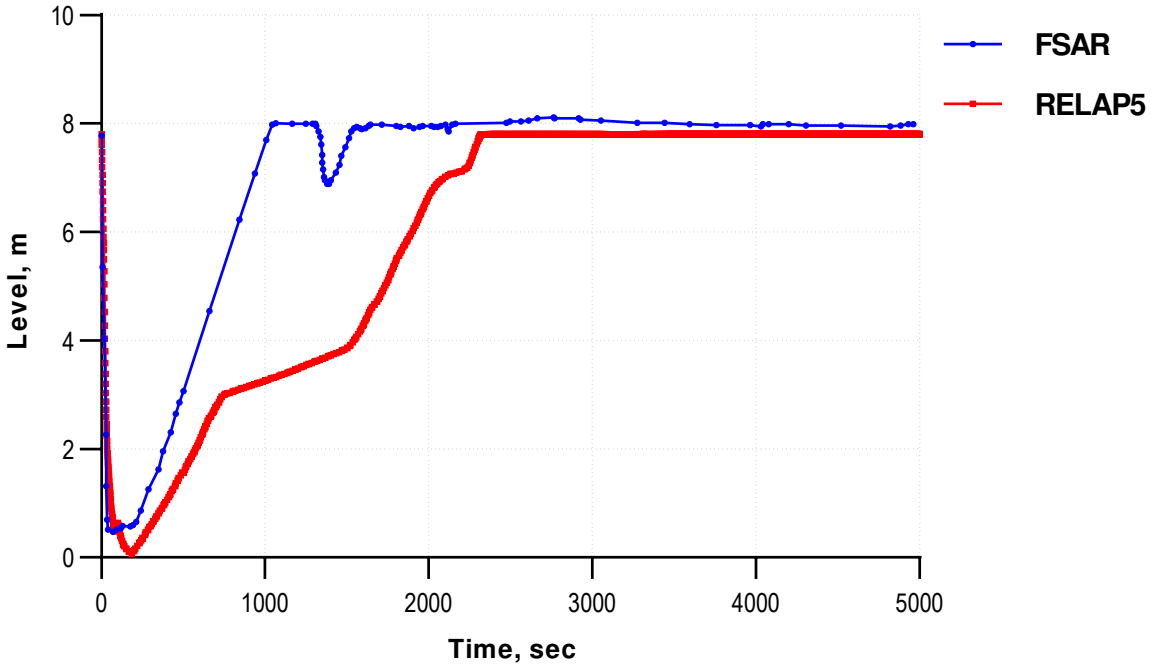

Fig. 5. PRZ level (Scenario 1)

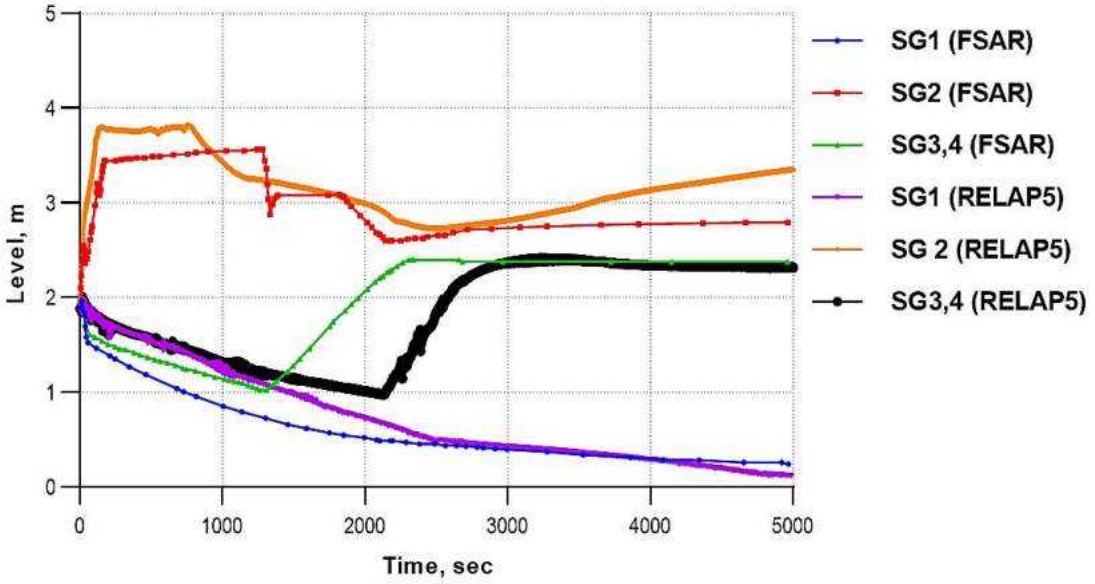

Fig. 6. Collapsed level of boiler water in SGs (Scenario 1)

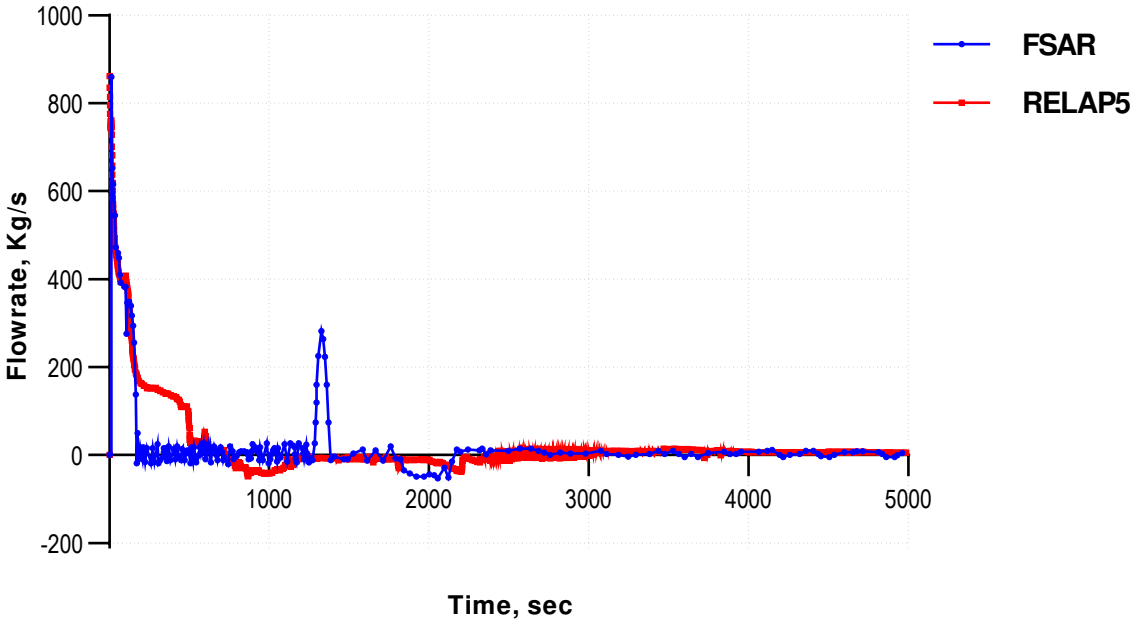

Fig. 7. Break of steam generator collector Dnom 100mm (Scenario 1)

Scenario 2: in this scenario, it is assumed that the BRU-A valves will not open when the pressure in the SGs increases. Therefore, the sequence of events until the 13th second will be similar to scenario 1. With the rise in temperature in the core of the reactor, the fuel clad temperature will reach CDC and the core will be damaged. The time obtained from the second scenario determines the time required for BRU-A valves to open to prevent core heat-up (scenario 3). Figure 8 shows the result of scenario 2. As can be seen, the fuel clad is damaged at 14100,0 seconds.

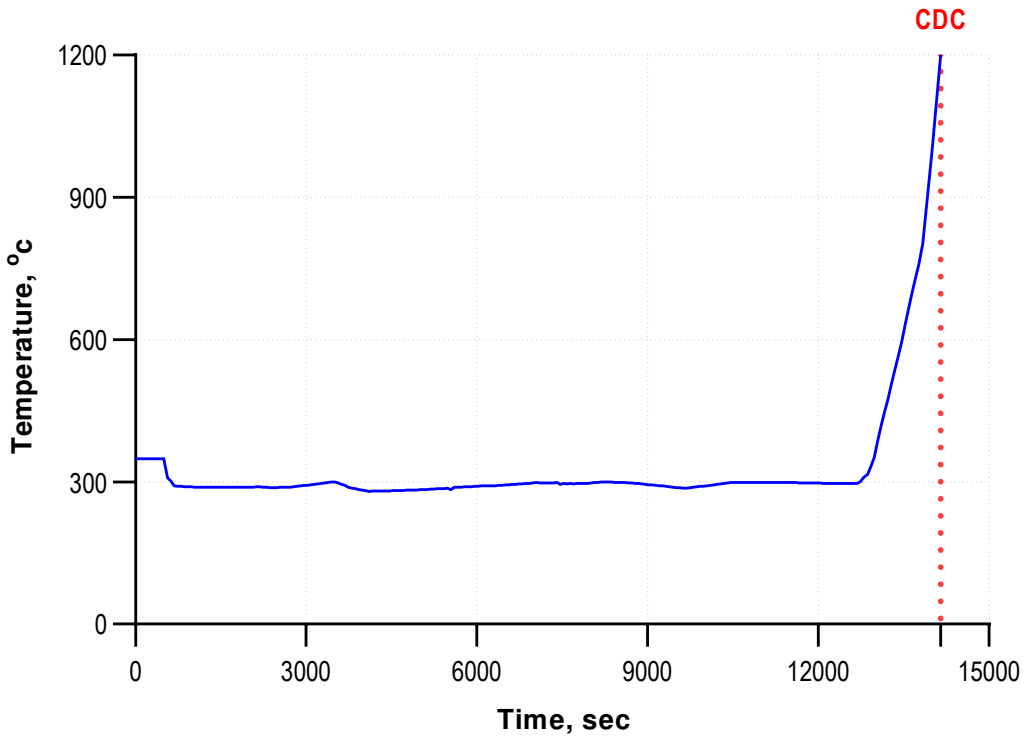

Fig. 8. Maximum fuel rod cladding temperature (Scenario 2)

Scenario3: in this scenario, it is assumed that only one valve (BRU-A, 1) out of 4 valves is opened within 3 hours and 40 minutes after the start of the accident, as a result, the temperature of primary side will decrease, and damage to the clad will be avoided. But if this time takes too long, opening the BRU-A valves will be useless. In Figure 9, it can be seen that by operating the BRU-A valve, the reactor will proceed toward cooling and reach a stable and controllable state.

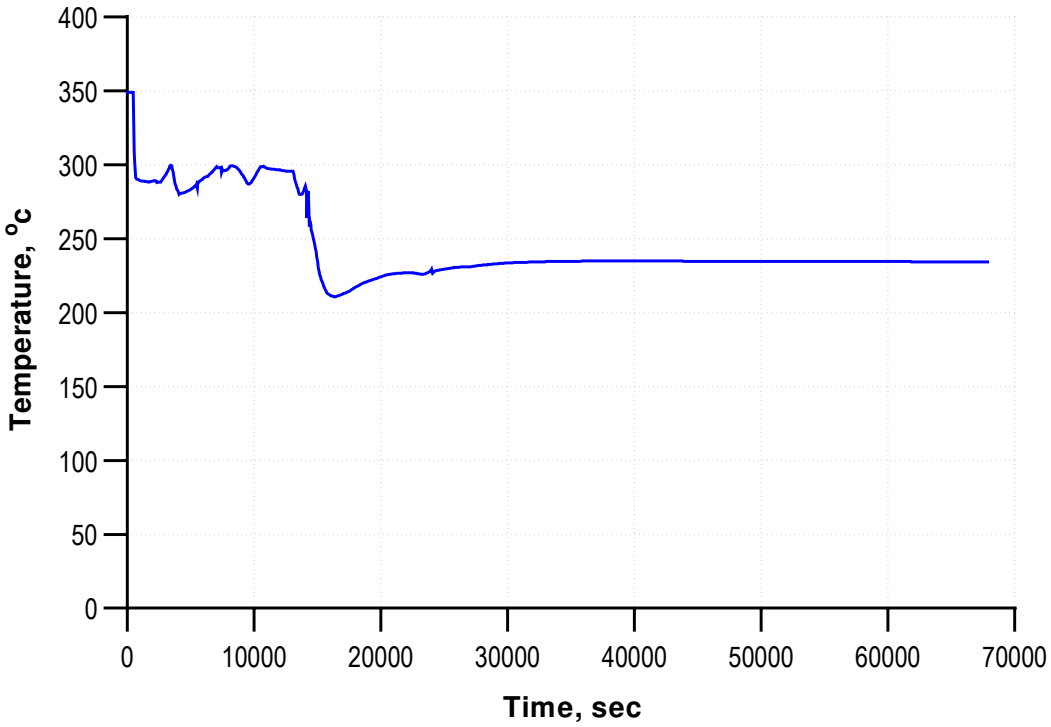

Fig. 9. Maximum fuel rod cladding temperature (Scenario 3)

In this accident, the BRU-A valve played a critical role in removing heat from the primary side. Therefore, the opening time of the BRU-A valves, which allows them to open without causing Core Damage (CD) is examined. This calculated duration, is referred to as Time Window (TW) in the reliability.

PSA Model

The Event Tree for the primary-to-secondary leak accident in a WWER-1000 nuclear power plant is shown in figure 10. The branch highlighted in this event tree is considered for IDPSA analysis. As you see, in the first step, it is assumed that BRU-K doesn't open, and the actuated of BRU-A is needed. For this assumption, there are two states: BRU-A success and BRU-A failure.

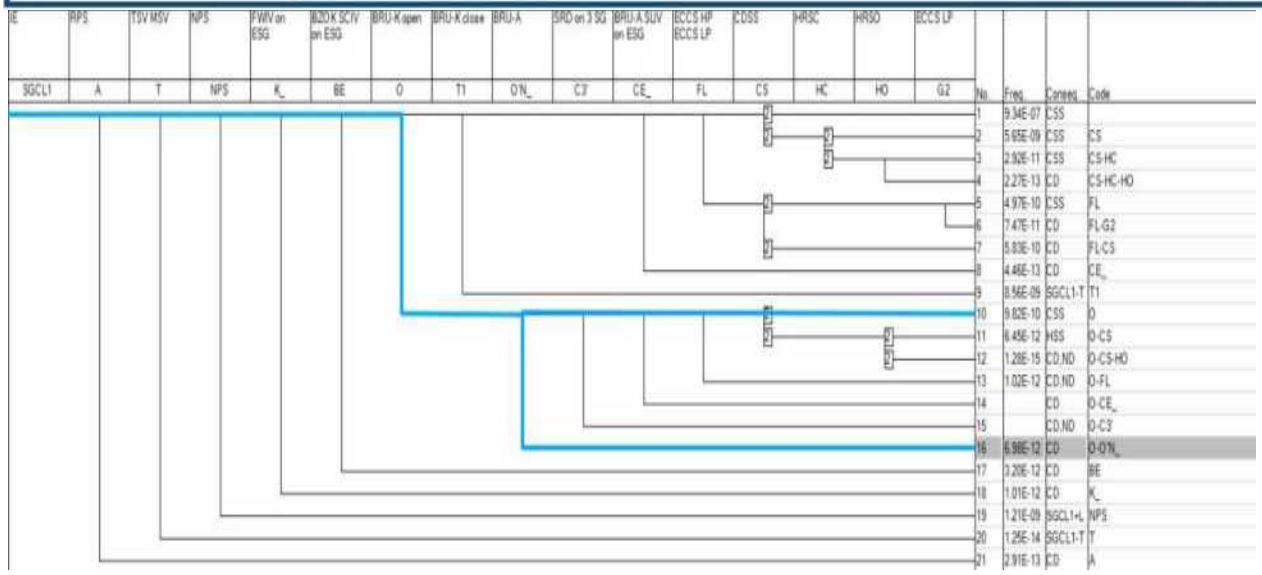

Fig. 10. Event Tree of leak primary to secondary accident in a WWER-1000 nuclear power plant

IDPSA

For branch failure of BRU-K and BRU-A, the mission time is equal to 24 hours (which is usually used for PSA level 1 calculation) and the core damage frequency is 4.30E-13. In this paper and related to the results of deterministic analysis by RELAP5, the mission time for the remaining one of 3 BRU-A valves and the non-opening of 2 other BRU-As in intact trains is 20.6 hours. By replacing this value with mission time in the PSA model, the core damage frequency According to this mission time is 6.98E-12

Conclusion

Based on the obtained results, it was observed that in case of automatic operation of the algorithm, there will be no damage to the core of the reactor (scenario 1), if the operation of the BRU-A valves is disturbed, there will be a possibility of damage to the core of the reactor (scenario 2).

The point that should be made about the deterministic analysis is that due to the decrease in the mission time of the BRU-A valve and replacing of PSA model, the CD frequency will also be decreased but on other side due to the consideration 2 valves out of service and loss of redundancy that are anticipated CD frequency will increase. Taking into account these two effects the CD frequency of the sequence has increased which shows that the loss of redundancy contribution is bigger.

References

[1] Akbari, R. and Cammi, A., 2024. The longevity of light water-cooled large-scale nuclear reactors: A holistic perspective. Nuclear Engineering and Design, 417, p.112830.

[2] S. Kordalivand, R. Akbari, M. Abbasi., quantifying the impact of risk mitigation measures using SPAR-H and RCM Approaches: Case study based on VVER-1000 systems, Nuclear Enginnering and Design, 2024, 113174.

[3] Enrico Zio, integrated deterministic and probabilistic safety assessment: Concepts, challenges, reserch directions, Nuclear Engineering and Design, Volume 280, 2014.

[4] A. Abaszadeh, F. Faghihi, study and assessement of the newly proposed passive management of MSLB + SBO accident for the VVER 1000/V446 NPP using the secondary side Deaerator tank, Annals of Nuclear Energy, 2023, 109545.

[5] BNPP-1 , Final Safety Analysis Report, FSAR, Ch 4, 2015.

[6] BNPP-1 , Final Safety Analysis Report, FSAR, Ch 6, 2015.

[7] BNPP-1 , Final Safety Analysis Report, FSAR, Ch 15, 2015.

[8] Nematollahi, M.R. and Zare, A., 2008. A simulation of a steam generator tube rupture in a VVER-1000 plant. Energy Conversion and Management, 49(7), pp.1972-1980.

ICNST 2024 International Conference on Nuclear Science and Technology
6- 8 MAY 2024 | Isfahan, Iran

Sensitivity and Uncertainty Analysis of Halden Reactor Fuel Using SUAP Code (Paper ID : 1268)

Fathi M.[1*], Saffari A.H[2]

[1] *Nuclear Reactors Fuel Company, Isfahan, Iran*

[2] *Advanced Nuclear Computing Center, Tehran, Iran*

Abstract

Probabilistic uncertainty and sensitivity analysis are frequently recommended for safety and reliability assessment of computer simulations. For this purpose, SUAP code (Sensitivity and Uncertainty Analysis using Probabilistic method) is developed. SUAP code is a powerful toolkit for uncertainty and sensitivity analysis of computer simulations, and in a joint work with the International Atomic Energy Agency, SUAP code is coupled with PART code (Performance Analysis of the fuel Rod in Transient conditions) which is developed by Advanced Nuclear Computing Center (ANCC) to perform sensitivity and uncertainty analysis, as well as automatically extract desired results from the output files. SUAP code provides support to properly quantify input uncertainties as to probability distributions and appropriate dependency functions. In this joint work, the Atomic Energy Organization of Iran succeeded in performing sensitivity and uncertainty analysis For the parameters related to the fuel rod. In this article, we intend to present the results related to the internal pressure of fuel rod at the peak power / burst node for the desired fuel rod (IFA 650.10) to simulate the LOCA scenario, and the results were in good agreement with the experimental results.

Keywords: Uncertainty and Sensitivities analysis, Monte-Carlo sampling, Spearman's rank ordered coefficient, fuel performance analysis, reliability and safety analysis.

Introduction

In deterministic safety analyses, it has become a common practice to apply best estimate computer codes for modeling. If a best-estimate code is used in combination with realistic input data, it is generally required that important uncertainties which may affect the computational result be considered and their influence on the result be quantified [1]. There are several sources of uncertainties which may affect the computational results. One of the most important sources is the model formulations implemented in a computer code. They are mostly based on a limited number of measurements in some specific condition, or may be rather simplified. So that, the accuracy level of such a model -even a validated model - may not be precisely known. The next effective uncertainty source is numerical solution algorithms which

commonly includes approximations and simplifications affecting the result, and usually are not exactly known. Another source that may have an inevitable role in the uncertainty of the results is geometrical tolerances that are acceptable in manufacturing process [2]. The most commonly used method to account for the uncertainty sources of a computational result and to get a quantification of their influence, is the Monte Carlo (MC) Method. It considers a range of values instead of just one value for each input parameter of the computer code subjected to uncertainty analysis. Each value selected for an uncertain input parameter is combined with values selected for other uncertain parameters and the whole package is supplied as input to corresponding computer code runs. Based on the sampled values finally provided for a computational result, a quantification of the uncertainty of the result is obtained by applying statistical methods [3,4,5,6]. To identify and prioritize the main uncertainty sources of a computational result, an additional sensitivity analysis is required [7,8]. It reveals the extent to which outputs from a simulation model depend on each uncertain input parameter. It also can show where to improve the state of knowledge in order to reduce the uncertainty of the computational result most effectively [9]. To facilitate the implementation of uncertainty quantification and sensitivity analysis based on the MC sampling method, the toolkit SUAP has been developed using LabVIEW [10]. SUAP has a comfortable graphical user interface (GUI) which enables the user to fully concentrate on the analysis input, i.e., the proper mathematically definition of those input parameters represent the uncertainty resources of the modeling. In addition, SUAP provides support to quantify the uncertainty ranges and to calculate sensitivity dependencies based on rank ordered correlations. The GUI has a branchlike structure which guides user through the main analysis steps. The analysis steps (branches) are displayed on top-left side of the first window and divided into two major parts (Fig. 1). The first part to select is “Project” where a new project has to be defined or an existing project could be called for further check and / or modification. As shown in Fig. 2, the next branch, “Uncertain input parameters”, is to be used in order to define the distribution characteristics of the uncertain input parameters. The interested input parameters, listed here, have been previously defined in a sample input file (template), which is to be entered in the “Code” branch by user. In addition, definition of the dependencies is so crucial, if any dependencies between uncertain parameters exists. These dependencies are to be formulated at the end of the sample (template) input file in a specific format shown here:

[language=Fortran] Dependency: F@(dspg F6.4) = 0.999*(F@(dco F6.4)-2*F@(thkcld F6.4)) :Dependency In this example parameter dspg is a function of two other parameters (dco and thkcld). The “F” before “@” refers to the type of parameter (F for Float/Real and I for Integer variables). In this example, user has also determined the printing format of each parameter (optional), here F6.4, which

means printing number within 6 columns (including decimal point) with 4 decimal digits. The only limitation in defining dependencies is that parameters in the righthand- side of equation shall be properly defined previously.

Fig. 1. Main (first) page of SUAP.

Fig. 2. Definition of uncertain parameters.

Four different probability distributions have been considered in the SUAP:

- Uniform Distribution
- Normal Distribution
- Triangular Distribution
- User-Defined Distribution (UDD)

Based on which PDF (Probability Distribution Function) user is desired to use, related sub-parameters vary. For instance, to define the first distribution (i.e., Uniform), it is sufficient to specify minimum and maximum values. While, in the case of Normal and/or Triangular distributions, some extra entries are required (Fig. 3). In all cases, the "Nominal" value is considered according to the information provided by the manufacturer as the fabrication characteristic. All Nominal values (for different uncertain input parameters) will be used to generate a specific input file assigned by 0000, which can be used as the

base line in future comparisons. By the way, Normal and Triangular distributions are to be truncated at the values identified as "Min" and "Max". And eventually, the UDD (User Defined Distribution) option is a table-based distribution at which accumulated probability values (sum up to 1) are listed and SUAP automatically calculates related probabilities using linear interpolation between two subsequent user defined values. In addition to all above mentioned capabilities, to check the accuracy of the defined PDFs, SUAP can plot a histogram graph according to the specifications inserted for each uncertain parameter for 25,000 samples (Fig. 4) [11].

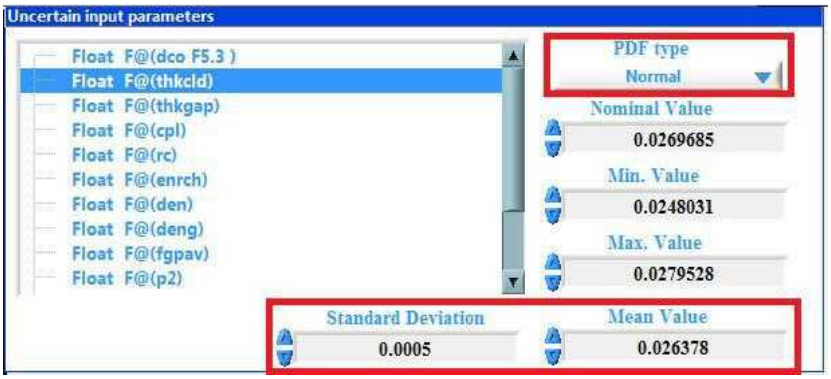

Fig. 3. Normal distribution definition.

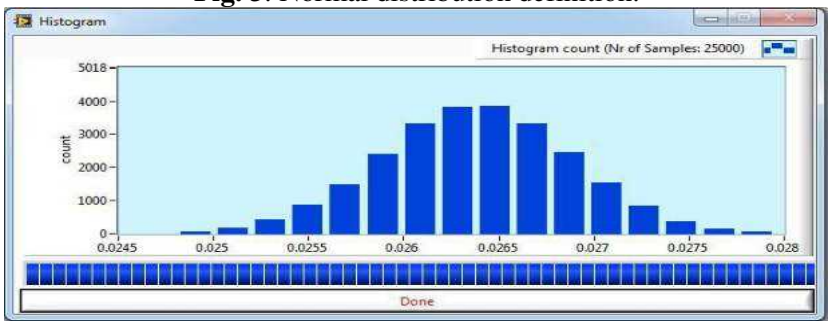

Fig. 4. Sample checking graph the accuracy of the inserted distribution data.

SUAP is capable of coupling with some frequently used nuclear codes (FRAPCON, FRAPTRAN, ...). In this study, performance analysis of the fuel rod in transient conditions (PART code) developed by the Advanced Nuclear Computing Center (ANCC) is coupled with the SUAP code. The method of pairing different codes with the SUAP code is that in the LabVIEW environment, the input and output formats of the desired codes are identified along with its executable file, and then, the desired operations are performed around the sensitivity and uncertainty analysis for the desired parameters. In Fig. 1, in the code section, we add the input file and executable file of the PART code to the SUAP code, and in order to perform sensitivity and uncertainty analysis for the desired parameters, we enter the specified tolerances (Table 3) into the SUAP code.

In this manuscript, the aim is to analyze the sensitivity and uncertainty for IFA 650.10 which was tested in the Halden reactor. The main purpose of this study is to validate and verify SUAP code with other sensitivity and uncertainty analysis codes used by other countries, as well as experimental results.

Research Theories

The detailed description of IFA-650.10 can be found in [12]. The test segment was cut from a standard PWR fuel rod test which had been irradiated in the PWR Gravelines 5 (900 MWe EDF, France) during five cycles from August 1988 to August 1995 to a burn-up of 61 MWd/kgU, with the pre-irradiation power history as shown in Fig. 5. The average linear heating rate during irradiation was 18 kW/m, and the average burnup was 56.2 MWd/kgU.

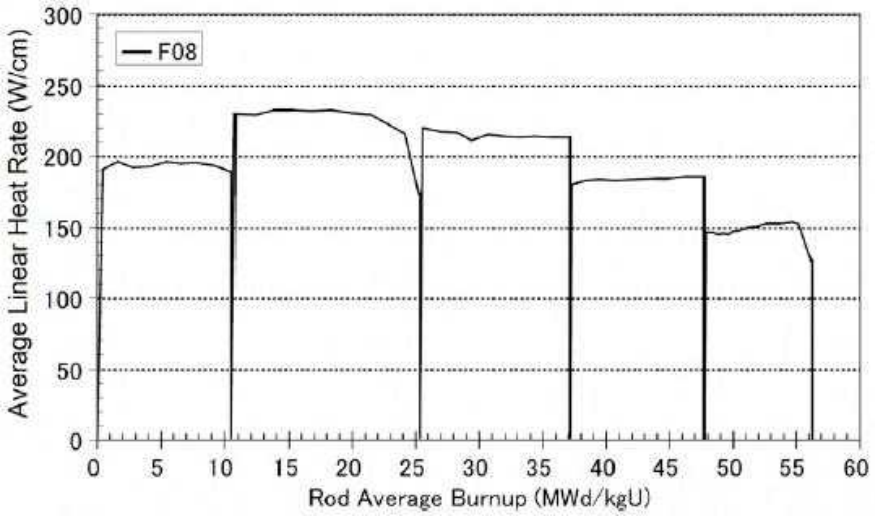

Fig. 5. Pre-irradiation power history for the IFA-650.10 fuel rod [13]

The operating conditions of the father rod were:

Coolant inlet temperature: 270 ℃

Coolant pressure: 15.5 MPa

Coolant inlet mass-flow rate: 3540 kg/s.m^2

The test fuel rod characteristics are compiled in Table 1. The father rod was from a typical Framatome 17x17 fuel assembly with an active length of 3658 mm. The length of the test rodlet fuel stack was ~ 440 mm and no end pellets were inserted. The test rodlet was filled with a gas mixture of 95 % argon and 5 % helium at 40 bars. Argon was chosen to simulate the fission gases, whereas a small amount of helium is required for the leak test of the rod. The rod plenum volume (free gas volume) was made relatively large to maintain stable pressure conditions until cladding

burst. The total free gas volume of ~17 cm^3 was thus practically all located in the plenum, outside the heated region.

Table 1. Rod Characteristics For IFA-650.10 [13]

Fuel rodlet design data	Value
Rod outer diameter (mm)	9.50
Rod inner diameter (mm)	8.36
Pellet diameter (mm)	8.19
Pellet height (mm)	13.78
Dish radius (mm)	3.0
Dish depth (mm)	0.32
UO_2 Enrichment (%)	4.49
Pellet density (%TD)	95.32
Pellet roughness (μm)	2.0
Cladding type	Zry-4
Cladding roughness (μm)	1.0
Rod pitch (mm)	12.6
Fuel average burnup (MWday/KgU)	61.0
Fill gas pressure at 295 K (MPa)	4.0
Rodlet initial LHGR (KW/m)	1.37
Peak cladding temperature (K)	1114.0
Heater initial LHGR (KW/m)	1.20
Coolant initial pressure (MPa)	15.5
Coolant initial inlet temperature (°C)	287.0
Coolant initial mass flux (Kg/m2.sec)	0.0
Fast flux (n/m^2.sec per KW/m)	4×10^{16}

The test was conducted in May 2010. At the start of the test, the axial power distribution was as shown in Fig. 6, with a peak to average power factor of ~1.05.

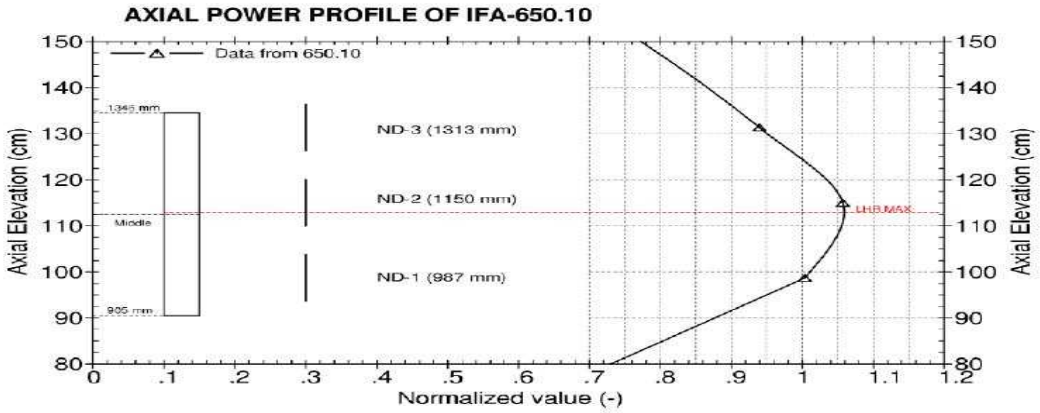

Fig. 6. Axial power profile at the start of the test of IFA-650.10 [13]

Table 2. The scenario of burst test

Time / Parameters	t_1	t_2	t_3	t_4	t_5
Definition	End of natural circulation	Beginning of blowdown	End of cooldown	After burst	End of calculations
Value	100.0 sec	101.0 sec	320.0 sec	350.0 sec	600.0 sec

Results and discussion

According to Table 2, the beginning of LOCA scenario is that in the 100th second, the natural circulation of the fluid ends and in the 101st second, the blowdown begins. The cooling process continues until the 320th second, and the simulation and modeling process continues until the 600th second, which is the end of the calculations. In this case, the fuel rod becomes plastic and ballooning occurs, the result of which is the bursting of the fuel rod.

After applying all the characterization of the fuel rod as well as the test conditions in the PART code (Table 1), the parameters in Table 3 were applied in the SUAP code to perform uncertainty analysis. The results related to the uncertainty analysis of the fuel rod internal pressure by AEOI and other countries are shown in Fig.7. According to Fig.7, the experimental data shows that in the considered scenario, the fuel rod burst incident occurs at 320 seconds, and the results obtained from the PART and SUAP code couple predict this incident at 304 seconds. Also, according to Fig.7, it can be seen that the behavior of the fuel rod before and after the bursting of fuel rod is very close and acceptable compared to the experimental data.

The reasons for the difference between the results of the countries and the experimental results can be

1. The lack of detailed information related to the models used in the fuel rod performance analysis code

for various phenomena in the test conducted in the Halden reactor, 2. The incomplete coding of fuel performance codes of other countries and the divergence of their results compared to experimental results. Nevertheless, the results obtained by the Atomic Energy Organization of Iran are in good agreement with the experimental results.

Also in Fig. 8, the uncertainty bandwidth of the rod internal pressure obtained by using the output code of SUAP code is compared with the results of other countries.

Table 3. Specification of the uncertainty parameters for IFA-650.10 [14,15]

Input uncertainty parameter	Uncertainty Range and Distribution				
	Mean or Nominal	Standard Deviation or Range	Type	Lower Bound	Upper Bound
Cladding outside diameter (mm)	9.50	0.01	Normal	9.48	9.52
Cladding inside diameter (mm)	8.36	0.01	Normal	8.34	8.38
Pellet outside diameter (mm)	8.19	0.01	Normal	8.18	8.22
Fuel theoretical density (Kg/m^3)	10457	50	Normal	10357	10557
U-235 Enrichment (%)	4.487	0.05	Normal	4.387	4.587
Filling gas pressure (MPa)	4.0	0.05	Normal	3.9	4.1
Plenum gas temperature (°C)	-	±20	Uniform	T-20	T+20

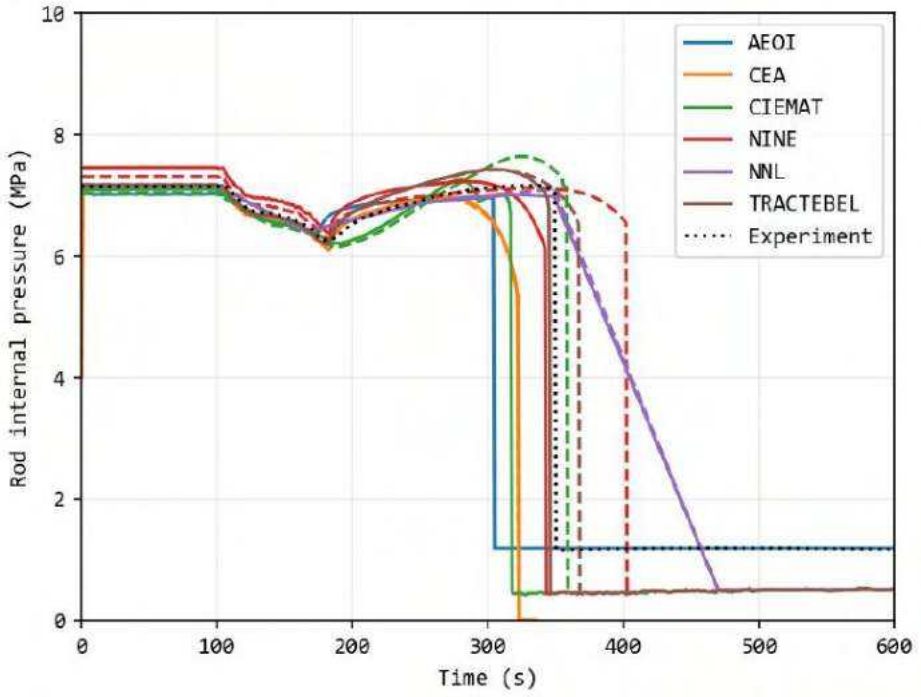

Fig. 7. Comparison of rod internal pressure by AEOI and other countries with **EXPERIMENTAL** data

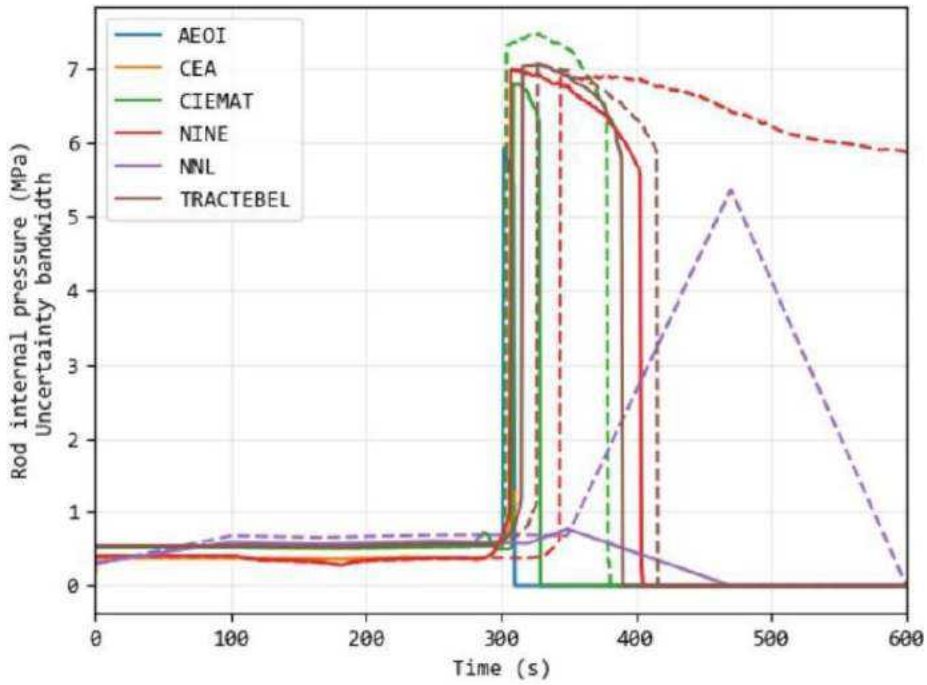

Fig. 8. Comparison of rod internal pressure for uncertainty bandwidth by AEOI and other countries

Statistical analysis of the results is based on Spearman's correlation coefficient, $r_s \in [-1, +1]$, which is defined as statistical relationship between the input and output parameters. Spearman formulation for calculating r_s is defined as follows:

$$r_s = 1 - \frac{6 \sum D_i}{m(m^2-1)} \quad (1)$$

where m is the number of pairs in the created rank; and D_i is the difference between i-th pair of values in the rank. The strength of monotonicity of the analysis has been defined according to absolute range of correlation coefficient (Table 4). As r_s goes to large values (in magnitude), it is concluded that dependency of the interesting output parameters to the related uncertain input parameter is stronger. The results related to the sensitivity analysis of fuel rod internal pressure parameter compared to uncertainty parameters (presented in Table 3) are presented in Table 5.

Table 4. Quantitative estimation of the absolute value of Spearman correlation coefficient

Range	Relation
[0.00, 0.20)	Very week
[0.20, 0.40)	Weak
[0.40, 0.60)	Average
[0.60, 0.80)	Strong
[0.80, 1.00]	Very strong

Table 5. Spearman's rank coefficients for fuel rod internal pressure in relevant to different uncertain input parameters for IFA-650.10

Uncertain input parameter	Spearman's rank ordered coefficient (absolute value)
Cladding outside diameter (mm)	0.48
Cladding inside diameter (mm)	0.46
Pellet outside diameter (mm)	0.36
Fuel theoretical density (Kg/m^3)	0.43
U-235 Enrichment (%)	0.44
Filling gas pressure (MPa)	0.48
Plenum gas temperature (°C)	0.89

Conclusions

The toolkit SUAP essentially facilitates the performance of probabilistic UA&SA based on Monte-Carlo sampling method. The comfortable branchlike GUI of SUAP guides user through the main analysis steps and contributes to comprehensibility and error prevention and, thus, to the quality assurance of an UA&SA. The Monte-Carlo sampling procedure is applicable for selecting sets of parameter values fulfilling the probability distributions and dependencies specified as input. SUAP can automatically transfer these sets of values to the input decks of the computer code and start the corresponding runs. The sensitivity analysis with SUAP is performed to the same sample data as generated for the uncertainty analysis preciously. Currently only one correlation related sensitivity index (i.e., Spearman rank ordered coefficient) has been predicted in SUAP. However, using the results of this part, the analyst will be capable of determining the importance of each input uncertainty on any crucial output parameter, and plan to improve the related knowledge and/or required technology more efficiently. All results of the uncertainty and sensitivity analysis can be exported as graphs or as raw tabulated data in the form of Excel files.

In this study, sensitivity and uncertainty analysis were performed for the internal pressure of fuel rod and the results were in good agreement with the experimental data. A future plan is to develop these analyzes for Accident Tolerant Fuel (ATF), which could use cases where Cr is doped into the fuel pellet or when a Cr layer is deposited on the fuel rod cladding. The use of ATF makes the fuel rod more resistant to accidents, and this can be the advantage of this technology when the reactor has an accident, and more time is available to the operator to direct the reactor and prevent severe accidents like the one that happened at the Fukushima reactor.

Acknowledgements

This work was conducted in the frame of IAEA's Coordinated Research Project on Testing and Simulation for Advanced Technology and Accident Tolerant Fuels (ATF-TS).

References

[1] D' Auria, F. S., Dusic, M., Dutton LM, C., et al. (2009). Deterministic Safety Analysis for Nuclear Power Plants. IAEA Specific Safety Guide. IAEA.

[2] Strydom, G. (2010). Use of SUSA in uncertainty and sensitivity analysis for INL VHTR coupled codes. Technical report, Idaho National Lab.(INL), Idaho Falls, ID (United States).

[3] Rusanov, V., Petkov, P., and Kamenov, K. (2018). Implementation of Uncertainty Analysis for Evaluation of Nuclear Reactors VVER-1000 Fuel Safety Margins during Normal Operation by FEMAXI-6 Computer Code Calculations. Journal of Physics and Technology, 2:19–36.

[4] Zhang, J., Umidova, Z., and Dethioux, A. (2015). Simulation of fuel behaviours under LOCA and RIA using FRAPTRAN and uncertainty analysis with DAKOTA. In Modelling of Water Cooled Fuel Including Design Basis and Severe Accidents, Proceedings of a Technical Meeting Held in Chengdu, China, 28 October–1 November 2013, pages 115–142.

[5] Veshchunov, M., Stuckert, J., Van Uffelen, P., et al. (2018). FUMAC: IAEAs Coordinated Research Project on Fuel Modelling in Accident Conditions. Trans. TopFuel.

[6] Helton, J. C., Johnson, J. D., Sallaberry, C. J., et al. (2006). Survey of sampling-based methods for uncertainty and sensitivity analysis. Reliability Engineering & System Safety, 91(10-11):1175–1209.

[7] Hofer, E. (1999). Sensitivity analysis in the context of uncertainty analysis for computationally intensive models. Computer Physics Communications, 117(1-2):21–34.

[8] Saltelli, A., Chan, K., and Scott, E. (2000). Wiley series in probability and statistics. Sensitivity analysis.

[9] Adams, B. (2020). DAKOTA, Multilevel parallel objectoriented framework for design ptimization, parameter estimation, uncertainty quantification, and sensitivity analysis: Version 6.13 user's manual. Technical Report SAND2020- 12495, Available online from http://dakota.sandia.gov/ documentation.html. Sandia National Laboratories, Albuquerque, NM 87185, Updated Nov. 2020.

[10] LabVIEW, F. (2010). National Instruments (NI), 373427G-01. Austin, Texas, pages 78730–5039.

[11] Khodadadi, H., Sabetghadam, K. (2023). Development of SUAP toolkit for performing uncertainty quantification and sensitivity analysis in fuel performance modeling. Radiation Physics and Engineering.

[12] LAVOIL, "LOCA Testing at Halden, the Tenth Experiment IFA-650.10", HWR-974, OECD Halden Reactor Project, December 2010.

[13] W. Wiesenack, "Summary of the Halden Reactor Project LOCA Test Series IFA-650," HPR-380, OECD Halden Reactor Project, May 2013.

[14] H. GLAESER, “GRS Method for Uncertainty and Sensitivity Evaluation of Code Results and Applications," Science and Technology of Nuclear Installations, Volume 2008, Article ID 798901,

[15] J. ZHANG, J. SEGURADO and C. SCHNEDESCH, "Towards an Industrial Application of Statistical Uncertainty Analysis Methods to Multi-physical Modelling and Safety Analyses," Proc. OECD/CSNI Workshop on Best Estimate Methods and Uncertainty Evaluations, Barcelona, Spain, 16-18 November 2011.

ICNST 2024 International Conference on Nuclear Science and Technology
6- 8 MAY 2024 | Isfahan, Iran

Design a Cold Crucible Induction Melting for an EXPERIMENTAL facility for testing corium interaction with the ex-vessel structures in severe accident of nuclear reactors (Paper ID : 1278)

Chakhmachi A.[1], Darestani Farahani N[1*]

[1] *Plasma and Nuclear Fusion Research School, Nuclear Science and Technology Research Institute, P. O. Box 14399-51113, Tehran, Iran*

Abstract

In severe accidents, corium composition and properties are crucial for understanding its behavior and interactions with reactor components. Accurate data on high-temperature chemical systems is challenging to obtain, requiring enhanced thermodynamic databases and precise equilibrium phase diagrams. These efforts are essential for improving the accuracy of simulation codes for severe accident conditions. Corium from severe accidents in different types of reactors can be produced and tested in an induction furnace with a cold crucible (IFCC) within a glove box.

Corium is distinguished by its high temperature, typically ranging from 2,200 to 2,800 degrees Celsius. This extreme temperature can lead to the melting of reactor components and concrete structures, posing significant safety risks. In this study, a proposal is made for an induction furnace with the appropriate frequency, power, and dimensions, taking into account the corium composition, specific heat capacity, and density.

Keywords: induction cold crucible, molten core, nuclear reactor, severe accident.

Introduction

A severe nuclear accident involving core melting, also known as a nuclear meltdown, is a catastrophic event in which the nuclear reactor core overheats and begins to melt. This can occur due to a variety of factors, such as a loss of coolant, a power outage, or a control system failure. When the core melts, it can release large amounts of radioactive material into the environment, potentially causing widespread contamination and health risks. The severity of the accident depends on the amount of radioactive material released and the prevailing weather conditions.

During a severe accident, such as a loss-of-coolant accident (LOCA), the reactor core can overheat, causing the fuel rods to melt and the cladding material to rupture. This molten material can then mix with other materials inside the reactor vessel, such as control rods, structural components, and coolant, forming a complex mixture known as corium. Corium is characterized by its high temperature, typically ranging from 2,200 to 2,800 degrees Celsius (4,000 to 5,000 degrees Fahrenheit). Due to its extremely high temperature, corium can melt through reactor components and concrete structures, posing a

significant safety risk. The behavior and properties of corium are complex and depend on various factors, including the specific composition of the fuel and structural materials, the temperature, and the presence of coolant or other materials. Understanding the behavior of corium is crucial for assessing the safety of nuclear power plants and developing strategies to mitigate the consequences of severe accidents. Corium is a hazardous material due to its high radioactivity and the potential for chemical reactions with air and water. Managing and containing corium during and after an accident is a critical challenge in nuclear safety. Various strategies, such as core catchers and sacrificial materials, are employed to mitigate the effects of corium and prevent its release into the environment.

The simulations of severe nuclear accidents involving an Induction Furnace with a Cold Crucible (IFCC) are important for understanding and preparing for potential risks and developing safety measures. These simulations can help in assessing the behavior of materials under extreme conditions and in designing effective safety protocols.

The IFCC is a technology offering a lot of possibilities of using for melting different materials. It is useful for melting the electrically conductive materials and non-conductive materials (oxides, glass, etc.). Of course, it is not a universal device. Prior to the design of a new device, it has to be absolutely clear what materials are going to be melted in it (1).

Using the IFCC for melting the electrically nonconductive materials is also possible: for a vitrification of radioactive waste or for a simulation of a severe nuclear accident with core melting. But there are also many nonnuclear applications, for example melting oxides of metals with a high melting point (2). For melting electrically nonconductive materials a starting phase of the melting process enters the melting. Electrically conductive material (for instance metallic zirconium) is added to the electrically nonconductive melted material.

The advantage of this technology is achieving high temperatures of melted material and obtaining highly pure melted product. The next indisputable advantage of this technology is the possibility to perform the melting process in a melting chamber which contains a different atmosphere or a vacuum. Therefore, it is possible to melt also highly reactive materials inside.

The IFCC technology is ideal for simulations of severe nuclear accidents with core melting because it is possible to achieve the temperature up to 3 000 ° C. The corium melting point is lower than this value. corium melting can be achieved and its behavior and material properties can be studied, which can be useful for preventing or minimizing the damage during severe nuclear accidents with core melting in a real reactor (3).

Udalov et al. (3) presented the results of the experimental study carried on molten corium and its crystallization products resulted from contact with sacrificial concretes. Experiments were carried out at COMETA installation using IFCC technology in air. The results of the physical-chemical analysis of the examined composite system U4+-U6+-Zr4+-Fe3+-Fe2+-Si4+-Al3+-Ca2+-O2− presented in that paper are based on computational diagram of fusibility of quasi ternary oxide systems.

In the Fig.1.a a photograph of the experiment progress with CORIUM melting in the IFCC Cometa is shown. The figure also shows the crust being formed on the surface of the melt, which was caused by the temperature decrease in the upper part of the workpiece. This using of the technology includes also Fig.1.b, which contains a photograph of a severe nuclear accident simulation but the upper part of the melt is completely melted and the surface is visible.

(a) (b)

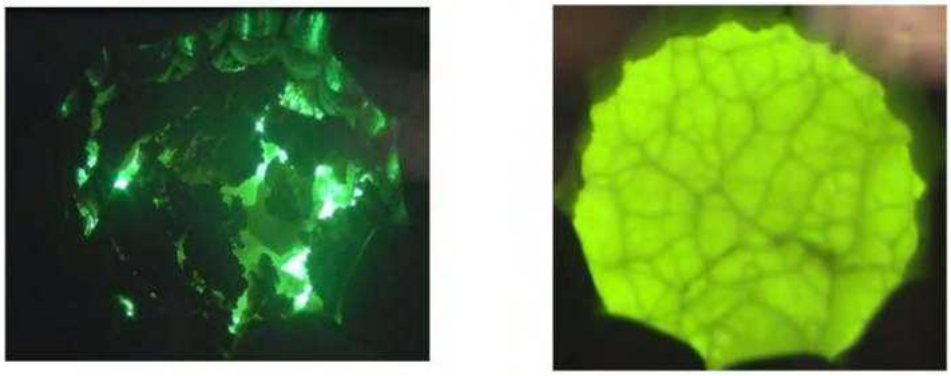

Fig. 1. Photograph of the melt during the **EXPERIMENTAL** melting of CORIUM. a) with the crust on the surface. b) without the crust on the surface. (2)

Description of Induction Furnace with Cold Crucible

Generally, there are two IFCC arrangements. The first of them is a cold crucible with an integrated inductor. The second one is a segmented cold crucible. Physical principle of the both types is the same however they have a different design. The following text will be devoted to the induction furnace with the segmented cold crucible.

In Fig.2, a basic geometric layout of the induction furnace with a segmented cold crucible is depicted. The section marked in red represents a two-turn inductor through which a time-varying electric current passes during the melting process. The frequency of the electric current varies based on the specific application. The inductor is water-cooled for efficient operation. The yellow area indicates the workpiece, which can be either electrically conductive or non-conductive, as previously mentioned. The

blue-marked sections depict the segments and the bottom of the cold crucible, both of which are actively water-cooled. This cooling process maintains a temperature of around 100°C at the contact point between the segments and the workpiece, preventing melting in this area and forming a protective layer known as a skull. This layer acts as a barrier, keeping the melt from touching the crucible wall, thereby ensuring high product purity. The segments and the bottom of the crucible are constructed from copper. In Fig.2, four segments have been omitted from the front of the device for clarity in illustration.

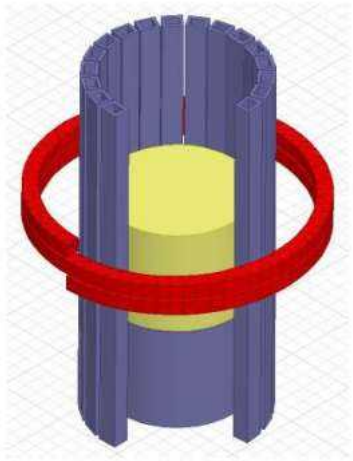

Fig. 2. Geometrical arrangement of the induction furnace with the cold crucible(2).

Fig. 3. The Induction furnace with the cold crucible developed in St. Petersburg University LETI(2).

A photograph of the real IFCC equipment developed and used in St. Petersburg University LETI is presented in the Fig.3. It was designed and developed by prof. Petrov from St. Petersburg University LETI. Two other IFCC installations are being constructed in the Research Centre at the time of writing of the article (2) with Output power of 160 kW and 240 kW.

Test facilities for severe accident corium for nuclear reactors

Experiments at UJV-COMETA facility

Within the ECOSTAR, SARNET and SARNET2 projects, severe accident corium for VVER type reactors can be produced and tested in the COMETA facility at ÚJV Rˇezˇ, a. s. (previously Nuclear Research Institute) (4). This uses induction heating in a cold crucible contained in a glove box (Fig. 4) (5). high-frequency tube generator provides 60 kW power in melt and a stable melting regime for the growth of large crystals.

Journeau et al. (6) discussed the transient interactions between boron carbide and molten uranium oxide. The cold crucible COMETA facility (7, 8) (Fig. 4, was constructed for the melting of powdered oxides with melting points of up to 3000°C. The facility was later adapted for operation with radioactive materials(in particular with UO2) and in particular for corium melt simulants. The COMETA cold crucible is serviced by a 60kW power, 4.5 MHz frequency generator, with a melt capacity of around 250cm^{3}and achieving temperatures of up to 3000°C. The COMETA facility was installed within a glovebox at the Nuclear research Institute (UJV) in Řež and, on formation of a solid crust at the melt surface, copper rods were used to break the crust to initiate the boron quenching. A quartz filter system was installed above the crucible for the capture of aerosolized particulates, liberated during the interaction, for post-test analysis (9).

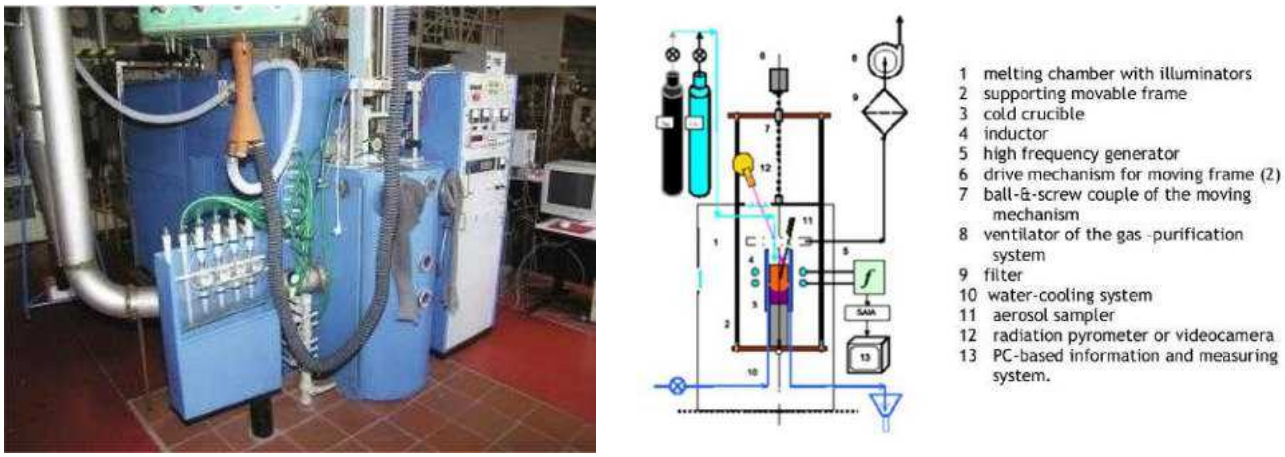

Fig. 4. Illustrations of the COMETA facility by (left) photograph and (right) schematic. 1: melting chamber; 2; supporting frame; 3: cold crucible; 4: inductor; 5: generator; 6: drive of frame (2); 7: ball and screw couple; 8: ventilator of the gas-purification system; 9: filter; 10: water cooling; 11:aerosol sampling; 12: pyrometer; 13: Digital Acquisition System(5).

ECO-NET program

An ECO-NET Network of high temperature facilities simulating severe accidents is presented in (10). This article discusses the ECO-NET program, which supports collaboration between French research laboratories and laboratories in Central and Eastern Europe. The program focuses on severe accidents in nuclear power plants and the experimental aspects related to prototypical corium material. Several high temperature facilities are described, including VITI, VULCANO, LAVA-B, and Laser Flash Apparatus. The article also discusses the development of a corium standard for material analyses and the use of modeling techniques to improve experiments.

THE «VCG-135» TEST BENCH

In (11), it is proposed to consider low-melting metals as a cooler (hereinafter, metals - coolers) for the organization of continuous cooling of corium. The conducted computer modeling showed the theoretical possibility to implement the proposed method of cooling corium in practice (12).

Small-scale experiments were conducted on the «VCG-135» test-bench at the first stage of experimental studies.

The metal-coolers (zinc, antimony and manganese) in the form of cylinders with a diameter of 6 mm and a height of 8 mm were used in the experiments. The powder of the crushed corium prototype taken from earlier conducted experiments was used as a corium melt (13).

During the experiments conducting, the liquid melt of corium was obtained by induction heating method of the powder to a temperature of 2250 °C. After reaching the required temperature, a two-minute exposure was conducted to equalize the temperature. After exposure, the induction heater was switched off and the metal was discharged on to liquid corium.

Lava-B facility

Skakov et al presents the results of computational and physical studies On the Possibility of Forming a Corium Pool by Induction Heating in a Melt Trap of the Lava-B Facility .The Lava-B facility is used to study the processes occurring during a severe accident at a nuclear reactor, with a focus on the separation of the stages of the reactor core corium formation and its interaction with other materials(13).

Fig.5 shows the physical form and layout of the Lava-B facility. The corium produced in an electric melting furnace (EMF) is drained into a melt trap located in the MR for further studying of its interaction with various structural materials. The trap is inserted in an inductor, which is used to simulate the decay heat in the corium in standard order.

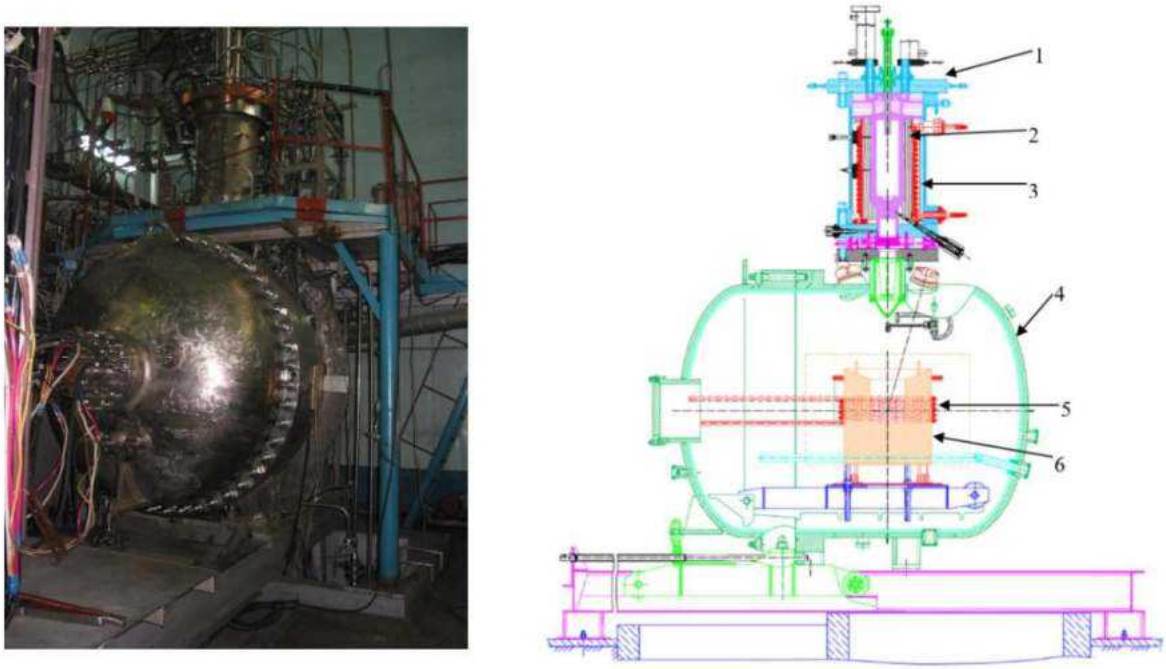

Fig.5. Physical form and layout of the Lava-B facility. 1: EMF (electric melting furnace), 2: crucible, 3: EMF inductor, 4: MR (melt receiver), 5: MR inductor, 6: concrete trap(13).

A structural feature of the Lava-B facility is that inductors of the EMF and MR are driven with a single variable frequency drive VFD 500-2.4-10000 with a capacity of 500 kW. The power of the MR's

induction heater can be sufficient not only to simulate the heat decay, but, also, to directly produce corium in the volume of the melt trap.

The melt trap is a cylindrical concrete structure inserted in the MR's inductor. A composition of materials for producing the corium with a total weight of 30.0 kg was loaded into the concrete trap.

The number of materials loaded into the trap:

- Uranium dioxide (UO2), kg 16.5;
- Zirconium (Zr), kg 7.5;
- Zirconium dioxide (ZrO2), kg 1.5;
- Steel (SS), kg . . . . . 4.5.

The initial data of induction heating for simulation were selected based on the averaged parameters of previously performed experiments (14, 15).By taking into account the technical capabilities of the Lava-B facility:

- The active power of the inductor was 120 kW;
- The inductor electrical efficiency was 45%;
- The inductor power factor was 0.9 considering the compensation.

Research Theories

An induction furnace with a cold crucible can be designed for the melting process simulation of the curium in a severe accident according to the following stages. In fact, the main parameters of the furnace and crucible will be calculated in this work.

Volume of the crucible: the minimum volume of the crucible is equal to the molten core volume. The volume of the molten core is obtained by dividing the curium mass by its density.

Crucible diameter and highness: regarding the induction furnace mass rate (furnace capacity), there is a specific ratio between the diameter and highness of the crucible (16-19). In the present work, the induction furnace mass rate (furnace capacity) is considered $30\frac{\mathrm{Kg}}{\mathrm{h}}$.

$\frac{h}{D} = 2$ For furnace mass rate (furnace capacity) $\leq 16\frac{\mathrm{Kg}}{\mathrm{h}'}$

$\frac{h}{D} = 1\,7$ For $16\frac{\mathrm{Kg}}{\mathrm{h}} <$ furnace mass rate $< 30\frac{Kg}{h}$,

$\frac{h}{D} = 1\,3$ For furnace mass rate $\geq 30\frac{\mathrm{Kg}}{\mathrm{h}'}$

Where, h and D are highness and diameter of the crucible, respectively. It is clear that based on the volume of the crucible and the specified value of the highness-diameter ratio, the highness and the diameter of the crucible can be easily calculated.

Total power of the induction furnace RF source: the thermal energy which is required to heat the corium from room temperature to a temperature of 3000 degrees centigrade is obtained by equation (1);

$$Q = mC_p\Delta T \qquad (1)$$

where Q, m, C_p, and ΔT are the required thermal energy, the corium mass, the specific heat capacity of the corium, and the temperature interval, respectively. In this regard, the required thermal power is obtained by time derivation of equation (1).

$$\dot{Q} = \dot{m}C_p\Delta T \qquad (2)$$

where $\dot{Q}$, and $\dot{m}$, are the required thermal power, and the furnace mass rate (the furnace capacity), respectively. In practice, the total power of the induction furnace RF source is calculated by;

$$P = \frac{\dot{Q}}{\eta_E \eta_T} F, \qquad (3)$$

where, η_E , η_T, and F are the electrical efficiency coefficient, the thermal efficiency coefficient, and the design coefficient, respectively. Based on the reported value of the literature, in this work the electrical efficiency coefficient, the thermal efficiency coefficient, and the design coefficient are considered as 15%, 45%, and 50%, respectively (18).

The operational frequency: The operation frequency can be calculated by using the skin depth relation (17). As reported by the literature, the skin depth of the radio frequency wave in the materials is the function of the material resistivity and frequency of the RF wave;

$$\delta = 503\sqrt{\rho / f}\ , \qquad (4)$$

where, ρ and f are the material resistivity in $(\Omega - m)$ and frequency in (Hz), respectively. On the other hand, it is experimentaly obtained that the RF wave skin depth is related to the crucible diameter (20, 21);

$$\delta = 0\,25D \qquad (5)$$

As a result, the operational frequency of the induction furnace is obtained by:

$$f = 40\,5 \times 10^5 \frac{\rho}{D^2} \qquad (6)$$

Results and Discussion

To execute the procedures mentioned in the last section to obtain the parameters of the designed IFCC, certain parameters of the corium matrix, such as density, heat capacity, and electrical resistivity, need to be defined.

The sum of materials loaded into the trap is considered to be 30 kg and consists of: Uranium dioxide (UO2) (16.5 kg), Zirconium (Zr) (7.5 kg), Zirconium dioxide (ZrO2) (1.5 kg), and Steel 316L(SS) (4.5 kg).

Molar volumes and masses of solid and liquid alloys can be expressed as the cumulative molar volumes and masses of each component of the solution (Vegard's law) as expressed in equations (7) and equations (8). Density of the mixture, which is the quotient of these two variables, is expressed by equation (9)(22). V^m is Molar Volume, x_i is composition of component i, V_i is partial molar volume of component i, $M$is molar mass and ρ is the density. Density of a material is dependent to the temperature and expressed by relations in equations (10) and (11). $\beta_{sol}\,[K^{-1}]$ is coefficient of volumetric thermal expansion for a solid phase, $\beta_{liq}\,[K^{-1}]$ is coefficient of volumetric thermal expansion for a liquid phase and T_m is the melting temperature (23).

$$V^m = \sum_{i=1}^{n} x_i V_i \qquad (7)$$

$$M = \sum_{i=1}^{n} x_i M_i \qquad (8)$$

$$\rho = \frac{\sum_{i=1}^{n} x_i M_i}{\sum_{i=1}^{n} x_i V_i} \qquad (\textstyle\sum_{i=1}^{n} x_i = 1) \qquad (9)$$

$$V_{Soild} = V_{25°C}(1 + \beta_{sol}(T - 25°C))(for\ solids) \qquad (10)$$

$$V_{liquid} = V_{mT_m}(1 + \beta_{liq}(T - T_m))(for\ liquids) \qquad (11)$$

if the specific heat capacities (C) and masses (m) of the individual components will be known, the specific heat capacity of the mixture ($C_{mixture}$) and be calculated by using the equation (12) where $m_1, m_2 \ldots, m_n$ are the masses of the individual components and $C_1, C_2 \ldots, C_n$ are their respective specific heat capacities.

$$C_{mixture} = \frac{m_1C_1 + m_2C_2 + \cdots + m_nC_n}{m_1 + m_2 + \cdots + m_n} \quad (12)$$

Thermophysical properties of liquid UO_2, ZrO_2 and corium are presented in Woong Kee Kim et al. work (24). Predicting the fate of accident-melted nuclear fuel-cladding requires the understanding of the thermophysical properties which are lacking or have large scatter due to high-temperature experimental challenges. They predicted the properties of melted UO2 and ZrO2 Using equilibrium classical molecular dynamics (MD) and compare them with the available experimental data and the predictive models. The existing interatomic potential models have been developed mainly for the polymorphic solid phases of these oxides, so they cannot be used to predict all the properties accurately. they compared and deciphered the distinctions of those MD predictions using the specific property-related autocorrelation decays. The predicted properties are density, specific heat, heat of fusion, compressibility, viscosity, surface tension, and the molecular and electronic thermal conductivities up to 5000 K. After the comparisons, they provided readily usable temperature-dependent correlations (including UO2-ZrO2 compounds, i.e. corium melt). by molecular dynamics and predictive models.
The proposed temperature–dependent correlations for liquid UO_2 and ZrO_2 density and heat capacity in Table 1(24).

Table 1: Temperature–dependent correlations for liquid UO_2 and ZrO_2 density and heat capacity using the Gross et al. and Hirai formula (24).

Property	UO_2	ZrO_2
Density(g/cm^3)	$\rho(T) = 4\,40 - 8\,31 \times 10^{-4}(T - 3120)$	$\rho(T) = 7.56 - 2\,86 \times 10^{-4}(T - 2988)$
Heat capacity (J/kg-K)	$C_V(T) = 390 - 0\,900 \times 10^{-4}T$	$C_V(T) = 940 - 3\,36 \times 10^{-2}T$

Shipkov et al. (25) suggested an approximate equation for the calculation of density ρ of liquid zirconium at different temperatures is:

$$\rho = 6\,0 - (T - 2121) \times 10^{-3}(\frac{g}{cm^3}) \quad (13)$$

Also online database such as NIST Chemistry WebBook (26) can be used for some materials. The heat capacity (J/kg-K) of zirconium based on NIST Chemistry WebBook:

$$C_p(Zr) = 41.84 + 3.95 \times 10^{-8}t - 9.2 \times 10^{-9}t^2 + 7.21 \times 10^{-10}t^3 + 4.57 \times 10^{-8}/\ t^2 \quad (14)$$

t=T/1000 T is temp in Kelvin

Temperature-dependent density of stainless steel Type-316L. is obtained from (27).:

$$\rho = 8.0842 - 4.2086 \times 10^{-4}T - 3.8942 \times 10^{-8}T^2 \quad (solid\ region)$$
$$\rho = 7.4327 + 3.9338 \times 10^{-5}T - 1.8007 \times 10^{-7}T^2 \quad (liquid\ region) \quad (15)$$

Where $\rho = density\ in\ g/\ cm^3$ and T is temp in Kelvin.

specific heat capacity of stainless steel Type-316L is obtained from (28) and is presented as fig.6.

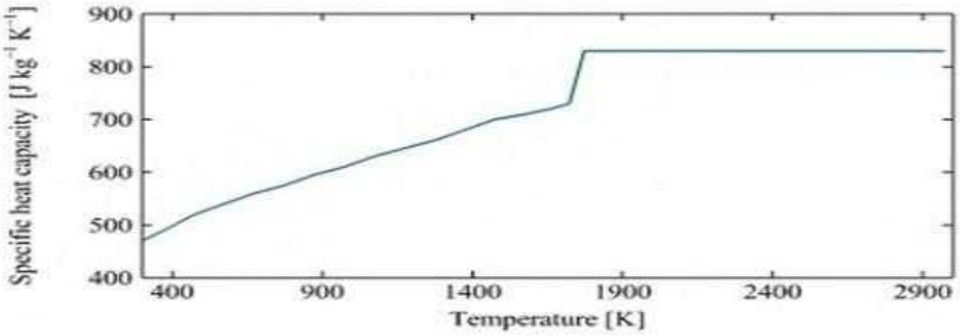

Fig. 6. The specific heat capacity of stainless steel Type-316L (28).

As mentioned, the sum of materials loaded into the trap is considered to be 30 kg and consists of: Uranium dioxide (UO2) (16.5 kg), Zirconium (Zr) (6.5 kg), Zirconium dioxide (ZrO2) (7.5 kg), and Steel 316L(SS) (4.5 kg). the specified parameters ale listed in table 2.

Table 2: specified parameters of the considered Corium composition (30 kg and consists of the Uranium dioxide (UO2) (16.5 kg), Zirconium (Zr) (6.5 kg), Zirconium dioxide (ZrO2) (7.5 kg), and Steel 316L(SS) (4.5 kg))

component	Mass(kg)	Melting point (°C)	boiling point (°C)	Density at 3000 °C(kg/m-3)	Specific Heat Capacity at 3000 °C (J/(kg.K)
Steel 316l	4.5	1375 - 1400°C	iron, the primary component of steel, vaporizes is around 2,800	5900	830

			degrees Celsius		
Zirconium (Zr)	7.5	1,855	4409	5123	458.6512
Uranium dioxide (UO2)	16.5	2,865	3527	4272	389.7054
Zirconium dioxide	1.5	2,715	4,300	7478	830.0222

Based on the data provided in table 2 and the formulas for mixture density and specific heat capacity, the resulting mixture parameters are as follows: 4769.7 kg/m³ for density and 495.0018 J/(kg·K) for specific heat capacity at 3000°C.

At the end, Based on the mentioned stages of the process and our calculated corium parameters, the main parameters of our proposed induction furnace with a cold crucible are represented in Table 3;

Table 3: The designed induction furnace parameters

Time of melting (h)	**Furnace frequency (kHz)**	**Furnace power (kW)**	**Crucible highness (cm)**	**Crucible Diameter (cm)**	**Furnace capacity (kg/h)**
1	6023	90.84	23.83	18.33	**30**
5	2059	90.84	40.7	31.3	**30**

Conclusion

During a severe accident, the composition and properties of corium play a crucial role in determining its behavior and its potential interactions with the reactor vessel and, subsequently, with the concrete basement or core catcher. Understanding these interactions necessitates a detailed knowledge of the phases present at high temperatures and their formation processes. However, obtaining accurate data on chemical systems at high temperatures is challenging and often uncertain. Therefore, there is a need for additional data to enhance thermodynamic databases (e.g., NUCLEA) and develop precise equilibrium phase diagrams. These efforts are essential for improving the accuracy of codes used to simulate severe accident conditions.

Corium from severe accidents in different types of reactors can be produced and tested in an induction furnace with a cold crucible (IFCC) within a glove box. Corium is distinguished by its high temperature, typically ranging from 2,200 to 2,800 degrees Celsius. This extreme temperature can lead to the melting

of reactor components and concrete structures, posing significant safety risks. In this study, a proposal is made for an induction furnace with the appropriate frequency, power, and dimensions, taking into account the corium composition, specific heat capacity, and density.

The composition of Corium is considered to be 30 kg and consists of: Uranium dioxide (UO2) (16.5 kg), Zirconium (Zr) (7.5 kg), Zirconium dioxide (ZrO2) (1.5 kg), and Steel 316L(SS) (4.5 kg). The density and specific heat capacity of the resulting mixture parameters are as follows: 4769.7 kg/m³ for density and 495.0018 J/(kg·K) for specific heat capacity at 3000°C. Based on the mentioned stages of the process and calculated corium parameters, A high-frequency tube generator to provides 90.84 kW power in melt and a stable melting regime for the growth of large crystals has been designed. The designed induction furnace parameters are presented in Table 3.

References

1. Mühlbauer A. 2008. HISTORY OF INDUCTION HEATING & MELTING: Vulkan-Verlag GmbH

2. HRBEK J. 2016. INTRODUCTION to Melting in Induction Furnace with Cold Crucible. In 20th International Student Conference on
Electrical Engineering. the Faculty of Electrical Engineering, Czech Technical University in Prague

3. Udalov YP, Poznyak I, Šrank J, Sázávaský P, Kiselová M, et al. 2014. Modifications in the Structure of Oxide Corium Melt and Phase Formation During Its Crystallization Caused by Interaction With Sacrificial Concretes of Core Catcher. Presented at International Conference on Nuclear Engineering

4. Bakardjieva S, Barrachin M, Bechta S, Bottomley D, Brissoneau L, et al. 2008. Improvement of the European thermodynamic database NUCLEA in the frame of EU-funded experiments. Presented at 3rd European Review Meeting on Severe Accident Research (ERMSAR 2008), Nesseber, Bulgaria

5. Bakardjieva S, Barrachin M, Bechta S, Bezdicka P, Bottomley D, et al. 2014. Annals of Nuclear Energy 74: 110-24

6. Journeau C, Kiselova M, Pozniak I, Bezdička P, Svora P, et al. 2021. Nuclear Materials and Energy 29: 101078

7. Journeau C, Kiselova M, Pozniak I, Svora P, Bechta S. 2018. First Experiment on Interaction of Molten Uranium Oxide with Solid Boron Carbide. Presented at 12th International Topical Meeting on Nuclear Reactor Thermal-Hydraulics, Operation and Safety (NUTHOS-12)

8. Petrov Y, Udalov Y, Subrt J, Selucky P, Piluso P, et al. 2005. New crystallization studies of UO 2-ZrO 2-Fe 3 O 4 system and the presumed melting diagram. Presented at Proceedings of the American Nuclear Society-International Congress on Advances in Nuclear Power Plants 2005, ICAPP'05

9. Udalov YP, Poznyak I, Schrank I, Kiselova M, Strejč M, Sazavsky P. 2016. Glass Physics and Chemistry 42: 484-9

10. Journeau C, Piluso P, Plevacova K, Ferry L, Kiselova M, et al. 2010. An ECO-NET Network of high temperature facilities simulating severe accidents. Presented at Proceedings of the 2010 International Congress on Advances in Nuclear Power Plants-ICAPP'10

11. Skakov MK, K. O.; Toleubekov, V. V. ;, Baklanov AV, Gradoboev AS, Akaev;, Beckmuldin. MK. 2022. Eurasian Physical Technical Journal 19: 69-77

12. Skakov M, Baklanov V, Toleubekov K, Akaev A, Bekmuldin M, Gradoboev A. 2023. Вестник НЯЦ РК: 49

13. Skakov M, Baklanov V, Akaev A, Kukushkin I, Bekmuldin M, et al. 2023. Applied Sciences 13: 2480

14. Maruyama Y, Tahara M, Nagasaka H, Kolodeshnikov AA, Zhdanov VS, Vassiliev YS. 2002. Recent results of MCCI studies in COTELS project. Presented at Proceedings of the NTHAS3: Third Korea-Japan Symposium on Nuclear Thermal Hydraulics and Safety Kyeongju, Korea

15. Kolodeshnikov A, Pivovarov O, Zhdanov V, Zuev V, Ignashev V, et al. 2002. Vestnik Natsional'nogo Yadernogo Tsentra Respubliki Kazakhstan 1: 5-17

16. Elliott M. 1996. Letter report: Cold crucible melter assessment, Pacific Northwest National Lab.(PNNL), Richland, WA (United States)

17. Elliott ML, Shafer PJ, Lamar DA, Merrill RA, Grunewald W, et al. 1996. Hanford high-level waste melter system evaluation data packages, Pacific Northwest Lab

18. Sugilal G, Sengar P. 2008. Cold crucible induction melting technology for vitrification of high level waste: development and status in India. Presented at Waste Management Symposium

19. Kobelev A, Stefanovskii S, Zakharenko V, Polkanov M, Knyazev O, et al. 2007. Atomic energy 102: 277-86

20. Roach J, Lopukh D, Martynov A, Polevodov B, Chepluk S. 2008. Advanced modeling of cold crucible induction melting for process control and optimization, Idaho National Lab.(INL), Idaho Falls, ID (United States)

21. Gopalakrishnan S, Thess A. 2012. International journal of thermal sciences 60: 142-52

22. Tesfaye F, Taskinen P. 2010.

23. Mills KC. 2002. Recommended values of thermophysical properties for selected commercial alloys: Woodhead Publishing

24. Kim WK, Shim JH, Kaviany M. 2017. Journal of Nuclear Materials 491: 126-37

25. Shipkov N, Kostikov V, Neproshin E, Demin A. 1979. Recrystallized graphite. Metallurgiya, Moscow

26. Technology NIoSa. 2023. NIST Chemistry WebBook. United States of America: U.S. Secretary of Commerce on behalf of the United States of America

27. Kim CS. 1975. Thermophysical properties of stainless steels, Argonne National Lab., Ill.(USA)

28. Ebrahimi A, Sattari M, Bremer L, Luckabauer M, Römer G-W, et al. 2022. The influence of laser characteristics on internal flow behaviour in laser melting of metallic substrates

ICNST 2024 International Conference on Nuclear Science and Technology
6- 8 MAY 2024 | Isfahan, Iran

Investigation of the Effect of Al2O3 Nanoparticles on Thermo-hydraulic Parameters in a Mini-Loop with Natural Circulation (Paper ID : 1282)

Nourashrafeddin S.A.[1*], Shayesteh M.[1]
[1]*Physics Science and Technology Center, Imam Hossein University, Tehran, Iran.*

Abstract

This research investigates the influence of aluminum oxide nanoparticles on thermohydraulic parameters in a mini-loop system with natural circulation, employing numerical simulations conducted with ANSYS Fluent. The study employs a simulation-based approach to analyze the thermohydraulic behavior of the system in the presence of aluminum oxide nanoparticles. The simulation methodology involves modeling the fluid flow, heat transfer using the ANSYS Fluent software. The mass flow rate, temperature difference across the heat source, and fluid velocity were compared for various power levels and for a fluid with different percentages of aluminum oxide nanofluid in this study. The results indicate that within the operational power range of this mini-loop, the mass flow rate decreases with an increase in nanoparticle percentage, resulting in an increase in the temperature difference across the heat source and a decrease in fluid velocity. Furthermore, at a power of 20 watts and at various inclination angles, the results were compared. The findings suggest that as the angle of inclination increases, the mass flow rate decreases, the temperature difference across the heat source increases, and the fluid velocity decreases.

Keywords: aluminum oxide, nanoparticles, mini-loop, natural circulation, ANSYS Fluent, Heat transfer.

Introduction

Leveraging the principles of fluid dynamics and gravity, the natural circulation loop forms the backbone of passive safety systems, eliminating the need for mechanical pumps by transferring heat from the source to the sink. This mechanism, fundamental to many innovative technologies, is particularly critical in the realm of nuclear applications, where the safety of the systems is intrinsically linked to their cooling capabilities. Despite the challenges associated with natural circulation, such as low driving force and flow instability, its potential for widespread use is significant if these issues are properly addressed. Numerous studies have been conducted on the sustainability of natural circulation systems. Initially, Vijayan et al. [1] examined the impact of loop diameter on the stability of the natural circulation system. They discovered that in single-phase systems, the stability of the natural circulation system decreases with an increase in diameter. However, in two-phase systems, stability increases with an increase in circuit diameter. In another study by Vijayan [2], the effect of flow direction on the stability of the

natural circulation system was investigated. This research examined steady-state analysis for clockwise and anti-clockwise circulation using a rectangular loop with a heat source and sink placed horizontally and vertically in the loop. Chen et al. [3] studied the stability of a rectangular loop by changing the height to width ratio and concluded that as this ratio approaches one, the loop tends to unstable conditions. Moussavian et al [4] investigated the stability behavior of the Genova natural circulation loop using the numerical solution method and compared it with experimental results in some cases. In the aforementioned studies, water has been used as the reference fluid. However, it should be noted that in the field of thermal management, the search for efficient heat transfer fluids is an ongoing subject. Traditional fluids often fall short in systems with high heat flux density, such as electronics and solar collectors, due to their low thermal conductivity and poor thermal performance. This has led to the discovery of nanofluids - fluids containing nanoparticles - which have been promising in enhancing the thermal properties of the base fluid [5,6]. This paper focuses on the effect of Al2O3 nanoparticles on the thermo-hydraulic performance of a mini-loop system with natural circulation. The mini-loop system, also known as a Natural Circulation Loop (NCL), is a system that transports thermal energy from a heat source to a heat sink without the need for a pump. The use of Al2O3 nanoparticles in such a system is a novel approach aimed at enhancing its thermo-hydraulic performance. Some of the latest publications in the field of thermal management using Al2O3 nanoparticles are: Prashanth, M. et al. investigate the effect of different weight percentages of Al2O3 nanoparticles, fill ratio, and heat input on the thermal performance of an Oscillating Heat Pipe (OHP) system. The results indicated that the highest influence factors are heat input and fill ratio, while the least is the weight percentage of Al2O3 nanoparticles [7]. Sufian, M. et al. utilized ANSYS Fluent for simulations, taking into account various input parameters in their study on the application of Al2O3-Water nanofluids in compact pipes. Their findings revealed that the two-phase simulation approach they employed was more effective compared to the conventional single-phase simulations used in other research. Notably, their approach demonstrated a significant enhancement in both heat flow and thermal conductivity [8]. M. Misale et al. conducted an experimental study on the thermal performance of a mini-loop system that employs natural circulation. The study utilized distilled water and Al2O3 nanofluid as working fluids. The findings revealed a strong alignment with Vijayan's correlation, which was originally developed for large-scale natural circulation loops [9]. In their experimental study, Doganay and colleagues explore the thermal performance of a Single-Phase Natural Circulation Mini Loop (SPNCmL). The findings reveal a significant enhancement in thermal performance, with the effectiveness factor increasing by 30%. This improvement was achieved through the use of Al2O3-DIW nanofluids as the working fluid under inclined conditions. Notably, this is the

first instance of such a performance boost in a nanofluid-based SPNCmL. This research holds potential for future applications and advancements in the field [10]. Koca et al. used a DIW based Ag nanofluid in an SPNCmL and compared the results with a DIW based Al2O3 nanofluid. SPNCmL using a lower concentration of Ag nanofluid (0.25 wt.%) had the same thermal stability with DIW as a working fluid. However, the Al2O3 nanofluid had an almost constant ε ratio at different heater powers while for higher concentrations of Ag-nanofluid, ε increased significantly with increasing heater power [11]. Sudi and colleagues in their experimental study, delve into the behavior of a two-phase natural circulation loop filled with both water and nanofluid. Their findings reveal that the mass flow rate within the natural circulation loop escalates in response to an increase in heat input during the single phase. Interestingly, they also observe that the transition from a single phase to a two-phase state occurs at lower heat inputs when the loop is filled with nanofluid [12]. Azher M. with their colleagues conducts a numerical analysis using ANSYS software to examine the fluid flow and heat transfer characteristics of nanofluids in a corrugated wavy channel within the turbulent range. Various nanoparticles, including Al2O3, CuO, SiO2, and ZnO, were employed and dispersed in different base fluids such as ethylene glycol, glycerin, and water [13]. Nagireddy, P and colleagues conducted a study on the thermal performance of a natural circulation loop filled with Al2O3/Water nanofluid. Their findings revealed that the use of Al2O3/Water nanofluid as a loop fluid led to an increase in mass flow rates and enhanced thermal characteristics in comparison to water. Notably, the time required to reach a steady state was reduced, and there was a significant improvement in the Nusselt and Grashof numbers [14]. Çobanoğlu, N., with their colleagues, conducted a study on the impact of geometrical parameters on the performance of nanofluid-based single-phase natural circulation mini loops (SPNCmLs). They used water-based Al2O3 nanofluid as the working fluid. Their findings revealed that the pipe diameter has a more substantial influence on heat transfer performance than the aspect ratio. Additionally, they found that nanofluids exhibit higher temperatures and effectiveness values compared to water [15]. Bejjam, R. B., et al. conducted a numerical investigation into the impact of the inclination angle on the thermal-hydraulic characteristics of a rectangular natural circulation loop (NCL). They discovered that the steady-state mass flow rate rises with particle concentration and falls with loop inclination angle at a specific power input. The Rayleigh number and the average heat transfer coefficient are improved with particle concentration. However, these effects are marginal at lower inclinations for any particle concentration [16]. Adarsh, R., and their colleagues focused their study on the stabilization of flow in Natural Circulation Loops (NCLs) at lower inclinations. They demonstrated that the presence of an orifice could achieve the flow stability of a higher inclination angle at a lower one. This was accompanied by a reduction in the loop's

mass flow rate and an increase in the temperature difference across the cooler [17]. In their study, Elnaggar, S., and colleagues validated a model using ANSYS Fluent, benchmarking it against experimental data. Their findings indicated that the software could qualitatively predict the thermal-hydraulic behavior, including the associated flow inversion phenomenon, in natural circulation loops [18]. In their research, Zhu, H., and colleagues conducted both theoretical and experimental studies under inclined conditions. They discovered that inclination constrained the overall circulation due to a decrease in the average altitude difference between the steam generators and the electric heater. Furthermore, they found that a loop design featuring a large altitude difference and a small width was more desirable to minimize the influence of inclination [19]. Nourashrafeddin et al. investigated the single-phase natural circulation mini-loop by simulation method with Ansys Fluent software and compared with experimental data. It was observed that the simulation results are in good agreement with the laboratory data [20]. In this study, the specifications of the natural circulation mini-loop from reference 11 were utilized for the simulation. Despite these extensive studies, gaps in knowledge still exist. For instance, the effect of different fluid properties on the stability of natural circulation systems is not fully understood. Furthermore, the impact of various system parameters, such as loop geometry and heat source characteristics, on system performance needs further investigation. This study seeks to address these research questions and contribute to the existing body of knowledge in this field. Specifically, it aims to examine how varying weight percentages of Al2O3 nanofluids, fill ratios, and heat inputs influence the thermal performance of the system. The ultimate objective is to offer insights that could enhance heat management in systems characterized by high heat flux density.

Simulation model

System description and assumptions

In this study, a rectangular mini-loop with a circular cross-section (as depicted in Fig.1) has been employed as a thermo-hydraulic system to investigated the natural circulation of fluid. The heat source is positioned at the bottom of the loop, delivering heat to the lower horizontal arm of the loop at a constant heat flux. The cooling component, a heat exchanger maintaining a constant wall temperature (Tc), is situated at the top of the loop and is expected to have the lowest temperature in the system. The heat flux and temperature (Tc) serve as two variable parameters for assessing the system's stability. The temperature differential between the two extremities of the heat source signifies the temperature difference between two points, T1 and T2, as illustrated in Fig.1. These two points are distanced 40 mm from the lower segment of the loop [21].

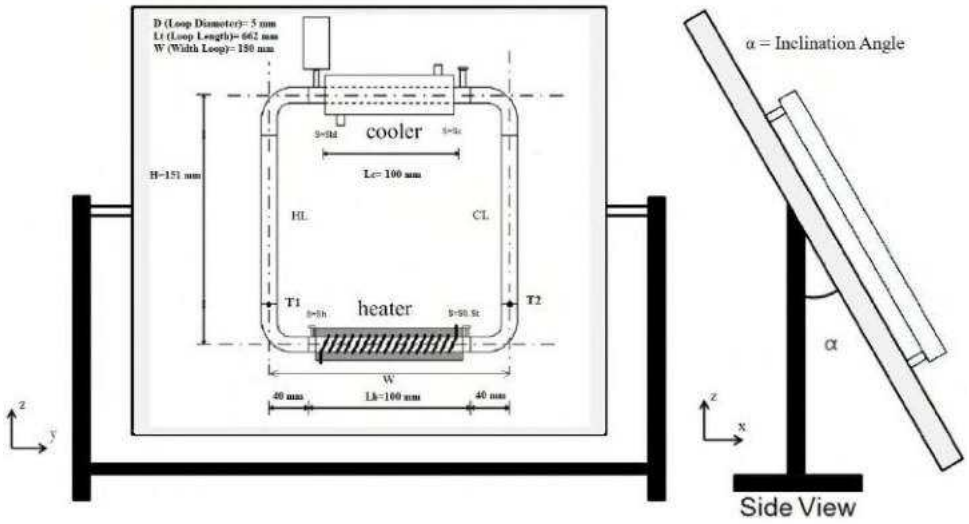

Fig.1 . Schematic view of the natural circulation mini-loop [21]

Simulation with Ansys Fluent

Ansys Fluent software is used as an accurate tool for modeling fluid flow, heat transfer, etc. The main task of Fluent software is to solve differential equations that cannot be solved analytically, which is called CFD. Below is a brief description of the mini-loop simulation setup using Ansys Fluent:

The geometry is imported into ANSYS Fluent and discretized into a mesh, the quality of which is vital for the simulation's accuracy. Fig.2 illustrates the temperature distribution in the mini loop simulated using ANSYS Fluent, and the mesh specifications of this mini loop are detailed in Table 1.

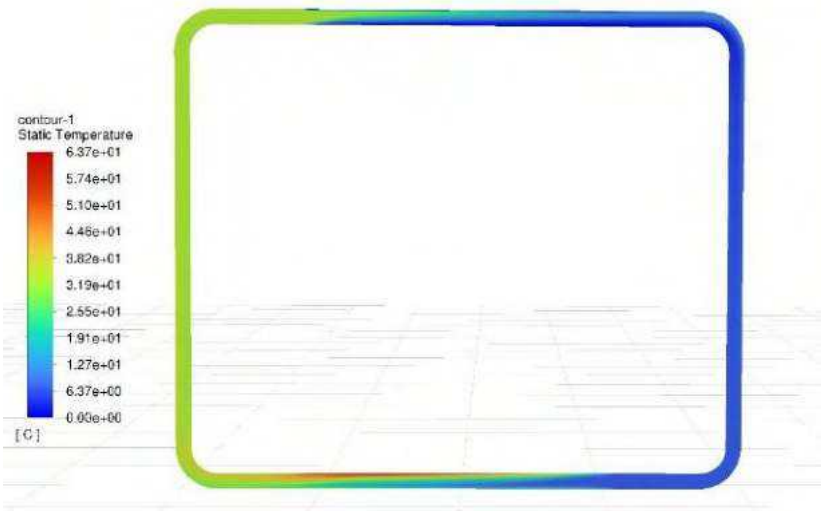

Fig.2 . Temperature distribution in the mini loop simulated using ANSYS Fluent

Table 1. Parameters related to mesh specifications of mini-loop

mesh specifications Parameters	Aspect Ratio	Skewness	Mesh number	Geometry Mesh
Mini-loop	1 2914	0.091259	99054	Quadrilateral Mesh

It's important to note that the specific parameters and boundary conditions, as well as the numerical methods and models, would be contingent on the specifics of the system being simulated, such as the type of fluid, the operating conditions, and the physical phenomena of interest. In this work, ANSYS Fluent used Pressure-Based Solver numerical method. This method is typically used for incompressible and mildly compressible flows. It solves the pressure-velocity coupling using an iterative method. Table 2 shows some parameters related to simulation with Ansys Fluent software for mini-loop.

Table 2. Parameters related to simulation with Ansys Fluent software for mini-loop

Ansys Fluent Parameters	Geometry	Flow Model	Solver	Spatial discretization type of pressure	Solving algorithm	The method of solving gradients
Mini-loop	3D Channel	$k-\omega(2eq)$	Pressure Based	Second Order	Coupled	least squares cell based

The reference fluid considered for the study of natural circulation in the mini-loop is distilled water, the thermodynamic properties of which are provided in Table 3. The goal of this study is to observe the impact of different percentages of aluminum oxide nanoparticles on various thermodynamic parameters of a natural circulation mini loop. The thermodynamic properties of uranium oxide nanoparticles are given in Table 4. Please note that it's important to consider the specific heat capacity, thermal conductivity, and other thermodynamic properties of the nanoparticles when analyzing their impact on the natural circulation of the fluid. These properties can significantly influence the heat transfer and fluid dynamics within the system.

Table 3. Thermo-physical properties of loop fluid at a temperature of 25℃ and a pressure of 1 atm

	$\rho(kg/m^3)$	$\mu(kg/ms)$	$C_p(J/kg℃)$	$\beta(K^{-1})$	Pr
Thermo-physical properties of fluid	997.1	0.00089	4183	0.00025	**6.3**

Table 4. Thermo-physical properties of Al_2O_3 nanoparticles

	$\rho(kg/m^3)$	$k(W\,m^{-1}K^{-1})$	$C_p(J/kg℃)$	$\beta(K^{-1})$
Al_2O_3	3970	25	880	0.85

1- The assumptions required to simulate this loop with Ansys Fluent are [21]:
2- Heat is supplied to the bottom of the loop (heat source) as a constant heat flux. The amount of this heat flux is changed to study the stability of the system.
3- The cooling part (heat well) in the upper part of the loop is considered as a heat exchanger with constant wall temperature (T_c), which has the lowest temperature in the system. T_c is considered as a variable parameter for stability study.
4- Considering that the range of temperature changes in the present problem is not large, the Boussinesq approximation[4] can be used. To increase the accuracy of the simulation calculations, the physical properties of the fluid were defined as a function of temperature with the 7th order polynomial function in the material properties section, and the results were not much different from the results of Boussinesq approximation. Therefore, this approximation has been used in the calculations.
5- It is assumed that the inner diameter of the loop is the same in all parts and equal to 5 mm.
6- Hot legs and cold legs are considered insulation.
7- Fluid axial heat transfer and thermal viscosity are omitted.

Results and discussion

Figure 3 compares the mass flow rate and fluid velocity in the loop for various power levels with fluids containing different weight percentages of aluminum oxide nanoparticles (1-3% by weight). The findings reveal that both the mass flow rate and fluid velocity increase proportionally to the power input. However, this increase is less pronounced in fluids with higher weight percentages of nanoparticles. In other words, as the power input increases, both the mass flow rate and fluid velocity increase. But this increase is less in fluids that have higher percentages of nanoparticles. This could be because the nanoparticles, by increasing the fluid's density, cause a decrease in the fluid's flow rate. This is an important finding as it can have a significant impact on the efficiency and performance of thermal systems that use these types of fluids.

[4] Boussinesq approximation is an approximation used in the analysis of fluid flows under the influence of buoyancy force. This approximation is based on the fact that the effect of fluid density changes in the momentum term can be ignored in the equation of motion and the effect of density changes can be considered only in parts of the fluid motion equation that are acceleration coefficients. In this approximation, it becomes much easier to solve the equation of fluid motion in conditions where there is a change in density.

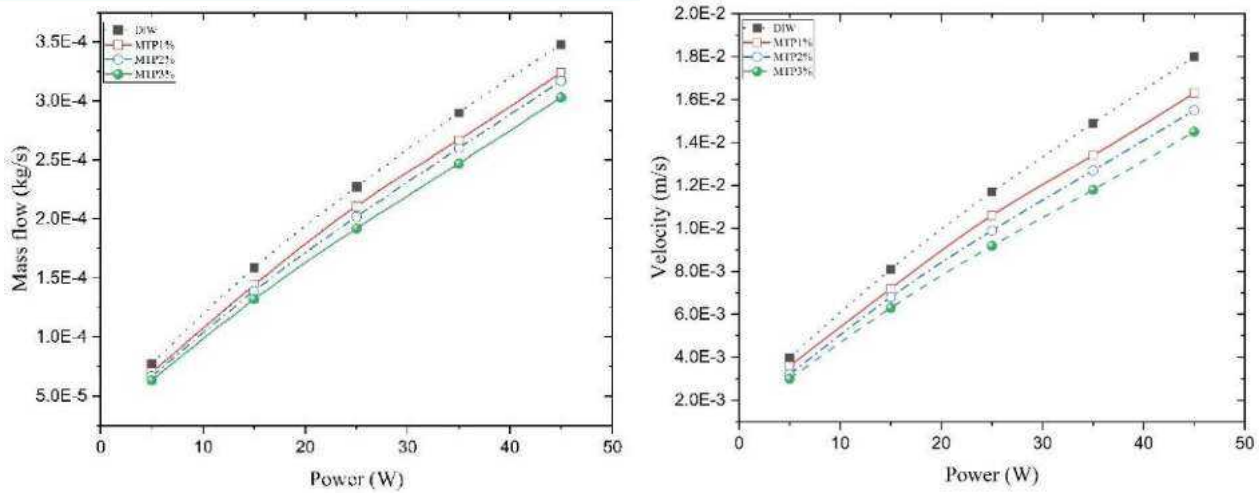

Fig.3. Mass flow rate and fluid velocity diagrams as a function of heat source power for distilled water with (1-3%) weight percentages of aluminum oxide nanoparticles.

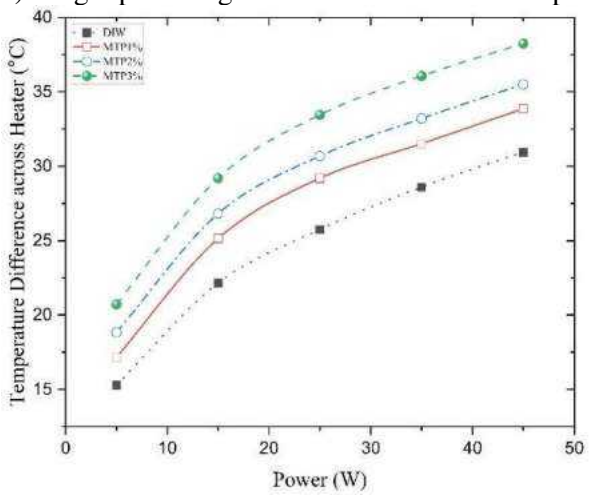

Fig.4. Comparison diagram of the temperature difference across heater in the loop as a function of input power and for fluids with different percentages of aluminum oxide nanoparticles.

The temperature difference across heater, as a function of input power, is depicted in Fig4. The results indicate that as the input power increases, the temperature difference across the heater also increases. This means that the heater becomes more effective at transferring heat as more power is supplied to it. Moreover, the increase in temperature difference is more significant for fluids with higher weight percentages of nanoparticles. This could be due to the enhanced thermal conductivity of nanofluids, which allows for more efficient heat transfer. Nanoparticles can distribute the heat more evenly throughout the fluid, leading to a larger temperature difference across the heater for a given power input. In practical terms, this suggests that using nanofluids in a heating system could potentially improve its efficiency, especially at higher power levels. However, further research would be needed to confirm this and to optimize the nanoparticle concentration for different applications. It's an interesting area of study in the field of thermal engineering.

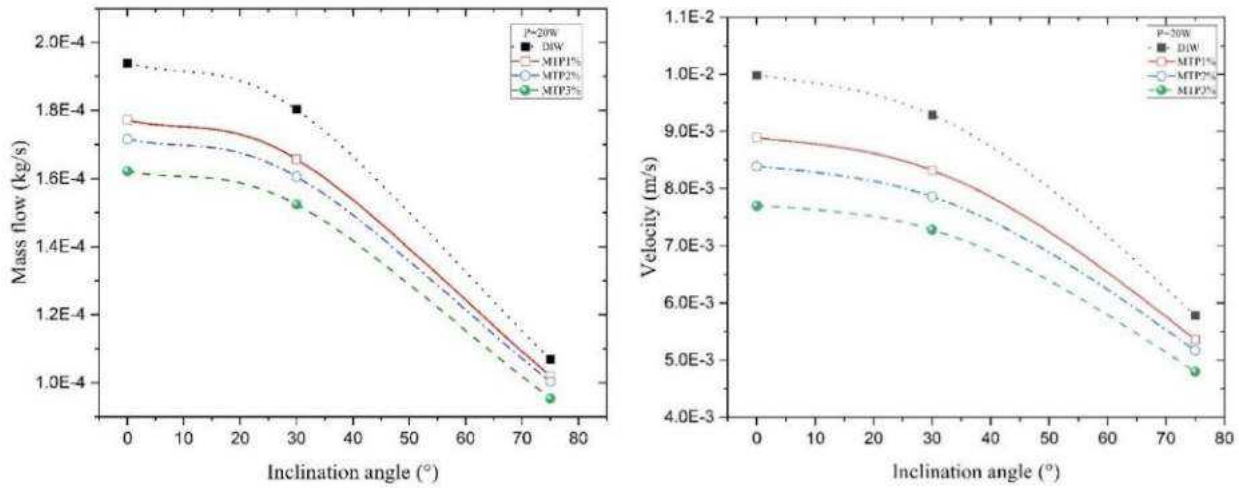

Fig.5. Mass flow rate and fluid velocity diagrams as a function of different inclination angles for distilled water with various weight percentages of aluminum oxide nanoparticles.

Continuing, for different inclination angles[5] of the mini-loop and considering a constant power (P=20W), diagrams depicting the fluid mass distribution, fluid velocity distribution, and the temperature difference heater are calculated for various powers. The results are presented in Figures 5-6.

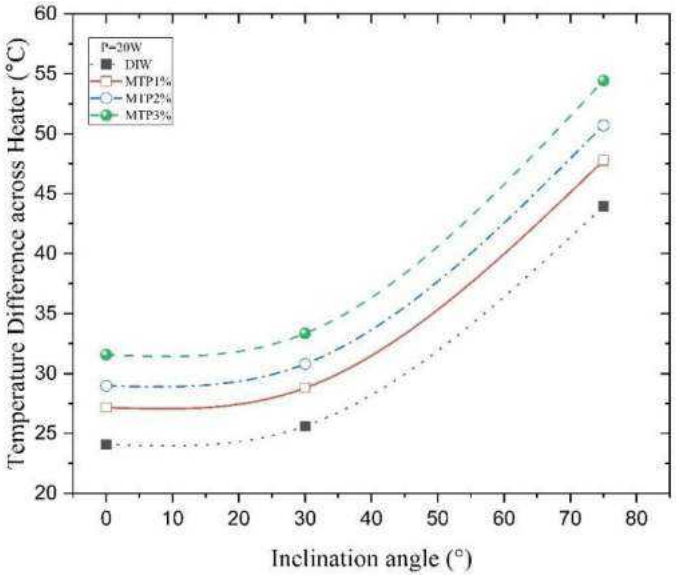

Fig.6. Comparison diagram of the temperature difference across heater in the loop as a function of various inclination angles and for fluids with different percentages of aluminum oxide nanoparticles.

Fig.5 shows that as the inclination angle increases, both the mass flow rate and fluid velocity decrease. This could be due to the fact that an increase in the inclination angle changes the gravitational force acting on the fluid, which in turn affects the fluid's flow rate and velocity. Interestingly, this decrease is more significant for fluids with higher weight percentages of nanoparticles. This might be because the

[5] Inclination Angle (α)

nanoparticles increase the fluid's density, which further reduces the fluid's flow rate and velocity at higher inclination angles. Fig.6, on the other hand, shows that the temperature difference between the two heat sources increases with an increase in the inclination angle. This suggests that the heat transfer efficiency of the system improves as the inclination angle increases. Moreover, this increase in temperature difference is more pronounced for fluids with higher weight percentages of nanoparticles. This could be due to the enhanced thermal conductivity of nanofluids, which allows for more efficient heat transfer, especially at higher inclination angles. In practical terms, these findings suggest that the inclination angle and nanoparticle concentration can significantly affect the performance of a fluid system. Therefore, these factors should be carefully considered when designing and optimizing such systems. However, further research would be needed to fully understand these effects and their implications for different applications. It's a fascinating area of study in the field of fluid dynamics and heat transfer.

Conclusions

In this paper, the impact of different weight percentages of aluminum oxide nanoparticles on the thermodynamic parameters of a mini-loop natural circulation system has been investigated. It was observed that when the loop is in a vertical position and the inclination angle is zero, both the mass flow rate and fluid velocity increase with the increase in power, and the magnitude of this increase is less pronounced for fluids with higher weight percentages of nanoparticles. Meanwhile, the temperature difference across heater is expected to increase with higher power, and the extent of this temperature difference will be greater for fluids with higher weight percentages of nanoparticles. Furthermore, the calculations at a constant power and for different inclination angles of the loop indicate that both the mass flow rate and fluid velocity decrease with an increase in the inclination angle, and the magnitude of this decrease is more significant for fluids with higher weight percentages of nanoparticles. On the other hand, the temperature difference across heater increases with an increase in the inclination angle, and the extent of this increase is more pronounced for fluids with higher weight percentages of nanoparticles. In summary, the results provide valuable insights into the thermodynamic behavior of the mini-loop under varying conditions, specifically highlighting the influence of different weight percentages of aluminum oxide nanoparticles.

References

[1] Vijayan, P., et al., (2008). Effect of Loop Diameter on the Steady State and Stability Behavior of Single-phase and Two-phase Natural Circulation Loops. Science and technology of nuclear installations.

[2] Vijayan, P., Sharma, M., Saha, D., (2007). Steady state and stability characteristics of single-phase natural circulation in a rectangular loop with different heater and cooler orientations. Exp. Therm. Fluid Sci. 31 (8), 925–945.

[3] Chen, K., (1985). On the oscillatory instability of closed-loop thermosyphons. ASME, Transactions, Journal of Heat Transfer 107, 826–832.

[4] Moussavian, S. K., Misale, M., D'Auria, F., & Salehi, M. (2003, January). Stability behavior of single-phase natural circulation loop. In ASME International Mechanical Engineering Congress and Exposition (Vol. 37157, pp. 119-131).

[5] Yılmaz Aydın, D., & Gürü, M. (2021). Nanofluids: preparation, stability, properties, and thermal performance in terms of thermo-hydraulic, thermodynamics and thermo-economic analysis. *Journal of Thermal Analysis and Calorimetry*, 1-34.

[6] Okonkwo, E. C., Wole-Osho, I., Almanassra, I. W., Abdullatif, Y. M., & Al-Ansari, T. (2021). An updated review of nanofluids in various heat transfer devices. *Journal of Thermal Analysis and Calorimetry*, *145*, 2817-2872.

[7] Prashanth, M., Madhu, D., Ramanarasimh, K., & Suresh, R. (2023). An investigation to evaluate the influence of Al2O3 nanoparticles on thermal performance of oscillating heat pipe using Box–Behnken design method. *Multiscale and Multidisciplinary Modeling, Experiments and Design*, 1-13.

[8] Sufian, M., & Ali, B. (2023). ANSYS Simulation of Enhanced Heat Transfer in Compact Pipes Using Al2O3-Water Nanofluids: ANSYS Simulation of Al2O3-Water Nanofluids. *Pakistan Journal of Emerging Science and Technologies (PJEST)*, *4*(4).

[9] Misale, M., Devia, F., & Garibaldi, P. (2012). Experiments with Al2O3 nanofluid in a single-phase natural circulation mini-loop: Preliminary results. *Applied Thermal Engineering*, *40*, 64-70.

[10] Doganay, S., & Turgut, A. (2015). Enhanced effectiveness of nanofluid based natural circulation mini loop. *Applied Thermal Engineering*, *75*, 669-676.

[11] Koca, H. D., Doganay, S., & Turgut, A. (2017). Thermal characteristics and performance of Ag-water nanofluid: Application to natural circulation loops. *Energy Conversion and Management*, *135*, 9-20.

[12] Sudi, V. S. S., Kupireddy, K. K., Balasubramanian, K., & Nagireddy, P. D. (2023). experimental Study on Transition of Single Phase to Two Phase in a Natural Circulation Loop Filled with Al2O3 Nanofluid. *Iranian Journal of Science and Technology, Transactions of Mechanical Engineering*, 1-11.

[13] Abed, A. M., Abdulkadhim, A., Mohammed, H. A., Hamzah, H. K., Farooq, H. A., Mejbel Abed, I., & Mahjoub Said, N. (2024). Numerical simulation on thermohydraulic performance of different types of nanofluids in a corrugated-triangular channel. *Journal of Taibah University for Science*, *18*(1), 2306671.

[14] Nagireddy, P. D., Chalamalasetti, S. R., & Kupireddi, K. K. (2021). Thermal performance of natural circulation loop filled with Al_2O_3/Water nanofluid. *International Journal of Nano Dimension*, *12*(3), 272-278.

[15] ÇOBANOĞLU, N., Alaboud, M., & Karadeniz, Z. H. (2021). Effect of geometrical parameters on the performance of nanofluid-based single phase natural circulation mini loops. *High Temperatures--High Pressures*, *50*(6).

[16] Bejjam, R. B., & Kiran Kumar, K. (2019). Numerical investigation to study the effect of loop inclination angle on thermal performance of nanofluid-based single-phase natural circulation loop. *International Journal of Ambient Energy*, *40*(8), 885-893.

[17] Adarsh, R., Raveesh, G., & Rupesh, S. (2020). Orifice enabled flow stabilization of natural circulation loop at lower inclinations. *Kerntechnik*, *85*(3), 140-146.

[18] Elnaggar, S. (2022). Validation of ANSYS Model of experimental Test Rig Simulating the Flow Inversion in RRs. *Archives of Current Research International*, *22*(4), 19-28.

[19] Zhu, H., Yang, X., Gong, H., & Jiang, S. (2013). Theoretical and experimental study on single-phase natural circulation under inclined conditions. *Journal of Nuclear Science and Technology*, *50*(3), 304-313.

[20] Nourashrafeddin, S. A., Shayesteh, M., Bahonar, M. (2023). Investigating the influence of inclination angle on thermohydraulic parameters of natural circulation laboratory mini-loop. In 29th Iranian nuclear conference, Shahid Beheshti University, Tehran, Iran.

[21] Nourashrafeddin, S. A., Shayesteh. (2024). Investigating the Influence of Inclination Angles on the Parameters of the Mini-Loop's Natural Circulation (Manuscript under review). Progress in Nuclear Energy.

ICNST 2024
International Conference on Nuclear Science and Technology
6- 8 MAY 2024 | Isfahan, Iran

Design of molten salt reactor core power controller using MPC method (Paper ID : 1300)

Safarzadeh O.[1*], Bakhtiari-Mehr M.[2]

[1] *Faculty of Engineering, Shahed University, Tehran, Iran*

[2] *Faculty of Engineering, Shahed University, Tehran, Iran*

Abstract

One of the most important operations in nuclear power plants is controlling the power of the reactor core. The molten salt reactor is one of the fourth generation reactors, which is superior to other reactors due to the use of liquid fuel. Model predictive control is a modern optimal control method that is widely used to control linear and nonlinear systems. In this article, the predictive control method of the model is used to control the core power of the molten salt reactor. For this purpose, the six-group model of neutron kinetics of this reactor was developed along with thermal feedbacks of fuel temperature and retarder. Then the linear model was extracted and using this model, a predictive control system was designed. The results show lower overshoot and settling time.

Keywords: Molten salt reactor, model predictive control, reactor power control,

Introduction

The heart of the reactor in a nuclear power plant is considered as a key part in the cycle of electricity generation from nuclear fuel. The inability of a nuclear power plant to perform optimal control over the reactor core can lead to higher operating costs or reduced system safety and reliability. In general, reactor core control includes power control and power distribution control in the reactor core. Molten salt reactor is one of the fourth generation reactors of nuclear power plants. In this reactor, molten salt is used as fuel and elemental graphite is used as an agent to slow down the interactions of nuclear reactions in the molten salt reactor. Since liquid fuel is used in this reactor, there is no need to prepare solid fuel pellets and enclose them in rod packages. The core power control of molten salt reactor with liquid fuel compared to other solid fuel reactors of the fourth generation has advantages such as the decay of delayed neutron precursors in the primary circuit and the reduction of the effective delayed neutron fraction. Also, compared to the current advanced light water reactors, molten salt reactors are far superior in terms of economy, safety, and compatibility with the environment.

Nuclear power plants have very complex, nonlinear and time-varying systems that have different characteristics at each level of operational power. Therefore, monitoring the input variables and applying restrictions for the stability of the system is a serious challenge in order to control the heart of the reactor. The aim of this paper is to design a predictive controller to control the core power of the molten salt

reactor. Controller design is difficult due to unpredictable disturbances. To avoid the above problems, the unknown parameters of the system should be estimated and the satisfied parameters should be included in the control algorithm. One of the ways to solve such problems is to develop a model predictive control that can achieve control goals by compensating the modeling error due to parameter uncertainties.

Research Theories

In recent years, several control methods have been used to control the core power of the molten salt reactor. Like the fuzzy-PID control method presented by Mr. Liu in 2009 [1]. Also, the PID control method based on the internal model was presented by Mr. Zheng in 2020 and Mr. Paradan in 2022 [2-3]. Also, the fuzzy-PID control method was also presented by Mr. Zheng in 2020 [4]. Singh et al presented a nonlinear model for molten salt reactor [5]. They used various sources for the suggestions and compared the simulation results with the laboratory results. In reference [6], molten salt reactor control strategies were investigated. Control loops for load tracking, rendering, and results are compared to the case where there is no control loop. Mr. Zarei presented a non-linear model for the molten salt reactor and then examined the differences between the linear and non-linear models [7]. Then, using the feedback linearization method, he provided a controller to control the power of the reactor. Reference [8] presented a fractional-order fuzzy-PID controller for reactor power control. Fuzzy adjustment was achieved using cuckoo optimization method.

The application of these control methods has been successful in controlling the core power of the molten salt reactor, but there are still challenges in controlling the power of the reactor core. Although traditional and hybrid PID control techniques are used to control molten salt reactor cores, adjusting the controllers in the control methods is a very difficult and time-consuming task.

Modeling and Governing Relations

As shown in Figure (1), the reactor core is divided into an inner zone and an outer zone. Based on the theory of point dynamics and the energy conservation principle of the reactor core, the nonlinear model of the reactor core for molten salt is presented.

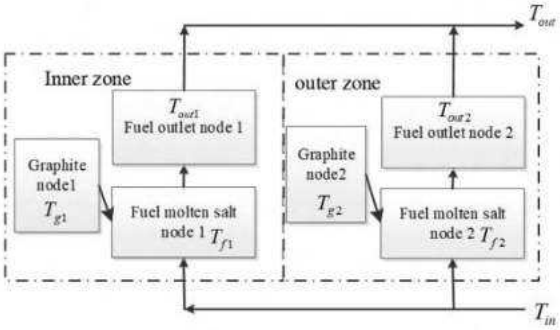

Fig. 1. Division of liquid molten salt reactor core

Nonlinear model of the reactor core

The nonlinear model of the reactor core is developed by adopting point dynamics with two groups of delayed neutron precursors and reactivity feedbacks due to changes in fuel temperature and coolant temperature.

$$\frac{dp(t)}{dt} = \frac{\rho(t)-\beta}{\Lambda} p(t) + \lambda_1 c_1(t) + \lambda_2 c_2(t) \quad (1)$$

$$\frac{\boldsymbol{dc_i(t)}}{\boldsymbol{dt}} = \frac{\boldsymbol{\beta_i}}{\boldsymbol{\Lambda}} \boldsymbol{p(t)} + \boldsymbol{\lambda_i c_i(t)} - \frac{\boldsymbol{1}}{\boldsymbol{\tau_c}} \boldsymbol{c_i(t)} \quad (2)$$

$$\boldsymbol{c_i(t-\tau_i) \approx c_i(t) - \tau_i \frac{dc_i(t)}{dt}} \quad (3)$$

$$\boldsymbol{\frac{dc_i(t)}{dt} = \frac{\beta_i}{\Lambda} p(t) + \lambda_i c_i(t) - \frac{\lambda_i}{a_i b_i} c_i(t) \quad i = 1\ 2} \quad (4)$$

where $\boldsymbol{a_i}$and $\boldsymbol{b_i}$ are equal to:

$$a_i = \frac{\lambda_i \tau_i}{\lambda_i \tau_i + 1 - \exp(-\lambda_i \tau_l)}$$

$$b_i = 1 + \frac{\tau_l}{\tau_c} \exp(-\lambda_i \tau_l)$$

In order to facilitate the application, equations (1) and (4) are simplified:

$$\boldsymbol{\frac{dp_r(t)}{d(t)} = \frac{\rho(t)-\beta}{\Lambda} p_r(t) + \lambda_1 c_{1r}(t) + \lambda_2 c_{2r}(t)} \quad (5)$$

$$\boldsymbol{\frac{dc_{ir}(t)}{d(t)} = \frac{\beta_i}{\Lambda b_i} p_r(t) - \frac{\lambda_i}{a_i b_i} c_{ir}(t) \quad i = 1, 2} \quad (6)$$

In which, $\boldsymbol{p_r(t) = p(t)/\ p_0}$represents the relative power of the heart to the initial average power at time t, $\boldsymbol{c_{ir}(t) = c_i(t)/\ c_{i_0}}$ indicating the precursor density compared to the initial average density at time t. p(t) and $\boldsymbol{c_i(t)}$ are the reactor core power and neutron precursor density of group i at time t. $\boldsymbol{p_0}$and $\boldsymbol{c_{i_0}}$ indicate the initial average power of the heart and the density of the initial average neutron precursor from group i , $\boldsymbol{\beta_i}$ and Λ indicate the delayed neutron fraction of group i and the time of neutron production. $\boldsymbol{\lambda_i}$ indicates the decay constant related to the delayed neutron group i, $\boldsymbol{\rho(t)}$indicates the reactivity of the reactor core at time t, $\boldsymbol{\tau_c}$and $\boldsymbol{\tau_l}$ indicate the transit time of the core and the external

transit time of the primary loop. Considering the movement of the control rods and the reactivity feedback caused by the changes in fuel temperature and coolant temperature, the following reactivity model is made:

$$\boldsymbol{\rho} = \boldsymbol{\rho_0} + \boldsymbol{\rho_{rod}} + \boldsymbol{\rho_t} \qquad (7)$$

$$\boldsymbol{\rho_0} = \sum_{i=1}^{2} \boldsymbol{\beta_i}\left[\mathbf{1} - \frac{\boldsymbol{\lambda_i}}{\boldsymbol{\lambda_i} + \frac{\mathbf{1}}{\boldsymbol{\tau_c}} \times (\mathbf{1} - \boldsymbol{exp}\,(-\boldsymbol{\lambda_i \tau_l}))}\right] \qquad (8)$$

$$\boldsymbol{\rho_t} = \boldsymbol{\alpha_f}\frac{[(T_{f1} - T_{f1}{}^{0})m_{f1} + (T_{f2} - T_{f2}{}^{0})m_{f2}]m_{f2}}{m_{f1}+m_{f2}} + \boldsymbol{\alpha_g}\frac{[(T_{g1} - T_{g1}{}^{0})m_{g1} + (T_{g2} - T_{g2}{}^{0})m_{g2}]m_{g2}}{m_{g1}+m_{g2}} \qquad (9)$$

$$\mu_{f1} = \frac{m_{f1}}{m_{f1}+m_{f2}} \quad , \quad \mu_{f2} = \frac{m_{f2}}{m_{f1}+m_{f2}}$$

$$\mu_{g1} = \frac{m_{g1}}{m_{g1}+m_{g2}} \quad , \quad \mu_{g2} = \frac{m_{g2}}{m_{g1}+m_{g2}}$$

where $\boldsymbol{\rho_0}$and $\boldsymbol{\rho_{rod}}$represent the initial steady state reactivity and control rod movement reactivity, respectively. $\boldsymbol{\alpha_f}$and $\boldsymbol{\alpha_g}$represent Doppler feedback coefficient and graphite feedback coefficient, respectively.

Linear model of reactor core

Before linearization, the linear model is designed as a single-output, single-input (SISO) model. The input and output are the reactivity change of the reactor control rods and the deviation of the relative power of the heart, respectively.

$$\frac{\boldsymbol{dp_r}}{\boldsymbol{dt}} = \frac{\boldsymbol{\rho(0)-\beta}}{\boldsymbol{\Lambda}}\boldsymbol{\delta p_r} + \boldsymbol{\lambda_1 \delta c_{1r}} + \boldsymbol{\lambda_2 \delta c_{2r}} + \frac{\boldsymbol{\alpha_{fp_r(0)}}}{\boldsymbol{\Lambda}}\left(\boldsymbol{\mu_{f1}\delta T_{f1}} + \boldsymbol{\mu_{f2}\delta T_{f2}}\right) + \frac{\boldsymbol{\alpha_{gp_r(0)}}}{\boldsymbol{\Lambda}}\left(\boldsymbol{\mu_{g1}\delta T_{g1}} + \boldsymbol{\mu_{g2}\delta T_{g2}}\right) + \frac{\boldsymbol{p_{r(0)}}}{\boldsymbol{\Lambda}}\boldsymbol{\delta \rho_{rod}} \qquad (10)$$

$$\frac{\boldsymbol{d\delta c_{ir}(t)}}{\boldsymbol{d(t)}} = \frac{\boldsymbol{\beta_i}}{\boldsymbol{\Lambda b_i}}\boldsymbol{\delta p_r(t)} - \frac{\boldsymbol{\lambda_i}}{\boldsymbol{a_i b_i}}\boldsymbol{\delta c_{ir}(t)} \qquad (11)$$

$$\begin{cases} \dfrac{m_{f1}c_{pf}}{2}\dfrac{d\delta T_{f1}}{dt} = G_{f1}C_{pf}\left(-\delta T_{f1}\right) + \dfrac{h_{fg}A_1}{2}\left(\delta T_{g1} - \delta T_{f1}\right) + \dfrac{K_f P_{10}\delta_{pr}}{2} \\ \dfrac{m_{f1}c_{pf}}{2}\dfrac{d\delta T_{out1}}{dt} = G_{f1}C_{pf}\left(\delta T_{f1} - \delta T_{out1}\right) + \dfrac{h_{fg}A_1}{2}\left(\delta T_{g1} - \delta T_{f1}\right) + \dfrac{K_f P_{10}\delta_{pr}}{2} \\ m_{g1}c_{pg}\dfrac{d\delta T_{g1}}{dt} = -h_{fg}A_1\left(\delta T_{g1} - \delta T_{f1}\right) + K_g P_{10}\delta_{pr} \end{cases}$$

According to formulas (10) to (11), the state space model is created:

$$A = \begin{bmatrix} A_{11} & A_{12} \\ A_{21} & A_{22} \end{bmatrix}$$

$$A_{11}=\begin{bmatrix} \frac{\rho(0)-\beta}{\Lambda} & \lambda_1 & \lambda_2 & \frac{\mu_{f1}\alpha_f p_r(0)}{\Lambda} \\ \frac{\beta_1}{\Lambda b_1} & \frac{-\lambda_1}{a_1 b_1} & 0 & 0 \\ \frac{\beta_2}{\Lambda b_1} & 0 & \frac{-\lambda_2}{a_2 b_2} & 0 \\ \frac{K_f P_{10}}{M_{f1} C_{pf}} & 0 & 0 & \frac{-2G_1 C_{pf}+h_{fg}A_1}{M_{f1}C_{pf}} \end{bmatrix} \quad A_{12}=\begin{bmatrix} 0 & \frac{\mu_{f1}\alpha_f p_r(0)}{\Lambda} & 0 & \frac{\mu_{g1}\alpha_g p_r(0)}{\Lambda} & \frac{\mu_{g2}\alpha_g p_r(0)}{\Lambda} \\ 0 & 0 & 0 & 0 & 0 \\ 0 & 0 & 0 & 0 & 0 \\ 0 & 0 & 0 & \frac{h_{fg}A_1}{M_{f1}C_{pf}} & 0 \end{bmatrix}$$

$$A_{21}=\begin{bmatrix} \frac{K_f P_{10}}{M_{f1} C_{pf}} & 0 & 0 & \frac{2G_1 C_{pf}-h_{fg}A_1}{M_{f1}C_{pf}} \\ \frac{K_f P_{20}}{M_{f1} C_{pf}} & 0 & 0 & 0 \\ \frac{K_f P_{20}}{M_{f1} C_{pf}} & 0 & 0 & 0 \\ \frac{K_g P_{10}}{M_{g1} C_{pg}} & 0 & 0 & \frac{h_{fg}A_1}{M_{g1}C_{pg}} \\ \frac{K_g P_{20}}{M_{g2} C_{pg}} & 0 & 0 & 0 \end{bmatrix}$$

$$A_{22}=\begin{bmatrix} -\frac{2G_1 C_{pf}}{M_{f1}C_{pf}} & 0 & 0 & \frac{h_{fg}A_1}{M_{f1}C_{pf}} & 0 \\ 0 & -\frac{2G_2 C_{pf}+h_{fg}A_2}{M_{f2}C_{pf}} & 0 & 0 & \frac{h_{fg}A_2}{M_{f2}C_{pf}} \\ 0 & \frac{2G_2 C_{pf}-h_{fg}A_2}{M_{f2}C_{pf}} & -\frac{2G_2 C_{pf}}{M_{f2}C_{pf}} & 0 & \frac{h_{fg}A_2}{M_{f2}C_{pf}} \\ 0 & 0 & 0 & -\frac{h_{fg}A_1}{M_{g1}C_{pg}} & 0 \\ 0 & \frac{h_{fg}A_2}{M_{g2}C_{pf}} & 0 & 0 & -\frac{h_{fg}A_2}{M_{g2}C_{pf}} \end{bmatrix}$$

Also, matrices B, C and D are equal to:

$$B=\left[\frac{p_{r(0)}}{\Lambda} \quad 0 \quad 0 \quad 0 \quad 0 \quad 0 \quad 0 \quad 0 \quad 0\right]^T \quad C=[1 \quad 0 \quad 0 \quad 0 \quad 0 \quad 0 \quad 0 \quad 0 \quad 0]$$

$D=0$

Controller design

PID controller

PID controller is one of the most common examples of control algorithm with feedback, which is used in many control processes such as DC motor speed control, pressure control, temperature control, etc. The PID controller calculates the "error" value between the process output and the desired input value (setpoint). The goal of the controller is to minimize the error by adjusting the process control inputs. PID consists of three separate parts named Proportional, Integral and Derivative, each of which takes the error signal as input and performs an operation on it, and finally their output is added together. The output of this set, which is the output of the PID controller, is sent to the system to correct the error. Among them, the proportional part can accelerate the response speed of the system, the integral part of

the catch can eliminate the steady state error of the system, and the derivative part of the catch can realize the advanced control of the system.

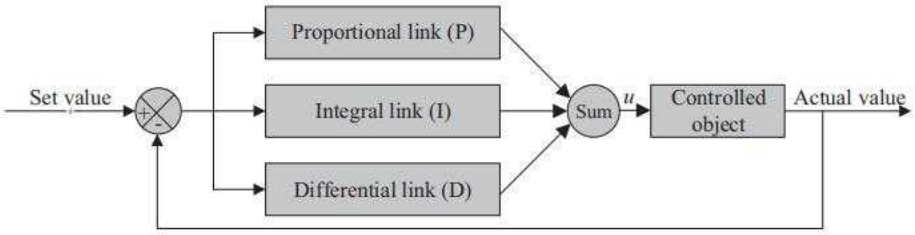

Fig. 2. PID control block diagram

According to the linear model of molten salt reactor heart and PID controller algorithm in SIMULINK section of MATLAB software, we design the controller.

Fuzzy controller

Fuzzy controller is a controller based on fuzzy logic. Fuzzy control is an intelligent control method based on the theory of fuzzy sets. As shown in figure (3), a two-dimensional fuzzy controller has been used to design the fuzzy controller of reactor core power. The fuzzy controller consists of three parts: fuzzification, fuzzy reasoning and defuzzification based on basic knowledge:

Fuzzification: The controller transforms the control input into a fuzzy input that can be recognized by the system for fuzzy logic reasoning.

Fuzzy reasoning: Fuzzy reasoning is the core of fuzzy control. According to the table of fuzzy rules, after fuzzification, the controller reasons the fuzzy input variables and finally obtains the desired control output.

De-fuzzification: Fuzzy output from fuzzy reasoning is converted to exact output value by maximum membership method, area center method or area division method. To choose the fuzzification method, this paper chooses the central region method with a smoother fuzzy reasoning mechanism.

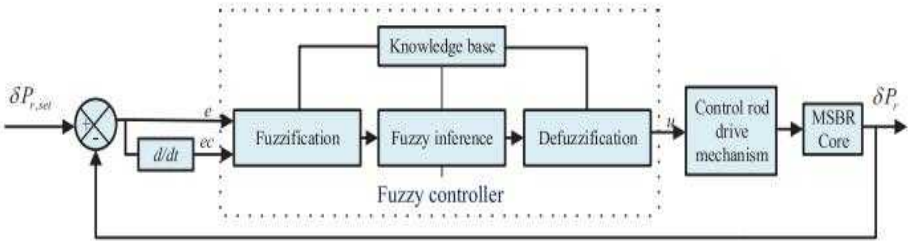

Fig. 3**.** Fuzzy control block diagram

Model predictive controller

Predictive control is actually the same as optimal control, but it performs real-time and online optimization. In predictive control, the control signal model is always obtained by solving a constrained optimization problem. Model predictive control works based on iterative (online) optimization of a cost function with a limited horizon of system performance. The figure below shows the working principles of this popular controller.

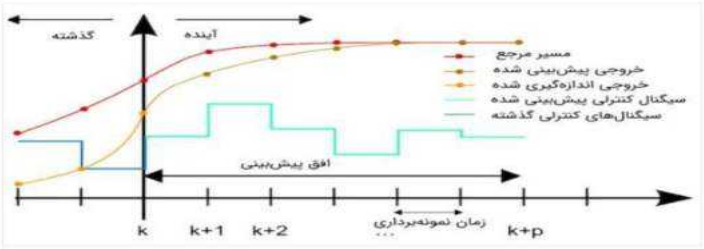

Fig. ٤. Model predictive control

The goal is to determine the control signal during the forecasting horizon to minimize the cost function and considering the constraints governing the system. In fact, in this case, the control horizon is equal to the forecast horizon. The control horizon specifies the length of an interval of the control signal, using which we want to minimize the cost function. But they often consider the control horizon less than the forecasting horizon. Various strategies have been mentioned for model predictive control, all of which use the following three principles:

*Explicit use of the process dynamic model to predict the future behavior of the system

*Calculation of the optimal control signal by optimizing the cost function and considering its constraints

* Principle of diminishing horizon

But their difference is in the following:

* Type of process model for prediction: Some algorithms use the step response of the system, others use the transform function model, and others use the system state space model for prediction.

* The method of considering disturbances on the system.

* Cost function type: The sum of squares of the tracking error and the control signal is often used as the cost function. But it is possible to consider the sum of absolute magnitudes of tracking error and control signal or any other cost function depending on the type of plant.

According to these differences, the most important predictive control strategies of the model to control the heart of the molten salt reactor are the PFC algorithm. The reason is that the linear state space model of the system is available.

Simulation

To simulate the linear model of molten salt reactor heart, we use SIMULINK section of MATLAB software. For this purpose, we use the PFC algorithm.

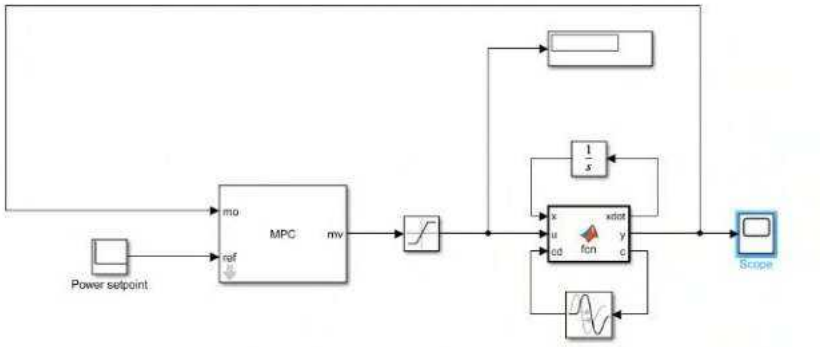

Fig. 5. Predictive controller design in SIMULINK environment

Figures (6) is relative power response curves under the control predictive controller. As shown in Figures (6), the controllers can control the relative power to the set value of the relative power in this short time.

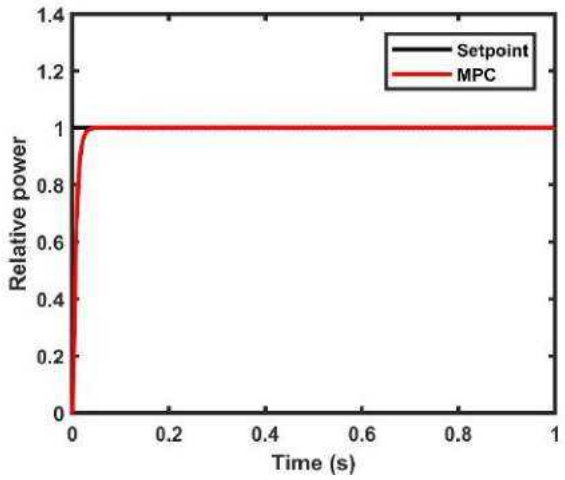

Fig. 6. Controller comparison

Results and discussion

It can be seen from the figures that three types of controllers can return the relative power to the initial relative power level in a short period of time. Also, according to the figures, it can be seen that the speed of reaching the desired power level is higher in the predictive control algorithm of the model compared to other controllers.

Conclusions

The nonlinear model of the liquid molten salt reactor core is created based on the division of the reactor core into internal and external regions. The linear model of the reactor core is also created and simplified by the small perturbation linearization method. In this article, an attempt was made to use control techniques based on model predictive control to quickly and accurately control the core power of the molten reactor. A model predictive controller designed using PFC algorithm has high robustness. The predictive controller has removed the effects of disturbances (uncertainties and noises) more effectively than other controllers. Also, as we expected, the overshoot in the predictive controller method is less.

References

[1] C. Liu, J.-F. Peng, F.-Y. Zhao, and C. Li, "Design and optimization of fuzzy-PID controller for the nuclear reactor power control." Nuclear Engineering and Design, vol. 239, no. 11, pp. 2311-2316, 2009, doi: 10.1016/j.nucengdes.2009.07.001.
[2] S. K. Pradhan, D. Acharya, and D. K. Das, "Internal model control based proportional-integral controller with class topper optimization for power control of molten salt breeder reactor core." Annals of Nuclear Energy, vol. 165, p. 108675, 2022, doi: 10.1016/j.anucene.2021.108675.
[3] W. Zeng, W. Zhu, T. Hui, L. Chen, J. Xie, and T. Yu, "An IMC-PID controller with Particle Swarm Optimization algorithm for MSBR core power control." Nuclear Engineering and Design, vol. 360, p. 110513, 2020, doi: 10.1016/j.nucengdes.2020.110513.
[4] W. Zeng, Q. Jiang, J. Xie, and T. Yu, "A fuzzy-PID composite controller for core power control of liquid molten salt reactor." Annals of Nuclear Energy, vol. 139, p. 107234, 2020, doi: 10.1016/j.anucene.2019.107234.
[5] V. Singh, A. M. Wheeler, M. R. Lish, O. Chvála, and B. R. Upadhyaya, "Nonlinear dynamic model of Molten-Salt Reactor Experiment – Validation and operational analysis." Annals of Nuclear Energy, vol. 113, pp. 177-193, 2018, doi: 10.1016/j.anucene.2017.10.047.
[6] V. Singh, M. R. Lish, O. Chvála, and B. R. Upadhyaya, "Dynamics and control of molten-salt breeder reactor," Nuclear Engineering and Technology, vol. 49, no. 5, pp. 887–895, Aug. 2017, doi: 10.1016/j.net.2017.06.003.
[7] M. Zarei, "Nonlinear dynamics and control in molten salt reactors," Nuclear Engineering and Design, vol. 332, pp. 289–296, Jun. 2018, doi: 10.1016/j.nucengdes.2018.03.042.
[8] O. Karahan, "Design of optimal fractional order fuzzy PID controller based on cuckoo search algorithm for core power control in molten salt reactors," Progress in Nuclear Energy, vol. 139, p. 103868, Sep. 2021, doi: 10.1016/j.pnucene.2021.103868..

ICNST 2024 International Conference on Nuclear Science and Technology
6- 8 MAY 2024 | Isfahan, Iran

An economic evaluation of Persian Gulf desalination coupled to different energy sources (Paper ID : 1304)

Ahmadi Esmailabadi.V, Zaidabadi nejad.M*,Khoshhal.A.R,
Department of Nuclear Engineering, Graduate University of Advanced Technology, Kerman, Iran

Abstract

Increasing population and industrial development in the Persian Gulf countries have caused a serious water crisis in these areas, so to solve this crisis, several desalination units have been used to desalinate seawater, one of which is the Iranian Persian Gulf desalination plant. This desalination plant is designed in several phases and each phase produces 200,000 cubic meters of fresh water per day using the RO method. In this paper, the economic evaluation of the connection of this desalination plant to different energy sources has been done by DEEP code in order to find the most economical energy source. For this purpose, first using the DEEP code, the minimum electrical and thermal power required to produce 200,000 cubic meters of fresh water per day was obtained. The desalination plant was then connected to five sources of coal, oil, gas, combined cycle and Nuscale nuclear reactor, and an economic evaluation was performed. Finally, in order to compensate for the weaknesses of the RO method in the quality of output water, the use of a combined desalination method was also investigated. The results of this evaluation showed that the use of nuclear reactors has the lowest cost of energy production and fresh water compared to other energy sources. Also, due to the low quality of fresh water produced by RO method, the use of RO + MED hybrid method was suggested and then The economic evaluation showed that the RO + MED process with a thermal / RO ratio of 0.26 can reduce the output TDS to 165 ppm.

Keywords: Desalination, Economic Evaluation, Nuscale Reactor, RO, DEEP.

1.Introduction

Water is a limited valuable resource that is the basis of human existence and an essential aspect of the development of production and the economy. Increasing demand for fresh water resources, along with stable water resources, has led to water shortages in many parts of the world, so that we will see water shortages in the world, especially in the Middle East and North Africa. If a significant reduction in this deficit is not possible, many countries in the world will be threatened by increasing food shortages, increasing social tensions and other problems such as the war for water [1]. An effective way to solve this problem is large-scale desalination of seawater (at the rate of about one hundred thousandth cubic meters per day or more), which can be implemented in countries with territories located near the seas

and oceans [2]. More than 150 countries are currently working to address their freshwater shortages using desalination options. Globally, at the end of 2015, about 80 million cubic meters of drinking water were produced daily by more than 18,000 desalination plants, of which 50% (40 million cubic meters per day) use seawater as a source [3] About half of this capacity (37.32 million cubic meters per day) is located in the Middle East and North Africa [4]. The global capacity of desalination plants is expected to increase steadily, from 21 million cubic meters per day of desalinated water in 2007 to 110 million cubic meters per day by 2030 [5]. However, desalination is an energy-intensive process. Most existing desalination plants use nonrenewable fuels as their main energy source, which is the main source of CO2 emissions [6]. Both solar and nuclear energy can be used as alternatives to fossil fuels in the desalination process. Although solar energy is often considered free and environmentally friendly, it is not easy to assess the feasibility and cost of solar desalination. The main disadvantages of climate dependent solar water distillers are high cost and the need for a lot of space [7]. Among All types of energy sources, nuclear energy has certain advantages over other sources and in this case can be quite competitive. Technically, any type of reactor can be used for nuclear desalination, although several types have been identified as the most practical, useful, and probable for this application [8].

There are several methods for desalination of seawater, but basically commercial desalination units are classified into two categories: thermal and membrane. To choose between desalination processes, especially in medium-tech countries, several factors must be considered such as total capacity, design, materials, feed water quality, energy consumption and output ratio. Estimation of energy consumption of different desalination methods is a function of several parameters such as temperature, desalination flow rate and salinity of seawater [9, 10].

Among the thermal processes, the multi-effect distillation process (MED) is the oldest desalination method, which is very efficient in terms of water, water flow, and thermodynamics. The MED process is performed in a series of evaporators called effects and uses the principle of reducing ambient pressure in various effects. This process allows the seawater to be fed several times after the first effect, without providing additional heat. Seawater enters the first effect and after heating in the pipes, its temperature rises to boiling point. Seawater is sprayed on the surface of the evaporator tubes to increase rapid evaporation. The pipes are heated by steam coming out of a conventional dual-purpose power plant [11,12].

Among the membrane processes, reverse osmosis (RO) is one of the most common methods in which osmotic pressure is overcome by applying external pressure higher than osmotic pressure on seawater. Thus, water flows across the membrane in the opposite direction of natural flow, passing soluble salts

as the salt concentration increases. The amount of fresh water that can be obtained from seawater varies between 30 and 75% of the volume of feed water depending on the quality of the initial water, the quality of the product required and the technology and membranes applied.

In order to evaluate the economics of desalination plants, various researches have been done so far, and several of them have been mentioned below:

In 2007, Gomez et al. examined the feasibility and economic development of replacing a CAREM reactor (PWR) for a CC gas power plant at a desalination plant in Argentina. They showed that the cost of producing 48,000 cubic meters of water per day by a nuclear desalination plant is $ 0.66 per day, which is less than the cost of $ 0.69 per day at the CC plant [13]. In 2007, Nissan and Dardor compared three desalination plants with MED technology, including PWR, HTR and CC, using DEEP 3 software economically. The results showed that water production costs by PWR and HTR are 46% and 42% lower than CC power plant [14]. In another study, Sadeghi et al. In 2020 compared five different types of desalination systems MED, RO, MSF, RO + MSF and RO + MED with connection to a nuclear power plant. The aim was to analyze the possible desalination options of Bushehr nuclear power plant using DEEP under special conditions in terms of cost. According to the results, MSF method is the most expensive option and RO method is the cheapest. Comparing their total costs, a combined RO + MED design with a thermal / RO ratio of 0.7 was suggested [15].

Iran is a large country covering an area of 1648195 square kilometers of the Middle East with a population of approximately 82 million people. Due to the importance of water in Iran, fresh water production has become an important issue for Iran and has created a strong incentive to install desalination units [17,16]. The main source of energy required for desalination plants in Iran is fossil power plants. In addition to environmental pollution, fossil fuel resources are limited and their use in other industries has dramatically increased the price of fossil fuels. Thus, as a result of these concerns about fossil fuels, other alternative energy sources have been created for future desalination needs, including nuclear energy. Iran is currently a member of the International Atomic Energy Agency (IAEA) and has expressed interest in nuclear desalination due to population growth and economic growth [15].

In this research, for the first time, an economic evaluation of the connection of Iranian Persian Gulf desalination water to different energy sources has been performed.

2. Materials and methods

2.1. DEEP code

The Desalination Water Economic Assessment Program (DEEP) is a water cost assessment package developed by the Department of Public Nuclear Physics on behalf of the International Atomic Energy Agency (IAEA). This program allows designers and decision makers to compare performance and estimate the cost of desalination in different models while connecting to nuclear power plants [18].

There are several different criteria for evaluating the economic feasibility of projects defined in a power plant using the DEEP code. One of the most important criteria used for economic evaluation is the Balanced Cost of Electricity (LCOE). LCOE is used to compare different power generation technologies. This method includes several parameters such as capital costs, operating and maintenance costs, fuel costs and carbon taxes (if any), which combine to estimate the final cost of energy production [19].

2.2. Persian Gulf desalination plant

The Persian Gulf desalination plant, as the largest desalination plant in Iran, aims to produce fresh water with a capacity of one million cubic meters of fresh water per day by RO method for consumption, That required information of each unit of this desalination plant is given in Table1 [20,21].

Table 1: Persian Gulf desalination parameters

Total desalination plant capacity 200,000	200,000	m3 /day
Total dissolved solids	40,000	ppm
Max brine temperature	70	°C
Product water TDS	210	ppm

2.3. Nuscale Nuclear Reactor

Today, the focus of the nuclear industry is on smaller reactors with less power, as well as the possibility of manufacturing in the factory and sending to the site of the reactor, for which the development of small modular reactors (SMR) was on the agenda of this industry. The advantages of this type of reactors over current power reactors include smaller size, relative simplicity, shorter construction time and variety of applications [22].

The NuScale small modular reactor is one of the most iconic SMR reactors. Due to its unique design, this reactor has special features that distinguish it from other SMR reactors. Some of its most important features are: use of a safety cover immersed in the water pool, integrated first circuit, scalable power plant design for different capacities, providing reactor safety up to 72 hours after severe accidents without the need External intervention and cooling of the reactor heart by natural flow method. A standard NuScale power plant consists of 12 modules that together provide about 924 MW of power,

although four-module and six-module power plants are now in operation. The thermal power generated is 125 MW and the electrical power generated by the generator is 45 MW for each small module [23].

2.4. Combined desalination plants

Desalination is a combination of the latest methods to remove salts and salts in seawater and brackish water and convert them to drinking and fresh water. Considering the advantages and disadvantages of each of the thermal and membrane methods in water desalination, the best solution is to use the advantages of several methods with each other, which can be the result in combined desalination water. Witnessed. In general, these methods refer to a combination of thermal methods and membrane methods, usually an RO + MED configuration or an RO + MSF configuration. These configurations are designed to improve product water quality and operational flexibility [24], and DEEP software allows them to be simulated through a combination of thermal and RO models. In this study, we used RO + MED hybrid method to compensate for the weaknesses of RO method and due to the useful features of combined methods such as improving the quality of production water and operational flexibility as an alternative to the independent RO method.

3. Simulations and results

The first step in this research is to calculate the minimum electrical and thermal power for fresh water production, which according to the results, it was determined what energy sources can be used to produce this volume of fresh water. For this purpose, the Persian Gulf desalination plant simulated in DEEP code and the minimum thermal and electrical power were obtained. Also, since a combined desalination method is presented at the end, simulations were performed in DEEP with a variety of desalination thermal methods in addition to RO, and the minimum thermal and electrical power of each of these methods. Were obtained. Table 2 shows the minimum capacity required to produce 200,000 cubic meters of fresh water per day by each of the desalination methods, including thermal, membrane and combined methods.

Table 2: Minimum capacity required to produce 200,000 cubic meters of fresh water per day

Process	Thermal ratio	Min. thermal power (MWth)	Min. electricity power (MWe)
MED	-	481	13.5
MSF	-	663	17.5
RO	-	130	30
RO+MSF	-	526	24.1
	0.3	338	18.7

RO+MED	0.5	241	22.1
	0.7	145	25.5

In the next step, the connection of different energy sources (with the required power) with the desired desalination water is simulated. Five different power plants, including fossil fuels (oil and coal) with boilers, combined cycle gas turbines and steam turbines (CC), gas cycle including gas turbines (GC) and Nuscale nuclear reactor as a source of power generation Used with desalination plant.

3.1. Results of economic evaluation of energy production

The results of economic evaluation of energy production in different ways to desalinate seawater by RO method are given in Figures 1 to 3.

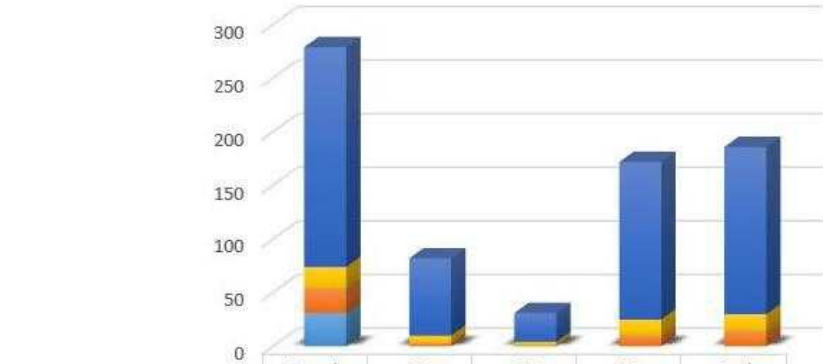

	Nuscale	CC	GC	FC	Coal
Overnight EPC costs	205	72	27	147	156
Owners costs	20	7	3	15	16
Contingency cost	0	0	0	0	0
Interest during construction	23	3	1	10	14
Decommissioning costs	31	0	0	0	0

Figure 1: Capital costs and ancillary costs of fossil and nuclear power plants

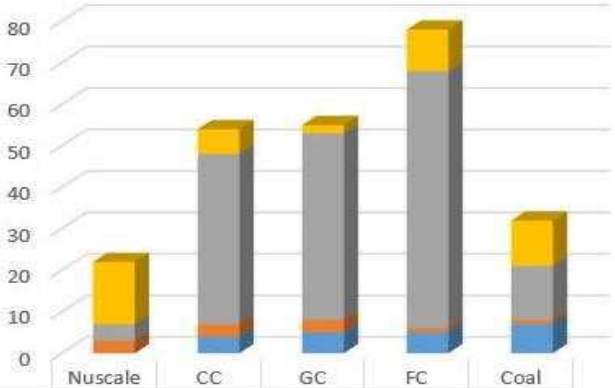

	Nuscale	CC	GC	FC	Coal
Annualized capital costs	15	6	2	10	11
Fuel costs	4	41	45	62	13
Operation & maintenance costs	3	3	3	1	1
carbon tax	0	4	5	5	7

Figure 2: Total annual cost of fossil and nuclear power plants

All the necessary parameters for calculating LCOE are given in Figures 3 and 4.

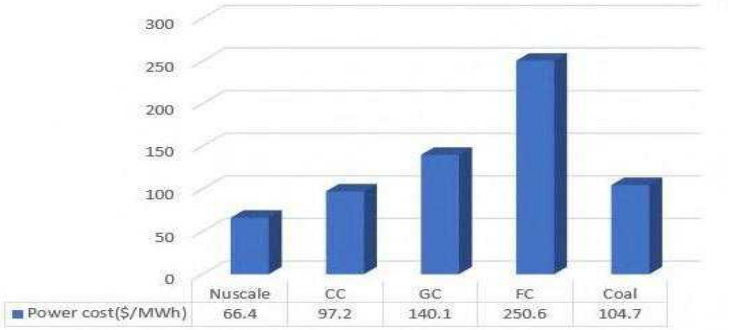

Figure 3: LCOE estimation for different fossil and nuclear power plants

3.2. Results of economic evaluation of fresh water production

The results of economic evaluation of energy production showed that NuScale reactor and CC method are the most cost-effective methods for fresh water production, so in order to economically evaluate the cost of fresh water production, only these two methods have been used. Figure 4 shows the capital costs of desalination plants, including construction costs, intermediate loop costs, input / output costs, water plant owners costs, potential water plant costs, and interest during construction.

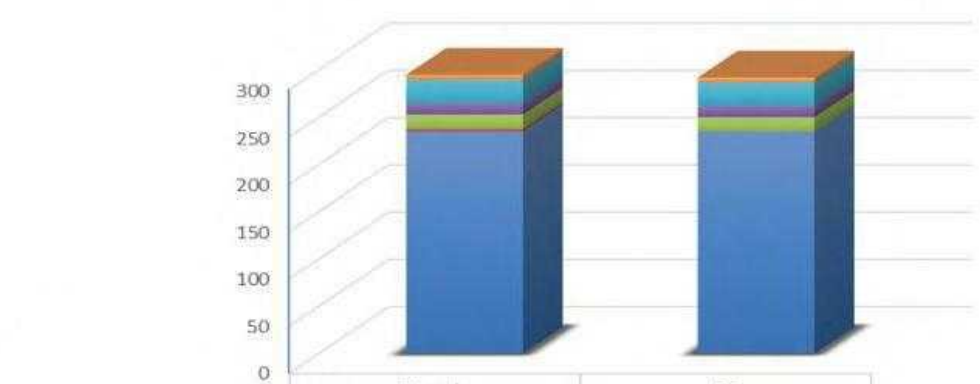

	Nuscale	CC
interest during construction	5	5
waterplant contingency cost	25	25
water plant owners cost	12	12
infall/outfall costs	15	15
intermediate loop cost	2.9	0
construction cost	235	235

Figure 4: Total capital costs for CC and Nuscale power plants

The part that has the largest share in the cost of capital is the cost of construction, which is similar between the two power plants. The main parameter that makes the cost difference between CC and

nuclear coupling desalination plants is the cost of the intermediate loop. Due to the radioactive nature of the running water in the reactor, the nuclear desalination plant requires the use of an intermediate loop to prevent radioactive contamination of the fresh water. Other economic parameters do not differ significantly between CC and nuclear power desalination plants.

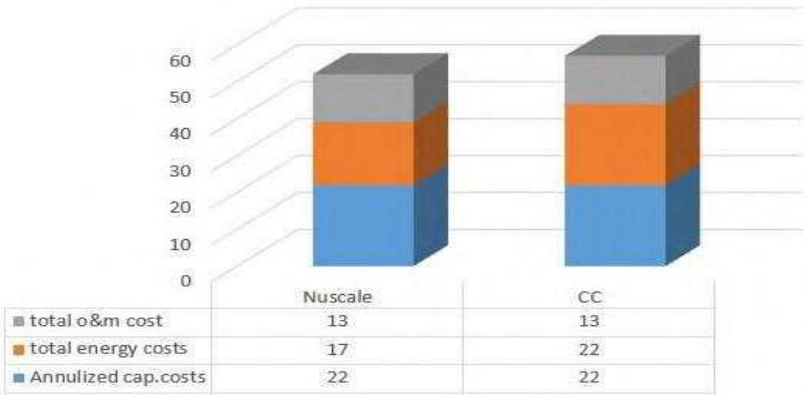

(a)

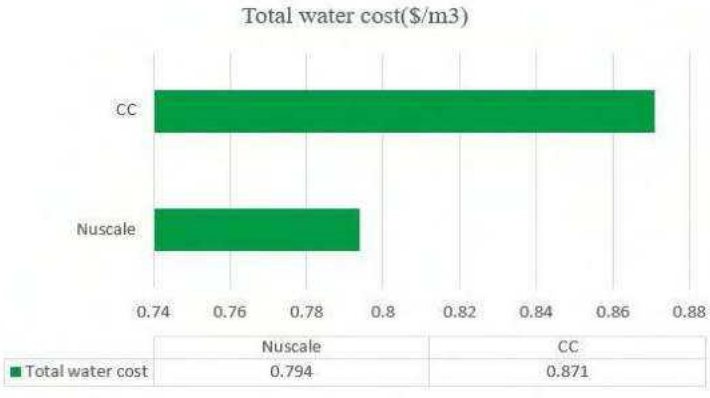

(b)

Figure 5: (a) Annual costs of desalination plants with CC and Nuscale energy sources, (b) Total water cost of desalination plants with CC and Nuscale energy sources

3.3. Evaluation results of using the combined desalination method

The quality of water produced by thermal methods is significantly higher than RO membrane method. In the final part of this research, the combined RO + MED method is tried to simulate the connection of Persian Gulf desalination water with Nuscale power plant as a source. The economic superiority of power generation and connection is chosen at the same time as the confectionery plant. Table 3 shows the quality of water produced for different thermal / RO ratios based on the amount of Total dissolved solids (TDS) along with the total cost of water production.

Table 3: Quality of produced water with different values of thermal ratio in RO + MED hybrid method

Power plant	Total capacity (m^3/ day)	Thermal ratio (RO+MED)٪	TDS (ppm)	Total water cost ($/$m^3$)
Nuscale	200000	10	193	0.786
		15	184	0.794
		20	176	0.801
		25	167	0.810
		26	165	0.811

4. Discussion and Conclusion

The results showed that among the fossil fuels, the most cost-effective method of energy production is CC method, but among all the sources simulated in this research, the most cost-effective method is energy production by nuclear method. Also, among all the modeled sources for fresh water production, it has been concluded that the use of nuclear water desalination in the Persian Gulf Desalination plant will be the most cost-effective method.

In using the combined method of water desalination, it can also be seen that as the ratio of fresh water production to thermal method increases compared to membrane method, the final cost of fresh water also increases slightly, but it should be noted that the quality of water output Increases, which can drastically reduce transmission and maintenance costs of transmission lines. According to these results, the increase in the cost of water production with different percentages from 10 to 26 percent has increased by only $ 0.03, but in contrast to the TDS quality of water production 30 ppm has improved, which can have a significant impact on reducing water transfer costs. Finally, after economic evaluation, it was shown that with RO + MED process with thermal / RO ratio of 0.26, the output TDS can be reduced to 165 ppm and by connecting it to the NuScale reactor, the most economical fresh water can be produced.

References

[1] M. Shatat, M. Worrall, and S. Riffat, "Opportunities for solar water desalination worldwide: Review," Sustainable Cities Soc. 9, 67–80 (2013).

[2] World Economic and Social Survey 2011 (UN DESA, New York, 2011).

[3] Desalination by the Numbers (Int. Desalin. Assoc., 2013).

[4] E. Jones, M. Qadir, M. T. H. van Vliet, V. Smakhtin, and S.-M. Kang, "The state of desalination and brine production: A global outlook," Sci. Total Environ. 657, 1343–1356 (2019).

[5] K. Zotalis, E. G. Dialynas, N. Mamassis, and A. N. Ange-lakis, "Desalination technologies: Hellenic experience," Water 6, 1134–1150 (2014).

[6] Nuclear Power in the World Today (World Nucl. Assoc., London, 2014).

[7] P. Compain, "Solar energy for water desalination," Procedia Eng. 46, 220–227 (2012).

[8] INTRODUCTION of Nuclear Desalination (IAEA, Vienna, 2000).

[9] Floating Nuclear Energy Plants for Seawater Desalination (Proc. Technical Committee Meeting, Obninsk, Russia, May 29–31, 1995) (IAEA, Vienna, 1995).

[10] Advanced Applications of Water Cooled Nuclear Power Plants (IAEA, Vienna, 2008), IAEA-TECDOC-1584.

[11] Antonyan, Martun. Energy footprint of water desalination. MS thesis. University of Twente, 2019.

[12] Al-Karaghouli, Ali, and Lawrence L. Kazmerski. "Energy consumption and water production cost of conventional and renewable-energy-powered desalination processes." Renewable and Sustainable Energy Reviews 24 (2013): 343-356.

[13] S.M. Gómez de Soler, L.B. Ramilo, A. Castellano, N. Coppari, C. Cabrera, Assessment. Nuclear desalination projects in Argentina and Latin America, International Atomic Energy Agency, IAEA-TECDOC-1561, Annex 1, Atomic Energy National Commission, Argentina, 2007.

[14] S. Nisan, S. Dardour, Economic evaluation of nuclear desalination systems, Desalination 205

[15] Sadeghi, Kh, et al. "Economic Assessment of the Possible Desalination Processes for the First Unit of Bushehr Nuclear Power Plant." Thermal Engineering 67.5 (2020): 271-281.

[16] N. A. Tir, F. Momeni, and G. T. Boboevich, "Explor-ing the effects of water sector investment in economic development in Iran," Procedia - Soc. Behav. Sci. 131, 396–405 (2014).

[17] H. Malekinezhad, "Study on the water availability in Iran, using the international water indicators," in Proc. 8th Int. Congr. on Civil Engineering, Shiraz, Iran, May 11–13, 2009 (Civil Environ. Eng., Shiraz, 2009).

[18] Naserbegi, A., and M. Aghaie. "Multi-objective optimization of hybrid nuclear power plant coupled with multiple effect distillation using gravitational search algorithm based on artificial neural network." Thermal Science and Engineering Progress 19 (2020): 100645.

[19] A. Rezaei, A. Naserbeagi, Gh. Alahyarizadeh, and M. Aghaie, "Economic evaluation of Qeshm island MED-desalination plant coupling with different energy sources including fossils and nuclear power plants," Desalination 422, 101–112 (2017).

[20] Mohamed Abouleish, Shakib Shariar, Reem Mohamed and Arnold L Gordon (2020), Impacts of brine disposal from water desalination plants on the physical environment in the Persian/Arabian Gulf, Published by IOP Publishing Ltd.

[21] www.was-co.ir.

[22] Mario D. Carelli, Daniel T. Ingersoll, (2015). Handbook of Small Modular Nuclear Reactors, Woodhead Publishing Series in Energy: Number 64.

[23] Zayermohammadi Rishehri, H., & Zaidabadi Nejad, M. (2022). Design and Neutronic, Thermal-Hydraulic Analysis of DSCF Assembly for a SMR and Investigation of the Effect on the Thermal Power Uprate. Nuclear Technology, 1-21.

[24] MOSER, H., "Design and operation of the largest hybrid desalination plant, Fujairah", International Desalination Association (IDA) Congress, Singapore (2005).

ICNST 2024 International Conference on Nuclear Science and Technology
6- 8 MAY 2024 | Isfahan, Iran

RELAP5 Code Investigation on Operational Characteristics of Passive siphon breaker line in Research Reactors under LOCA Conditions (Paper ID : 1330)

Shahabinejad A.[1,2*], Rahimian A.[1] Aminmozafari M.[1] Eghbal M.M.[1]

1Reactor and Nuclear Safety Research School, Nuclear Science and Technology Research Institute, 1439951113, Tehran, Iran
2Department of Nuclear Engineering, School of Mechanical Engineering, Shiraz University, 7193616548, Shiraz, Iran

Abstract

Currently, passive safety systems are critical for enhancing nuclear reactor safety and dependability. To limit the chance of the core being uncovered in pool-type research reactors, a siphon pipe with a penetration in the pool wall higher than the core level can be used as the pool outlet pipe. Using a siphon breaker as a passive safety system is vital. The hydraulic study of the siphon breaker line passive safety system for a pool-type research reactor is carried out using the RELAP5 code. The hydraulic analysis and modeling are carried out on a 16-inch coolant outlet siphon pipe, taking into account 16-inch and 8-inch break diameters, as well as siphon breaker line diameters of 2, 2.5, 3, and 4 inches. As a consequence, the undershooting height for a 16-inch break and a 4-inch siphon breaker line is -36.7 cm. The undershooting height is -51.4 cm when using an 8-inch break and a 2-inch siphon breaker line. Compared with the findings to the reference experimental data, the largest difference is -3.1 cm and the smallest difference is -0.1 cm. The findings obtained indicate a substantial agreement between the simulated and experimental results.

Keywords: Breaker, Passive, RELAP5, SBL, LOCA

Introduction

Since the first nuclear power plants went into operation, scientists and activists in this field have been examining the safety of nuclear reactors utilizing passive technology. Furthermore, the system's stability and ability to maintain the core of research reactors cooled and protect against radiation after an accident resulting in coolant loss improve the reactor's level of safety. According to the International Atomic Energy Agency's recommendations in the field of research reactor safety, the cooling piping should not be left at the bottom of the pool to reduce the risk of draining the reactor pool coolant in the event of an accident or coolant loss. Instead, it should be left through a siphon tube by creating a hole in the pool

wall at a height higher than the core. The siphon breaker line is employed as a passive safety mechanism to prevent the coolant from draining completely in the case of a break in the outlet pipe, as well as to restrict the outflow from the pool to keep the pool water level higher than the core. A LOCA[1] condition occurs when an outlet pipe in a pool-type research reactor's cooling system fails. However, if the water level in the reactor pool remains above the level of the core and the emergency shutdown mechanism trip the reactor, the decay heat of the reactor core can be removed by natural convection flow, avoiding the repercussions of a Loss of Coolant Accident.

In 1991, there was consideration of passive safety systems [1], in the International Atomic Energy Agency's conference titled "Nuclear Energy Safety: Future Strategy." The use of passive systems can result in system simplicity and overall cost benefits, as well as a reduction in human error as compared to active systems. As a result, passive safety systems have been studied for several kinds of research reactors. In 1993 [2], Neil et al. evaluated the siphon breaker line on a small scale and modeled the system with the RELAP5 safety analysis algorithm. However, they were unable to obtain satisfactory findings, so they abandoned modeling and merely presented the results of experiments. In 1999 [3], Sakurai et al. conducted an experimental and numerical evaluation of a small-scale siphon breaker line with a pool height of approximately 6.5 meters and a break distance to the pool top of 19.5 meters. The numerical findings were satisfactory in terms of accuracy when compared to the experimental test results using the SBAP[2] software.

From 2011 until 2017 [4-7], Lee et al. conducted experimental and simulation studies on the siphon breaker line for a real-scale research reactor, as shown in Fig. 1. In these studies, the break diameters ranged from 6 to 16 inches, the siphon breaker line sizes varied from 2 to 6 inches, and the pool outlet pipe size was 16 inches. As a consequence, UH[3] were measured in two experimental and simulation modes at various break sizes, with a maximum error of 13 cm and a minimum error of 1 cm.

[1] Loss of Coolant Accident
[2] Siphon Breaker Analysis Program
[3] Undershooting Height

Fig. 1. Siphon break experimental facility

In 2018 [8], Kim et al. conducted an experimental examination of a small-scale siphon facility and numerical analysis by using SBSP4. According to the obtained findings, in the size of the siphon breaker line of 0.375 inches and 0.5 inches, the tank sweeping mode was relatively small and partially, while in the size of 0.25 inches, the tank was completely empty and the change of the air sweeping mode was not easy. Furthermore, the simulation UH differed from the practical test results by decreasing the diameter of the siphon breaker line, with a minimum average error of 16 mm and a maximum relative inaccuracy of 48%. In the lower diameters of the siphon breaker line, the difference grows with an increase in the C factor equation mentioned in reference [8], and the SBSP program is appropriate for usage in the design range of 100,000 to 420,000.

In 2022 [9], Samiran et al. investigated the siphon breaker line on a small scale using both experimental and numerical methods. The numerical solution was performed using the RELAP5/Mod3.2 code, and experimental and numerical analysis were performed with various break diameters. The numerical and experimental findings were in satisfactory compliance, demonstrating that RELAP5 is capable of modeling the siphon breaker line in a small-scale facility.

[4] Siphon Breaker Simulation Program

According to the literature and what was mentioned about the significance of passive systems, as well as the complexity of the two-phase behavior of the flow in this phenomenon, the two-phase phenomenon of this system has been studied experimental in many countries since 1993. Several numerical analyses have been carried out using diverse programs and codes, such as: RELAP5, CFD, OpenFOAM [10–12], and special codes have also been developed [13, 14]. However, in real-scale pool type research reactors, the simulation and validation of two-phase flow in siphon pipe have not been provided in a valid manner by RELAP5 code, therefore in the present work, the mentioned simulation and analyses are performed and validated with the reference experimental results [6] in real-scale.

Thermohydraulic Analysis of The Siphon Breaker Line System

Reference Siphon Breaker Line

In this section, the reference siphon breaker system is initially introduced. Then the applied configuration and nodalization in the safety analysis RELAP5 code is discussed. Finally, the analysis method in RELAP5 is addressed. According to Fig. 2, the first break is 11.6 meters from the entrance of the siphon breaker line, whereas the second break is 6.6 meters away. Both line and hole type were considered for siphon breaker in the reference (for the present work, just line type included). The break size in the line type siphon breaker was 16 inches, 10 inches, 8 inches, and 6 inches, and for the hole type siphon breaker, a 10-inches line with siphon breaker hole sizes of 30, 35, 40, 45, 50, and 55 mm was built and analysed. The siphon's main pipe had a diameter of 16 inches, and the pool's capacity was 57.6 m^3 at a height of 4 meters. The siphon breaker line was sizes (0.5, 1, 1.5, 2, 2.5, 3, 4, 5, and 6) inches, and the flow rate variations have been measured using an ultrasonic flow meter.

This research simulates the break position of LOCA #1 with diameters of 16 and 8 inches and models the siphon breaker line with sizes of (2, 2.5, 3 and 4) inches, as shown in Fig. 2. The sizes and dimensions of the siphon system are fully discussed in the final report of reference [4] and the article [5].

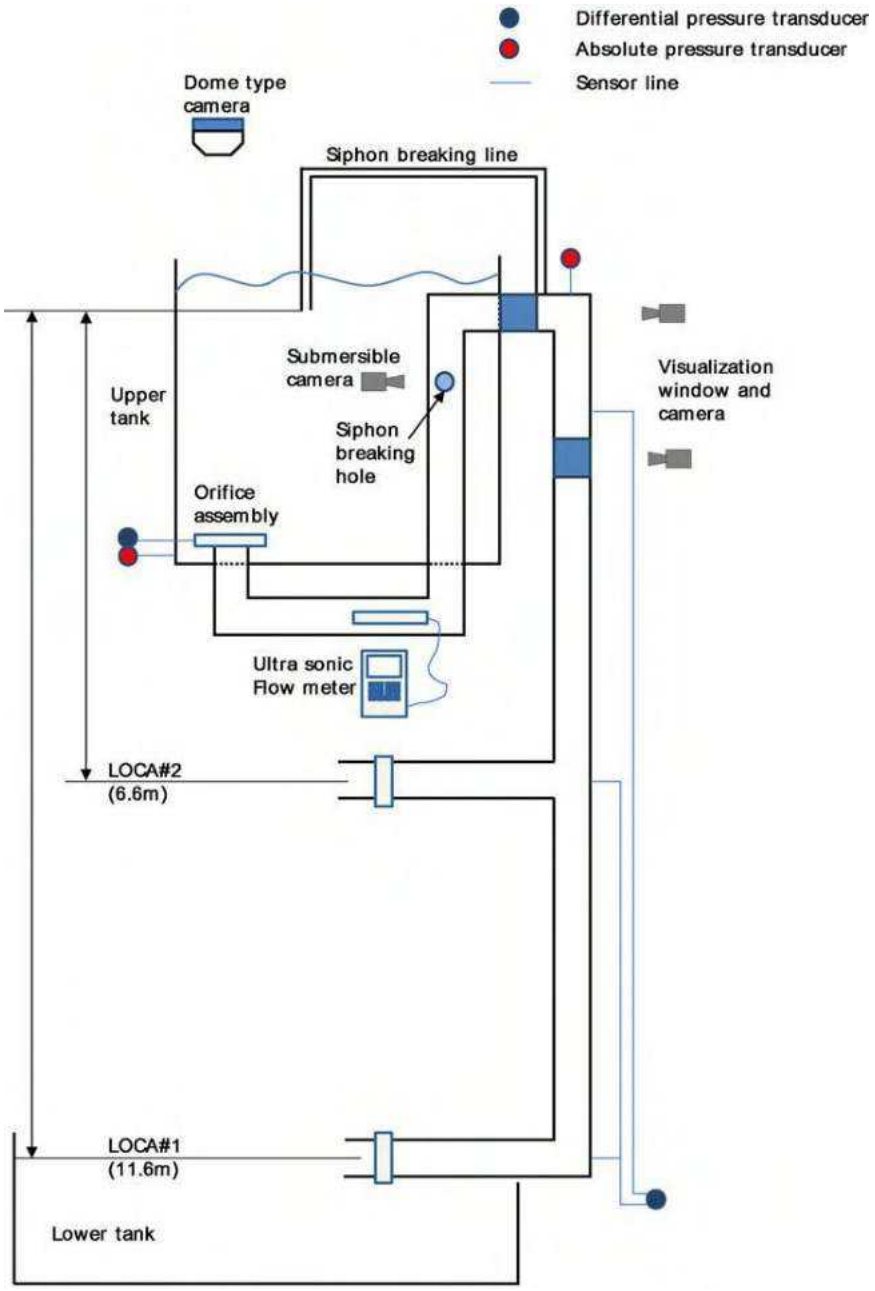

Fig. 2. Siphon loop in real scale

Modeling and Designing the Reference Passive Safety System

The system schematic in Fig. 3 is obtained by the reference data [15], including the system's dimensions, height, volume, diameter, and connections, as well as the break position [4-7]. Position 1 refers to the pool's water level, which is initially set to 4 meters.

The siphon breaker line's entry within the pool is indicated with position 0 in Fig. 3, at a height of 3.3 meters, which is the same height as the bottom of the highest horizontal part of the 16-inch siphon pipe. Position 2 is where the siphon breaker line connects to the siphon pipe. Position 3 is the system's break position, and the test facility's height is approximately 17.67 meters.

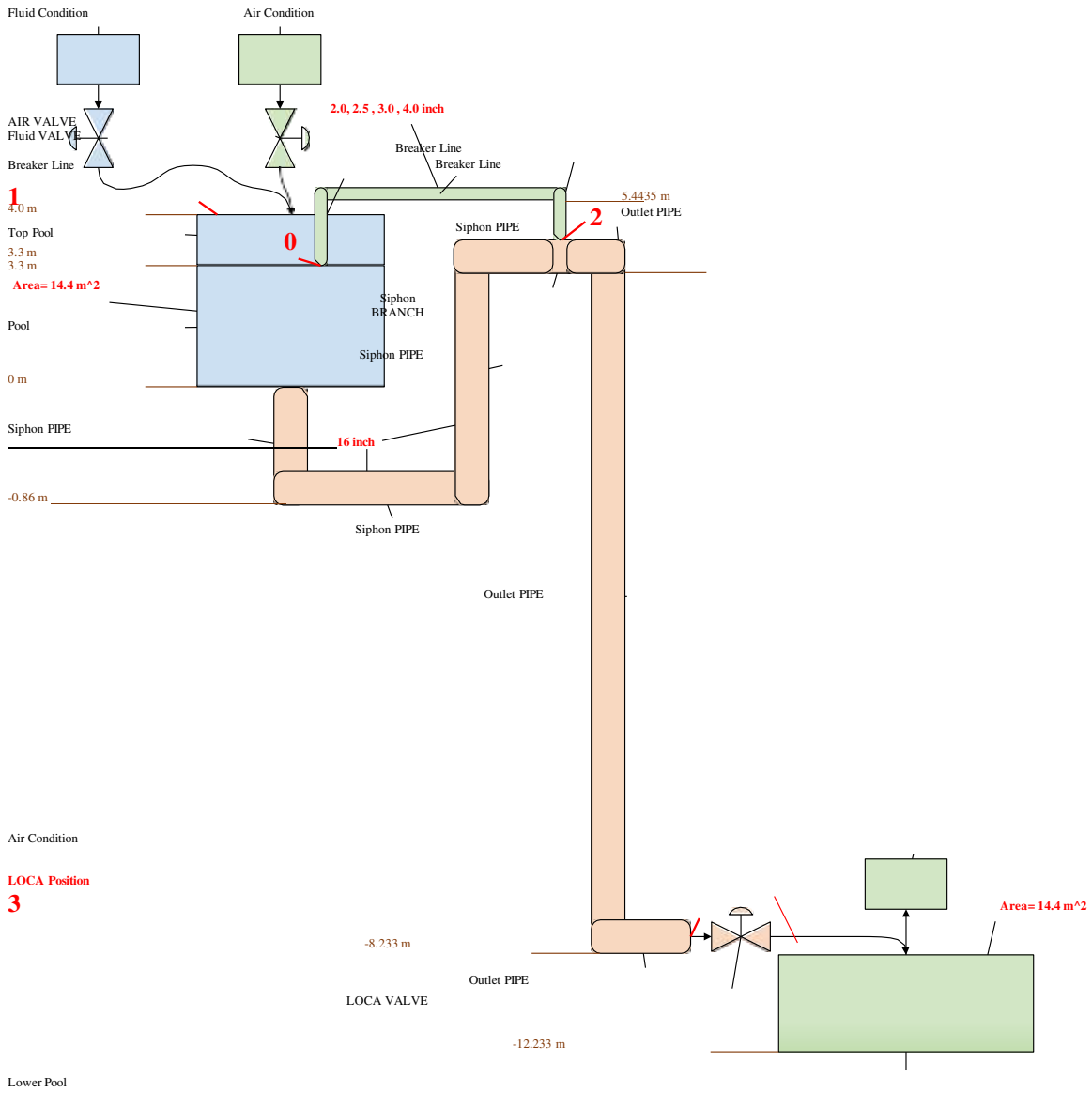

Fig. 3. Siphon loop and siphon breaker line

Nodalization of the Siphon Breaker Line System in the RELAP5 Code

Fig. 4 depicts siphon loop nodalization for simulation with RELAP5 code. The ambient air boundary conditions are connected to valve number 222 and branch number 424 via TDVs 111 and 515, respectively. Valve No. 222 remains open from the start of the simulation until the end of the computations. Valve 414 represents the break in the outlet pipe in the lowest location. The boundary conditions of the water entering the pool are connected to the surface of the pool via TDV No. 333 and valve No. 444. Branch 555 indicates the volume of the pool above the siphon breaker line's entry, whereas branch 777 represents the volume of the pool below it. The end of branch 777 is connects to pipe 888, which represents the 16-inch siphon outlet pipe, and the top to pipe 616, which represents the siphon breaker line input. Pipe 909, whose specifications are shown in Table 1, is connected to pipe 313 (the location of the break) via SNJ 212, and the diameter of the break is assumed to be 16 and 8 inches, respectively, in the aforementioned pipe. It should be noted that for a 16-inch broken siphon pipe, the diameters of the siphon breaker line are 4, 3, and 2.5 inches, respectively, and for an 8-inch broken siphon pipe, the diameters of the SBL[5] are 2.5 and 2 inches.

Table 1. Specifications of Pipe No. 909

Area (m^2)	Length (m)	Vertical angle (degrees)	Elevation change (m)	Wall roughness (m)	Pressure (Pa)	Temperature (K)
0.1297171	11.533	-90.0	-11.533	0.000046	1.0e5	293.15

[5] Siphon Breaker Line

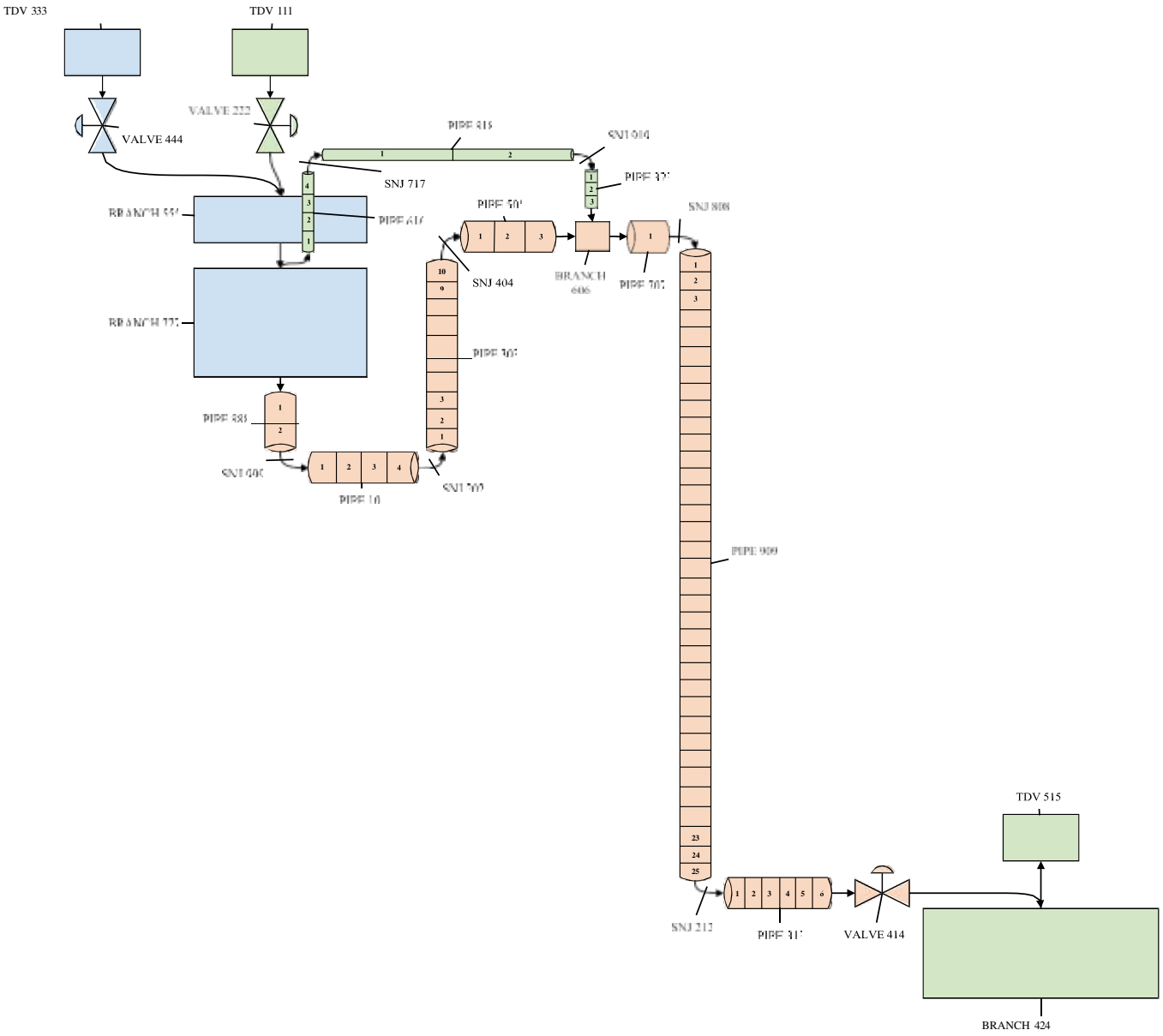

Fig. 4. Siphon loop nodalization for simulation in RELAP5

Analysis Method

The RELAP5 safety analysis code's solution approach was used to analyze momentum equations in a heterogeneous way owing to changes in fluid velocity in two phases. The general form of the inhomogeneous two-phase momentum equation is shown in equation (1).

$$\rho_i\left(\frac{\partial v_i}{\partial t}+v_i.\nabla v_i\right)=-\nabla P_i+\rho_i F_i+\sum j\neq i\,\alpha_{ji}\left(\rho_j-\rho_i\right)g_i+\Gamma_i-M_i \qquad (1)$$

The parameters of equation (1) are defined below:

ρ_i: density of phase i
v_i: velocity vector i
F_i: external force affecting phase i
Γ_j: is the velocity term or exit term in the governing equation
M_i: surface mass transfer between two phase surfaces
P_i: pressure of phase i
α_{ji}: surface concentration between two phases ji
ρ_j: density of phase j
g_i: is the acceleration vector of gravity

The control variable card is used to calculate the UH in the RELAP5 code input and represents it graphically in the results. UH is defined as the pool water level difference with respect to the breaker line entrance (the bottom of the highest horizontal siphon pipe), which corresponds to pipe 505, after stabilizing the pool water level.

Results and Discussion

This section presents the RELAP5 code results in two parts: first for an 8-inch break and subsequently for a 16-inch break:

Fig. 5 compares five versions of RELAP5 for analyzing a passive siphon breaker system with break size of 8 inches and siphon breaker line size of 2.5 inches. According to the results of this figure, three versions of RELAP5 with the numbers 3.2 ai, 3.2 pt, and 3.3 ds have the solution with minimal error when compared to the experimental result. In Fig. 5, two indices are used: (N) indicates a nonhomogeneous solution approach (two velocity momentum equations), and (H) represents a homogeneous solution approach (single velocity momentum equation). In the homogeneous approach, there is a substantial difference between the experimental data and 3.3 ds (H) version. Furthermore, there is a greater deviation between SCDAP versions and experimental result.

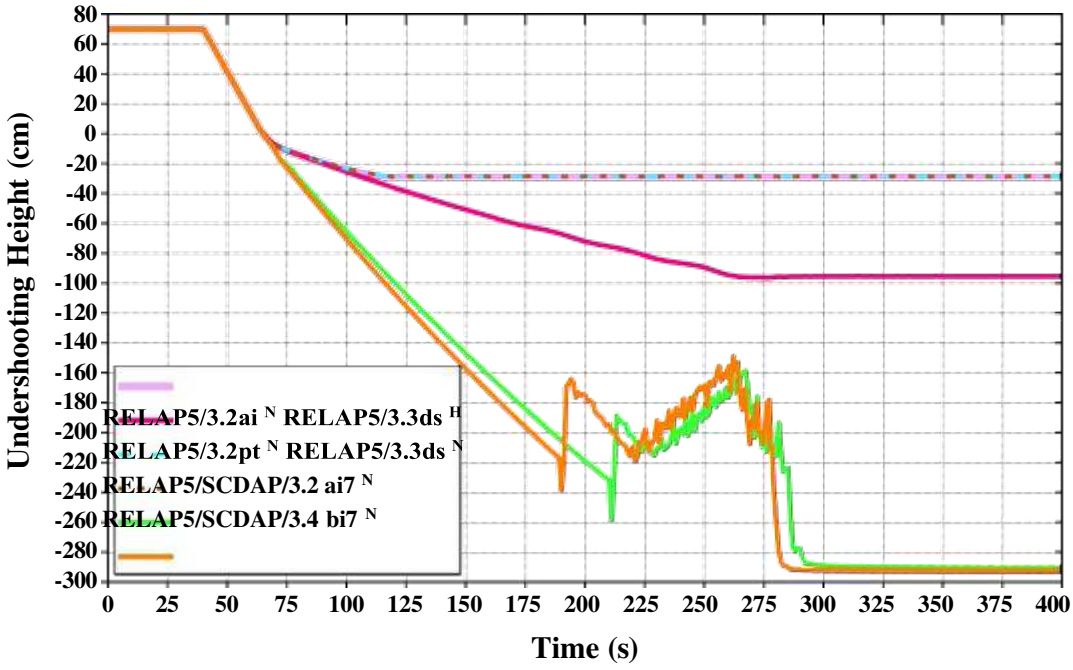

Fig. 5. UH in different RELAP5 versions

Fig. 6 shows the pressure variations for the break diameter of 8 inches and the siphon breaker line size of 2.5 inches. From the beginning of the modeling until 40 seconds (the moment of the accident), the pressure at the top of the siphon pipe drops to 0.72 bar, and then, due to air entering pipe number 909, the pressure rises to atmospheric pressure. The void fraction variations occurs at the two-phase area from 3.3 to 3 m water pool level until the fluid stabilizes and gas phase dominates.

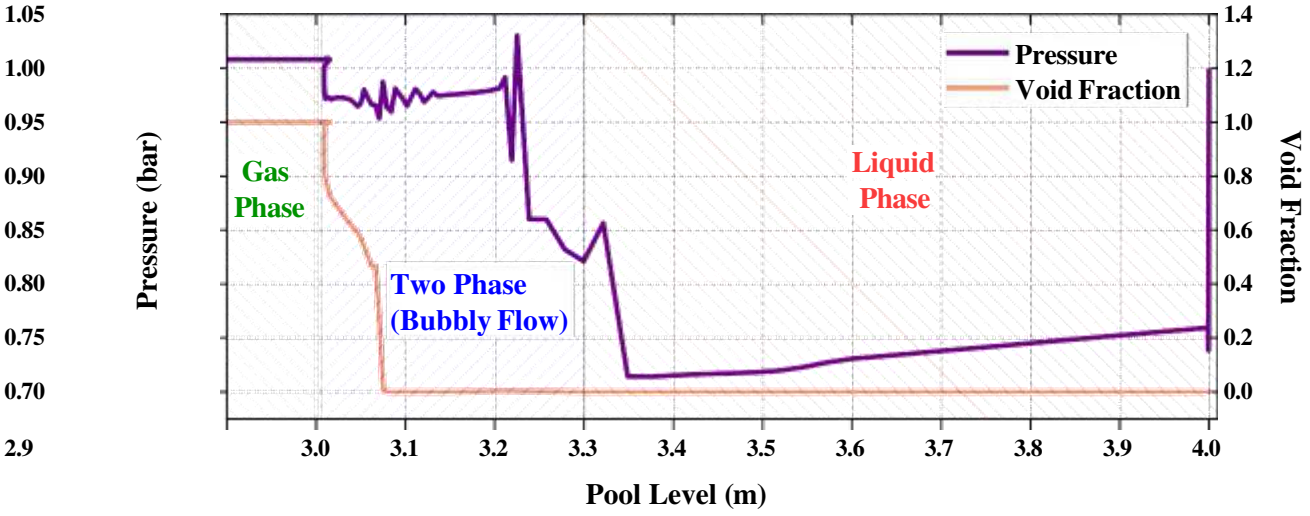

Fig. 6. Pressure and void fraction in break size of 8 inches

Fig. 7 shows the pool water level for an 8-inch break and a 2.5-inch siphon breaker line, which stabilizes approximately at the pool level of 3 meters after the breaker functions, and on the right side, due to air entrance into the siphon pipe and the flow stoppage, the UH value for a 2.5-inch diameter siphon breaker line is -28.9 cm.

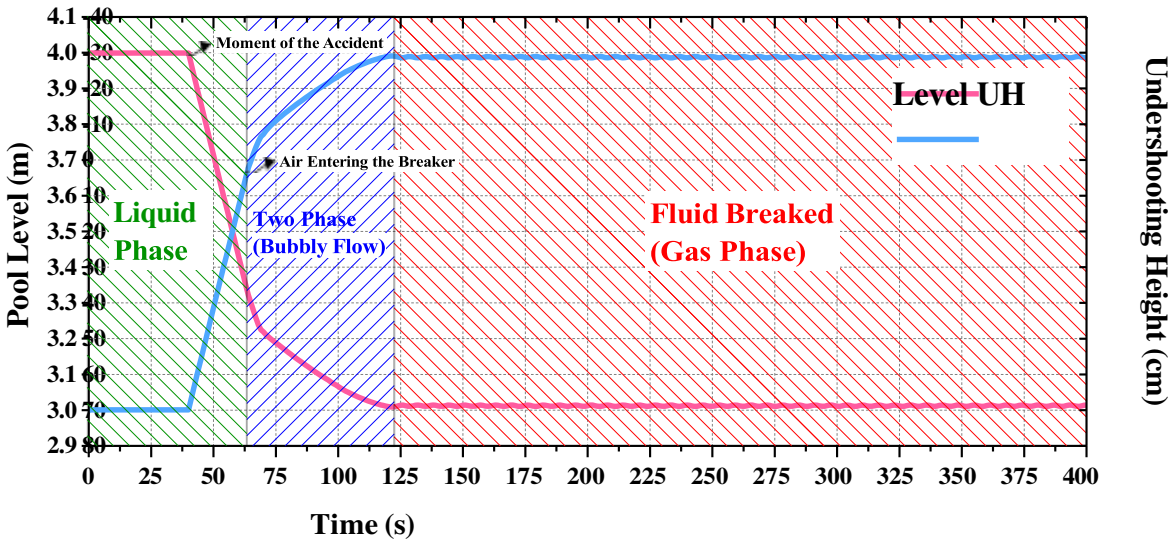

Fig. 7. Pool level and UH in break size of 8 inches

According to Fig. 8, on the left side, the outlet flow rate from the siphon pipe for the break size of 8 inches, reduces form approximately 410 kg/s, to zero after air entrance and the flow breakage at the level of 3 meters. On the right side, the fluid velocity variations are indicated, reaching to zero value after flow breakage.

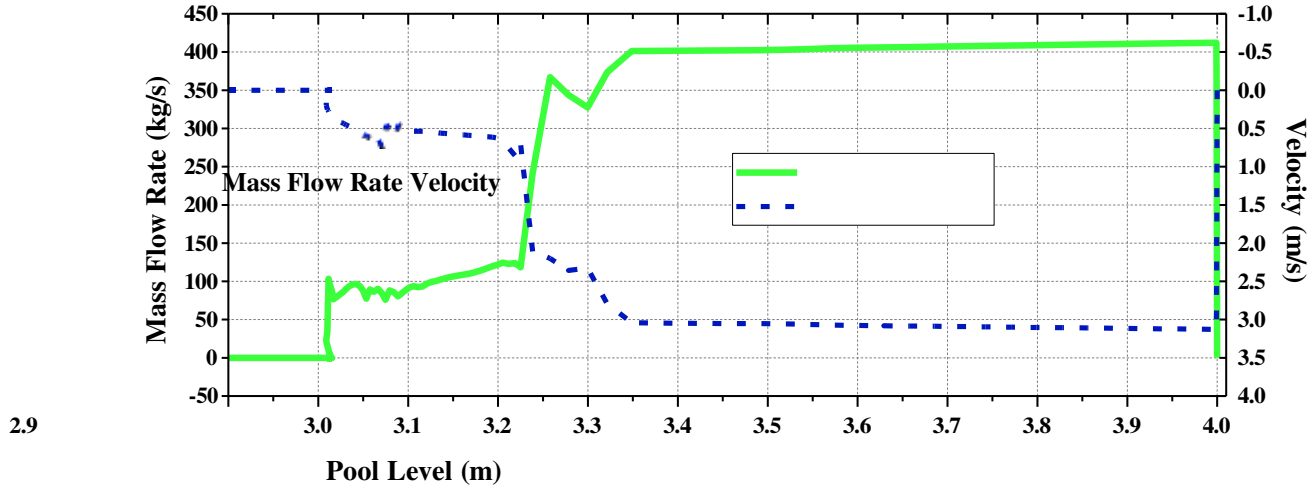

Fig. 8. Mass flow rate and velocity in break size of 8 inches

In Fig. 9, the left side shows pressure fluctuations for a break size of 16 inches and a siphon breaker line size of 2.5 inches. From the start of the modeling to the 50 seconds, the pressure in the top of the siphon pipe is reduced to 0.2 bar, and after 175 seconds, when the pool outlet is stopped due to air entering pipe number 909, the pressure at the top of the siphon pipe equals atmospheric pressure. On the right side, the void fraction variations are displayed which its value changes from zero to one by air entrance into siphon pipe leading to changing liquid phase to two-phase and finally gas phase.

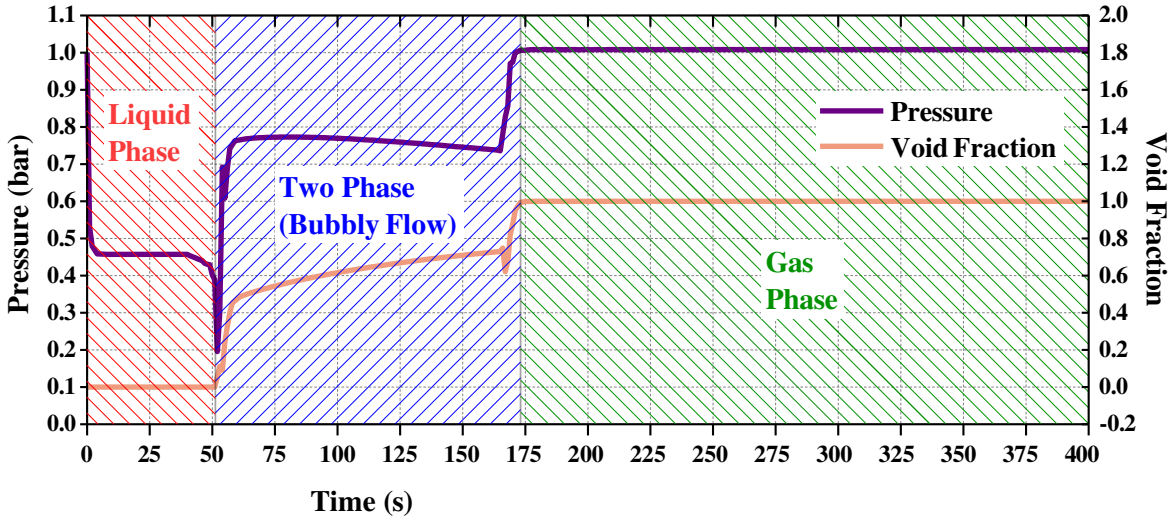

Fig. 9. Pressure and void fraction in break size of 16 inches

Fig. 10 shows that the pool water level for the break size of 16 inches in three cases of the breaker line sizes of 4, 3 and 2.5 inches. The pool's water level reaches 2.933 meters approximately 40 seconds after the pool inlet flow stops in the case of 4-inch diameter siphon breaker line. Pool water level stabilizes in 2.491 meters in the case of the 3-inch diameter siphon breaker line and 1.948 meters in the case of the 2.5-inch diameter siphon breaker line, approximately 70 and 110 seconds following the initiation of the incident, respectively. With a break diameter of 16 inches and the assumption of a siphon breaker line with sizes of 4 inches, 3 inches, and 2.5 inches, UH has been illustrated in Fig. 11. The water level is 70 cm above the siphon breaker line's entry before the flow into the pool is stopped. After stopping the flow into the pool, it was discovered that the water level of the pool stabilized faster using a larger diameter siphon breaker line. UH is equal to -36.7 in a 4-inch line, -80.9 in a 3-inch line, and -135.2 cm in a 2.5- inch line regarding siphon breaker line diameters.

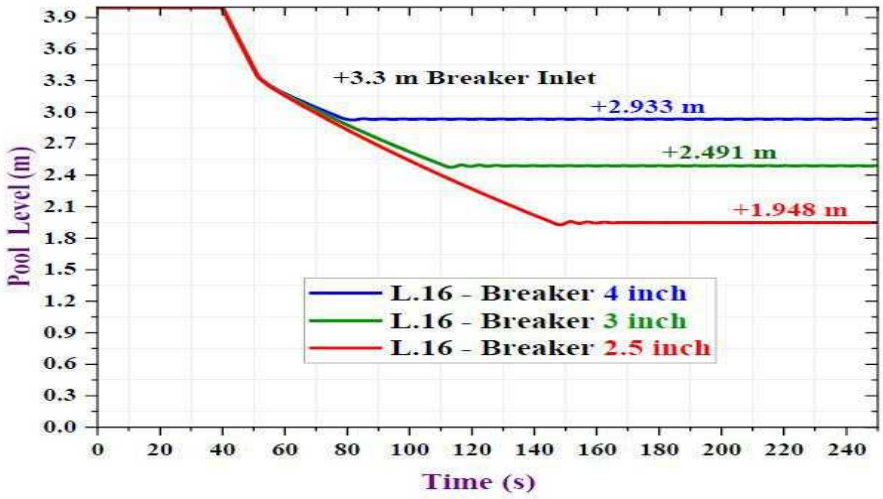

Fig. 10. Pool level in 16-inch break size

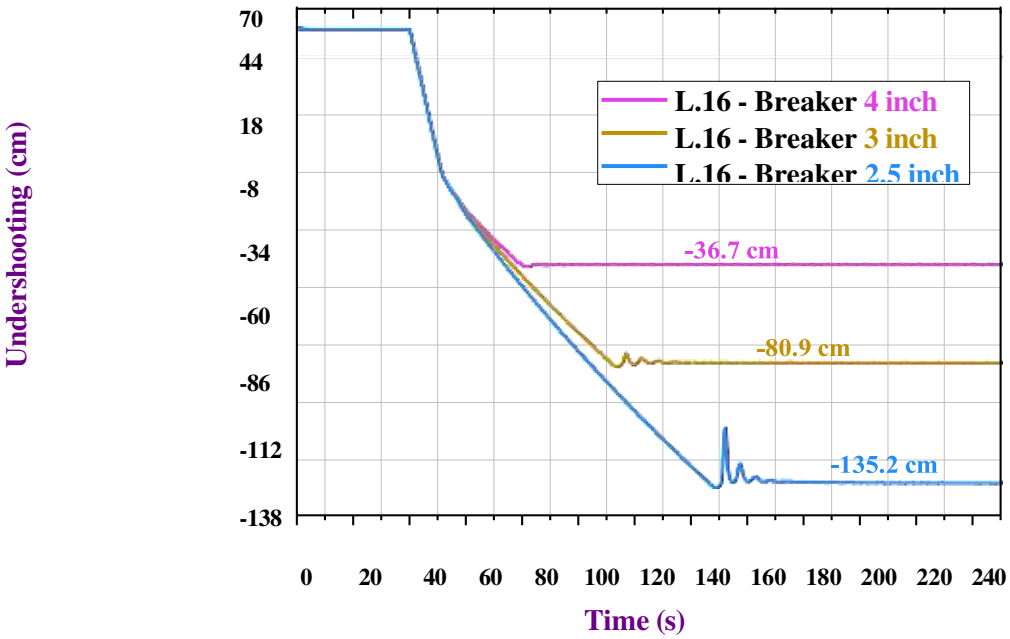

Fig. 11. Undershooting height in 16-inch break size

According to Fig. 12, in the left side, the outlet mass flow rate from the siphon pipe with the break size of 16 inches, is approximately 840 kg/s. The fluid flow breaks at 175 seconds, at which point the flow rate is zero. With a breaking size of 16 inches on the right side, the outlet velocity drops to zero when the flow breakage occurs.

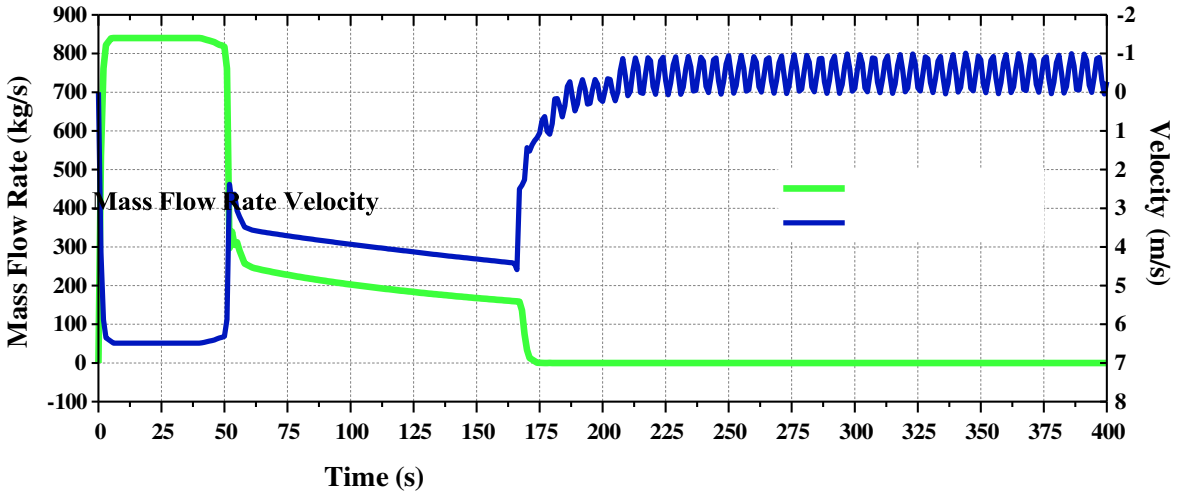

Fig. 12. Mass flow rate and velocity in break size of 16 inches

Table 2 shows the validation of the simulation results by comparing the simulation results carried out in this work with the experimental results reported in reference [6]. The accuracy of the simulation is demonstrated by the fact that the largest difference in UH between the simulation and reference results is equal to -3.1 cm, while the smallest difference is equal to -0.1 cm.

Table 2. Comparison of experimental results and simulation results

Size (inch)			UH (cm)		
Siphon Pipe	Break	SBL	Experiment	RELAP5/ Mod3.2 ai(N)	Difference
16	16	4	-35	-36.7	+1.7
16	16	3	-84	-80.9	-3.1
16	16	2.5	-138	-135.2	-2.8
16	8	2.5	-29	-28.9	-0.1
16	8	2	-53	-51.4	-1.6

Conclusion

According to this research, the heterogeneous solution approach has fewer errors and is more accurate than the homogeneous solution. By adjusting the parameters of the break size and the size of the siphon breaker line and taking a wide range of numbers into consideration, it is concluded that the amount of UH is increased with the increase of break size or the decrease of the size of the siphon breaker line.

The main result and originality of this study was to demonstrate that the RELAP5/Mod3.2ai thermohydraulic code is capable of modeling this kind of accident on a large scale and to arrive at the findings of previous experiments that have been conducted. Research centers worldwide are presently investigating and developing this problem using two-phase approximations. Special programming has been developed for this test facility, taking into account the complexity of this phenomenon in two-phase state with gravity flow and with increasing mass flux in case of increasing the break size to increase the accuracy of calculations. This study presents a numerical solution of the RELAP5/Mod3.2 code simulating the siphon breaker line type of this system. The UH is equal to -36.7 cm in a break size of 16 inches and a breaker line size of 4 inches, and it is equal to -51.4 cm with an 8-inch break size and a 2- inch breaker line. The largest difference is -3.1 cm, and the smallest difference is -0.1 cm, based on a comparison of the numerical findings with the experimental results [6]. The simulation results showed an acceptable degree of conformance with the experimental data.

References

[1] V. Proc. of a Conf., "The Safety of Nuclear Power Strategy for the Future," *INTERNATIONAL ATOMIC ENERGY AGENCY,* 1991.

A. G. S. D.T. Neil, "Siphon breaker design requirements final report," *DOE/ER/12820-T1, pp. 1- 222,* 1993. [Online]. Available: https://doi.org/10.2172/10140472,.

[2] F. Sakurai, "Study for improvement of performance of the test and research reactors," Japan Atomic Energy Research Inst., 1999.

S. H. Kang, Kim, Moo Hwan, Seo, Kyoung Woo, Lee, Kwon Yeong, and Chi, Dae Young, "Final report of experimental studies on siphon breaker, JORDAN RESEARCH AND TRAINING REACTOR," 2011. [Online]. Available: https://www.osti.gov/etdeweb/servlets/purl/21560925

K. Seo *et al.*, " experimental and numerical study for a siphon breaker design of a research reactor," *Annals of Nuclear Energy,* vol. 50, pp. 94-102, 2012.

[3] K.-Y. Lee and W.-S. Kim, "Theoretical study on loss of coolant accident of a research reactor,"

[4] *Nuclear engineering and design,* vol. 309, pp. 151-160, 2016.

[5] K.-Y. Lee and W.-S. Kim, "Study of siphon breaker experiment and simulation for a research reactor," *JoVE (Journal of Visualized Experiments),* no. 127, p. e55972, 2017.

D.-Y. Ji, S. hoon Kim, K.-Y. Lee, and D. K. Park, " experimental study of small scale siphon breaker to verify Siphon Breaker Simulation Program (SBSP)," *Annals of nuclear energy,* vol. 121, pp. 406-413, 2018.

S. Sengupta, V. Kumar, and S. Bhattacharya, experimental *and Numerical studies of Siphon breaker in an* experimental *Test facility*. 2022.

[6] S. Park, H. Kim, C. Park, and J. Yoon, "RELAP5/Mod3. 3 and MARS3. 0a Modeling of a Siphon Break Experiment," 2011.

[7] H. Park, K. Seo, S. Kim, and D. Chi, "Cfd analysis of siphon break in a research reactor," in

[8] *Transactions of the Korean Nuclear Society Spring Meeting*, 2014, pp. 1-2.

[9] D. Ramajo, S. Corzo, P. Alberto, C. Mocciaro, M. Saez, and N. M. Nigro, "Numerical simulation of siphon breaker of an open-pool type research reactor," *Mecánica Computacional,* vol. 35, no. 31, pp. 1809-1825, 2017.

[10] K.-Y. Lee and W.-S. Kim, "Development of siphon breaker simulation program for investing loss of coolant accident of a research reactor," *Annals of Nuclear Energy,* vol. 101, pp. 49-57, 2017.

[11] J.-P. Park and I. K. Park, "Parametric Study for Interfacial Drag on Siphon break Phenomena in a Research Reactor," 2020.

[12] Kang, S. H., et al. (2014). "Investigation on effects of enlarged pipe rupture size and air penetration timing in real-scale experiment of siphon breaker." Nuclear Engineering and Technology 46(6): 817-824.

ICNST 2024 International Conference on Nuclear Science and Technology
6- 8 MAY 2024 | Isfahan, Iran

Development of a Model for Calculation of Radial Burnup Distribution in VVER-1000 Reactor Fuel Rod Using Monte Carlo Method (Paper ID : 1354)

Mohsen Pourramezan Shahabaldini, Ahmad Pirouzmand*, and Maryamsadat Hosseini

Department of Nuclear Engineering, School of Mechanical Engineering, Shiraz University, Shiraz, Iran

pirouzm@shirazu.ac.ir

Abstract

In this paper, a model is developed for calculating the radial distribution of burnup and the actinide densities in the VVER-1000 fuel rod type. For this purpose, an MCNPX model for 1.6% fuel enrichment of VVER-1000 reactor is prepared and then the values are calculated for radial distribution of cross sections, neutron flux, burnup and atomic densities. Also, using the MCNPX data, correlations are developed to calculate the radial changes of absorption, capture and fission cross sections of actinides in different values of fuel burnups.

Using developed cross section correlations and taking into account the governing differential equations, a model is developed in MATLAB software to calculate the radial atomic density of actinides in a fuel pellet. Then using the calculated atomic densities and fission cross sections, the amount of radial changes of power density with fuel burnup are calculated. Finally, we evaluate the outcome by calculating the radial distribution of fuel burnup and comparing it with the MCNPX data. The comparison show that the model has an acceptable accuracy for predicting the radial distribution of fuel burnup within the VVER-1000 fuel rods.

Keywords: The MCNPX code, Radial distribution of atomic density, Radial distribution of burnup, VVER-1000 nuclear reactor.

Introduction

Increasing the fuel burnup in fuel pellets, primarily composed of uranium oxide (UO_2), imposes certain operational limitations that require investigation. Among these limitations are the formation of radial profiles of fuel burnup, power, and other actinides in the fuel pellet [1, 2]. This distribution causes the formation of a rim effect in the peripheral region of the fuel pellet, and it also affects the thermal and mechanical properties of the fuel pellet [1, 3]. Therefore, this issue should be considered in the process of thermal-mechanical analysis of fuel rods in light water reactors, and the change of fuel pellet characteristics with radial distribution of fuel burnup should be properly modeled. In fact, in all the codes

developed in the field of thermal-mechanical analysis of fuel rods, a model is used to estimate the radial consumption of fuel, power, and concentration of actinides [1, 3-5]. In these models, the radial distribution of fuel burnup, power distribution, and the concentration of various fission products in the fuel pellet are calculated by taking into account the fuel pellet geometry, fuel enrichment, concentration of burnable poisons, and other operational parameters. These radial calculations are used to estimate changes in the thermal mechanical parameters of the fuel [4, 5].

Regarding the radial fuel burnup calculations in water reactors, extensive research has been conducted. This research involves developing models and simulations to calculate radial fuel burnup and investigate the parameters that affect it. Pirouzmand et al. (2016) utilized the MCNPX code to examine the radial distribution of fuel burnup in the VVER-1000 reactor fuel rod. The results obtained by the MCNPX code showed acceptable agreement with the results obtained in the benchmark problem [4]. Concurrently, Brian et al. (2016) investigated a model for radial variations in fuel burnup and source conditions in the fuel for both BWR and PWR reactors under high burnup conditions [6]. Later, Sierjelati et al. (2019) investigated a model for the shape changes of fuel rods caused by fuel burnup and their influence on the transient behavior of the VVER-440 reactor, considering both mechanical and thermal aspects. They used the FRAPCON and HEXTRAN reactor dynamics codes, which included initial data on the behavior of the FINIX fuel [7].

Various research studies in the field of simulation and calculation of the radial distribution of fuel burnup and the concentration of radionuclides in fuel pellets indicate that these calculations are of great importance in the thermal-mechanical analysis of fuel rods. On the other hand, the development of a simple model that can rapidly compute these quantities based on data obtained from the accurate Monte Carlo method is highly significant. In this article, considering the excellent accuracy of the Monte Carlo method in modeling complex geometries and utilizing continuous neutron cross section libraries, the MCNPX computational code is employed to investigate the behavior of fuel pellets during the operational cycle of fuel rods. Subsequently, these data are used to develop a model capable of accurately and rapidly computation, the mentioned quantities under various operational conditions.

Theory

1. Description of VVER-1000/VVER-446 fuel assemblies

In VVER-1000/VVER-446 reactor, fuel assemblies are hexagonal. These fuel assemblies consist of 311 cylindrical fuel rods. Depending on the type of fuel assembly and its location within the reactor core, various types of fuel rods are utilized. This variation is intended to distribute power throughout the entire reactor core. In reactor core design, it is essential to consider that higher enriched fuel rods are employed in regions where neutron flux is low. This practice ensures a uniform neutron flux in those regions, resulting in a consistent power distribution across the entire reactor core. The specifications of various fuel assemblies in the VVER-1000 reactor core are provided in Table 1 [8]. In this paper, the fuel assembly type 16 is chosen as a case study.

Table 1. Specifications of fuel assemblies in first fuel cycle of VVER-1000/VVER-446 reactor [8]

Type of fuel assemblies	Average enrichment (%)	Number of fuel rods type 1	Number of fuel rods type 2	The number of BARs*	Density in BAR (g/cm^3)
16	1.6	311 (1.6)	–	–	–
24	2.4	311 (2.4)	–	–	–
36	3.62	245 (3.7)	66 (3.3)	–	–

*Burnable Absorbers

2. Governing equations

Considering the great importance of radial burnup calculation of fuel in thermo-mechanical analyses of fuel pins, this section introduces the governing equations for the radial calculation of actinides atom densities. These equations play a crucial role in calculation of the radial distribution of power density and fuel burnup. Additionally, significant parameters affecting their solution are presented. According to one-group and one-dimensional diffusion theory, the equilibrium equations for fissile and fertile nuclides density such as ^{235}U, ^{238}U, ^{239}Pu, ^{240}Pu, ^{241}Pu, and ^{242}Pu can be expressed as follows:

$$\frac{\partial}{\partial t}N_{235}(t,\ r) = -N_{235}(t,\ r)\sigma_a^{235}(t,\ r)\phi(t,\ r) \quad (1)$$

$$\frac{\partial}{\partial t}N_{238}(t,\ r) = -N_{238}(t,\ r)\sigma_a^{238}(t,\ r)\phi(t,\ r) \quad (2)$$

$$\frac{\partial}{\partial t}N_{239}(t,\ r) = -N_{239}(t,\ r)(\sigma_a^{239}(t,\ r)\phi(t,\ r) + \lambda_{239}) + N_{238}(t,\ r)\sigma_c^{238}(t,\ r)\phi(t,\ r) \quad (3)$$

$$\frac{\partial}{\partial t}N_{240}(t,\ r) = -N_{240}(t,\ r)(\sigma_a^{240}(t,\ r)\phi(t,\ r) + \lambda_{240}) + N_{239}(t,\ r)\sigma_c^{239}(t,\ r)\phi(t,\ r) \quad (4)$$

$$\frac{\partial}{\partial t}N_{241}(t,\ r) = -N_{241}(t,\ r)(\sigma_a^{241}(t,\ r)\phi(t,\ r) + \lambda_{241}) + N_{240}(t,\ r)\sigma_c^{240}(t,\ r)\phi(t,\ r) \quad (5)$$

$$\frac{\partial}{\partial t}N_{242}(t,\ r) = -N_{242}(t,\ r)(\sigma_a^{242}(t,\ r)\phi(t,\ r) + \lambda_{242}) + N_{241}(t,\ r)\sigma_c^{241}(t,\ r)\phi(t,\ r) \quad (6)$$

In the above equations, $N_i(t, r)$ represents the atomic density of nuclide i (in atoms/m³), $\sigma_a{}^i$ is the neutron absorption cross section of nuclide i, $\sigma_c{}^i$ denotes the neutron scattering cross section in nuclide i, λ_i stands for the decay constant of nuclide i (in s^{-1}), and $\phi(t, r)$ represents the one-group neutron flux (in n/cm²s). To solve the above set of equations, it is necessary to consider the dependence of the cross section and neutron flux with enrichment, fuel burnup, and radius in fuel pellet.

The one-group neutron flux $\phi(t, r)$ can be assumed to be constant in the radial direction and expressed as a function of power density (POWDEN in unit of W/cm³), fuel burnup (BU in unit of MWD/(kgU)), and ^{235}U enrichment level (*EN* in unit of wt.%) [1]:

$$\phi(t,\ r) = \left((C_1^n + C_2^n EN + C_3^n EN^2) + C_4^n BU + C_5^n BU^2\right)POWDEN \quad (7)$$

The values of C_i are constant.

The absorption cross sections of ^{235}U, ^{239}Pu, and ^{241}Pu, as well as the fission cross sections of ^{235}U, ^{239}Pu, and ^{241}Pu can be expressed in terms of radial position, fuel burnup, and ^{235}U enrichment. For the cross section of the interaction between nuclide i and nuclide j:

$$\sigma_j^i(t,\ r) = f_j^i(r)\sigma_j^i(t) \quad (8)$$

where functions $\boldsymbol{f_j^i}$ and $\sigma_j{}^i$ are radial and time-dependent functions, respectively. Since the $\boldsymbol{f_j^i}$ function depends on ^{235}U enrichment, it is assumed that a third-order polynomial models the radial changes and a first-order polynomial models the ^{235}U enrichment as follows:

$$f_j^i(r) = C_1^a + C_2^a EN + (C_3^a + C_4^a EN)r + (C_5^a + C_6^a EN)r^2 + (C_7^a + C_8^a EN)r^3 \quad (9)$$

Also, the time-dependent function $\sigma_j{}^i$ can be expressed as a function of burnup and enrichment of ^{235}U as follows:

$$\sigma_j^i(t) = (C_1^b + C_2^b EN + C_3^b EN^2)(C_4^b + \left(C_5^b + C_6^b EN\right)BU + (C_7^b + C_8^b EN)BU^2) \quad (10)$$

Methodology

In this section, the steps of the work are explained. First, we utilize the MCNPX code to simulate various fuel assemblies of the VVER-1000/VVER-446 reactor during the initial reactor cycle, ensuring representation of different fuel enrichments. In the next step, we radially divide fuel rods in each assembly to simulate the radial distribution of neutron flux, fuel burnup, and actinide changes in the MCNPX code. Subsequently, we extract data related to the radial distribution of neutron flux, absorption and scattering cross sections, fuel burnup, and actinide densities. Next, we calculate the neutron absorption and scattering cross sections using the MCNPX model. In the subsequent stage, we fit the variations of cross-sections and neutron flux using suitable polynomial functions based on fuel burnup, enrichment level, and radial position using MATLAB software. Finally, we solve the system of equations described in the theoretical foundations using the provided cross section functions from equations (7) to (10) via MATLAB. Additionally, we compare the results obtained from the MCNPX model with the data from MATLAB to assess the accuracy of the radial distribution model for nuclear densities.

1. MCNPX model for VVER-1000/VVER-446 fuel assemblies

In this article, for modeling the calculations of radial fuel burnup, we require neutronic calculations using the reactor physics code MCNPX. This enables us to simulate the radial burnup of nuclear fuel and the products resulting from fission. In this study, three fuel assemblies from the VVER-1000 reactor, containing 1.6%**,** 2.4%**,** 3.3%**,** and 3.7% enrichment, are modeled in the MCNPX code. During reactor cycle calculations, the flux distribution must be divided into time intervals such that flux variations within each interval are considered constant. To ensure a realistic analysis, all fuel assembly components and details must be modeled with actual dimensions and sizes. All the details used in the input file can be extracted from FSAR chapter 4.

According to Fig. 1-a, fuel assembly No. 16 is designed so that all fuel rods within it have a uranium enrichment of 1.6%. Fig. 1 illustrates the arrangement of fuel with 1.6% uranium enrichment in assembly 16, where the fuel rods are discretized radially using the MCNPX code. In the fuel rod's cell card, nodalization is performed in each cell. As we approach the end of the fuel pellet, increase the number of nodes. As shown in Fig. 1-b, we have increased the discretization in the fuel periphery to enhance computational accuracy. This allows us to observe the fuel's rim effect.

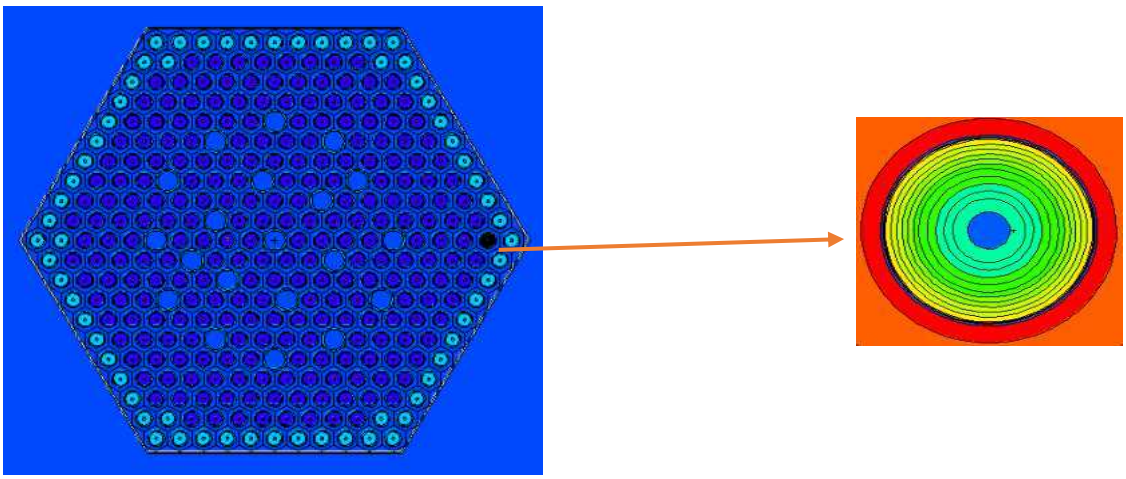

(a) (b)

Fig. 1. (a). Modeled fuel assembly (No. 16) and **(b).** Radial nodalization of a fuel rod using MCNPX code

It is worth mentioning that neutronic cross sections are modified using MAKXSF utility for different temperatures.

1.1. Cross section generation

Since we need to calculate effective cross sections, we perform these calculations using *F4* tallies in the MCNPX code. After simulating the computations and the desired geometry, we utilize the *F4* tally to obtain the desired cross sections. The *F4* tally is defined as follows: (w_i: weight of each particle, N: total number of particles, v: volume of each area)

$$F4 = \frac{1}{N}\sum_{i=1}^{N}\frac{w_i}{v} \tag{11}$$

Using the *FMn* tally card, we calculate the desired reaction rate for that desired substance and then divide the *FM4* by *F4* to get the cross section of the reaction for that desired isotope. The format of the *FMn* tally card for *FM4* is displayed as follows: ($\phi(\boldsymbol{E})$: energy-dependent flux in terms of neutron/cm^2, *Rm(E)* is an operator to add or multiply a function in the flux, C: the density of the material, m: the desired item number, r: the desired reaction number we need to calculate)

$$C\int \phi(E)Rm(E)dE \tag{12}$$

$$FM4 \;\; c \;\; m \;\; r_1 \;\; r_2 \tag{13}$$

$$\phi = \frac{R}{\Sigma} \tag{14}$$

$$\sum_{t_i} = \frac{\int \phi(E) \sum_i(E) dE}{E \int \phi(E) dE} = \frac{FM4}{F4} \quad (15)$$

2. Modeling the radial distribution of fuel burnup using MATLAB

2.1. Cross section calculations

In order to determine the constants in the equations governing changes in cross section and neutron flux (equations (7) to (10)), we used the cftool function in MATLAB, considering the variables of fuel burnup, enrichment level, and radius. In this toolbox, the constants in the above equations have been selected to minimize errors using data obtained from the MCNPX model and curve fitting.

2.2. Solving coupled differential equations

In this article, for solving equations (1) to (6), we have utilized the ode45 solver method in MATLAB, considering the fuel burnup time interval and the initial atomic density of 235U and 238U. After performing coupled calculations, the atomic densities of 235U, 238U, 239Pu, 240Pu, 241Pu, and 242Pu have been obtained during the various radial fuel burnup at different enrichments. After calculating atomic density, we proceed to calculate the reaction rate and then determine the power density of actinides. Also, by calculating the radial distribution of fuel burnup and comparing it with MCNPX data, the results of the model are evaluated. Finally, using the atomic density of fissile materials, the fission interaction rate, the power density, and consequently the radial distribution of burnup in the fuel rod are calculated.

Results and discussion

As an example, some results for radial changes in the absorption cross sections and atomic densities of ^{238}U and ^{235}U for 1.6% enrichment fuel are presented. Additionally, the radial distribution of fuel burnup is shown using the developed model and compared with data obtained from the MCNPX model.

1. MCNPX results

In this section the result of MCNPX model for 1.6% enrichment for ^{235}U and ^{238}U is presented as an example. Similar results have been extracted for other isotopes, including ^{239}Pu, ^{240}Pu, ^{241}Pu, ^{242}Pu for various burnups and enrichment values. It is worth mentioning that the maximum value of the statistical error for all cases in the MCNPX model for infinite multiplication factor calculation is equalto 3.0×10^{-4}. As shown in Fig. 2-a, as the fuel burnup increases, the absorption cross section of ^{235}U decreases radially. Depending on the amount of fuel burnup, the range of the cross section increases from the innermost

radius to the outermost radius. According to Fig. 2-b, the absorption cross section of ^{238}U increases radially with increasing fuel burnup. According to the amount of fuel burnup, the resonance absorption cross section of neutrons at the fuel pellet edge also increases with radius and fuel burnup. The increase in cross section leads to a decrease in atomic density and saturation of fuel burnup at the pellet edges (rim effect), resulting in increased plutonium production. Fig. 2-c illustrates the changes in radial capture cross section in ^{238}U with a 1.6% enrichment during the burnup of various fuels using the MCNPX model. Considering this figure, similar to the absorption cross section curve for ^{238}U, we can infer that there are minor effects on the radial changes of cross section in different fuel burnup. Additionally, the capture cross section for ^{238}U will increase at the fuel edges.

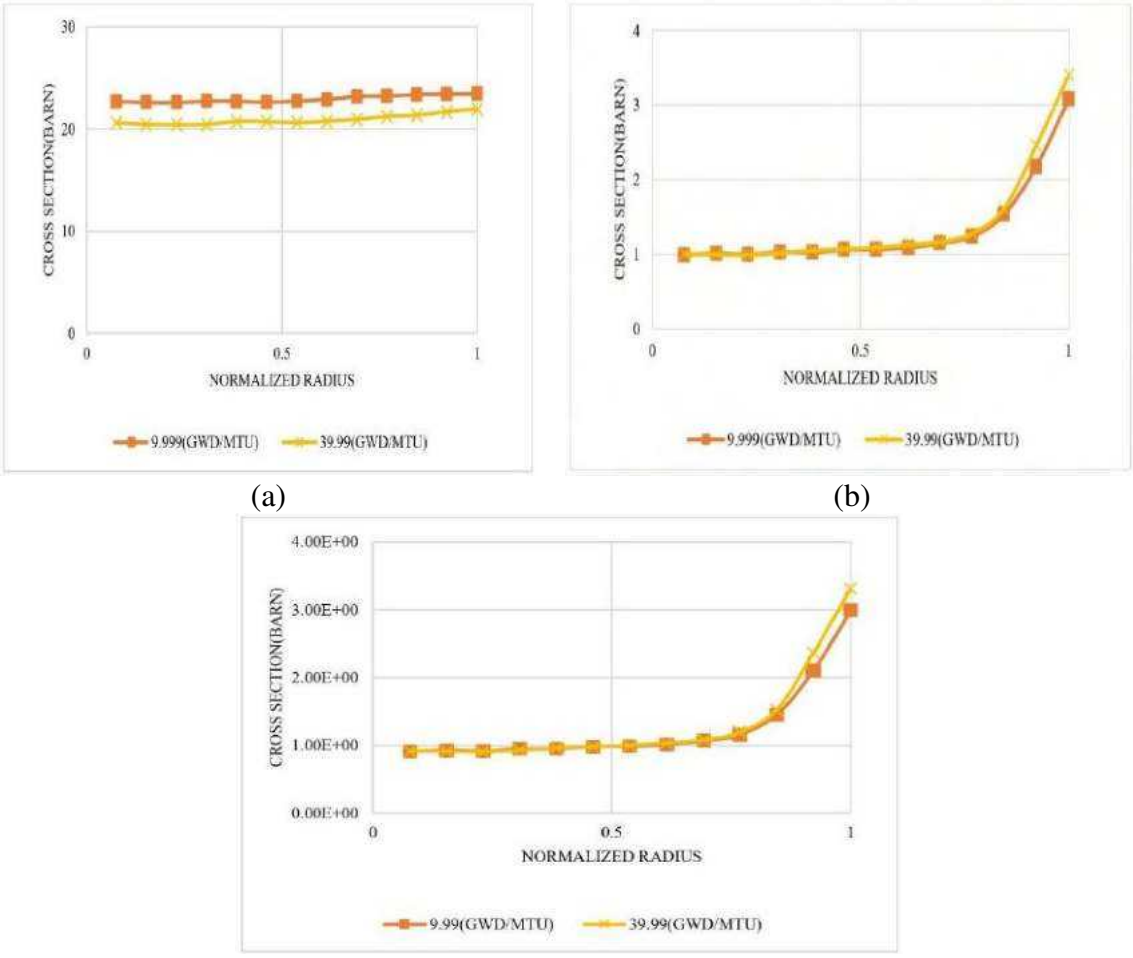

Fig. 2. Radial changes of **(a).** absorption cross section of ^{235}U **(b).** absorption cross section of ^{238}U **(c).** capture cross section of ^{238}U, with 1.6% enrichment at two fuel burnup

According to Fig. 3, the atomic densities of ^{235}U and ^{238}U decrease radially with increasing fuel burnup at 1.6% enrichment. Additionally, it can be stated that as fuel burnup increases, the atomic density

decreases. In the radial direction, a sharp decrease in atomic density is observed at the fuel pellet edges due to the saturation of ^{235}U and ^{238}U absorption.

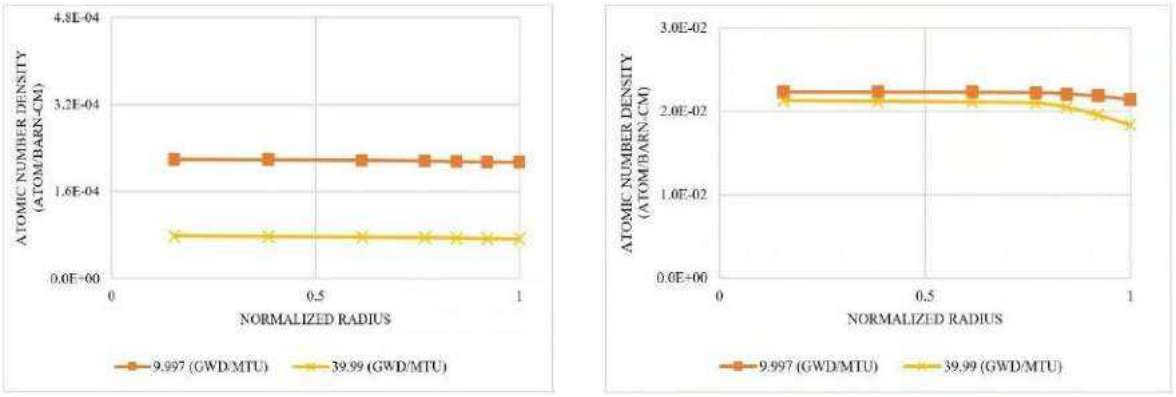

(a) (b)

Fig. 3. Radial changes in atomic density of **(a).** ^{235}U and **(b).** ^{238}U with 1.6% enrichment at two fuel burnup

2. Comparison of result obtained by MCNPX and MATLAB

In this section, as an example, the results of developed model are presented for a fuel enrichment of 1.6% and burnup values of 9.999 and 39.999 (GWD/MTU).

2.1. Cross section

In this subsection, constant values are obtained to estimate absorption and capture cross sections based on the correlations presented in the theoretical section. Subsequently, the results from these correlations are compared with data obtained from the MCNPX model.

According to Fig. 4, the observed results for radial changes in the absorption and capture cross sections using the model presented with MATLAB and MCNPX exhibit a high degree of agreement.

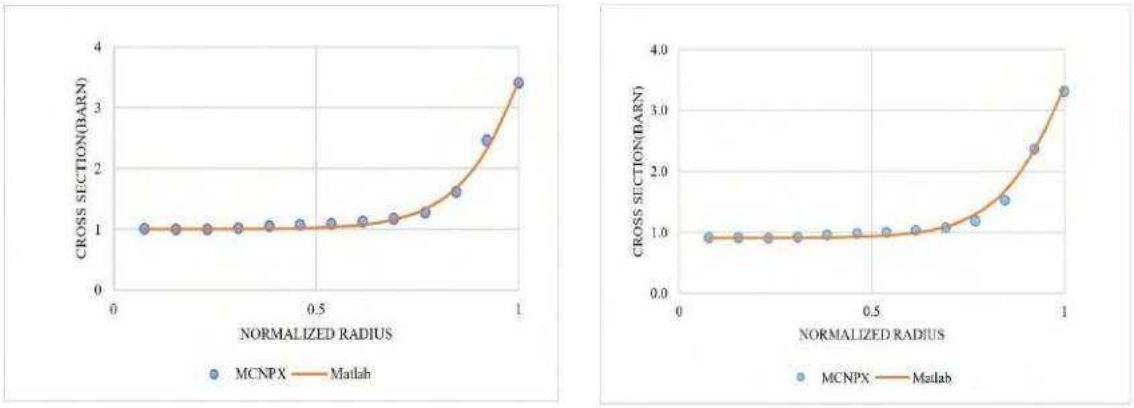

(a)

(b)

Fig. 4. Comparison of radial changes in **(a).** absorption cross section of ^{238}U and **(b).** capture cross section of ^{238}U, using MATLAB and MCNPX for fuel burnup of 39.999 (GWD/MTU) with 1.6% enrichment.

2.2. Atomic density

In this subsection, the results of radial distribution of atomic density calculations using the developed model in this article are compared with data obtained from the MCNPX model.

According to Fig. 5, it is observable that the relative error of atomic density along the radial direction using the model presented with MATLAB and MCNPX is 11.5% for 235U and 0.6% for 238U. The difference is due to the MCNPX code capability to accurately model the geometry and using continuous-energy cross section data.

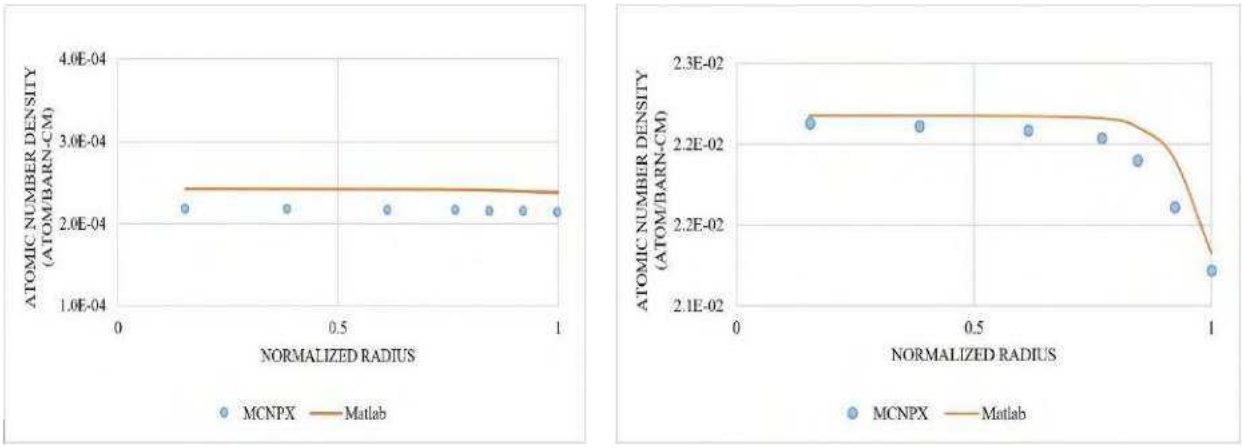

(a) (b)

Fig. 5. Comparison of the atomic density obtained using MATLAB and MCNPX in the radial direction for: **(a).** ^{235}U, **(b).** ^{238}U with 1.6% enrichment in fuel burnup 9.999 (GWD/MTU)

2.3. Burnup

In this subsection, the results of radial distribution of burnup calculations using the developed model in this article are compared with data obtained from the MCNPX model (results for a fuel enrichment of 1.6%).

Fig. 6 illustrates the radial variations in fuel burnup obtained from MATLAB and MCNPX for a 1.6% enrichment, corresponding to burnup rates of 39.99 and 14.99 (GWD/MTU). This figure indicates that the burnup level increases with the increasing burnup time along the radial direction in a discretized fuel rod; the burnup level rises. This increase is more pronounced at lower enrichments compared to higher

enrichments. Based on the comparison of data between MATLAB and MCNPX in Fig. 6, it can be concluded that the proposed model demonstrates reasonable accuracy, with an error rate below 2%.

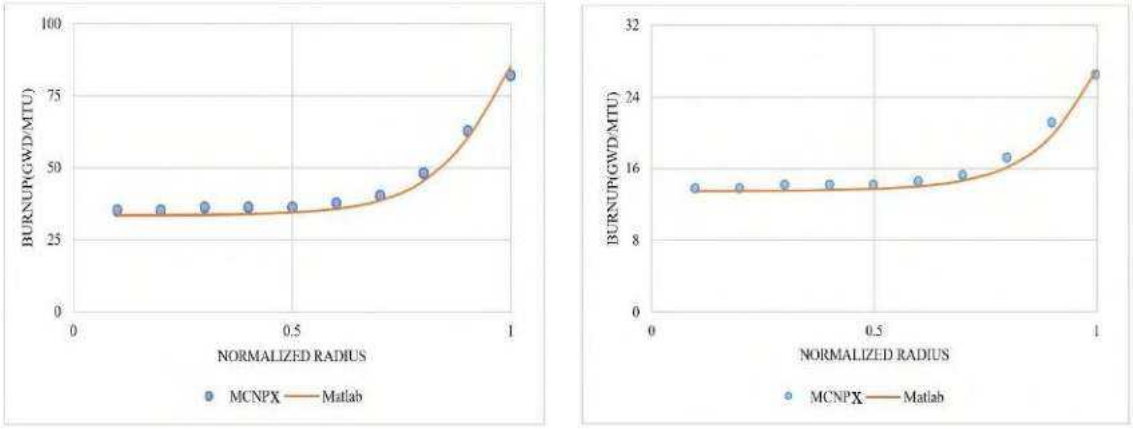

(a) (b)

Fig. 6. Radial fuel burnup changes obtained from MATLAB and MCNPX at 1.6% enrichment with fuel burnup rate **(a).** 39.99 (GWD/MTU) **(b).** 14.99 (GWD/MTU)

Conclusions

Given the significance of analyzing fuel rod behavior during high burnup from safety and economic perspectives by the thermomechanical analysis codes of the fuel rod, and its dependence on the radial distribution of fuel burnup in the fuel pellet, this research utilized data from a developed model in the MCNPX code for fuel rods in VVER-1000/VVER-446 reactors at different enrichments. The goal was to develop a model for rapid and accurate calculation of the radial distribution of fuel burnup. The proposed model predicted the radial distribution of neutron flux and the radial variations of one-group absorption cross sections quite well. Additionally, it closely aligned with the results obtained from the MCNPX model. The final model presented for calculating the radial distribution of fuel burnup is capable of reasonably estimating these quantities by changing of radius, power density, average fuel burnup, and fuel enrichment.

References

[1] C. B. Lee, D. H. Kim, J. S. Song, J. G. Bang, and Y. H. Jung, "RAPID model to predict radial burnup distribution in LWR UO2 fuel," *J. Nucl. Mater.*, vol. 282, no. 2–3, pp. 196–204, 2000.

[2] T. S. & P. G. Juan J. SERNA , Pekka TOLONEN , Sadaaki ABETA , Seiichi WATANABE , Yuji KOSAKA and To, " experimental observations on fuel pellet performance at high burnup," *J. Nucl. Sci. Technol.*, vol. 43, no. 9, pp. 1045–1053, 2006.

[3] F. N. Kryukov, G. D. Lyadov, O. N. Nikitin, V. P. Smirnov, and A. P. Chetverikov, "Radial distribution of the burnup and content of plutonium in VVÉR fuel pellets," *At. Energy*, vol. 100, no. 1, pp. 1–7, 2006.

[4] A. Pirouzmand and F. Roosta, "Calculation of radial burnup and nuclides atom density distributions in a VVER-1000 fuel rod using Monte Carlo method," *Prog. Nucl. Energy*, vol. 88, pp. 321–331, 2016.

[5] K. Lassmann, C. O'Carroll, J. van de Laar, and C. T. Walker, "The radial distribution of plutonium in high burnup UO2 fuels," *J. Nucl. Mater.*, vol. 208, no. 3, pp. 223–231, Feb. 1994.

[6] B. J. Ade, "RADIAL VARIATION OF BURNUP AND SOURCE TERMS IN HIGH BURNUP LWR FUEL," pp. 1–6, 2016.

[7] E. Syrjälahti, T. Ikonen, and V. Tulkki, "Modeling burnup-induced fuel rod deformations and their effect on transient behavior of a VVER-440 reactor core," *Ann. Nucl. Energy*, vol. 125, pp. 121–131, 2019.

[8] AEOI, "Final Safety Analysis Report (FSAR) for BNPP-1", Chapter 4, 2015.

ICNST 2024 International Conference on Nuclear Science and Technology
6- 8 MAY 2024 | Isfahan, Iran

Investigation on Delayed Neutron Grouping Effects: Numerical Solution (Paper ID : 1373)

Narjes Zare Yarji1, 2*, Daryiush Rezaey Uchbelagh1 (ddrezaey@aut.ac.ir), Mohammad Arkani2 (markani@aeoi.org.ir)

1- Department of Energy Engineering & Physics, Amirkabir University of Technology (Tehran Polytechnic), Tehran, Iran.

2- Nuclear Science & Technology Research Institute (NSRTI), Tehran, Iran. P.O. Box: 143995-1113 (✉ markani@aeoi.org.ir)

Abstract

Delayed neutrons have a small fraction of the total neutrons produced in a fission reaction. The relatively long life of the delayed neutrons (in comparison with prompt neutron lifetime) is mainly for the sake of the nuclear decay of the precursor nuclides. This significant feature has an important impact on the reactor dynamics. Generally, delayed neutron parameters in light water reactors are divided into six groups. This is represented in fifteen groups in heavy water reactors (extra nine groups for delayed photo neutrons). Within the last few decades, the development of digital computers has been accelerated. Therefore, the traditional group wise models for reactor dynamics can be considered in more few details or complexity without any difficulties in computation time, hardware resources or software capabilities. In the present research, different group wise models have been reflected to solve the kinetic equations of a typical thermal reactor using fourth order Runge-Kutta numerical method. The MATLAB software engineering tool is applied to implement the method. The results are compared with each other.

Keywords: Point Kinetic Equation, Delayed Neutron, Nuclear Reactor Dynamics, Kinetic Parameter.

Introduction

Delayed neutrons are produced from some fission fragments, which is called delayed neutron precursors. Delayed neutron precursors decayed by beta emission with different half-lives and shortly after that emit neutrons. After each fission, it takes roughly the average lifetime of the delayed neutron precursors to produce each neutron. Since the time needed to produce these neutrons is much longer than the time required to produce fast neutrons, these neutrons are called delayed neutrons. Each reactor has special features of delayed neutrons according to the characteristics of its core and fuel composition, hence the parameters of delayed neutrons of each reactor core are unique. Although delayed neutrons form a small fraction of the neutrons produced in the reactor core, they have a significant effect on the reactor period, resulting in the time needed to control the reactor by control systems as a result of the effect they have

on the average life of neutrons in the reactor core. Due to the fact that delayed neutrons directly affect the kinetic response of the reactor core, it plays an important role in related measurements (e.g., measuring the reactivity of the reactor core as a result of disturbance using the kinetic response analysis of the reactor core). To analyse the behaviour of the reactor core, delayed neutrons are grouped based on their half-lives [Keppin, 1957, Keepin 1972). Delayed neutrons are mostly classified into six and eight groups (from about a fraction of a second to more than 50). Group-wise modelling of delayed neutrons dates back to the early years of the models for nuclear reactor dynamics and the development of information about nuclides producing delayed neutrons. Since then, the information of nuclear libraries as well as computing tools and methods has advanced a lot. In this research, data related to delayed neutrons were extracted from nuclear libraries, then this information was classified into different groups. In the next step, the effect of the grouping of delayed neutrons on the dynamic behaviour of the nuclear reactor core has been investigated by stiff equation-solving methods. The main tool for this purpose is the MATLAB software engineering tool. The obtained results have been compared and verified with the corresponding experimental results in In Tehran Research Reactor.

Six-Group approach of delayed neutrons

The concept of delayed neutrons and their half-life groupings was first proposed by G. R. Keepin et al., [6]. Delayed neutrons are traditionally classified into six groups, and their yields and decay constants (λ) are obtained through nonlinear least squares fitting using experimental measurements. While the six-group parameter set still satisfies the requirements of reactor physics calculations, these calculations are performed to achieve higher accuracy than previous computations.

Eight-Group approach of delayed neutrons

In April 1997, an international workshop on delayed neutrons was held at the Institute of Physics and Power Engineering (IPPE) in Obninsk, Russia [2]. The research conducted by Spriggs et al., [2] examined the parameters of delayed neutrons using an eight-group classification scheme and validated the results. The study, published in 2002, investigated the grouping of delayed neutron constants for 20 fissile isotopes, comprising a total of 245 experimental data points. The data was analysed using a non-linear least square fitting method, resulting in the division of the data into eight distinct groups based on their characteristics. The results of this grouping are presented in Table 2 in supplementary data.

Point kinetic equation

The equations encapsulate the categorization of delayed neutron sources into six distinct groups based on their respective half-lives. This classification scheme serves to capture the diverse temporal scales associated with delayed neutron emission, thereby enhancing the fidelity of neutron population calculations. Each delayed neutron-producing nucleus is assumed to undergo decay by emitting a single delayed neutron, which imparts a level of simplicity to the modelling of neutron production and facilitates the estimation of the delayed neutron fraction.(Hetrick and Jarvis 1972) Holistically, the point kinetic equations furnish a robust framework for investigating reactor behaviour, playing a vital role in reactor design, operation and safety analyses. Their application contributes to figure out and predict neutron kinetics, thereby subjecting to the advancement of nuclear reactor technology.

$$\begin{cases} \frac{dn(t)}{dt} = \frac{(1-\beta)}{\Lambda} n(t) + \sum_{i=1}^{6} \lambda_i c_i - \frac{n}{l} \\ \frac{dc_i(t)}{dt} = \frac{\beta_i}{\Lambda} n(t) - \lambda_i c_i \quad i = 1\ 2 \ldots\ 6 \end{cases} \tag{1}$$

In their research, Spriggs et al. (2002) [2] indicated that 17 delayed neutron generator nuclei with longer half-lives are deliberated, then divided into groups of six, eight, and once with 17 Delayed neutron generator nuclei are grouped. Each group may contain several nuclei producing delayed neutrons, but the half-lives of each group need to be relatively close to each other. Initially, the number of delayed neutrons released in the decay (neutrons in each decay) and the probability of the release of delayed neutrons in each decay have been extracted from nuclear libraries.

First, the number of delayed neutrons in each decay are extracted from nuclear libraries such as NDS.

$$Neutron\ per\ decay = \frac{p_n}{100} \tag{2}$$

Then the number of neutrons emitted in each fission is obtained by equation 3.

$$Neutron\ per\ fission = yeild * \frac{p_n}{100} \tag{3}$$

The sum of all the neutrons emitted in one fission is called the yield of the total delayed neutrons, which for uranium 235 is as follows:

$\sum \beta_i$=0.0158

(4)

Calculation of fraction of delayed neutrons

Delayed neutron fraction is the ratio of total delayed neutrons emitted to total neutrons resulting from fission, which is it has been shown by the abbreviation β.

$$\beta = \frac{Neutron\ per\ fission}{\nu} \quad (5)$$

ν: The number of neutrons produced in fission

In the next step, the following relationship is used to calculate the relative interest (Abundance) of each group.

$$Abandance = \frac{\beta_i}{\beta_{total}} \quad (6)$$

Half-life averaging method

One of the most important parts of this study is averaging the half-life of delayed neutrons. For this purpose, β was used as the basis and averaging was done using relation7.

$$halflife = \frac{\sum_1^i Beta\ i * \lambda_i}{\sum_1^i Betai} \quad (7)$$

Using MATLAB software, this method has been implemented in different groupings of delayed neutrons, the accuracy and precision of this method with a similar model presented by (Hetrick and Jarvis 1972)and fast power equations without Feedback are compared.

The parameters related to the nuclei producing delayed neutrons are grouped in 6, 8, and 17 ones, respectively, and their results are detailed in Tables 2, 3, and 4, respectively.

Digram 1 indicates a comparison between the changes in the density of nuclei producing delayed neutrons in terms of time for the six groups of delayed neutrons obtained in this research using the common six -group model.

Figure ١ shows a comparison between the diagrams of the 6, 8 and 17 group models of delayed neutrons obtained in this research using the common six- group model.

The common six-group model is the six-group model that is commonly used in nuclear calculations and discussed in details in Kipnis ' Reactor Dynamics book.

Notably, these calculations are only used to figure out the conformity of the grouping results of the recommended delayed neutron parameters in this group with the grouping parameters of the common 6-group model and the validation of the results will be done using the experimental tests.

The expansion process was tested by experimental data for the thermal fission of uranium-235. Initially, the results were compared and evaluated with the six-group model recommended in this research. The second fitting was done using the 8-group model and the third fitting was done for 17 nuclei producing delayed neutrons without grouping. Fig 1 features out a comparison of the fit diagrams of the six Keepin groups and the fit of 6 and 8 of the 17 developed groups in the mode.

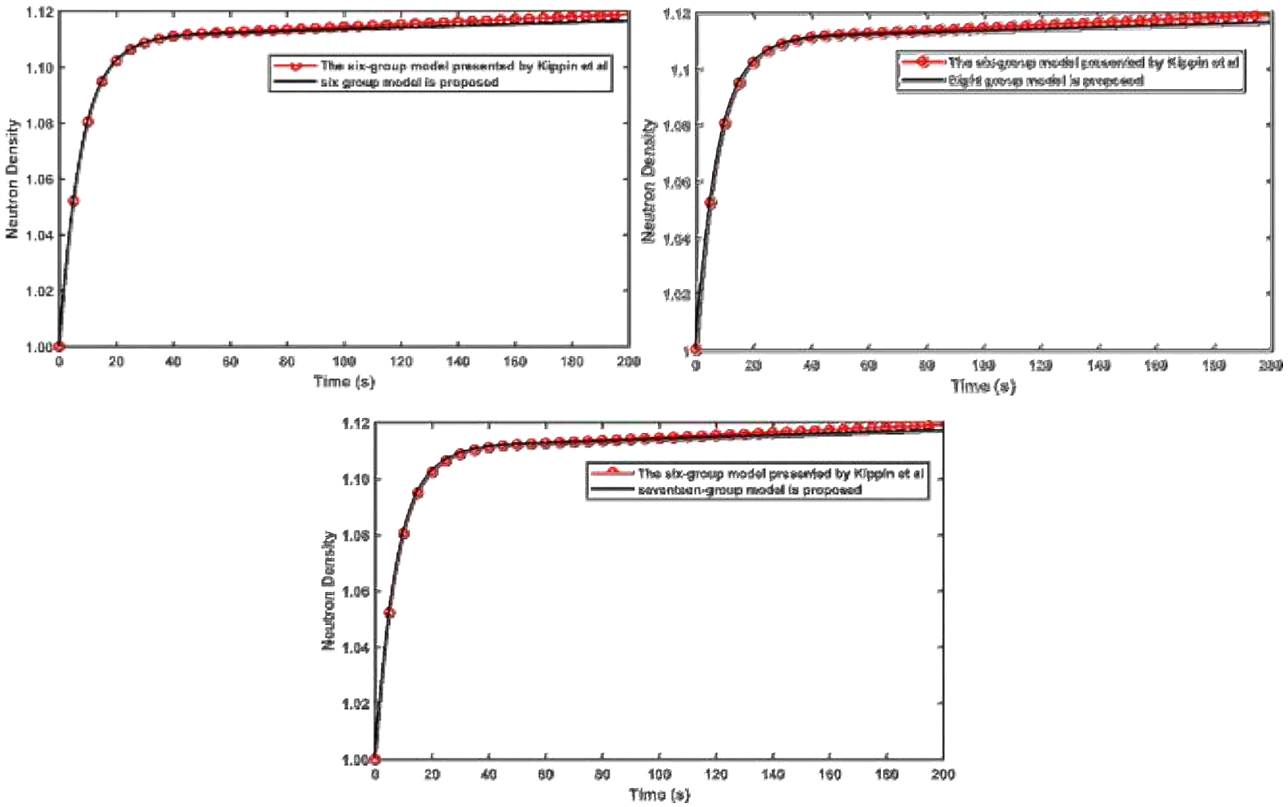

Figure 1. Comparison of the diagram of delayed neutron density versus time based on the data of the developed 6, 8, 17 group model with the common six group model in each positive reaction injection of $0.1.

Validation using Experimental tests

To adjust the power of the reactor (less than 1 kW), we remove the tested rod with a height of 65 cm completely (100%) from the heart and make the reactor critical with other control rods. The estimated duration of the fall of the control rod is 350-800 milliseconds in In Tehran Research Reactor. The swiftness of the control rod and the resulting negative reactivity is entered into the centre of the reactor, the power of the reactor is first decreased by a large slope and with the appearance of delayed neutrons, its slope is gradually declined and stabilized.

Initially, we should calculate the integral value of the safety control rod selected for the test using equation (8) to achieve the results with more accuracy. Next, the reactivity functions in terms of time for the control rod. We draw, enter the obtained values for reactivity into equation (1) and verify the results with the results of numerical calculations.

$$\rho(z) = \rho(H) \times \left[\frac{Z}{H} - \frac{1}{2\pi}\sin\left(\frac{2\pi Z}{H}\right)\right] \quad (8)$$

(H): The total value of the reactivity of the control rod

Z: The rate of rod exit from the reactor core

H: Effective height of the reactor core

$\frac{Z}{H}$: Fraction of the control rod from the core

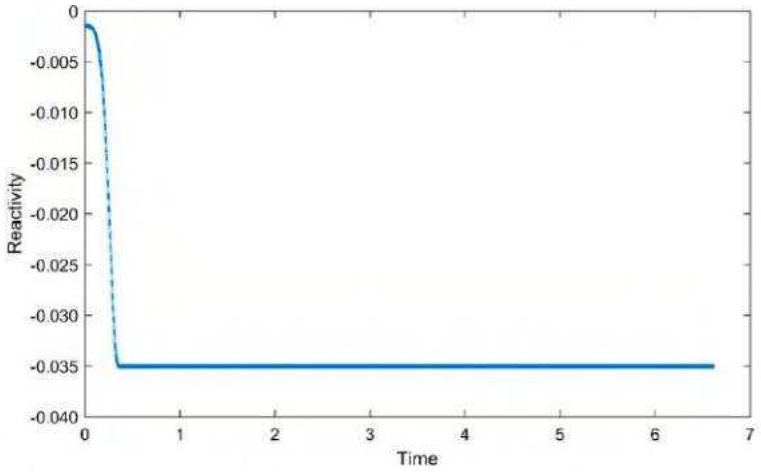

Fig.2. changes of reactivity during the time interval.

Fig. 2 illustrates the reactivity values in terms of time. By placing the reactivity values in the point kinetic equation, the density of delayed neutrons in group states 6, 8, and 17 is obtained. Then, the results taken from the experimental tests with the results from the simulation have been compared. In this method, the instantaneous jump theory in the reactor can be used to determine the integral value of the entire control rod. For this purpose, we adjust the power of the reactor (less than 1 kW). We remove the test rod with a height of 65 cm completely (100%) from the core and make the reactor critical with other control rods. The estimated duration of the control rod falls in In Tehran Research Reactor is 350 to 800 milliseconds with the sudden fall of the control rod and entry The resulting negative reactivity to the core of the reactor, the power of the reactor first decreases with a large slope, and with the appearance of delayed neutrons, its slope gradually decreases and stabilizes. The expansion process was tested using experimental data for the thermal fission of U-235. At first, the results were compared and evaluated with the six-group model recommended in this research. The second fitting was done using the 8-group

model and the third fitting was done for 17 nuclei producing delayed neutrons without grouping. It is necessary to remember that since there is not enough information available in the numerical simulation to obtain the integral value of the control rod, we had to perform the numerical simulation for a short time (6.615 milliseconds). In the experimental mode, information such as the height of the control rod, the reactivity of the input to the core, the rate of the rod leaving the core, etc., are completely available, so the results of the experimental tests are more reliable. By comparing fig. 6, 7, and 8, it is demonstrated that there are slight differences in the presented models with the model simulated by numerical calculations, these differences are expected to some extent. However, both provide suitable methods to describe the decay curve of the delayed neutron, but it is not expected that the obtained models are exactly in accordance with the original model of 6 groups. Nonetheless, the data of the three models 6, 8, and 17 groups should be similar to the data of the simulated model using numerical calculations, as a result, it is specified that the reason for the difference in the curve obtained from experimental tests and numerical simulation is the lack of information in numerical simulation.

Nevertheless, it is not expected that the models obtained in experimental mode and numerical simulation are exactly similar to one another. However, they should match each other well. As a result, it can be specified that the reason for the difference between the curve obtained from experimental tests and numerical simulation is the lack of information in numerical simulation. However, there is a very good agreement between the two curves from 300 ms to 6.615 s with time steps of 0.001 s.

It should be noted that diagram number ۳shows the results of experimental tests with models 6, 8, and 17 groups of delayed neutron generator nuclei.

In fact, it can be concluded that the agreement of the results of experimental tests with numerical simulations allows the user to, according to the type of problem and its complexities, from the models of 6, 8 and 17 groups of delayed neutron generator nuclei. use.

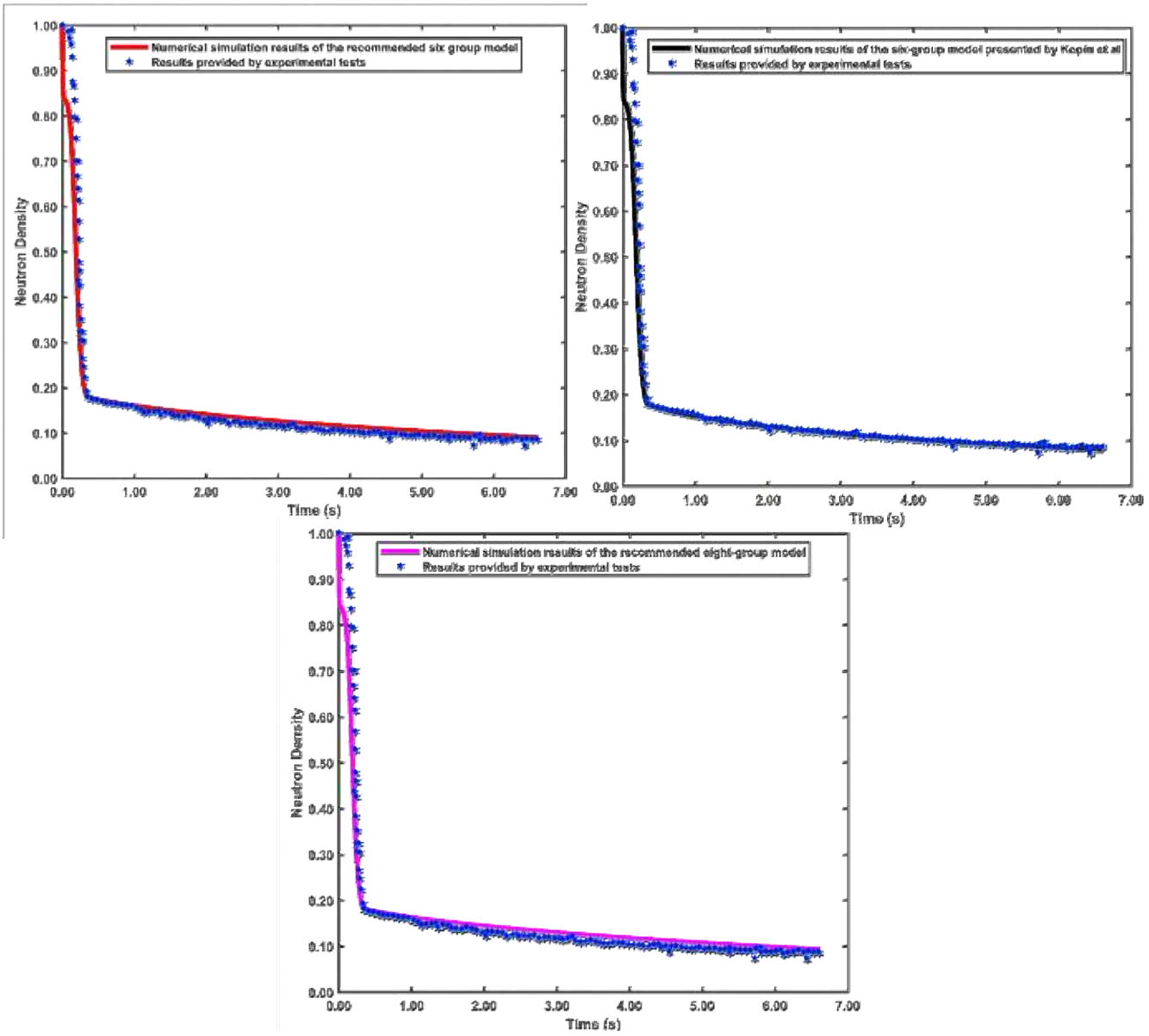

Fig. 3. Comparison of the data of 6,8,17 extended groups experimentally and using numerical simulation

Discussion

Power control of nuclear reactors is very important caused by the importance of safety issues and the increasing use of nuclear energy in optimal energy production. Nuclear reactors are designed to operate in a steady state for almost their entire lifetime. Nonetheless, reactors always subject to disturbances that can cause a transient. The two basic terms used to describe the time-dependent phenomena of nuclear reactors are kinetics and dynamics. As a result of the fission of nuclei such as uranium 235, uranium 238, thorium 232, and plutonium 239, 2 to 3 neutrons are produced on average. Depending on the time of birth, neutrons resulted from fission are divided into two groups, prompt neutrons and delayed neutrons.

The source of neutron emission is instantaneous fission and its emission occurs immediately after the fission process. Meanwhile, delayed neutrons are emitted by the fission fragments sometime after the fission process (several hundred seconds to less than a minute). The release of delayed neutrons is one of the most important aspects of nuclear reactor control because if all the neutrons from Ana fission are produced after fission, the reactor becomes impossible to control. In order to facilitate reactor physics calculations, it is common to classify delayed neutrons into 6 groups and in some sources into 8 groups. In the present analysis, the 4th-order Rang Kuta method was used by MATLAB software to solve the point kinetic equations. By solving these equations in models 6, 8, and 17, it has been demonstrated that the comparison results of the models presented in this research are in good agreement with the experimental results with the expansion of nuclear libraries and the updating of software and calculation methods. The grouping parameters of all three models are summarized in Tables 3, 4 and 5 respectively. It can be observed that there are very close agreements between the three delayed neutron approaches with the experimental results.

Conclusion and suggestions

In the design of all nuclear reactors, Kinetics parameters such as the average production time of delayed neutrons, the fraction of delayed neutrons and the decay constant of delayed neutrons, the concentration of delayed neutrons, etc. play a very important role. Therefore, in this study, the Kinetics and neutronic parameters related to the grouping of delayed neutrons have been averaged. With the contribution of MATLAB software and the 4th-order Rang-Kutta method, the answers to point kinetic equations have been obtained and the results achieved from them have been verified with the corresponding experimental results in In Tehran Research Reactor. Although the response of the kinetic equations is an approximate point and does not consider the spatial dependence of the flux, from the comparison of the computational results and the experimental results, we find that there is a good agreement between the recommended models using numerical simulation and the results obtained from the experimental tests. It has also been indicated that it is possible to develop delayed neutrons without grouping, this approach has been carried out using the latest data available in the NDS library. The current research includes two parts of numerical calculations and validation through experimental tests. By comparing the behaviour of reactor power distribution in all three approaches using numerical calculation methods and validation through experimental tests, the results are satisfactory. However, the choice of half-life is still debatable. To choose the half-life , it is essential to consider where the numerical modelling of delayed neutrons is a stable basis for comparing the results of numerical solutions with the results of experimental

experiments while using half- life. However, until new data are collected, the expansion process presented in this paper simply allows us to obtain an improved delayed neutron model. The results of this research can be used in the dynamic calculations of nuclear reactors; There fore, it is hoped that by presenting this article in the near future, we will witness valuable activities in the direction of developing new and efficient models of delayed neutron generator nuclei for reactor physics applications.

References

[1] Akcasuh, Z. (2012). Mathematical methods in nuclear reactor dynamics, Elsevier.

[2] Arkani, M. (2015). "Measurement of Tehran and Esfahan research reactors kinetic parameters using reactor noise diagnostic methods." Nuclear Science and Technology Research Institute, Ph. D. Thesis.

[3] Arkani, M. (2021). "Diagnostic methods applied to Esfahan light water subcritical reactor (ELWSCR)." Nuclear Engineering and Technology **53**(7): 2133-2150.

[4] Arkani, M. (2022). "Simulation of Pulsed Neutron Source Experiment in In Tehran Research Reactor Core (TRR)." Journal of Nuclear Science and Technology (JonSat) **43**(1): 171-180.

[5] Bell, G. I. and S. Glasstone (1970). Nuclear reactor theory, US Atomic Energy Commission, Washington, DC (United States).

[6] Bhat, M. (1992). Evaluated nuclear structure data file (ENSDF). Nuclear Data for Science and Technology: Proceedings of an International Conference, held at the Forschungszentrum Jülich, Fed. Rep. of Germany, 13–17 May 1991, Springer.

[7] Birch, M., et al. (2015). "Evaluation of Beta-Delayed Neutron Emission Probabilities and Half-Lives for Z= 2–28." Nuclear Data Sheets **128**: 131-184.

[8] Boer, B., et al. (2008). "RAPHAEL Core Physics: Neutronic and thermal-hydraulic simulation of the HTR-10 and AVR reactors."

[9] Brady, M. C. (1988). Evaluation and application of delayed neutron precursor data, Texas A&M University.

[10] Brown, D. A., et al. (2018). "ENDF/B-VIII. 0: the 8th major release of the nuclear reaction data library with CIELO-project cross sections, new standards and thermal scattering data." Nuclear Data Sheets **148**: 1-142.

[11] Caballero-Folch, R., et al. (2018). "First determination of β-delayed multiple neutron emission beyond A= 100 through direct neutron measurement: The P 2 n value of Sb 136." Physical Review C **98**(3): 034310.

[12] Cahalan, J. and K. Ott (1973). "Delayed neutron data for fast reactor analysis." Nuclear Science and Engineering **50**(3): 208-215.

[13] Campbell, J. M. and G. D. Spriggs (1998). A few-group delayed neutron model based on a consistent set of decay constants, Los Alamos National Lab.(LANL), Los Alamos, NM (United States).

[14] Hetrick, D. L. and R. Jarvis (1972). Dynamics of nuclear reactors, American Institute of Physics.

Keepin, G. R. (1972). "Physics of Delayed Neutrons—Recent experimental Results." Nuclear Technology **14**(1): 53-58.

Lamarsh, J. R. (1975). INTRODUCTION to Nuclear Engineering Addison, Wesely publishing company. Polytechnic Institute of New York, USA.

[15] Mathieu, L., et al. (2012). "New neutron long-counter for delayed neutron investigations with the LOHENGRIN fission fragment separator." Journal of Instrumentation **7**(08): P08029.

[16] Plompen, A. J., et al. (2020). "The joint evaluated fission and fusion nuclear data library, JEFF-3.3." The European Physical Journal A **56**(7): 1-108.

[17] Robert W, A. (1972). Mathematical Methods in Nuclear Reactor Dynamics, Taylor & Francis.

[18] Rudstam, G. (1982). "Six-group representation of the energy spectra of delayed neutrons from fission." Nuclear Science and Engineering **80**(2): 238-255.

[19] Rudstam, G., et al. (1993). "Delayed-neutron branching ratios of precursors in the fission product region." Atomic Data and Nuclear Data Tables **53**(1): 1-22.

[20] Spriggs, G. D. and J. M. Campbell (2002). "A summary of measured delayed neutron group parameters." Progress in Nuclear Energy **41**(1-4): 145-201.

ICNST 2024 International Conference on Nuclear Science and Technology
6- 8 MAY 2024 | Isfahan, Iran

Optimal selection of the core baffle and barrel materials for a typical PWR reactor with 300MW by investigation of the reactor core neutronic parameters (Paper ID : 1374)

Sardooie Nasab M.J.[1], Mirian S.F.[2*], Ayoobian N.[1]
[1]*Departmen of nuclear engineering, Faculty of physics, University of Isfahan, Isfahan, Iran*
[2]*Nuclear Reactors Fuel company (NRF), Atomic Energy Organization of Iran (AEOI), Isfahan, Iran*

Abstract

In this research, the neutronic parameters of the typical reactor core with 300 MW electrical power were calculated in order to choose an optimal material for the core barrel and baffle. The core barrel belongs to the lower core support structure because it houses a reactor core. Other lower core support structures are attached to the core barrel, which transmits the weight of the core to the reactor vessel. Core baffle forms the interface between the core and the core barrel. The core barrel is made of low carbon, chromium-nickel stainless steel because it is situated in a corrosive environment (primary coolant comprises boric acid), and the material should not get oxidized. Since different materials can be chosen as baffles and barrels of the core, it is necessary to investigate the effects of these materials on different neutronic parameters of the core. In this regard, the typical reactor core was completely simulated by the MCNP code. The core of the reactor consists of 121 fuel assemblies with a 15x15 square arrangement. At first, various neutronic parameters of the reactor core, including the effective multiplication factor, neutron flux, and radial Power Peaking Factor (PPF) for the reference core were calculated by considering SS-304L as the material of Barrel and Baffle, and the obtained results were validated. Then, various alloy materials including 0Cr18Ni11Ti, 18Cr10NiTi, SS-347, SS-409, Inconel-718, Inconel-625 and 08X18H10T were considered as the material of the core barrel and baffle. According to the results, SS-304L leads to the most effective multiplication factor, Inconel-625 leads to the most thermal to fast neutron flux ratio, while, 08X18H10T leads to the lowest PPF. Finally, by performing optimization on various neutronic parameters of the reactor core, the alloy 08X18H10T was introduced as the optimal material for the core barrel and baffle.

Keywords: Core Barrel; Core Baffle; Neutronic Design; MCNP code.

Introduction

There are a variety of materials that are used as a reflecting medium for neutrons in nuclear reactors. In general, reflector materials are normally not fissionable and have high scattering cross-section and low absorption cross-section [1]. Reflector material must possess the following properties to be effective: low absorption cross-section, high reflection coefficient, radiation stability and resistance to oxidation [2].

Essentially, for thermal reactors, a good moderator is also a good reflector because most of the moderators also possess the properties mentioned above of a good reflector. Water, heavy water, beryllium, or graphite are commonly used as reflectors [3]. In pressurized water reactors, water serves as an axial reflector. This axial reflector does not form any special device, and the neutrons are simply reflected by the core inlet and outlet coolant. On the other hand, common water volume cannot be used as a reflector in radial direction because it is of the highest importance to maintain high flow rates in the core and not bypass fuel assemblies. Therefore, the neutron reflectors are installed in PWR and BWR reactor cores. The design of neutron reflectors can be distinguished between two basic types: core baffle and heavy reflector (core barrel) [4].

Core baffle consists of the baffle and former assembly consisting of vertical plates called baffles, and horizontal support plates called formers. This assembly forms the interface between the core and the core barrel, and there is water between the baffle and the core barrel. Since the coolant flow in the former region is significantly reduced by the former, the high flow rate through fuel assemblies is maintained. A secondary benefit is that water in the former region reduces the neutron flux on the pressure vessel, which causes irradiation embrittlement of pressure vessel material [5-6].

The heavy reflector is a structure that is installed inside a core barrel (similarly to a core baffle). But the heavy reflector is a wall made of stainless-steel slabs stacked vertically surrounding the reactor core. Due to higher atomic number density, heavy reflectors reduce neutron leakage (especially of fast neutrons) from the core more efficiently than the core baffle. This provides additional protection of the reactor vessel from irradiation embrittlement, caused especially by fast neutrons. While acting as a neutron shield, the heavy reflector is heated due to the absorption of gamma radiation. The heat in the reflector is removed by water flowing through cooling channels drilled through the reflector to avoid overheating [6-7].

Since different materials can be chosen as baffles and barrels of the core, it is necessary to investigate the effects of these materials on different neutronic parameters of the core. In this regard, the typical reactor core was completely simulated by the MCNP code. The core of the reactor consists of 121 fuel assemblies with a 15x15 square arrangement. At first, various neutronic parameters of the reactor core, including the effective multiplication factor, neutron flux, and radial Power Peaking Factor (PPF) for the reference core were calculated by considering SS-304L as the material of barrel and baffle, and the obtained results were validated. Then, various alloy materials including 0Cr18Ni11Ti, 18Cr10NiTi, SS-

347, SS-409, Inconel-718, Inconel-625 and 08X18H10T were considered as the material of the core barrel and baffle

Research Theories

In this research, the typical reactor core with 300MW electrical power and 1000MW thermal power was considered as a case study. Main characteristics and features of this reactor is presented in Table 1.

Table 1. Main characteristics and features of a typical reactor core [8-9]

Parameters	Value
Reactor core heat output	998.6 MWt
System pressure, nominal	15.2 MPa
Reactor inlet temperature	288.5 ℃
Average rise in reactor vessel	27 ℃
Average temperature in reactor vessel	302 ℃
Average linear power	135.9 W/cm
Peak linear power for normal operation	366.9 W/cm
Average power density	70.9 kW/liter of core
Specific power	27.8 kW/kgU
Fuel rod array	15*15
Number of fuel assemblies	121
Number of fuel rods per assembly	204
Rod pitch	13.3 mm
Overall dimensions of fuel assembly (mm)	199.3*199.3*3500
Fuel weight	40746 kg
Clad weight	10515 kg
Loading scheme	3 region nonuniform
Number of fuel rod	24684
Outside diameter of fuel rod	10 mm
Diametral gap	0.17 mm
Cladding thickness	0.7 mm
Cladding material	Zr-4
Material of fuel pellet	UO2 sintered
Density, % of theoretical	95
Diameter of fuel pellet	8.43 mm
Length of fuel pellet	10 mm
Neutron absorber in RCCA	Ag-In-Cd
Cladding material of absorber rod	OCr18Ni11TiS.S
Cladding thickness of absorber rod	0.5 mm
Number of RCCAs	37
Number of absorber rods per RCCA	20
Number of BAR	576
Material of BAR	Borosilicate glass
Outside diameter of BAR	10 mm
Inner tube O.D of BAR	5.6 mm
Clad material of BAR	0Cr18Ni11Ti
Inner tube material of BAR	0Cr18Ni11Ti

Also, fuel loading pattern for the first cycle and burnable absorber rods pattern in the reactor core are shown in Figure 1 and Figure 2, respectively.

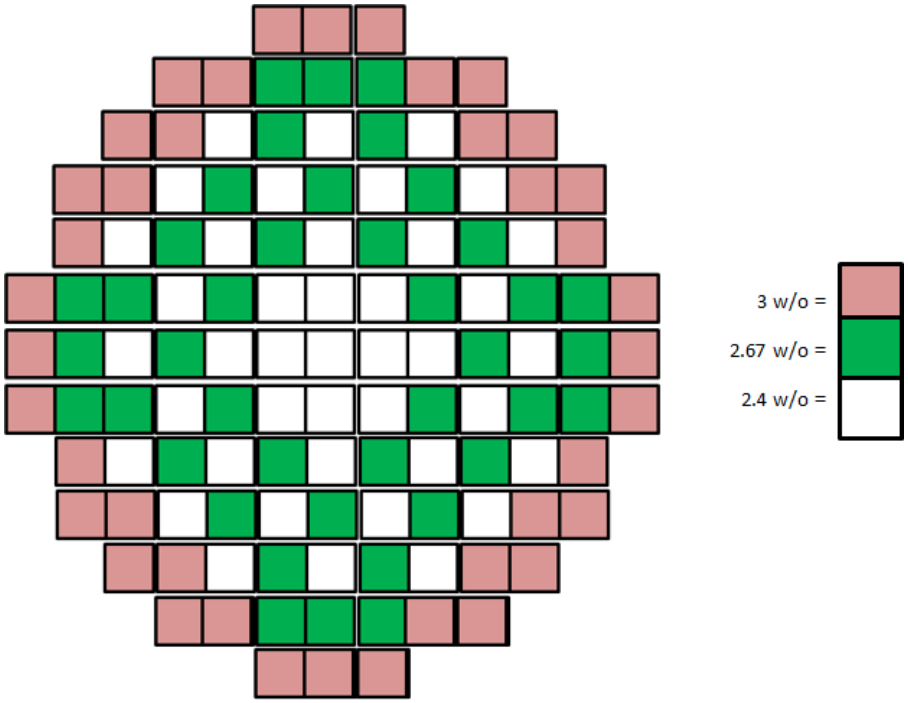

Figure 1. Fuel loading pattern of the reactor core for the first cycle

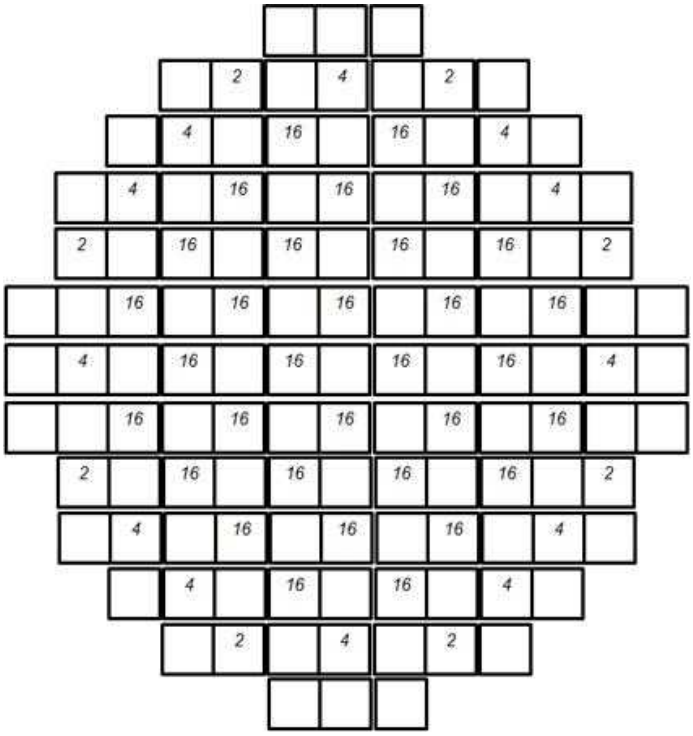

Figure 2. Burnable absorber rods pattern in the reactor core for the first cycle

In order to select the best material for baffle and barrel for mentioned reactor core, different alloy materials including 0Cr18Ni11Ti, 18Cr10NiTi, SS-347, SS-409, Inconel-718, Inconel-625 and 08X18H10T were simulated in MCNP code. Figure 3 shows top views of the reactor core and fuel rods simulated using MCNP code. Also, Table 2 shows different baffle and berrel material chemical composition which were used in material card of the MCNP code.

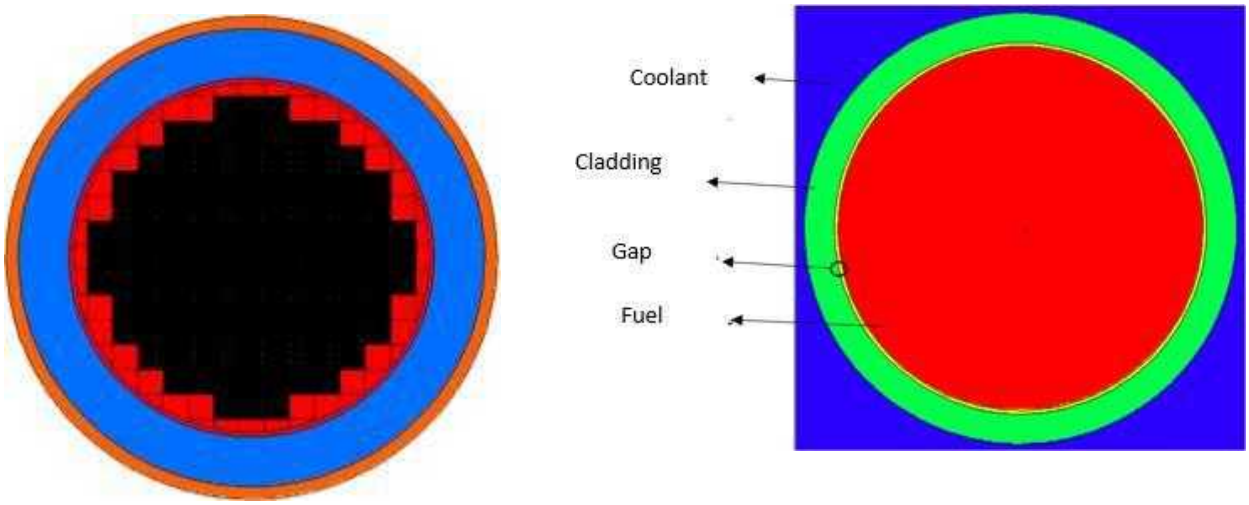

a b

Figure 3. Top views of the a) reactor core b) fuel rod simulated using MCNP code

Table 2. Chemical composition of different Barrel and Baffle Materials

Barrel and Baffle Materials	Chemical Composition
SS-347	Fe 64.86% Cr 19% Ni 12% Mn 2% Si 1% Nb 1% C 0.08% P 0.045% S0.015%
SS-409	Fe 85.23% Cr 11.75% Ni 0.5% Mn 1% Si 1% C 0.08% P 0.045% S0.045% Ti 0.75%
18Cr10NiTi	Fe 66% Cr19% Ni 11% Mo 0.5% C 0.12% Mn 2% Si 0.8% P 0.035% S 0.02% Cu 0.4%
08X18H10T	Fe 65.865% Cr 19% Ni 11% Mo 0.3% C 0.08% Si 0.8% Mn 2% P 0.035% S 0.002% W 0.2% Ti 0.7%
Inconel-625	Ni 58% Cr 21% Fe 5% Mo 10% Nb+Ta 3.15% C 0.1% Mn 0.5% Si 0.5% P 0.015% S 0.015% Al 0.4% Ti 0.4% Co 0.92%
Inconel-718	Ni 55% Cr 17% Fe 17% Mo 2.8% Nb+Ta 4.75% C 0.08% Mn 0.35% Si 0.35% P 0.015% S 0.015% Al 0.8% Ti 0.84% Co 1%

In order to perform neutronic investigation of the reactor core, different parameters including effective multiplication factor, neutron flux, and radial Power Peaking Factor (PPF) were calculated [10]. At first, neutronic results of the reference core were obtained and validated. Then neutronic parameters for different core baffle and barrel materials were calculated.

Results and discussion

Table 3 shows neutronic results of the reference core. According to the results, there is good agreement between the results obtained from the simulation of the reference core and the values reported in the reference core documents.

Table 3. neutronic results of the reference core obtained from MCNP simulation

Parameter	State	MCNP simulation results	Reference results
Effective multiplication factor	CZP	1.21254	1.21485
	HZP	1.16121	1.15928
	HFP	1.14163	1.14100
Axially averaged neutron flux (neutron/cm^{2}sec)	CZP	2.5×10^{14}	2.53×10^{14}
Radial PPF	CZP	1.180	1.217

Table 4 presents the effective multiplication factor, ratio of the flux of thermal neutrons to fast neutrons (Nth/Nf) and radial PPF for different baffle and barrel material. According to the results, using 0Cr18Ni11Ti, 18Cr10NiTi, SS-347, SS-409 and 08X18H10T leads to increase in effective multiplication factor, while, using Inconel-718 and Inconel-625 leads to decrease in effective multiplication factor. Among all materials for baffle and barrel, 08X18H10T and Inconel-625 have the highest and the lowest effective multiplication factor, respectively. Also, SS-347, Inconel-625 and 08X18H10T have more (Nth/Nf) than the reference baffle and barrel. From PPF point of view, Inconel-625 and 08X18H10T have lower PPF than the reference baffle and barrel.

According to the results and by considering that in the most favorable conditions, the reactor core has the highest effective multiplication factor, the highest (Nth/Nf) ratio and the lowest PPF value, the alloy 08X18H10T is introduced as the optimal material for the core barrel and baffle.

Table 4. Neutronic parameters for different baffle and barrel material

Baffle and Barrel Material	Effective Multiplication Factor at BOC	(Nth/Nf)	Radial PPF
SS-304L	1.21254	1.244223	1.114440
0Cr18Ni11Ti	1.21391	1.185107	1.220964
18Cr10NiTi	1.21345	1.216629	1.240585
SS-347	1.21306	1.258203	1.251286
SS-409	1.21690	1.232055	1.142734
Inconel-718	1.21195	1.209998	1.114865
Inconel-625	1.21017	1.300030	1.087082
08X18H10T	1.21367	1.244415	1.061206

Conclusions

In this research, a typical reactor core with 300MWe was simulated in detail using MCNP code. In order to select optimum material for baffle and barrel of this reactor core, neutronic investigation was done. In this regard, different neutronic parameters such as the effective multiplication factor, neutron flux, and radial PPF were calculated for reference core and various baffle and barrel materials. According to the results, 08X18H10T and Inconel-625 had the highest and the lowest effective multiplication factor, respectively. Also, using SS-347, Inconel-625 and 08X18H10T as baffle and barrel material leads to increase in (Nth/Nf) in comparison with the reference baffle and barrel, while Inconel-625 and 08X18H10T had lower PPF than the reference baffle and barrel. Finally the alloy 08X18H10T was determined as the optimal material for the core barrel and baffle.

References

[1] Zhong, Y., Norman, P. and Wu, W. (2022). A feasibility study of SMART reactor power performance optimizations-part 2: Reflector material selection. Frontiers in Energy Research, 10:987513.

[2] Khoshahval, F. and Salari, F. (2016). Sensitivity analyses of the use of different reflector materials on the neutronics parameters of Tehran research reactor. Progress in Nuclear Energy, 93:351-361.

[3] Privas, E. and Chabert, L. (2018). Reflector features and physics consideration issued from the Jules Horowitz Reactor design analyses. Nuclear Sciences and Technologies, 4:18.

[4] Chellaiah, S., Viskanta, R., Ranganathan, P. and Anand, N.K. (1988). Analysis of core and core barrel heat-up under conditions simulating severe reactor accidents. Nuclear Engineering and Design, 105(3):259-267.

[5] Filonova, Y., Dubyk, Y., Filonov, V. and Kondratjuk, V. (2020). mproved Computational Fluid Dynamics Framework for Reactor Core Baffle Swelling Assessment. Journal of Nuclear Engineering and Radiation Science, 7(1): 011404.

[6] Altstadt, E., Kumpf, H., Weiss, F.P., Fischer, E., Nagel, G. and Sgarz, G. (2004). Analysis of a PWR core baffle considering irradiation induced creep, Annals of Nuclear Energy, 31(7):723-736.

[7] Tahara, Y., Kanagawa, T. and Sekimoto, H. (2000). Two-Dimensional Baffle/Reflector Constants for Nodal Code in PWR Core Design. Journal of Nuclear Science and Technology, 37(11):986-995.

[8] Hengra, N.H., Ilyas, M. and Inayat, M.H. (2022). Severe accident analysis of the Qinshan Nuclear Power Plant and evaluation of boundary conditions for ex-vessel heat transfer. Progress in Nuclear Energy, 143:104032.

[9] Ahmad, I., Ilyas, M. and Akram, Z. (2014). Pressurized water reactor core thermal-hydraulics model for flow coastdown transient. Proceedings of the Institution of Mechanical Engineers, Part A: Journal of Power and Energy, 228(5).

[10] Mirian, S.F. and Ayoobian, N. (2020). Investigations on a typical small modular PWR using coupled neutronic-thermal-mechanical evaluations to achieve long-life cycle-length. Progress in Nuclear Energy, 119:103176.

ICNST 2024 International Conference on Nuclear Science and Technology
6- 8 MAY 2024 | Isfahan, Iran

Optimal selection of the ATF cladding for a typical PWR reactor with 300MW by investigation of the reactor core neutronic parameters (Paper ID : 1375)

Sardooie Nasab M.J.[1], Mirian S.F.[2*], Ayoobian N.[1]

[1]Departmen of nuclear engineering, Faculty of physics, University of Isfahan, Isfahan, Iran

[2]Nuclear Reactors Fuel company (NRF), Atomic Energy Organization of Iran (AEOI), Isfahan, Iran

Abstract

For many decades, PWR fuels have consisted of uranium dioxide (UO2) pellets surrounded by zirconium (Zr)-alloy cladding. Mainly after Fukushima Daiichi Nuclear Power Plant accident in 2011, the concept of Accident-Tolerant Fuels (ATF) has been proposed and widely investigated. One approach of ATF progress is developing oxidation-resistant monolithic or layered cladding materials. Considering the extent of these materials, the effects of using these materials as fuel cladding on the neutronic parameters of the reactor core should be investigated. In this regard, the typical reactor core was completely simulated by the MCNP code. The core of the reactor consists of 121 fuel assemblies with a 15x15 square arrangement. At first, various neutronic parameters of the reactor core, including the effective multiplication factor, neutron flux, and radial Power Peaking Factor (PPF) for the reference core were calculated by considering Zr-4 with 0.7 mm thickness as the cladding material, and the obtained results were validated. Then, various ATF claddings including FeCrAl, SS-347, SS-348, SS-409, Inconel-625, Inconel-718, SiC, 18Cr10NiTi and 0Cr18NiTi with different thicknesses (0.3 to 0.7mm) were considered as the cladding material. According to the results, changing the thickness of the SiC cladding had a very small effect on the effective multiplication factor. In general, SiC cladding leads to a slight improvement in the effective multiplication factor compared to the reference cladding. Among the steel-based claddings, the SS-409 cladding had the best neutronic status. Finally, by optimization based on different neutronic parameters, the optimal cladding was selected as SiC with 0.5 mm thickness.

Keywords: ATF Cladding, Neutronic Design, SiC Cladding, FeCrAl Cladding, MCNP code.

Introduction

The concept of Accident Tolerated Fuels (ATFs) emanates from the nuclear catastrophe, which was as a following results of earthquake and severe tsunami in Japan in 2011. The station blackout accident (SBO) leads to failure of the cooling system. Without sufficient quality of coolant water, the fuel cladding finally reached the failure temperature and then lead to the reaction between coolant water and Zircaloy cladding. This threatening oxidation reaction released massive heat and promoted the cladding

temperature to higher level. Furthermore, hydrogen was also released by this reaction and accumulated to a hazardous point. As a consequence, a hydrogen explosion finally occurred and all the safety barriers were destroyed, fission products were released to the ocean [1].

This infrequent event caused very drastic controversy in the United States and soon expanded to the world. Again, the significance of the safety warranty for nuclear plants is accentuated and boosted into a new high level. Accordingly, ATF concept was suggested and is becoming the most favorable strategy to meet current challenges.

Zirconium-based alloys have been extensively used as materials for commercial light water reactors (LWRs) fuel cladding owing to their low thermal neutron absorption cross-section, rational corrosion performance under normal operation, and good mechanical properties under neutron irradiation [1]. However, the disadvantages of zirconium alloys such as high-speed oxidation reaction in high temperature steam condition and the resulting hydrogen production cannot be enhanced by altering only its alloy composition or manufacturing process.

In order to dominate this restriction of zirconium alloys, most present studies have concentrated on two areas: the development of an alternative material and the application of a protective layer. Nuclear research industries, including Westinghouse, General Electric, General Atomic, KAERI, CEA, CNNC, UKRI, and AREVA (FRAMATOME), as well as nuclear research groups in several universities, including MIT, Tsinghua University, and University of Wisconsin-Madison, have conducted research on this new technology [1-2].

To obtain oxidation resistance in high-temperature steam, which is very significant for improving accident resistance, the type and characteristics (density, growth rate, etc.) of an oxide film generated in a high-temperature steam environment must be controlled. Recent developments, referred to as alternative cladding materials, include iron-based alloys such as FeCrAl and SiC–SiC composites. The crucial point to reduce development time and costs, is to secure improved accident tolerance beyond the performance of zirconium alloy without compromising its stability in normal operation [2-3].

Since a wide range of materials have been proposed for ATF claddings in recent years, the effects of using them on the neutronic parameters of the reactor core should be evaluated. In this regard, the typical reactor core was completely simulated by the MCNP code. The core of the reactor consists of 121 fuel assemblies with a 15x15 square arrangement. At first, various neutronic parameters of the reactor core, including the effective multiplication factor, neutron flux, and radial Power Peaking Factor (PPF) for the reference core were calculated by considering Zr-4 with 0.7 mm thickness as the cladding material, and

the obtained results were validated. Then, various ATF claddings including FeCrAl, SS-347, SS-348, SS-409, Inconel-625, Inconel-718, SiC, 18Cr10NiTi and 0Cr18NiTi with different thicknesses (0.3 to 0.7mm) were considered as the cladding material.

Research Theories

In this research, the typical reactor core with 300MW electrical power and 1000MW thermal power was considered as a case study. Main characteristics and features of this reactor is presented in Table 1.

Table 1. Main characteristics and features of a typical reactor core [4-5]

Parameters	Value
Reactor core heat output	998.6 MWt
System pressure, nominal	15.2 MPa
Reactor inlet temperature	288.5 ℃
Average rise in reactor vessel	27 ℃
Average temperature in reactor vessel	302 ℃
Average linear power	135.9 W/cm
Peak linear power for normal operation	366.9 W/cm
Average power density	70.9 kW/liter of core
Specific power	27.8 kW/kgU
Fuel rod array	15*15
Number of fuel assemblies	121
Number of fuel rods per assembly	204
Rod pitch	13.3 mm
Overall dimensions of fuel assembly (mm)	199.3*199.3*3500
Fuel weight	40746 kg
Clad weight	10515 kg
Loading scheme	3 region nonuniform
Number of fuel rod	24684
Outside diameter of fuel rod	10 mm
Diametral gap	0.17 mm
Cladding thickness	0.7 mm
Cladding material	Zr-4
Material of fuel pellet	UO2 sintered
Density, % of theoretical	95
Diameter of fuel pellet	8.43 mm
Length of fuel pellet	10 mm
Neutron absorber in RCCA	Ag-In-Cd
Cladding material of absorber rod	OCr18Ni11TiS.S
Cladding thickness of absorber rod	0.5 mm
Number of RCCAs	37
Number of absorber rods per RCCA	20
Number of BAR	576
Material of BAR	Borosilicate glass
Outside diameter of BAR	10 mm
Inner tube O.D of BAR	5.6 mm
Clad material of BAR	0Cr18Ni11Ti

Inner tube material of BAR	0Cr18Ni11Ti

Also, fuel loading pattern for the first cycle and burnable absorber rods pattern in the reactor core are shown in Figure 1 and Figure 2, respectively.

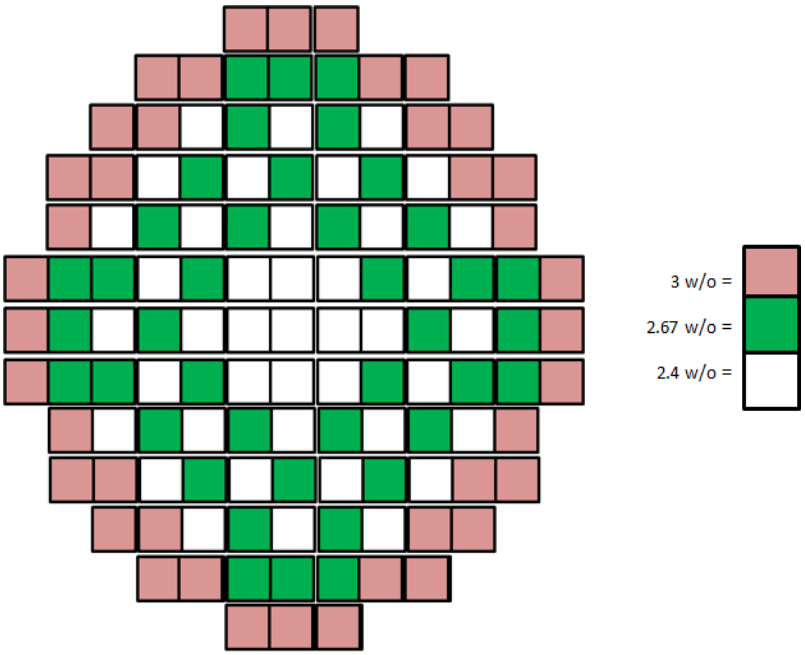

Figure 1. Fuel loading pattern of the reactor core for the first cycle

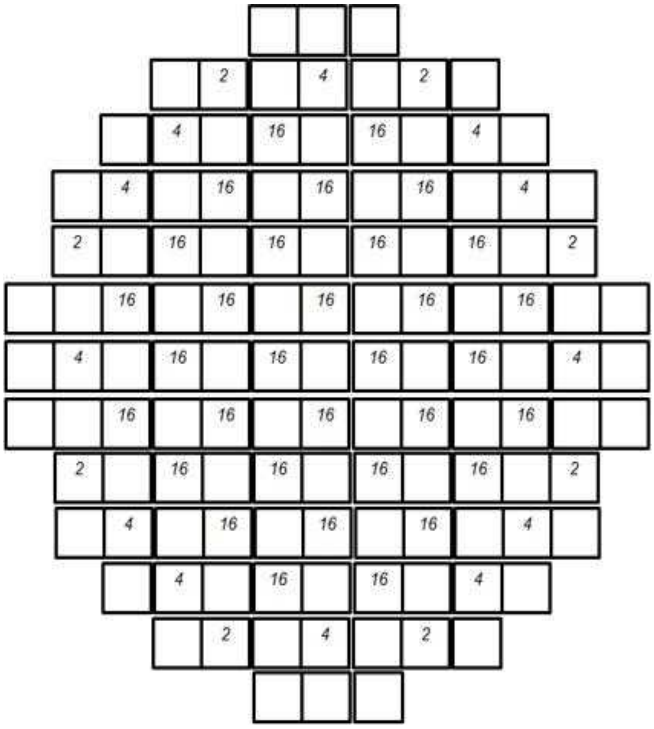

Figure 2. Burnable absorber rods pattern in the reactor core for the first cycle

In order to select optimum ATF cladding for mentioned reactor, various ATF claddings including FeCrAl, SS-347, SS-348, SS-409, Inconel-625, Inconel-718, SiC, 18Cr10NiTi and 0Cr18NiTi with different thicknesses (0.3 to 0.7mm) were considered as the cladding material in MCNP simulation of the reactor core. Figure 3 shows top views of the reactor core and fuel rods simulated using MCNP code. Also, Table 2 shows different ATF claddings chemical composition and density which were used in material card of the MCNP code.

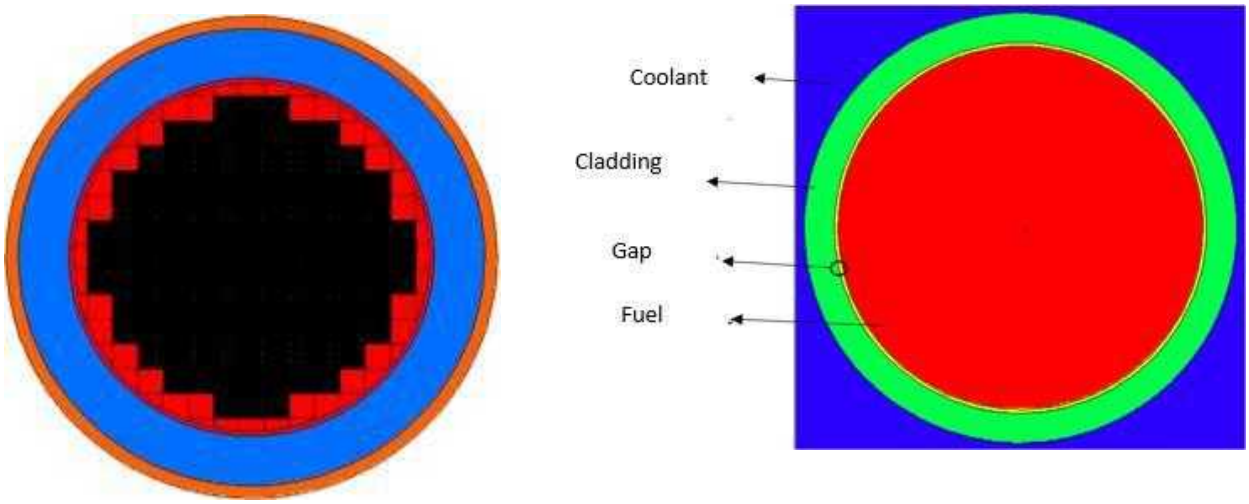

a b

Figure 3. Top views of the a) reactor core b) fuel rod simulated using MCNP code

Table 2. Chemical composition and density of different ATF claddings

ATF Cladding	Density (g/cm^3)	Chemical Composition
SS-347	7.96	Fe 64.86% Cr 19% Ni 12% Mn 2% Si 1% Nb 1% C 0.08% P 0.045% S0.015%
SS-348	8.00	Fe 65.745% Cr 19% Ni 11% Mn 2% Si 1% Nb+Ta 1% C 0.08% P 0.045% S0.03% Co 0.2% Ta 0.1%
SS-409	7.61	Fe 85.23% Cr 11.75% Ni 0.5% Mn 1% Si 1% C 0.08% P 0.045% S0.045% Ti 0.75%
18Cr10NiTi	7.92	Fe 66% Cr19% Ni 11% Mo 0.5% C 0.12% Mn 2% Si 0.8% P 0.035% S 0.02% Cu 0.4%
FeCrAl	7.15	Fe 72.2% Cr 22% Al 5.8%
Inconel-625	8.44	Ni 58% Cr 21% Fe 5% Mo 10% Nb+Ta 3.15% C 0.1% Mn 0.5% Si 0.5% P 0.015% S 0.015% Al 0.4% Ti 0.4% Co 0.92%
Inconel-718	8.17	Ni 55% Cr 17% Fe 17% Mo 2.8% Nb+Ta 4.75% C 0.08% Mn 0.35% Si 0.35% P 0.015% S 0.015% Al 0.8% Ti 0.84% Co 1%

In order to perform neutronic investigation of the reactor core, different parameters including effective multiplication factor, neutron flux, and radial Power Peaking Factor (PPF) were calculated [6]. At first,

neutronic results of the reference core were obtained and validated. Then neutronic parameters for different ATF claddings were calculated. Finally, by optimization based on different neutronic parameters, the optimal cladding was selected.

Results and discussion

Table 3 shows neutronic results of the reference core. According to the results, there is good agreement between the results obtained from the simulation of the reference core and the values reported in the reference core documents [4-5].

Table 3. neutronic results of the reference core obtained from MCNP simulation

Parameter	State	MCNP simulation results	Reference results
Effective multiplication factor	CZP	1.21254	1.21485
	HZP	1.16121	1.15928
	HFP	1.14163	1.14100
Axially averaged neutron flux (neutron/cm^{2}sec)	CZP	2.5×10^{14}	2.53×10^{14}
Radial PPF	CZP	1.180	1.217

Figure 4 shows effective multiplication factor for various ATF claddings with different thickness (0.3-0.7mm). According to the results, in all claddings, except for SiC, the effective multiplication factor has increased with the decrease in thickness. The effective multiplication factor for SiC is independent of thickness. In general, all other non-zirconium claddings lead to acute reduction in the effective multiplication factor. Meanwhile, Inconel-625 and Inconel-718 had the best and the worst conditions, respectively.

Table 4 presents the ratio of the flux of thermal neutrons to fast neutrons (Nth/Nf) and radial PPF for different claddings with reference thickness. According to the results, all the non-zirconium claddings, except for SiC, have a lower (Nth/Nf) than the Zr-4 cladding. Meanwhile the SiC has better (Nth/Nf) than the Zr-4 cladding. Also, in the case of radial PPF, FeCrAl and SiC claddings have the lowest value, while SS-409 shows the highest value.

According to the obtained results, in order to find the optimum cladding, there is a need to compromise between different parameters. Considering that in the most favorable conditions, the reactor core has the highest effective multiplication factor, the highest (Nth/Nf) ratio and the lowest PPF value, the following

cost function can be defined by standardizing the data and assuming the equal importance of each of the neutronic parameters.

$$CostFunction = \sqrt{\frac{(PPF)^2}{(keff)^2 + (\frac{Nth}{Nf})^2}} \quad (1)$$

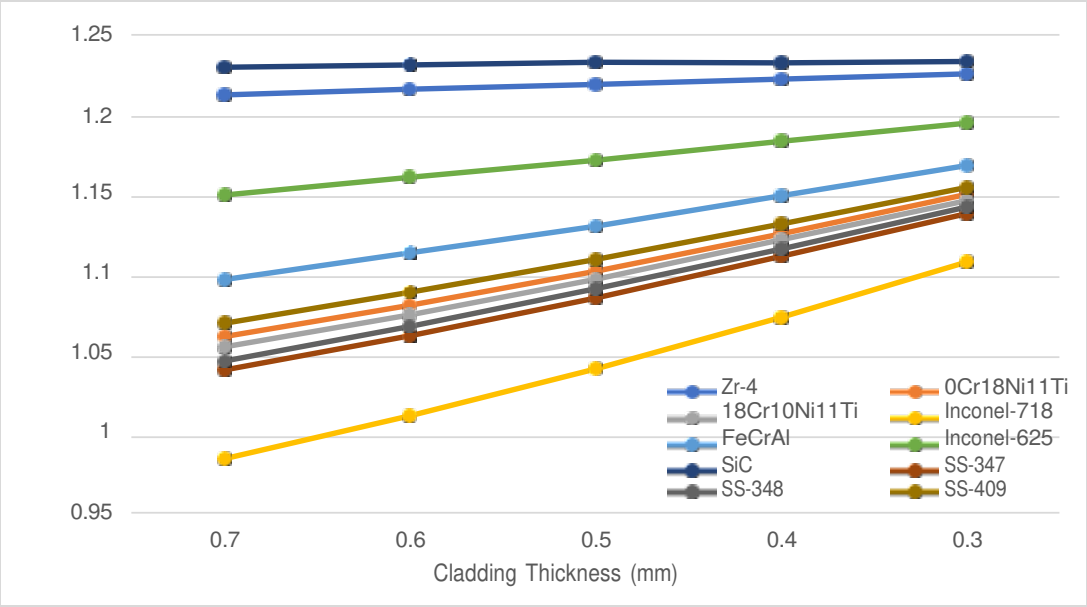

Figure 4. effective multiplication factor for various ATF claddings

Table 4. (Nth/Nf) and Radial PPF for different ATF claddings

ATF Claddings	(Nth/Nf)	Radial PPF
Zr-4	1.241289	1.180248
18Cr10Ni11Ti	1.065107	1.234087
0Cr18Ni11Ti	1.083374	1.18652
Inconel-718	1.021122	1.13265
Inconel-625	1.141806	1.129579
FeCrAl	1.072297	1.121274
SiC	1.284147	1.125573
SS-347	1.069254	1.237131

SS-348	1.070231	1.271681
SS-409	1.077378	1.304983

According to the obtained results and also by using equation 1, the optimum cladding was selected as SiC with a thickness of 0.5 mm.

Conclusions

In this research, a typical reactor core with 300MWe was simulated in detail using MCNP code. In order to select optimum ATF cladding for this reactor core, neutronic investigation was done. In this regard, different neutronic parameters such as the effective multiplication factor, neutron flux, and radial Power Peaking Factor (PPF) were calculated for reference core and various ATF claddings with different thickness. According to the results, all non-zirconium claddings lead to reduction in the effective multiplication factor, except SiC which had no effects on effective multiplication factor.Also, all the non-zirconium claddings, had a lower (Nth/Nf) than the Zr-4 cladding. Meanwhile the SiC has better (Nth/Nf) than the Zr-4 cladding. Finally, by performing optimization, the optimal cladding was selected as SiC with 0.5 mm thickness. In future researches, the effects of ATF claddings on the thermohydraulic and thermomechanical parameters of the fuel should be investigated in order to select the best ATF cladding from three perspectives: neutronic, thermohydraulic, and thermomechanical.

References

[1] Qiu, B., Wang, J., Deng, Y., Wang, M., Wu, Y. and Qiu, S.Z., (2020). A review on thermohydraulic and mechanical-physical properties of SiC, FeCrAl and Ti3SiC2 for ATF cladding. Nuclear Engineering and Technology, 52(1):1-13.

[2] Alraisi, A., Yi, Y., Lee, S., Alameri, S.A., Qasem, M., Paik, C.Y. and Jang, C. (2022). Effects of ATF cladding properties on PWR responses to an SBO accident: A sensitivity analysis. Annals of Nuclear Energy, 165:108784.

[3] Nguyen, X.H., Jang, S. and Kim, Y. (2020). Impacts of an ATF cladding on neutronic performances of the soluble-boron-free ATOM core. International Journal of Energy Research, 44(10):8193-8207.

[4] Hengra, N.H., Ilyas, M. and Inayat, M.H. (2022). Severe accident analysis of the Qinshan Nuclear Power Plant and evaluation of boundary conditions for ex-vessel heat transfer. Progress in Nuclear Energy, 143:104032.

[5] Ahmad, I., Ilyas, M. and Akram, Z. (2014). Pressurized water reactor core thermal-hydraulics model for flow coastdown transient. Proceedings of the Institution of Mechanical Engineers, Part A: Journal of Power and Energy, 228(5).

[6] Mirian, S.F. and Ayoobian, N. (2020). Investigations on a typical small modular PWR using coupled neutronic-thermal-mechanical evaluations to achieve long-life cycle-length. Progress in Nuclear Energy, 119:103176.

ICNST 2024 International Conference on Nuclear Science and Technology
6- 8 MAY 2024 | Isfahan, Iran

Investigation of the neutronic parameters of a typical PWR reactor with 300MW using different cladding coatings as ATF cladding (Paper ID : 1377)

Sardooie Nasab M.J.[1], Mirian S.F.[2*], Ayoobian N.[1]
[1]*Departmen of nuclear engineering, Faculty of physics, University of Isfahan, Isfahan, Iran*
[2]*Nuclear Reactors Fuel company (NRF), Atomic Energy Organization of Iran (AEOI), Isfahan, Iran*

Abstract

For many decades, PWR fuels have consisted of uranium dioxide (UO2) pellets surrounded by zirconium (Zr)-alloy cladding. Mainly after Fukushima Daiichi Nuclear Power Plant accident in 2011, the concept of Accident-Tolerant Fuels (ATF) has been proposed and widely investigated. One approach of ATF progress is developing oxidation-resistant monolithic or layered cladding materials. Another obvious and more near-term approach could be the modification of the surface of existing and available Zr alloy claddings, typically by protective coatings, to improve the oxidation resistance, as it does not significantly alter the existing UO2/Zr-based alloy cladding fuel design. Considering the extent of coating materials, the effects of using these claddings on the neutronic parameters of the reactor core should be investigated. In this regard, the typical reactor core was completely simulated by the MCNP code. The core of the reactor consists of 121 fuel assemblies with a 15x15 square arrangement. At first, various neutronic parameters of the reactor core, including the effective multiplication factor, neutron flux, and radial Power Peaking Factor (PPF) for the reference core were calculated by considering Zr-4 (with 0.7 mm thickness without any coatings) as the cladding material, and the obtained results were validated. Then, various coating materials on Zr-4 Cladding including Cr, CrN, FeCrAl, Mo4VAlC4 (MAX material), SiC, Ti2AlC, Ti3SiC and TiN with 5 to 20 micron thickness were simulated. According to the results, the effects of cladding coating on various neutronic parameters of the reactor core were insignificant. This is a remarkable advantage compared to using non-zirconium-based materials (such as steel or inconel) for reactor fuel claddings. Among different coatings, SiC coating had the best neutronic performance.

Keywords: ATF Claddings, Cladding Coatings, Neutronic Design, MCNP code.

Introduction

The concept of Accident Tolerated Fuels (ATFs) emanates from the nuclear catastrophe, which was as a following result of earthquake and severe tsunami in Japan in 2011. The station blackout accident (SBO) leads to failure of the cooling system. Without sufficient quality of coolant water, the fuel cladding finally

reached the failure temperature and then lead to the reaction between coolant water and Zircaloy cladding. This threatening oxidation reaction released massive heat and promoted the cladding temperature to higher level. Furthermore, hydrogen was also released by this reaction and accumulated to a hazardous point. As a consequence, a hydrogen explosion finally occurred and all the safety barriers were destroyed, fission products were released to the ocean [1]. This infrequent event caused very drastic controversy in the United States and soon expanded to the world. Again, the significance of the safety warranty for nuclear plants is accentuated and boosted into a new high level. Accordingly, ATF concept was suggested and is becoming the most favorable strategy to meet current challenges.

Zirconium-based alloys have been extensively used as materials for commercial light water reactors (LWRs) fuel cladding owing to their low thermal neutron absorption cross-section, rational corrosion performance under normal operation, and good mechanical properties under neutron irradiation. However, the disadvantages of zirconium alloys such as high-speed oxidation reaction in high temperature steam condition and the resulting hydrogen production cannot be enhanced by altering only its alloy composition or manufacturing process [1].

In order to dominate this restriction of zirconium alloys, most present studies have concentrated on two areas: the development of an alternative material and the application of a protective layer. Nuclear research industries, including Westinghouse, General Electric, General Atomic, KAERI, CEA, CNNC, UKRI, and AREVA (Framatome), as well as nuclear research groups in several universities, including MIT, Tsinghua University, and University of Wisconsin-Madison, have conducted research on this new technology [1-2]. The first approach, new cladding concepts, represent a long-term strategy that requires significant engineering redesign to the cores. Meanwhile more near-term approach, protective coatings, does not significantly alter the existing UO2/Zr-based alloy cladding fuel design [2]. To obtain oxidation resistance in high-temperature steam, which is very significant for improving accident resistance, the type and characteristics (density, growth rate, etc.) of an oxide film generated in a high-temperature steam environment must be controlled. [3-4].

Since a wide range of materials have been proposed for ATF claddings protective layer in recent years, the effects of using them on the neutronic parameters of the reactor core should be evaluated. In this regard, the typical reactor core was completely simulated by the MCNP code. The core of the reactor consists of

121 fuel assemblies with a 15x15 square arrangement. At first, various neutronic parameters of the reactor core, including the effective multiplication factor, neutron flux, and radial Power Peaking Factor (PPF) for the reference core were calculated by considering Zr-4 with 0.7 mm thickness as the cladding material, and the obtained results were validated. Then, various coating materials on Zr-4 cladding including Cr, CrN, FeCrAl, Mo4VAIC4 (MAX material), SiC, Ti2AlC, Ti3SiC and TiN with 5 to 20 micron thickness were simulated.

Research Theories

In this research, the typical reactor core with 300MW electrical power and 1000MW thermal power was considered as a case study. Main characteristics and features of this reactor is presented in Table 1.

Table 1. Main characteristics and features of a typical reactor core [5-6]

Parameters	**Value**
Reactor core heat output	998.6 MWt
System pressure, nominal	15.2 MPa
Reactor inlet temperature	288.5 °C
Average rise in reactor vessel	27 °C
Average temperature in reactor vessel	302 °C
Average linear power	135.9 W/cm
Peak linear power for normal operation	366.9 W/cm
Average power density	70.9 kW/liter of core
Specific power	27.8 kW/kgU
Fuel rod array	15*15
Number of fuel assemblies	121
Number of fuel rods per assembly	204
Rod pitch	13.3 mm
Overall dimensions of fuel assembly (mm)	199.3*199.3*3500
Fuel weight	40746 kg
Clad weight	10515 kg
Loading scheme	3 region nonuniform
Number of fuel rod	24684
Outside diameter of fuel rod	10 mm
Diametral gap	0.17 mm
Cladding thickness	0.7 mm
Cladding material	Zr-4
Material of fuel pellet	UO2 sintered
Density, % of theoretical	95
Diameter of fuel pellet	8.43 mm
Length of fuel pellet	10 mm
Neutron absorber in RCCA	Ag-In-Cd
Cladding material of absorber rod	OCr18Ni11TiS.S
Cladding thickness of absorber rod	0.5 mm
Number of RCCAs	37
Number of absorber rods per RCCA	20
Number of BAR	576
Material of BAR	Borosilicate glass
Outside diameter of BAR	10 mm
Inner tube O.D of BAR	5.6 mm
Clad material of BAR	0Cr18Ni11Ti
Inner tube material of BAR	0Cr18Ni11Ti

Also, fuel loading pattern for the first cycle and burnable absorber rods pattern in the reactor core are shown in Figure 1 and Figure 2, respectively.

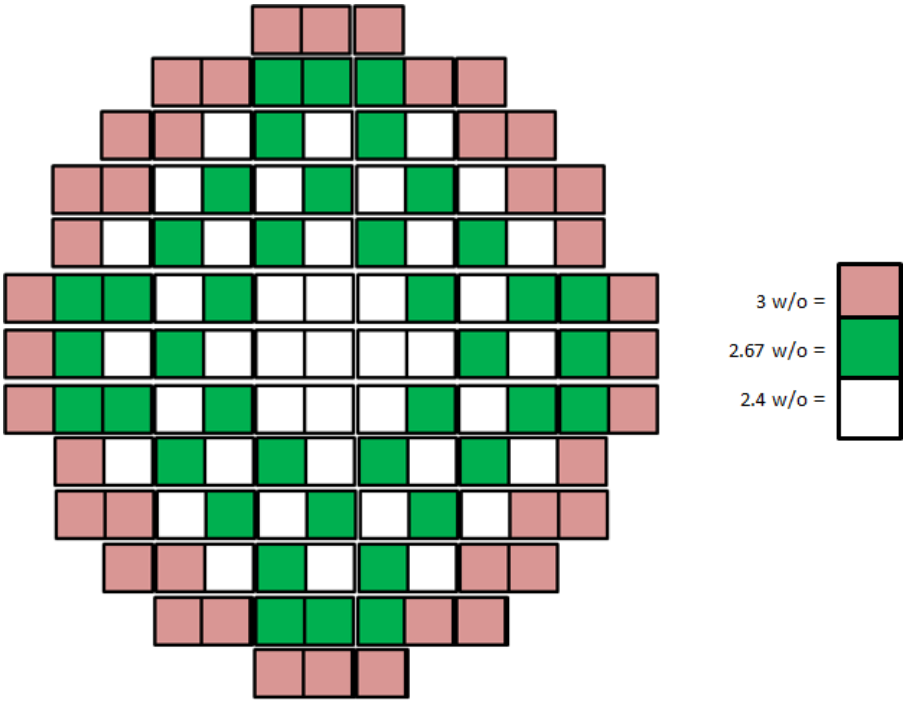

Figure 1. Fuel loading pattern of the reactor core for the first cycle

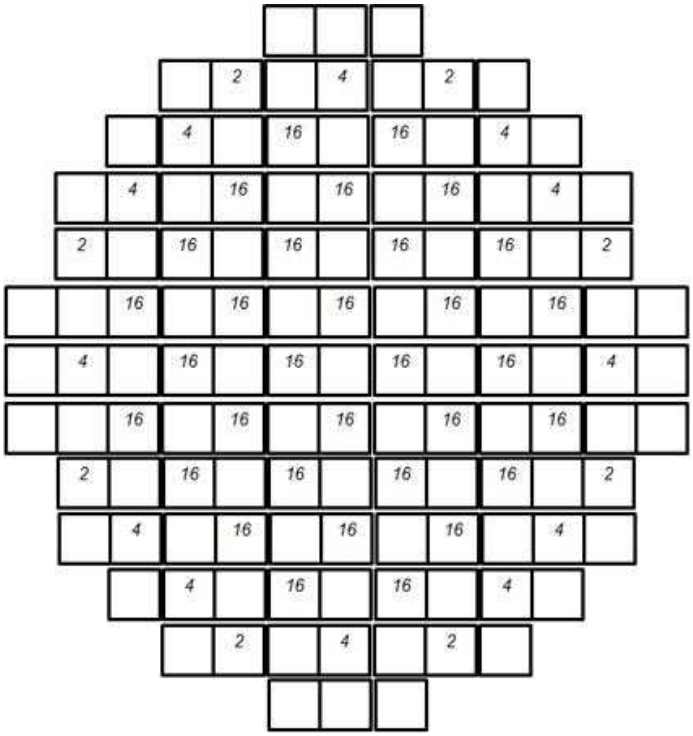

Figure 2. Burnable absorber rods pattern in the reactor core for the first cycle

In order to select optimum ATF cladding coating layer for mentioned reactor, various coating materials on Zr-4 cladding including Cr, CrN, FeCrAl, Mo4VAIC4 (MAX material), SiC, Ti2AlC, Ti3SiC and TiN with 5 to 20 micron thickness were simulated in MCNP code Figure 3 shows top views of the reactor core and fuel rods simulated using MCNP code.

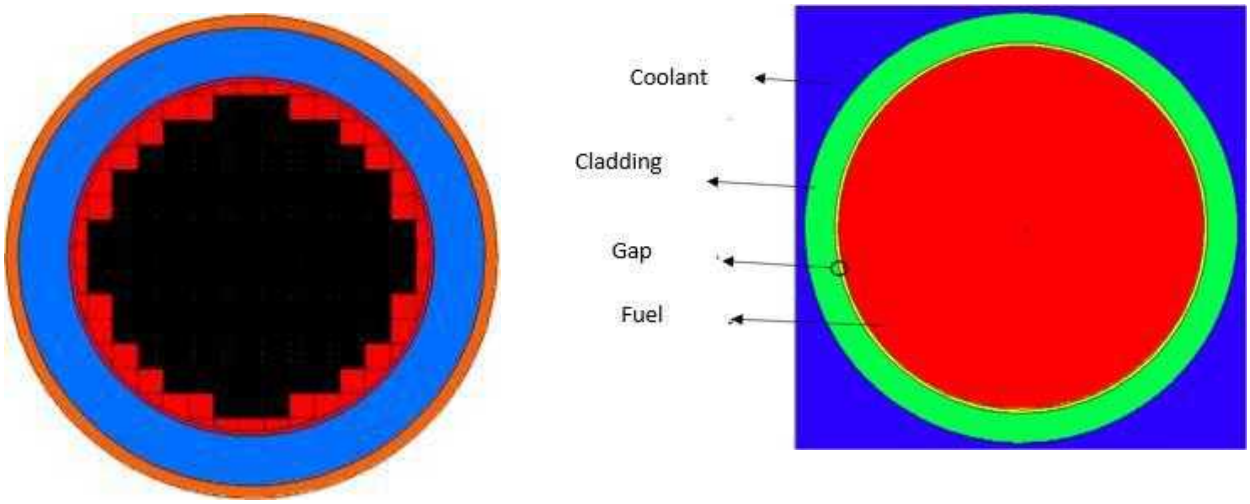

a b

Figure 3. Top views of the a) reactor core b) fuel rod simulated using MCNP code

In order to perform neutronic investigation of the reactor core, different parameters including excess reactivity, neutron flux, and radial Power Peaking Factor (PPF) were calculated [7]. At first, neutronic results of the reference core were obtained and validated. Then neutronic parameters for Zr-4 cladding with different coatings were calculated.

Results and Discussion

Table 2 shows neutronic results of the reference core. According to the results, there is good agreement between the results obtained from the simulation of the reference core and the values reported in the reference core documents.

Table 2. neutronic results of the reference core obtained from MCNP simulation

Parameter	State	MCNP simulation results	Reference results
Effective multiplication factor	CZP	1.21254	1.21485
	HZP	1.16121	1.15928
	HFP	1.14163	1.14100
Axially averaged neutron flux (neutron/cm^{2}sec)	CZP	2.5×10^{14}	2.53×10^{14}
Radial PPF	CZP	1.180	1.217

Figure 4 shows excess reactivity for various Zr-4 cladding with various coatings and different layer thickness (5-20 micron). According to the results, in all claddings with coatings, the excess reactivity was decreased with the increase in thickness. The cladding with SiC as coating had the most excess reactivity value, meanwhile, the cladding with TiN coating had the least excess reactivity value.

Table 4 presents the ratio of the flux of thermal neutrons to fast neutrons (Nth/Nf) and radial PPF for Zr-4 cladding with various coatings. According to the results, all claddings with coatings, except for cladding with SiC layer, have a lower (Nth/Nf) than the Zr-4 cladding (which is 1.241289). Meanwhile the SiC has better (Nth/Nf) than the Zr-4 cladding. Also, in the case of radial PPF, all claddings with coatings lead to slight increase in PPF. Accordingly, among different coatings, SiC coating had the best neutronic performance.

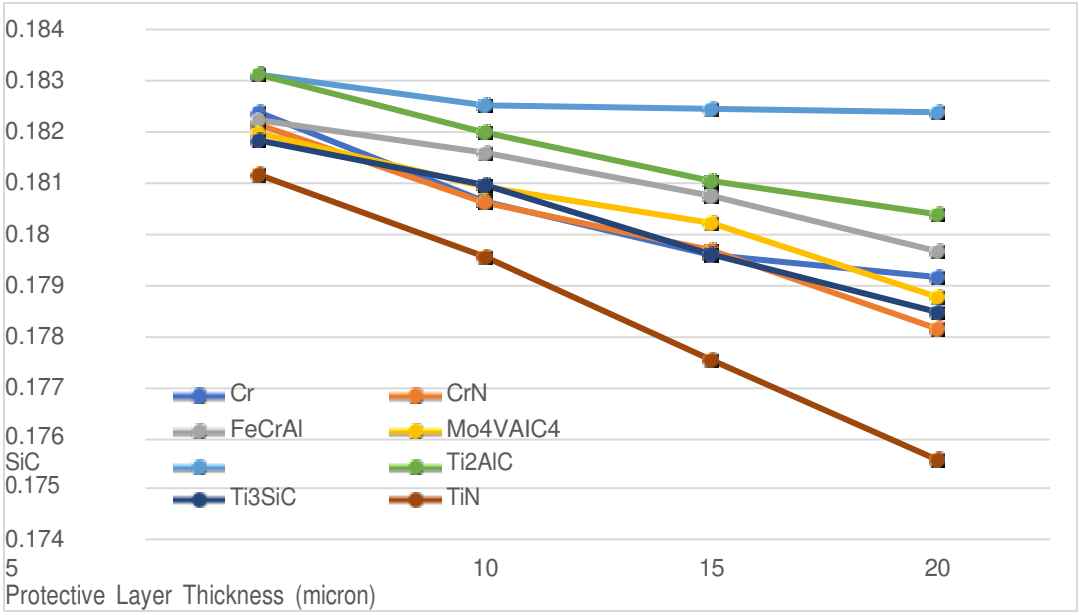

Figure 4. Excess reactivity for various coatings

Table 4. (Nth/Nf) and Radial PPF for different ATF claddings

Zr-4 Cladding coatings	(Nth/Nf)	Radial PPF
Cr	1.224976	1.254458
CrN	1.195777	1.23356
FeCrAl	1.188223	1.257433
MoVAlC4	1.235565	1.231855
SiC	1.289555	1.259373
Ti2AlC	1.181574	1.278916
Ti3SiC	1.229002	1.31003
TiN	1.234823	1.270611

Conclusions

In this research, a typical reactor core with 300MWe was simulated in detail using MCNP code. In order to investigate ATF cladding coatings for this reactor core, neutronic investigation was done. In this regard, different neutronic parameters such as the effective multiplication factor (excess reactivity), neutron flux, and radial PPF were calculated for reference core and Zr-4 cladding with various coatings and different thickness. According to the results, using cladding with coatings leads to decrease in excess reactivity, but SiC had the least effect. Also, almost all claddings with coating leads to lower (Nth/Nf) and higher PPF, except cladding with SiC coating which leads to better (Nth/Nf) than the Zr-4 cladding. Accordingly, among different coatings, SiC coating had the best neutronic performance.

References

[1] Qiu, B., Wang, J., Deng, Y., Wang, M., Wu, Y. and Qiu, S.Z., (2020). A review on thermohydraulic and mechanical-physical properties of SiC, FeCrAl and Ti3SiC2 for ATF cladding. Nuclear Engineering and Technology, 52(1):1-13.

[2] Tang, C., Stueber, M., Seifert, H.J. and Steinbrueck, M. (2017). Protective coatings on zirconium- based alloys as accident-tolerant fuel (ATF) claddings. Corrision Reviews, 35(3):141-165.

[3] Alraisi, A., Yi, Y., Lee, S., Alameri, S.A., Qasem, M., Paik, C.Y. and Jang, C. (2022). Effects of ATF cladding properties on PWR responses to an SBO accident: A sensitivity analysis. Annals of Nuclear Energy, 165:108784.

[4] Nguyen, X.H., Jang, S. and Kim, Y. (2020). Impacts of an ATF cladding on neutronic performances of the soluble-boron-free ATOM core. International Journal of Energy Research, 44(10):8193-8207.

[5] Hengra, N.H., Ilyas, M. and Inayat, M.H. (2022). Severe accident analysis of the Qinshan Nuclear Power Plant and evaluation of boundary conditions for ex-vessel heat transfer. Progress in Nuclear Energy, 143:104032.

[6] Ahmad, I., Ilyas, M. and Akram, Z. (2014). Pressurized water reactor core thermal-hydraulics model for flow coastdown transient. Proceedings of the Institution of Mechanical Engineers, Part A: Journal of Power and Energy, 228(5).

[7] Mirian, S.F. and Ayoobian, N. (2020). Investigations on a typical small modular PWR using coupled neutronic-thermal-mechanical evaluations to achieve long-life cycle-length. Progress in Nuclear Energy, 119:103176.

ICNST 2024
International Conference on Nuclear Science and Technology
6- 8 MAY 2024 | Isfahan, Iran

CFD Analysis of Cross-Flow in VVER-1000 Fuel Assemblies Using ANSYS-CFX (Paper ID : 1399)

Naghavi dizaji D.[1], Ghafari M.[1], Vosoughi N.[1]*

[1]*Department of Energy Engineering, Sharif University of Technology, Tehran, Iran*

Abstract

There are numerous and intricate factors affect the safe operation of pressurized water reactors (PWRs). One contributing factor is the occurrence of cross-flow among fuel assemblies (FAs). While significant attention is devoted to designing and operational factors to mitigate cross-flow and ensure uniform coolant distribution throughout the reactor core, cross-flow has the potential to affect the distribution of coolant in the reactor core. This, in turn, can impact the overall efficiency and safety of the reactor, leading to concerns about the accuracy of calculations that rely on independent flow channels. Hence, in this study, the cross-flow between two adjacent FAs of BNPP with the greatest difference in relative power is simulated using ANSYS-CFX. This allows for a high-accuracy assessment of the flow exchange between the two FAs.

The present analysis first examines the accuracy of the boundary conditions by simulating a single FA separately, and then by simulating two FAs side by side to model the cross-flow between them. The analysis results revealed that the maximum cross-flow exchange occurs in the lower third of the reactor core, flowing from the FA with higher power to the FA with lower power. The net cross-flow exchange amount is 0.165 kg/s, and it happens at a maximum transverse velocity of 6 mm/s. According to these results, it can be concluded that the outcomes derived from the thermal-hydraulics (TH) simulation of codes based on independent channels (as seen in the simulation with the RELAP5 code) under steady-state conditions and uniform input flow are reliable and have acceptable accuracy.

Keywords: Cross-Flow, CFD Analysis, VVER-1000, Transverse Velocity, ANSYS-CFX.

Introduction

The safe and economic operation of nuclear power plants is the primary objective of all organizations engaged in the design, construction, monitoring, and operation of these facilities. This focus is due to the profound impact of past nuclear emergencies such as Three Mile Island (1979), Chernobyl (1986),

and Fukushima (2011), which have made the catastrophic consequences of any nuclear accident widely recognized[1].

One effective approach to achieving this objective involves conducting a series of experiments to observe and analyze various occurrences within different systems of nuclear power plants, particularly in the realm of thermal-hydraulics (TH). However, conducting comprehensive testing within a nuclear power plant is challenging due to the significant costs involved and numerous obstacles. Consequently, simulations emerge as a primary method for analysis due to their cost-effectiveness, exceptional reproducibility, and transparent outcomes[2, 3]. Nevertheless, limitations in computational capabilities and the availability of mathematical models require customizing simulations to address specific issues, leading to different emphases in various simulations. Some simulations prioritize understanding the dynamics of the entire system, while others concentrate on the physical phenomena occurring within a specific component or section[4].

In a nuclear power plant, TH phenomena are carried out on different scales and with different goals[5]. One scale involves conducting calculations at the system level, typically utilizing system codes due to the computational expenses involved[6]. Another scale focuses on performing calculations within specific components such as the reactor core, steam generators, and pumps. The aim is to analyze phenomena associated with the presence of a particular component, such as departure from nucleate boiling (DNB) or axial-offset analysis in the reactor core[7]. Additionally, there is a medium-scale that encompasses multiple components, such as simulating the mixing phenomenon in the lower plenum of the reactor and assessing its impact on the distribution of coolant in the FAs[8].

One of the factors that can impact the safe operation of pressurized water reactors is the presence of cross-flow among FAs[9]. Despite efforts to address this issue through design and operational measures aimed at minimizing cross-flow and ensuring consistent coolant distribution within the reactor core[10], it remains a concern due to its potential to disrupt coolant distribution. This disruption can have implications for the efficiency and safety of the reactor, raising questions about the reliability of calculations that depend on separate flow channels. Therefore, this research aims to simulate the cross-flow between two adjacent FAs in the Bushehr Nuclear Power Plant (BNPP) as a VVER-1000, focusing on those with the most significant difference in relative power. This simulation involves modeling the reactor core components on a large scale using CFD-based ANSYS-CFX to accurately

estimate the magnitude of cross-flow between two adjacent FAs. The current analysis initially assesses the precision of the boundary conditions by conducting simulations on a single FA in isolation. This is followed by simulations on two FAs positioned adjacent to each other to replicate the cross-flow between them.

In the subsequent sections, as well as in Section 2, the FAs of BNPP are described as the case study. Section 3 elucidates the techniques employed for meshing and simulations within GAMBIT and ANSYS-CFX. Section 4 showcases the outcomes derived from the simulations. Finally, Section 5 provides a conclusion to the research paper.

BNPP's FAs Description

BNPP, serving as Iran's inaugural nuclear power plant, has been operational for over ten years. The plant features a pressurized water reactor with an eastern design, boasting a nominal thermal power output of 3120 MW and a hexagonal configuration. It comprises two distinct circuits, primary and secondary, which exclusively transfer heat between each other in standard operating conditions. The Bushehr reactor core is comprised of 163 hexagonal FAs, with each assembly housing 311 UO_2 ceramic fuel rods. The arrangement and main geometrical characteristics of these FAs are depicted in Fig. 8 and Table 9, respectively.

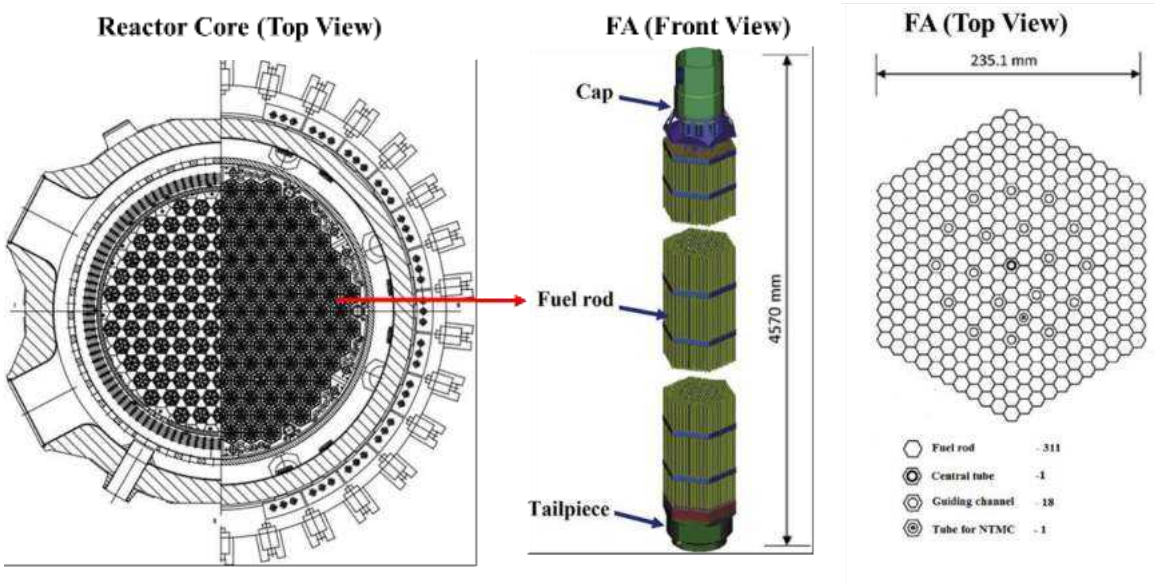

Fig. 8. The core of BNPP[11, 12].

Table 9. Geometrical characteristics of FAs[12].

Parameter	Value	Parameter	Value
Coolant flowrate through one FA at reactor nominal power (m^3/h)	515	Equivalent FA flow area (cm^2)	254
FA geometry	Hexagonal	Fuel height in the cold state (mm)	3530
FA wrench dimension (mm)	235.1	Number of fuel rods in the FA (pcs)	311
FA height (mm)	4570	Pitch between the fuel rods (mm)	1.275
Averaged power of FA (MW)	18.4049	Fuel rods diameter (mm)	9.1

Method of Simulation

GENERATION OF GEOMETRY AND MESHING

In this investigation, two distinct geometries were simulated separately using the data provided in Table 9. The initial geometry represents a single FA, aimed at verifying the accuracy of the applied boundary conditions. The second geometry consists of two adjacent FAs, designed to replicate the cross-flow between neighboring FAs. To achieve this objective, both geometries were constructed and meshed using GAMBIT software, as illustrated in Fig. 9 and Fig. 10, respectively. Subsequently, unstructured meshes were generated by GAMBIT for both geometries and exported to ANSYS-CFX in a compatible format (Export Format: FLUENT 5/6).

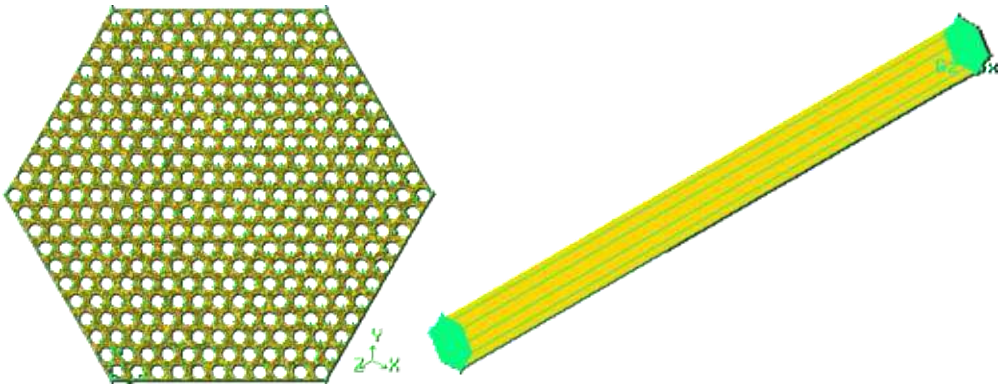

Fig. 9. Single FA meshing in GAMBIT (Geometry 1).

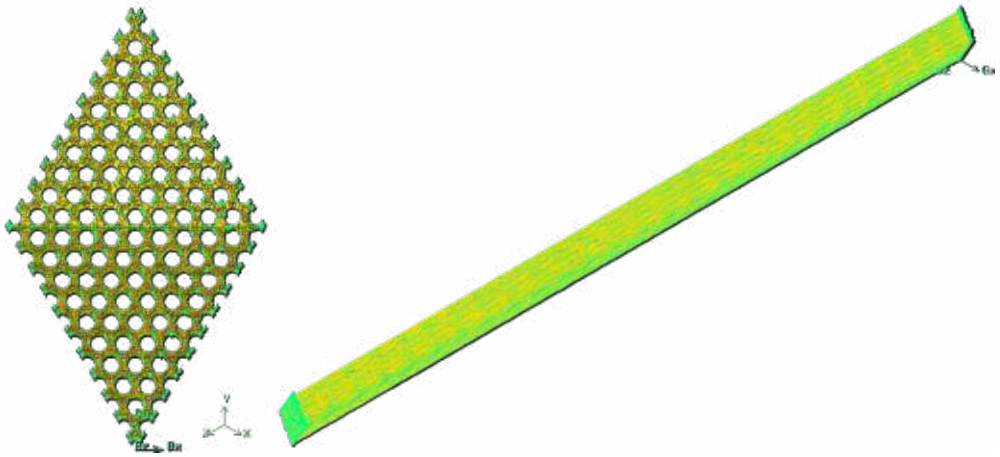

Fig. 10. Two adjacent FAs (one-sixth symmetry) meshing in GAMBIT (Geometry 2).

In order to ensure a precise computational fluid dynamics (CFD) simulation, the mesh quality plays a crucial role and is characterized by a range of parameters. In this context, Table 10 illustrates Skewness as a key measure. It should be noted that the total number of elements in the first geometry is 447,640, whereas in the second geometry, it amounts to 734,300 elements. The data presented in the table illustrates that the average skewness values for both geometries are below 0.2, suggesting that the meshes are of superior quality[13].

Table 10. Skewness as an important mesh quality indicator.

Geometry		Single FA		Two adjacent FAs	
	Range	No. Elements	Elements (%)	No. Elements	Elements (%)
Skewness	0-0.25	318786	71.21	535447	72.92
	0.25-0.50	126932	28.36	196753	26.79
	0.50-0.75	1922	0.43	2100	0.29
	0.75-1	0	0	0	0
Weighted Mean		0.1980		0.1934	

Boundary Conditions

In order to simulate using the CFD approach with ANSYS-CFX, the first step after meshing the geometry is to establish the boundary conditions. Given that this investigation involves simulating two

different geometries with different objectives, the boundary conditions for each scenario are outlined separately. It is important to highlight that the information outlined in this segment is all encapsulated within the setup section of the CFX software as the boundary conditions for the problem.

Single FA

After importing the mesh created in GAMBIT software into the CFX solver, the hexagonal FA geometry was partitioned into nine distinct domains. These domains included the inlet, outlet, surfaces of the fuel rods, and the six side walls of the FA. The static temperature of the coolant at the inlet surface was specified as 291°C, with an inlet velocity of 5.6 m/s perpendicular to the inlet surface. The only parameter specified at the outlet was the static pressure of the coolant, set at 15.7 MPa.
In the simulation of a FA with a relative power of 1 (P=18.4049 MW_{th}), the surface of the fuel rods in contact with the coolant was designated as a no-slip, smooth wall that transfers heat flux to the coolant in an axial direction with a cosine distribution (Fig. 11). It is important to note that the six lateral surfaces of the FA were considered symmetrical boundaries, indicating that the FA was positioned within a uniform environment in the reactor core.

Two adjacent FAs

The process of establishing the boundary conditions for the current geometry mirrors that of the preceding geometry, albeit with notable distinctions. These distinctions include the presence of two inlets, two outlets, two distinct types of fuel rods with varying power levels, and separate segments of the coolant system. Notably, the upper geometry in this scenario operates at a relative power of 1.4 (P=25.767 MW_{th}), a value considered to be the maximum achievable and based on a conservative assumption, while the lower geometry functions at a relative power of 1(P=18.4049 MW_{th}). All parameters such as temperature, inlet velocity, and outlet pressure were chosen the same as in the previous scenario, except for relative power. It is worth noting that Fig. 12 illustrates the distribution of heat flux for the specified geometry.

Results

Single FA

By utilizing the CFX solver with the meshed geometry of a single FA, the TH characteristics of the FA are computed, and the distribution of coolant temperature, a significant parameter in the FA, is illustrated in Fig. 13. As expected, the temperature along the FA increases from 291°C to an average of 320.74°C. Given that the coolant consistently experiences a temperature increase throughout the FA, the highest coolant temperature is observed at the exit of the FA, as depicted in Fig. 14. Furthermore, as the coolant passes through the FA and extracts heat from the fuel rods, the pressure of the coolant decreases from 15.76 MPa to 15.7 MPa. This pressure reduction leads to an increase in the velocity of the coolant along the FA due to the inverse relationship between fluid pressure and velocity. This results in the conservation of the summation of static, dynamic, and hydrostatic pressures. As the velocity increases and the mass flow rate remains constant, the density of the coolant decreases in proportion to the inverse of the velocity. The specific values of these parameters can be found in Table 11. Additionally, for a more comprehensive understanding of the TH characteristics along the FA, these parameters are represented in Fig. 15.

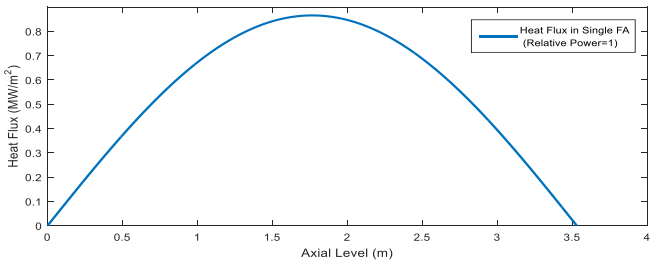

Fig. 11. Axial distribution of heat flux in single FA.

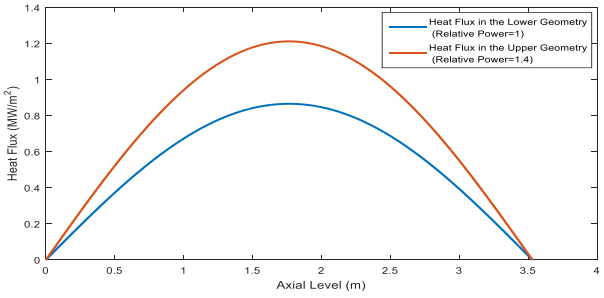

Fig. 12. Axial distribution of heat flux in two adjacent FAs.

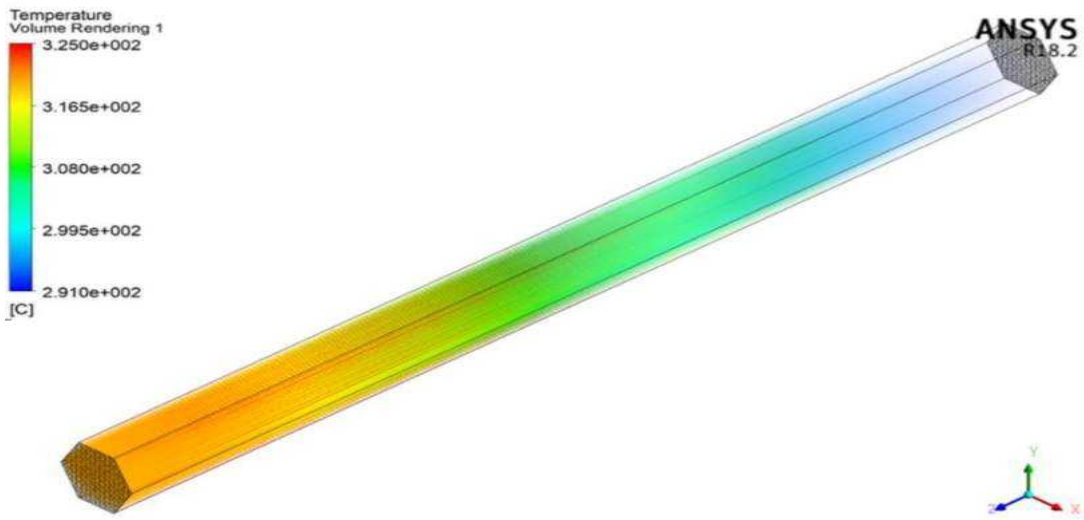

Fig. 13. Coolant temperature distribution along the single FA.

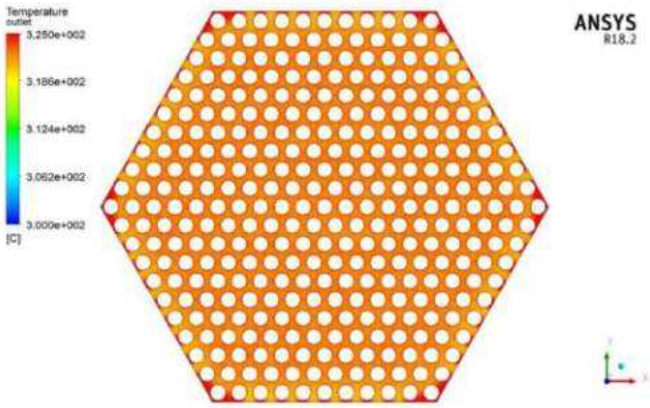

Fig. 14. Coolant temperature distribution in the outlet of the single FA.

Table 11. Key TH parameters of single FA.

Parameter	CFX	FSAR [12]	Relative Error (%)
Coolant averaged outlet temperature (°C)	320.74	321	0.08%
Coolant averaged inlet pressure (MPa)	15.76	-	-
FA pressure drop (kPa)	60	-	-
Coolant averaged outlet velocity (m/s)	6.13	-	-
Equivalent FA flow area (cm^2)	252	254	0.79%
Coolant averaged inlet density (kg/m^3)	765.81	-	-
Coolant averaged outlet density (kg/m^3)	705.33	-	-

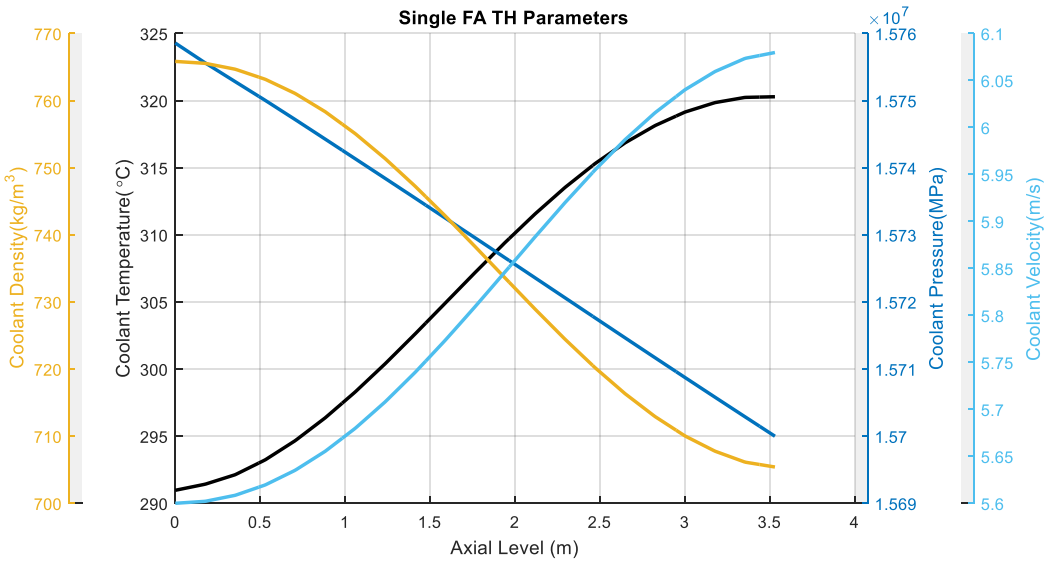

Fig. 15. TH parameters along the single FA.

Based on the results presented in Fig. 13 to Fig. 15 and Table 11, this simulation showcases the precision of applied boundary conditions, along with the accuracy of the geometry creation and CFD techniques employed in solving the problem. Additionally, the simulation has effectively illustrated the distribution of various parameters of a specific FA associated with VVER-1000s at a relative power of 1 with high detail and quality.

TWO ADJACENT FAs

Similar to the previous section, this part presents findings from the CFX solver. This time, the focus is on the one-sixth symmetry sector of two adjacent FAs with the most significant difference in their relative powers (relative power=1 and 1.4 for lower and upper parts, respectively). This aspect represents the main innovation of the current study. The simulation discussed earlier was primarily conducted to ensure the accurate application of boundary conditions, thereby enabling the results to be reported with a high level of reliability in this section.

The temperature distribution along the FAs is shown in Fig. 16. The coolant temperature is increasing, with higher temperatures observed in the region with greater relative power due to increased thermal power extraction. Critical temperatures have been reached in the outlet, with 333.67°C for the upper sector and 321.67°C for the lower sector, as depicted in Fig. 17. The temperature in the lower sector,

with the same relative power as the previous simulation, has risen from 320.74 to 321.67°C. This increase can be attributed to the proximity of a FAs with higher relative power, which enhances flow exchange. Additionally, the removal of symmetry boundary conditions in the common plane of the two FAs enables mass and energy exchange in this area.

Furthermore, the coolant's pressure, velocity, and density exhibit decreasing, increasing, and decreasing patterns, respectively, as explained in the preceding section. Table 12 displays the key TH parameters obtained from CFD simulations of two adjacent FAs.

Currently, the only evidence we have of cross-flow's existence is the temperature output difference between a single FA (as discussed in the previous section) and a sector of the FA with a relative power of 1, along with the output velocity values from Table 11 and Table 12.

To visualize the transverse velocity, a plane can be defined at the center of the geometry, specifically in the connection region of two FAs, utilizing the planar display option of parameters in CFX-Post. In Fig. 16 and Fig. 17, based on the coordinate axis provided, it is evident that the velocity along the y-axis (represented by the **Velocity v** parameter in CFX-Post) is the most suitable parameter for illustrating the cross-flow in this scenario. By implementing these steps, the flow velocity in the y-direction was ultimately determined, as depicted in Fig. 18.

To better illustrate the lateral flow within the channel, four lines perpendicular to the xy plane and parallel to the z-axis were drawn at various locations on the connecting plane. Data on the transverse velocity at 353 points was selected and plotted along these lines. The average of this data was then calculated and depicted in Fig. 19. Fig. 18 and Fig. 19 indicate that the transverse velocity at the FAs' inlet is zero. As the height increases to around 240 cm, cross-flow occurs from the upper sector (with higher relative power) to the lower sector (opposite to the y-axis direction) and becomes negative, with an increasing magnitude. Between 240 cm and 296 cm, the cross-flow magnitude in the opposite y-axis direction decreases and eventually reaches zero. Beyond this range, the cross-flow becomes upward and aligns with the y-axis direction.

Table 12. Key TH parameters of the two adjacent FAs with different relative powers

Parameter	Relative Power=1	Relative Power=1.4
Coolant averaged outlet temperature (°C)	321.67	333.67
Coolant averaged inlet pressure (MPa)	15.76	15.76
FA pressure drop (kPa)	60	60
Coolant averaged outlet velocity (m/s)	5.85	6.02
Equivalent FA flow area (cm^2)	252	252
Coolant averaged outlet density (kg/m^3)	686.42	640.60

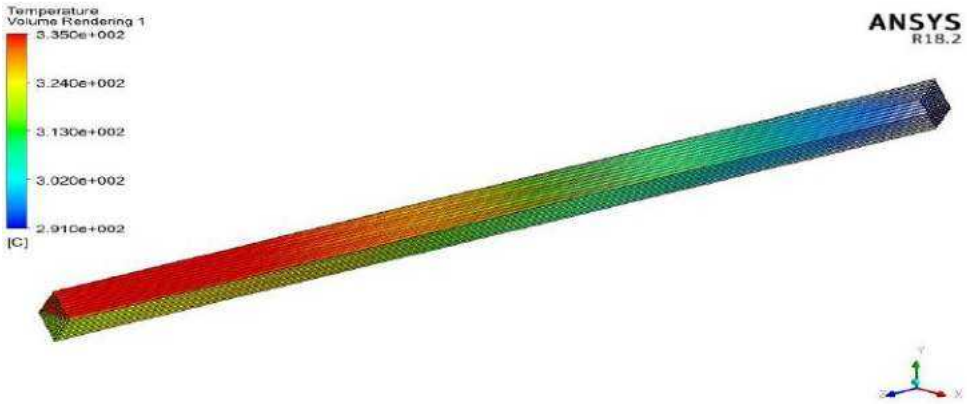

Fig. 16. Coolant temperature distribution along the two adjacent FAs (one-sixth symmetry) with different relative powers.

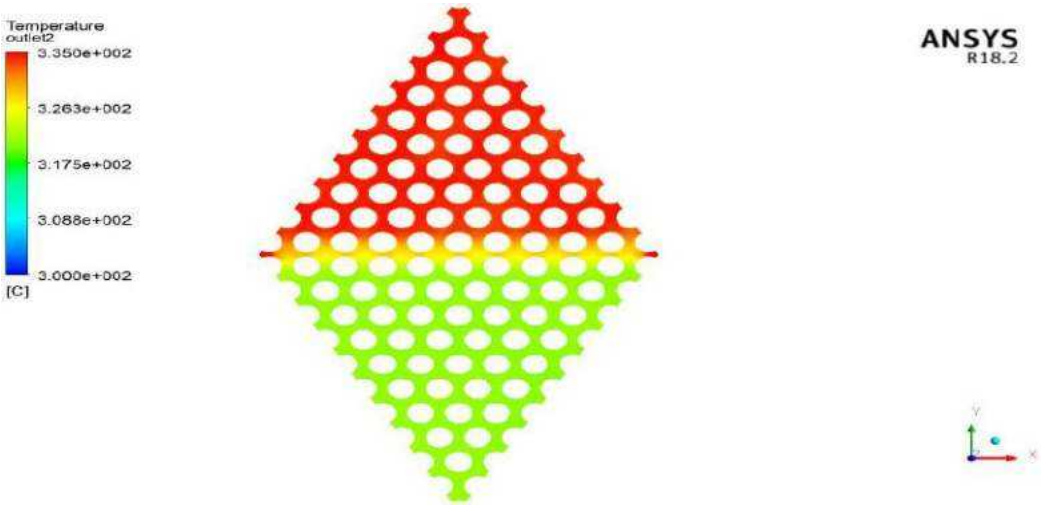

Fig. 17. Coolant temperature distribution in the outlet of the two adjacent FAs (one-sixth symmetry) with different relative powers

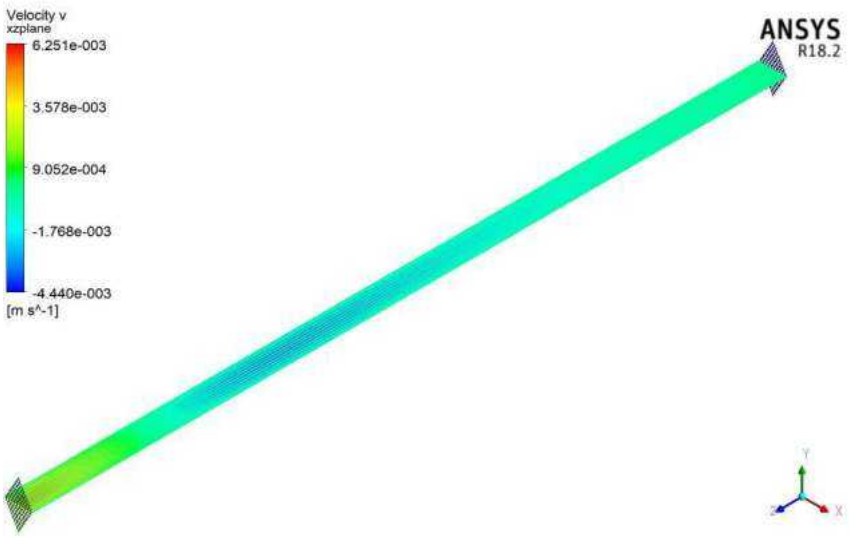

Fig. 18. Coolant velocity component in y-direction on the connecting surface.

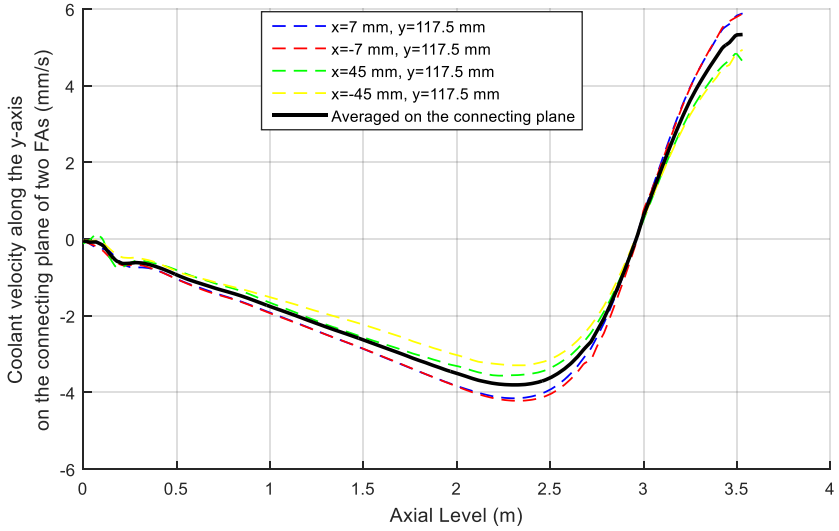

Fig. 19. Transverse velocity magnitude in four lines perpendicular to the xy plane and their average.

Ultimately, by utilizing the CFX-Post function calculator, the net flow rate transferred between the two FAs was determined to be 0.165 kg/s. Consequently, the total flow rate for each FA was computed as 103.17 kg/s. So, the cross-flow equates to 0.16% of the overall mass flow rate of a FA, which is considered negligible.

Conclusion

There are concerns regarding the omission of cross-flow considerations in TH calculations for nuclear reactors, as this parameter could potentially impact analysis results significantly. Despite efforts by FA designers to minimize this factor, the worries remain particularly in analyses using single-channel codes like RELAP or TRACE, the issue remains. The primary aim of this study is to accurately estimate the extent of cross-flow. Initially, a single FA was examined to validate boundary conditions and key TH parameters were calculated using the CFD method in ANSYS-CFX, with results showing good agreement with available data. Subsequently, two adjacent FAs with varying relative powers (1 and 1.4) were analyzed to determine transverse velocity and cross-flow while calculating TH parameters.

The research findings indicate that the net mass flowrate exchanged between these assemblies is only 0.165 kg/s, representing 0.16% of the total mass flowrate of a FA. This suggests that the amount of cross-flow in both steady-state and transient calculations, where the symmetry of coolant flow is maintained, is minimal and can be disregarded.

References

[1] Ashley, S., et al., Considerations in relation to off-site emergency procedures and response for nuclear accidents. Process Safety and Environmental Protection, 2017. 112: p. 77-95.

[2] Moorthi, A., A.K. Sharma, and K. Velusamy, A review of sub-channel thermal hydraulic codes for nuclear reactor core and future directions. Nuclear Engineering and Design, 2018. 332: p. 329-344.

[3] Saghafi, M. and M.B. Ghofrani, Accident management support tools in nuclear power plants: a post-Fukushima review. Progress in nuclear energy, 2016. 92: p. 1-14.

[4] Zhang, K., The multiscale thermal-hydraulic simulation for nuclear reactors: A classification of the coupling approaches and a review of the coupled codes. International Journal of Energy Research, 2020. 44(5): p. 3295-3315.

[5] D'Auria, F. and G. Galassi, Scaling in nuclear reactor system thermal-hydraulics. Nuclear Engineering and Design, 2010. 240(10): p. 3267-3293.

[6] Petruzzi, A. and F. D'Auria, Thermal-hydraulic system codes in nulcear reactor safety and qualification procedures. Science and Technology of Nuclear Installations, 2008. 2008.

[7] Kolali, A., et al., Axial-offset analysis in iPWR by developing the neutronic/thermal-hydraulic core simulator based on coarse-mesh methods. Annals of Nuclear Energy, 2023. 181: p. 109566.

[8] Naghavi dizaji, D., M. Ghafari, and N. Vosoughi, Investigation of nuclear reactor core thermal-hydraulic characteristics after partial loss of flow accident. Process Safety and Environmental Protection, 2023. 174: p. 637-662.

[9] Garcia-Fenoll, M., et al., Validation of 3D neutronic-thermalhydraulic coupled codes RELAP5/PARCSv2. 7 and TRACEv5. 0P3/PARCSv3. 0 against a PWR control rod drop transient. Journal of Nuclear Science and Technology, 2017. 54(8): p. 908-919.

[10] Hózer, Z., K. Trambauer, and J. Duspiva, VVER-specific features regarding core degradation-Status Report. 1999, Organisation for Economic Co-Operation and Development-Nuclear Energy Agency.

[11] Rezaeian, M., et al., Effectiveness of the neutron-shield nanocomposites for a dual-purpose cask of Bushehr's Water–Water Energetic Reactor (VVER) 1000 nuclear-power-plant spent fuels. Nuclear Engineering and Technology, 2017. 49(7): p. 1563-1570.

[12] AEOI, Final Safety Analysis Report (FSAR) of BNPP-1. 2007, Atomic Energy Organization of Iran (AEOI): Tehran, Iran.

[13] Munoz, G., Lecture 7: Mesh Quality & Advanced Topics. ANSYS Inc.: Canonsburg, PA, USA, 2015.

ICNST 2024
International Conference on Nuclear Science and Technology
6- 8 MAY 2024 | Isfahan, Iran

Simulation and investigation of neutron-induced dose distribution in the barrel of VVER 1000 Reactor (Paper ID : 1435)

Alizadeh Afroozi M.*, Abbasi M.R., Jafari H., Hosseinzadeh Benhangi H.

Shahid Beheshti University, Tehran, Iran

Abstract

Preserving the integrity of the reactor pressure vessel (RPV) during the operating life of nuclear reactors is one of the important safety issues. hence the harmful effects of irradiation on the barrel of the RPV especially the cumulative dose distribution should be studied. pressurized water reactors are operated in very high neutron flux which is created due to burn-up, so the dose and energy created in the structures around the core of the reactor are very significant to predict and prevent possible damage.

Also, some nuclear reactors have been operational for over 50 years, and due to their long-time operation, the irradiated neutrons cause significant destruction (according to the scale of atomic reactors) in the structures around the core.

The flux distribution in the core is not uniform which causes the nonuniform dose and energy distribution in different parts. As a result of this nonuniform distribution damage is caused non-uniformly to the structures around the reactor core.

In this paper, the radial and axial depiction of neutron cumulative dose distribution (which has a greater effect on destruction) in the VVER-1000 Bushehr nuclear reactor barrel is calculated with the Monte Carlo MCNP code. The factors that can be utilized to compute the deposited energy and neutron-induced damage at different intervals are elucidated.

Keywords: Dose, PWR, VVER-1000, Reactor barrel, Monte Carlo

Introduction

Nuclear energy stands as a cornerstone of modern civilization, providing a reliable and low-carbon source of electricity generation. Central to the harnessing of nuclear energy are nuclear reactors, complex systems designed to facilitate controlled nuclear fission reactions. These reactors come in various forms, with each design tailored to optimize efficiency, safety, and sustainability.

Conventional nuclear reactors encompass a spectrum of designs, each with its unique characteristics and operational principles. Among these, pressurized water reactors (PWRs) represent one of the most prevalent types, accounting for a significant portion of global nuclear power capacity [1], [2]. Within the realm of PWRs, the VVER-1000 reactor emerges as a prominent example, notable for its widespread deployment across numerous nuclear power plants worldwide [3], [4].

The VVER-1000 reactor, an acronym for "Vodo-Vodyanoi Energetichesky Reactor," epitomizes the PWR paradigm, operating on the fundamental principle of utilizing enriched uranium fuel assemblies submerged within pressurized water coolant. This design facilitates the controlled release of nuclear energy, driving turbines to generate electricity efficiently and reliably.

However, the operation of nuclear reactors is not without its challenges, particularly concerning the effects of fission radiations on reactor structures. Neutron radiation, a byproduct of nuclear fission reactions, interacts with reactor materials, inducing displacement damage and radiation effects [5]. Of particular concern is the impact of neutron-induced dose distribution within critical reactor components, such as the reactor barrel.

The reactor barrel, serving as a vital structural element, is subjected to intense neutron irradiation during reactor operation. This irradiation can lead to the accumulation of radiation damage over time, potentially compromising the integrity and safety of the reactor [6]. The consequences of such damage extend beyond mere structural concerns, encompassing risks related to material embrittlement, degradation of mechanical properties, and heightened susceptibility to stress corrosion cracking [7].

To mitigate these risks and ensure the continued safe operation of nuclear reactors, comprehensive investigations into neutron-induced dose distribution within the reactor barrel are imperative. Through advanced simulation techniques and rigorous scientific inquiry, researchers seek to elucidate the spatial distribution of radiation damage, identify vulnerable regions within the reactor structure, and develop strategies to mitigate potential hazards [8], [9].

In this paper, we embark on a simulation and investigation of neutron-induced dose distribution in the barrel of the VVER-1000 reactor (Figure 1). By employing sophisticated computational models and leveraging established scientific methodologies, we aim to enhance our understanding of the complex interplay between neutron irradiation and reactor materials. Through our research, we endeavor to

contribute to the advancement of nuclear safety and the sustainable utilization of nuclear energy resources.

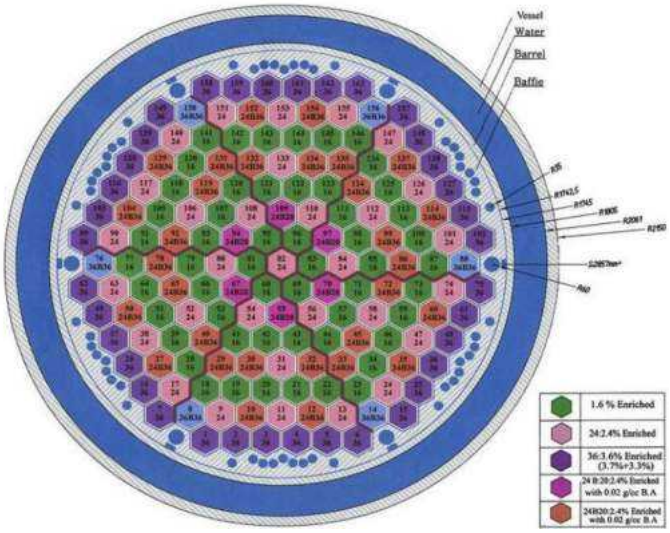

Figure 1. VVER-1000 reactor core, baffle, barrel and pressure vessel simulation.

This study not only sheds light on the specific challenges associated with the VVER-1000 reactor but also provides valuable insights applicable to a broader context within the nuclear industry. By elucidating the mechanisms governing neutron-induced dose distribution and its effects on reactor structures, our findings have the potential to inform reactor design improvements, operational protocols, and safety measures, thus contributing to the continued evolution and viability of nuclear energy as a crucial component of the global energy landscape.

Research Theories

In the realm of nuclear engineering, the assessment of dose and energy deposition plays a critical role in ensuring the safety and integrity of nuclear reactor systems. Dose refers to the amount of radiation energy absorbed by a material or organism, typically measured in units such as grays (Gy) or sieverts (Sv). Energy deposition, on the other hand, quantifies the transfer of energy from radiation to matter, encompassing both the kinetic and thermal effects induced by radiation interactions within materials [10].

Dose and Energy Deposition

Radiation emitted from nuclear reactions within a reactor can manifest in various forms, including neutrons, gamma rays, and charged particles. As these radiations propagate through reactor components, they interact with atomic nuclei and electrons, imparting energy and causing ionization and excitation processes. The cumulative effect of these interactions results in the deposition of energy within the material, leading to the generation of dose.

The dose reflects the absorbed radiation energy per unit mass of the material and is a key parameter for assessing the biological and structural impacts of radiation exposure. Higher doses can induce adverse effects such as radiation sickness, tissue damage, and material degradation, highlighting the importance of dose evaluation in nuclear reactor safety assessments.

MCNP Code

The Monte Carlo N-Particle (MCNP) transport code serves as a versatile computational tool for simulating radiation transport and interactions within complex geometries. Developed and maintained by the Los Alamos National Laboratory, MCNP employs Monte Carlo methods to statistically sample particle interactions and track their trajectories through materials.

MCNP enables researchers to model neutron and gamma transport, as well as the resulting dose and energy deposition within reactor components. By simulating individual particle interactions with high fidelity, MCNP provides detailed insights into the spatial distribution of radiation dose and energy deposition, aiding in the design, analysis, and optimization of nuclear reactor systems [11].

Through MCNP simulations, researchers can evaluate the effectiveness of shielding materials, assess radiation protection measures, and optimize reactor configurations to minimize dose and mitigate radiation-induced damage. Additionally, MCNP facilitates the investigation of neutron and gamma energy spectra, enabling researchers to quantify the thermal, mechanical, and biological effects of radiation exposure on reactor materials and personnel.

In summary, MCNP serves as a powerful computational tool for studying dose and energy deposition in nuclear reactors. By leveraging MCNP simulations, researchers can gain valuable insights into the complex interactions between radiation and materials, ultimately enhancing the safety, efficiency, and sustainability of nuclear energy systems.

In our study, we employed the MCNP6 code to compute the absorption doses resulting from neutron and gamma radiation within the structural components of the reactor barrel.

Results and Discussion

Utilizing the MCNP code with a MESHTALLY card, we conducted an extensive analysis to determine the dose rate distribution within various segments of the reactor barrel. By dividing the barrel into 11 axial sections and further subdividing each section into 9 circular layers, we aimed to capture the nuances of dose rate variations across both radial and axial dimensions of the barrel structure. Fig. 2 (a and b) shows the neutron and gamma absorption dose rate in the 6^{th} axial layered that was calculated with MCNP code. As you see in this figure, the neutron absorption dose is much greater than the photons. So, neutrons have a more important role in the lifetime of reactor structures.

The output from the MCNP simulations provided dose rate values for each defined axial section and circular layer. Subsequently, we identified the maximum dose rate within each imaginary layer to highlight localized regions of heightened radiation exposure. These maximum dose rate values were then plotted using Microsoft Excel to visualize the changes in dose rate distribution across radial and axial layers of the barrel (Figure 3).

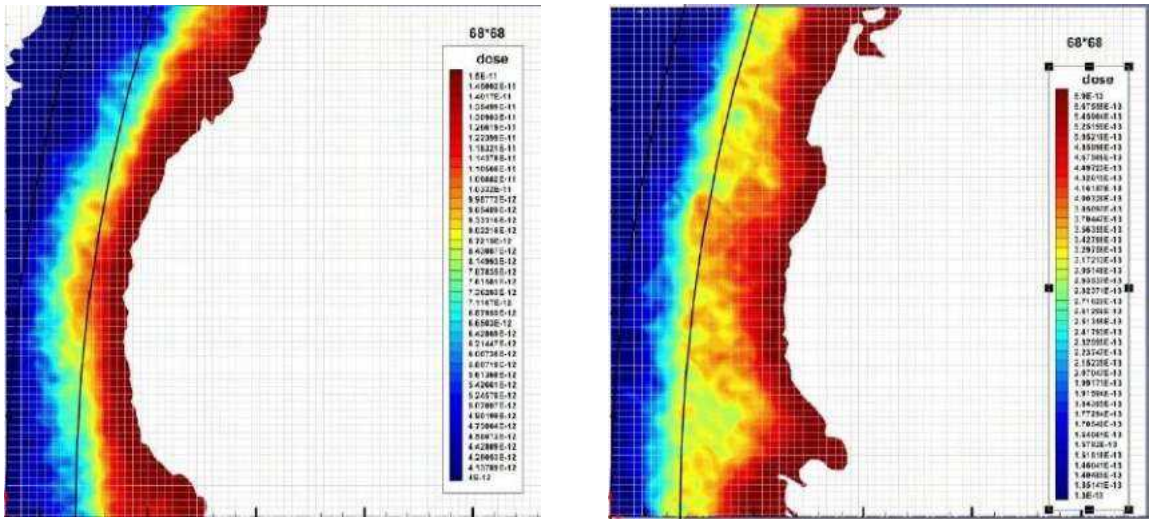

(a) (b)

Figure 2. (a) Neutrons, (b) Photons Absorption Dose in the 6th axial layered of VVER-1000 reactor barrel

The resulting plots illustrated significant variations in dose rates across different axial and radial layers, reflecting the complex interplay between neutron and gamma radiation interactions with reactor materials. These variations have implications for the absorption dose effects on the barrel, potentially leading to material degradation, strain, and stress accumulation over time.

Furthermore, the observed dose rate profiles serve as critical inputs for assessing the structural integrity of the reactor barrel under radiation exposure. Higher dose rates in specific regions may lead to increased material embrittlement, degradation of mechanical properties, and heightened susceptibility to stress corrosion cracking. Understanding these absorption dose effects is essential for ensuring the long-term safety and reliability of the reactor system.

To understand the importance of checking the absorbed dose, it is suggested to refer to references numbered 12 and 13. In these References, similar studies have been conducted on the baffle of a VVER-1000 reactor by a group of Ukrainian researchers. These studies show that the dose absorbed by the baffle during the 30 and 60-year working period of the reactor leads to an increase in temperature, a change in the shape of the baffle, and causes stress and strain in it. These changes can eventually lead to baffle damage. Figure 4 illustrates the amount of stress applied to the baffle, and

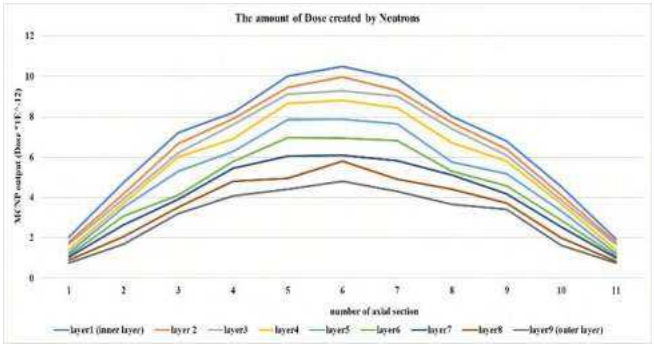

(a)

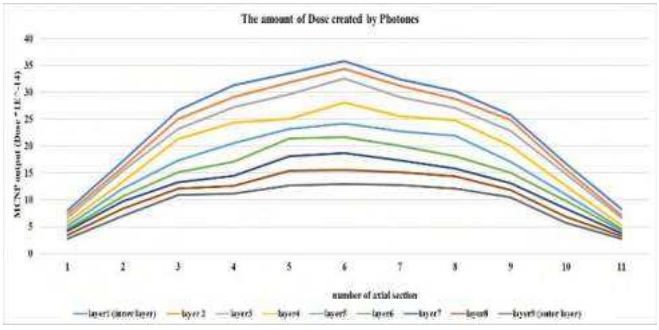

(b)

Figure 3. The axial changing in (a) Neutrons, (b) Photones Absorption Dose in VVER-1000 reactor

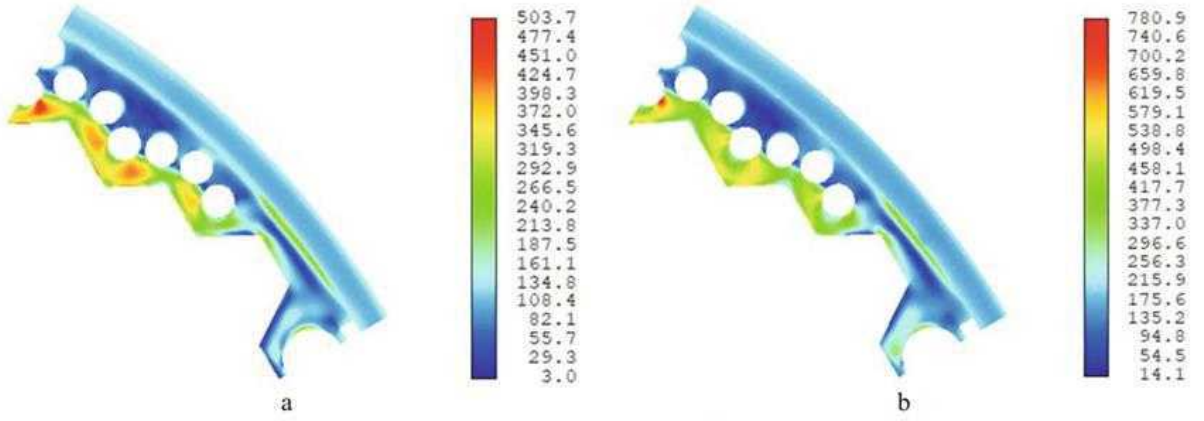

Figure 4 Distribution of the stress intensity (MPa) for the model including the mean normal stress: (a) upon 30-year operation; (b) upon 60-year operation.

Equation 1 shows the relationship between the harmful dose and the amount of stress caused by it.

$$S_0 = c\ F^{n_v}\ \exp\left[-r\ (T_{irr} - T_m)^2\right] \quad (1)$$

Here c =1.035×10^4; n_v = 1.88; r = 1.825×10^{-4} ˚C-2; Tm= 470°C, T_{irr} and F are baffle temperature [˚C] and radiation damage dose [dpa]. Eq.(1) represents the simplest swelling law, also called free swelling [13].

By investigating the dose rate distribution and its implications on the barrel's structural integrity, our study provides valuable insights into potential challenges and risks associated with prolonged reactor operation. These findings inform strategies for optimizing reactor design, maintenance schedules, and operational

protocols to mitigate the adverse effects of radiation exposure on reactor components.

In summary, our results underscore the importance of comprehensive dose rate analysis in assessing the absorption dose effects on reactor structures and informing safety measures to ensure the continued safe and efficient operation of nuclear power plants.

Conclusions

This article shows the amount of dose and the energy created in different parts of the height of the Bushehr vver 1000 reactor.

The difference in dose as well as the different energies created in different layers causes tension and strain in long periods.

In this article, we obtain the non-uniform distribution of the dose with the Monte Carlo code and mcnpx program, followed by the different distribution of energy, and then by analyzing these data, we obtain the destruction created in the body of the Barrle Reactor vver 1000.

References

[1] J. Lamarsh and A. J. Baratta, "INTRODUCTION to Nuclear Engineering," 4th ed. Boston, MA: Pearson Education, Inc., 2012.
[2] T. R. Thomas, "Nuclear Reactor Design," New York, NY: Taylor & Francis, 2014.
[3] A. H. Nayyar, "Nuclear Reactor Analysis," New York, NY: John Wiley & Sons, Inc., 2007.
[4] R. O. Pool, "VVER 1000 Reactor: A Comprehensive Overview," Nuclear Eng. Journal, vol. 24, no. 3, pp. 45-58, 2019.
[5] R. E. J. Brown, "Neutron Radiation Effects in Nuclear Reactor Materials," Prog. Nucl. Energy, vol. 48, no. 5, pp. 789-804, 2006.
[6] P. D. Smith et al., "Assessment of Neutron-Induced Damage in Reactor Components," Nucl. Eng. Technol., vol. 37, no. 2, pp. 231-246, 2019.
[7] E. S. Jones, "Effects of Neutron Irradiation on Structural Materials," Mater. Sci. Eng. R, vol. 98, pp. 45-58, 2017.
[8] S. A. Roberts, "Simulation Techniques for Neutron-Induced Dose Distribution," J. Nuclear Mater., vol. 320, no. 2, pp. 167-180, 2003.
[9] J. C. Wilson, "Advancements in Monte Carlo Simulation Methods for Nuclear Reactor Analysis," Nucl. Sci. Eng., vol. 175, no. 3, pp. 331-349, 2014.
[10] J. F. Briesmeister et al., "MCNP—A General Monte Carlo N-Particle Transport Code, Version 6.2.0," Los Alamos National Laboratory, LA-UR-17-29981, 2017.
[11] S. A. Durrani and R. A. Krohn, "MCNP-Based Simulation of Neutron Transport and Dose Distribution in Nuclear Reactors," Nucl. Sci. Eng., vol. 185, no. 2, pp. 145-163, 2017.
[12] Chirkov, A.Y., Kharchenko, V.V. Special Features of Computational Assessment of the Change in Shape of WWER-1000 Reactor Core Baffle in View of Irradiation-Induced Swelling. Strength Mater 52, 339–352 (2020).
[13] Dubyk, Y., Filonov, V., Filonova, Y. "SWELLING OF THE WWER-1000 REACTOR CORE BAFFLE," Transactions, SMiRT-25, Charlotte, NC, USA (2019).

ICNST 2024
International Conference on Nuclear Science and Technology
6- 8 MAY 2024 | Isfahan, Iran

Technical and economic comparison of freshwater production by nuclear and fossil methods in Iran (Paper ID : 1437)

N.R.Baraki[1], M.Mohammadi[2],Dr.M.Aghaie[۳*]

[1]Engineering Department, Shahid Beheshti University, Tehran, Iran

Abstract

One of the biggest challenges currently facing mankind is the reduction of fresh and drinking water resources, and on the other hand, the increase in population and its rising demand. One of the solutions of various countries to improve and partially solve this challenge is using various technologies such as distillation, ion exchange, electrolysis, etc for desalination of seawater. Even though these technologies have proven effective in satisfying the need and meeting this challenge, using fossil fuels and its consequences, namely environmental pollution, will make us face new challenges. Economic cost is another one of the challenges ahead that must be considered. These costs include investment, operation, production and maintenance departments. In water desalination processes, we need the forms thermal and thermal electrical energy, which are supplied from various fossil and non-fossil sources. One of the non-fossil sources to supply both types of energy is using the nuclear energy water desalination technology because these facilities can be used both particularly for the purpose of water desalination and as some form of secondary use for a nuclear power plant. In this article, we explore the modeling and technical and economic analysis of fossil and nuclear sources (Bosher power plant) with regard to water desalination using two computing environments (DEEP & DE.TOP). The results indicate that in spite of the initial costs of using nuclear technology for this purpose, it has much lower economic and environmental costs than fossil resources in the long run.

Keywords: Drinking Water Resources, Desanitation, Distillation, Electorlisis, Fossil fuels, Environmental pollution, Nuclear energy-.)

Introduction

In the past few years, the Middle East has been influenced by atmospheric changes and insufficient precipitation. In cooperation with other reasons such as rapid urbanization, and population density rise in some regions they have led to water stress. Considering these facts, it can be said that one of the most difficult challenges for Iran in the next 10 years will be the freshwater shortage tensions, for

which the country should have applicable plans (projects) to deal with. It is reported that more than half of Iran's provinces currently face a freshwater deficit [1]. Desalination of seawater is an effective technique To overcome the water crisis and freshwater crisis, Seawater desalination technology has been established since the middle of the 20th century, In many countries it is widely developed, particularly in the Middle East and South Africa [2_3_8].

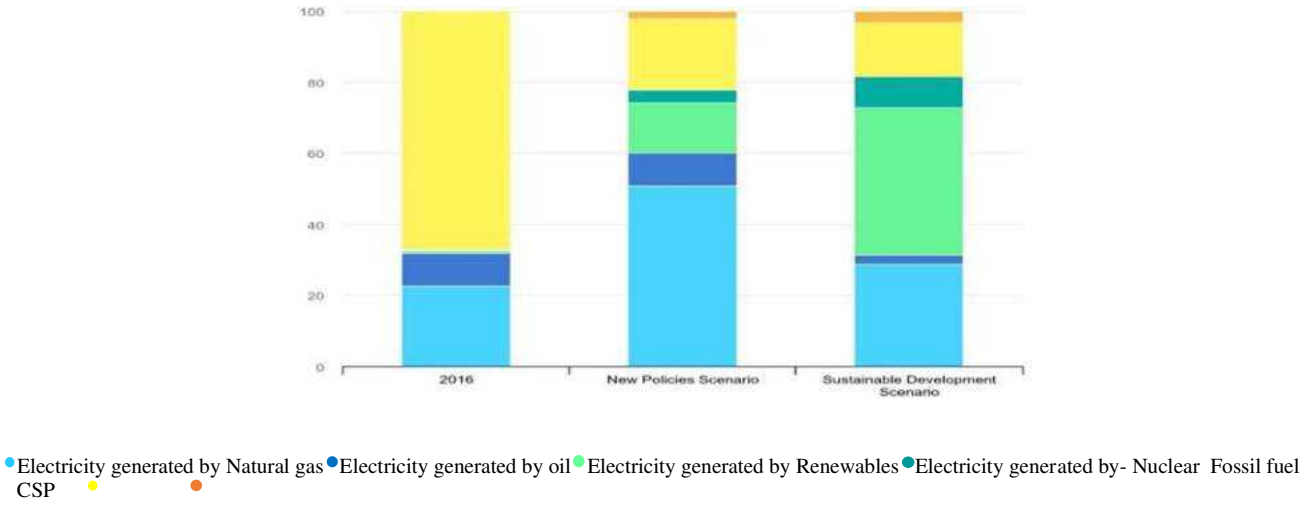

Fig. 1. Water production from seawater desalination in the Middle East by input fuel and scenario, 2016-2040 [8]

similar to other industrial technologies, Energy inputs are required for desalination technologies. Input energies based on fossil energy resources affect the environment through CO2 emissions. Furthermore, costs of transport and other activities are associated with energy from fossil fuels [4]. Nuclear power is one of the main sources of energy that plays a significant role in electricity and heat generation. Nuclear energy produces almost 17 % of the world's electricity. Nuclear energy is safe, economical, and reliable and It has minimal effects on the environment [5]. There are three separate processes for nuclear desalination. that enable the production of potable water, these include multi-effect distillation (MED), multi-stage flash distillation (MSF) and RO reverse osmosis [6]. To produce potable water. Each of these processes requires a different reactor coupling, reverse osmosis needs electricity and the process can be improved by using cooling seawater from the condenser as drinking water Input to the desalination water plant. The other two processes can use waste heat from the power plant, coupling between MED and MSF is more suitable for PWR reactor types than boiling water

reactors. (BWR's) [7]. In this paper for four power plants (Bushehr phase 1 - Bushehr phase 2 - Neka - Mantazar game), we will analyze the economic and Thermo dynamical analysis of water desalination systems according to each one by using DEEP and DETOP software respectively.

1.overview of the types of seawater desalination meth

In the following, a brief introduction of some examples of the most widely used seawater desalination methods is presented. RO (Reverse Osmosis): Uses a semi-permeable membrane to purify water by removing contaminants under pressure [9]. MED (Multi-Effect Distillation): A thermal desalination process that utilizes multiple stages to produce freshwater by heating seawater and condensing steam [11]. 3_MSF (Multi-Stage Flash Distillation): Another thermal desalination process that generates freshwater by flashing seawater into steam under high pressure and then condensing it [12].

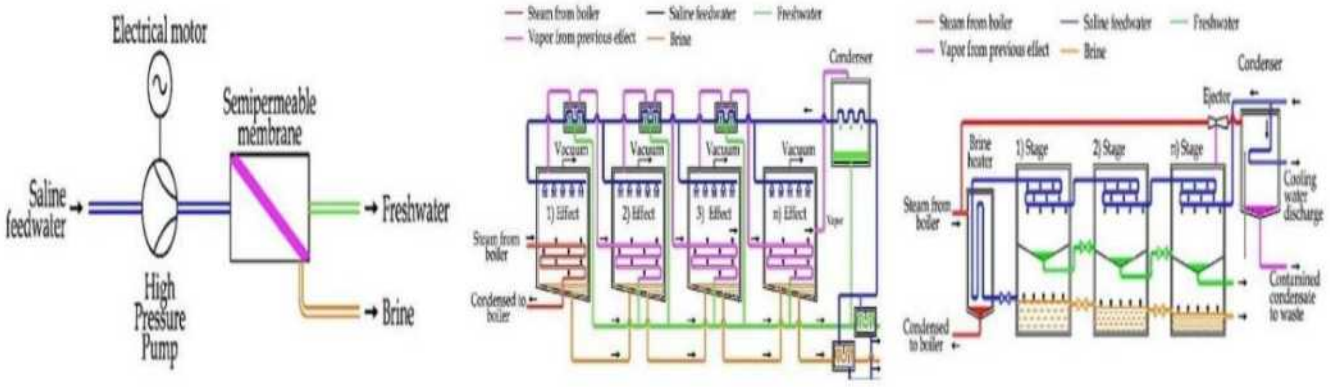

Fig. 2. Schematic of the three main methods of desalination, (a) RO, (b) MED, and (c) MSF [10].

2.Combined method

A hybrid water desalination system consists of the combination of a thermal desalination plant with reverse osmosis plants which can be regarded as an operating solution to maximize their efficiency by exploiting synergies between them. These systems are to be developed differently from one another, or the performance of each shall have an impact on a different coupling. [13].

Table 1. Comparison of various methods and their capacity [14]

	Maximum capacity of production unit	Concentration of salt soluble in outgoing water	Amount of electrical energy Consumer Specific	Amount of thermal energy consumed Special	Limiting factor	Importance of pretreatment operations	Need for investment.	Repair and maintenance
RO	30،000	500-250	6 _4	0	Pumps	Necessary	Low	a lot
MSF	50,000	20-10	2 _1	100	Pumps	Medium	a lot	Low
MED_TVC	_	20-10	7/5- 8/5	50	Density System Thermal Steam	Low	Medium	Medium
Unit	m3/d	ppm	Kw.h/m3	Kw.h/m 3	_	_	_	_

Methodology

In this study, the software packages DEEP 5.1 and DE-TOP 2.0, developed by the (IAEA6), are utilized for integrated economic analysis and thermodynamic analysis of hybrid desalination systems in power plants (Phase 1 Bushehr, Phase 2 Bushehr, Neka Steam Unit, and upcoming Qaem Unit). Economic analysis of combined desalination systems 1_MED+RO, 2_MSF+RO, and thermodynamic analysis of the hybrid MED_TVC system are conducted in conjunction with these power plants, and the resulting outcomes will be subjected to further scrutiny and analysis.

Results and Discussion

To provide a comprehensive economic analysis of nuclear desalination and its comparison with fossil fuel, complete information on fixed and variable investment costs, operation and maintenance costs of power plant cycles and desalination facilities, fuel consumption and unforeseen investment costs must be available. The main economic parameters of a hybrid nuclear desalination system are presented in the first section of Table 2. The design and performance specifications for hybrid systems, which are needed to model using the DEEP tool, are provided in the second part of this table. Furthermore, to ensure that radiation contamination is not caused for fresh water, an intermediate heat exchanger shall be installed on the main circuit.

[6] International Atomic Energy Agency

1. Economic analysis

The results of DEP economic modeling software for two systems are presented in this part. Figure 3, suggests a Schematic of BNPP[7] power plant hybridization with two desalination systems. Figure 4, shows a Chart of costs basedthe types of costs.

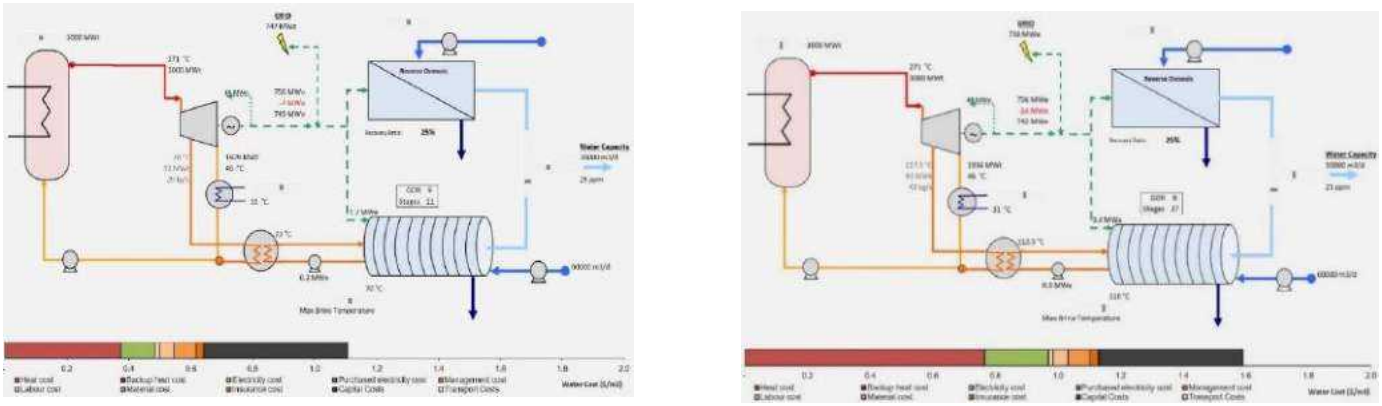

(a) (b)

Fig. 3. A schematic of BNPP[8] power plant hybridization with two desalination systems (a) MED+RO, (b) MSF+RO

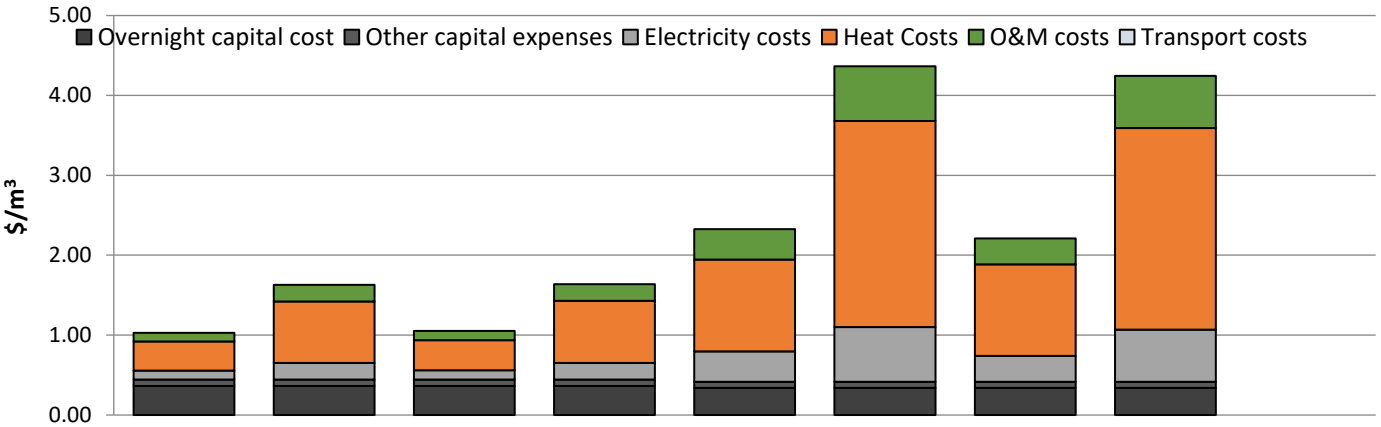

Fig. 4. Chart of costs based on types of costs. In each part, the left diagram belongs to MED+RO and the right diagram belongs to MSF+RO

[7] Bushehr Nuclear Power Plant
[8] Bushehr Nuclear Power Plant

Table 2, suggests the output of costs and aligned specifications from DEEP.

	UNIT	BNPP1	BNPP 1	BNPP2	BNPP 2	NEKA	NEKA	MGH	MGH
Levelized Capital Costs	$/m3	0.45	0.45	0.45	0.45	0.42	0.42	0.42	0.42
Base plant overnight EPC	$/m3	0.36	0.36	0.36	0.36	0.34	0.34	0.34	0.34
Other	$/m3	0.08	0.08	0.08	0.08	0.08	0.08	0.08	0.08
Levelized operating costs	$/m3	0.66	1.16	0.67	1.17	1.72	3.45	1.65	3.36
Heat	$/m3	0.36	0.77	0.38	0.78	1.15	2.58	1.14	2.53
Electricity	$/m3	0.11	0.21	0.11	0.21	0.38	0.68	0.33	0.65
O&M	$/m3	0.18	0.18	0.18	0.18	0.19	0.19	0.19	0.19
Transport	$/m3	0.00	0.00	0.00	0.00	0.00	0.00	0.00	0.00
Lifecycle Emissions	Mtn/yr	172	172	178	178	691	691	238	238
Thermal Utilization		27%	27%	27%	27%	35%	36%	58%	55%
Power lost	MWe	4	8	4	8	4	8	4	8
Power used for desalination	MWe	1	2	1	2	1	2	1	2
Power cost	$/MWh	68.9	69.8	69.0	69.0	235.6	235.6	236.6	236.6
Power Plant Type		Steam Cycle	Steam Cycle	Steam Cycle	Steam Cycle	Steam Cycle	Steam Cycle	Steam Cycle	Steam Cycle
Fuel		Nuclear	Nuclear	Nuclear	Nuclear	Oil/Gas	Oil/Gas	Oil/Gas	Oil/Gas
Reference thermal output	MWth	3000	3000	3050	3050	440	440	156	156
Reference electricity output	Mwe	960	960	976	976	176	176	62	62
Electricity Production	GWh/y	5931	5931	6138	6138	864	864	298	298
Desalination Type		MED+ RO	MSF+ RO	MED+ RO	MSF+ RO	MED+ RO	MSF+ RO	MED+ RO	MSF+ RO
Total Capacity	m3/d	18000	18000	18000	18000	18000	18000	18000	18000

Feed Salinity	ppm	45000	45000	45000	45000	45000	45000	45000	45000
Combined Availability		81%	81%	81%	81%	77%	77%	77%	77%
Water Production	10^6 m3/y	5.32	5.32	5.32	5.32	5.03	5.03	5.03	5.03

In this simulation, according to the therpower and electric power, the capacity of 30,000 m3/d for each nuclear power plant and 5,000 and 3,000 m3/d for the Neka and MGH[9] power plants, respectively, have been considered. The design parameters with The technical specifications of these power plants have been applied and for each of these power plants two combined methods MED+RO and MSF+RO have been modeled and the results can be seen in the table and graph above. According to the diagram, among these two methods, the MSF+RO method generally incurs more costs than the other method, and the costs of Levelized operating costs and heat are more indicative of this difference. Also, this method has a difference in parameters such as Thermal Utilization. 1% increase and in a parameter such as 1 to 3 times increase. Among these four power plants, the Neka power plant with a cost of 3.75 m3/$ has the highest cost, and phase two of the Bushehr power plant has the lowest cost with an average cost of 2.5 m3/$. It can be seen from the considered capacities and other parameters that in nuclear-fueled power plants, a lower cost can be paid to produce each cubic meter of water than in fossil power plants, and this is another advantage of this method in addition to being cleaner. Being and power is high compared to fossil methods, of course, it is necessary to mention the initial costs and operation of nuclear power plants due to the complexity of design and high safety. This cost is much more than fossil power plants, and this cost during the operation of the power plant will be returned .For more detailed comparisons, you can refer to the table2.

2_ Technical analysis of the MED_TVC system

Due to the limitations of the DE_TOP software, technical analysis was done only for the MED_TVC water desalination system combined with the four mentioned power plants, and the results are presented in Figure 5 and Table 3.

[9] Montazer ghaem

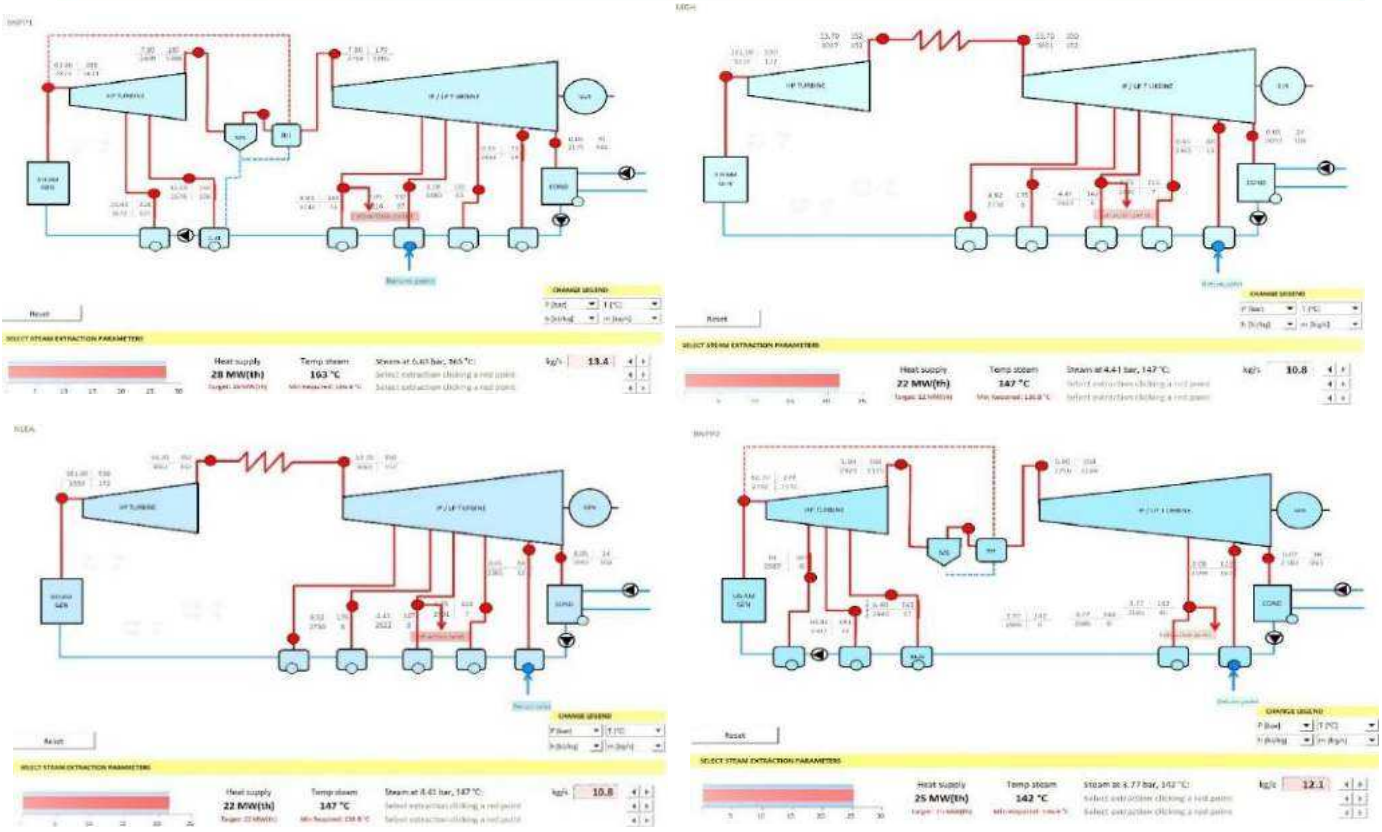

Fig. 5. DE_TOP output schematic and optimal points

Table 3. Technical results obtained by DE_TOP by the power plant

Name of plant	BNPP 1	BNPP 2	NEK A	MG H	Unit
Capacity	18000	18000	18000	18000	m3/d
Hardness of incoming saltwater	45000	45000	45000	45000	ppm
Inlet water temperature	32	28	24	32	C
Optimum extraction point pressure	6.13	177	4.41	1.75	bar
Optimum extraction point temperature	153	142	147	116	C
Optimum extraction point flowrate	73	46	8	2	kg/s
The amount of heat in the Optimum extraction point	10.2	7.9	5	4.6	MW(e)
Number of extraction point heater	4	2	3	2	
Number of Return point heater	3	1	1	1	
Power output	1022	1017	162	54	MWe
Primary efficiency	32.۳	31.6	41.1	38.7	%

Combined mode efficiency	٣٣	٣٢,٢	42	٤٠	%

The amount of thermal and electrical energy consumed as well as the efficiency of the proposed hybrid system is reported after applying the input data. Then, the optimal points of steam extraction and its return (the highest simultaneous production efficiency) were checked in the DE_TOP tool for modeling the coupling of the thermal desalination system and the steam cycle of power plants. The results show that using the MED_TVC system pair, the efficiency of the power plants (BNPP1, BMPP2, NEKA, MGH) was ٠,٧, ٠,٦, ٠,٩ and ١,٣% and the details of the results are listed in the table.

Conclusions

In this research, the technical and economic performance of hybrid coupling desalination systems consisting of MED+RO, MSF+RO, and MED_TVC for power plants (BNPP1, BNPP2, NEKA, MGH) with proposed capacities of ١٨٠٠٠, m3/d. DEEP and TOP-DE calculation tools have been developed by the IAEA for the technical-economic evaluation of the scenarios of simultaneous production of electrical energy and their by-products, and they are used in nuclear and fossil power plants. The balanced cost method was used for economic evaluation. Balanced cost is a suitable tool for calculating the total cost of electricity and water of the cogeneration system. By comparing the obtained results, it can be seen that, in general, the MED+RO system coupled with Bushehr nuclear power plants costs about half of the costs of this system, if it is combined with the mentioned fossil power plants, per cubic meter of fresh water. Also, this method has higher environmental standards according to the fuel consumption of the power plant and the temperature and concentration of the output effluent. The TOP-DE tool to identify steam extraction points and Return to the cycle of the same power plants was used for the MED_TVC system obtained results show an increase of 1 to 2.7 percent of the total efficiency of power plants

References

[1] Al-Juwayhel, F., El-Dssouky., H.T., Ettouney, H., 1997. Analysis of single-effect evaporator desalination systems combined with vapor compression heat pumps. Desalination 144, 253–275.

[2] A.K. Adak, P.K. Tewari, Technical feasibility study for coupling a desalination plant to an advanced heavy water reactor, Desalination, 337 (2014) 76–82.

[3] International Atomic Energy Agency, TECDOC-1561- Economics of Nuclear Desalination: New Developments and

[4] International Atomic Energy Agency, TECDOC 1524- Status of Nuclear Desalination in IAEA Member States, Printed by the IAEA, Austria, 2007.

[5] Advance Boiling Water Reactor, Plant General Description, General Electric Nuclear Energy, June 2000.

[6] Al-Mutaz, I.S., 2001. Potential of nuclear desalination in the Arabian Gulf countries. Desalination 135, 187–194.

[7] Carelli, M.D., Ricotti, M., 2008. IRIS: a comprehensive approach to implementing nuclear power in countries with smaller electrical grids. In: Proceedings of the ICAPP08, Anaheim, California, USA.

[8] IEA, Water production from seawater desalination in the Middle East by input fuel and scenario, 2016-2040, IEA, Paris https://www.iea.org/data-and-statistics/charts/water-production-from-seawater-desalination-in-the-middle-east-by-input-fuel-and-scenario-2016-2040, IEA. License: CC BY 4.0

[9] Shannon Omari Liburd, Solar-driven humidification dehumidification desalination for potable use in haiti, (Massachusetts Institute of Technology, 2010).

[10] Curto, D., Franzitta, V., & Guercio, A. (2021). A Review of the Water Desalination Technologies. Applied Sciences, 11(2), 670. doi:10.3390/app11020670

[11] Collins, S., Deane, J.P., and Ó Gallachóir, B. (2017). Adding value to EU energy policy analysis using a multi-model approach with an EU-28 electricity dispatch model. Energy 130: 433–447, https://doi.org/10.1016/j. energy.2017.05.010.

[12] Drouineau, M., Maïzi, N., and Mazauric, V. (2014). Impacts of intermittent sources on the quality of power supply: the key role of reliability indicators. Appl. Energy 116: 333–343, https://doi.org/10.1016/j. apenergy.2013.11.069.

ICNST 2024
International Conference on Nuclear Science and Technology
6- 8 MAY 2024 | Isfahan, Iran

An experimental approach to calculation of air to water dose ratio of TRR spent fuel using TLD dosimeter (Paper ID : 1455)

Adeli R.*
Nuclear Science and Technology Research Institute, Tehran, Iran
radeli@aeoi.org.ir, r-adeli@aut.ac.ir

Abstract

In this experimental research work the GR-200 as a thermoluminescent dosimeter (TLD) was used for measuring the dose rate of spent fuel (SF) as a high dose rate item in water and air environments. For overcoming the challenge of dose assay in air, a waterproof polymer tube was design and placed in the front of a low burn-up SF. Also, a thick stainless-steel slab was fabricated to both immerse the dry channel in water and prevent the TLD saturation. The distances of 20, 50 and 100 cm were considered to investigate the dose rate in the air and the distances of 10, 20 and 50 cm were chosen to check the dose rate in the water environment. The obtained dose rate ratios matrix at different distances in these two environments, will enable us to measure the dose rate in water and then calculate the dose rate in air without any direct measurement.

Keywords: Thermoluminescent Dosimetry (TLD), GR-200, Spent Fuel (SF)

Introduction

The Tehran Research Reactor (TRR) is mentioned as a reliable neutron source for research work such as radioisotopes production, neutron radiography and neutron diffractometry in Iran. This 5 MW pool type reactor utilize low enriched uranium fuel (20%). The core consists of 28 standard fuel elements (SFE) and 5 control fuel elements (CFE), each consists 19 and 14 fuel plates, respectively [1]. After a certain irradiation history, each fresh fuel converts to a spent fuel (SF) with a specific burn-up. Dealing with the spent nuclear fuel is one of the most challengeable issues in the peaceful use of nuclear technology, both in terms of protection of public and the environment from hazard effects of ionization radiation.

During the process of nuclear fission, hundreds of fission isotopes are created in the SF. However, most of them have short half-life and will completely decay within a few days or weeks of interim

storage period [2]. in the opposite side, high half-life radionuclides such as Cs-137 will maintain their long-term radioactivity effects [3, 4].

Meanwhile the recent studies on SFs are based on photon and neutron emissions, the use of gamma emission is commonly used because of the wide range of gamma detectors, conventional calibration and ease of work. Calculations such as SF burn-up, validating the nuclear materials in the fuel, or fuel dosimetry are some studies. Thermo-luminescent dosimeters (TLDs) are one of available tools for these purposes [5, 6]. The TLD dosimeters are commonly applied in both personal and environmental radiation monitoring. These dosimeters are able to report the cumulative dose over a certain period of time.

In our previous research investigation, the effect of some parameters such as fuel burn-up, radiation history and cooling time on the ratio of air to water environmental dose has been simulated by using the Monte Carlo code (MCNPX) [1]. The dosimetry of specific TRR spent fuel, based on gamma radiation is the purpose of this experimental work. Accordingly, by using a TLD, the delivered dose by the SF will be obtained in water and air environments. Finally, the matrix (at different distances) of the dose rate ratio will be reported. By having this matrix, it is possible to measure the dose rate in water and then calculate the dose rate in air for some purposes, including radioactive waste management purposes [7, 8] in determining the decay heat for its storage; nuclear safeguards [9] in order to irradiate fuel assemblies whose dose rate falls down below a certain limit; or in cask design [2, 10] in the decay heat calculations.

Experimental

The dosimeter used in this research was GR-200 (Beijing P.R, China) thermo-luminescent type (LiF:Mg,Cu,P) which is sensitive to both gamma and beta radiations. This type of dosimeter, which has higher sensitivity and wider linear range than TLD-100 (personal dosimeter), is mostly used in environmental dosimetry studies. The linear range for GR-200 is 10^{-6}-10 Gy (R^2=0.9997) while this range for TLD-100 is 10^{-5}-1 Gy [11-13].

There is no radiation safety challenge, when the SF dosimetry was carried out in water. However, in measuring the dose rate of these high radioactive items in the air environment, high radiation exposure will be unavoidable. In this regard, decreasing the pool water level will also be an impractical solution,

because it will increase the dose level beyond the dose limit. In order to overcome this challenge, in a creative strategy, the air was transferred (by dry channel) to the water (storage pool) instead of transferring the SF to the open environment. Therefore, a waterproof polymer (with minimum radiation attenuation) tube as a dry channel was design and placed in the front of the SF in question. Figs. 1 shows three TLD pellets (each in a plastic bag) placed in the sealed dry channel.

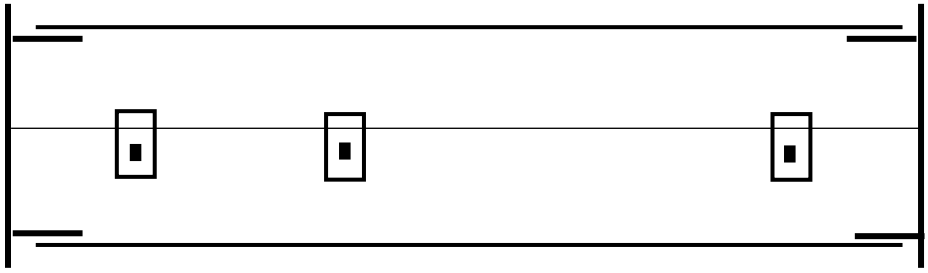

Fig. 1. The view of 3 TLD packs on the central wire in dry channel

For doing SF dosimetry, the TLDs were first coded and placed in plastic zipper bags. Then the pellets were fixed at the certain distances on a wire which was passed through the middle of the dry channel caps. Finally, the tube was sealed and placed in front of SF in storage pool. In this experimental work, the distances of 20, 50 and 100 cm were considered to investigate the dose in the air.

Fig. 2 shows a side view of the dosimetry process in the storage pool. The dry channel and shield are moved and steered by a crane into the storage pool. The low burn-up SF assembly came out from its position and moved to the corner of the pool and fixed by a fuel holding rod. In the following, the dry channel is set exactly in front of and at the central plane of the SF for a certain period of time. This position has highest gamma flux and consequently cause the highest TLD absorbed dose due to its high fuel burn-up [4]. To measure the SF dose in water medium, the experiment was done in a same manner but without the presence of the dry channel. In this phase, distances of 10, 20 and 50 cm were considered to investigate the dose rates in the water. Also, another TLD as witness is used for background measurement.

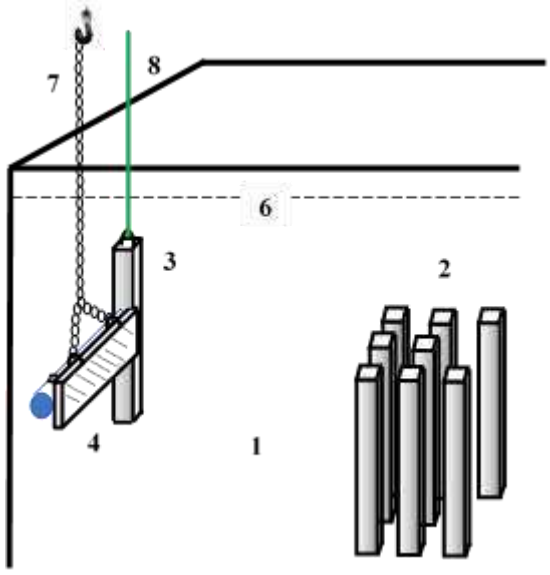

Fig. 2. Side view of the dosimetry arrangement in the storage pool. 1: pool, 2: Other SFs in the rack, 3: SF in question, 4: Shield, 5: Dry channel, 6: Water level, 7: Crane, 8: Fuel holding rod.

After the ending of irradiation phase, the dosimeters were sent to the TLD reading laboratory (Harshaw-4500 TLD Reader).

Results and discussion

In this experimental work, the distances of 20, 50 and 100 cm were considered to investigate the dose rate in the air and the distances of 10, 20 and 50 cm were considered to check the dose rate in the water environment. The distances were chosen in such a way that we do not have the challenge of dosimeters saturation. In addition, two distances of 20 cm in water and 100 cm in air have been emphasized as reference distances which are important in TRR safeguards measurements. Since the pellets were irradiated with no badge (tissue equivalent filter), the reportable dosimetry quantity will be the environmental dose. Due to the radiation weighting factor of 1 for both gamma and beta radiations, the absorbed dose is mentioned as equivalent dose (mSv). Table 1 shows the dosimetry results for a low burn-up SF in two environments. As mentioned before, this will be the maximum value (in front of and at the central plane position) for absorbed dose. Taking into account the radiation exposure time, dose rate quantity could be achievable.

Table 1. TLD dosimetry results of SF

TLD Code	Irradiation time (hr)	environment	Distance (cm)	Dose rate (mSv/hr)
I12			20	427.95
J11	2:35’	Air	50	67.67
J12			100	10.26
I10			10	308.35
I8	7:00	Water	20	97.09
I1			50	4.43

Since our purpose is to calculate the air to water dose rate ratio, coefficients such as reference lights, ECC and CF in Eq. 1 will practically have no effect on the results. According to Table 1, the ratio of air to water dose rate (f) will be easily obtained. For example, calculating this ratio in 100 cm of air to 20 cm of water will be equal to:

$$f \equiv \frac{D_{air(100)}}{D_{w(20)}} = 0.106 \cong 0.11 \quad (3)$$

It should be mentioned that this ratio (0.11) has been previously obtained by Monte Carlo simulation [1]. Table 2 gives the matrix of gamma dose rate ratios (air to water) at different distances from the SF.

Table 2. Air-to-water gamma dose ratios (f) at different distances from the SF

		Distance in water (cm)		
		10	20	50
Distance in air (cm)	20	1.39	4.40	96.52
	50	0.22	0.70	15.27
	100	0.03	0.11	2.32

Conclusions

The most common approach to store materials with high and very high dose rate is to store them under water. The SFs are not excluded from this. The dosimetry of these very high dose rate items is particularly complicated, especially during short cooling times. In this research work, direct

measurement of the gamma dose rate from a low burn-up SF was carried out in two environments (water and air) by TLD dosimeters (GR-200). A stainless steel slab shield was designed for not only reduce the background radiation, but as a tool for immersing the light weight dry channel in water. While the dosimetry process was carried out under water, the challenge of direct dosimetry in the air environment was overcome by designing a dry channel. Finally, the matrix of dose rate ratios at different distances in these two environments were obtained (Table 2.). As a validation, it should be mentioned that the calculating this ratio in 100 cm of air to 20 cm of water (f=0.11) has been previously obtained by Monte Carlo simulation. By having this matrix, it is possible to measure the dose rate in water and then calculate the dose rate in air with an acceptable estimation. It should be mentioned that the dosimetry system has passed the trumpet curve standard, which will ensure that reported doses have an acceptable uncertainty (95% confidence level) but as a complementary suggestion, using at least 3 dosimeters in each plastic bag makes the statistical calculations possible.

Acknowledgements

It would not have been possible to do this experimental work without the cooperation of the TRR operators, especially Mr. Kivani, Shahoseini and Moasesi. The author also thanks to Ms. Vahhabi for reading the TLD dosimeters.

References

1. Gholamzadeh, Z., R. Adeli, and M. Keivani, Investigation of the air to water conversion factor dependency to the spent fuel cooling time, irradiation history and burnup for gamma dose rate determination of TRR spent fuels. Radiation Physics and Engineering, 2021. **2**(1): p. 1–7.
2. Sobolev, A.V. and P.A. Danilov, Problems of radiation safety calculations related to spent nuclear fuel transport casks. Nuclear Energy and Technology, 2020. **6**: p. 43.
3. Favalli, A., et al., Determining initial enrichment, burnup, and cooling time of pressurized-water-reactor spent fuel assemblies by analyzing passive gamma spectra measured at the Clab interim-fuel storage facility in Sweden. Nuclear Instruments and Methods in Physics Research Section A: Accelerators, Spectrometers, Detectors and Associated Equipment, 2016. **820**: p. 102-111.

4. Terremoto, L., et al., Gamma-ray spectroscopy on irradiated MTR fuel elements. Nuclear Instruments and Methods in Physics Research Section A: Accelerators, Spectrometers, Detectors and Associated Equipment, 2000. **450**(2-3): p. 495-514.

5. Ohno, A. and S. Matsuura, Measurement of the gamma dose rate distribution in a spent fuel assembly with a thermoluminescent detector. Nuclear Technology, 1980. **47**(3): p. 485-493.

6. Pergreffi, R., et al., Gamma dose rates from a spent UO2 fuel Assembly: Calculations vs measurements. Annals of Nuclear Energy, 2022. **165**: p. 108755.

7. Tupasela, T., et al., Passive neutron albedo reactivity measurements of spent nuclear fuel. Nuclear Instruments and Methods in Physics Research Section A: Accelerators, Spectrometers, Detectors and Associated Equipment, 2020: p. 164707.

8. Bell, M. and A.M. Macfarlane, Fixing the nuclear waste problem? The new political economy of spent fuel management in the United States. Energy Research & Social Science 2022. **91**(3): p. 102728.

9. Willman, C., Applications of gamma ray spectroscopy of spent nuclear fuel for safeguards and encapsulation, in Faculty of Science and Technology. 2006, Acta Universitatis Upsaliensis. p. 82.

10. Trtik, P., et al., Sample container for high-resolution neutron imaging of spent nuclear fuel cladding sections. Rev. Sci. Instrum., 2020. **91**.

11. McKeever, S.W., M. Moscovitch, and P.D. Townsend, Thermoluminescence dosimetry materials: properties and uses. 1995.

12. Horowiz, Y. and A. Horowitz, Characterisation of LiF: Cu, Mg, P (GR-200) for personnel thermoluminescence dosimetry. Radiation Protection Dosimetry, 1990. **33**(1-4): p. 279-282.

13. ISO. (2013). Practice for use of a thermoluminescence – dosimetry system (TLD system) for radiation processing. ISO/ASTM 51956. 2013.

ICNST 2024
International Conference on Nuclear Science and Technology
6- 8 MAY 2024 | Isfahan, Iran

Neutronic Analysis of two-channel cooled Annular Fuel in the Core of the Bushehr reactor in the MCNPX (Paper ID : 1471)

Z.Tayyari-Sadegh, F. Zolfagharpour
University of Mohaghegh ardabili, Ardabil, Iran

Abstract

In this article, the use of annular fuel instead of the current solid fuel in the core of the Bushehr reactor is investigated. Five types of annular fuel with different inner and outer radii as well as solid fuel currently used in BNPP, are simulated in MCNPX.2.6.0 code. By comparing the results of solid fuel burnup during 300 days with FSAR data, the simulation has been validated. Then, for annular fuels, some neutronic parameters have been calculated, such as; effective multiplication factor, radial and axial changes of neutron flux, production of neutron poisons and negative reactivity caused by them and the burnup during 300 days of reactor operation. By examining the results, the optimal geometry has been selected from the proposed annular geometries. The criterion for choosing the optimal fuel geometry is based on the volume close to the current fuel rod volume and increasing the surface-to-volume ratio in order to increase burnup, without changing the current operating power. The results showed that while the operating power of the reactor is kept constant and other neutronic parameters remain close to solid fuel, the burnup increases by using annular fuel instead of solid fuel.

Keywords: *Annular Fuel, Solid Fuel, BNPP, Burnup, MCNPX.*

1. Introduction

In recent years, due to the increase in electricity demand, efforts have been made to increase the power of nuclear plants. One of the ways to increase the power of the reactor is to increase the fuel enrichment or increase the number of fresh fuels. In addition to that, increasing Burnup, is one of the ways to increase power, while the fuel cycle is maintained and it is economical [1].

Increasing the ratio of surface to volume in fuel rods, causes an increase in burnup. For increase the ratio of surface to volume of fuel, we can reduce the size of the fuel and increase their number. But this is not recommended due to reduction in rigidity of rods against vibrations, and avoid the penalty of corrosion of thinner cladding [2-4].

Another way to increase the surface-to-volume ratio is to change the geometry of the fuel from solid to annular with the ability to cool from two channels, which was proposed and led by MIT and funded by the U.S. DOE Nuclear Energy Research Initiative (NERI), in 2006 [5].

Also, it has been proposed for light-water reactors (LWR) by Blinkov et al. to achieve higher average power density without increasing reactor vessel dimensions [6].

The researches show that annular fuel with both internal and external cooling channels, achieve better temperature distribution and leads to high linear heat generation rate [7]. It has also been observed that annular fuel pellets has low fission gas release and raised MDNBR [2].

H. T. Kim et al. have investigated the effect of reducing the maximum temperature ofannular fuel in the LOCA Accident [8].

In the present work, we simulated the core of BNPP reactor in MCNPX.2.6.0 code, using annular fuels with different radii and pitches, and extracted some neutronic parameters. The reactor was considered at first cycle of operation which the control rods are out of the core right top of core, and in operation temperature 300 ℃. The way to enter the temperature in the MCNPX code is by writing the energy in units of Mev in the KT relation (K is the Boltzmann's constant and T is temperature in unit Kelvin). The input “TEMP” for cladding and fuel in code is tmp=4.91 2e-8 and tmp=7.522e-8, respectively.

Similar this work, N. El-Sahlamy et al. did in [9]. They used the MCNP6 code to evaluate the neutronic design and basic safety parameters of the annular fuel. They compared standard solid fuel with a new annular fuel performance in the core of a PWR. Also M.Amin Mozafari and F.Faghihi, used MCNP5 to find neutronic parameters of the core with annular fuel rods applicable to VVER-1000 type reactors [10].

By comparing the results of solid fuel burnup during 300 days with FSAR data, the neutronic simulation has been validated. After validation, some neutronic parameters have been calculated, such as; effective multiplication factor, radial and axial changes of neutron flux, production of neutron poisons and negative reactivity caused by them and the burnup during 300 days of reactor operation. By examining the results, the optimal geometry has been selected from the proposed annular geometries. The criterion for choosing the optimal fuel geometry is based on the volume close to the current fuel rod volume and increasing the surface-to-volume ratio in order to increase burnup, without changing the current operating power or the size of core. Then, by analyzing the

results, we selected and introduced the optimal geometry among the 5 types of proposed geometries.

2. Explanation about BNPP core

BNPP is a LWR reactor that supplies nuclear electricity. That is a VVER type of pressurized water reactors that developed in Russia in the 1960s [11,13]. The name comes from the abbreviation of Water-Water Energy Reactor (WWER), which translates into Russia as Voda-Voda Energo Reactor (VVER). VVER is one of the most prosperous and influential branches of nuclear power plant development (NPP). And the technology is widely used worldwide [13].

The core of BNPP is composed of 163 fuel assemblies. The geometry of core and assemblies are hexagonal. Each assembly consists of 331 hexagonal channels which 311 fuel rods located in 311 channels. The one of 20 special channels is the central channel and one of them is used to place neutron measuring sensors. The remained 18 channels are guiding channels where Control Protection System (CPS) absorbing rods move at them [13].

Details of the fuel assembly types used for BNPP core are presented in Table 1.

The main characteristics of BNPP core, are presented in Table 2.

The highest enrichment of ^{235}U in the fuel rod is 3.6%. More details about the isotopic compositions of other material's structure is presented in the FSAR [14].

3. Modeling method

MCNPX code is based on Mont Carlo method for nuclear simulation and calculations which can track so many types of particles such as photons, mesons, leptons (including electrons), and hadrons (including neutrons) and transport them. One can use this code for design, shielding, nuclear safety, and other proposes. This code works using evaluated cross-sections introduced in the form of an ENDF library [12].

In this work, evaluated neutron data based on ENDF/B-VII.1 was used as the data source.

The horizontal and vertical scheme of core geometry simulated in MCNPX code, are presented in Figs. 1-2. And the horizontal cross-section view of quarter detailed structure of the core is shown in Fig. 3.

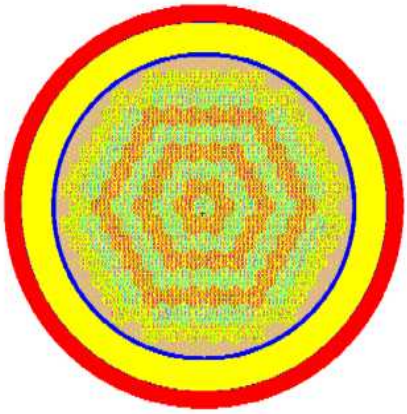

Fig 1. Horizontal cross-section of BNPP core simulated by MCNPX.

Table 1. Description of the six different types of fuel assemblies in BNPP core [14].

FA. Type	Number of fuel rods	U-235 enrichment (Wt %)	Number of BARs	Content of boron (natural) in absorbing material (g/cm^3)	Number of CPS ARs	Number of GCs
FA16	311	1.6	-	-	18	2
FA24	311	2.4	-	-	18	2
FA36	311	3.6	-	-	18	2
24B20	311	2.4	18	0.020	-	2
24B36	311	2.4	18	0.036	-	2
36B36	311	3.6	18	0.036	-	2

Table 2.
The BNPP core description [14].

The main core Characteristics	Value
Core & FA form in a plane	Hexagonal
Number of fuel assemblies	163
FA pitch in core (cm)	23.6
Fuel rod pitch in assembly (mm)	12.75
Core equivalent diameter (cm)	316
Temperature at the inlet (˚C)	291
Fuel pellet material	UO^2
Cladding material	Alloy Zr+1%Nb
Cladding outside diameter (mm)	7.73
Fuel pellet outside diameter (mm)	7.57
Hole diameter in the fuel pellet (mm)	1.5
Fuel pellet density (g/cm^3)	10.4…10.7
Absorbing material in CPS AR (combined)	B_4C+($Dy_2O_3TiO_2$)
$Dy_2O_3TiO_2$ absorber height in control rod (cm)	30
B_4C absorber height in control rod (cm)	320
Absorbing material in BAR	CrB_2+Al

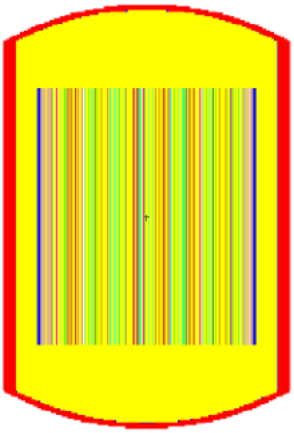

Fig2. Vertical cross-section of BNPP core simulated by MCNPX.

We simulated the real operation conditions of the reactor by adjusting POWER and PFRAC cards in the code. By calculating burnup under the same adjusting, we observed that the outputs are in good agreement with FSAR. This conformity of the results showed that the conditions considered in the input of the code simulate the real operation conditions of the reactor. Thus the MCNPX model of the BNPP core validation was performed and the following parameters were calculated in mentioned validated conditions. This validation in detailed is shown in Fig.4. In the Fig.4 the burnup results in MCNPX is compared with Burnup data in FSAR duration 300 days operation.

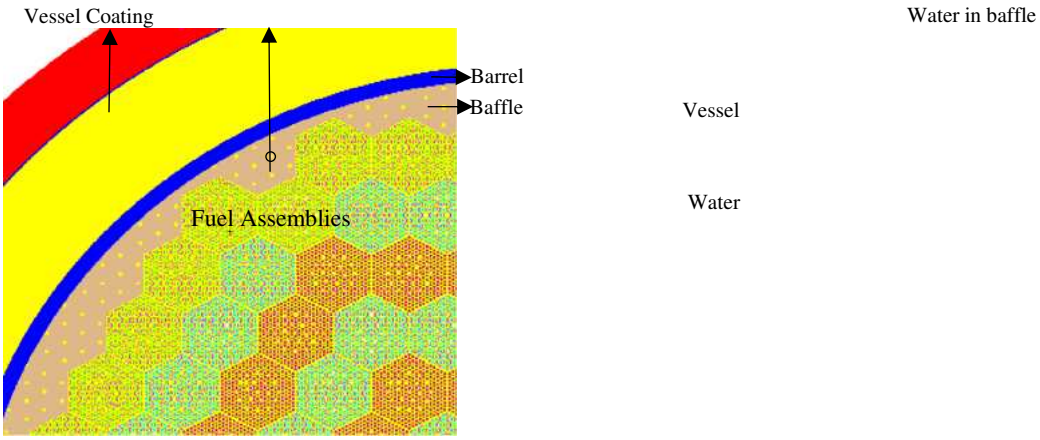

Fig.3. Horizontal cross-section of BNPP core simulated by MCNPX code.

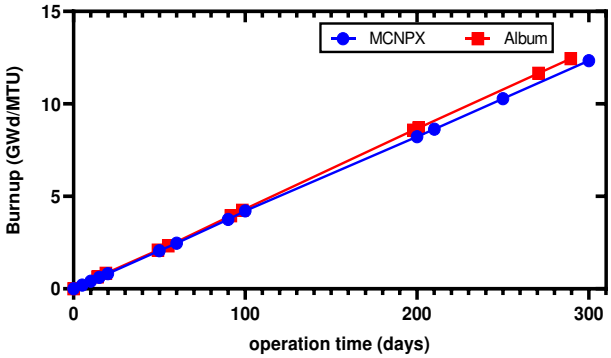

Fig. 4. Comparison of Bushehr FSAR (Neutronic Album) and MCNPX output Burnup.

Five types of annular fuels are proposed in this work. Suggested annular geometries are different in terms of internal and external radii and rod pitches in the assembly. The selection criterion of these data is based on maintaining the volume of fuel used in the Solid case, and increasing the area of the fuel surface. After ensure from accuracy of simulation in MCNPX, we designed and simulated the core of reactor with proposed annular fuels. The simulated assemblies with annular fuels are zoomed in and shown in Fig. 5. And the geometric characteristics of annular fuels, along with solid fuel, are given in Table 3.

The selection criterion is based on choosing the volume of the rods close to the current solid fuel volume in order to increase the surface-to-volume ratio, while for the diameter of the water in the inner and outer channel of the annular fuel, different values have been considered.

Table 3. Characteristics of annular fuels and solid fuels.

Fuel type	Inner radius (mm)	Outer radius (mm)	Fuel thickness (mm)	Fuel volume (cm^3)	Number of fuels in assembly	Total mas of fuel in assembly (kg)	Total mass of fuel in core (t)
Type 1	4.25	5.62	1.37	149.955	210	330.65	53.896
Type 2	4.25	5.62	1.37	149.955	162	255.07	41.576
Type 3	4.55	5.85	1.3	149.93	162	255.03	41.57
Type 4	4.75	6	1.25	149.01	162	253.466	41.314
Type 5	5.35	6.5	1.15	151.126	120	190.418	31.038
Solid	Central hole radius 0.75	3.785	3.035	152.637	311	498.436	81.245

It is emphasized that the size of the core and the assemblies and assembly pitches (=23.6 cm), remain intact, as well as the materials. And we have only changed the geometry of the fuel rods

and therefore the fuel numbers and pitches in the assembly.The fuels in more detailed are presented in table 4.

4. Neutronic Analysis

4. 1. Multiplication factor; Time Changes

Considering only fuel burnup, the effective multiplication factor will certainly decrease over time. Plotting the output data of the code also shows the same in Fig 6. This figure also shows the closest effective multiplication factor to the solid fuel. It is the annular fuel type 1 that has closest data to solid fuel.

Of course, the reduction of the multiplication factor is compensated by chemical shim which the concentration of the boron shim must be reduced to keep the reactor critical [15].

Table 4. The more details of fuels[10].

	Type1	**Type2**	**Type3**	**Type4**	**Type5**	**solid**
Fuel pitch (mm)	15.94	16.64	17.1	17.4	18.6	12.75
Number of fuels	210	162	162	162	120	311
Diameter of inner channel (mm)	7	7	7.6	8	9.02	No inner channel
Minimum distance between outer neighbor cladding (mm)	3	3.7	3.7	3.7	3.7	3.65
Fuel thickness (mm)	1.37	1.37	1.3	1.25	1.15	3.035
Outer cladding thickness (mm)	0.8	0.8	0.8	0.8	0.9	0.685
Inner cladding thickness (mm)	0.7	0.7	0.7	0.7	0.8	Without inner cladding
Outer Helium thickness (mm)	0.05	0.05	0.05	0.05	0.05	0.08
Inner Helium thickness (mm)	0.05	0.05	0.05	0.05	0.04	Helium radius in central hole **= 0.75**

[10] In this table, the pitch of fuels has been changed, it may have an effect on the working conditions of the reactor, so it may be necessary to check the extent of this effect in a separate research.

4. 2. Uranium isotopes Depletion

Using the output data of the code, the mass of U isotopes were manually calculated via calculation of their density. The mass variation of U(235) and U(238) isotopes trough 300 days burnup, have been determined for Annular and Solid fuels are presented in Figs. 7-8.

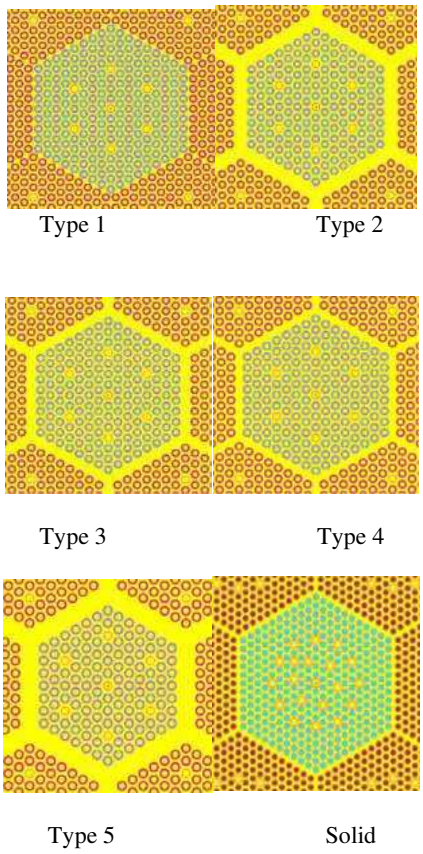

Fig. 5. Simulated assemblies with annular and solid fuels in MCNPX.

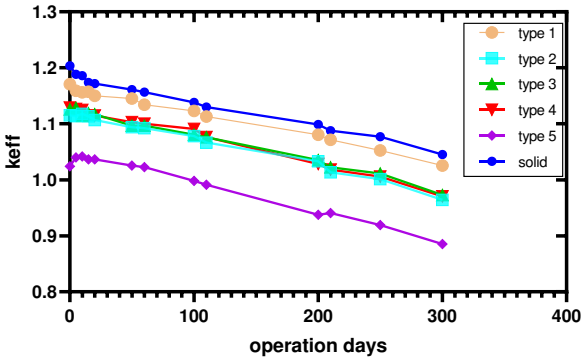

Fig 6. Time change of k_{eff} due to "burnup" only.

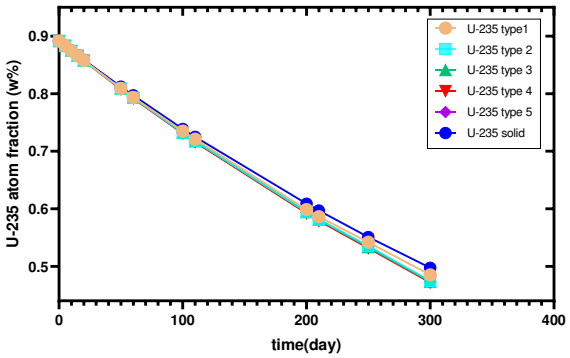

Fig 7. U-235 depletion versus time operation.

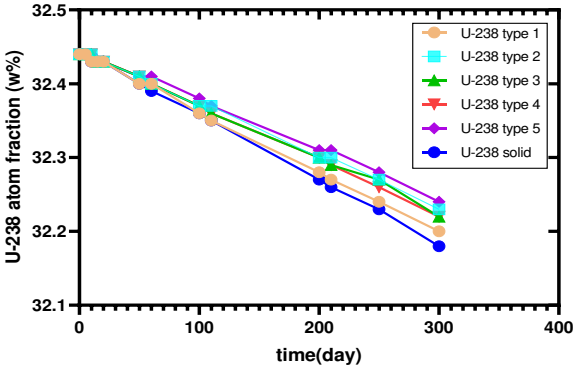

Fig 8. U-238 depletion versus time operation.

$$M_{(UO_2)} = 0\,024 \times 235 +$$

$$+0\,975 \times 238 +$$

$$+2 \times 16 = 269\,69\ g$$

4. 2. Pu-239 Production

According to the Fig 9, in all cases an increase is observed for 239Pu isotopes as the operation time and the burnup increases. This is true because 239Pu is produced from 238U transmutation and the 238U becomes transmuted as reactor operates and time goes.

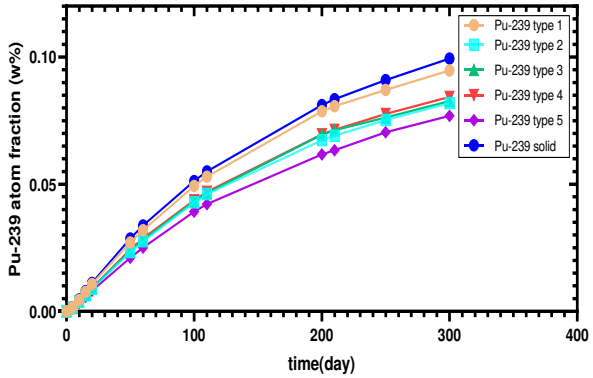

Fig 9. Pu-239 production versus time operation.
In all cases at first, amount of ^{239}Pu increases gradually then the gradient of graph decreases. This is true because as time goes, the amount of ^{239}Pu itself fissions with thermal neutrons.

4. 3. Neutron poisons; Negative reactivity

Again, using the output data of the code, the mass of some non-actinide isotopes such as ^{135}Xe and ^{149}Sm as fission productions, were manually calculated via calculation of their density.

Xe-135 and Sm-149 atom densities:

$$\rho_{(UO_2)} = 10\,5\ {}^{g}/_{cm^3}$$
$$N_{(UO_2)} = 0\,0234 \times 10^{24}\ atm/cm^3$$
$$N_{(Xe)} = atom\ fraction(output\ file) \times N_{(UO_2)}$$
$$N_{(Sm)} = atom\ fraction(output\ file) \times N_{(UO_2)}$$

$$N_{(UO_2)} = \frac{\rho_{(UO_2)} N_A}{M_{(UO_2)}}$$

ρ: mass density
N: atom density

It is important to know the information about the negative reactivity variations to adjust the reactor criticality. The negative reactivity is defined as relative reduction in multiplication factor.

Xe-135 and Sm-149 negative reactivity:

$$\rho_{Xe,Sm} = -\frac{\Sigma_{a,Xe,Sm}}{\Sigma_{a,U235}} f$$

$$f < 1 \qquad f \approx 1$$

$$\frac{\Sigma_{a,Xe,Sm}}{\Sigma_{a,U235}} = \frac{N_{Xe,Sm}}{N_{U235}} \times \frac{\sigma_{a,Xe,Sm}}{\sigma_{a,U235}}$$

$$\frac{N_{Xe,Sm}}{N_{U235}} = \frac{N_{Xe,Sm}}{N_{UO_2}} \times \frac{N_{UO_2}}{N_{U235}}$$

$$N_{U235} = 0\ 0244 N_{UO_2}$$

$$|\rho_{Xe,Sm}| = \frac{\text{atom fraction}}{0\ 0244} \times \frac{\sigma_{a,Xe,Sm}}{\sigma_{a,U235}}$$

$$\frac{N_{Xe,Sm}}{N_{UO_2}} = \text{atom fraction (from output file)}$$

$$\sigma_{a,Xe} = 2\ 6 \times 10^6\ b$$

$$\sigma_{a,Xe} = 2\ 6 \times 10^6\ b$$

ρ: reactivity
f: thermal utilization

Because the both of ^{135}Xe and ^{149}Sm have very high thermal neutron absorption cross sections [15], these non-actinide isotopes are named "neutronic poisons". The high absorption cross section of non-actinides, causes a reduction in multiplication factor.

Injection of negative reactivity by neutron poisons are given in Figs 10-11. These plots are the results of the manual calculations mentioned above. In these calculations, the output data of the code is entered.

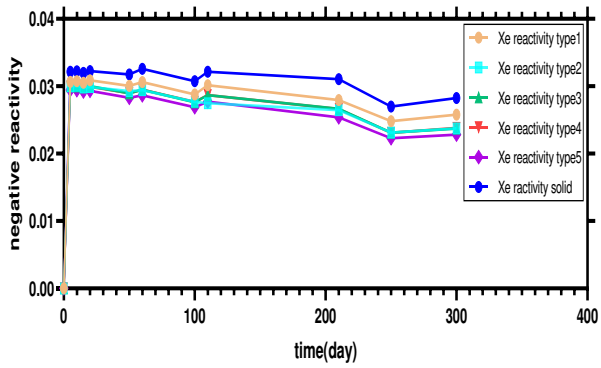

Fig 10. Negative reactivity due to Xe-135 production.

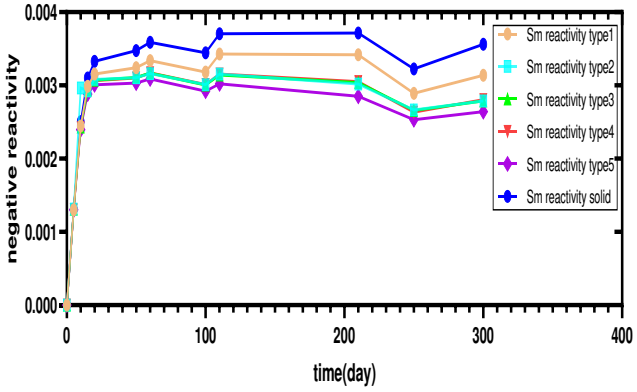

Fig 11. Negative reactivity due to Sm-149 production

Comparing Figs 2 and 3 shows that in all cases, Xe-135 reaches stability earlier than Sm-149. But Sm-149 injects higher negative reactivity into the reactor. These results are in agreement with theoretical and experimental data [15].

4. 4. Thermal neutron flux

The flux distribution of the core, is determined using MESH tally superimposed on the axial mid plane of the full core. The radial and axial thermal neutron flux distributions of all cases are shown in Figs 12 -13 respectively.

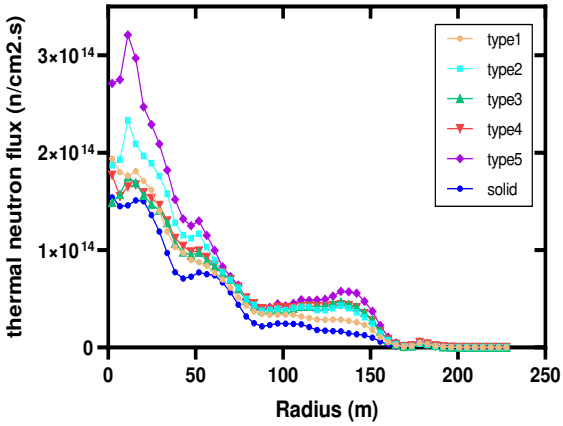

Fig. 12. The thermal neutron flux distribution along radius (RFD) of core using MESH tally in MCNPX.

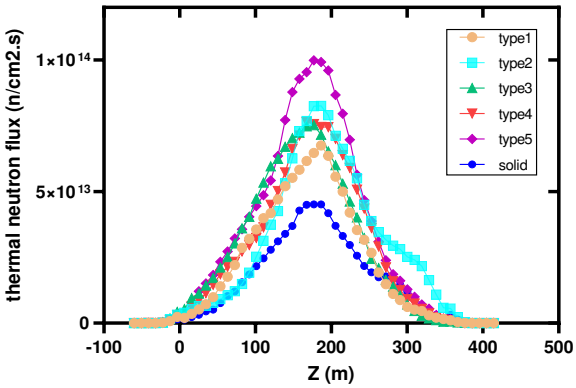

Fig. 13. The thermal neutron flux distribution along Height (HFD) of core using MESH tally in MCNPX.

The power of reactor is determined by neutron flux level [15]. Then the local power depends on the local neutron flux level. Thus can be concluded that the power distribution depends on neutron flux distribution and to achieve the flattened power distribution, the neutron flux distribution must be flattened.

The Figs 12-13 show explicitly that the radial as well as axial neutron flux in annular Type 1 case is more flattened compared with others.

4. 5. Burnup calculations

Also, for the proposed types of annular fuels, we calculated burnup, during 300 days of reactor operation. The calculation performed in units gigawatts days per metric ton uranium (GWd/MTU) by MCNPX code and the results are shown in Fig 14, which compares the amount of burnups for various annular and solid fuels. And also compare them with FSAR data.

As can be seen from the figure, the amount of burnup has increased significantly in the annular fuel and the highest increase in Burnup, has occurred for annular fuel Type1.

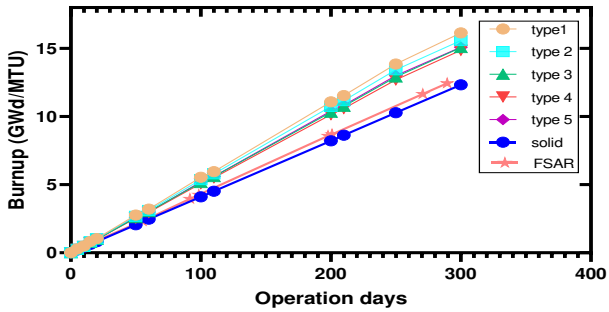

Fig 14. Burnup comparison between annular types and solid fuels.

6. Conclusion

In this work, the use of annular fuel instead of solid fuel was investigated from the neutronic point of view in MCNPX. The results showed that among five proposed annular fuel, the annular fuel type1 has the closest neutronic parameters to the solid fuel while it causes an increase in fuel burnup. This will cause an increase in the length of the working cycle of the reactor. Also it has a significant economic benefit because the total mass of the fuel used is reduced, while the total power and the size of the core and the size of the assemblies remain unchanged. Thus the annular fuel type1 is proposed for use in reactor.

References

[1] Bo Feng, Mujid S. Kazimi, "On the Use of High Performance Annular Fuel in PWRs", Massachusetts Institute of Technology, June 2008.

[2] Kazimi, M.S., P. Hejzlar, et al., "High Performance Fuel Design For Next Generation PWRs: Final Report", MIT-NFC-PR-082, Center for Advanced Nuclear Energy Systems, MIT (Jan 2006).

[3] P.Hejzlar, M.S.Kazimi, "Annular Fuel for High-Power-Density Pressurized Water Reactors: Motivation and Overview", October 2007 Nuclear Technology 160(1):2-15.

[4] Kazimi, Mujid S., et al., "High Performance Fuel Design for Next Generation PWRs: Final Report", Massachusetts Institute of Technology. Center for Advanced Nuclear Energy Systems. Nuclear Fuel Cycle Program, 2006-01.

[5] D. Feng, et al., "Thermal-Hydraulic Design of High PowerDensity Annular Fuel in PWRs", Nuclear Technology, Vol.160, pp.16~44, 2007.

[6] Blinkov, V., et al., "Prospects for using annular fuel elements in nuclear power engineering". Thermal Engineering, 2010. Vol. 57: p. 213-218.

[7] N. Todreas and M. Kazimi, Nuclear System, Volume 1 "Thermal Hydraulic Fundamentals", Maaschussets Institute of Technology (2011).

[8] H. T. Kim et al., ''Performance of internally and externally cooled annular fuel in loss of coolant accident,'' Proc. International Congress on Advanced Nuclear Power Plants, Hollywood, Florida, USA, June 9–13, 2002 (2002).

[9] N. El-Sahlamy, M. Hassan and A. Khedr, "Comparison between standard Solid Fuel and a new Annular Fuel performance in the Core of a PWR", Kerntechnik, De Gruyter, February 23,2021.

[10] M.Amin Mozafari, F.Faghihi, "Design of annular fuels for a typical VVER-1000 core: Neutronic investigation, pitch optimization and MDNBR calculation", Annals of Nuclear Energy, Volume 60, October 2013, Pages 226-234.

[11] Katona, T.J., 2011. "Long-term operation of VVER power plants", In: Tsvetkov, P.v.(Ed), Nuclear Power – Deployment. Operation and Sustainability, In Tech, pp. 153-196.

[12] Milad Afzali, et al., "Optimization and burnup calculations of BNPP's reactor core with the new generation fuels (TVS-2M) by artificial neural network", Progress in Nuclear Energy 150 (2022) 104209.

[13] Heba K. Louis, Esmat Amin, "Burnup and neutronic analysis for UOX and MOX fuel assemblies in VVER reactor", Annals of Nuclear Energy 164 (2021) 108586.

[14] Atomic Energy Organization of Iran (AEOI), 2003, Final Safety Analysis Report (FSAR) for Bushehr VVER-1000 Reactor. John R. Lamarsh, "INTRODUCTION to NUCLEAR REACTOR THEORY", NEW YOBK UNIVERSITY ADDISON-WESLEY PUBLISHLNG COMPANY Readmg.

ICNST 2024
International Conference on Nuclear Science and Technology
6- 8 MAY 2024 | Isfahan, Iran

Investigation of Temperature distribution and DNBR Safety margin in two-channel cooling Annular Fuel in VVER-1000 reactor (Paper ID : 1474)

Z.Tayyari-Sadegh, F. ZolfagharpourWe
University of Mohaghegh ardabili, Ardabil, Iran

Abstract

In this article, the annular fuel geometry, has been investigated from a thermohydraulic point of view, for use in the Bushehr reactor, instead of solid fuel. The annular geometry of the fuel has two external and internal cooling channels, and the heat exchange between the fuel and cooling, occurs through two surfaces. The geometrical simulation of the hottest solid and annular fuel rod, as well as their meshing, has been done in ANSYS and the solution of the Navier-Stokes equations has been done in FLUENT. For validating the simulation, the results of solving the solid fuel problem in Fluent were compared with the corresponding results in the COBRA code. By ensuring the accuracy of the simulation, the results of solving the annular fuel problem by Fluent, were evaluated in CFD-Post processing. The results showed that while the operating power of the reactor is kept constant, the DNBR safety margin for annular fuel increases, and the maximum temperature in center of annular fuel decreases.

Keywords: *Annular Fuel, Solid Fuel, BNPP, DNBR, ANSYS FLUENT.*

1. Introduction

In recent years, due to the increase in electricity demand, efforts have been made to increase the power of nuclear plants. One of the ways to increase the power of the reactor is to increase the fuel enrichment or increase the number of fresh fuels. In addition to that, the way which is also economical, is the increase of Burnup, while the fuel cycle is maintained [1].

Increasing the ratio of surface to volume in fuel rods, causes an increase in burnup. For increase the ratio of surface to volume of fuel, the size of the fuel can be reduced and their number increased.

But this is not recommended due to reduction in rigidity of rods against vibrations, and avoid the penalty of corrosion of thinner cladding [2-4].

Another way to increase the surface-to-volume ratio is to change the geometry of the fuel from solid to annular with the ability to cool from two channels, which was proposed and led by MIT and funded by the U.S. DOE Nuclear Energy Research Initiative (NERI), in 2006 [5].

Also, it has been proposed for light-water reactors (LWR) by Blinkov et al. to achieve higher average power density without increasing reactor vessel dimensions [6].

The researches show that annular fuel with both internal and external cooling channels, achieve better temperature distribution and leads to high linear heat generation rate [7]. It has also been observed that annular fuel pellets has low fission gas release and raised MDNBR [2].

H. T. Kim et al. have investigated the effect of reducing the maximum temperature ofannular fuel in the LOCA Accident [8].

In this work, the thermohydraulic analysis of the use of anular fuel, which it's characteristics will be defined later, is presented, For this purpose, the hottest annular fuel rod has been simulated in ANSYS FLUENT and its results have been compared with the corresponding results for solid fuel. For validation of thermohydraulic simulation, the COBRA-EN code is used and the BNPP core with solid fuels was simulated, then the results was compared with the results of FLUENT. The results showed a decrease in the maximum temperature of annular fuel center and an increase in the safety margin DNBR compared to solid fuel. These results were in agreement with the results of O.C.Joseph et al. work, who presented analytical model in their research about temperature distribution of annular fuel and used ANSYS APDL to validation [9].

2. Description of BNPP core

BNPP is a LWR reactor that supplies nuclear electricity. That is a VVER type of pressurized water reactors that developed in Russia in the 1960s [10]. The name comes from the abbreviation of Water-Water Energy Reactor (WWER), which translates into Russia as Voda-Voda Energo Reactor (VVER). VVER is one of the most prosperous and influential branches of nuclear power plant development (NPP). And the technology is widely used worldwide [11].

The core of BNPP is composed of 163 fuel assemblies. The geometry of core and assemblies are hexagonal. Each assembly consists of 331 hexagonal channels which 311 fuel rods located in 311

channels. The one of 20 special channels is the central channel and one of them is used to place neutron measuring sensors. The remained 18 channels are guiding channels where Control Protection System (CPS) absorbing rods move at them [12].

Details of the fuel assembly types used for BNPP core are presented in Table 1.
The main characteristics of BNPP core, are presented in Table 2.
The highest enrichment of ^{235}U in the fuel rod is 3.6%. More details about the isotopic compositions of other material's structure is presented in the FSAR [13].
The core of reactor with annular and solid fuels was designed and simulated in MCNPX.2.6.0 code. MCNPX code is based on Mont Carlo method for nuclear simulation and calculations which can track so many types of particles such as photons, mesons, leptons (including electrons), and hadrons (including neutrons) and transport them. One can use this code for design, shielding, nuclear safety, and other proposes. This code works using evaluated cross-sections introduced in the form of an ENDF library. In this work, evaluated neutron data based on ENDF/B-VII.1 was used as the data source.

The simulated assemblies with annular fuels are zoomed in and shown in Fig. 1. And the geometric characteristics of annular fuels, along with solid fuel, are given in Table 3. The criterion of these characteristics selection is based on choosing the volume of the rods close to the current solid fuel volume in order to increase the surface-to-volume ratio, while for the diameter of the water in the inner and outer channel of the annular fuel, different values have been considered.

Table 1. Description of the six different types of fuel assemblies in BNPP core [13].

FA. Type	Number of fuel rods	U-235 enrichment (Wt %)	Number of BARs	Content of boron (natural) in absorbing material (g/cm^3)	Number of CPS ARs	Number of GCs
FA16	311	1.6	-	-	18	2
FA24	311	2.4	-	-	18	2
FA36	311	3.6	-	-	18	2
24B20	311	2.4	18	0.020	-	2
24B36	311	2.4	18	0.036	-	2
36B36	311	3.6	18	0.036	-	2

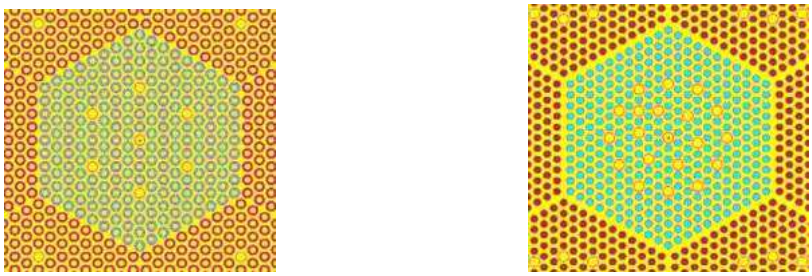

Annular fuel Solid fuel

Fig 1. Annular and solid fuel simulated in MCNPX.

It is emphasized that the size of the core and the assemblies and assembly pitches (=23.6 cm), remain intact, as well as the materials. It has changed only the geometry of the fuel rods and then the fuel numbers and pitches in the assembly have changed.The fuels in more detailed are presented in table 4.

Table 2.
The BNPP core description [15].

The main core Characteristics	Value
Core & FA form in a plane	Hexagonal
Number of fuel amblies	163
FA pitch in core (cm)	23.6
Fuel rod pitch in assembly (mm)	12.75
Core equivalent diameter (cm)	316
Temperature at the inlet (˚C)	291
Fuel pellet material	UO^2
Cladding material	Alloy Zr+1%Nb
Cladding outside diameter (mm)	7.73
Fuel pellet outside diameter (mm)	7.57
Hole diameter in the fuel pellet (mm)	1.5
Fuel pellet density (g/cm^3)	10.4…10.7
Absorbing material in CPS AR (combined)	B_4C+($Dy_2O_3TiO_2$)
$Dy_2O_3TiO_2$ absorber height in control rod (cm)	30
B_4C absorber height in control rod (cm)	320
Absorbing material in BAR	CrB_2+Al

Table 3. Characteristics of annular fuels and solid fuels.

Fuel type	Inner radius (mm)	Outer radius (mm)	Fuel thickness (mm)	Fuel volume (cm^3)	Number of fuels in assembly	Total mas of fuel in assembly (kg)	Total mass of fuel in core (t)
Annular	4.25	5.62	1.37	149.955	210	330.65	53.896
Solid	Central hole radius 0.75	3.785	3.035	152.637	311	498.436	81.245

Table 4. The more details of fuels.

	Fuel pitch (mm)	Number of fuels	Diameter of inner channel (mm)	Minimum distance between outer neighbor cladding (mm)	Fuel thickness (mm)	Outer cladding thickness (mm)	Inner cladding thickness (mm)	Outer Helium thickness (mm)	Inner Helium thickness (mm)
Annular	15.94	210	7	3	1.37	0.8	0.7	0.05	0.05
Solid	12.75	311	No inner channel	3.65	3.035	0.685	With out inner cladding	0.08	Helium radius in central hole = **0.75**

3. Thermohydraulic Analysis

After study of some neutronic and nuclear behavior of all types of fuels, Type 1 annular fuel is chosen and introduced for use in reactor. But it should also be studied from a thermohydraulic point of view to determine its safety margins and safety coefficients.

In the following, some important parameters like temperature distribution and DNBR calculations for annular fuel Type1 were investigated and compared with corresponding parameters for Solid fuel in CFD code.

3. 1. Modeling in FLUENT

In addition to neutronic analysis, the annular fuel properties were also investigated from thermohydraulic point of view. The Thermohydraulic analysis of the problem leads to the Navier-Stokes equations, which requires the CFD codes to solve. These equations are:

Continuity equation:

$$\nabla . \vec{V} = 0$$

Momentum equation:

$$\frac{\partial V}{\partial t} + (\vec{V} . \nabla)\vec{V} = -\frac{1}{\rho}\nabla P + \nu\nabla^2\vec{V}$$

where $\vec{V}$ denotes the velocity vector, P the pressure, and the ρ and ν are the density and kinematic viscosity, respectively.

FLUENT is one of the CFD codes which uses the FVM to solving the Navier-Stokes equations [14], and in this work the hottest annular Type1 and solid fuel rods were modeled in ANSYS FLUENT.

For modeling, the fuels geometries were designed in Design Modeler and in order to obtain the high quality of meshing, some properties of geometry were introduced in UDF code. After successfully sketching, the geometry was meshed by ANSYS Meshing with Orthogonal Quality about 0.65 which are shown in Fig 2.

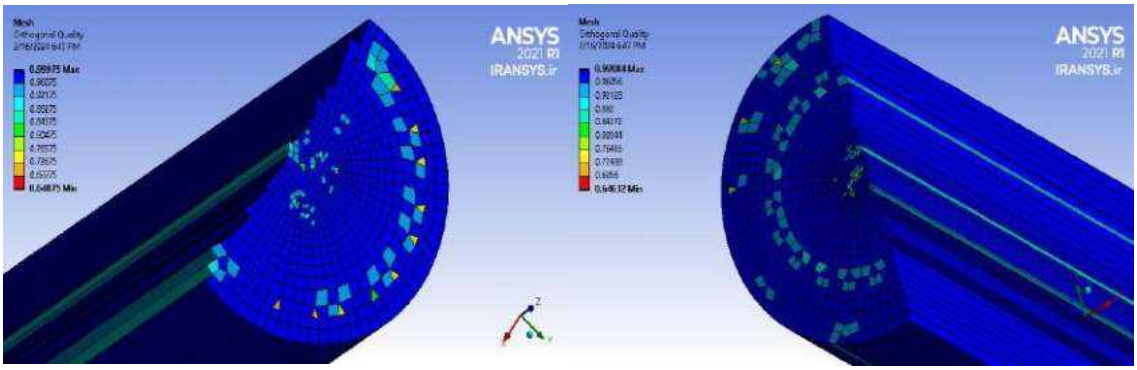

(a) (b)

Fig 2. Fuel rod meshing (a) Solid, (b) Annular

Some operation conditions were considered which were presented in table 5. And the materials which are used fuel rods in FLUENT, and their characteristics are presented in table 6.

Table 5. Operation considered in FLUENNT.

Operation condition	Temperature	pressure	Gage Pressure
	564 K	2200 psia	15067768 Pa

Table 6. Material characteristics which are used in FLUENT [15].

Material	Density (kg/m^3)	Specific heat (J/kg.K)	Conductivity (W/m.K)	Viscosity (kg/m.s)
Water	714	5650	0.545	8.59 e-5
Cladding (Zircalloy-IV)	6450	183	10.7	-
He	9	5.1	0.2	-
UO_2	10500	221	2.4	-

The axial power distribution in BNPP reactor along rods [16] is presented in Fig 16. Since the operation power of the reactor is not changed in this work, the power distribution presented in Fig.3, has been calculated for 210 annular Type1 in assembly and is used in UDF as source term.

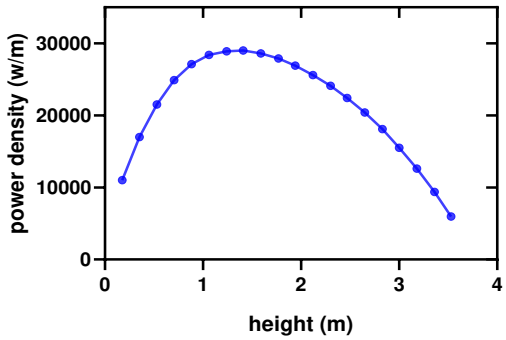

Fig 3. Power distribution of fuel rod in BNPP [16].

The solution in FLUENT was converged after 89 iteration for Solid case, and 853 iteration for Annular case, which are shown in Figs 4-5 respectively.

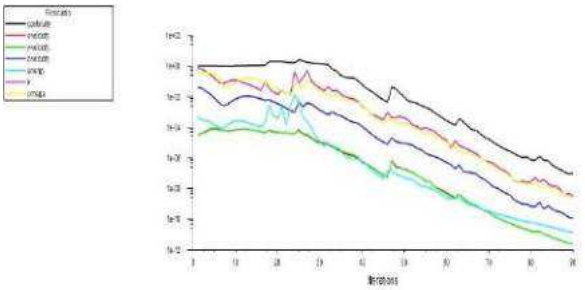

Fig 4. Solution convergence diagram for Solid case.

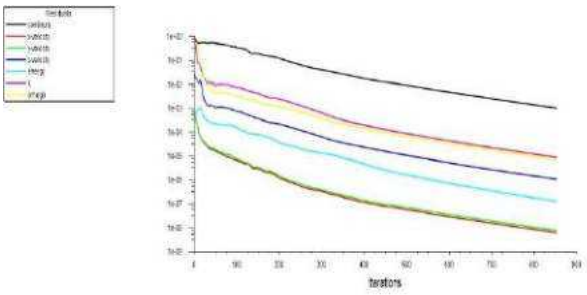

Fig 5. Solution convergence diagram for Annular case.

3. 2. **Temperature distribution**

The attempts for reduction in fuel center temperature is the main motivation to investigate about Annular Fuels. The low maximum temperature in the center of fuel is very important in the LOCA to prevent the fuel from melting. Thus after solution in FLUENT, some results, such as temperature distributions were studied by CFD Post-Processing. In addition to simulation in FLUENT, the solid fuel was simulated in COBRA-EN code. Then, the results of solid fuel simulation were compared in FLUENT with corresponding output data in COBRA by plotting them as shown in next figures.

Here, the radial distribution of temperature in fuel was presented, as well as axial distribution of temperature in fuel center, fuel surfaces, cladding surface and in coolant. These are shown in Figs 19-22. In Fig 6, which is plotted by CFD Post-Processing, the comparison of radial distribution of temperature in middle of height, between solid and annular fuel Type1 is presented,

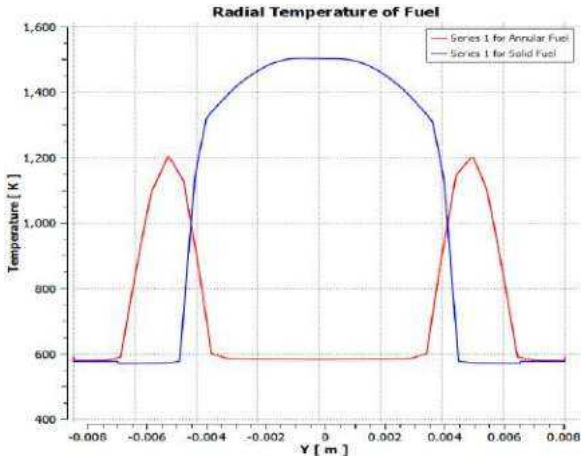

Fig 6. Radial distribution of temperature in fuel.

The center of fuel rod has chosen to check the axial temperature distribution in fuel. By extracting the relevant data from CFD-Post Processing, it was plotted in Prism. The result is shown in Fig 7.

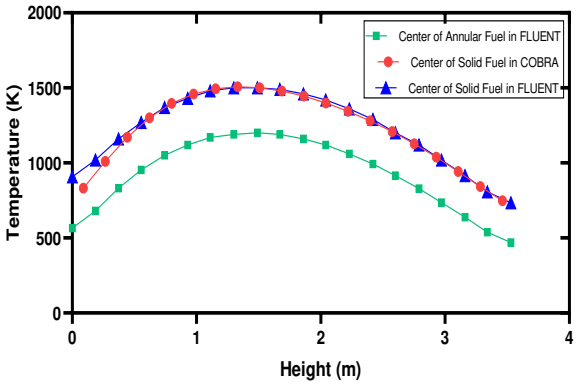

Fig 7. Axial distribution of temperature in fuel center.

Also, as it can be seen from Figs 6-7, the maximum temperature of the annular fuel center is much lower than the solid fuel center temperature.

Then, the axial distribution of temperature in fuel surfaces was plotted. This is shown in Fig 8.

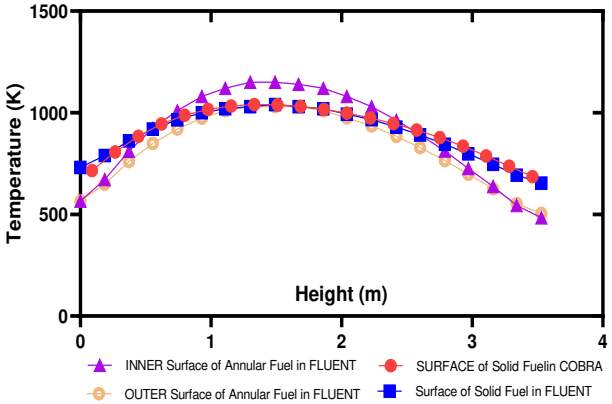

Fig 8. Axial temperature in fuel surface.

As it can be seen from Fig 8, the maximum temperature of INNER surface of annular fuel, is higher than OUTER surface temperature and is higher than solid surface temperature. This is reasonable because the smaller the thickness of fuel, the surface temperature of the fuel will be closer to the center temperature. Also, due to the spread of heat on the surface, the concentration of heat on the smaller surface will be higher and therefore the temperature of the inner surface is higher than outer surface temperature.

The heat exchange between the water and the fuel rod is done through the rod cladding. Therefore, the cladding surface temperature is an important quantity and plays an important role in the heat flux from the cladding surface.

The axial distribution of temperature in cladding surfaces, are plotted in Fig 9.

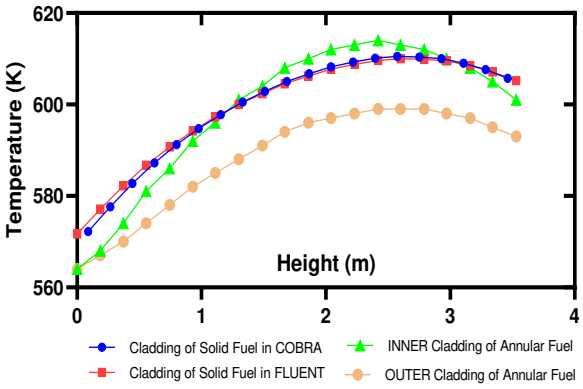

Fig 9. Axial temperature of cladding surface.

According to the Fig 9, the maximum temperature of outer cladding in annular fuel, is higher than solid fuel cladding but it is still below the boiling point of water at 15.7 Mpa pressure, and safety is not compromised.

In the next step, the axial temperature distribution of water was checked. The resulting diagram is shown in Fig 10. According to this figure, the temperature changes in the axial direction of the water for annular fuel is the same as solid fuel, but the maximum temperature in the inner channel is higher than all others. This means that heat flux from the inner channel of the annular fuel is more than others.

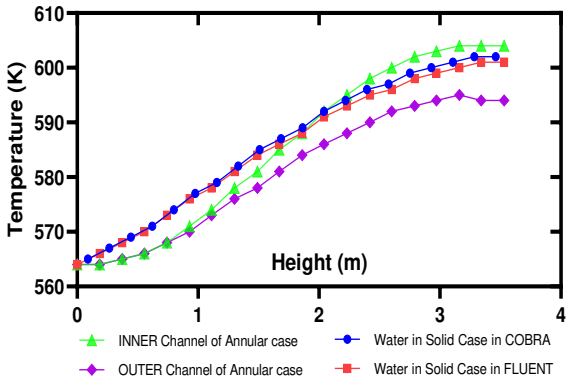

Fig 10. Axial distribution of temperature in water.

The Fig 11. Shows the contour of temperature in horizontal cut of fuel in middle of height for annular and solid fuels, which are extracted from data in CFD-Post Processing.

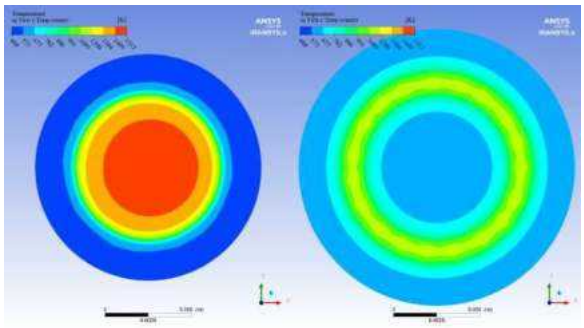

Fig 11. Contour of temperature. Annular (right) solid (left).

3. 3. Pressure drop

Then, the pressure data were exported from CFD-Post Processing to Prism and the pressure drop in the internal and external channels were plotted and compared it with the corresponding values of the solid case in Fig 12.

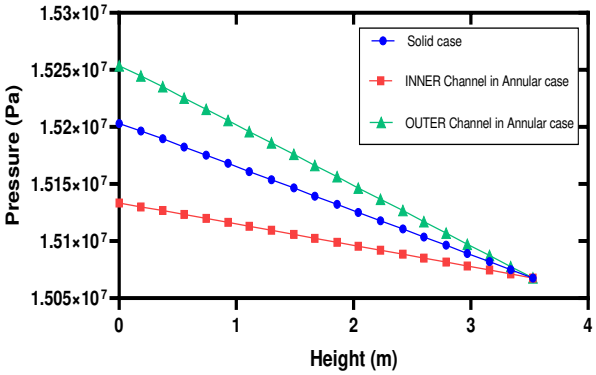

Fig 12. Pressure drop.

Since the Pressure Outlet boundary condition was considered to solve the problem in Fluent, for all three cases of the channels, the pressure at the outlet of the rods is considered the same, and based on that, the changes and pressure drop in all three cases are calculated. According to the Fig 12, the pressure drop at inner channel is less than solid case, and pressure drop at outer channel is more than solid case. Therefore, to compensate for this difference in pressure drop compared to the solid case, it is necessary to adjust the water pumping power accordingly.

3. 4. DNBR calculations

The ratio of critical heat flux to local heat flux DNBR is one of the most important safety margins:

$$DNBR = \frac{q_c''}{q_{actual}''}$$

In this ratio, q_c'' is the critical heat flux (CHF) along the hottest coolant channel, and q_{actual}'' is the actual surface heat flux along this channel [17].

In this work the CHF is obtained from COBRA output file (CHF=4.28 MW/m^2), and q_{actual}'' from FLUENT data in CFD Post-Processing. These results are plotted and are shown for annular and solid fuel cases in Fig 13. It can be seen from this figure that amount of DNBR in each inner and outer channel in annular fuel case is much than solid fuel case and this is one of the important motivations for using annular fuel in reactor.

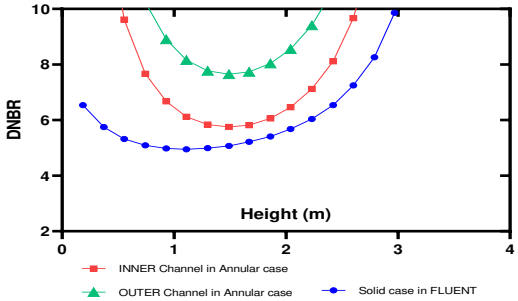

Fig 13. Departure from Nucleat Boiling Rate.

3. 5. Thermohydraulic analysis Summary

Here, the summary of averaged quantities which provided above, were presented in tables 7-11.

Table 7. Averaged temperature in fuel center.

Fuel Type	Averaged temperature (˚C)
Solid in COBRA	953
Solid in FLUENT	949
Annular	647

Table 8. Averaged temperature of cladding.

Fuel Type	Averaged temperature (˚C)
Solid in COBRA	327
Solid in FLUENT	326
inner cladding of Annular	325
outer cladding of Annular	316

Table 9. Averaged temperature in water.

Fuel type	Averaged temperature (˚C)
Solid in COBRA	313
Solid in FLUENT	312
inner channel of Annular	313
outer channel of Annular	308

Table 10. Pressure drop.

Fuel type	**Pressure drop (bar)**
Solid case in COBRA	1.2
Solid case in FLUENT	1.3
Inner channel in annular case	0.65
Outer channel in annular case	1.8

Table 11. Departure from Nucleat Boiling.

Fuel type	**DNBR**
Solid case in COBRA	5.38
Solid case in FLUENT	5.24
Inner channel in annular case	7.47
Outer channel in annular case	8.27

6. Conclusion

In this work, the use of annular fuel instead of solid fuel was investigated from the thermohydraulic point of view in ANSYS FLUENT. The results showed that the use of annular fuel instead of solid fuel leads to favorable changes in thermohydraulic parameters. Among other things: It has a significant

economic benefit because the total mass of the fuel used is reduced, while the total power and the size of the core and the size of the assemblies remain unchanged. It causes to decrease the maximum temperature of the fuel center which is very important in terms of safety in LOCA. And it causes high extraction of heat from fuel and thus increases efficiency. It also increases the amount of DNBR significantly.

References

[1] Bo Feng, Mujid S. Kazimi, "On the Use of High Performance Annular Fuel in PWRs", Massachusetts Institute of Technology, June 2008.

[2] Kazimi, M.S., P. Hejzlar, et al., "High Performance Fuel Design For Next Generation PWRs: Final Report", MIT-NFC-PR-082, Center for Advanced Nuclear Energy Systems, MIT (Jan 2006).

[3] P.Hejzlar, M.S.Kazimi, "Annular Fuel for High-Power-Density Pressurized Water Reactors: Motivation and Overview", October 2007 Nuclear Technology 160(1):2-15.

[4] Kazimi, Mujid S., et al., "High Performance Fuel Design for Next Generation PWRs: Final Report", Massachusetts Institute of Technology. Center for Advanced Nuclear Energy Systems. Nuclear Fuel Cycle Program, 2006-01.

[5] D. Feng, et al., "Thermal-Hydraulic Design of High PowerDensity Annular Fuel in PWRs", Nuclear Technology, Vol.160, pp.16~44, 2007.

[6] Blinkov, V., et al., "Prospects for using annular fuel elements in nuclear power engineering". Thermal Engineering, 2010. Vol. 57: p. 213-218.

[7] N. Todreas and M. Kazimi, Nuclear System, Volume 1 "Thermal Hydraulic Fundamentals", Maaschussets Institute of Technology (2011).

[8] H. T. Kim et al., ''Performance of internally and externally cooled annular fuel in loss of coolant accident,'' Proc. International Congress on Advanced Nuclear Power Plants, Hollywood, Florida, USA, June 9–13, 2002 (2002).

[9] Odii Christopher Joseph, Agyekum Ephraim Bonah, Afornu Bright Kwame, "Effect of Dual Surface Cooling on the Temperature Distribution of a Nuclear Fuel Pellet", Key Engineering Materials Vol. 769, ISSN: 1662-9795, Vol. 769, pp 296-310, 2018 Trans Tech Publications, Switzerland.

[10] Katona, T.J., 2011. "Long-term operation of VVER power plants", In: Tsvetkov, P.v.(Ed), Nuclear Power – Deployment. Operation and Sustainability, In Tech, pp. 153-196.

[11] Obaidurrahman. K., Doshi, J.B., 2011. "Spatial instability analysis in pressurized water reactors", Annals of Nuclear Energy 38, 286-294.

[12] Heba K. Louis, Esmat Amin, "Burnup and neutronic analysis for UOX and MOX fuel assemblies in VVER reactor", Annals of Nuclear Energy 164 (2021) 108586.

[13] Atomic Energy Organization of Iran (AEOI), 2003, Final Safety Analysis Report (FSAR) for Bushehr VVER-1000 Reactor.

[14] Botond et al., "Coupled Population Balance-CFD Modelling of a Continuous Precipitation Reactor", Computer Aided Chemical Engineering, volum 33, 2014, Pages 187-192.

[15] W.G. Luscher and K.J. Geelhood, "Material Property Correlations: Comparisons between FRAPCON-3.5, FRAPTRAN 1.5, and MATPRO (NUREG/CR-7024, Revision 1), Office of Nuclear Regulatory Research U.S. Nuclear Regulatory Commission Washington DC 20555-0001, October 2014.

[16] S. H. Sangestani et al., "Study of Fast Transient Pressure Drop in VVER-1000 Nuclear Reactor Using Acoustic Phenomenon", January 2018, Science and Technology of Nuclear Installations, 2018(2):1-11.

John R. Lamarsh, "INTRODUCTION to NUCLEAR REACTOR THEORY", NEW YOBK UNIVERSITY ADDISON-WESLEY PUBLISHLNG COMPANY Readmg.

ICNST 2024
International Conference on Nuclear Science and Technology
6- 8 MAY 2024 | Isfahan, Iran

The effect of radiation induced swelling on the heat transfer performance of nuclear fuel plate (Paper ID : 1499)

Roustaii B. [1*], Naghshnejad Z. [1], Dabiri J. [1]

[1] Nuclear reactor and safety School, Nuclear Science and Technology Research Institute, Tehran, Iran.

Abstract

Dispersion fuel plates are widely used in various research reactors. In dispersed fuel, the fuel particles are located in a bed of base materials that can be metal or ceramic, which improves their heat transfer properties. Temperature distribution and heat transfer in fuel plates and fuel assemblies are important in reactor safety. Due to the harsh environment inside the reactor core and the effects of radiation on the fuel elements, like the swelling of the fuel plates due to the presence of fission products that cause dimensional changes of the fuel plates must be considered in the temperature distribution and heat transfer calculations. In this article, by using the corrected model of fuel radiation induced swelling for high burnups and applying it to the calculations, the temperature distribution of the fuel element is obtained for the values of initial burnups to high burnups (about 120MW/KgU) and is compared with similar works that high burnup corrections is not included on the fuel swelling model. This comparison shows that the radiation induced swelling effect in the burnup of 120MW/KgU can cause an increase of about 6 ˚C in temperature of the fuel plate center.

Keywords: radiation induced swelling, heat transfer, dispersion fuel plate, high burnup.

Introduction

When the nuclear fuel inside the reactor is exposed to radiation, many changes occur in its microstructure. When nuclear fission occurs, various products are produced in the fuel. Some of these products are rare gases such as xenon and krypton, elements with a lower amount such as Pd, Ru Rh, Tc and Mo also cause the swelling of fuel particles as solid fission products. In higher burnups and in areas with High Burnup Structure or HBS, the swelling effect of gas products increases. Thermal conductivity, which is one of the most important properties of nuclear fuel, has a great effect on the working temperature, efficiency and behavior of the fuel. In general, thermal conductivity of fuel is affected by several factors such as temperature, porosity, solid and gaseous products of fission, change of fuel microstructure and HBS and radiation damage. Among these factors, determining the effect of porosity, which is influenced by gas products and swelling, on thermal conductivity is a complex process. The existing relationships do not correctly predict the fuel swelling behavior and its thermal

conductivity at high burnups. In the article of the present author, these relationships have been corrected for the high burnups and its results are used in this article. The research shows that the increase in the temperature of the fuel plate, with taking into account the swelling of the fuel and the reduction of the thermal conductivity of the fuel particles with the increase of burnup due to the production of fission products, is significant, So that for dispersion type fuels, the internal microstructure of the fuel must be evaluated due to the effects of fissile fuel particles and metallic matrix on thermal performance. Therefore, it is important to investigate these effects from the point of view of reactor safety. Because the thermal properties of most materials change with temperature, as a result, this analysis is usually non-linear. Many commercial finite difference or finite element software such as ANSYS, ABAQUS, etc., as well as many nuclear codes such as FRAPCON, DART, TRANSURANUS, etc., perform thermal analysis or thermo-mechanical analysis. There are many articles on the thermal analysis of rod fuels, but less has been addressed to plate-type fuels.

In the Similar article, using ANSYS software, heat transfer calculations and the effect of induced swelling of fuel radiation on it have been performed for a dispersion fuel with UO2 fuel particles, zircaloy matrix metal and clad. However, in this article, the fuel swelling model and the thermal conductivity model for UO2 fuel particles, zircaloy matrix metal and clad are corrected according to reference for high burnups and the temperature distribution in the fuel element is calculated and compared with reference. (The reason for choosing UO2 and Zircaloy is the availability of information needed for these materials to perform calculations but in general, this calculation method can be used for other fuels and different casing materials.).

Methods and Materals

Geometric model of fuel element and heat transfer relationship

Due to the very small thickness of the fuel plate compared to its length and width, the produced heat energy is mainly transferred from the upper and lower surfaces of the fuel plate to the coolant water. As a result, the upper and lower surfaces are the most important boundaries of plane-dispersed fuel. To investigate the effects of fuel particles and base metal on the thermal performance of the fuel, the modeling should include the microstructure of the fuel. Assuming that the fuel particles are alternately distributed along the length and width of the fuel plate, a model can be considered as shown in Figure 1, where the model is chosen to have a repeating size (in the meso-scale) along the length and width direction. And the actual size (on the macro scale) is in the thickness direction. For simplicity, it is assumed that the spherical particles of the fuel are arranged as shown in Figure 1b.

To increase the calculation speed, the finite element model is selected as 1/8 according to the symmetry in the model. The plane Z=0 is the middle plane of the fuel plate and Z=H⁄2 is the outer surface of the fuel plate, which is in contact with the coolant water. Considering that the planes X=0, X=a⁄2, Y=0, Y=a⁄2 and Z=0 have symmetry, the adiabatic boundary condition should be applied to them in the form of -k ∂T/∂n=0. The plane Z=H⁄2 is the convection boundary, and this boundary condition is expressed

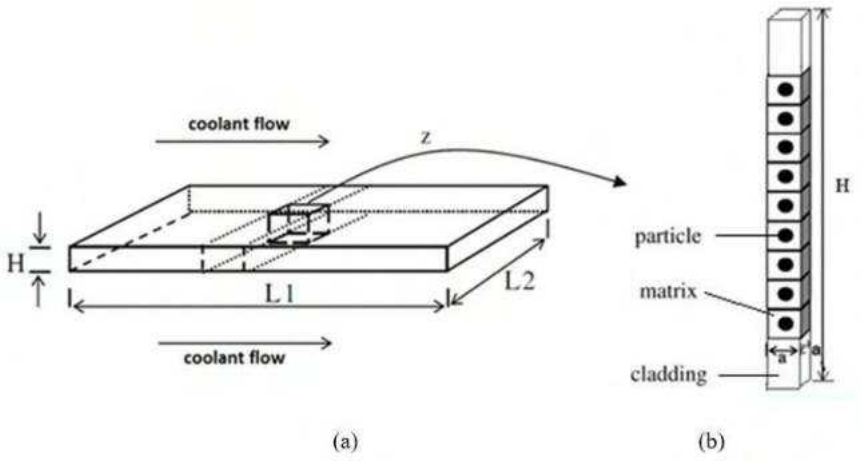

Figure 1. a) Dispersed type fuel plate geometry, b) the model

by the equation -k ∂T/∂n=h(T-T_f). Where h is the heat transfer coefficient and T_f is the temperature of the coolant water and n indicates the outer vertical direction of the boundary surface. Also, the temperatures and heat fluxes are continuous along the vector perpendicular to the common boundary of the matrix metal and the clad, and also along the perpendicular vector to the common boundary of the fuel and the matrix metal.

The conduction heat transfer equation in steady state for fuel, matrix metal and clad can be written as equations (1) and (2), respectively:

$$\nabla.\ (K_P(T)\nabla T) + \dot{q} = 0 \qquad (1)$$

$$\nabla.\ (K_{m\ or\ c}(T)\nabla T) = 0 \qquad (2)$$

Where K(W/mK) is the thermal conductivity, T(K) is the temperature and (W/m3) q ˙is the rate of heat production per volume unit and K_P (T), Km (T) and Kc (T) are respectively the thermal conductivity of the fuel, matrix metal and clad.

The rate of heat production per unit volume of fuel particles corresponds to the rate of fission, taking into account that 200 MeV of heat energy is released from each fission and 1eV=1.602×10-19J, the rate of heat production in the fuel particle can be calculated as q ṗ calculated in terms of J/m3s (W/m3) using the equations q ṗ=c.f ˙and c=3.204 ×10 -11. Where c is the amount of thermal energy produced

in each fission in terms of J/fission, f ˙shows the fission rate of fuel particles per unit of time and volume (fission/m3s).

Fuel swelling relations

According to Ref. from present author, the swelling relationship is obtained. Porosity defines as the ratio of voided volume over the total volume. Total porosity *P* is composed of two contributions: One comes from pores P_v including as-fabricated voids as initial porosity with no contribution to the matrix swelling and the other named swelling porosity P_s stems from the irradiation induced fission gas bubbles contributing to the matrix swelling. If $\Delta V^{\text{gas bubble}}/V_0^{\text{matrix}}$ represents the fractional fuel matrix swelling due to fission gas bubbles, where V_0^{matrix} denotes the initial matrix volume, and $\Delta V^{\text{gas bubble}}$ is the increase of matrix volume due to bubble formation, then by definition the swelling porosity P_s is give by:

$$P_s = (\Delta V^{\text{gas bubble}}/V_0^{\text{matrix}}) / (1 + \Delta V^{\text{gas bubble}}/V_0^{\text{matrix}}) \quad (3)$$

Taking the unirradiated fuel volume as the reference state in the fuel swelling calculation, the pore P_v may be obtained by the following expression given in [12]

$$P_v = 1 - (1 + \Delta V^{\text{matrix}}/V_0^{\text{matrix}})(\rho/\rho_{\text{th}}), \quad (4)$$

where ρ is the bulk fuel density and ρ_{th} is the theoretical density of UO_2, and $\Delta V^{\text{matrix}}/V_0^{\text{matrix}}$ represents the total fractional fuel matrix swelling caused by both solid ($\Delta V^{\text{solid}}/V_0^{\text{matrix}}$) and gaseous ($\Delta V^{\text{gaseous}}/V_0^{\text{matrix}}$) fission products as follows:

$$\Delta V^{\text{matrix}}/V_0^{\text{matrix}} = \Delta V^{\text{solid}}/V_0^{\text{matrix}} + \Delta V^{\text{gaseous}}/V_0^{\text{matrix}} \quad (5)$$

With $\Delta V^{\text{gaseous}}/V_0^{\text{matrix}}$ representing the total fractional gas swelling resulting from both gas atoms in the dynamic solution and the fission gas bubbles as follows

$$\Delta V^{\text{gaseous}}/V_0^{\text{matrix}} = \Delta V^{\text{gas atom}}/V_0^{\text{matrix}} + \Delta V^{\text{gas bubble}}/V_0^{\text{matrix}} \quad (6)$$

The swelling due to solid fission products is given by :

$$\Delta V^{\text{solid}}/V_0^{\text{matrix}} = 0.0032 * Bu(\text{GWd/tM})/10, \quad (7)$$

where *Bu* depicts the fuel burnup. To estimate the swelling due to gaseous fission products, an analytical approach to fuel element swelling developed in the low temperature condition (T < 850 K) is used.

Hence the total porosity $P = P_s + P_v$ takes the following form:

$$P = 1 - (1 + \Delta V^{\text{matrix}}/V_0^{\text{matrix}})(\rho/\rho_{\text{th}}) + (\Delta V^{\text{gas bubble}}/V_0^{\text{matrix}}) / (1 + \Delta V^{\text{gas bubble}}/V_0^{\text{matrix}}) \quad (8)$$

To study the evolution of porosity with burnup using Eq. (8), one needs to calculate the terms associated with the matrix swelling.

The porosity in Eq. (8) is calculated Ref. as Fig. 2 and is applied in the thermal conductivity model for the present article.

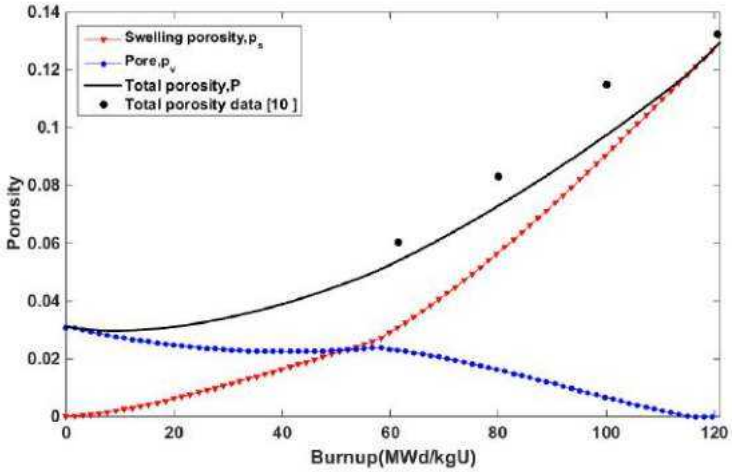

Fig. 2 Formation of pore P_v, swelling porosity P_s, and total porosity P as a function of burnup

The thermal conductivity models of UO2 and Zr

A common and widely used model for thermal conductivity of UO2 irradiated fuel was proposed by Lucuta et al., which includes six terms according to equation (9). It should be noted that using equations (3) in the high burnups where HBS is formed has limitations and is not correct.

$$k^{Lucuta}\left(\frac{W}{mK}\right) = k_0 \kappa_S \kappa_P \kappa_{RD} \kappa_{DP} \kappa_{PP} \qquad (9)$$

Where k_0 is the thermal conductivity of fresh UO2 fuel at 100% theoretical density. κ_S is related to the effect of deviation from stoichiometry and under normal operating conditions of the reactor, κ_S=1. κ_P as a porosity coefficient shows the effect of porosity on thermal conductivity and according to reference it is equal to $\kappa P=(P-1)/(1+(\sigma-1)P)$ where P is the fraction of porosity (p=0.05)) and σ is the shape factor of the porosity (for spherical pores σ=1.5). κRD is due to the effect of radiation damage and the increase of network defects and subsequently the reduction of thermal conductivity [64]. κDP is the effect of fission products dissolved in fuel and κPP is the effect of fission products deposited in fuel.

Equation (9) is modified for high burnups in Ref. with using of Fig. 2. The effect of evolution of as-fabricated porosity and gas porosity caused by fission on the thermal conductivity of fuel particles can be entered as a correction porosity factor ($\kappa_{P\text{- modified}}$) in the thermal conductivity of fuel particles (Fig .3).

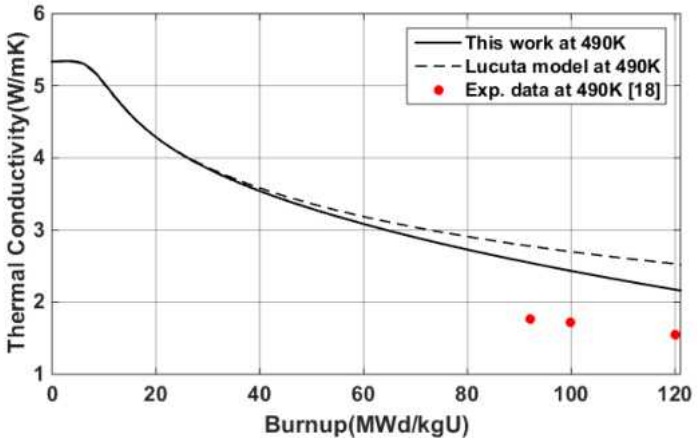

Fig. 3. UO2 fuel thermal conductivity based on Lucuta model vs. burnup with porosity evolution included in comparison to the case with constant porosity and experimental data.

The thermal conductivity for zircaloy is as:

$$K_{Zr} = 7.51 + 2.09 \times 10^{-2}T - 1.45 \times 10^{-5}T^2 + 7.67 \times 10^{-9}T^3 \qquad (10)$$

By considering the as-fabricated porosity in the matrix metal and taking it into account on its thermal conductivity relationship can be drawn Fig.4 in vs. of temperature for Zr. It can be seen that the thermal conductivity of Zr metal decreases with the increase of initial porosity p. For 10% initial porosity (p=10%), a 26% reduction is predicted for the thermal conductivity of the base metal.

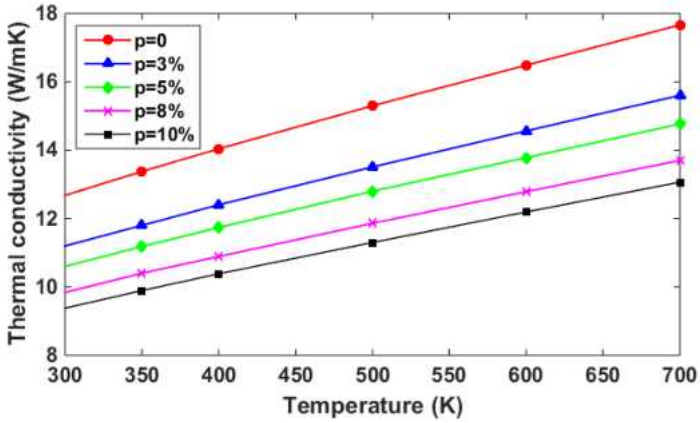

Fig. 4 The thermal conductivity of zircaloy vs. Temperature for different %porosity.

Results and discussion

With considering Fig.5 path 1 on the model and using fuel swelling and the modified thermal conductivity, can obtain temperature distribution in fuel element.

The dimensions of the fuel model in Figure 5, including the radius of the fuel particles, the thickness of the fuel meat, and the thickness of the sheath are equal to 50µm, 0.625mm, and 0.4mm respectability. In addition, the volume fraction of fuel particles is 20%. To take into account the thermal analysis boundary conditions, the heat transfer coefficient h and the coolant water temperature T_f are needed, which are $2x10^4$ W/m^2 and 573 K respectively. Also, the rate of heat production is assumed to be equal to 3.204×10^9 W/m^3.

Fig. 6 is a benchmark and indicates effect of swelling of fuel particles on temperature distribution of fuel element on reference results [10] and reproduction values in present work.

Fig. 7 indicates the effect of swelling of fuel particles on the temperature distribution of the fuel element in the present work for burnup U% 5 and 10, taking into account the correction of the thermal conductivity of the matrix metal (applying the initial porosity of 10% in the base metal) and compared it with the reference reproduction results.

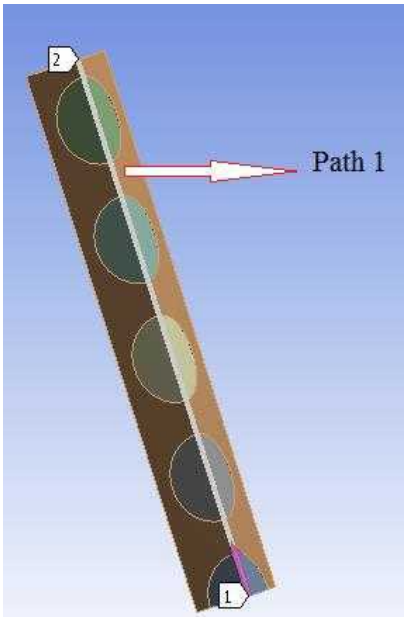

Fig.5 fuel element model

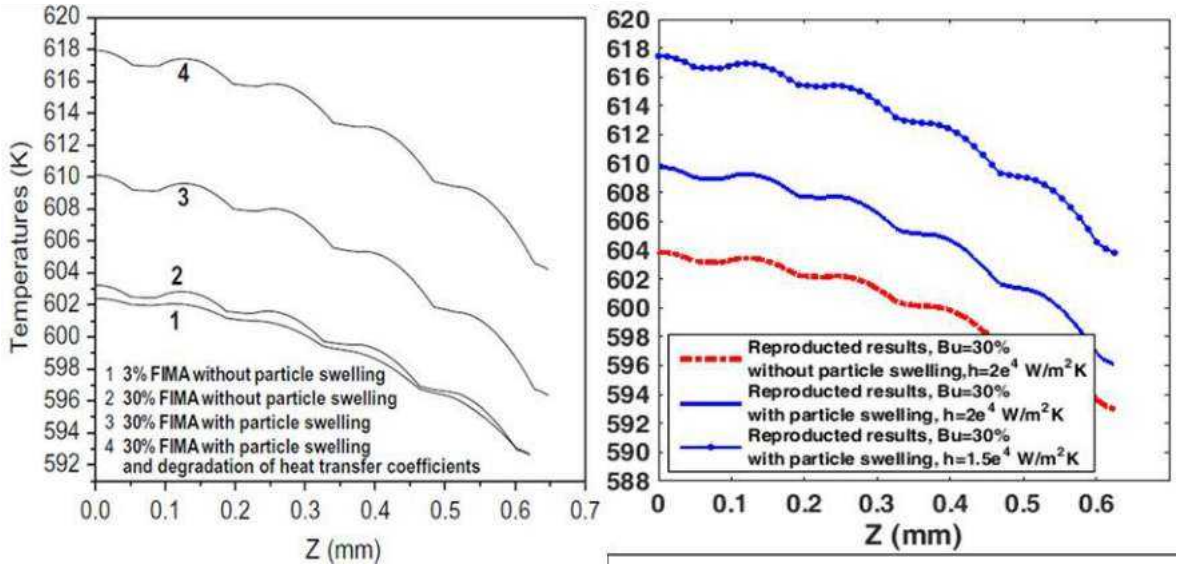

(a) (b)

Fig.6 Effect of swelling of fuel particles on temperature distribution of fuel element a) reference results [**Error! Bookmark not defined.**] and b) reproduction values.

Fig. 7 The effect of swelling of fuel particles on the temperature distribution of the fuel element in the present work for burnup U% 5 (50 MWd/KgU) and 10 (100 MWd/KgU), taking into account the correction of the thermal conductivity of the matrix metal (applying the initial porosity of 10% in the base metal) and comparing it with the reference reproduction results [**Error! Bookmark not defined.**].

Fig.8 shows the fuel element temperature distribution for burnup U% 12.8 (120 MWd/KgU)in the present work.

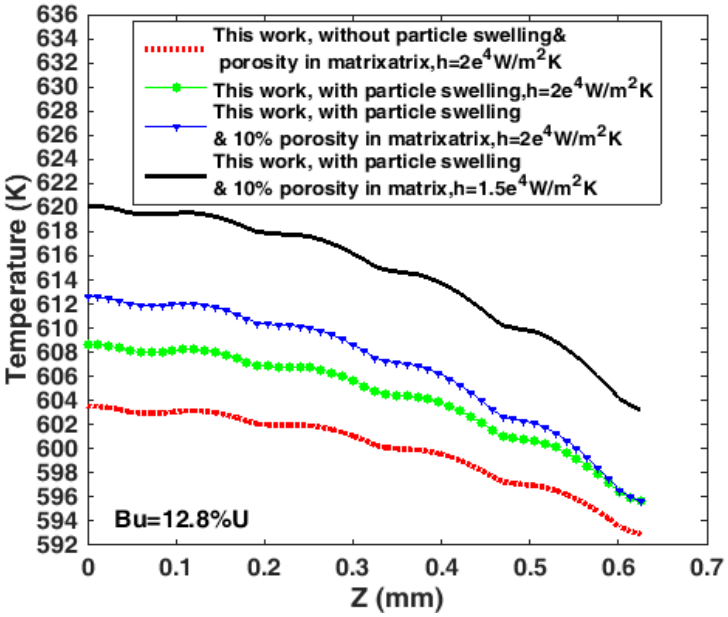

Fig.8 Fuel element temperature distribution for burnup U% 12.8 (120 MWd/KgU)in the present work.

Conclusions

In this work, by using the corrected model of fuel radiation induced swelling for high burnups and applying it to the calculations, the temperature distribution of the fuel element is obtained for the values of initial burnups to high burnups (about 120MW/KgU) and is compared with similar works that high burnup corrections is not included on the fuel swelling model. This comparison shows that the radiation induced swelling effect in the burnup of 120MW/KgU can cause an increase of about 6 ˚C in temperature of the fuel plate center.

References

[1] H.J.Matzke, Oxygen potential in the rim region of high burn-up UO2 fuel, Journal of Nuclear Materials, 208 (1994) 18-24.

[2] C. Ronchi, M. Sheindlin, D. Staicu, M. Kinoshita, Effect of burn-up on the thermal conductivity of uranium dioxide up to 100.000 MWd/t, Journal of Nuclear Materials, 327 (2004) 58–76.

[3] P.G. Lucuta, Hj. Matzke, R.A. Verrall, Modelling of UO_2-based SIMFUEL thermal conductivity The effect of the burnup, Journal of Nuclear Materials 217 (1994) 279-286.

[4] P.G. Lucuta, Hj. Matzke, I.J. Hastings, A pragmatic approach to modelling thermal conductivity of irradiated, UO_2 fuel, Journal of Nuclear Materials, 232 (1996) 166-180.

[5] B.Roostaii, H. Kazeminejad, and S. Khakshournia. "Influence of porosity formation on irradiated UO2 fuel thermal conductivity at high burnup." *Journal of Nuclear Materials* 479 (2016): 374-381.

[6] J. Rest, "The DART Dispersion Analysis Research Tool: A Mechanistic Model for Predicting Fission-Product-Induced Swelling of Aluminum Dispersion Fuels", ANL-95/36, Argonne National Laboratory, (1995).

[7] K. J. Geelhood, W.G. Luscher, FRAPCON-3.5: A Computer Code for the Calculation of Steady-State, Thermal-Mechanical Behavior of Oxide Fuel Rods for High Burnup,NUREG/CR-7022, (2014).

[8] K. Ito, et al. "FEMAXI-III, a computer code for fuel rod performance analysis." Nuclear engineering and design 76.1 (1983): 3-11.

[9] Lassmann, K. "TRANSURANUS: a fuel rod analysis code ready for use." Journal of nuclear materials 188 (1992): 295-302.

[10] S. Ding, Y. Huo, X. Yan, Modeling of the heat transfer performance of plate-type dispersion nuclear fuel elements, Journal of Nuclear Materials, 392 (2009) 498–504.

[11] S. Ding, X. Jiang, Y. Huo, L. Li, Reliability analysis of dispersion nuclear fuel elements, Journal of Nuclear Materials, 374 (2008) 453–460.

ICNST 2024
International Conference on Nuclear Science and Technology
6- 8 MAY 2024 | Isfahan, Iran

A study on the thermal properties of irradiated UO2 fuel (Paper ID : 1500)

Roustaei B. [1*]

Nuclear Science and Technology Research Institute, Tehran, Iran.[1]

Abstract

Due to the development of the nuclear industry and the emergence of various types of reactors and nuclear fuels, UO2 fuel is still used as one of the most important conventional fuels with simpler and more well-known manufacturing technology. One of the most important fuel characteristics is its thermal conductivity . According to experimental observations, when the fuel reaches a burnup higher than around 60 MWd/KgU, microstructural changes occur in positions of the fuel with temperature lower than 1000K, where is called high burn-up structure (HBS). Since the edges of the fuel pellets have higher burn-ups and lower temperatures than the center of the fuel, these microstructural changes occur more often there, and it is also known as the rim effect. In many fuel performance codes, thermal conductivity correlation are correct at low burnups and cannot provide exact predictions for high burn-ups. In this article, an existing correlation for the UO2 thermal conductivity is developed for use in high burn-ups. The irradiated UO2 thermal conductivity model based on the Maxwell-Eucken correlation for porosity factor is selected as a case study and the calculation of porosity evolution with burnup is carried out. It is shown that taking into account the formation of porosity with burnup compared to the case with constant porosity equal to as-fabricated value leads to a decrease in the UO2 fuel thermal conductivity up to about 15% at high burnup values of 120 MWd/kgU. Results of the calculations are also compared with the available experimental data and good agreement was found. The conducted parametric study clearly demonstrated the impact of the key parameters on the results of the present investigation.

Keywords: UO2 thermal conductivity, high burnup, fuel performance code, porosity

Introduction

The thermal conductivity is one of the most important properties of fuel that has great influence on the fuel operating temperature, performance and behavior. In general, ceramic fuels as UO2 have rather low thermal conductivity that is affected by several factors such as temperature, porosity, dissolved and precipitated solid fission products, changing in fuel microstructure and establishment of high burnup structure, radiation damage and stoichiometry. The porosity effect on thermal conductivity, among other factors, is one of the most difficult properties to characterize. In fact the oxide fuel is generally fabricated by sintering pressed powdered U02 at high temperature. By controlling the sintering conditions, material of any desired density, usually around 90% of the maximum possible or theoretical density of the solid, can be produced. As a result, as-fabricated porosity is already present in unirradiated fuel. The fission gas atoms resulted from the fission process, are known to be insoluble in the fuel matrix and to precipitate into intragranular and intergranular bubbles, which contribute to fuel swelling and porosity generation. With increasing burnup under low temperature condition, UO2

fuel is known to undergo irradiation-induced recrystallization process by which more grain boundaries are formed to accommodate fission gas atoms. Recrystallization initiates from the boundary of the grain and proceeds toward its center until the grain is totally consumed. Large grains turn into small fine grains so as to absorb gas atoms in the grain boundary effectively, thus large intergranular bubble will be produced and make a major contribution to the gas bubble swelling and corresponding porosity generation [1-5].

Various equations, both empirical and analytical have been developed to describe the effect of porosity on the thermal conductivity. Taking a unit cell of porous material represented as a cube of the solid material surrounding a gas pore, Loab [6] and Kampf et al. [7] derived an analytical expression for the porosity effect on thermal conductivity. Studies on thermal conductivity of high burnup structure and experimental observations of increasing porosity in the rim region of UO2 pellet led to proposing some correlations for porosity evolution with burnup in this region [8]. Lee et al. [9] studied the effect of calculated porosity of rim region of UO2 pellet on thermal conductivity degradation assuming that all generated fission gas atoms in the rim region are retained in the rim pores. Using the HALDEN thermal conductivity model, they found that the rim porosity yields a thermal conductivity decrease of about 20% at high burnups. Recently, based on the relevant experimental data obtained by Spino et al. [10], Lemes et al. [11] developed an empirical expression for porosity of UO2 fuel as a function of local burnup ranging from 60 to 300 MWd/kgU, including the possible effects of pellet-cladding mechanical interaction.

In this paper, an attempt is made to quantify the influence of porosity on the thermal conductivity of UO2 matrix. This is achieved using a model for determining porosity evolution based on the work of Spino at al. [12] as well as the Rest model [2,4,5] for UO2 swelling with progressive recrystallization. Then as a case study, the Lucuta model [13] for UO2 thermal conductivity is selected to evaluate the effect of calculated porosity evolution on the thermal conductivity up to the local burnup of 120MWd/kgU.

Models and methods

Lucuta model of thermal conductivity

The model of irradiated UO2 thermal conductivity developed by Lucuta et al. [13] can be expressed as:

$$k = k_0 \kappa_B \kappa_S \kappa_{RD} \kappa_P \quad (1)$$

where k_0 is unirradiated UO2 thermal conductivity and for a fully dense UO2 (100% of theoretical density) as a function of temperature is given by the expression [13]

$$k_0 = \frac{1}{0.0375+2.165\times10^{-4}T} + \frac{4.715\times10^{9}}{T^2}\exp\left(-\frac{16361}{T}\right) \quad (2)$$

where T is the temperature in Kelvin.

κ_B is the burnup dependence factor that consists of the following two contributions:

$$\kappa_B = \kappa_{DS}\,\kappa_{PS}$$

$$\kappa_{DS} = \left(\frac{1\,09}{Bu^{3\,265}} + \frac{.0643}{\sqrt{Bu(\%)}}\sqrt{T(K)}\right) \arctan\left(\frac{1}{\frac{1\,09}{Bu(\%)^{3\,265}} + \frac{.0643}{\sqrt{Bu(\%)}}\sqrt{T(K)}}\right) \quad (3)$$

$$\kappa_{PS} = 1 + \frac{0\,019Bu(\%)}{(3-0\,019Bu(\%))}\,\frac{1}{1+\exp\left(-\frac{T(K)-1200}{100}\right)} \quad (4)$$

where κ_{DS} and κ_{PS} denote the effect of the dissolved and precipitated solid fission products, respectively and Bu is the fuel burnup in percent .

κ_S is associated to the effect of deviation from the stoichiometry on the thermal conductivity that is important for accident conditions and fuel defects. In both cases, the fuel becomes hyper stoichiometric and thermal conductivity would decrease accordingly [13], but no deviation from the stoichiometry under normal operating conditions is observed, so that under these conditions $\kappa_S = 1$

κ_{RD} refers to the effect of the radiation damage from the neutrons, α-decay which increases lattice defects and consequently reduces the fuel thermal conductivity. κ_{RD} can be expressed as [13]:

$$\kappa_{RD} = 1 - \frac{0\,2}{1+\exp\left(\frac{(T(K)-900)}{80}\right)} \quad (5)$$

κ_P indicates the porosity effect on the fuel thermal conductivity. The expression for κ_P, according to Maxwell-Eucken formula [13] consists of a pore shape factor, σ, that equals to 1.5 for the spherical pores and hence the total porosity P given by:

$$\kappa_P = \frac{1-P}{1+(\sigma-1)P} \quad (6)$$

In the present study, we examine the effect of porosity evolution with burnup on the thermal conductivity as expressed by the factor κ_P in the Lucuta formula for irradiated UO2 fuel thermal conductivity.

Porosity

Porosity is defined as the ratio of voided volume over the total volume. Total porosity P is composed of two contributions: One comes from pores P_v including as-fabricated voids as initial porosity with no contribution to the matrix swelling and the other named swelling porosity P_s stems from the irradiation induced fission gas bubbles contributing to the matrix swelling. If $\Delta V^{\text{gas bubble}}/V_0^{\text{matrix}}$ represents the fractional fuel matrix swelling due to fission gas bubbles, where V_0^{matrix} denotes the initial matrix volume, and $\Delta V^{\text{gas bubble}}$ is the increase of matrix volume due to bubble formation, then by definition the swelling porosity Ps is given by:

$$P_s = (\Delta V^{\text{gas bubble}}/V_0^{\text{matrix}}) / (1 + \Delta V^{\text{gas bubble}}/V_0^{\text{matrix}}) \quad (7)$$

Taking the unirradiated fuel volume as the reference state in the fuel swelling calculation, the pore P_v may be obtained by the following expression given in [12]

$$P_v = 1 - (1 + \Delta V^{\text{matrix}}/V_0^{\text{matrix}})(\rho/\rho_{\text{th}}), \quad (8)$$

where ρ is the bulk fuel density and ρ_{th} is the theoretical density of UO_2, and $\Delta V^{\text{matrix}}/V_0^{\text{matrix}}$ represents the total fractional fuel matrix swelling caused by both solid ($\Delta V^{\text{solid}}/V_0^{\text{matrix}}$) and gaseous ($\Delta V^{\text{gaseous}}/V_0^{\text{matrix}}$) fission products as follows:

$$\Delta V^{\text{matrix}}/V_0^{\text{matrix}} = \Delta V^{\text{solid}}/V_0^{\text{matrix}} + \Delta V^{\text{gaseous}}/V_0^{\text{matrix}} \quad (9)$$

With $\Delta V^{\text{gaseous}}/V_0^{\text{matrix}}$ representing the total fractional gas swelling resulting from both gas atoms in the dynamic solution and the fission gas bubbles as follows

$$\Delta V^{\text{gaseous}}/V_0^{\text{matrix}} = \Delta V^{\text{gas atom}}/V_0^{\text{matrix}} + \Delta V^{\text{gas bubble}}/V_0^{\text{matrix}} \quad (10)$$

The swelling due to solid fission products is given by [14] :

$$\Delta V^{\text{solid}}/V_0^{\text{matrix}} = 0\,0032 * \text{Bu}(\text{GWd/tM})/10, \quad (11)$$

where Bu depicts the fuel burnup. To estimate the swelling due to gaseous fission products, an analytical approach to fuel element swelling developed in the low temperature condition (T < 850 K) is used [5,15].

Hence the total porosity P =Ps+Pv takes the following form:

$$P = 1 - (1 + \Delta V^{\text{matrix}}/V_0^{\text{matrix}})(\rho/\rho_{\text{th}}) + (\Delta V^{\text{gas bubble}}/V_0^{\text{matrix}}) / (1 + \Delta V^{\text{gas bubble}}/V_0^{\text{matrix}}) \quad (12)$$

To study the evolution of porosity with burnup using Eq. (12), one needs to calculate the terms associated with the matrix swelling.

Matrix swelling before grain recrystallization

An analytical approach in the low burnup regime to obtain fission gas induced swelling was developed in references [4,5,12]. For completeness, this approach is outlined in this Section.

In this approach, fission gas swelling is a function of the fission gas atoms and bubbles concentration and lattice size in the fuel matrix. The density of the gas in the intragranular bubbles change by

irradiation time and can be written as the sum of the two equations, representing the time evolution of the fission gas bubble density c_b and of the gas atoms content in bubbles n_b as follows [4,5,12]:

$$\frac{dc_b(t)}{dt} = \frac{16\pi f_n D_g r_g c_g(t) c_g(t)}{n_b(t)} - \frac{b}{2} c_b(t) \quad (13)$$

$$\frac{dn_b(t)}{dt} = 4\pi r_b(t) D_g c_g(t) - \frac{b}{2} n_b(t) \quad (14)$$

where f_n ($\approx 10^{-4}$) is the bubble nucleation factor, b is related to the effects of fission-induced gas atom resolution and is the rate of gas atoms ejected from the bubble, and c_g, D_g, r_g and r_b are the concentration of the intragranular gas atom, diffusion coefficient and radii, respectively.

In present work, the system of Eqs. (13) and (14), with initial conditions (cb=nb=0) is solved numerically the by Runge Kutta-4 to obtain c_b and n_b .The first term on the RHS of Eq. (14) represents the creation rate of intragranular bubbles with an average size of r_b. The last terms on the RHS of Eqs. (13) and (14) are a loss due to the whole bubbles destruction and a loss term due to gas atom chipping from bubbles, respectively.

The concentration of gas atoms within grain $c_g(t)$, according to Rest [2] is formulated as

$$c_g(t) = \frac{-(1+f_s)+\left[(1+f_s)^2+64\pi f_n r_g D_g \alpha \dot{f} t/b\right]^{\frac{1}{2}}}{32\pi f_n r_g D_g/b}, \quad (15)$$

where $\dot{f}(\text{fission}/\text{m}^{-3}\text{sec}^{-1})$ is the fission density rate, α is the number of gas atoms produced per fission event and f_s is the fraction of the gas that diffuses to the grain boundary of diameter d_g and can be approximated by [4]

$$f_s = \frac{8}{d_g}\left(\frac{D_g t}{\pi}\right)^{\frac{1}{2}} - \frac{6}{d_g^2} D_g t \qquad \frac{4\pi^2 D_g t}{{d_g}^2} \le 1 \quad (16)$$

$$f_s = 1 - \frac{{d_g}^2}{60 D_g t} + \frac{{d_g}^2}{2 D_g t} \exp\left(-\frac{4\pi^2 D_g t}{{d_g}^2}\right) \qquad \frac{4\pi^2 D_g t}{{d_g}^2} > 1 \quad (17)$$

To obtain the bubble concentration on the grain boundary, $C_b(t)$, one can use an approximate relation as [4,5,12]:

$$C_b(t) = \left(\frac{8zaK}{12^{1/3}\pi^2 \xi D_g \delta}\right)^{\frac{1}{2}}, \quad (18)$$

where $\frac{a^3}{12}$ is the average atomic volume in UO2 [12], a is the lattice constant, z is the number of sites explored per gas-atom jump, δ is the width of the boundary, ξ is a grain-boundary diffusion

enhancement factor, and K is the diffusion flux of gas-atoms from grain interior to the grain boundary given by [12]:

$$K = \frac{d_g}{3}\frac{dc_g}{dt}\frac{d(f_s t)}{dt}, \quad (19)$$

with

$$\frac{dc_g}{dt} = \frac{\alpha \dot{f} - c_g df_s/dt}{1 + f_s + 32\pi f_n r_g D_g c_g / b} \quad (20)$$

The gas concentration on the grain boundaries, C_g, is given by:

$$C_g(t) = \frac{d_g}{3} f_s(t) c_g(t) \quad (21)$$

And the average number of gas atoms in a grain boundary bubble is

$$N_b = \frac{C_g(t)}{C_b(t)} \quad (22)$$

The radius of the intragranular bubble rb can be calculated using the modified Van der Waals gas law as:

$$\frac{2\gamma}{r_b}\left(\frac{4\pi r_b^3}{3} - h_s B n_b\right) = n_b kT \quad (23)$$

where B is the Van der Waals constant for Xe, k is Boltzmann's constant, T is the absolute temperature, γ is the surface tension and h_s is a fitting parameter that for a given T makes Eq. (23) equivalent to the hard sphere equation of state [12].

An approximate solution to Eq. (23) for intragranular bubbles in the nanometer size range is given by

$$r_b(t) = \left(\frac{3 h_s B n_b(t)}{4\pi}\right)^{1/3}, \quad (24)$$

where B is the Van der Waals constant for Xe, k is Boltzmann's constant, T is the absolute temperature, γ is the surface tension and h_s is a fitting parameter that for a given T makes Eq. (23) equivalent to the hard sphere equation of state [12].

The radius of the intergranular bubble Rb can be obtained by numerically solving Eq. (23) written on the grain boundary while substituting nb and rb with N_b and R_b, respectively.

Finally, the total fractional gaseous swelling defined by Eq. (4) is given as [12]

$$\left(\frac{\Delta V^{gaseous}}{V_0^{matrix}}\right)_g = \frac{c_g a^3}{4} + \frac{4\pi}{3}\left(r_b^3 c_b + \frac{3R_b^3 C_b}{d_g}\right) \quad (25)$$

The first term on the RHS of Eq. (25), represents the swelling due to gas atoms in the dynamic solution and does not contribute to the swelling porosity Ps, and the second term represents the contribution of intragranular and intergranular bubbles to the matrix swelling leading to swelling porosity formation, respectively.

Matrix swelling with grain recrystallization

In low temperature, high burnup conditions, irradiation induced recrystallization process wherein the as-fabricated micron-size grains are transformed to submicron-sized grains accelerates the fission gas swelling. This is due to a combination of short diffusion distances which further facilitates gas depletion, increased grain-boundary area per unit volume, and greater intergranular bubble growth rates as compared to that in the grain interior. The initiation of the recrystallization has been observed to occur predominantely along the preexisting grain boundaries at a fission density of F_{dx} estimated as [2,5]

$$F_{dx} = 4 \times 10^{24} \dot{f}^{2/15} . \quad (26)$$

Subsequently, the recrystallization front moves toward the grain center eventually consuming the entire grain. Thus, the volume fraction of recrystallized material is a function of the irradiation time as well as the initial grain size given by [2,5]

$$V_r = 1 - \left[1 - \frac{96\gamma B_2 (F_d - F_{dx})}{d_g C_A C_\rho} \sqrt{\frac{f(\nu)}{2\pi}}\right]^3 , \quad (27)$$

where F_d and $F_{dx} = \dot{f}t_x$ are the fission density related to the irradiation time, t, and onset of the recrystallization time, t_x respectively, $f(\nu) = (1 - \nu/2)/(1 - \nu)$, where υ is poisson's ratio, C_A is 3 for the cubic cells, C_ρ is within a factor of unity [2,5], B_2 is a parameter in the expression for the fission induced microscopic creep, $\dot{\varepsilon} = B_2 \dot{f} \sigma$, and stress, σ, is a function of the lattice displacement, $\sigma = E\, \Delta a/a_0$, where E is the bulk modulus of fuel material [3]. After the onset of the recrystallization, the original grain is divided into two regions of the recrystallized and unrecrystallized grain. The total fractional gas swelling can be expressed as

$$\left(\frac{\Delta V^{gaseous}}{V_0^{matrix}}\right)_{TOT} = (1 - V_r)\left(\frac{\Delta V^{gaseous}}{V_0^{matrix}}\right)_g + V_r \left(\frac{\Delta V^{gaseous}}{V_0^{matrix}}\right)_{gx} , \quad (28)$$

where V_r is given by Eq. (27), $\left(\frac{\Delta V^{gaseous}}{V_0^{matrix}}\right)_g$ indicates the gaseous swelling within the unrecrystallized zone which is still composed of both the intragranular and intergranular bubbles given by Eq. (25),

and $(\frac{\Delta V^{gaseous}}{V_0^{matrix}})_{gx}$ denotes the gaseous swelling within the recrystallized area which is due to the Xe depletion in the fuel matrix steming from the intergranular bubbles only, and can be calculated by [2,5]

$$(\frac{\Delta V^{gaseous}}{V_0^{matrix}})_{gx} = 4\pi R_{bx}^3 \left(\frac{C_b}{d_g} + \frac{C_{bx}}{d_{gx}} + \frac{1}{3d_{gx}^3} \right) \quad (29)$$

where R_{bx} and C_{bx} are the radius and the density of the intergranular fission gas bubble and d_{gx} is the grain size after the recrystallization. For evaluation of C_{bx}, Eq. (18) is used , and Eq. (23) is numerically solved for R_{bx}, with as fabricated grain size d_g replaced with the recrystallized grain size d_{gx} and N_b with N_{bx} which is obtained by the modified expression given by Yi Cui et al. [16] as follows:

$$N_{bx} = \frac{\alpha \dot{f} t}{3\left(\frac{C_b}{d_g} + \frac{C_{bx}}{d_{gx}} + \frac{1}{3d_{gx}^3} \right)} . \quad (30)$$

In Eq. (30), it was assumed that in the recrystallized region of the fuel, the majority of the generated gas is on the grain boundaries. This assumption is consistent with the fractional gas release calculated using Eq. (17) for $\frac{4\pi^2 D_g t}{{d_g}^2} > 1$ [4].

Results and discussion

Matrix swelling

The values of the parameters used in the present calculations are listed in Table 13. Fig. 17 depicts the total matrix swelling of UO2 fuel as a function of the local burnup calculated at a representative temperature of 800K for various recrystallized grain sizes. It is seen that after initiation of recrystallization, the fuel matrix swelling rate increases showing a “Knee” in the corresponding curve as would be expected. Moreover, the increase of recrystallized grain **Fig. 18** shows the total matrix swelling as a function of temperature for various burnups. In fact high temperature will induce the large intergranular bubble radius leading to high gaseous bubble swelling.

Porosity evolution

Having determined the gas bubble swelling $\Delta V^{gas\ bubble}/V_0^{matrix}$ as well as the total fractional matrix swelling $\Delta V^{matrix}/V_0^{matrix}$ we can now calculate the swelling porosity Ps , pore contribution Pv ,and the total porosity P by virtue of Eqs.(7), (8), and (12), respectively, with the relative immersion density ρ/ρ_{th} for the local burnups in the range 15-100 MWd/kgU estimated by the following expression [12].

$$\rho/\rho_{th} = \left(0\,9383 - 1\,71 \times 10^{-4} Bu^{3/2}\right)^{1/2}, \quad (31)$$

where Bu is burnup in MWd/kgU.

Table 13. Values of various parameters used in the calculations.

Parameter	Value	Unit	Reference
α	0.26	-	[14]
b_0 *1	10^{-23}	m^3	[12]
D_0 *2	$1\,2 \times 10^{-39}$	m^5	[12]
r_g	$2\,16 \times 10^{-10}$	m	[14]
ξ	$1\,65 \times 10^{3}$	-	[12]
δ	2×10^{-9}	m	[2]
γ	1	Jm^{-2}	[14]
B	$8\,5 \times 10^{-29}$	$m^3 atom^{-1}$	[14]
f_n	10^{-2}	-	[12]
h_s	0.6	-	[12]
d_g	5×10^{-6}	m	[5]
$\dot{f}$	2×10^{19}	$m^{-3}s^{-1}$	This work
B_2	1×10^{-34}	$m^5\,N^{-1}$	[2]
ν	0.31	-	[17]
d_{gx}	$0\,15 \times 10^{-6}$	m	[18]

*1 $b = b_0\dot{f}$,
*2 $D_g = D_0\dot{f}$

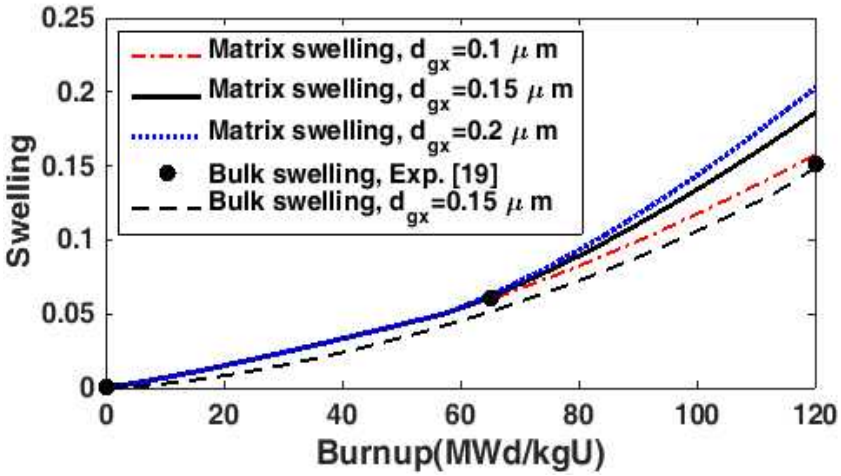

Fig. 17. Total matrix swelling of UO_2 fuel calculated for different recrystallized grain sizes at T=800K ($\Delta V^{matrix}/V_0^{matrix} = \left(\frac{\Delta V^{gaseous}}{V_0^{matrix}}\right)_{TOT} + \left(\frac{\Delta V^{solid}}{V_0^{matrix}}\right)$) in addition UO_2 bulk swelling calculated and data.

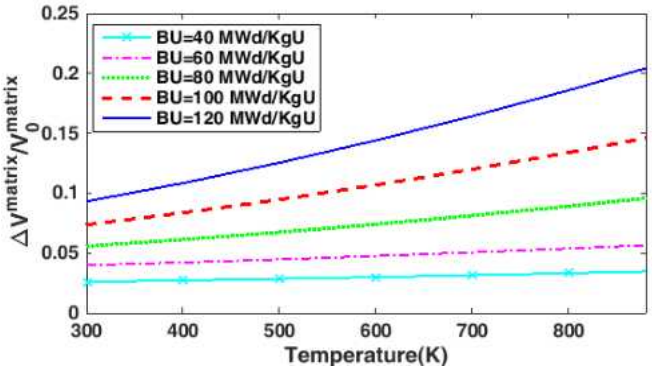

Fig. 18. Total matrix swelling of UO_2 fuel as a function of temperature for different burnups with $\mathbf{dgx = 0\ 15\ \mu m}$.

Fig. 19 displays the calculated swelling porosity P_s, pore P_v, and the total porosity P as a function of burnup compared with the experimental data [10]. It is seen that at the high burnups owing to the increase of gas bubble swelling contributed by the intergranular bubbles gathered in the recrystallized grain boundary, the swelling porosity increases, resulting in an increase in the total porosity. As shown in Fig. 3, the calculated total porosity values follow the trend of the porosity data as a function of burnup.

Thermal conductivity

The thermal conductivity of this work was obtained with calculation of total porosity (by using Eq. (12)) that is indicated in **Fig. 19** and by placing in the Maxwell-Eucken formula, Eq. (6). **Fig. 20**a and b compare the evolution of UO_2 thermal conductivity based on the Lucuta model Eq. (1) as a function of the local burnup for two cases: a constant volume porosity of 5% and a varying porosity computed by the present methodology for T=490K and T=800K. It can be seen that taking into account the evolution of porosity with burn up leads to a decrease in the thermal conductivity of about 15% at a local burnup of 120MWd/kgU for T=490K and 800K. In addition, it has better agreement with the trend of (33)

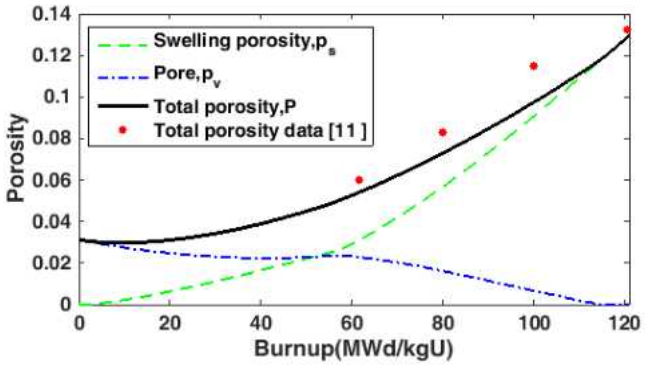

Fig. 19. Formation of pore P_v, swelling porosity P_s, and total porosity P as a function of burnup at 800K in addition total porosity data.

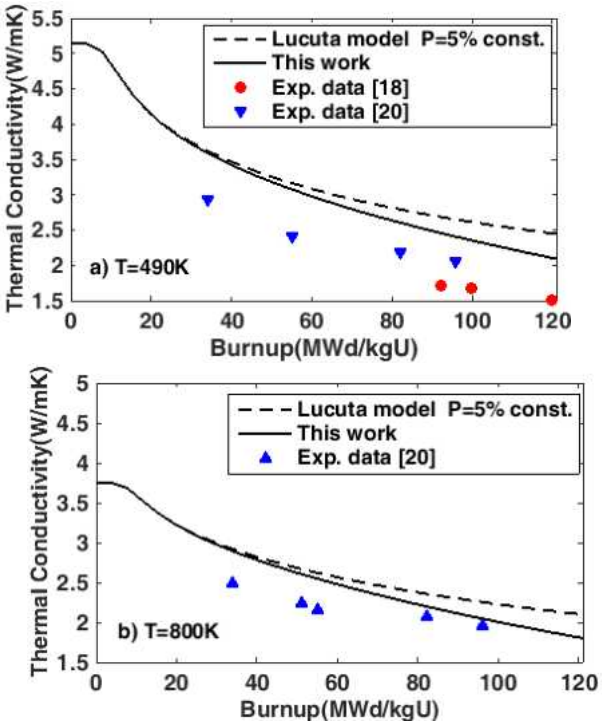

Fig. 20. UO_2 thermal conductivity based on Lucuta model vs. burnup with porosity evolution included in comparison to the case with constant porosity 5% and experimental data at a) 490K, b) 800K.

Experimental data of thermal conductivity by Walker et al. [18] and Ronchi et al. [20] rather than original Lucuta model.

The thermal conductivity of present work is normalized from the 97% theoretical density to 95% by using the following relations that is the general form of the relation in Ref. [21]:

$$k_0 = \frac{1+(\sigma-1)(1-d)}{d} k_d \qquad (32)$$

$$k_{d'} = \frac{d'}{1+(\sigma-1)(1-d')} k_0,$$

where k_0 and k_d are the thermal conductivity at 100% and d% theoretical density, respectively. $k_{d'}$ is the thermal conductivity at the percentage of theoretical density, d'. The term, $\frac{1+(\sigma-1)(1-d)}{d}$, adjusts the thermal conductivity from d% to 100% theoretical density. So, for this case d is 97% and d' is 95%. The shape factor, σ, is 1.5 for spherical pore shape [13].

Conclusions

In this paper the volume porosity formation of irradiated UO_2 fuel with burnup was estimated using the existing gaseous swelling model. It was found that at high burnups, around 120MWD/kgU, total porosity of the order of 15% can be produced as a result of the swelling porosity generated due to speeding up the formation of intergranular bubbles gathered on the boundary of recrystallized grains. In order to study the influence of the porosity formation on the irradiated UO_2 thermal conductivity, the Lucuta model for UO_2 thermal conductivity consisting of a porosity correction factor was applied. It was found that a decrease in the UO_2 thermal conductivity up to about 15% at local burnup levels of around 120MWd/kgU compared to the case with as fabricated porosity during irradiation time T=490 and 800K occurs. The obtained results were consistent with the trends of the available data. A parametric study conducted into the key parameters used in the calculations indicated that although, in general, these parameters have a considerable impact on the calculated matrix swelling after the grain recrystallization, but their impact on the calculated thermal conductivity (due to porosity factor) turned out to be very limited.

It is expected that the degradation of thermal conductivity due to formation of porosity increases for local burnups higher than 120MWd/kgU. The model presented can be incorporated into fuel modeling codes to improve calculations of fuel thermal conductivity and in turn fuel operating temperature under normal and accident conditions at extended burnup.

References

[1] J. Rest, An alternative explanation for evidence that xenon depletion, pore formation, and grain subdivision begin at different local burnups , J. Nucl. Mater, 277 (2000) 231-238.
[2] J. Rest, A model for the effect of the progression of irradiation-induced recrystallization from initiation to completion on swelling of UO2 and U–10Mo nuclear fuels, J. Nucl. Mater, 346 (2005) 226–232.
[3] J. Rest, Derivation of analytical expressions for the network dislocation density, change in lattice parameter, and for the recrystallized grain size in nuclear fuels ,J. Nucl. Mater, 349 (2006) 150–159.
[4] J. Rest, G. Kagana, A Physical description of fission product behavior in fuels for advanced power reactors, ANL-07/24, Argonne National Laboratory, 2007, p. 21-26.
[5] J. Rest, editor: Rudy J. M. Konings, Comprehensive Nuclear Materials, Vol.3, Elsevier (2012) 579-627.
[6] A. L. Loeb, Thermal Conductivity: VIII, A theory of thermal conductivity of porous materials, J. Amer. Ceram. Soc., 37 (1954) 96-99.
[7] H. Kampf, G. Karsten, Effects of different types of void volume on the radial temperature distribution of fuel pins, Nucl. Appl. Technol., 9 (1970) 288-300.

[8] M. Owaki N. Ikatsu, K. Ohira, N. Itagaki, Development of a fuel rod thermal-mechanical analysis code for high burn up, IAEA-TECDOC-1233, Session 6 (2000) 375-385.
[9] B.H. LEE, Y. H. KOO, D. S. SOHN, Rim characteristics and their effects on the thermal conductivity in high burnup UO2 fuel, J. Nucl. Sci. Tech, 38(2001)45-52.
[10] J. Spino, A. D. Stalios, H. Santa Cruz, and D. Baron, Stereological evolution of the rim structure in PWR-fuels at prolonged irradiation: Dependencies with burnup and temperature, J. Nucl. Mater, 354 (2006) 66-84.
[11] Martín Lemes, Alejandro Soba, Alicia Denis, An empirical formulation to describe the evolution of the high burnup structure, J. Nucl. Engin. Tech, 456 (2015) 174-181.
[12] J. Spino, J. Rest, W. Goll, C. T. Walker, Matrix swelling rate and cavity volume balance of UO2 fuels at high burnup, J. Nucl. Mater, 346 (2005) 131-144.
[13] P.G. Lucuta, Hj. Matzke, I.J. Hastings, A pragmatic approach to modelling thermal conductivity of irradiated UO_2 fuel: review and recommendations, J. Nucl. Mater. 232 (1996) 166-180.
[14] D.R. Olander, Fundamental aspects of nuclear fuel elements, Technical Information Center & Energy Research and Development Administration (publisher), USA, 1976, pp. 193-194.
[15] J. Rest, A model for the influence of microstructure, precipitate pinning and fission gas behavior on irradiation-induced recrystallization of nuclear fuels, J. Nucl. Mater, 346 (2004) 175-184.
[16] Yi Cui, Shurong Ding, Zengtao Chen, Yongzhong Huo, Modifications and applications of the mechanistic gaseous swelling model for UMo fuel, J. Nucl. Mater, 457 (2015) 157-164.
[17] J. Rest, A microstructurally-based model for the evolution of irradiation-induced recrystallization in U-Mo monolithic and Al-dispersion fuels, RERTR-2004 International Meeting on Reduced Enrichment for Research and Test Reactors, USA, Argonne National Laboratory, 2004, p. 17.
[18] C.T. Walker, D. Staicu, M. Sheindlin, D. Papaioannou , W. Goll, F. Sontheimer, On the thermal conductivity of UO2 nuclear fuel at a high burnup of around 100 MWd/kgHM, J. Nucl. Mater, 350 (2006) 19-39.
[19] M. L. Bleiberg, R. M. Berman, and B. Lustman, Effects of high burn-up on oxide ceramic fuels, insymp. on radiation damage in solid and reactor materials, Proc. Series, IAEA, Venice (1963), p. 319.
[20] C. Ronchi, M. Sheindlin, D. Staicu, M. Kinoshita, Effect of burn-up on the thermal conductivity of uranium dioxide up to 100.000 MWd/t, J. Nucl. Mater., 327 (2004) 58–76.
[21] K. J. Geelhood, W.G. Luscher, FRAPCON-3.5: A Computer Code for the Calculation of Steady-State, Thermal-Mechanical Behavior of Oxide Fuel Rods for High Burnup, Pacific Northwest National Laboratory, (2014), p. 2.18.

ICNST 2024
International Conference on Nuclear Science and Technology
6- 8 MAY 2024 | Isfahan, Iran

Point defect effects on the phonon thermal conductivity of Zr-1%Nb single crystal by Reverse non-equilibrium Molecular dynamics (Paper ID : 1501)

M. Rajabi, M. Hassanvand[11]*, M. Asadi Asadabad[2], M. A. Amirkhani[2]
1 Department of physics, Isfahan University of Technology, Isfahan, Iran
2 Reactor and Nuclear Safety Research School, Nuclear Science and Technology Research Institute, Tehran, Iran

Abstract

The thermal conductivity of the Zr-1%Nb alloy that is used in the construction of the fuel cladding of the VVER-1000 reactor, is very important for the safe and efficient operation of the reactor. This feature is gradually reduced under the influence of hard working conditions of reactors as well as neutron irradiation. experimental analysis of such changes is difficult due to the various defect contributions. In addition, the existing theoretical models do not cover all aspects of the interaction of thermal carriers and defects. In this work, with using the Reverse Non-Equilibrium Molecular Dynamics (RNEMD) method and Angular Dependent Potential (ADP), the thermal conductivity coefficient of Zr-1%Nb alloy for different concentrations of Vacancy, interstitial, and Frenkel pair defects, in different temperatures and different crystallographic orientations are studied in detail with considering the finite size effect. It was seen that reduction of thermal conductivity occurs anisotropically in different crystallographic directions. For the same concentrations, vacancy defects have a greater effect on the reduction of the average thermal conductivity coefficient than other defects. At high defect concentration condition, the temperature does not affect the thermal conductivity too much.

Keywords: Thermal Conductivity-Point defect- RNEMD- Zr-1%Nb

[11] * *Corresponding Author name*: M. Hassanvand
E-mail address: hassanvand@iut.ac.ir

Introduction

The nuclear fuel cladding plays a very important role in preventing the leakage of radioactive fission products to the surrounding environment and the corrosion of the fuel pellets by the coolant [1]. A group of materials used to make these cladding are based on zirconium which is due to its good mechanical and thermal properties, the low cross-section of thermal neutron absorption and their high resistance to corrosion [2, 3]. Although adding a small amount of niobium to zirconium increases the corrosion resistance and improves its mechanical properties [4, 5], due to the low concentration of niobium, the alloy has almost the same properties as pure zirconium and hexagonal close-packed (HCP) structure at low temperature. Also, at high pressures, the distribution of niobium is almost single and uniform [6].

Nuclear fuel cladding works in extreme condition such as high temperature and pressure, high corrosiveness and various types of irradiation caused by the fission of nuclear fuel elements. The most important part of irradiation damage by high-energy neutrons is displacement damage, in which atoms of the target material are displaced from their positions in the crystal structure [7, 8]. Displacement damage leads to the creation of point defects, displacement cascades and dislocation loops. These microstructural changes also cause the formation of gross structural defects such as swelling, cracking, embrittlement, growth and creep.

These macroscopic damages will have significant effects on the performance, lifetime and safety of the fuel cladding [9-12].

Thermal conductivity is an important physical property to the heat transfer of nuclear fuel cladding that affects the safe and optimal operation of the reactor [13]. This quantity depends on the atomic and molecular structure of the material, alloy composition, crystal defects and impurities, as well as environmental parameters such as temperature and pressure. Defects caused by irradiation damage act as a barrier against thermal carrier (electron, phonon etc.) thereby reducing thermal conductivity. Calculation of thermal conductivity, especially for an irradiated alloy, is one of the most difficult calculations and requires knowing all aspects of the interaction of carriers with each other and with defects and the effect of various parameters on this quantity. In addition, interpretation of experimental results is difficult due to different contributions of defects [14, 15].

Simulation offers us an easier, cheaper and safer way. Molecular dynamics (MD) simulation is one of the suitable ways to calculate this quantity. In this method, thermal conductivity coefficient, kappa, is calculated by equilibrium (EMD) and non-equilibrium (NEMD) approaches [13-24]. Non-equilibrium

methods are based on Fourier's law. These methods calculate thermal conductivity using heat flux and temperature gradient. The equilibrium method is also based on the Green-Kubo relationship [15]. In general, the non-equilibrium methods are both cheaper and simpler than the equilibrium method [13, 14]. So far, many researches have been done using different MD methods to calculate the thermal conductivity of different materials with different potentials. However, little research has been done on the thermal conductivity of zirconium, especially on Zr-1%Nb under conditions of radiation damage with NEMD [13-24]. We also studied effects of Point defects, Vacancy, interstitial, and Frenkel pair on the phonon thermal conductivity of Zr-1%Nb single crystal. In this work, with using RNEMD method (one of the non-equilibrium methods) the thermal conductivity coefficient of Zr-1%Nb alloy for different concentrations of defects, in different temperatures and different crystallographic orientations are studied in details with considering the finite size effect. In this way, we used large-scale atomic/molecular massively parallel simulator (LAMMPS) package and Angular Dependent Potential (ADP) for simulation. ADP potential is generalization of Embedded Atom Method (EAM) potential that includes dipole and quadrupole distortions of the local environment of an atom and predict Zr-1%Nb mechanical properties correctly [6], [25-27]. The structure of this paper is as, in general, in the first part, we explain the simulation method and details, and in the second part, we examine the results obtained for total thermal conductivity of perfect Zr-1%Nb then study reduction of phonon thermal conductivity for different defects in different directions and affected by temperature.

Methodology

Total thermal conductivity of perfect Zr-1%Nb

The total thermal conductivity of alloy is:

$$\kappa_{total} = \kappa_e + \kappa_{ph} \qquad (1)$$

κ_e is electronic thermal conductivity and κ_{ph} is phonon thermal conductivity. We calculated κ_e from the well-established Wiedemann-Franz (W-F) law, that link κ_e with the electrical resistivity [28]:

$$\kappa_e = \frac{LT}{\rho_e} \qquad (2)$$

where $L = 2.44 \times 10^{-8} W\,\Omega / K^2$ is Lorenz number, T is temperature. ρ_e is Electrical resistivity that can be estimated by the equation (3) listed below in the temperature range from 300 K to 1100 K [29];

$$\rho_e \times 10^8 (\Omega \cdot m) = -9.08 + 0.2535\,T - 2.0391 \times 10^{-4} T^2 + 9.505 \times 10^{-8} T^3 \quad (3)$$

Reverse Non-Equilibrium Molecular Dynamics (RNEMD) method

Reverse non-equilibrium molecular dynamics (RNEMD) method, one of the non-equilibrium methods in LAMMPS used to calculate phonon thermal conductivity. This method like other non-equilibrium methods, is based on Fourier's law [14]:

$$\kappa = -\frac{J}{\nabla T} \quad (4)$$

Here, J is the heat flux and ∇T temperature gradient. So, in order to calculate kappa from equation (1), we need to calculate heat flux and temperature gradient. In the usual non-equilibrium methods, the procedure is similar to the experimental process, where the temperature gradient is imposed to the system and the heat flux is measured. But in RNEMD method, the cause and effect is reversed. In fact the "effect", the heat flux, is imposed on the system and the "cause", the temperature gradient is obtained from the simulation [14]. This method has several advantages other non-equilibrium methods, such as compatibility with periodic boundary conditions, conservation of total energy and total linear momentum, and the sampling of a rapidly converging quantity (temperature gradient) rather than a slowly converging one (heat flux) [14].

To generate a heat flux profile and a temperature profile, the simulation box is divided into N layers perpendicular to the heat flux direction as shown in Figure (1) [24].

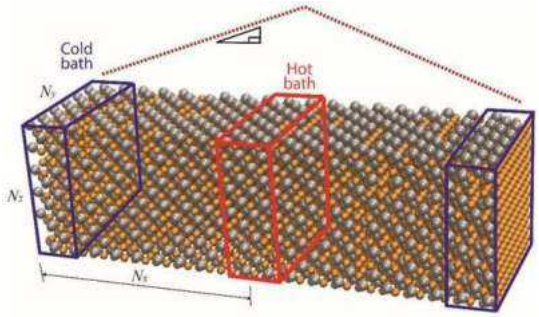

Figure 1: Division of periodic simulation box into slabs. The slabs 1 and N are "cool" and Slab N/2 is "hot"

In the next step, the coldest atom in the hot layer and the hottest atom in the cold layer are considered and then their velocities are exchanged to generate heat flow. This velocity exchange leads to an unphysical flux that gradually creates hot and cold layers and establishes a temperature gradient. After reaching a steady state, the exchanged energy is exactly balanced by the opposite heat flux, then the heat flux is calculated from equation (5)

$$J = \frac{\Delta\varepsilon}{2AWt} \quad (5)$$

Where $\Delta\varepsilon$ is the average exchange energy after reaching the steady state that are exchanged in each W step, t is the time interval of the MD step and A is the area of the normal plate on heat flux. The coefficient 2 is due to the periodic boundary condition and indicates that the heat flux is established in two directions.

For temperature gradient calculation, using statistical mechanics, the temperature of each region can be written as follows:

$$T_k = \frac{1}{3 n_k k_B} \sum_{i \in k}^{n_k} m_i v_i^2 \qquad (6)$$

Where the sum extends over the n_k atoms i in slab k with masses m_i and velocities v_i, k_B is Boltzmann's constant. The temperature profile is then calculated by time averaging and the temperature gradient can be calculated.

In the RNEMD method, if the length of the super cell along the heat flux direction is not sufficiently greater than the mean free path of the phonon, the finite size effect appears. The calculated thermal conductivity, κ is a function of the length of the super cell, L along the heat flux direction:

$$\frac{1}{\kappa} = \frac{a}{L} + b \qquad (7)$$

a and b are constant values [23, 24]. In order to extrapolate the phonon thermal conductivity from finite samples, super cells with different lengths should be designed. The phonon thermal conductivity of the infinite system is equal to the inverse of b, which can be obtained by extrapolating the fitting straight lines to 1/L = 0.

Data files generation with ATOMSK

In order to simulate the thermal conductivity, first with using ATOMSK, zirconium super cells with dimensions of 8*6*30, 8*6*40 and 8*6*60 units cell (with lattice parameters a=b=3.213 Å , c=5.164 Å [25]) was generated. The total atoms of these super cells are 5720, 7680 and 11520. Periodic boundary conditions

are applied in x, y, and z along the $[2\bar{1}\bar{1}0]$, $[01\bar{1}0]$ and $[0001]$ directions respectively.

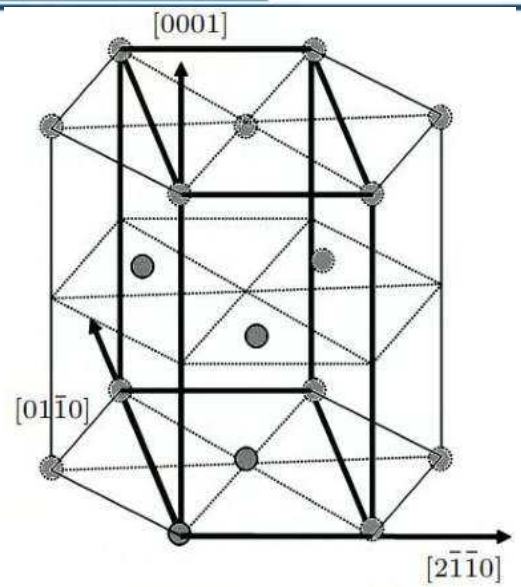

Figure 2: Unit cell of Zr-1%Nb

Then one atomic percent of zirconium atoms was randomly replaced with niobium to create Zr-1%Nb super cells. To produce vacancy defects, a certain percentage of zirconium atoms in the perfect structure are randomly removed. For interstitial defects, the certain percentage of zirconium atoms is added to the structure. Also, to produce Frenkel pair defects, a certain percentage is removed and a certain percentage is added. Defect concentration (nv) is defined as the ratio of the number of defects created to the total number of atoms in the super cell. Four defect concentrations are considered in this work, they are 0.5%, 1%, 1.5% and 2%. In the figure 1, you see a schematic picture of the production 1% of different defects [23].

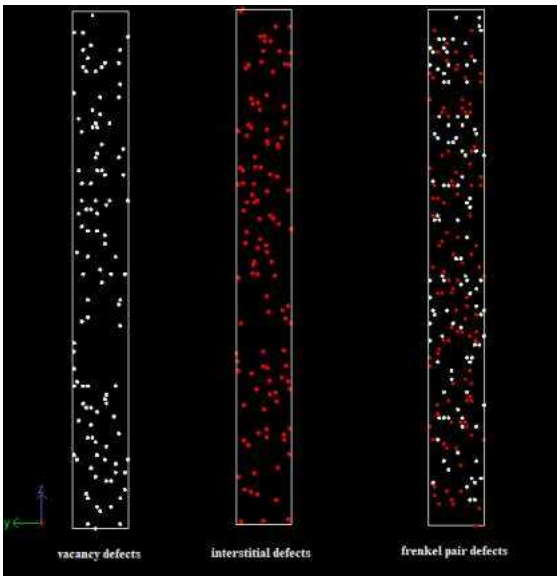

Figure 3: nv=1% of different point defects in super cell with 8×6×60 cells (11520 atoms)

To calculate the average phonon thermal conductivity, we calculate the thermal conductivity in three directions x, y and z along the $[2\bar{1}\bar{1}0]$,directions, respectively. In order to calculate the $[0001]$ and $[01\bar{1}0]$ kappa in each direction, we created a super cell corresponding to that direction by copying the appropriate unit cell, for example, to calculate the kappa along thephic orientation, the crystallogra $x = [2\bar{1}\bar{1}0]$ dimensions of the simulated block are 30×6×8, 40×6×8, 60×6×8 cells with the numbers of atoms being 5720, 7680, 11520, respectively. In the same way for the direction of y and z is done. The simulation temperature was set to 600 and 800 K.

Finally the phonon kappa, which is the average kappa in three directions, can be calculated using the following relationship

$$\kappa_{ph} = \frac{\kappa_x + \kappa_y + \kappa_z}{3} \quad (8)$$

To evaluate the results of our calculations, we used the relationship of total kappa in terms of temperature in the literatures [29]:

$$\kappa_{total}[W/(m \cdot K)] = 23.5 - 0.0192\,T + 1.68 \times 10^{-5} T^2 \quad (9)$$

LAMMPS parameters details

First NVT ensemble is applied initially to equilibrate the system for 0.1 ns. During this stage, the total number of atoms N, the volume of the system V, and the temperature T are kept as constants. The target temperatures of the MD simulation was 600 K and 800 K. Next, the RNEMD method is used to calculate the thermal conductivity of Zr-1%Nb with an NVE ensemble. In this stage, the total number of atoms N, total volume of the system V, and the total energy E are kept as constants. The time step of all the simulation processes was 2 fs and the total simulation time was 1 ns (5×10^5 MD steps).

Results and discussion

Total thermal conductivity of perfect Zr-1%Nb

The calculated results for electron thermal conductivity are given in Table 1

Table 1: electron thermal conductivity of Zr-1%Nb in 600 and 800 kelvin

Temperature (K)	$\kappa_e(W/mK)$
600	16.1
800	17.43

The simulation results of phonon kappa for perfect Zr-1%Nb in three directions and three sizes is shown in figure 4. For each line of this graph, kappa is calculated by reversing b in equation 4. The second diagram is a repetition of the first diagram at a temperature of 800 K.

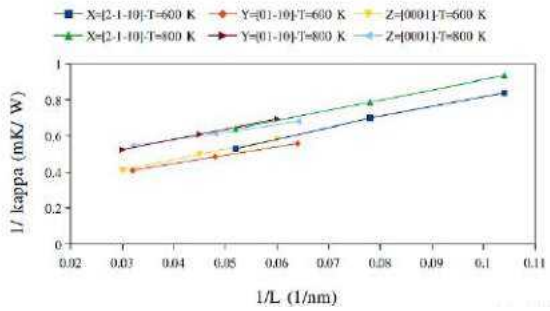

Figure 4: Variations of the inverse of phonon thermal conductivity of perfect Zr-1%Nb with the inverse of the dimension along heat flux in three direction at temperature 600 K and 800 K

The calculated results from graphs are given in Table 2.

Table 2: phonon thermal conductivity of perfect Zr-1%Nb at 600 K and 800 K for different crystallographic orientation

Direction	$\kappa_i (W / mK)$	
	T=600 K	T=800K
$[2\bar{1}\bar{1}0]$	4.5	2.89
$[01\bar{1}0]$	4.21	2.82
$[0001]$	3.87	2.42

The evaluation results have been presented in the table 3

Table3: total thermal conductivity of perfect Zr-1%Nb in 600 and 800 kelvin

Temperature (K)	$\kappa_{total} (W / mK)$		
	This work	Literature[29]	Relative error
600	20.3	18.03	12.5 %
800	20.14	18.9	6.6 %

Average phonon thermal conductivity of Zr-1%Nb with various point defect concentrations

In this section, we investigated the effect of defect concentration and temperature on the thermal conductivity. The results (Figure 5) showed that, for all three types of defects, thermal conductivity decreases with increasing concentration, which was expected, because the increase in defect concentration causes more dispersion of heat carriers and the reduction of the mean free path of the phonons. Vacancy

defects have a greater effect on the reduction of the average thermal conductivity coefficient than other defects. The reduction of the average thermal conductivity of interstitial defects and frenkel pairs at a temperature of 600 K has a relatively similar behavior, but with increasing temperature to 800 K, frenkel pairs behave similar to vacancy defects.

For temperature effect it can also be understood with increasing temperature, the thermal conductivity decreases for all defects. The reason is that with increasing temperature, the number of phonons and collisions between them increases, and therefore the phonon mean free path decreases, so the thermal conductivity also decreases. Also, as the temperature increases, the dependence of the thermal conductivity on the concentration of defects (all three defects) decreases, which occurs more for interstitial defects. Also, at high concentrations, the temperature dependence decreases for all three types of defects, which is less for vacancy defects.

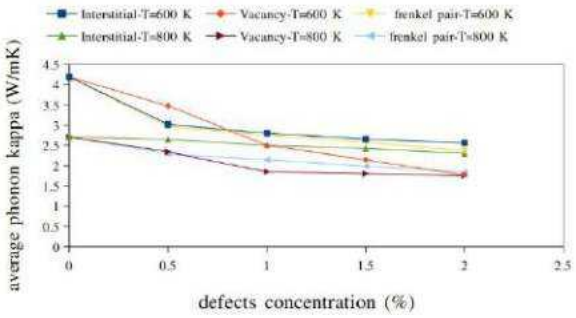

Figure 5: variation of average phonon thermal conductivity with concentration of different defects and different temperature

Anisotropy of phonon thermal conductivity reduction

From the obtained results, we found that the decrease in thermal conductivity occurs anisotropically, which depends on the type of defects and temperature. Vacancy defects reduce thermal conductivity in three directions to an almost equal and significant compared to other defects (Figure 6). Interstitial defects have a significant decrease in thermal conductivity in the $[0001]$direction, but in the other two directions, the decrease is relatively the same and low (Figure 7). Frenkel pairs in $[0001]$and $[01\bar{1}0]$direction have a relatively similar and good reduction (Figure 8).

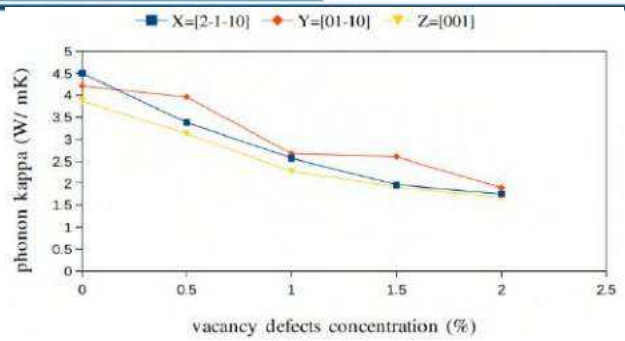

Figure 6: Variations of phonon thermal conductivity with vacancy defects concentration at 600 K and in different orientation

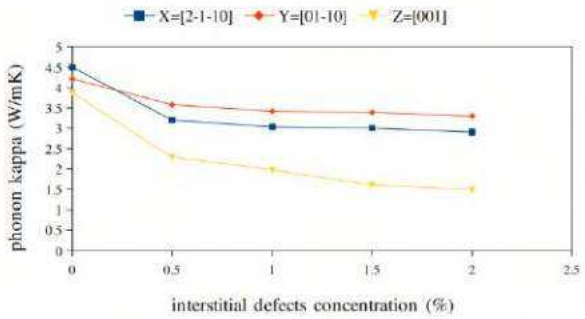

Figure 7: Variations of phonon thermal conductivity with interstitial defects concentration at 600 K and in different orientation

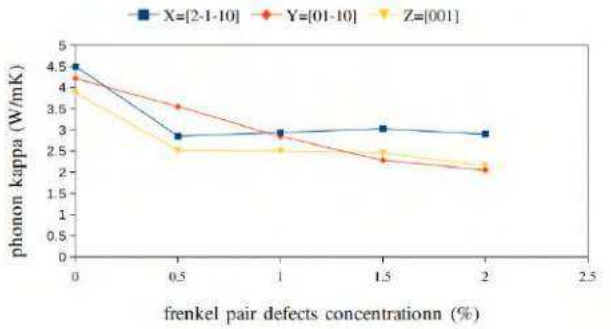

Figure 8: Variations of phonon thermal conductivity with Frenkel pair defects concentration at 600 K and in different orientation

Conclusion

In this work, with using Reverse Non-Equilibrium Molecular dynamics (RNEMD) method and Angular Dependent Potential (ADP), we investigated the thermal conductivity of Zr-1% Nb alloy for different concentrations of vacancy defects, interstitials and Frenkel pairs, at different temperatures and different crystallographic orientations. We understand that point defects reduce the thermal conductivity of the Zr-1% Nb alloy. This reduction takes place anisotropically depending on the type of defects and temperature. Vacancy defects in three directions reduce the thermal conductivity by an equal and significant amount. Interstitial defects have a significant decrease in thermal conductivity in the $[0001]$direction, but in the other

two directions, the decrease is relatively the same and low. Frenkel pairs in $[0001]$ and $[01\bar{1}0]$ direction have a relatively similar and good reduction. The average thermal conductivity of the alloy decreases more for vacancy defects than for other defects. The reduction of the average thermal conductivity of interstitial defects and Frenkel pairs at a temperature of 600 K has a relatively similar behavior, but with increasing temperature, Frenkel pairs behave similar to vacancy defects. As the temperature increases, the dependence of the thermal conductivity on the concentration of defects (all three defects) decreases, which occurs more for interstitial defects. Also, at high concentrations, the temperature dependence decreases for all three types of defects, which is less for vacancy defects.

References

1. C. Evans, "Micromechanisms and micromechanics of Zircaloy-4", Imperial College London 2014.

2. O. Northwood, "The development and applications of zirconium alloys ".Materials Design 6 58–70, 1985.

3. H. G. Rickover, et al, "History of the development of zirconium alloys for use in nuclear reactors", Technical Reports TID-26740, Energy Research and Development Administration , 1975.

4. B. Lustman and F. Kerze, "The Metallurgy of Zirconium", McGraw-Hill Book Company, 1955.

5. B. D. C. Bell, et. al, "The influence of alloying elements on the corrosion of Zr alloys",Corrosion Science 105, pp. 36-43, 2016.

6. M. R. Basaadat, M. Payami , "The study of the Analysis of Irradiation Induced Defect Clusterization for Zr-1%Nb" Alloy Using Atomistic Simulation. JONRA, Vol. 3, No. 2, P 15-21, 2023.

7. I. Chant, K.L. Murty, "Structural materials issues for the next generation fission reactors", JOM 62 (9) , 2010.

8. P. Yvon, F. Carré, "Structural materials challenges for advanced reactor systems", J. Nucl. Mater. 385 (2) ,2009.

9. F. Onimus, J. Béchade, "radiation effects in zirconium alloys", Comprehensive Nuclear Materials, Elsevier, Oxford, 2012.

10. M. Fregonese, et al, "Failure mechanisms of irradiated Zr alloys related to PCI: activated slip systems, localized strains, and iodine-induced stress corrosion cracking", ASTM Spec. Tech. Publ. 377–39, 2000.

11. T.S. Byun, et al," Deformation in metals after low-temperature irradiation: part ii c irradiation hardening, strain hardening, and stress ratios", Acta Mater. 56 (5) 1056–1064, 2008.

12. C.R.F. Azevedo, "A review on neutron-irradiation-induced hardening of metallic Components", Eng. Fail. Anal. 18 (8) (2011) 1921–1942.

13. M. Yichen, et al, "Point defect effects on the thermal conductivity of β-SiC by molecular dynamics simulations". Nuclear Materials and Energy, Volume 20, 2019, 100683

14. F. Muller Plathe, "A simple nonequilibrium molecular dynamics method for calculating the thermal conductivity" 1997 J. Chem. Phys. 106 6082

15. P. K. Schelling et al, "Comparison of atomic-level simulation methods for computing thermal conductivity". 2002 Phys. Rev. B 65
144306

16. A. Maiti et, " Dynamical simulations of nonequilibrium processes — Heat flow and the Kapitza resistance across grain boundaries" Solid State 1997

17. P. Heino and E. Ristolainen, "Thermal conduction at the nanoscale in some metals by MD" Microelectron. J. 34 773, 2003.

18. G. J. Wagner, et al, "An atomistic-to-continuum coupling method for heat transfer in solids"Comput. Methods Appl. Mech. Eng. 197 3351-2008

19. H. Kaburaki, et al, "Thermal Conductivity of Solid Argon by Classical Molecular Dynamics" 1999 Mater. Res. Soc. 538 503

20. A. Maeda and T. Munakata, "Lattice thermal conductivity via homogeneous nonequilibrium molecular dynamics" 1995 Phys. Rev. E 52 234

21. A. R. Abramson, et al, " Interface and Strain Effects on the Thermal Conductivity of Heterostructures A Molecular Dynamics Study" 2002 J. Heat Transfer 124 963

22. M. P. Zhang, et al, "Enhancement effect of asymmetry on the thermal conductivity of double-stranded chain systems" 2011 Chin. Phys. B 20 100508.

23. M. Yichen, et al, "Vacancy defects effect on thermal conductivity of α-zirconium crystal. Mater". Res. Express 6 (2019) 116531

24. W. T. Yu, et al, "Study of lattice thermal conductivity of alpha-zirconium by molecular dynamics simulation". Chin. Phys. B Vol. 22, No. 7 (2013) 076601

25. D. Smirnova, S. Starikov. "Defect and Diffusion Forum. Study of niobium diffusion and clusterization in hcp zr-nb dilute alloys". Trans Tech Publ. 375, P 167–174, 2017.

26. M. R. Basaadat, M. Payami, " The study of the properties of point defects in pure-Zr and Zr-1% Nb alloy using density-functional theory and atomic simulation". Iranian Journal of Physics Research. 20 (1), P 57–64, 2020

27. M. R. Basaadat and M. Payami. "Elastic stiffness tensors of Zr–x Nb alloy in the presence of defects: A molecular dynamicsstudy", International Journal of Modern Physics C 31.02, 2050028, (2020).

28. O. Kahveci, et al, "Measurement and Prediction of the Thermal and Electrical Conductivity of Al-Zr Overhead Line Conductors at Elevated Temperatures", Materials Research. 2018; 22(1): e20180513

29. INTERNATIONAL ATOMIC ENERGY AGENCY, "Thermophysical Properties of Materials for Nuclear Engineering": A Tutorial and Collection of Data, Non-serial Publications , IAEA, Vienna (2008)

ICNST 2024
International Conference on Nuclear Science and Technology
6- 8 MAY 2024 | Isfahan, Iran

Calculation of neutron flux along the beam line of PGNAA system of Isfahan Miniature Neutron Source Reactor Department of Physics, Isfahan University of Technology, Isfahan, Iran, 8415683111 (Paper ID : 1553)

S. Attabi[1], S.Z Kalantari[1], M.H. Choopan Dastjerdi[2], J. Mokhtari[2]

1Department of Physics, Isfahan University of Technology, Isfahan, Iran, 8415683111

2Reactor and Nuclear Safety Research School, Nuclear Science and Technology Research Institute, AEOI, Iran

Abstract

In recent years, various beam tubes have been added to the Isfahan Miniature Neutron Source Reactor (MNSR) for purposes such as neutron radiography (NR), Prompt Gamma Neutron Activation Analysis (PGNAA), and irradiation of large samples outside the reactor core. For experiments like PGNAA and NR. The design of each beam tube should be such that it has optimal parameters at the beam outlet for the intended application. Neutrons and gamma rays generated in the reactor core enter the beam tube, along this path the neutron and gamma flux and dose will have some changes, usually decreasing. Since characteristics of the neutron beam at different points is very important for optimal operation of the beam tubes, methods for measurement or simulation of the neutron and gamma ray flux and dose should be investigated.

In this research the Isfahan MNSR is simulated in detail using MCNP code and thermal, epithermal and fast neutron flux are calculated at the different heights of the beam tube. Results show that the order of magnitude of the thermal neutron flux change from 10^{11} to 10^{6} n/cm^2.s along the height of the PGNAA beam tube, and the calculation errors were lower than 4%. Further results and analysis are presented for epithermal and fast neutron fluxes. Finally, to validate of the simulation results, thermal neutron fluxes were measured for the places in front of the reactor core by indium neutron activation method.

Keywords: Neutron flux, Neutron beam, MCNP, MNSR, PGNAA

Introduction

The MNSR research reactor in Isfahan is considered one of the most important neutron production sources inside the country, which is used in the fields of education, research, production of short-lived radioisotopes, neutron activation analysis, and neutron radiography. The MNSR reactor, which was used as the neutron source in this study, has several beam tubes for different applications. The beam tube studied in this research is the PGNAA beam tube, which is used for prompt gamma neutron activation analysis [1-5]. PGNAA is a nondestructive method for analysis of elements such as Gd, Cd, Ca, N, H, C, B which are difficult or even

impossible to detect with other methods like NAA, and takes much less time compared to NAA since the emitted gamma rays are measured during neutron irradiation [6]. PGNAA technique is used in several areas like analysis of food materials, medicine, environment, materials science, safety and security.

The goal of this study is to obtain neutron flux by calculation method in the PGNAA channel of the MNSR reactor. The MCNP code was used for high detail simulation of the reactor and calculation of neutron flux in thermal, epithermal and fast energy ranges.

Also, we will compare our results for thermal neutron flux of the PGNAA beam outlet of the MNSR reactor with the PGNAA beam outlet of the several reactors around the world.

Materials and Methods

MNSR Reactor

The MNSR research reactor in Isfahan is a tank-in-pool research reactor with a maximum nominal power of 30 kW that uses high enriched (90.2%) UAl_4 as fuel, beryllium reflector, and light water as moderator and coolant. This reactor includes 343 fuel rods, a cadmium control rod, 5 inner irradiation sites, 2 large outer irradiation sites, 3 small outer irradiation sites and 4 regulator rod tubes with diameters of 1.55 cm, 1.95 cm, 1.55 cm and 2.2 cm, respectively. The inner and outer irradiation sites are used for in-core irradiation. The locations of the inner irradiation sites are inside the beryllium reflector surrounding the core, while the outer irradiation sites are located outside the beryllium reflector. At the maximum 30 kW power, the neutron flux at the inner irradiation site (the closest location to the reactor core) is 1×10^{12} n/cm^2.s and at the outer irradiation site it is 5×10^{11} n/cm^2.s. In the initial design of the reactor, there was no channel for irradiation outside the core, but in recent years channels with various applications such as a dry channel for irradiation of large samples, a neutron radiography channel and the PGNAA channel have been added to the reactor [3, 7, 8] . In previous studies, the neutron flux at the beam outlet has been calculated on the order of 10^6 n/cm^2.s. In this study the variations of the neutron beam flux, has been calculated in 3 energy ranges along the PGNAA channel. Figure 1 shows schematic view of the MNSR reactor.

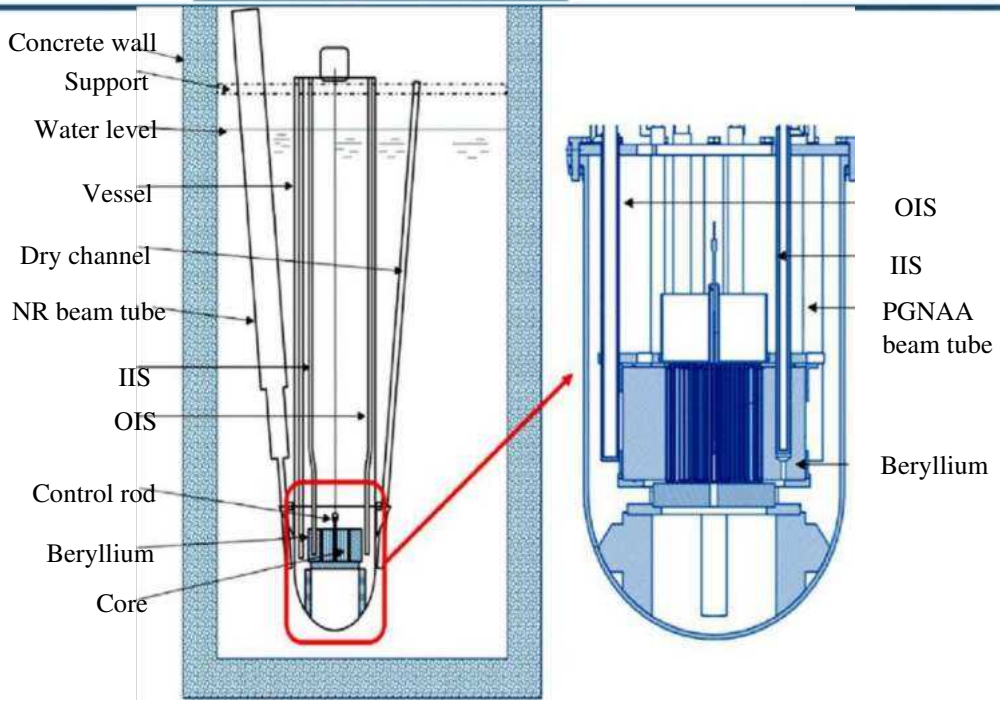

Fig. 1. schematic view of the MNSR reactor

Calculation of Neutron Flux in the PGNAA Channel

The MCNP Monte Carlo code is a multifunctional and powerful code for particle transport calculations [9]. The MCNP code can be used to simulate complex reactor geometries, flux and power distributions in the reactor and the effective multiplication factor.

In this study, at first a 3D model containing all components of the MNSR reactor was simulated using MCNP code. The Kcode critical source card and F5 tally (particle flux at a point) were used to calculate the neutron flux. The input file contains 100 cycles with 10 inactive cycles and one million histories per cycle. The flux distribution analysis was performed using three energy groups including 0 - 0.625 eV for thermal, 0.625 eV- 10^5 keV for epithermal, and 10^5 –10^7 keV for fast neutrons. In this study, the neutron flux at 42 points along the PGNAA channel has been calculated. It should be noted that the MCNP code normalizes the results per one particle from the source, so in order to calculate the total neutron flux, the MCNP results must be multiplied by the MNSR reactor neutron production rate which is equal to 2.38 × 10^{15} n/s. The neutron production rate (N) for the MNSR 30 Kw power reactor is calculated as follows:

$$N = 30 \times 10^3 \frac{J}{S} \times \frac{1eV}{1.6\times10^{-19}J} \times \frac{1\ fission}{2\times10^8 eV} \times \frac{2.45\ n}{1\ fission} = 2.38\times 10^{15}\ (n/s)$$

Figure 2 shows The MCNP model of MNSR

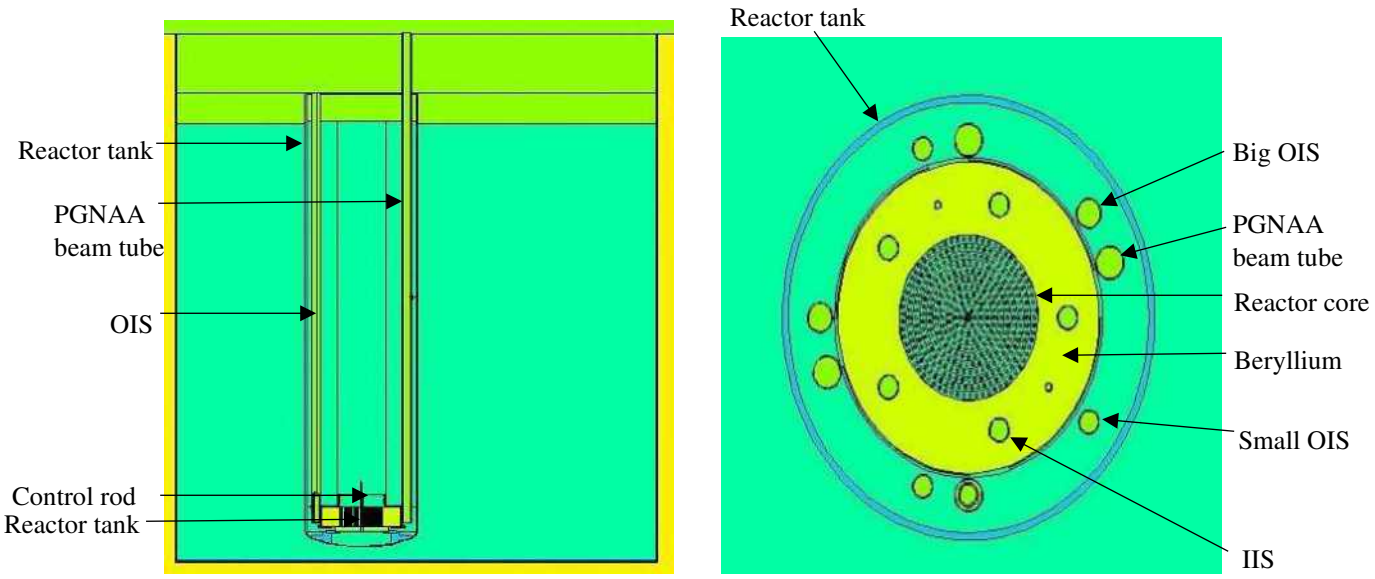

Fig. 2. Shows the MCNP model of MNSR. Cross sectional view (right) and lateral view (left)

Results and Discussion

Tables 1 to 3 present the results of neutron flux calculations in the thermal, epithermal and fast energy ranges, and Figures 3 to 5 show the neutron flux variations in the 3 energy ranges. As expected, the neutron flux is high near the core and decreases exponentially with distance from the core similarly for all 3 energy ranges. Moreover, since the PGNAA channel is located outside the beryllium reflector in the water, as the distance from the core increases with channel height, some neutrons collide with the channel wall and surrounding water and reflect back into the channel. Additionally, interactions between high energy neutrons with air and water molecules around the channel and the channel wall increases the percentage of thermal neutrons in the neutron beam.

The thermal neutron flux at the output of the PGNAA channel was obtained as 2.33×10^6 (n/cm^2.s), which is comparable with the thermal neutron flux value for the other reactors for PGNAA applications.

Table 1 . The computational results of the thermal neutron flux as a function of the distance from the bottom of the PGNAA beam tube

Height (cm)	ϕ thermal neutron (n/cm^2.s)	Error (%)	Height (cm)	ϕ thermal neutron (n/cm^2.s)	Error (%)	Height (cm)	ϕ thermal neutron (n/cm^2.s)	Error (%)
2.2	5.33×10^{11}	0.22	98.7	2.07×10^{8}	2.11	218.7	1.81×10^{7}	1.26
8.7	5.25×10^{11}	0.2	108.7	1.47×10^{8}	2.96	228.7	1.59×10^{7}	2.73
13.7	4.58×10^{11}	0.21	118.7	1.13×10^{8}	1.97	258.7	1.22×10^{7}	3.03
18.7	3.61×10^{11}	0.2	128.7	8.93×10^{7}	1.2	288.7	9.42×10^{7}	2.69
23/7	2.43×10^{11}	0.24	138.7	6.95×10^{7}	1.12	318.7	7.37×10^{6}	1.85
28/7	1.36×10^{11}	0.31	148.7	5.6×10^{7}	2.01	348.7	5.79×10^{6}	1.67
38.7	3.89×10^{10}	0.52	158.7	4.29×10^{7}	1.9	378.7	4.33×10^{6}	1.2
48.7	1.14×10^{10}	0.91	168.7	3.72×10^{7}	2.27	408.7	3.63×10^{6}	0.28
58.7	3.67×10^{9}	1.49	178.7	3.27×10^{7}	1.69	438.7	2.94×10^{6}	0.35
68.7	1.38×10^{9}	2.34	188.7	2.74×10^{7}	2.29	468.7	2.65×10^{6}	0.2
78.7	6.31×10^{8}	3.16	198.7	2.30×10^{7}	3.39	498.7	2.15×10^{6}	0.4
88.7	3.46×10^{8}	3.77	208.7	2.01×10^{7}	2.43	528.7	1.87×10^{6}	0.31

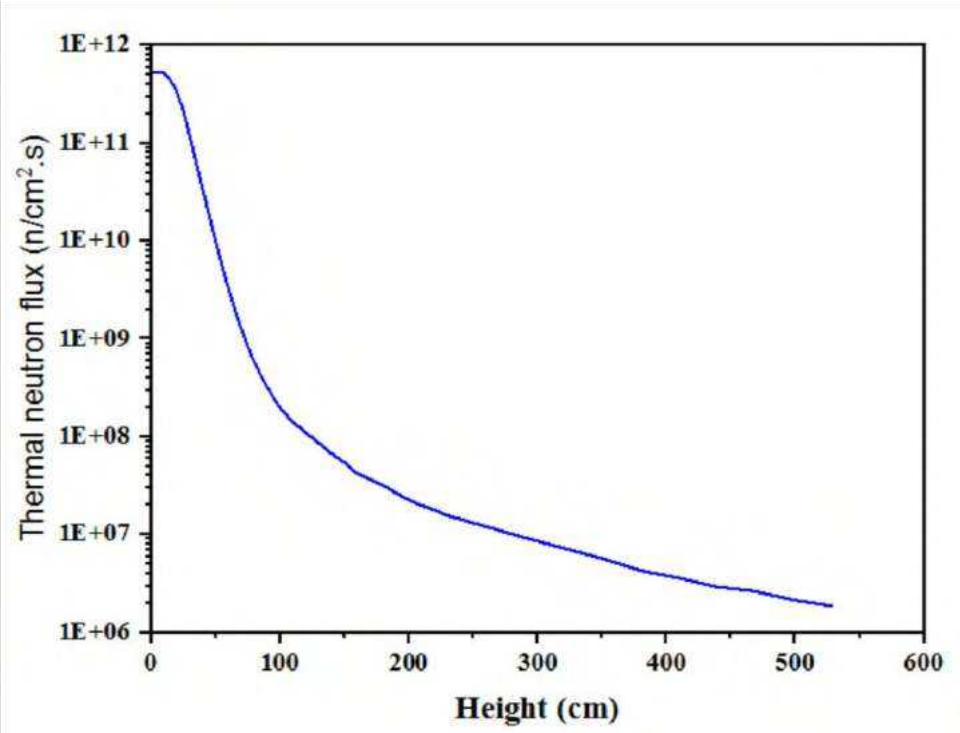

Fig.3. The changes of thermal neutron flux at different heights of PGNAA beam tube.

Table 2. The computational results of the epithermal neutron flux as a function of the distance from the bottom of the PGNAA beam tube

Height (cm)	ϕ epithermal neutron (n/cm².s)	Error (%)	Height (cm)	ϕ epithermal neutron (n/cm².s)	Error (%)	Height (cm)	ϕ epithermal neutron (n/cm².s)	Error (%)
2.2	6.29×10^{10}	0.26	98.7	1.44×10^{7}	2.15	218.7	1.51×10^{6}	0.56
8.7	6.51×10^{10}	0.25	108.7	1.07×10^{7}	4.98	228.7	1.34×10^{6}	0.67
13.7	5.33×10^{10}	0.27	118.7	8.03×10^{6}	3.17	258.7	9.96×10^{5}	0.67
18.7	3.69×10^{10}	0.31	128.7	6.60×10^{6}	4.79	288.7	7.66×10^{5}	0.57
23/7	2.06×10^{10}	0.55	138.7	4.97×10^{6}	1.56	318.7	6.01×10^{5}	0.58
28/7	1.52×10^{10}	0.81	148.7	4.08×10^{6}	0.76	348.7	4.84×10^{5}	0.59
38.7	2.01×10^{9}	1.61	158.7	3.60×10^{6}	2.52	378.7	3.99×10^{5}	0.59
48.7	5.49×10^{8}	2.73	168.7	2.89×10^{6}	0.76	408.7	3.31×10^{5}	0.6
58.7	1.83×10^{8}	4.36	178.7	2.54×10^{6}	2.37	438.7	2.80×10^{5}	0.6
68.7	7.53×10^{7}	2.82	188.7	2.26×10^{6}	3.1	468.7	2.36×10^{5}	0.62
78.7	3.49×10^{7}	3.61	198.7	2×10^{6}	2.88	498.7	2.02×10^{5}	0.62
88.7	2.28×10^{7}	2.94	208.7	1.77×10^{6}	3.11	528.7	1.76×10^{5}	0.62

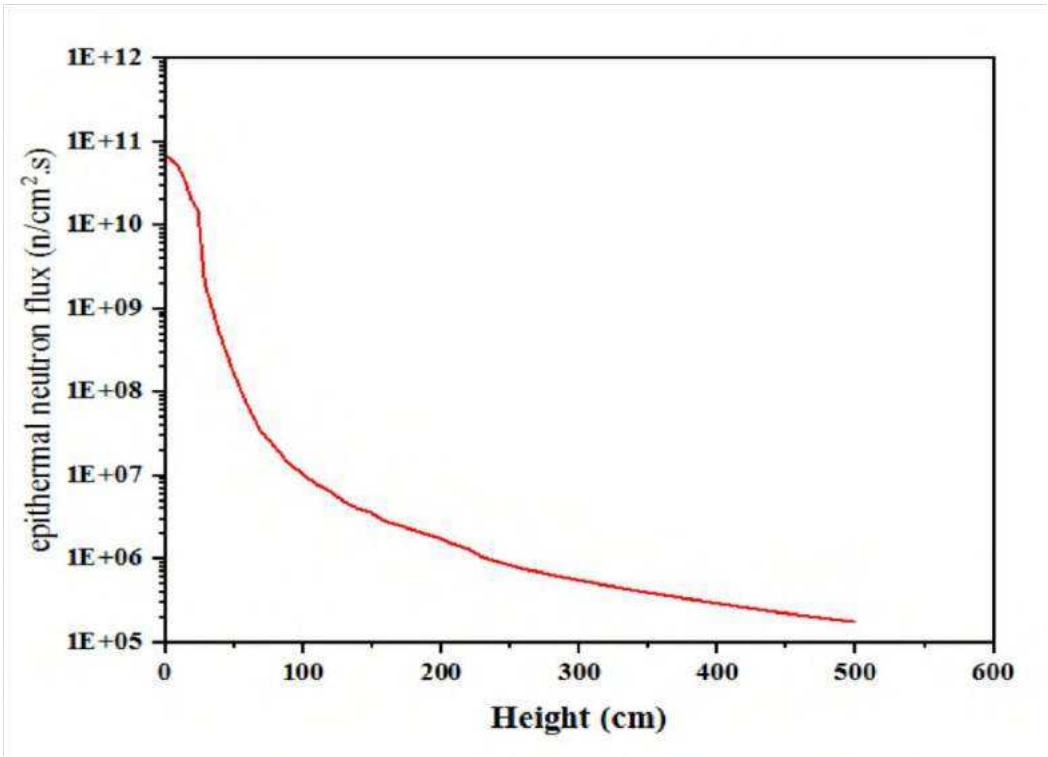

Fig.4. The changes of Epi-thermal neutron flux at different heights of PGNAA beam tube.

Table 3. The computational results of the fast neutron flux as a function of the distance from the bottom of the PGNAA beam tube

Height (cm)	φ fast neutron (n/cm².s)	Error (%)	Height (cm)	φ fast neutron (n/cm².s)	Error (%)	Height (cm)	φ fast neutron (n/cm².s)	Error (%)
2.2	8.99×10^{10}	0.18	98.7	1.67×10^{7}	3.44	218.7	1.52×10^{6}	0.65
8.7	9.36×10^{10}	0.17	108.7	1.13×10^{7}	1.38	228.7	1.35×10^{6}	0.58
13.7	7.82×10^{10}	0.19	118.7	8.74×10^{7}	3.11	258.7	9.87×10^{6}	0.55
18.7	5.45×10^{10}	0.22	128.7	7.02×10^{6}	2.33	288.7	7.46×10^{5}	0.56
23/7	3.13×10^{10}	0.35	138.7	5.70×10^{6}	2.73	318.7	5.85×10^{5}	0.57
28/7	1.49×10^{10}	0.49	148.7	4.45×10^{6}	2.53	348.7	4.69×10^{5}	0.58
38.7	3.83×10^{9}	0.93	158.7	3.66×10^{6}	2.21	378.7	3.88×10^{5}	0.6
48.7	1.05×10^{9}	1.57	168.7	3.02×10^{6}	0.69	408.7	3.22×10^{5}	0.59
58.7	3.21×10^{8}	2.44	178.7	2.61×10^{6}	1.38	438.7	2.72×10^{5}	0.6
68.7	1.15×10^{8}	3.19	188.7	2.29×10^{6}	2.86	468.7	2.32×10^{5}	0.61
78.7	5.41×10^{7}	4.47	198.7	1.95×10^{6}	1.1	498.7	2×10^{5}	0.61
88.7	2.66×10^{7}	3.36	208.7	1.71×10^{6}	0.63	528.7	1.74×10^{5}	0.62

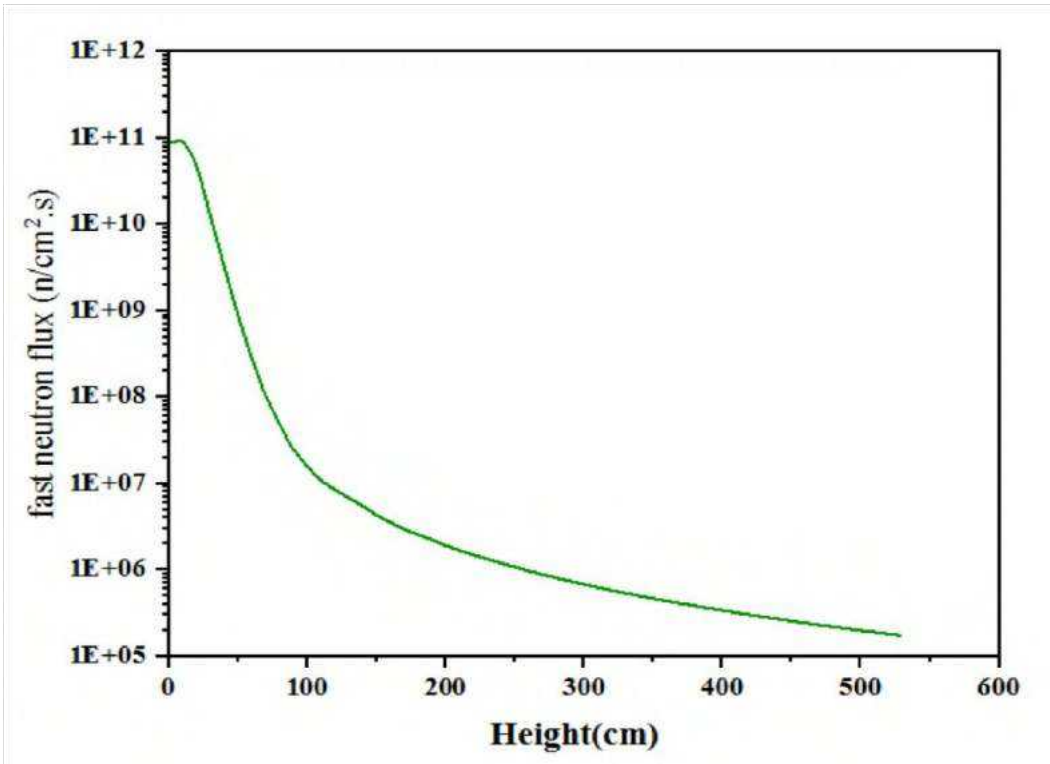

Fig.5. The changes of fast neutron flux at different heights of PGNAA beam tube.

The thermal neutron flux measured by neutron activation method. This measurement was done for 6 points in front of the reactor core.In Figure 6, the comparison of simulation and measurement results for thermal neutron flux is presented. It is shown that the simulation and experimental results are in good agreement with each other, especially in places far from the reactor core.

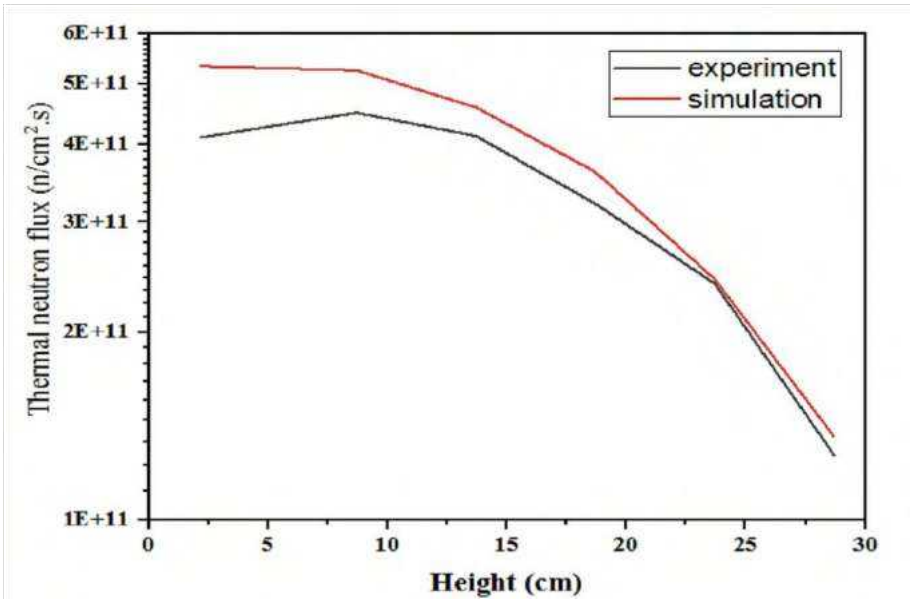

Figure 6. Comparison of experimental and simulation results for thermal neutron flux in PGNAA beamtube

Conclusion

In this study the variation of neutron flux along the height of neutron beamline of PGNAA beam tube in Isfahan MNSR has been investigated. The MCNP code has been used to simulate and calculate the different neutron energy ranges at different positions of PGNAA beamline. A complete model has been defined to simulate the reactor and beamline and the Kcode critical source card and F5 tally (particle flux at a point) have been used to calculate the neutron flux.

The simulations and calculations have been done in such a way that the errors remain as low as possible. The results have been analyzed to determine the flux changes and reduction at every points through the height of beamline, i.e. from the near of core to up the beamline outlet for three neutron energy groups.

In table 4 the specifications of several reactor which are used for PGNAA is summarized. According to the outlet thermal neutron flux of the PGNAA beam of the MNSR reactor)~ 2×10^6 n/cm^2.s) and the comparison in table 4, it can be concluded that due to the much lower power of the MNSR reactor compared to other reactors, the thermal neutron flux of the beam outlet is very suitable for PGNAA and the design of the beam line done with high precision.

Table 4. Review of some PGNAA facilities in the world [10-18].

Country/ reactor	Reactor power	Thermal neutron flux (n/cm^2.s)
USA/ TRIGA Argentina /Ra-3	1 MW 8 MW	9.3×10^5 10^9
Switzerland /FRM II		3.61×10^8 –
Brazil /TRIGA IPR-R1	100-250 kW	6.07×10^{10}
Thailand /TRR-1/M1	1.2 MW	5.6×10^6
Vietnam /DALAT	500 kW	7.8×10^6
Indonesia /TRIGA	2 MW	2.1×10^7
Indonesia /kartini	100kW	10^7
Morocco /TRIGA MARK II	250 kW	1.164×10^7 $3\times10_{11}$

References

[1] Vatani, M., Hassanvand, M., Mokhtari, J. and Dastjerdi, M.C., 2023. Design of an in-tank thermal neutron beam for PGNAA application at Isfahan MNSR. Nuclear Engineering and Design, 412, p.112451.

[2] Ghasemi, Z., Hassanvand, M., Dastjerdi, M.C. and Mokhtari, J., 2023. Design of a radiation shield for an HPGe detector for a reactor-based PGNAA facility. Radiation Physics and Chemistry, 210, p.111045.

[3] Dastjerdi, M. C., Mokhtari, J., & Toghyani, M. (2023). Design, construction, and characterization of a Prompt Gamma Neutron Activation Analysis (PGNAA) system at Isfahan MNSR. *Nuclear Engineering and Technology*, *55*(12), 4329-4334.

[4] Dastjerdi, M. C., Mokhtari, J., Toghyani, M., & Soleimani, B. (2023). Feasibility study on PGNAA experiments using a prototype neutron beam at Isfahan MNSR. *Journal of Instrumentation*, *18*(07), P07031.

[5] Rahmati, E., Barough, M. S., Dastjerdi, M. C., & Mokhtari, J. (2023). Design of an out-of-tank neutron beam line for prompt gamma neutron activation analysis at low-power Miniature Neutron Source Reactor. *Journal of Instrumentation*, *18*(09), P09036.

[6] Jafari, M., Jafari, H., Dastjerdi, M. C., & Mokhtari, J. (2024). Designing a system of boron concentration measurement in solution samples by the PGNAA facility of the Isfahan MNSR reactor. *Nuclear Engineering and Design*, *416*, 112782.

[7] Dastjerdi, M.C., Mokhtari, J., Asgari, A. and Ghahremani, E., 2019. A neutron radiography beamline relying on the Isfahan Miniature Neutron Source Reactor. Nuclear Instruments and Methods in Physics Research Section A: Accelerators, Spectrometers, Detectors and Associated Equipment, 928, pp.2025.

[8] Mokhtari, J., Dastjerdi, M.C., 2023. Development and characterization of a large thermal neutron beam for neutron radiography at Isfahan MNSR. Nucl. Instrum. Methods Phys. Res. Sect. A Accel. Spectrom. Detect. Assoc. Equip. 1051, 168209.

[9] Waters, L. S. (2002). MCNPX user's manual. *Los Alamos National Laboratory*, *124*.

[10] Gonçalves-Carralves, M.L.S., Gadan, M.A., Bortolussi, S., Pinto, J., Ojeda, J., Langan, S., Quintana, J. and Miller, M.E., 2011. Development of a prompt gamma neutron activation analysis facility for 10B concentration measurements at RA-3: Design stage. *Applied Radiation and Isotopes*, *69*(12), pp.1928-1931.

[11] Canella, L., 2011. *Optimisation of the PGAA instrument at FRM II for low background and 2D measurements* (Doctoral dissertation, Technische Universität München).

[12] Inyang, O.E., Reece, W.D., Poston, J.W. and Walker, M.A., 2010. *Development of a Promptgamma, Neutron-activation Analysis Facility at the Texas A & M University Nuclear Science Center* (Doctoral dissertation, Texas A & M University).

Tegas, S., 2015. Beam modeling for PGNAA experimental facility at Kartini reactor. *Jurnal Iptek Nuklir Ganendra*, *18*(2), pp.107-113.

[13] Mghar, M., Chetaine, A., Maghnouj, A. and Darif, A., 2017. Design of a new collimator used in the PGAA nuclear technique. *Physics AUC*, *27*, p.39.

[14] Nguyen, C.H., Nguyen, N.D., Tran, T.A., Pham, N.S., Ho, H.T. and Vuong, H.T., 2019. Characteristics of the new prompt gamma neutron activation analysis facility at the Dalat research reactor.

[15] Permana, S., 2021, February. Characterization of neutron and gamma beams at the tangential beam port of TRIGA 2000 reactor using Monte Carlo methods. In *Journal of Physics: Conference Series* (Vol. 1772, No. 1, p. 012024). IOP Publishing.

[16] Sangaroon, S., Ratanatongchai, W., Picha, R., Khaweerat, S. and Channuie, J., 2017, June. The MCNP Simulation of a PGNAA System at TRR-1/M1. In *Journal of Physics: Conference Series* (Vol. 860, No. 1, p. 012037). IOP Publishing.

[17] Leal, A.S., Campolina, D. and Revay, Z., FEASIBILITY OF THE PROMPT-GAMMA NEUTRON ACTIVATION ANALYSIS FACILITY AT TRIGA IPR-R1 REACTOR IN BRAZIL.

[18] EXPERIMENTAL Measurement of Tehran Research Reactor Fuel Evolution (BURNUP), Using Iodine Detector and ORIGEN2.1 and MCNPX2.6 Software (Paper ID : 1568)

ICNST 2024
International Conference on Nuclear Science and Technology
6- 8 MAY 2024 | Isfahan, Iran

Compressive properties of Zr-Nb alloy produced by multidirectional free hot forging (Paper ID : 1587)

Ali Rajaie[1*], Mohsen Asadi Asadabad[2]
[1]*Department of Materials Engineering, Hakim Sabzevari University, Sabzevar, Iran.*
[2]*Nuclear Science and Technology Research Institute, Tehran, Iran.*

Abstract

In this study, the compressive strength of Zr-Nb alloy as a vital structural material for nuclear reactors was investigated. For this purpose, the alloy samples were subjected to multi-directional free forging. Subsequently, different samples were extracted from the billet at 0, 30, 60, and 90 degrees with respect to the forging direction. The microstructure, phase changes, hardness, and compressive strength of the forged samples were studied. The results of the experimental tests showed that the microstructure of forged samples included alpha grains elongated in the direction of forging and secondary spherical alpha grains. It was also found that at 60-degree direction, the severe plastic deformation induced during forging caused the nucleation of a high fraction of new secondary fine alpha grains. The hardness measurement results showed that the highest hardness is related to the zero degree in the direction of forging. The results of the compression tests showed that the highest and lowest compressive strength values were obtained for sample 60-degree and sample 30-degree, respectively.

Keywords: Zr-Nb alloy; Multidirectional free hot forging; Compressive strength

Introduction

Zr–Nb alloys are mainly employed for production of nuclear cladding tubes and pressure tubes (cooling tubes). The tubes work in severe operating conditions, where they experience the load of the fuel pellets, high-pressure cooling water flow at high temperature, and oxidative medium. Therefore, they must show good mechanical and corrosion properties in addition to having a stable microstructure in elevated operating temperatures. In pressurized heavy-water reactors (PHWRs), leak-before-break (LBB) criteria are required for the reactor operation. This can be achieved by maintaining a minimum level of tube fracture toughness during the reactor service. Improved strength and excellent corrosion resistance of high-pressure, cladding, and calandria tubes are attained by adding niobium to the zirconium alloys. This improvement in properties depends on niobium content, annealing temperature, and the fabrication process [1].

According to the concentrations of niobium and zirconium alloys are divided into three categories. First, zirconium-low niobium (0.2-0.3 wt% Nb) alloys that do not undergo the formation of β-phase or

precipitates within the matrix and are not affected by annealing. Second, zirconium-medium niobium (0.5-0.8 wt%) alloys that can be precipitation-hardened. Third, zirconium-high niobium (1.0-2.0 wt%) alloys, which can be annealed to form β-zirconium phases (dual-phase microstructure) [1].

In a study, Kondo et al. [2] investigated the microstructure and mechanical properties of as-cast Zr-Nb alloys. The results of microstructural investigations showed that in Zr-(3-6)Nb alloys, an acicular morphology was observed within the coarse coaxial grains. The acicular structure increased with enhancing the Nb up to 9 wt%. Furthermore, a lens-shaped morphology was observed, which was mainly detected in Zr-(16-24)Nb alloys.

Kučeráková et al. [3] studied the preferential orientation in a Zr alloy deformed by uniaxial tensile test at both ambient temperature and 300 °C from 0 to 30% strain. They observed that the poles of {0002} planes in the normal direction are significantly preferred to the transverse direction for all the preferred samples, which are not affected by altering the tensile test conditions. It was also observed from texture studies that tensile twinning of {10-12}<10-11> occurs only by the deformation at 300 °C. By elevating the tensile test temperature from ambient temperature to 300 °C, the overall texture sharpness increased. They concluded that the final resulting texture increases the rate of deformation progression.

In another recent study, Zeng et al. [4] investigated the effect of primary orientation on the dynamic recrystallization (DRX) of Zr-1Sn-0.3Nb alloy during hot deformation. For this purpose, the alloy sheet was compressed in both normal and transverse directions so that the grains in the <c> axis were parallel to the loading direction (zero angle) and the grains in the <c> direction were perpendicular to the loading direction (90 degrees). The samples were then subjected to a hot compressed test at a temperature of 700 °C and a strain rate of 1 s^{-1}. Based on these results, they discovered that the initial crystal orientation strongly affects the recrystallization mechanisms and the mechanisms are highly affected by the loading direction. In addition, it was seen that discontinuous dynamic recrystallization (DDRX) increased with the activation of <c+a> prismatic slip via increasing the dislocation density and the large Burgers vector of <c+a> dislocations. This increase led to high energy storage, hence the grain boundary density readily enhanced, where became the preferred sites for DDRX nucleation. At high strains, due to the lower stored energy, they develop around the primary grain boundaries. Consequently, the DRX mechanism changes from discontinuous to continuous. Moreover, a high resistance to DDRX was found in sample 90-degree, where the prismatic slip, base plane, and pyramid plane <a> activated during the early stages of deformation. Therefore, the work-hardening rate of this sample was lower than that of sample zero-degree and continuous dynamic recrystallization (CDRX) by grain rotation improved as the dominant mechanisms.

Additionally, the work-hardening induced by the texture during the early stages of deformation masks the softening caused by DDRX. All in all, the study results revealed the effect of hot deformation on the alloy grain-refinement and its ultimate properties.

The main purpose of the current investigation was to study the microstructure and compressive properties of Zr-1Nb alloy after hot forging process at different directions.

Materials and Methods

2.1. Alloy preparation

In this research, a cylinder ingot with a height of 120 cm and a diameter of 35 cm of Zr alloy containing 1 wt% of Nb was prepared by vacuum arc remelting, in a way that the oxygen content of the alloy was less than 1200 ppm. The chemical composition of the alloy is brought in Table 1.

Table 1 chemical composition of the Zr-Nb alloy

Element	N	Al	Be	B	Hf	Fe	Cd	Ca	P	Si	Li	Mg	Cu
wt%	0.002	0.004	0.001	0.00005	0.004	0.017	0.00002	0.003	0.002	0.002	0.0001	0.001	0.001
Element	Mo	Ni	Pb	Sn	Ti	C	Cl	Cr	H	F	O	Nb	Zr
wt%	0.004	0.002	0.002	0.02	0.002	0.0150	0.002	0.0048	0.001	0.0015	0.089	1.01	Ball.

2.2. Multidirectional free forging process

The as-cast ingot was first homogenized at 830 °C for 20 h in the heat treatment furnace under inert gas and cooled in the air. Then, the ingot was preheated at 870 °C for 2 hours to improve the deformability during the hot forging process. The process was carried out as a multi-directional free isothermal forging using a pneumatic forging machine. Before forging, MoS_2 powder was applied on the ingot surface as the. The forging process was carried out as a single-cycle process with a three-pass flow. Between each pass, the billet was reheated to the forging temperature for 30 min. The reduction of the ingot diameter was about 15% for each pass and a total of six forging passes were performed. The actual strain for each pass was calculated as $\varepsilon = \ln H/h$ (where H and h represent the billet heights before and after the forging, respectively). Thus, the cumulative strain for the total of six passes was approximately equal to 1.07. The billet was then cooled in air after the process. For sampling, the forged billet was cut in four directions of 0, 30, 60, and 90-degrees with respect to the forging direction.

2.3. Mechanical properties

To evaluate the compressive behavior of the alloy in different forging directions, the compression test was performed by Zwick Roell 25-Ton universal machine (model Z250, Germany) at ambient temperature and strain rates of 0.001, 0.01, 0.1, and 1 s^{-1} on the samples extracted in directions of 0, 30, 60 and 90 degrees with respect to the forging direction. The compression test samples were sub-sized with a height of 10 mm and a diameter of 5 mm according to the ASTM E9/E9M standard. Graphite powders were placed as the lubricant on the contact surfaces of the sample and machine jaws to reduce the friction. Furthermore, to validate the obtained data, the compression tests were repeated three times and the calculated average values were reported.

2.4. Microstructure characterization

The samples were ground by 100-1500 grit SiC sandpapers, polished using diamond paste, and etched with an etchant solution (90% ethanol, 8% nitric acid, and 2% hydrofluoric acid) for 8 s via swabbing method. The microstructure of the samples was captured by an Olympus optical microscope.

Results and Discussion

Figure 1 shows the microstructure of the as-cast Zr-Nb sample at different magnifications. As can be seen, the microstructure includes alpha phase with different colonies, as well as allotriomorphic α grains, forming along the β grain boundaries and inside β grains. A limited fraction of very fine secondary α is also seen within the β matrix. In the higher magnification micrograph (Figure 1) Nb-rich regions and martensite blades, resulting from high cooling rates during beta transformation are evident. It is evident that the as-cast sample shows large coaxial grains with grain sized up to several millimeters. The higher magnification micrograph (Figure 1) indicates that the microstructure consists of coarse lenses, clusters of parallel laths. Although the microstructure has the structural features of basket-weave Widmanstätten, this type of Widmanstätten appears mostly in Zr alloys with low cooling rates after β-phase heat treatment [5].

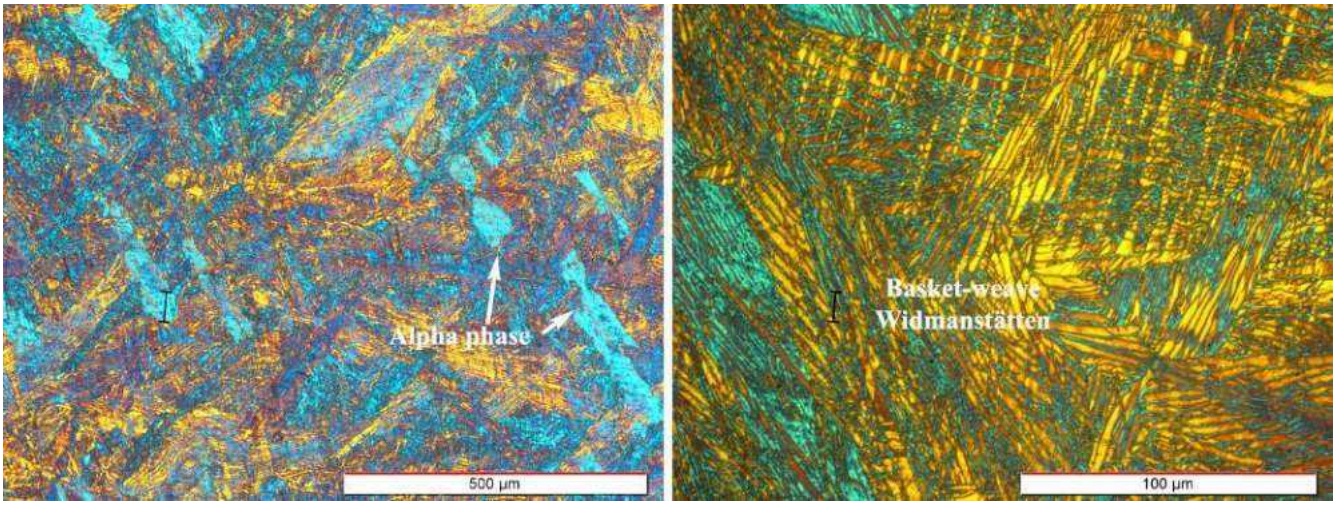

Fig. 1. OM micrographs of the as-cast sample with different magnifications: left (100X) and right (500X)

Figures 2a and b shows the optical micrograph of the microstructure of the sample obtained from the forged specimen at zero-degree. As can be seen, after forging, the microstructure includes a wide range of alpha grains stretched along the forging direction in the form of fiber. During the forging process, the flow localization phenomenon occurs in the microstructure due to severe plastic deformation, short deformation time and low deformation temperature. In the deformation process, an obvious work-hardening effect is induced in the sample, encouraging the flow localization phenomenon. The phenomenon implies the occurrence of a severe non-uniform deformation [6]. While for sample 30-degree, the volume fraction of the stretched alpha grains has decreased and the size of the colonies has increased. Severe deformation and high cooling rate have been the controlling factors of the microstructure [7]. In the micrograph with a higher magnification, the non-uniform size of the lath and various extents of twisting can be seen in the microstructure, which is mainly due to the phase transformation of the alloy during rapid cooling. For sample 60-degree, the decrease in the volume fraction of the stretched alpha grains is less than that of sample 30-degree, and larger colonies can be observed. Meanwhile, the microstructure of sample 90-degree contains the highest volume fraction of the stretched alpha grains. It can be said that the high strain rate induced during forging caused the nucleation of secondary alpha grains within the alpha grains elongated in the forging direction. Also, refined secondary alpha laths can be observed between primary alpha grain boundaries during thickness reduction. A similar microstructure was reported for Zr-2.5Nb alloy hot-rolled and cooled in air [8]. In a general, it can be said that the hot forging characteristics of the alloy is similar to those of hot rolling for Zr-Nb and Zr-Ti binary alloys, observing primary alpha grains in the beta matrix.

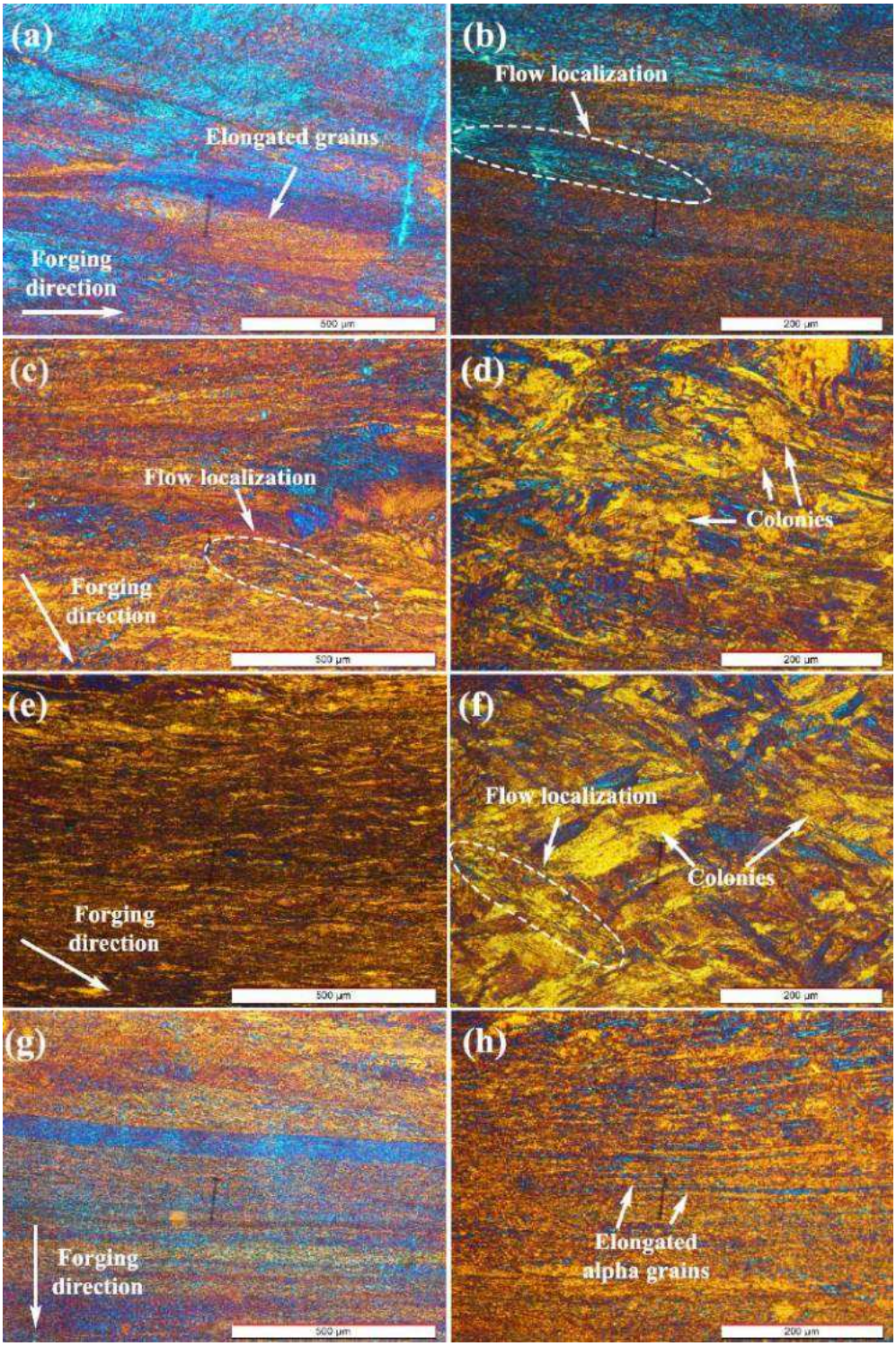

Fig. 2. OM micrographs of the forged samples with different directions: (a and b) 0 degree, (c and d) 30 degree, (e and f) 60 degree, and (g and h) 90 degree.

In Figure 3, the hardness measurement results for as-cast and forged samples in the directions of 0, 30, 60 and 90 degrees are presented. The hardness of the as-cast sample was 153 HV, while it was 184, 160, 171, and 207 HV for samples forged at 0, 30, 60, and 90 degrees, respectively. By comparing the hardness of as-cast sample compared to the forged samples, it is evident that the hardness of forged samples increased significantly. Noticeably, severe plastic deformation induced by the forging process causes an increase in hardness by the mechanism of increasing the density of dislocations. The measured hardness results were consistent with previous investigations [9–11]. As can be seen, the highest hardness was obtained for sample 90-degree. This corresponds to the microstructures presented in Figures 1. By comparing the microstructures of the forged sample at different angles, it is evident that the grains are refined during the forging process. Different microstructures observed in different directions indicate different conditions of dislocation motion and obstacles. Additionally, the change in the volume fraction of the alpha phase and its morphology (spherical or elongated) can change the hardness of the alloy. Results displayed that the microstructure was refined for sample zero-degree, while for samples 30-degree and 60-degree, the microstructures were coarsened. Finally, sample 90-degree showed recrystallized grains.

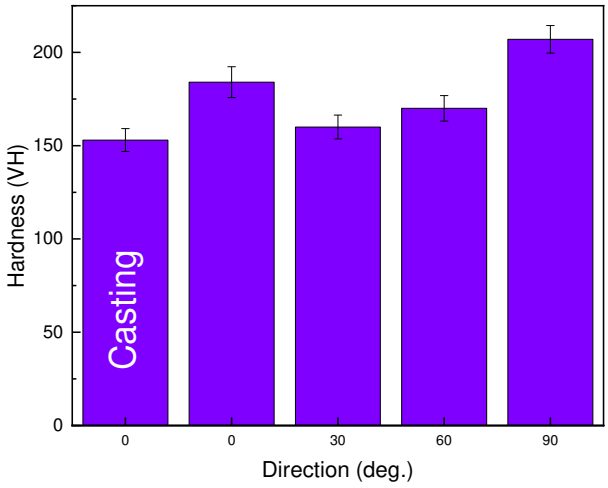

Fig. 3. Hardness changes for samples with different direction.

Figure 4 shows the stress-strain diagram of different samples. According to the figure, it is clear that the highest compressive strength is related to sample 60-degree, followed by samples 90 and 0-degree with an insignificant difference. However, the lowest strength is related to sample 30-degree. It can be seen that different yield strengths and flow stresses were obtained for different directions, indicating significant mechanical anisotropy in polycrystalline Zr alloy. According to the trend of diagrams, strain hardening during deformation can be detected. Additionally, the stress-strain diagrams generally display an

preliminary rise in the stress values by elevating the strain, which is shadowed by a sudden enhancement in the stress via work-hardening. This can be related to the impediment of the dislocation motion caused by dislocation pile-up during deformation, resulting in strength improvement [12–14]. The phenomenon lasts until the alloy arrives to a steady state, where the strain hardening rate stablized by the dislocation annihilation, resulting in a slight decrease in the stress [12–14].

At the initial deformation stage, the shear stress of sample 90-degree was higher than that of sample 60-degree, which is consistent with hardness results. At strain values higher than 0.4, the flow stress of sample 60-degree was slightly higher than that of sample 90-degree.

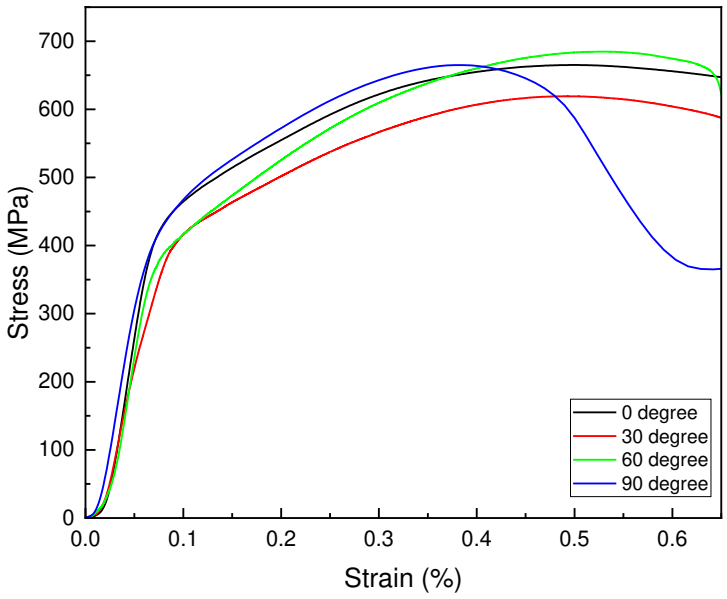

Fig. 4. Compressive stress-strain diagram at ambient temperature for samples at different directions (strain rate 0.001 s^{-1}).

Figures 5a and b show the optical micrograph of sample zero-degree after the compression test at ambient temperature. The figure shows very fined primary α grains with distributed β phase at the grain boundaries. In the micrograph with a higher magnification, it is evident that a part of the microstructure consists of elongated grains, corresponding to the material deformed a low strain rate and the lower temperature region of the two-phase region. In a previous study, a similar microstructure was reported for Zr alloy after hot-compression [15]. However, in some areas of the microstructure, the fragmentation of α grains distributed in the primary α phase are detected. While in other areas the fragmented grains are stretched perpendicular to the compression direction, which can be attributed to the low strain rate.

Figures 5c and e reveal the microstructures of the forged alloy at 30 and 60-degree direction after the compression test at ambient temperature. Moreover, a microstructure of the interlaced alpha surrounded by large β-grain boundaries was seen. By comparing the microstructures of samples 30 and 60-degrees, it can be seen that sample 30-degree contains larger primary α grains compared to sample 60-degree. In the micrograph with the higher magnification, it is clear that the width of the planes is approximately less than 1.5 μm, and the average length is about tens of microns. The interlaced α planes of have a large number of interfaces, indicating a high interface energy of the sample. Figure 5f shows the microstructures of the forged alloy at 90-degree direction after the compression test. A very small fraction of primary α phases with dispersed β phase are seen at the grain boundaries, corresponding to material deformed at low temperature of two-phase region. By comparing samples 60-degree and 90-degree, it is apparent that the size and shape of the grains or plates may be the only variations.

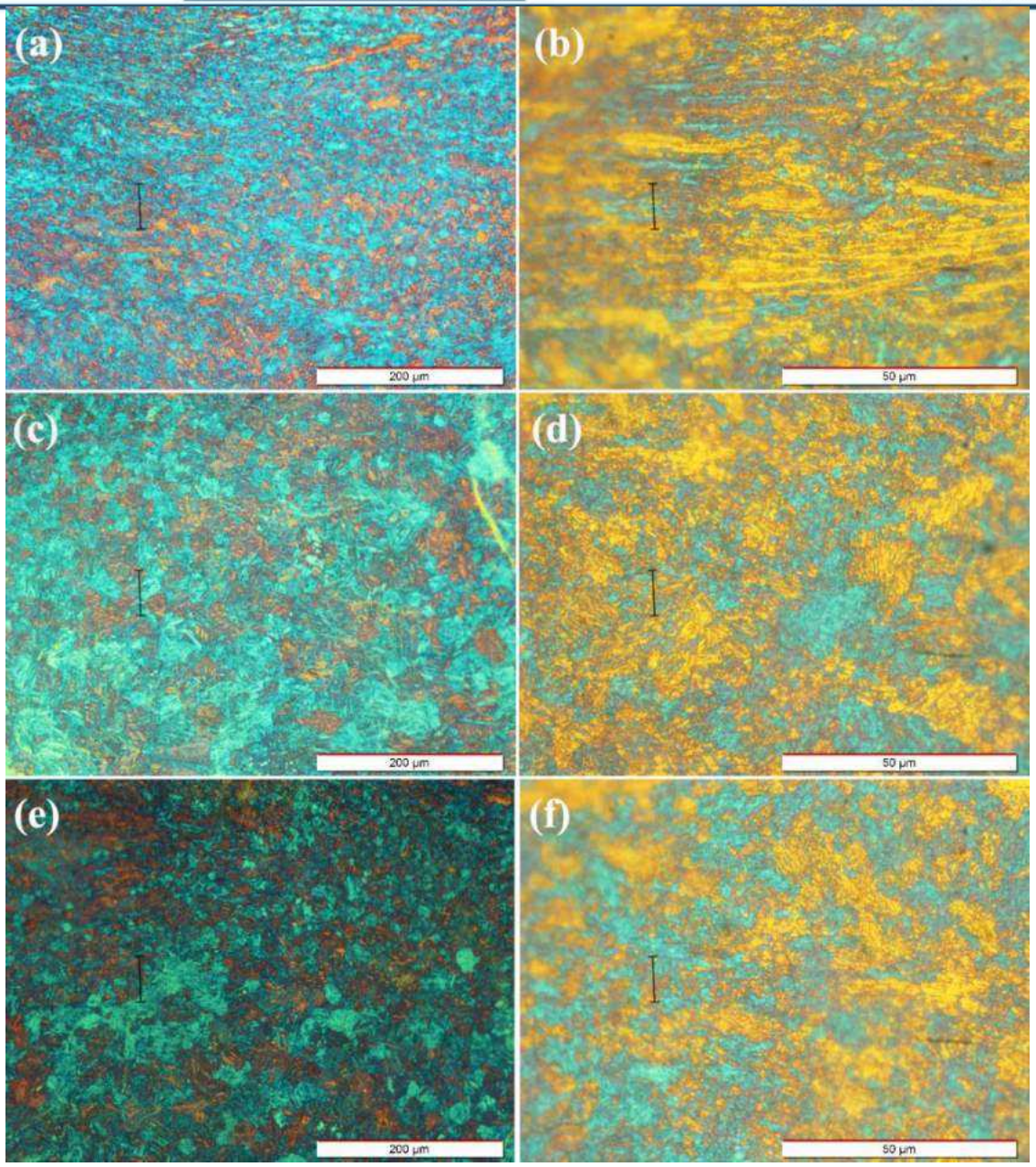

Fig. 5. OM micrographs of the forged samples with different directions after compression tests: (a and b) 0 degree, (c and d) 30 degree, (e) 60 degree, and (f) 90 degree.

Conclusions

In the current study, the compressive strength of Zr-Nb alloy after multi-directional free forging. The samples were extracted from the billet at 0, 30, 60, and 90 degrees with respect to the forging direction. The results showed that the microstructure of forged samples includes alpha grains elongated in the direction of forging and secondary spherical alpha grains. It was also found that in the direction of 60 degrees, the high strain rate created during forging caused the nucleation of a high fraction of new secondary

fine alpha grains. The hardness results showed that the highest hardness is related to the zero degree in the direction of forging and due to the high volume fraction of the alpha phase as well as its morphology and refinement caused by the forging process. The compression tests results showed that the highest compressive strength is related to the 60° sample and the lowest compressive strength is related to the 30° sample, which showed that the compressive strength of samples with different directions is affected by the mechanism and kinetics of recrystallization and different initial orientations between the loading direction and the ⟨c⟩ axes of the grains.

Acknowledgements

Acknowledgements of people, grants, funds, *etc.* should be placed here. The names of funding organizations should be written in full.

References

[1] [1] K.K. Saxena, V. Pancholi, Zr–Nb Alloys and Its Hot Deformation Analysis Approaches, Met. Mater. Int. 27 (2021) 2106–2133. 10.1007/s12540-020-00812-8.

[2] [2] R. Kondo, N. Nomura, Suyalatu, Y. Tsutsumi, H. Doi, T. Hanawa, Microstructure and mechanical properties of as-cast Zr–Nb alloys, Acta Biomater. 7 (2011) 4278–4284. https://doi.org/10.1016/j.actbio.2011.07.020.

[3] [3] M. Kučeráková, S. Vratislav, L. Kalvoda, Z. Trojanova, Analysis of preferential orientation in zirconium samples deformed by uniaxial tension using neutron and X-ray diffraction, Powder Diffr. 30 (2015). 10.1017/S0885715614001316.

[4] [4] Q. Zeng, B. Luan, Y. Wang, X. Zhang, R. Liu, K.L. Murty, Q. Liu, Effect of initial orientation on dynamic recrystallization of a zirconium alloy during hot deformation, Mater. Charact. 145 (2018) 444–453. https://doi.org/10.1016/j.matchar.2018.09.008.

[5] [5] Y. Cui, Z. Yang, W. Zhang, H. Liu, Effect of β-Phase Heat Treatment on Microstructure of Zr-Sn-Nb-Fe Alloy BT - Proceedings of the 23rd Pacific Basin Nuclear Conference, Volume 1, in: C. Liu (Ed.), Springer Nature Singapore, Singapore, 2023: pp. 219–230.

[6] [6] X. Zhou, K. Wang, X. Li, X. Gao, M. Zhong, R. Feng, Study on hot deformation behaviour and microstructure of Zr-4 alloy, IOP Conf. Ser. Mater. Sci. Eng. 768 (2020) 22028. 10.1088/1757-899X/768/2/022028.

[7] [7] J. Liu, G. He, A. Callow, K. Li, K.L. Moore, H. Nordin, M. Moody, S. Lozano-Perez, C.R.M. Grovenor, The role of β-Zr in a Zr-2.5Nb alloy during aqueous corrosion: A multi-technique study, Acta Mater. 215 (2021) 117042. https://doi.org/10.1016/j.actamat.2021.117042.

[8] [8] C.S. Daniel, A. Garner, P.D. Honniball, L. Bradley, M. Preuss, P.B. Prangnell, J. Quinta da Fonseca, Co-deformation and dynamic annealing effects on the texture development during alpha–beta processing of a model Zr-Nb alloy, Acta Mater. 205 (2021) 116538. https://doi.org/10.1016/j.actamat.2020.116538.

[9] [9] P. Han, Y. Xing, G. Yuan, X. Zhu, X. Wang, Effects of Specimen Size, Strain Rate and Temperature on the Deformation Behaviors at Micro-/Mesoscale in Ultrafine-Grained Pure Zr, Trans. Indian Inst. Met. 75 (2022) 2409–2417. 10.1007/s12666-022-02618-1.

[10] [10] C. PROFF, Aspects microstructuraux de l´oxydation d´alliages de zirconium, University DE Grenoble, 2006.

[11] [11] S.O. Rogachev, R. V Sundeev, S.A. Nikulin, Effect of severe plastic deformation by high-pressure torsion at different temperatures and subsequent annealing on structural and phase transformations in Zr-2.5% Nb alloy, J. Alloys Compd. 865 (2021) 158874. https://doi.org/10.1016/j.jallcom.2021.158874.

[12] [12] J.H. Cai, S.W. Xin, L. Li, L. Zou, H.Y. Yang, J. Chen, Effect of Strain Amounts on Cold Compression Deformation Mechanism of Ti-55531 Alloy with Bimodal Microstructure, Mater. Sci. Forum. 1035 (2021) 182–188. 10.4028/www.scientific.net/MSF.1035.182.

[13] [13] Z. Zeng, J.-F. Nie, S.-W. Xu, C. H. J. Davies, N. Birbilis, Super-formable pure magnesium at room temperature, Nat. Commun. 8 (2017) 972. 10.1038/s41467-017-01330-9.

[14] [14] H.-G. KIM, I.-H. KIM, J.-Y. PARK, Y.-H. KOO, INFLUENCE OF ALLOY COMPOSITION ON WORK HARDENING BEHAVIOR OF ZIRCONIUM-BASED ALLOYS, Nucl. Eng. Technol. 45 (2013) 505–512. https://doi.org/10.5516/NET.07.2012.055.

[15] [15] R. Gostariani, M. Asadi Asadabad, Studying the Hot Deformation Behavior of Zr-1Nb Alloy Using Processing Map and Kinetic Analysis, J. Mater. Eng. Perform. 32 (2023) 2151–2164. 10.1007/s11665-022-07267-5.

ICNST 2024
International Conference on Nuclear Science and Technology
6- 8 MAY 2024 | Isfahan, Iran

Numerical analysis of a novel passive flow limiter for nuclear heating reactors (Paper ID : 1592)

Hadipour A[1*], Hashemiyan M[2], Mostafaei Z[1]

[1]National Center of Quality system and Atomic Standards of Iran, Tehran, Iran
[2]Faculty of Mechanical Engineering, Semnan University, Iran

Abstract

The purpose of this study is to design a novel passive flow limiter for the NHR200-II nuclear heating reactor to reduce the break mass flow rate in loss-of-coolant accidents (LOCAs). In this work, mathematical analysis was conducted first to identify important geometric and hydraulic parameters of the passive flow limiter. Then a series of numerical simulations were carried out to find the relationship between hydraulic performance and geometric parameters of the passive flow limiter. The flow limiter is mainly composed of a multisection cylindrical flow passage and an internal movable ball, and the flow passage would be blocked automatically by the movable ball while the flow in the passage was accelerated during a LOCA transient. Important geometric parameters, such as the axial distance H, the shape of the throat section, the blockage ratio of the ball in the pipe, and the front length L were studied numerically to optimize the structure of the passive flow limiter.

Keywords: Passive flow limiter, Loss-of-Coolant Accident, Small modular reactor

Introduction

Many studies have been conducted to improve the safety of small modular reactors. A water-cooled SMR can be more resistant to a loss-of-coolant accident (LOCA) once the mass flow rate in possible leakage points can be passively controlled and reduced. This feature can be achieved with a variety of passive fluidic devices installed in the pipeline, such as the venturi tubes or the vortex diodes. So far, many studies have been done on Venturi tubes [1-4]. Venturi tubes have been installed on nozzles of pressure vessels of various nuclear reactors, to reduce the mass flow rate in postulated accidents. The pressure loss coefficient of venturi tubes is small at a low flow rate and large at a high flow rate since the flow is choked when the pressure difference is greater than the critical value.

The flow control mechanism of the fluidic device is due to change in the flow resistance inside a vortex chamber of the fluidic device. The benefit of the fluidic device is the elimination of LPSI (low pressure safety injection) pump from the safety injection system. The vortex device using the vortex flow effect was

invented in 1928 [5]. Vortex diode is a fluidic device that creates a diode-like pressure drop behavior, i.e., the pressure loss coefficient depends on the direction of the fluid flow. The pressure loss coefficient is small for a positive flow rate but is significantly high in the reverse direction. [1] employed the CATHENA program to simulate the effect of the vortex diode in the case of LOCA in the design optimization of the Canadian heavy water reactor CANFLO. The results showed that the vortex diode at the inlet pipeline of the pressure vessel can lower the peak fuel temperature during the accident, compared to conventional CANDU600 reactors.

On the contrary, a fluidic device with a significantly higher pressure loss coefficient at a low flow rate than the high flow rate was also purposed [6] They designed the passive flow controlling safety injection tank for the APR1400 reactor, and the pressure loss coefficient of the passive flow controlling safety injection tank was almost 10 times higher at a low flow rate than the high flow rate [7].

In this work, mathematical analysis was conducted first to identify important geometric and hydraulic parameters of the passive flow limiter. Then a series of numerical simulations were carried out to find the relationship between hydraulic performance and geometric parameters of the passive flow limiter.

Specifications of Passive Flow Limiter

Figure 1 shows a diagram of the passive flow limiter. To be compatible with the integral RPV (Reactor Pressure Vessel) of the NHR200-II reactor, the structure of the passive flow limiter was designed as compact as possible. The passive flow limiter is mainly composed of an upward cylinder shell, a movable ball, and an x-shaped support frame. At a low flow rate, the ball rests on the x-shaped frame due to its own weight, and the force of the fluid acting on the ball is not enough to drive the ball upward. As the fluid is accelerated in LOCA, the ball moves upward along the axis of the cylinder and stops at the throat due to the pressure difference, and the flow is blocked.

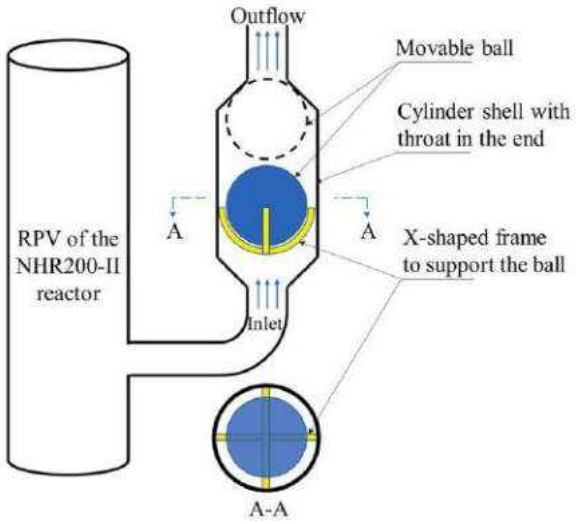

Fig. 1. Schematic of the passive flow limiter

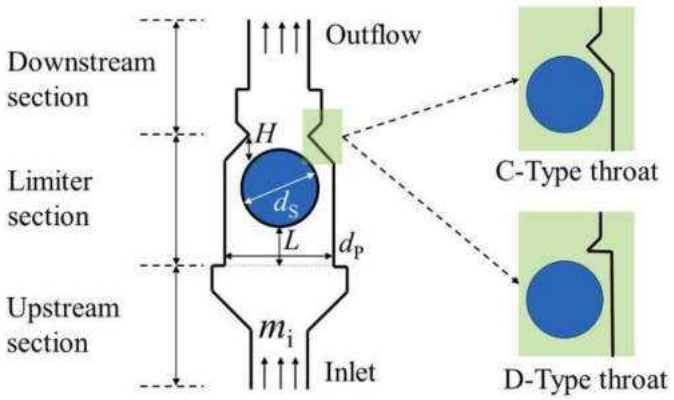

Fig. 2. Structure of the passive flow limiter

The most important design objective of the passive flow limiter is the critical flow rate at which the ball starts to be driven upward by the accelerated fluid. The critical flow rate can either be measured experimentally or calculated according to the balance of force. Figure 1 also show the structure of the passive flow limiter. The passive flow limiter has three sections from bottom to top, namely the upstream section, the limiter section, and the downstream section. A throat was designed at the end of the limiter section to stop the ball under a large pressure difference. Many structural parameters shown in Fig. 2 affect the value of dimensionless critical flow rate η, among which the important ones are: (1) front length L, which is the length from the starting point of the limiter section to the ball, (2) the blockage ratio $BR = d_s/d_p$, where d_s and d_p are the diameters of the ball and the pipe respectively, (3) the axial distance H between the ball and the throat, and (4) shape of the throat. Two types of throats were designed for the passive flow limiter. The first type is a tapered section with a cone angle of 45◦(C-type in Fig. 2). The second throat design has a sudden contraction at the end of the limiter section (D-type in Fig. 2). For the criterion of operability, the passive flow limiter should act correctly within the full operation range of pressure and temperature of the NHR200-II reactor. Since the lowest temperature and pressure of the reactor is 20 ◦C at 0.1 MPa, and the maximum temperature and pressure is 280 ◦C at 8 Mpa

Solution Method

The aim of this study is to design a novel passive flow limiter for the NHR200-II nuclear heating reactor to reduce the break mass flow rate in loss-of-coolant accidents. For this purpose, NHR200-II nuclear heating

reactor has been considered. The flow fields are predicted by the RNG (Renormalization Group) k–ε turbulent model with the enhanced wall treatment. Recent studies [11,12] have shown that the renormalization group (RNG) k–ε model offers superior performance to other turbulent models to predict hydrodynamic data with a higher convergence speed.

The numerical simulation is performed by solving the threedimensional governing equations including the following continuity, momentum, and energy conservation equations[15]:

$$\frac{\partial(\rho u_i)}{\partial x_i} = 0 \quad (1)$$

$$\frac{\partial(\rho u_i u_j)}{\partial x_j} = -\frac{\partial p}{\partial x_i} + \frac{\partial}{\partial x_j}\left(2\mu S_{ij} - \rho\overline{u_i' u_j'}\right) \quad (2)$$

$$\frac{\partial(\rho c_p u_i T)}{\partial x_i} = \frac{\partial}{\partial x_j}\left(K\frac{\partial T}{\partial x_i} - \rho C_p\overline{u_i' T'}\right) \quad (3)$$

where *ui* and *P* are the average velocity and static pressure, respectively. *u′ i* and *u′ j* represent fluctuating velocity components. In the following equation, *Sij* is the mean strain rate tensor

$$S_{ij} = \left[\frac{u_{i\,j} + u_{j\,i}}{2}\right] \quad (4)$$

The accuracy and high convergence speed of this model can come from some modifications including new constants and an additional term on the right-hand side of the ε equation compared to the standard *k*–ε model. It is noted that through an appropriate meshing near the wall regions, all advantages of the RNG k–ε model are achievable.

$$\frac{\partial(\rho k)}{\partial t} + \frac{\partial(\rho k u_i)}{\partial x_i} = \frac{\partial}{\partial x_i}\left\{\left(\mu + \frac{\mu_t}{\sigma_k}\right)\frac{\partial k}{\partial x_j}\right\} + p_k - \rho\varepsilon \quad (5)$$

$$\frac{\partial(\rho\varepsilon)}{\partial t} + \frac{\partial(\rho\varepsilon u_i)}{\partial x_i} = \frac{\partial}{\partial x_i}\left\{\left(\mu + \frac{\mu_t}{\sigma_\varepsilon}\right)\frac{\partial \varepsilon}{\partial x_i}\right\} + C_{1\varepsilon}\frac{\varepsilon}{k}p_k - C_{2\varepsilon}\rho\frac{\varepsilon^2}{k} - \frac{C_\mu\eta^3\left(1 - {}^{\eta}/_{\eta_0}\right)}{1+\beta\eta^3}\frac{\varepsilon^2}{k} \quad (6)$$

$$P_k = \left[2\mu_t S_{ij} - \frac{2}{3}\rho k S_{ij}\right]\frac{\partial u_j}{\partial x_i} \quad (7)$$

The computational mesh for an example of the studied cases was shown in Fig. 3. The SIMPLEC (Semi-Implicit Method for Pressure Linked Equations-Consistent) algorithm39 is used for pressure–velocity coupling. When residuals for the mass, momentum, energy, and turbulent equations become less than 10^{-7}, the numerical simulation is converged.

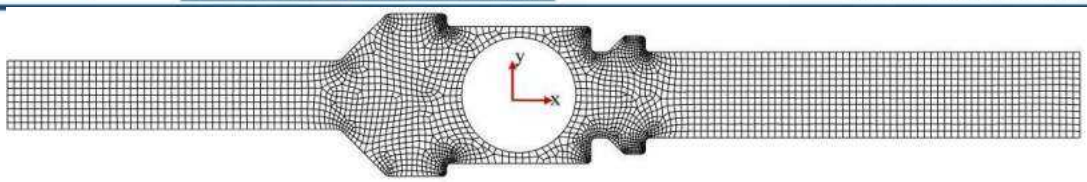

Fig. 3. Example of computational grids

Results and Discussion

The throat shape of the passive flow limiter also has a significant impact on the dimensionless critical flow rate. For the D-type and C type throat, the flow distribution with stream lines were depicted in Figs 4 and 5. Comparing with the flow distribution and pressure, it can be revealed that the critical flow rate for D-type throat is obviously larger than the C-type throat when the imensionless axial distance H=5 mm, while the dimensionless critical flow rate for D-type throat is smaller when the dimensionless axial distance H=15, especially for fluid at 20 ◦C.

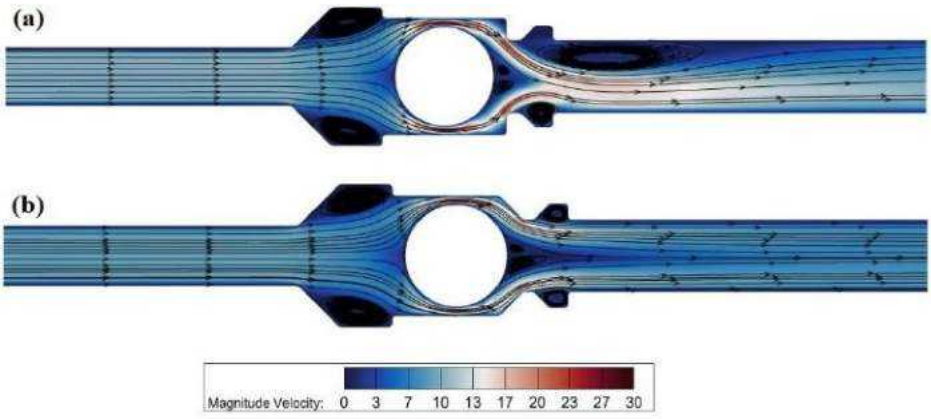

Fig. 4. Flow distribution with stream lines for H=15mm, (a) D-type, (b) C type

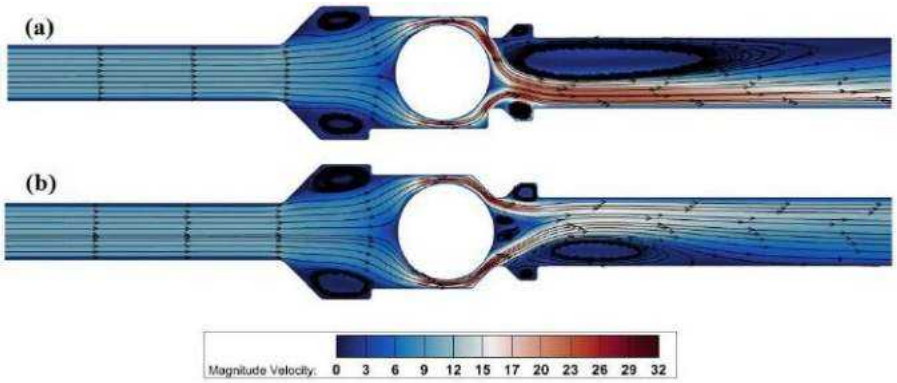

Fig. 5. Flow distribution with stream lines for H=5mm, (a) D-type, (b) C type

The trend in Figs. 4 to 7 can be explained by the pressure distribution and velocity profile around the ball. As the axial distance H between the ball and the throat increases, the gap velocity decreases rapidly, therefore, the downstream pressure around the rear side of the ball increases significantly , and the drag coefficient C_D of the ball decreases. It is worth mentioning a decrease in the drag coefficient C_D causes the increase in the dimensionless critical flow rate.

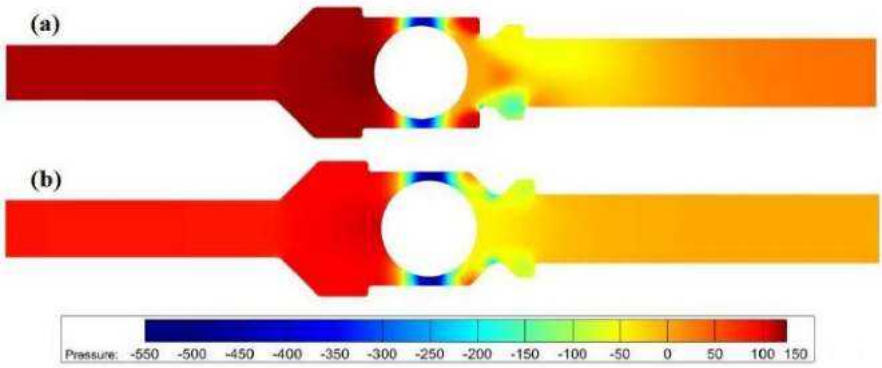

Fig. 6. Pressure contours of the passive flow limiter for H=15mm, (a) D-type, (b) C type

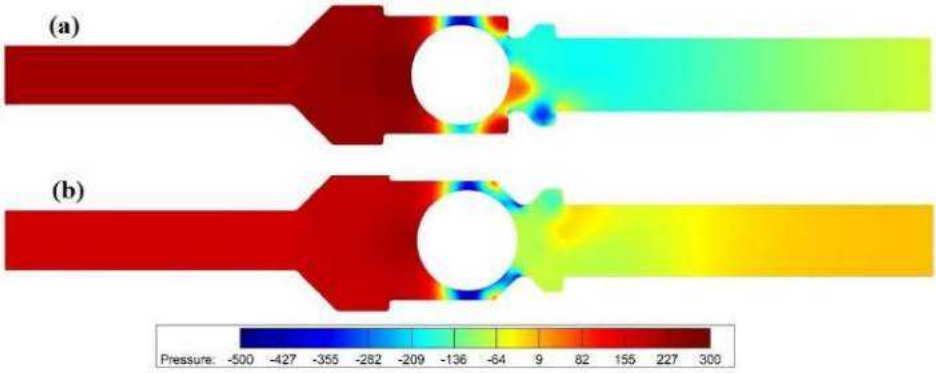

Fig. 7. Pressure contours of the passive flow limiter for H=5mm, (a) D-type, (b) C type

As shown in Figures 4 to 7 the velocity profile upstream of the ball becomes more flattened as the front length increases, i.e., the axial velocity at the centerline of the pipe decreases as the front length L increases. Therefore, the pressure near the front of the ball increases as the centerline velocity decreased, and the subsequent increase of the drag coefficient of the ball caused the decrease of the dimensionless critical flow rate.

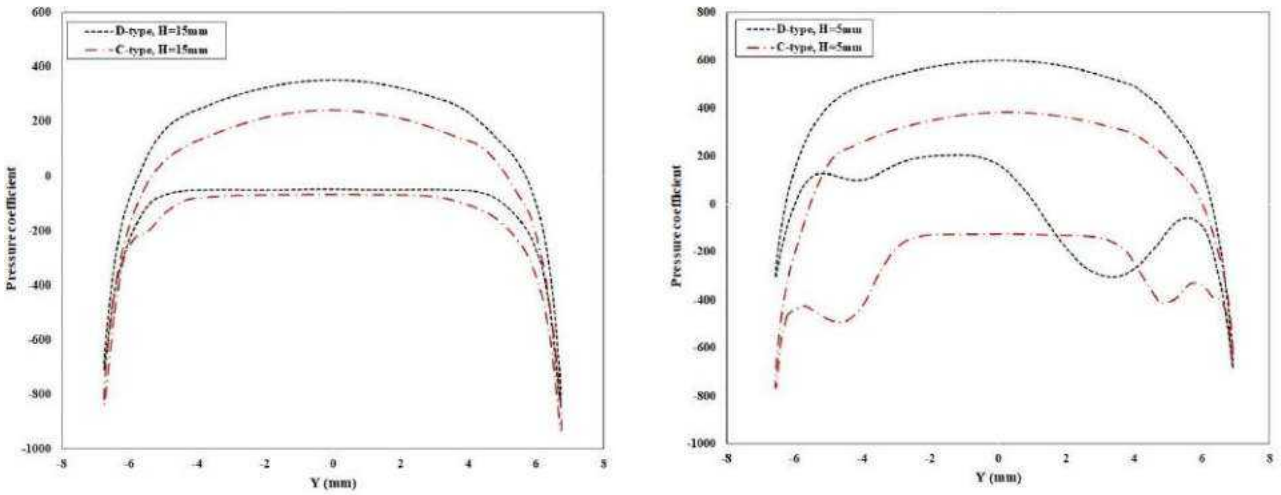

Fig. 8. Pressure coefficient distribution on the ball for different conditions investigated

Conclusions

In this study, novel passive flow limiter was proposed for the NHR200-II reactor to limit the coolant loss in postulated LOCA. A series of parametric numerical simulations were conducted to discuss the influences of important geometric of the passive flow limiter, including the axial distance H, the shape of the throat, the blockage ratio BR. The highlights obtained in this study are summarized as follows:

- The critical flow rate is very sensitive to the axial distance H, increases rapidly with the axial distance.
- The downstream throat shape of the passive flow limiter affects the performance of the limiter. A throat with a flat end (D-type) outperforms the throat with a tapered end (C-type).
- The flow rate decreases with the increasing front length, which can be attributed to the more flattened velocity profile in front of the ball.
-

References

[1] Spinks, N.J., Barclay, F.W., Allen, P.J., Yee, F., 1988. A CANDU designed for more tolerance to failures in large components.

[2] Meng, J., Xu, J., Lin, S., Song, Y., 2014. Design improvement and test verification of steam flow limiter of steam generator. Nucl. Tech. 37 (7), 95–98.

[3] Hwang, H.J., Park, J., Min, J.K., 2021. A numerical study on the flow control characteristic of a cavitating venturi with one- and two-stage diffusers. J. Mech. Sci. Technol. 35 (4), 1463–1472.

[4] Stratta, E., Belliard, M., 2017. Thermal-hydraulic Study of Passive Safety Systems Based on the Hydraulic Diode Principle for the Management of Large-Break Loss of Coolant Accidents.

[5] Thoma, D., June 1928. Vorrichtung zur Behinderung des Ruchstromens. Deutsche Patentschrift No. 507,713.

[6] Chu, I.-C., Song, C.-H., Cho, B.H., Park, J.K., 2008. Development of passive flow controlling safety injection tank for APR1400. Nucl. Eng. Des. 238 (1), 200–206.

[7] Cho, S.J., Kim, B.S., Kang, M.G., Kim, H.G., 2000. The development of passive design features for the Korean Next Generation Reactor. Nucl. Eng. Des. 201 (2), 259–271.

ICNST 2024
International Conference on Nuclear Science and Technology
6- 8 MAY 2024 | Isfahan, Iran

Application of the IDON Shielding Optimization Tool (ISOT) for the Primary and Secondary Shielding of a Research Reactor (Paper ID : 1611)

César Hueso[1,2*], Christian Garido[2], Omar Bouhasun[2]
[1]Department of Energy Engineering, Basque Country University, Bilbao, Spain
[2]IDON, Consulting, Engineering & Architecture, S.A.U., Bilbao, Spain

Abstract

The goal of the work presented at the 47th Annual Meeting of the Spanish Nuclear Society regarding the IDON Shielding Optimization Tool (ISOT) was to introduce the development, applications, and capabilities to automate the shielding design procedure using multi-objective genetic algorithms. The tool was tested on a very simple shielding problem using different Monte Carlo codes. The preliminary results were promising, and the capability of testing and validating the performance of ISOT in more complex shielding problems becomes achievable.

In order to assess the performance of ISOT in real-life shielding design, the tool has been used to optimize the primary and secondary shields of a research reactor. The calculations have been performed using SCALE, a new Monte Carlo code in ISOT (easily included in the system due to the modular nature of the tool). In the design of the primary shield, the objective was to minimize the neutron and photon dose outside the reactor core while also minimizing the total mass shield, taking into account the size constraints. For the secondary shield, the objective was to minimize the operational dose received by the operators while also minimizing the weight of the shield by optimizing the thickness of the shield in different zones.

The model, results, and methodology of ISOT calculations using SCALE related to primary and secondary shielding optimization will be presented. ISOT has been able to generate multiple optimal solutions not easily foreseen by expert shielding engineers. Those results indicate the potential of the tool to facilitate the process of real-life shielding design.

Keywords: Shielding, optimization, genetic algorithm, dose rate.

Introduction

The primary and secondary shielding in a research nuclear reactor are the layers of material that protect the operators and the environment from the harmful radiation emitted by the fission process. The primary shielding is the layer that surrounds the reactor core itself and is usually made of materials that can withstand high temperature and neutron interaction. The secondary shielding is the layer that covers the primary shielding and the rest of the reactor components, such as the steam generators, pumps, valves,

and piping. The secondary shielding is usually made of lead or other heavy metals that can absorb gamma rays and other forms of radiation.

A preliminary design of both shieldings for a research reactor was already provided in PhD Dissertation by the author [1]. The main goal was to improve both designs in terms of dose rates and weight. Moreover, the dose rates in different rooms also needed to be optimized, as well as the operational dose received by the operators.

Optimization of Primary Shielding

The optimization of the primary shielding is very similar to the multi-layer problem presented in the 47th Annual Meeting [2]. The main difference resides in the number of layers and materials considered.

The goal was to enhance the neutron shielding efficiency of the preliminary design by an order of magnitude while maintaining the photon shielding efficiency and trying to minimize the weight.

The geometry consists of concentric cylinders, of which the inner layers represent the vessel with the active core, the core shroud and the thermal insulation and the outer layers represent 10 layers of shielding materials. For simplicity, the fuel, coolant and structural materials in the active core are homogenized.

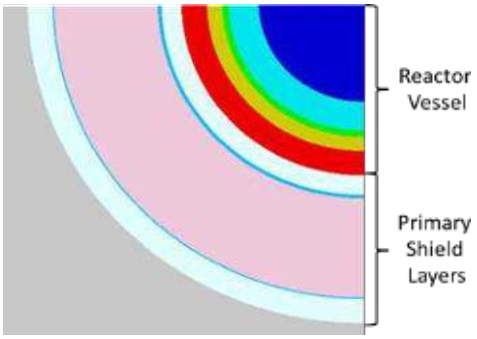

Fig. 1. Primary Shielding Geometry

The optimization problem involves finding the optimal material and thickness for each shielding layer, subject to two constraints:

The total shielding thickness must be lower than 110 cm

The total linear weight[1] of the shield must be lower than 341 g/cm (corresponding to the linear weight of the existing shielding)

A total of 6 different materials were considered:

Concrete

Water

[1] Linear weight is defined as the mass per unit length along the axial direction

Steel

Lead

Two different boron doped composites The objectives were to minimize:

The neutron dose rate after the shielding layers

The photon dose rate after the shielding layers

The weight of the shielding

Given the symmetry of the problem, these dose rates were provided by point detectors.

The genetic algorithm of ISOT was run for 30 generations of 150 individuals each. As seen in Figure 2, while in the initial generations the population is randomly scattered, with more generations the population starts converging to a set of optimal solutions (Pareto Front[2]).

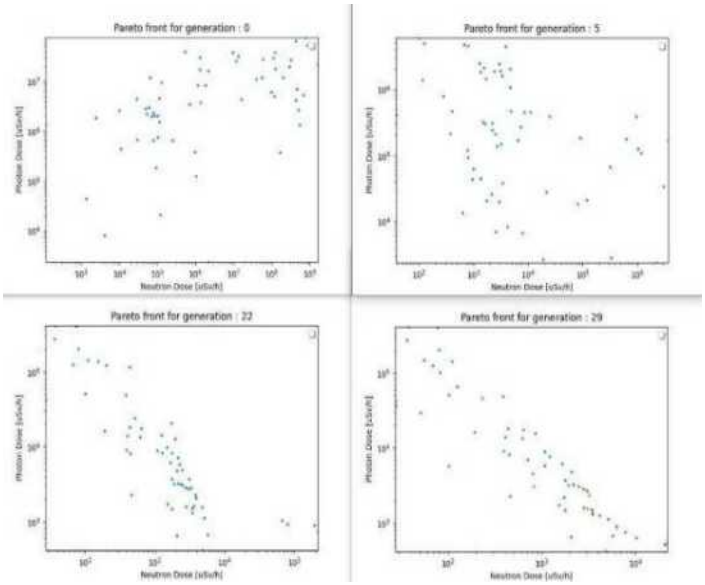

Fig. 2. Evolution of the Pareto Front

In the final generation, a set of 150 optimal solutions that respect the constraints was obtained. Figure 3 shows some of these solutions. These solutions were analyzed in order to find those that obtain an improvement on the neutron efficiency by 10 times while maintaining the Photon efficiency of the preliminary shield provided.

[2] Pareto Front is a curve that represents a set of non-dominated solutions, where no solution is better than another in all objectives.

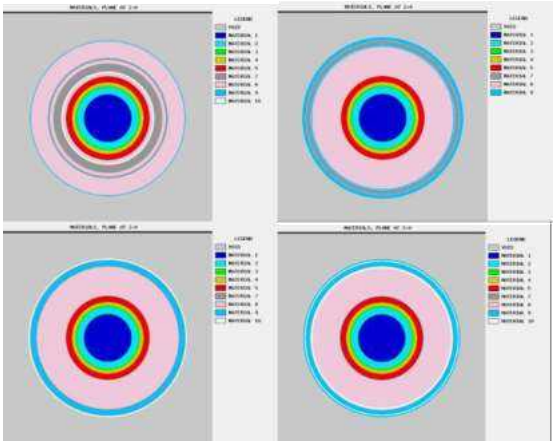

Fig. 3. Some optimal solutions

After this analysis, it was found that from the 150 solutions, 50 of them reach the goals. These 50 solutions were further evaluated for their constructability in terms of feasibility, considering material compatibility (e.g. materials with low melting point cannot be in hot zones close to the core), structural stability, etc. Finally, after all these analyses, the final selected configuration was obtained, shown in Figure 4. This configuration increases the neutron shielding efficiency by 18 times and also increases the photon shielding efficiency by 4 times, all this with a reduction on the linear weight of 40 g/cm.

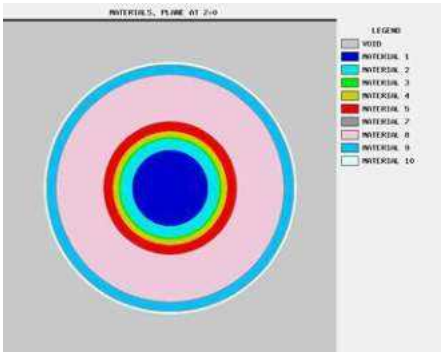

Fig. 4. Selected solution

Optimization of Secondary Shielding

The preliminary secondary shield design only considered shielding the walls of the room containing the reactor. Therefore, an opportunity to reduce the shield weight by adding shielding closer to the radiation source, such as the primary coolant pipes, steam generators and other equipment, was identified.

To optimize the secondary shielding and minimize the operational doses, an ISOT optimization model was set up. The first step was to simplify the detailed model to have a fast-running case. Then, the simplified

model was parametrized according to the design variables, constraints and objective functions defined in the ISOT model.

Model Simplifications.

The simplified model was based on the detailed model, but with some components removed or homogenized to reduce the complexity and computational time, while still capturing the relevant physics accurately.

The main simplifications were:

Removal of all small equipment from the reactor room.

Simplification of primary water circuits geometry, keeping the same total length and water inventory.

Homogenization of water, structural materials and fuel in the vessel (including primary shield).

Homogenization of primary water, secondary fluid and steel in the tube bundle zone of the Steam Generators (SG).

Figure 5 shows two cut views of the simplified model. The major components important for radiation transport, such as pipes, pressurizer, and steam generators, are still present. The lead in the secondary shielding is highlighted in green.

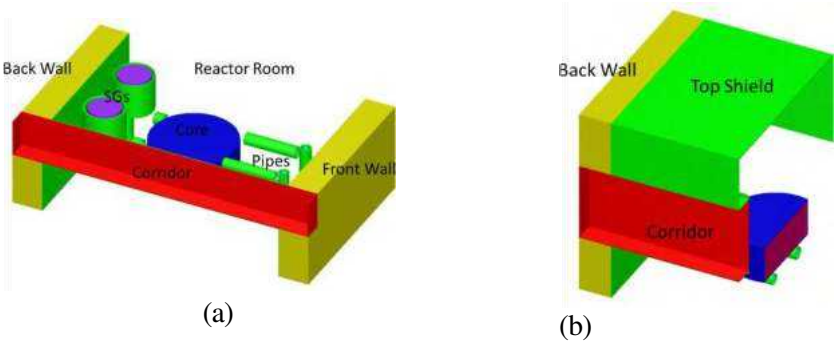

Fig. 5. Simplified model for secondary shield optimization

Four radiation sources are considered in this simplified model:

Gamma source from the core: This source was located on the external surface of the Primary shielding of the vessel. It included the gamma radiation from the activated primary coolant inside the vessel, the gamma particles that leaked through the primary shielding from the fuel and the secondary gammas generated by neutron interactions.

Gamma source from activated primary coolant in the pipes and bottom of SGs (primary water inlet and outlet): this source was located inside the pipes, and it included the gamma radiation from the activated primary coolant inside the pipes.

Gamma source from activated primary coolant inside the tubes of the SGs: this source was located in the tube bundle zone at the top of the SGs. It included the gamma radiation from the activated primary coolant inside the tubes of the steam generators.

Gamma source from activated primary coolant inside the pressurizer: this source was located at the bottom part of the pressurizer. It was assumed that 60% of the Pressurizer was filled with water, of which 5% was activated primary coolant. It included the gamma radiation from the activated primary coolant inside the pressurizer.

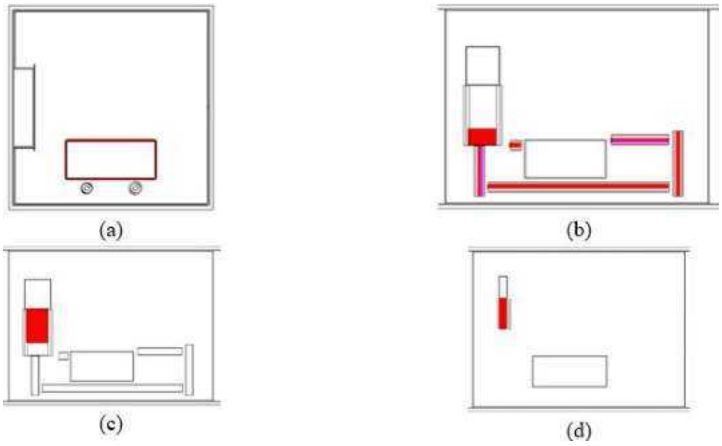

Fig. 6. Source terms

The strength and spectrum of these sources was obtained from previous calculations.

Since most of the neutrons were blocked by the primary shield and more gamma particles passed through, the neutron source could be neglected. Previous calculations showed that the dose rate from neutrons was about a billion (1E9) times lower than that from gamma particles.

Finally, three cartesian mesh tallies covering the corridor and adjacent rooms to the reactor room were used to estimate the dose rate map.

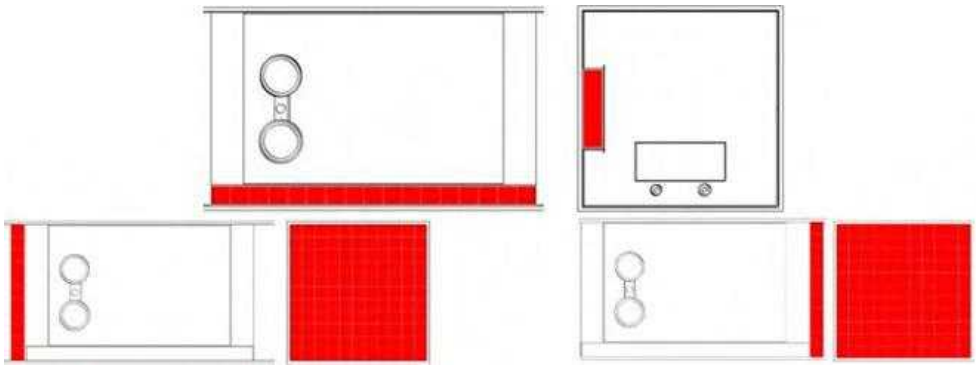

Fig. 7. Detection areas

During the operation of the reactor, operators work in the adjacent rooms to the reactor. Therefore, the constrains for the problem are:

Dose in the adjacent rooms and the corridor below the limit for its classification as Prohibited Radiological Zone.

Total weight of the secondary shield bellow 240 MT.

Furthermore, operators may need to cross the reactor room through the corridor while in operation. Therefore, the operational dose was estimated by considering residence time of the operator in each room and the corridor, and the maximum dose rate obtained in each of the tallies on each of theses sections. The following objective function, set as the linear combination of the maximum value in the different mesh tallies, was developed in ISOT for this purpose:

$OF = \sum Ti\max\ (MTi)$

Where OF is the objective function, Ti is the residence time in the section i, and MTi is the Mesh Tally in section i.

In the optimization of the operational dose for this configuration there is various sources of asymmetry:

The residence time in each room is different,

The steam generators are located close to the back room

The corridor is on one side of the reactor room.

For this reason, the thicknesses of the secondary shield in each loop can be optimized separately. Therefore, a total of 9 optimization variables are considered:

The shield thickness of each steam generator (x2)

The shield thickness of each primary system pipe loop (x2)

The shield thickness of the walls facing the front and back rooms (x2)

The shield thicknesses of the corridor walls facing the reactor room. (x3) The objectives were to minimize:

The operational dose of the operator

The weight of the shielding

Again, the genetic algorithm of ISOT was run for 30 generations of 150 individuals each.

After the analysis of the feasibility of the solutions provided, a secondary shield solution was obtained that met the constrains and reduced the total weight by 240 MT. This solution also lowered the operational dose to 60% compared to the preliminary design.

Conclusions

ISOT has been successfully used for the optimization of the primary and secondary shields of a research reactor.

For the primary shield optimization, a multilayer problem with 10 shielding layers, 6 different materials, three objective functions and two fatal constraints was setup. The genetic algorithm was run for 30 generation of 150 individuals. After analysis of the 150 solutions provided in the pareto front, the final selected configuration increased the neutron shielding efficiency by 18 times and also increased the photon shielding efficiency by 4 times, while reducing the linear weight of 40 g/cm.

For the secondary shield optimization, a simplified model of the whole reactor building was set up. The thicknesses of the secondary shield in each loop was optimized separately, giving a total of 9 optimization variables. The operational dose of the operator was optimized while minimizing also the shielding weight. A specific objective function, set as the linear combination of the maximum value in the different mesh tallies, was developed in ISOT. After the analysis of the feasibility of the solutions provided, a secondary shield solution was obtained that met the constrains and reduced the total weight by 240 MT. This solution also lowered the operational dose to 60% compared to the preliminary design.

Acknowledgements

The author would like to thank Dr. Nima Ghal-Eh from Department of Physics, Faculty of Science, Ferdowsi University of Mashhad for his kind invitation to ICNST2024.

References

C. Garido, O. Bouhasun, C. Hueso. (2022) Development and Verification of the Idon Shielding Optimization Tool (ISOT), 47ª Reunión Anual de la Sociedad Nuclear Española, Cartagena, Región de Murcia.

Hueso, C. (2022) Optimization of shielding calculations in mobile reactors through the determination of the contribution of influencing parameters, PhD Dissertation, http://hdl.handle.net/10810/57452

ICNST 2024
International Conference on Nuclear Science and Technology
6- 8 MAY 2024 | Isfahan, Iran

Computational Fluid Dynamics Simulation of Siphon Breaker Performance in a Research Reactor (Paper ID : 1659)

Parvin Arehjani [1], Seyed Mahmoud Mousavi [2], Amjad Sazgar [3*], Samaneh Heidaryan[4]

[1] Department of Chemical Engineering, Amirkabir University of Technology, Tehran, Iran
[2] Department of Mechanical Engineering, University of Zanjan, Zanjan, Iran
[3]Nuclear Fuel Cycle Research School, Nuclear Science and Technology Research Institute (NSTRI), Tehran, Iran
[4]MSc.in Materials Engineering, Department of Materials and Metallurgical Engineering, Amirkabir University of Technology, Tehran, Iran

Abstract

In an open-pool type reactor, the main accident that can occur is a loss of coolant accident (LOCA). This accident happens when there is a rupture in the primary cooling system components. In such cases, the outlet of the reactor core is designed as a siphon, and it is taken out of the pool at a height higher than the reactor core, so that in case of pipe rupture, the height of the water is maintained and the core is immersed in water to prevent of core melting. But still, the phenomenon of siphoning causes the flow to continue and the water in the pool to be empty. To prevent this phenomenon, considering a branch or hole in the siphon as a siphon breaker, will be useful. Many parameters affect the height of the pool water, including the diameter of the siphon breaker, the connection position of the siphon breaker, the height of the siphon pipe entrance, etc. In this research study, the effect of the siphon breaker diameter (50, 100, and 150 mm) on the height of the pool water was investigated. In this work, the computational fluid dynamics has been done using Fluent software. The simulation results show that the siphon breaker diameter significantly affects the undershooting height and bypass flow rate. The undershooting height, in the case where the diameter of the siphon breaker was considered to be 150 mm, had the lowest value, and the bypass flow rate had the highest value for this siphon breaker.

Keywords: Open Pool Research Reactor, Siphon Breaker, undershooting height, Computational Fluid Dynamics (CFD).

Introduction

A research reactor is important in advancing nuclear science and technology in a country. Typically, these reactors are used for educational purposes and provide instruction in the fundamentals of nuclear reactors. In addition, it serves as a valuable resource for conducting research and development efforts. A scientific reactor with neutron emission capabilities

facilitates the discovery of new materials. Another advantage is its ability to produce radioisotopes that are widely used in various industries and medical applications [1]. Currently, there are 820 operational scientific reactors worldwide [2]. Among these reactors, a significant number use fuel plate, which has been increasing recently. For easy cooling of this type of fuel, the research reactor must have a downward flow core. This adjustment is crucial to maintaining a positive suction head in the primary cooling system. As a result, some facilities must be located below the reactor. However, there is a potential hazard if a pipe rupture occurs in the primary cooling system below the surface of the reactor. This can create a siphon effect and continuously drain water, potentially dewatering the reactor core. This scenario prevents the removal of residual heat, which would lead to a severe accident. Therefore, to reduce the risk of accidental loss of coolant (LOCA), the safety measures must be considered. One of these safety features is the siphon breaker. This device effectively prevents water from draining by using air flow, which is known as the anti-siphon system. Two types of siphon breakers are commonly used in research reactors: siphon break lines (SBL) and siphon break holes (SBH). SBL consists of a small size tube. In certain designs, one end of the tube (tube inlet) is immersed in the open pool reactor, while in others, this end is open to the air. The other end of the pipe (pipe outlet) is connected to a high U-bend located on the outlet side of the cooling pipe. On the other hand, SBH is a small hole drilled on the inlet side of the cooling pipe. During normal operation, both the inlet ends of the SBL (in certain designs) and the SBH are fully immersed in the pool. In addition, the SBL can be equipped with valves to regulate the bypass flow [3, 4]. The performance of the siphon breaker is affected by two parameters: (1) undershooting height and (2) bypass flow.

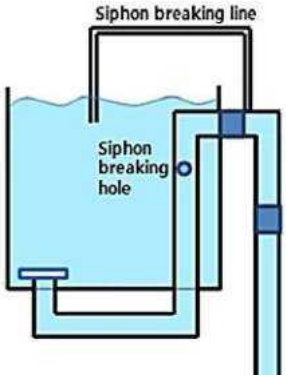

Fig. 1. Siphon breaker line and hole types.

The undershooting height refers to the difference in height between the entrance of the siphon break line (SBL) and the water level in the upper tank after the siphon breaking process. Essentially, it indicates how much the water level decreased during the siphon-breaking event. Consequently, the undershooting height is a crucial parameter as it directly facilitates the determination of the quantity of coolant loss [5].

Under steady-state operating conditions, the siphon breaker remains open, allowing for a bypass flow while the reactor is in operation. This bypass flow results in a portion of the primary coolant not passing through the reactor core but instead entering the primary loop directly through the siphon breaker. To ensure that coolant flows through the core as intended, the diameter of the siphon breaker should be minimized while still being large enough to break the siphon phenomenon effectively [6].

The siphon-breaking effect can be significantly influenced by various parameters such as the siphon breaker type, its diameter and height [5].The optimal selection of the siphon breaker diameter is crucial based on the information provided. Since the coolant water with a high flowrate passes through the main siphon pipe, choosing a siphon breaker diameter that is excessively small may cause a delay in breaking the siphon effect (high undershooting height) or even prevent its break before reaching the core level. Conversely, selecting a large siphon breaker diameter may result in a significant portion of the coolant bypassing the siphon breaker, reducing the amount of coolant passing through the core [4].

To investigate the siphon breaker, McDonald and Marten (1958) [7] experimented to validate the performance of the siphon breaking valve as an actively operated mechanism. Their objective was to prevent the reverse flow of sodium in a sodium graphite reactor. In another study, Neill and Stephens (1993) [8] investigated the siphon breaker as a passively operated device within a small pipe. They utilized various sizes of orifices to regulate the flow rate of water and air. To interpret their experimental findings, they introduced the concept of air sweep-out mode, which included zero sweep-out mode, partial sweep-out mode, and full sweep-out mode. Additionally, Sakurai (1999) [9] proposed an analytical model to analyze the siphon breaking process, employing a fully separate air-water flow model. Their model demonstrated reasonable agreement with experimental data. However, it is worth noting that only two experiments were conducted, and the scale of the experimental setup was relatively small compared to actual research reactors. Seo and colleagues have been conducting research on siphon breakers since 2011. In their initial work, Seo et al. (2011) [10] discussed the type

of breaker required for different types of nuclear reactors. They reported that for upward-flow reactors (where the flow passes through the core from bottom to top), both passive siphon break holes (SBH) or siphon break lines (SBL) can be installed in both the inlet and outlet pipes of the reactor. However, for downward-flow reactors (where the flow crosses the core from top to bottom), an SBH or SBL can be installed at the inlet, but a siphon -breaking valve (SBV) is necessary at the outlet to ensure the required net positive suction head (NPSH). In a subsequent study, Seo et al. (2012) [11] constructed a real-scale facility to investigate the siphoning effect on the Jordan Research and Training Reactor (JRTR). The experimental facility comprised a 60 m^3 open pool filled with water and 16 inches" diameter coolant pipe with several elbows. They simulated a loss of coolant accident (LOCA) of 10 inches in the main pipe and measured surface velocity, pressure at various positions in the main pipe, and pool level evolution to quantify undershooting (the distance from the pool level to the end of the SBL). Several SBL diameters (1, 1.5, 2, and 2.5 inches) were experimentaly studied, and some were also simulated using Computational Fluid Dynamics (CFD). They conducted simulations with Fluent using the Volume of Fluid (VOF) method and the Euler-Euler two-phase model. Despite discrepancies between the results of Seo et al. (2012) and experimental data, they concluded that the VOF method overpredicted undershooting, while the Euler-Euler method underpredicted it. They also noted that discrepancies were more pronounced for SBLs with smaller diameters.

More recently, Kang et al. (2013) [12] conducted experimental tests on the same facility but with different configurations. They reduced the diameter of the siphon break line (SBL) to as small as 0.5 inches and increased the size of the loss of coolant accident (LOCA) rupture to 6 and 8 inches. Additionally, they conducted tests using both siphon break lines (SBL) and siphon break holes (SBH), as well as combinations of both systems. When only the SBL was used, the undershooting height was significantly affected by the SBL size. As the size of the SBL decreased, the undershooting height increased significantly. The effect was so significant that with a 1-inch SBL, the siphon effect never broke. However, when both the SBL and the SBH were used simultaneously, the undershooting height decreased, and even with a 1-inch SBL size, the siphon effect was broken. In 2014, Kang et al. (2014) [13] continued their testing with various rupture sizes for loss of coolant accidents (LOCA) (12, 14, and 16 inches) and different sizes of siphon break lines (SBL) (fb = 3, 4, 5, and 6 inches). They concluded that the

undershooting height depends largely on the size of the SBL but is almost independent of the rupture size.

The extensive experimental data collected by Seo et al. (2012), Kang et al. (2013), and Kang et al. (2014) prompted Lee and Kim (2017) [14] to develop an ad-hoc code for designing and calculating siphon breakers. This code considers a range of basic structural parameters and enables quick estimation of the undershooting height evolution, pressure at various points, and coolant mass flow. However, this code is limited to basic rectangular pool configurations despite its utility, and does not account for core configuration. Additionally, it only models coolant circuit layouts involving pipes and elbows. Given the significance of siphon breakers, this code should be regarded as an initial estimation tool, and the final design should be evaluated using more reliable methods. Finally, in 2017, Ramajo et al. [15] conducted a Computational Fluid Dynamics (CFD) study on the siphon breaker of an open-pool nuclear research reactor, validating the model against experimental data previously obtained by Lee and colleagues in Korea. The calculations were performed using the Open FOAM code. The model accurately predicted key parameters such as the occurrence of the siphon breaker, undershooting height, and liquid mass flow rate using the Volume of Fluid Method (VOF) and k-epsilon turbulence modeling. Results exhibited excellent agreement with experimental findings, highlighting the model's reliability in assessing passive safety systems.

experimental studies on siphon breakers are costly and time-consuming. Since this phenomenon involves two-phase flow and transient conditions, simulating and modeling it is challenging and prone to significant errors. Nevertheless, it is necessary to exert further effort to address the existing issues in this field so that the problems can be resolved. This would enable us to utilize simulation results to select optimal conditions before experimental studies. In this paper, the siphon breaker is simulated as a pipe, and the effect of varying the pipe diameter on the undershooting height is investigated using CFD simulations of the Ansys fluent software.

Simulation of the Siphon Breaking Phenomena

Computational Fluid Dynamics (CFD) simulations of siphon breaker implemented using Ansys Fluent software (version 2022).

Fig. 2 shows the geometry used in the simulations. The reactor pool, constructed from a steel plate, has a water capacity of approximately 35.3 m^3, with a diameter and depth of 3 and 5

meters, respectively. The main pipe has a diameter of 18 inches. The height difference between the end of the siphon breaker line and the siphon main line is 10.5 meters. Siphon breaker lines ranging from 50 to 150 mm are connected to the horizontal part of the inverted U-tube region of the main drainage pipe.

On the pool and pipe walls, a smooth non-slip wall condition was defined because the fluids of this simulation are viscous, and considering this boundary condition, the velocity of the fluid near the wall will be considered zero, which makes the simulation more realistic. The fluids were considered as air and water at 25 °C, and the gravity was defined as −9.81 m/s. Due to the nature of the problem and the effect of time changes on fluid conditions, transient simulation was performed for the simulation. The Volume of Fluid (VOF) method was selected to simulate the multiphase condition of the siphon and siphon breaker. The volume of fluid (VOF) method represents a robust method for tracking the air-water interface. It offers several alternatives for reconstructing the interface with accuracy while conserving the fractional volume of fluid, which is suitable for this simulation. As mentioned before, in this simulation, there are two phases, water and air and water is selected as the first phase. The k-ε model for turbulence is the most common to simulate the mean flow characteristics for turbulent flow conditions that were used in this study. In other studies, it has been concluded that the k-ε model, to solve the conditions of this problem, has less error and leads to more accurate results. At both the top and bottom of the pool air at atmospheric pressure was defined with flow direction set as allowed only normal to the surface and with a 5% turbulence intensity for inwards flow.

The calculation starts from the initial condition of the stagnant flow of the pool water and is progressed by the head of the pool water and outflow to the outlet.

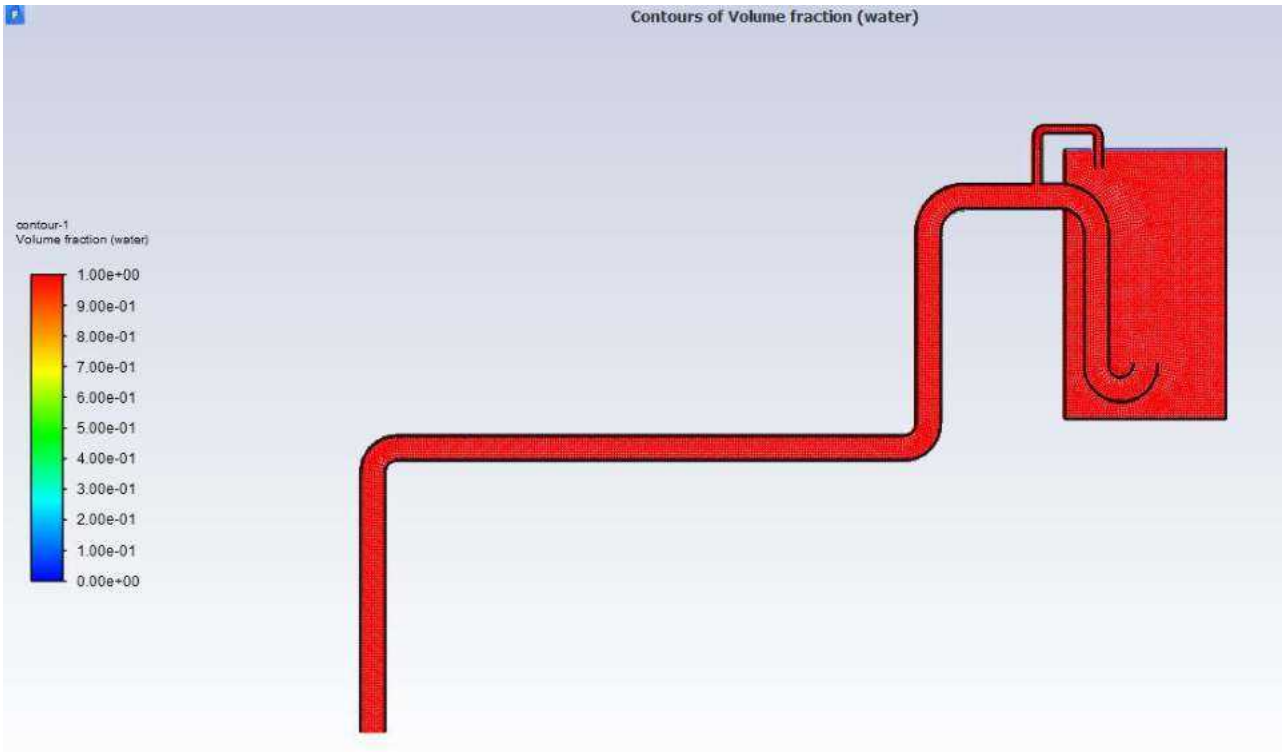

Fig. 2. The geometry used in the simulations.

Results and discussion

Fig. 3 shows the flow rate of output water from the end of the siphon pipe for the three SBL sizes (50, 100, and 150 mm). As depicted in the chart, the outlet water flow rate before the onset of the siphon- breaking phenomenon is highest in the simulation with a siphon breaker diameter of 150 mm. This indicates a higher amount of bypass flow in this scenario. Before the onset of the siphon breaking phenomenon, the outlet water flow rate with a siphon breaker pipe size of 50 mm is approximately 5000 kg/s, while for a siphon breaker pipe size of 150 mm, it is 6000 kg/s at the same moment. Therefore, there is a difference of 1000 kg/s in the bypass flow rate between these two scenarios.

After initiating of the siphon breaker phenomenon, the decrease in flow rate for the diameter of 150 mm is more severe and abrupt, followed by the 100 mm and then 50 mm diameter pipes, respectively. Additionally, due to the significant fluctuation and variation in the outlet water flow rate, approximately from second 3.8, the air has entered the siphon breaker pipe, and the siphon breaking phenomenon has occurred.

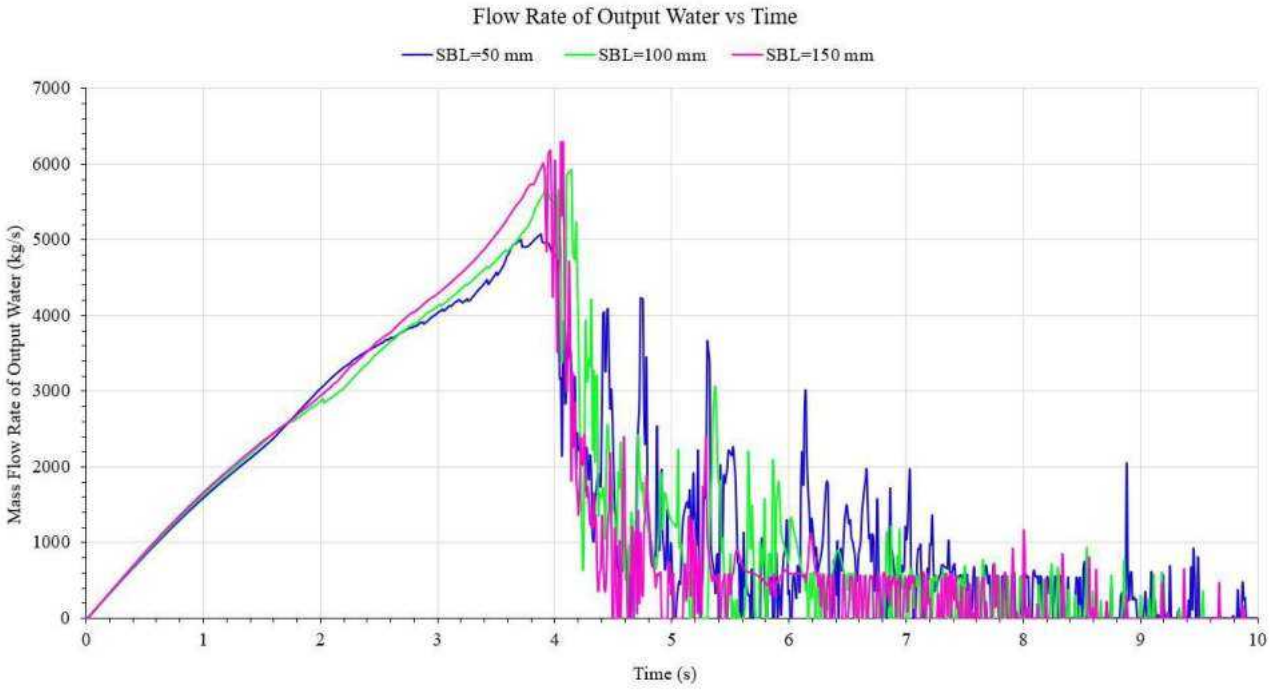

Fig. 3. Mass flow rate of output water for the SBL sizes of 50, 100, and 150 mm.

Figures 4 and 5 illustrate the changes in the pool water level for three different sizes of siphon breakers. As observed, the pool water level has reached its minimum value for a diameter of 50, thus experiencing the greatest undershooting height. Accordingly, the undershooting height of 50, 100, and 150 mm diameters is 1.2, 0.9, and 0.6 m, respectively.

As previously explained, a smaller diameter of the siphon breaker pipe results in less airflow entering the siphon breaker, making the siphon phenomenon more difficult to break. The simulation results also confirm this fact.

Fig. 6. shows the conture of volume fraction, dynamic pressure, and velocity magnitude at 0.5, 2, and 3.5 S times for the SBL size of 50 mm. Using this figure, it is possible to determine at which points the pressure and velocity have the highest and lowest values at any moment of the process, and their approximate values can be obtained.

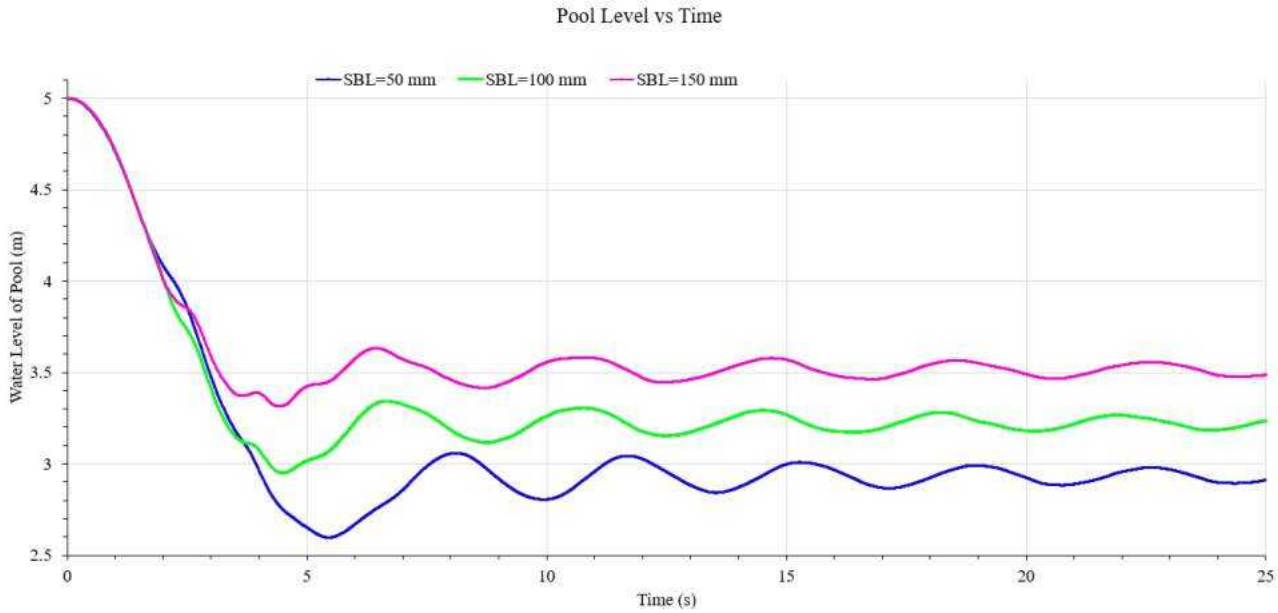

Fig. 4. Pool water level for the SBL sizes of 50, 100, and 150 mm.

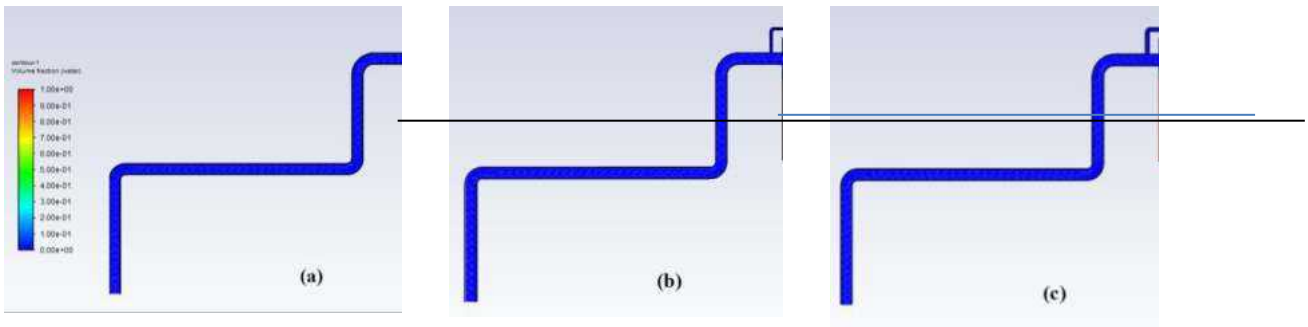

Fig. 5. The simulation results for the volume fraction of water in the pool for the SBL sizes of (a) 50 mm, (b) 100 mm, and (c) 150 mm.

Time	Conture of volume fraction	The dynamic pressure of the mixture	The velocity magnitude of the mixture
0.5 s	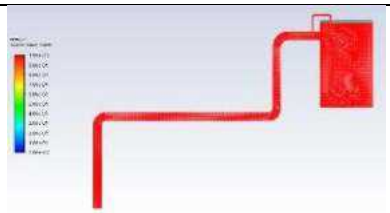	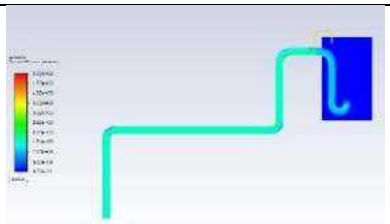	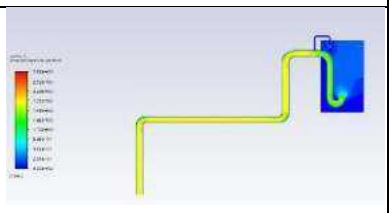
2 s	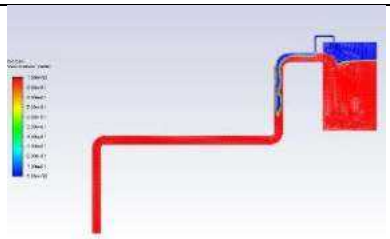	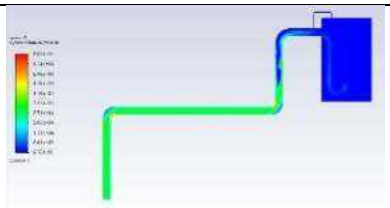	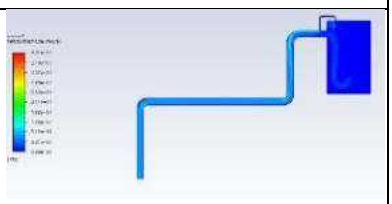
3.5 s	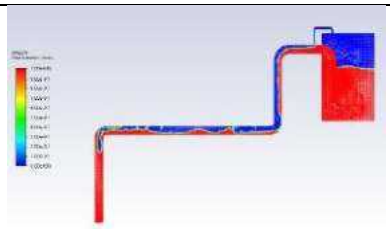	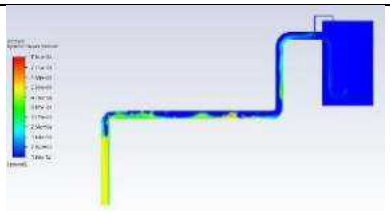	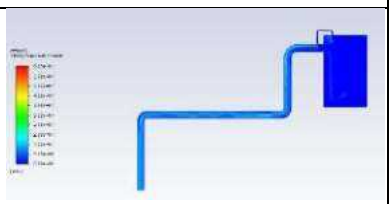

Fig. 6. Conture of volume fraction, dynamic pressure, and velocity magnitude for different simulation times.

Conclusions

This paper investigated the impact of siphon breaker diameter on the performance and safety of open pool-type research reactors. Simulation results demonstrate that the siphon breaker diameter significantly affects the bypass flow rate and undershooting height. Larger diameter siphon breakers (150 mm) allow for higher bypass flow rates (1000 kg/s relative to the diameter of 50 mm) under normal conditions but result in more undershooting height (0.6 m in comparison with the diameter of 50 mm) during siphon breaking. In contrast, smaller diameter siphon breakers exhibit lower bypass flow rates leading to smaller undershooting heights during siphon breaking. Therefore, precise selection of the siphon breaker diameter is crucial for achieving a balance between bypass flow rate and undershooting height to enhance the performance and safety of research reactors.

References

[1] Antariksawan, A. R., & Wahyono, P. I. (2018, February). Steady-state and LOCA analysis of Kartini reactor using RELAP5/SCDAP code: The role of passive system. In Journal of Physics: Conference Series (Vol. 962, No. 1, p. 012048). IOP Publishing.

[2] https:// world- nuclear.org/ information- library /non-power -nuclear- applications/ radioisotope sresearch research-reactors. aspx#:~:text=About %20820%20 research %20 and %20 test, USA%20 and % 20121 % 20 in % 20 Russia.

[3] Lee, K. Y., & Kim, W. S. (2016). Theoretical study on loss of coolant accident of a research reactor. Nuclear engineering and design, 309, 151-160.

[4] Ramajo, D., Corzo, S., Alberto, P., Mocciaro, C., Saez, M., & Nigro, N. M. (2017). Numerical simulation of siphon breaker of an open-pool type research reactor. Mecánica Computacional, 35(31), 1809-1825.

[5] Lee, K. Y., & Kim, W. S. (2017). Study of siphon breaker experiment and simulation for a research reactor. JoVE (Journal of Visualized Experiments), (127), e55972.

[6] Yue, Z., & Ji, S. (2017). Thermal hydraulic analysis of 49-2 Swimming Pool Reactor with a passive siphon breaker.

[7] McDonald, J., & Marten, W. (1959). A siphon break as a blocking valve. Atomics International.

[8] Neill, D. T., & Stephens, A. G. (1993). Siphon breaker design requirements (No. DOE/ER/12820-T1). Idaho State Univ., Pocatello, ID (United States).

[9] Sakurai, F. (1999). Study for improvement of performance of the test and research reactors (No. JAERI-RESEARCH--99-016). Japan Atomic Energy Research Inst.

[10] Seo, K. W., Lee, K., Yoon, H., Jeong, N., Park, Y. C., Chi, D. Y., & Yoon, J. H. (2011, May). Estimation on a siphon breaker type of a research reactor. In Transactions of the Korean Nuclear Society Spring Meeting (pp. 103-104).

[11] Seo, K., Kang, S.H., Kim, J.M., Lee, K.Y., Jeong, N., Chi, D.Y., Yoon, J. and Kim, M.H. (2012). experimental and numerical study for a siphon breaker design of a research reactor. Annals of Nuclear Energy, 50, 94-102.

[12] Kang, S.H., Ahn, H.S., Kim, J.M., Joo, H.M., Lee, K.Y., Seo, K., Chi, D.Y., Yoon, J., Jeun, G.D. and Kim, M.H. (2013). experimental study of siphon breaking phenomenon in the real-scaled research reactor pool. Nuclear Engineering and Design, 255, 28-37.

[13] Kang, S.H., Lee, K.Y., Lee, G.C., Kim, S.H., Chi, D.Y., Seo, K., Yoon, J., Kim, M.H. and Park, H.S., (2014). Investigation on effects of enlarged pipe rupture size and air penetration timing in the real-scale experiment of siphon breaker. Nuclear Engineering and Technology, 46(6), 817-824.

[14] Lee, K. Y., & Kim, W. S. (2017). Development of siphon breaker simulation program for investing loss of coolant accident of a research reactor. Annals of Nuclear Energy, 101, 49-57.

[15] Ramajo, D., Corzo, S., Alberto, P., Mocciaro, C., Saez, M., & Nigro, N. M. (2017). Numerical simulation of siphon breaker of an open-pool type research reactor. Mecánica Computacional, 35(31), 1809-1825.

ICNST 2024
International Conference on Nuclear Science and Technology
6- 8 MAY 2024 | Isfahan, Iran

Examining the nuclear reactors of Iran and the world in terms of technical knowledge, geographical location, power generation capacity, security considerations, environmental issues and economic benefits (Paper ID : 1681)

Yavari M. Correspondent[1*], Araghchi M. Co-Author[2]

[1] Department of Energy Systems Engineering, University of Science and Technology, Tehran, Iran

[2] Nuclear Science And Technology Research Institute, Tehran, Iran

Abstract

Today, the progress and development of nuclear power plants technology, along with other renewable energies, is a serious solution for reducing greenhouse gas emissions such as (CO2) emissions and controlling global warming in international forums worldwide and is considered as an indicator of the quality of the environment. Advantages such as providing a very impressive amount of electrical energy with very little fuel consumption, ensuring access to the fuel source, and from an economic point of view, low production costs such as construction, investment, operation, waste management, and dismantling the site after completion. Reactors should be considered as a suitable option for supplying electricity. In this article, the most important peaceful applications of nuclear technology for electricity generation, radiopharmaceutical production, and heavy water production in nuclear power plants or reactors are reviewed. Bushehr nuclear power plant, with a power plant unit with a capacity of 1000 megawatts, has delivered more than 61 billion kilowatt hours of electricity to the country's grid since the beginning of its operation in 1390, which has saved $33.5 billion in oil during its operation, while the construction cost It is estimated to be equivalent to 4 billion dollars. This means that this power plant unit has earned more than 1 billion dollars for Iran. With the production of nuclear power in this period of time, the equivalent of 97 million barrels of crude oil has been saved and the release of about 60 million tons of polluting gases into the atmosphere has been prevented. Iran is planning to produce 20,000 megawatts of nuclear power until the horizon of 2041, but in the peaceful cycle of nuclear technology, in addition to facing technical problems, in recent years, it has repeatedly faced biased policies and industrial vandalism based on world-class technology, which This issue shows the necessity of observing the safety and security laws and geographical considerations of power plants and electricity generation reactors.

Keywords: Nuclear fuel cycle, enriched uranium, waste disposal, nuclear reactors, renewable energy, greenhouse gases

Introduction

With the passage of more than half a century of world scientists' efforts and considering the very significant advantages of nuclear energy, today the need to achieve peaceful nuclear technology in securing the security and development of countries is an undeniable issue. Due to the global energy crisis caused by the increase in energy prices and instability in the oil and gas market, the unprecedented increase in energy demand has caused countries to have a wide competition to supply the energy they need to maintain their security and resources. Also, since fossil fuels are running out, we need to look for alternatives. Possessing nuclear technical knowledge, in addition to self-sufficiency in the field of energy supply through nuclear fuel, will lead to progress in other knowledge and technologies in the energy market and future security. In 2021, on the eve of the Glasgow Summit, Rafael Grossi, Director General of the International Atomic Energy Agency, emphasized the importance of nuclear energy in the economy and solving the energy crisis in the future, and emphasized the global guarantee of security and stability for the use of this amazing phenomenon [1]. From an environmental point of view, the increase in the concentration of greenhouse gases caused by human activities and the use of fossil fuels has caused increasing concerns about the increase in the temperature of the Earth's atmosphere, and experts always warn of global dangers. Global warming is the name of the phenomenon that has led to an increase in the average temperature of the earth and the surface of the oceans. In terms of climate change, the International Atomic Energy Agency, according to the Paris Agreement, has obliged all countries to reduce the Earth's temperature to 1.5 or 2 degrees Celsius, which is not possible without nuclear energy.

Research Theories

Due to the limitation of fossil fuels, it is necessary to pay attention to new sources of energy, especially renewable energy. But achieving these energies is limited both in terms of technology and cost. In this regard, attention has been paid to the energy caused by nuclear fission and nuclear fusion. Since 2013, Iran's nuclear program has strengthened along with other industrialized countries, and in these years, the first unit of Bushehr power plant was completed and put into operation in 2018, and it was connected to the national electricity grid. The construction of the second unit started in 2016 and is expected to be put into operation by 2026, and the third unit is also in the initial stages of construction. The Arak heavy water complex, which includes a power plant and a research reactor, is the only heavy water

production center in the Middle East that operates under the supervision of an international agency. Considering that the Tehran research reactor (which was started about 40 years ago with a power of 5 MW) is nearing the end of its working life, the Arak heavy water research reactor has been designed. The production capacity of this complex is 20 tons of heavy water product with high purity and isotopic richness of 88.99% per year. After the successful exploitation, from the heavy water produced for the deuterium source, deuterium-labeled isotopic compounds have been produced. Stable isotopes are widely used in the medical industry, nuclear science, geology, agriculture, pharmaceuticals, and scientific research. Iran plans to increase the capacity of nuclear power plants to about 20 thousand megawatts by 2041, and for this purpose, 5 new nuclear power plants are planned in the 5 coastal provinces of Khuzestan, Bushehr, Hormozgan, Sistan and Baluchistan and in the north of the country only Golestan province. has been taken Two types of nuclear power plants are being built in the world, the first type is known as traditional power plants and it is built in three levels below 300 MW, 300 to 700 MW and above 700 MW. In addition, Another type of nuclear reactors was introduced in 2000, called small power plants. In these small-scale power plants, the technologies required to generate electricity from nuclear energy are designed and manufactured in a factory [2].

Experimental

Advantages and applications of nuclear energy

During the last half century and under the efforts of scientists around the world, this technology has played an important role in the development of industry, agriculture, medicine and other fields. In addition to providing clean energy, nuclear technology helps improve medical diagnosis. Human diseases should be cured, human nutrition should be increased, water resources should be developed, agricultural productivity should be improved, industrial quality control should be strengthened, environmental science should progress and in a word, prosperity and happiness. has brought to human life. The applications of nuclear energy go far beyond electricity generation, treatment of various diseases such as cancer and the production of radiopharmaceuticals, access to fresh water sources, agricultural advancement, etc. and include many scientific and industrial fields.

Advantages of nuclear energy:

• A small amount of nuclear fuel is capable of producing very high energy.

• Cleanliness and non-pollution of the environment with dangerous gases such as CO2, CO, NO2, SO2

• More economical compared to fossil power plants (means lower operating cost)

• The use of nuclear technology in other peaceful fields besides nuclear power plants

• They do not need continuous fuel injection. • It does not need air to burn.

Disadvantages of nuclear energy:

• Limited uranium resources • Unusability of atomic waste • More difficult maintenance

• Environmental pollution in terms of radioactive materials and Thermal pollution

• Multiple stages of fuel processing before use • High investment cost

• Special and constant control and monitoring • Special equipment to prevent radioactive radiation

The status of countries in the use of nuclear electricity

Despite the suitability of nuclear energy for energy production, due to the production of nuclear waste and other risks, its use has not been expanded. Like Italy, they want to reduce the use of nuclear energy.nuclear energy. Figure (1) shows the situation of different countries in the use of nuclear energy.

Countries using nuclear power Countries building new reactors

Countries planning ne reactors Countries without reactors are planning to build new reactors

They have no plans to reduce or increase reactors They plan to disable all their reactors

They intend to disable part of their reactors No reactor [3].

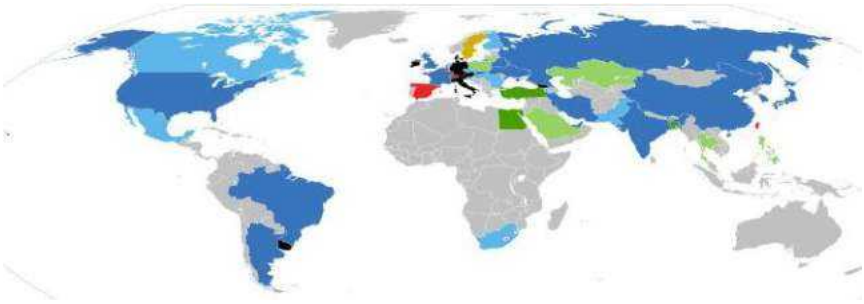

Fig. 1. Countries with nuclear power plants or programs

Economic efficiency of nuclear reactors in the world

The energy crisis has become more obvious with the increase in population and the development of industry. One of the actions of advanced countries is investing in nuclear

technology. 80 tons of uranium in the Bushehr reactor produces electricity equal to 17 million barrels of crude oil. In a smaller comparison, the energy from nuclear fission of a 12 gram fuel pellet with 3.5% enrichment is equivalent to the energy from burning one ton of coal or 2.5 tons of wood or 476 cubic meters of natural gas [4]. The development of nuclear power plants in the world has experienced five stages:

The first and second generation of nuclear reactors:

First-generation reactors were developed in the 1950s and 1960s, and the last first-generation reactor was shut down at the end of 2015. In this generation of reactors, natural uranium was used as fuel and graphite as fuel. Second generation reactors make up most of the current nuclear fleet in the United States. This generation of reactors uses enriched uranium fuel and is primarily water-cooled and moderated.

The emergence of the third generation of nuclear reactors with high safety:

The third generation of nuclear technology with higher safety was born after the Three Mile Island Unit 2 accident (in 1979) and the Chernobyl accident (in 1986). The first advanced reactors of the third generation are in operation in Japan, China, Russia and the United States, and the rest of the reactors of this generation are under construction or ready to be ordered. This generation of reactors is the result of the development of second generation reactors with high safety.

fourth generation reactors:

In the fourth generation of reactors, which is still on paper, used fuel from previous generations is used to produce hydrogen. This generation is characterized by a closed fuel cycle and the burning of long-lived actinides, so that the fission products are only high-level waste (very low radiation) that can no longer be used. Of the seven such reactor designs, four or five will be fast neutron reactor designs, operating with fluoride or liquid metal coolants at low pressure. These reactors have much higher temperatures than current water-cooled reactors.

Geographical location of nuclear reactors in the world

Nowadays, location studies have become very common for all power plants. In such studies, various criteria are considered to choose the best place to build a power plant:

Access to large volumes of sea water or rivers full of water:

Light water is the most commonly used liquid for the cooling system for power generation reactors. For example, Bushehr nuclear power plant produces about three thousand megawatts of heat. Out of these three thousand megawatts, one thousand megawatts is converted into

electricity in the generator, and the other two thousand megawatts must be discharged in some way from the second cycle of the power plant, and this work requires a large volume of water, and accordingly, the power plant was built next to the Persian Gulf. At the same time, environmental considerations require that the temperature of the water used to cool the reactor of the power plant is not too high when returning to the sea.

Earthquake:

In addition to paying attention to the above criteria, the earthquake-prone areas of the world are important and these areas are an almost definite area on the planet. In the most general classification, these areas are divided into 3 categories, but in a more detailed classification, there are 5 cities or points in the world. , are considered the most earthquake-prone cities in the world,which shows the main seismic belts of the earth along with the focal depth of the earthquakes on the figure (2) It is clear [5].

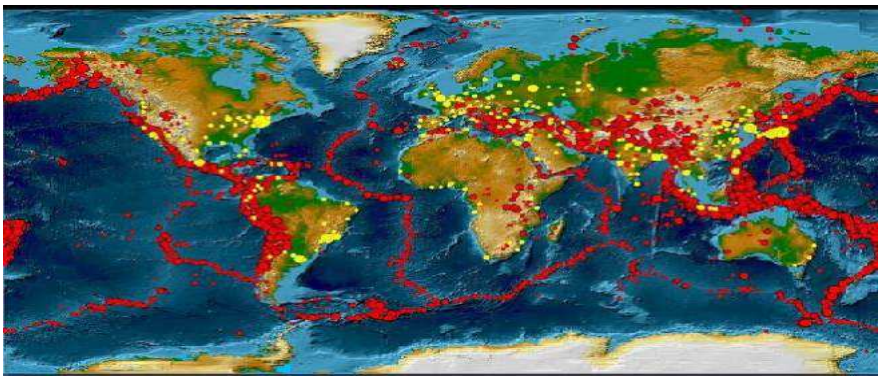

Fig. 2. Map of the areas with earthquakes and their intensity in different levels of the world

Power plant reactor structure

In the reactor core, there are about 50,000 fuel rods, each 3-4 meters long and composed of enriched uranium pellets with a diameter of about 2 cm and a height of 1 cm. The reactor core of the power plant also includes a moderator, or in other words, a neutron speed reducer, which is called a moderator. The substance used as Moderator is generally normal water or light water. In some cases, solid graphite is used, and in less cases, heavy water is used. The nuclear fission process is an incremental chain process. Also, the energy produced in the reactor is absorbed by the coolant, which means the element that absorbs heat or cools the reactor, and this heat is transferred outside. Coolant can be light water or heavy water or a gas such as helium or a metal such as sodium.

Types of power plant reactors:

The two main groups of nuclear reactors are power reactors and research reactors. Power reactors produce electricity, and research reactors are used for basic nuclear research, applied analytical studies, and isotope production. Power reactors are divided into two main groups: thermal (slow) reactors and fast (fast) reactors. In thermal (slow) reactors, in addition to the activity retarder, there are also nuclear fuel, steam tank and its transfer pipes, protective walls and control and observation equipment of the reactor system and it is divided into three categories. Pressurized ducts in RBMK and CANDU reactors that can be refueled during reactor operation, or have a high-pressure hot steam tank, as in most nuclear power plants and naval reactors (ships, aircraft carriers, or submarines). is used, or a gaseous liquid is used instead. of water Helium or nitrogen and carbon dioxide are often used to cool the reactor. In a PWR type plant, ordinary water is used both as a neutron moderator and as a coolant (see Figure 3). The coolant inside the reactor of this power plant absorbs the thermal energy produced by the reactor under high pressure and maintains its liquid state due to its high pressure. This heat is transferred to the boiler of the power plant in order to produce the steam needed for the turbine of the power plant in the heat exchange with the water of the boiler. Light water is water in which there is only ordinary hydrogen. BWR is not much different from pressurized water reactor, except that in BWR there is only one cooling cycle and the water boils directly in the heart of the reactor.

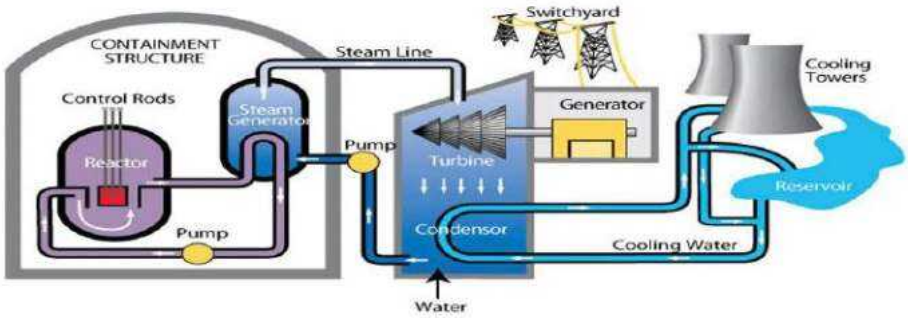

Fig. 3. Power plant with PWR reactor

The water pressure in BWR is lower than PWR, water boils at 285 degrees Celsius. The coolant absorbs the heat of the reactor, turns into steam, and the steam produced in the reactor is directly transferred to the steam turbine. BWR reactors are designed in such a way that between 12 and 15% of the water inside the reactor core is placed in the form of steam in its upper part. Pressurized heavy water reactor (PHWR) is one of the types of nuclear energy industrial reactors produced in the world and like the hive reactor, they use natural uranium fuel. But

instead of using calandria pressure tubes, they use a common pressure chamber. Candu Heavy Water Reactor (CANDU) is made in Canada. In this power plant, condo electricity generation is similar to a fossil fuel power generation station (See figure 4). Steam Generating Heavy Water Reactor (SGHWR) is one of the pressure tube type nuclear reactors with heavy water moderator and normal (light) water cooling. Graphite is widely used in nuclear industries due to its high purity and good resistance to high temperatures. The advanced gas cooling reactor (AGR) is a generation of gas cooling reactors that use graphite as a neutron moderator and carbon dioxide as a coolant. The (RBMK) is a class of graphite nuclear power reactors designed and built by the Soviet Union in which the core is surrounded by an annular steel vessel instead of a large steel pressure vessel surrounding the entire core. The cylinder is surrounded by a concrete vault, and each fuel assembly is enclosed in a separate tube with a diameter of 8 cm (inner). The channels also contain coolant and are surrounded by graphite. The reactor (PBMR) is a specific design of the Pebble Bed Reactor and includes gas turbine and heat transfer laboratories and a high pressure and high temperature helium test rig. Fast reactors are nuclear reactors in which fast neutrons are used to carry out nuclear fission reactions and do not require a neutron moderator and require a higher-rich fuel to produce heat.Fast reactors are divided into three categories, fast reactors (LMFR) in which the retarder is not necessary, but the cooling of molten metal is sodium.In this reactor, plutonium 239 is used as fuel and it is very advanced, and fast reactors (SFR), which is a fast neutron reactor cooled by liquid sodium, and the third category of reactors (BFR) or bioactive foam reactor, which uranium 238 to The title of fuel is used in it (See figure 5). In fact, the purpose of this reactor is to produce plutonium or uranium 233. The core fuel of this technology consists of uranium, oxygen and carbon particles covered with ceramic and carbon materials. The reactor (CARR) is one of China's new nuclear reactors, and has a complex and 12 year-old light water tank unit. The nuclear reactor (ADS) has the ability to convert nuclear waste including ultra-uranium elements and nuclear fission fragments into low-risk elements with low half-life and radiation poisoning. Also, its important advantage compared to other nuclear reactors is its safety and the sensitivity of the neutron parameters of the reactor core to the change of some accelerator parameters. Reactor (SMR) can produce 160 megawatts of electricity, and the process of building 32 reactors of this type in England with a capacity to produce 5.1 gigawatts of electricity by 2050 has started. The US is also expanding reactors (AP1000) due to their cheaper and faster modular construction and the ability to build from scratch on site instead of in a factory.

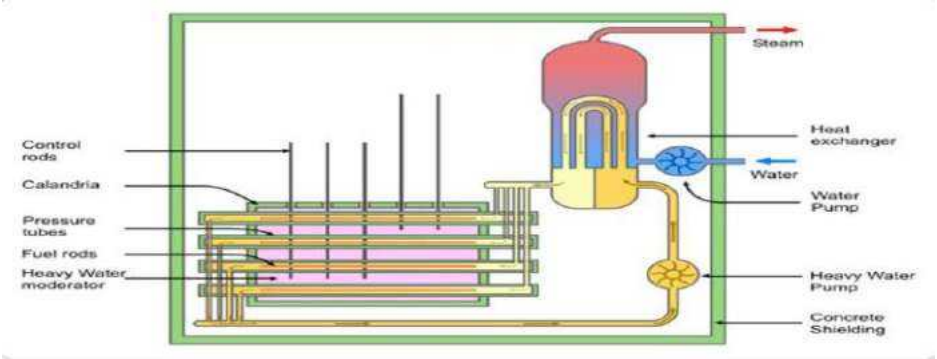

Fig. 4. Power plant with CANDU reactor

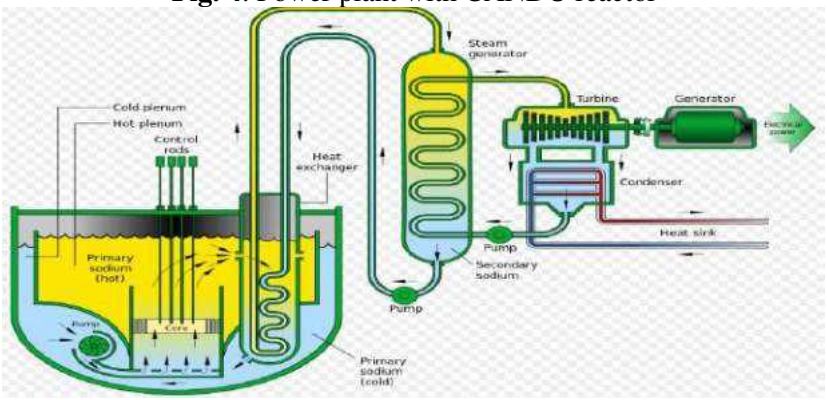

Fig. 5. Sodium cooled fast reactor (SFR)

Iran's nuclear power generation capacity: Iran has a nuclear power plant that uses nuclear fission of uranium to generate electricity. Bushehr nuclear power plant in the south of Iran includes an active unit with a capacity of producing about 1000 megawatts of electricity [6].

Nuclear fuels for power plant reactors

The main fuel of nuclear power reactors is uranium, which is used in different reactors in different combinations. Enriched uranium is uranium whose isotope 238 has been artificially reduced. Uranium metal is often used with uranium dioxide (UO2). In homogeneous reactors (fuel and moderator form a single unit) always and without exception, uranium enriched in solution (UO2SO4) is used. These fuels are often used in the form of rods, belts and pellets.There are five fissile nuclides currently used in reactors: Pu^{239}, U^{238}, U^{235}, U^{233}, Th^{232}. Some of these nuclides are for fission caused by thermal neutrons and some are for fission caused by fast neutrons. Table (1) shows the fuel of all types of reactors.

Table 1. Types of nuclear reactors in the world in terms of structure

Type Reactor	Coolant Reactor	Moderator Reactor	Fuel Reactor
PWR	H2O	H2O	U_{235} 3% --- 5%
BWR	H2O	H2O	U_{235} 3% --- 5%
PHWR	D2O	D2O	U_{238}----
SGHWR	H2O	D2O	Th_{232}
CANDU	D2O	D2O	U_{238}
Magnox	CO2	Graphite	U_{238}----
AGR	CO2	Graphite	Th_{232}
RBMK	H2O	Graphite	U_{238}
HTR	He	Graphite	U_{235} 3%
LMFR	Na	-------	U_{235} 1.8%
SFR	Na	-------	U_{235} 7% -- 1.8% PU 239 U 233- PU 239 U238
FBR	Na	-------	

Power generation capacity from nuclear reactors

Today, 445 nuclear reactors produce 10% of the world's electricity. After the Fukushima disaster in 2011, Japan has reduced its nuclear power plants, but France is looking to increase its nuclear capacity. The 10 nuclear power plants in the world that produce the most electricity are shown in Table (2).

Table 2. Types of nuclear reactors in the world in terms of structure

Rank	Country	Nuclear Energy (TWh)	% of Total
1	USA	772	29%
2	China	383	14%
3	Farnce	363	14%
4	Russia	208	8%
5	South	150	6%
6	Korea	87	3%
7	Canada	81	3%
8	Ukraine	65	2%
9	Germany	61	2%
10	Japan	54	2%
	Spain		

Destroy nuclear power plants

Some of the world's nuclear power plants are aging. In the past decade, several nuclear reactors have been shut down permanently. Decommissioning a nuclear power plant involves removing and safely storing spent nuclear fuel, decontaminating the plant to reduce residual radioactivity, dismantling the plant structures, transporting contaminated materials to disposal facilities, and then long-term release of the asset. According to the regulations of a nuclear power plant It takes decades to 60 years to retire.

Risk of cancer

In a nuclear power plant, there is a special type of radiation called ionizing radiation, which is emitted both naturally from uranium and as part of the nuclear fission process, and can remove electrons from atoms. These very low doses of nuclear radiation increase the risk of cancer.

Security and environmental protocols of nuclear reactors in the world

Nuclear safety and security are a set of rules, principles and sciences that must be observed in order to keep centers, facilities and activities related to nuclear technology safe. Accidents related to nuclear activities must have a high safety factor due to their deadly and long-term effect on humans and nature. The main goal of nuclear security is to protect employees, people and the environment from the destructive effects of radioactive materials by establishing and maintaining effective defense measures in facilities. To achieve nuclear safety, the following technical and organizational steps are implemented:

• Accurate control of the amount of radiation and release of radioactive materials in the environment..

• Preventing the occurrence of an accident • Reducing the consequences of the accident if it occurs.

Some field activities of environmental monitoring and environmental protection are carried out in the following areas in the power plant [7] :

• Environmental monitoring through sampling and online equipment for radiation monitoring

• Measurement of physical and chemical parameters of surface water and well water in the region

• Measurement of environmental dose rate using dosimeters (TLD)

• Measurement of ambient radiation status with mobile environmental monitoring laboratory

• Measurement of surface pollution of the environment using portable devices

• Environmental monitoring through sampling and analysis of environmental samples

Economic benefits of operating nuclear power plants for the cost of electricity generation

The State of the World Nuclear Industry report estimates that the cost of generating nuclear power in 2021 will be between $112 and $189 per MWh, while the cost of solar will be between $36 and $44 and onshore wind will be between $29 and $56. But according to the International Energy Agency's cost of electricity generation reports, the most expensive nuclear power generation is cheaper than a combined cycle plant, which includes a 3 percent discount rate. In addition, saving fossil energy resources, reducing greenhouse gases and global warming are among the achievements of nuclear reactors. In Iran, the Bushehr nuclear power plant has not only paid for its construction from oil savings, but has also brought billions of dollars in profits for Iran. Operation of Bushehr nuclear power plant has produced more than 61 million megawatt hours and has saved 97 million barrels of oil consumption. It has also prevented the production of 60 million tons due to the non-emission of polluting gases.

Nuclear waste

Among the environmental effects of nuclear energy, nuclear waste is the most notorious. Nuclear waste at every stage of processing and use of nuclear energy, including low-level waste (LLW)[1] from spent nuclear fuel and uranium mill tailings (radioactive sand waste containing heavy metals and radium) production as well as high-level waste (HLW)[2] that is produced from nuclear weapons or contaminated radioactive materials or neutron radiation in a radioactive nuclear power plant.

Spent nuclear fuel is fuel from a nuclear reactor that is no longer efficient in generating electricity because the fission process has slowed [8].

---

[1] Nuclear waste according to the type of contents, thermal production potential and radiation intensity at low level.

[2] Nuclear waste according to the type of contents, thermal production potential and radiation intensity at the high level.

Results and discussion

Nuclear technology with the aim of providing clean energy in the last half century has contributed a lot to agricultural productivity, treatment of some diseases, improvement of human nutrition, development of water resources and industrial quality control and has contributed to the prosperity of mankind and on the other hand, nuclear energy It does not pollute the environment in any way. Leakage of nuclear waves occurs due to technical defects or natural disasters such as earthquakes and floods. One kilogram of uranium-235 produces about 40,000 kilowatt-hours of electricity, which is equivalent to 10 tons of coal or 50,000

gallons of oil. Currently, two types of nuclear power plants are being built in the world, the first type of which is called the traditional power plant, and another type of nuclear reactor has been put on the agenda since 2000 under the title of small power plants, in which small-scale technologies It is required to generate electricity from integrated nuclear energy. By building a fleet of Small Electrical Modular Nuclear Reactors (SMR) or (AP1000) with capacities of 100 to 300 MW of nuclear power, this project can be developed while overcoming the energy crisis. In Iran, about 81% of electricity production capacity depends on fossil fuel supply and 14% of electricity production capacity (hydroelectric power plants) depends on the existence of water reserves due to the limitations of fossil fuel supply, especially in the cold. Seasons of the year and limitations of hydropower production due to drought, sustainable electricity is provided only by the development of nuclear power plants.

Citation

Nuclear power plants emit 90% less pollution than coal and 80% less than fossil power plants and are among the clean energy sources of the environment. Although solar, wind and geothermal energy do not produce as much pollution as nuclear or coal, they are not sustainable energy. The technologies used in small nuclear reactors (SMR) include water-cooled reactors (WCR) and high-temperature gas-cooled fast neutron reactors (HTGR), with international attention to this advanced technology and its relative advantages over large reactors. Traditional, despite its shortcomings and problems, has been considered and expanded as one of the energy production options.

References

[1] Ramazani, A. (2022). The development status of nuclear technology applications in Iran and the world. Islamic Council Research Center. Strategic Studies, No. 18676.

[2] Expert sources of Atomic Energy Organization. (2023). Arak heavy water facility, Marwaridi in the center of Iran. science and technology site.

[3] Wikipedia. (2016). List of countries using nuclear electricity. English encyclopedia, No. 12.7.2016.

[4] President of Bushehr Nuclear Power Plant Operation Company. (2023). Bushehr Nuclear Power Plant produced 6 million megawatt hours of electricity. Islamic Republic News Agency No.402.1.20

[5] Al Daoud,S.(2018). Familiarity with earthquake-prone areas of the planet. Earthquake magazine, Hamshahri, news code 93582

[6] Akhvian Tehrani,A. (2022). Nuclear flow in the energy network of the country. Jam Jam, number 6325, first page group, page number 1.

[7] Ahmadi,A. Bahmani,A.(2015). Investigation of nuclear energy and the effects of nuclear pollution on the environment and humans. National Conference on Power Engineering and Nuclear Power Plants, first session.No.2015.11

[8] Amini, A. (2022). Effects of nuclear power plants on the environment. Journal of Jokul, Nov. 7

Climate Change & The Role of Nuclear Power

ICNST 2024
International Conference on Nuclear Science and Technology
6- 8 MAY 2024 | Isfahan, Iran

Innovative Carbon Dioxide Removal from the Air Utilizing Methane Dry Reforming via Plasma Technology (Paper ID : 1464)

Davari H. Correspondent[1*], Davari D. Co-Author[1], Davari M. Co-Author[1], Taheri AH. Co-Author[1]

[1]Emam Reza Innovation Center, Isfahan, Iran

Abstract

This paper introduces a novel technology for the removal of carbon dioxide from the atmosphere using plasma technology, inspired by the dry methane reforming method. Carbon dioxide and methane are the primary greenhouse gases responsible for climate change on Earth's surface. Dry reforming of methane (DRM) entails the simultaneous conversion of methane and carbon dioxide into synthesis gas and higher hydrocarbons. We employ plasma technology to activate chemical reactions and eliminate carbon dioxide, providing a sustainable and efficient alternative to conventional methods. In this article, we explore the potential applications and environmental implications of carbon dioxide removal through various types of hot and cold plasmas. Additionally, we investigate the future prospects of this innovative technology in the realms of nuclear energy and environmental sustainability. For example, the utilization of microwave plasma shows promising implications for carbon capture and storage in nuclear energy applications. The objective of this article is to examine new scientific methods of plasma technology for carbon dioxide removal and its synergy with energy technologies, such as hot plasma in fusion machines. Furthermore, we will compare the performance, conditions, and consequences of employing different types of cold and hot plasma for carbon dioxide removal, providing explanations for each approach. Ultimately, through the presentation of the proposed model, we assert that plasma technology has the capacity to effectively eradicate carbon dioxide, demonstrating its innovative nature, adaptability, and ability to address current global challenges. This technology represents a sustainable and long-lasting solution.

Keywords: Carbon dioxide absorption, methane dry reforming, synthesis gas production, nuclear environment modification, greenhouse gas reduction, sustainable nuclear applications, reducing the carbon effect in nuclear facilities.

\

Introduction

Global interest is growing in low temperature plasmas because of their potential energy and environmental uses, especially in the conversion of CO_2 into chemicals and fuels. The switch to renewable energy sources produces a clean source of electricity, which makes plasmas appropriate for chemically storing intermittent renewable energy. One of the biggest challenges of the twenty-first century is the rising atmospheric CO_2 concentrations brought on by the combustion of fossil fuels, which in turn causes global environmental climate changes.

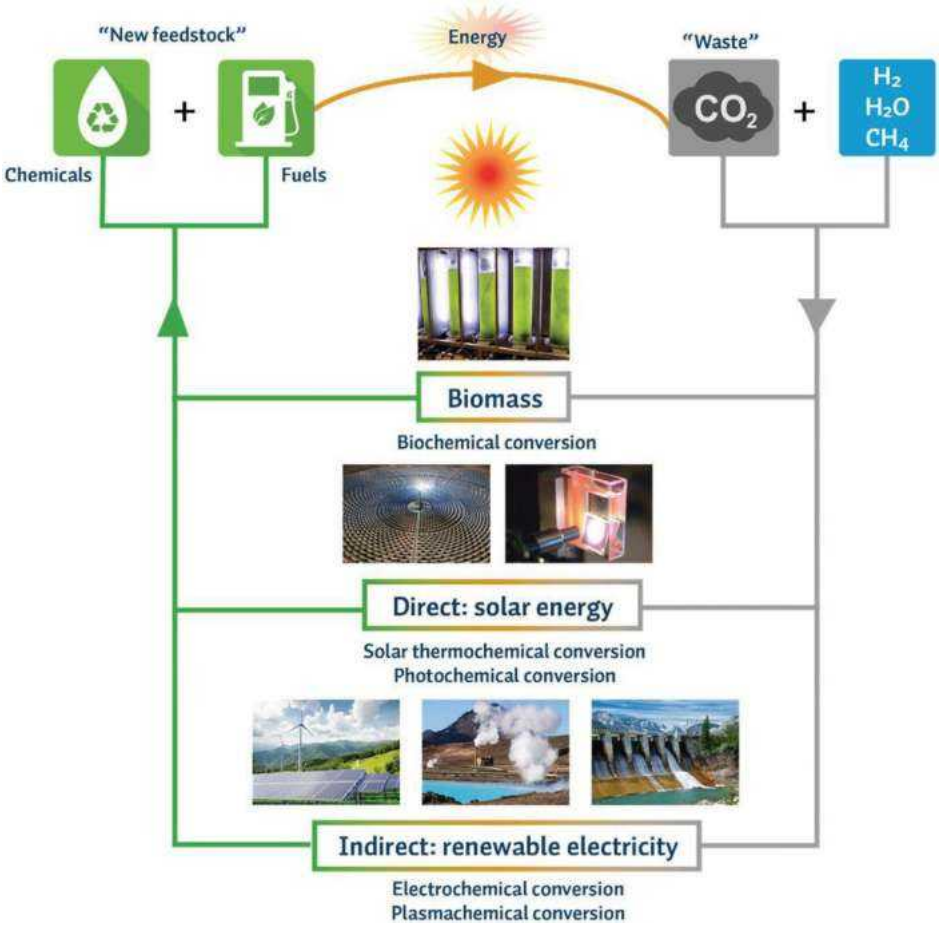

Fig. 20. Overview of the different novel technologies and their principal use of renewable energy for the conversion O2 in a carbon neutral cycle[1].

In order to combat climate change and reduce our reliance on fossil fuels, one of the main challenges is the conversion of CO_2 into liquid fuels and value-added chemicals. Making use of trash and transforming it into new feed stocks aligns with the cradle-to-cradle notion and sustainable and green chemical frameworks. The cradle-to-cradle concept has resulted in a surge in interest in technology that can transform CO_2 into goods with additional value. In carbon dioxide capture, storage, and utilization, CO_2 has further uses, including fixation and

technological application. Alternative technologies, including non-thermal plasma techniques, are being researched. These include electrochemical, photochemical, solar thermochemical, and biological routes. These alternatives include interactions with other gases, such as CH_4, H_2, or H_2O, with the goal of producing syngas and useful oxygenates, as well as pure CO_2 splitting into CO and O_2.

Traditional thermal conversion approaches, such as combustion and pyrolysis, rely on the high temperatures produced by the combustion of fossil fuels to drive the reactions that convert CO_2 to O_2 and CO. In contrast, new technologies such as nuclear energy and plasma offer more sustainable and efficient means of providing the heat needed for these transformations. For example, nuclear energy provides a low-carbon alternative to harnessing the power of nuclear reactions to generate heat and power chemical processes without burning fossil fuels. Plasma technology, on the other hand, uses ionized gases to generate high temperatures and accelerate chemical reactions. While traditional thermal approaches are resource-intensive and can have a negative impact on the environment, new technologies such as nuclear power and plasma aim to convert CO_2 into O_2 and CO, improving energy efficiency and reducing emissions, represents innovative solutions that prioritize environmental sustainability. A possible solution can be found in carbon capture and utilization (CCU) [2], where greenhouse gasses such as CO_2 and CH_4 can be recycled for the production of chemicals instead of being emitted into the atmosphere, thus contributing to a circular economy. An interesting reaction is the so-called dry reforming of CH_4 (DRM) (Eq. 1) to produce syngas, a mixture of H_2 and CO.

$$CO_2 + CH_4 \longrightarrow 2CO + 2H_2 \qquad \Delta H_0 = 247\ kJ/mol \tag{1}$$

Syngas can be further processed, for example into synthetic fuels through the Fischer-Tropsch process.

Plasma-based DRM is interesting because it offers many advantages. It is electrically powered and is a turnkey process that can be quickly turned on and off and scaled depending on the amount of renewable energy available [1,3-4]. Plasma-based DRM has already been studied in various experimental settings. In so-called warm plasmas, such as sliding arc plasma (GA), microwave plasma (MW), atmospheric pressure glow discharge (APGD), or pulsed nanosecond discharge (NPD), gas temperatures can reach up to 4000 K or even higher. There is a gender. The main reaction product is actually syngas [5-10]. On the other hand, cold plasma, similar to dielectric barrier discharge (DBD), mainly produces synthesis gas, but especially the catalyst is integrated in the plasma zone [10-12].

Although experiments are valuable for the development of plasma-based DRMs, insights into the chemical processes are limited. Additional information can be obtained using kinetic modeling of the experimental setup. This provides insight into the influence of specific plasma type chemistry, reactor design, and experimental parameters. However, this model only considers specific experimental conditions. B. Fluid mechanics and heat transfer. Provides specific information regarding reactor design and operating conditions. Although the model is useful for understanding experimental work, the limited parameters used do not allow further optimization of chemical transformations. Example: Cleiren et al. study. [13] Wanten et al. [14] analyzes his DRM for GA and APGD plasmas, but focuses only on gas temperatures between 2000 and 2700 K. The main limitation is the maximum CH4 content of 35% due to experimental limitations. A lower temperature range of 1600–2200 K is also used to more accurately represent the experimental reactor. Liu et al. [15] modeled a gas mixture with CH_4 content up to 50%, but the plasma temperature is limited to 2500 K. These experiments show that CO, H_2, and H_2O are the main products formed in these gas mixtures, with small amounts of C_2H_2, C_2H_4, C_2H_6 and O2. Other studies include adding O_2 or N_2 as the main component or impurity in the gas mixture [16-18].

This study aims to provide a more comprehensive understanding of the influence of plasma parameters on the chemical kinetics of DRMs, regardless of the experimental setting. High-temperature plasma conditions are preferred in GA, MW, APGD, and NPD due to their better energy efficiency compared to low-temperature plasmas [1]. It should be noted that no comprehensive studies of reaction kinetics have been performed in these warm plasmas, but only in low-temperature His DBD plasmas [17, 19-20]. We explore a wide range of plasma environments, including different reactor designs and a wide range of gas conditions, including: B. Temperature, power density, and gas mixture. These include gas mixtures from 90% CO_2 to 90% CH_4, a new concept in hot plasma research. We analyze the differences and similarities between thermal gas chemistry and plasma-based conversion kinetics. Thermochemistry is important for conversion processes in plasma systems [15]. We updated previous studies and developed a new chemical kinetics scheme. We validate the kinetic scheme through refinement through a literature review and through detailed balancing and comparison of steady-state concentrations and thermodynamic equilibrium.

Model Description

The purpose of this study is to investigate the influence of different parameters. This study focuses on the effects of gas temperature, plasma power, and CO_2/CH_4 ratio on the chemical composition of the plasma, regardless of the reactor configuration. Therefore, zero-dimensional chemical kinetics model is suitable for this. The ZDPlasKin code [21] was used to perform calculations of various parameters within a simple model setup, ensuring reasonable computation times. This model solves the mass conservation equation for all plasma species by calculating the change in number density due to chemical reactions. Eq. (2) represents the temporal change in number density n of species s with respect to time t due to reaction j. This change is determined by the coefficients of species s on the right ($\boldsymbol{a_{si}^R}$) and left ($\boldsymbol{a_{si}^L}$) sides of reaction i and the corresponding reaction rate R_i. The reaction rate is calculated using the Eq. (3) in which it is the product of the rate coefficient k and number densities of the reactants n_s.

$$\frac{\partial n_s}{\partial t} = \sum_{i=1}^{j}\left[\left(a_{si}^R - a_{si}^L\right)R_i\right] \quad (2)$$

$$R = k\prod_s n_s^{a_s^L} \quad (3)$$

For electron impact reactions, by using Eq. (4) rate coefficient are calculated where ε is the electron energy, σ_c is the collision cross section, f_e is the electron energy distribution function (EEDF), and v is the electron velocity. The EEDF is calculated using BOLSIG+, which is integrated into the ZDPlasKin code [22]. BOLSIG+ uses a binomial approximation to calculate the EEDF from the reduced electric field (E/N) using the Eq. (6) where n_{tot} is the total species number density, P/V is the input power density, and σ is the plasma conductivity. The latter is calculated using Eq. (7) with μ the electron mobility obtained from BOLSIG+, n_e is the electron density, and e is the elementary charge.

$$k = \int_{\epsilon_{th}}^{+\infty} \sigma_c(\varepsilon)\, f_e(\varepsilon)\, v(\varepsilon)\, d\varepsilon \quad (4)$$

$$v(\varepsilon) = \sqrt{\frac{2\varepsilon}{m_e}} \quad (5)$$

$$\left(\frac{E}{N}\right) = \frac{1}{n_{tot}}\sqrt{\frac{P/V}{\sigma}} \quad (6)$$

$$\sigma = \frac{\mu}{n_{tot}}.\, n_e\, e \quad (7)$$

In the context of reactions involving heavy species (excluding electrons), rate coefficients are determined through analytical equations such as modified Arrhenius equations or fall-off functions. Plasma power and gas temperature are treated as distinct and autonomous input

variables, maintaining a steady state at consistent levels during simulations. As a result, gas temperature is not dynamically computed using the thermal equilibrium equation, thereby dissociating plasma power from gas heating. This approach offers a clearer understanding of individual parameter effects, allowing for independent evaluation of their impacts.

In our research, the simulations are based on an assumption of uniform plasma characteristics without variations in temperature or power density. ZDPlasKin utilizes a batch reactor model, where species number densities evolve over time through the solution of conservation equations. However, the total number density is affected by temperature fluctuations and chemical reactions, necessitating adjustments to uphold pressure equilibrium. To address this, ZDPlasKin applies a correction factor β to the calculated number densities of all species at each time step to maintain the total number density in accordance with the ideal gas law at atmospheric pressure and the specified temperature. By maintaining a constant temperature in our simulations, we emulate the behavior of a batch reactor operating under constant pressure conditions.

$$\boldsymbol{\beta} = \frac{\boldsymbol{T_g(0)\sum_i n_i(0)}}{\boldsymbol{T_g(t)\sum_i n_i(t)}} \qquad (8)$$

In our simulations, the temperature remains constant throughout, meaning the initial temperature (Tg(0)) and the temperature at any given time (Tg(t)) are the same in Eq.(8). This methodology mirrors the behavior of a batch reactor running under steady pressure conditions. In a flow reactor scenario, this adjustment would mirror the compression or expansion of gas volume caused by chemical reactions, leading to changes in velocity within the plasma flow. This constant temperature setting in our simulations allows for a simplified representation of the system dynamics, akin to a batch reactor operating under stable pressure conditions. In contrast, in a flow reactor setup, such constant pressure conditions would translate to alterations in gas volume due to chemical reactions, consequently affecting the flow velocity within the plasma environment.

Overview of the Simulations

This study delves into the kinetics within the active plasma zone, specifically excluding considerations of afterglow or post-plasma effects. Gas temperature variations ranging from 1000 to 4000 K, typical for warm plasmas, were explored across five different CO2/CH4 ratios (10/90, 30/70, 50/50, 70/30, 90/10). Four sets of simulations were conducted for different

power density levels: thermal (0 W/cm3) and plasma (500, 1000 and 1500 W/cm3), aligning with established norms for warm plasma systems. The "Thermal" simulations focus on gas-phase thermal decomposition without electron or ion involvement, solely emphasizing neutral species due to the high gas temperature. By comparing these thermal simulations with plasma simulations at a residence time of 10 ms, consistency with the literature and realistic estimates of residence time distribution are maintained. While the heavy species kinetics reach a steady state with extended simulation times up to 1010 s, serving as a validation against thermodynamic equilibrium concentrations, uncertainties in reaction rate coefficients can impact the accuracy of the model's outcomes. These uncertainties, ranging from 10% to over 100%, emphasize the importance of interpreting trends and relative values of species densities rather than relying solely on absolute values.

In comparing our thermal and plasma simulations with thermodynamic equilibrium calculations, we evaluate the deviation in species concentrations using the mean absolute deviation formula. To address the impact of numerous low-density species on the mean value, a weighted mean approach is applied to prioritize higher density species. This weighted mean absolute deviation (wMAD), Eq.(9), is determined by considering the concentration differences (Δcs) for each species (s) with corresponding weights (ws), such as utilizing thermodynamic equilibrium concentrations as weights when comparing with those results. When contrasting thermal and plasma simulations, the weights are based on the thermal concentrations for accuracy in evaluation.

$$wMAD = \frac{\sum_s (w_s | \Delta c_s |)}{\sum_s w_s} \quad (9)$$

This weighted mean absolute deviation method helps to accurately assess the deviations in species concentrations by giving more importance to species with higher densities, thereby highlighting significant differences in simulation results compared to thermodynamic equilibrium calculations. By incorporating appropriate weighting factors, such as using thermal concentrations as weights when comparing thermal and plasma simulations, a more nuanced and precise evaluation of the discrepancies between different modeling scenarios is achieved, enhancing the reliability and robustness of the comparative analysis.

The calculation of CO2 or CH4 conversion is determined by an Eq. (10) that involves the number densities of CO2 or CH4 at the simulation's inlet or outlet, alongside a correction factor denoted as β. This formula, outlined in the research, aims to quantify the extent of conversion

for CO2 or CH4 throughout the simulation duration by considering the initial and final number densities in conjunction with the correction factor.

$$\chi_s = \left(1 - \frac{n_s^{out}}{\beta \cdot n_s^{in}}\right). 100\% \quad (10)$$

Results and Discussion

We compare different simulations of DRM chemistry, both with and without plasma power, focusing on the comparison of plasma and thermal kinetics over short timescales of up to 10 ms. As indicated in Fig.1, we find that above 2400K, the plasma concentrations match the thermodynamic equilibrium concentrations. However, at lower temperatures, certain species like CO2 and CH4 are not fully dissociated, resulting in the formation of other compounds such as H2O, C2H2, and C2H4. These will eventually react away and reach thermodynamic equilibrium given sufficient time. Thermal conditions show no conversion below 1400K, while plasma conditions exhibit conversion in this temperature range, with slightly higher conversion for CH4 than CO2.

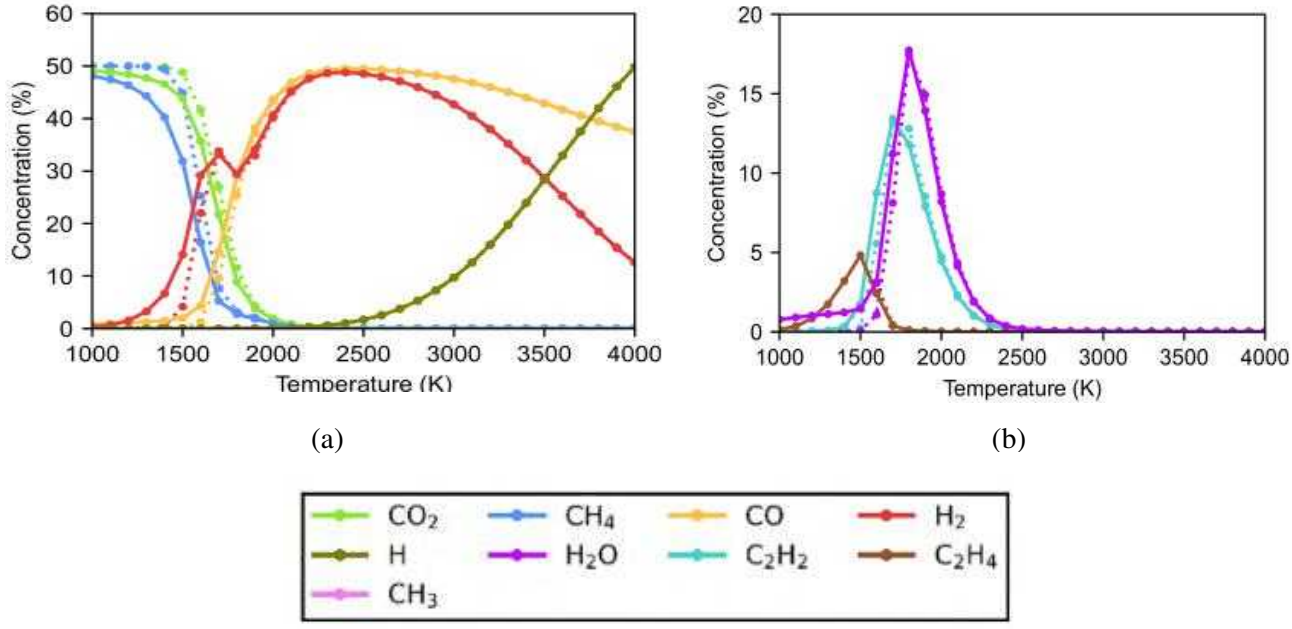

Fig. 2. The concentrations of the primary plasma components were determined for temperatures between 1000 and 4000 K with an equal CO2/CH4 ratio, considering a 10 ms duration, under both thermal conditions (shown as dotted lines) and plasma conditions with a power density of 1000 W/cm3 (represented by solid lines)[24].

As temperature increases from 1400-1600K, there is a sharp increase in CO2 and CH4 conversion for both thermal and plasma conditions, leading to the formation of products such as H2, CO, C2H2, and H2O (Fig2.a). Syngas (CO and H2) is found to be the dominant product, although H2O formation is also significant, particularly at 1800K (Fig2.b). At temperatures

above 2400K, the concentrations of C2H2 and H2O decrease dramatically, becoming negligible. Additionally, the concentrations of H2 and CO reach their peak values. Calculations indicate that the concentrations of thermal and plasma conditions converge above 2000K. Lastly, it's worth noting that the effects of plasma activation diminish as temperature rises, and thermal reactions begin to predominate above 1500K, ultimately reaching thermodynamic equilibrium at very high temperatures.

The comparison between plasma and thermal kinetics reveals variations influenced by the gas mixture composition. In mixtures favoring CH4 excess, such as 30/70 and 10/90 CO2/CH4 ratios, the weighted mean absolute deviation (wMAD) peaks at 11% and 13% at 1500 K, respectively. Conversely, mixtures with excess CO2 exhibit peak deviations at slightly higher temperatures: 1600 K for the 70/30 ratio (8.1%) and 1700 K for the 90/10 ratio (12%) (Fig.3). Notably, deviations between thermal and plasma kinetics become negligible above 2000 K, except for the 90/10 mixture showing a minor deviation at temperatures from 2000 to 3000 K. The influence of power density is evident, with wMAD increasing slightly with higher densities, ranging from 4.1% to 6.4% for 500 W/cm3 and 12% to 19% for 1500 W/cm3 in different mixtures.

These findings highlight the significance of plasma kinetics in DRM reactions below 2000 K, with deviations between thermal and plasma kinetics amplifying at longer residence times and higher power densities. Above 2000 K, the chemical processes predominantly follow thermal pathways. This suggests that for plasma conditions with temperatures exceeding 2000 K, typical in certain plasma sources like GA, MW, and APGDs, describing the DRM process may suffice by focusing solely on thermal kinetics. However, the study notes that while thermal kinetics dominate at higher temperatures, the role of electron impact collisions in plasma heating mechanisms should not be disregarded due to the unaddressed energy balance in the current analysis.

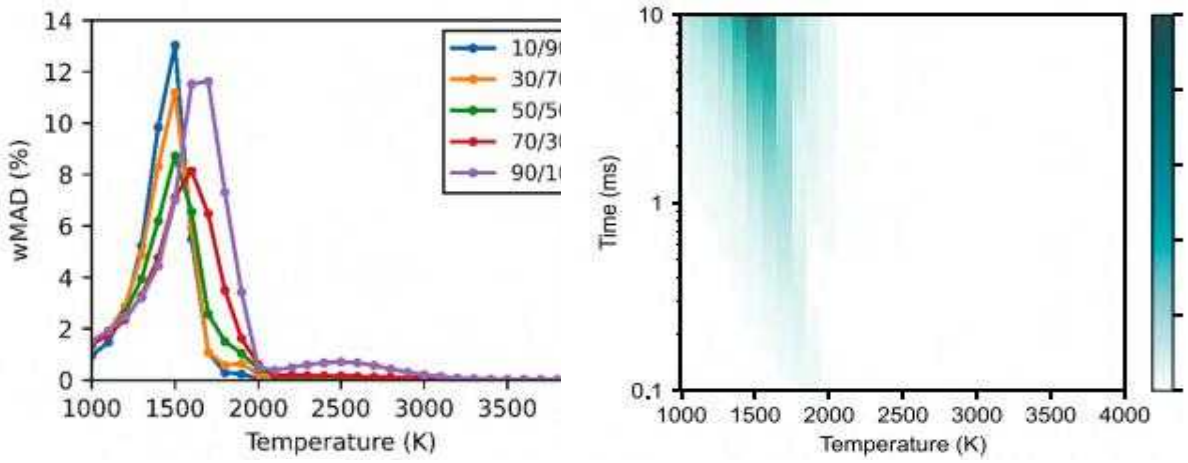

(a) (b)

Fig. 3. The weighted mean absolute deviation (wMAD) was calculated for the species concentrations under thermal and plasma kinetics conditions (1000 W/cm3) within a 10 ms residence time, spanning temperatures from 1000 to 4000 K, (a) across five varied CO2/CH4 ratios (90/10, 70/30, 50/50, 30/70, 10/90) (b) stoichiometric (50/50) CO2/CH4 ratio[24].

The conversion of CO2 is primarily driven by electron impact dissociation below 1500 K, with substantial contributions from direct electron impact dissociation and dissociative attachment. However, the actual CO2 conversion remains low within this temperature range, increasing significantly beyond 1500 K due to reactions with H radicals (Fig.4). For CH4, conversion occurs through heavy species reactions, with main dissociation reactions involving O and OH at 1000 K but reducing with temperature (Fig.5). Below 1500 K, the origin of O radicals from CO2 dissociation and OH from CH4 dissociation highlights the interconnected reactions between CO2 and CH4, leading to higher CH4 conversion compared to CO2 at lower temperatures.

Above 1500 K, loss reactions for CH4 involve reactions with H, CH3, and C2H3, with varying contributions at different temperature ranges. The dominance of H radicals in CH4 dissociation, despite fluctuations in contribution rates, underscores their significance throughout the temperature range, even up to 4000 K. While direct dissociation of CH4 through electron impact reactions is not crucial in the specified conditions, the interrelation between O and OH radicals underscores the coupled process between CO2 and CH4 in DRM reaction pathways.

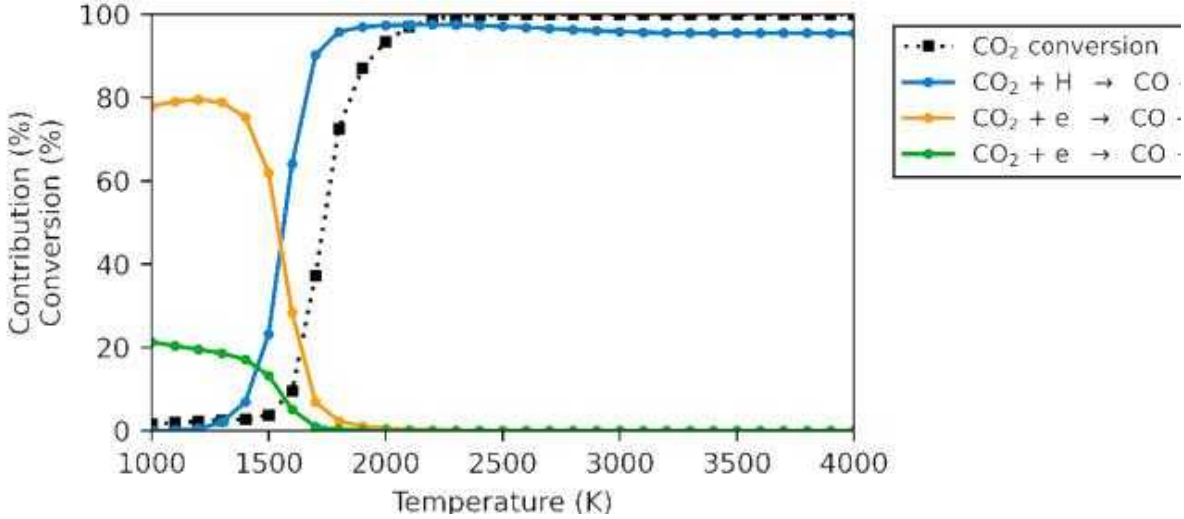

Fig. 4. The conversion of CO_2 (indicated by dotted black lines) and the proportionate impacts of major loss reactions (>5%) derived from time-integrated net reaction rates (refer to legends), are illustrated across varying temperatures in plasma simulations with a power density of 1000 W/cm^3, considering a 50/50 ratio of CO_2/CH_4 over a 10 ms residence time[24].

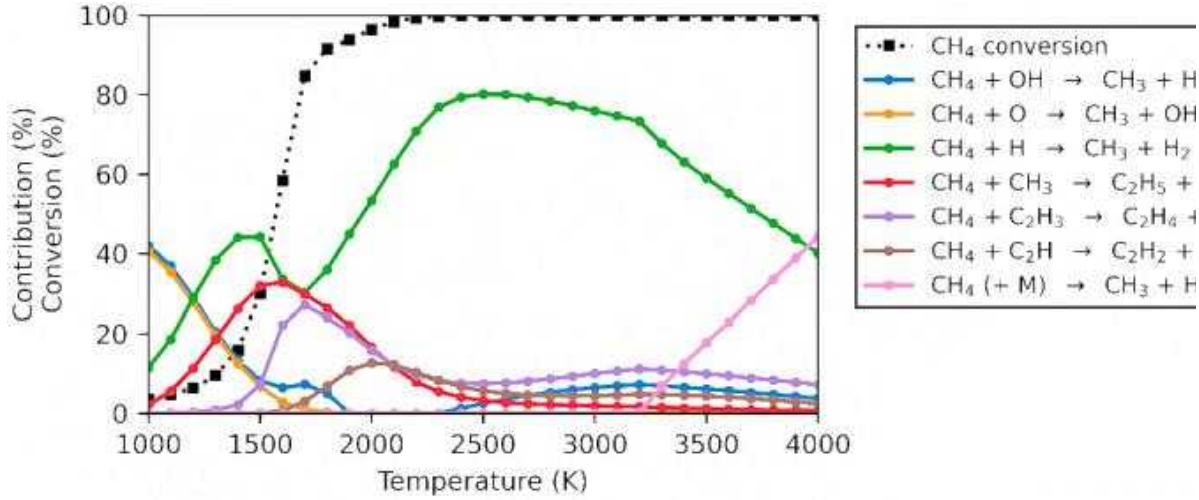

Fig. 5. The conversion of CH4 (indicated by dotted black lines) and the proportionate impacts of major loss reactions (>5%) derived from time-integrated net reaction rates (refer to legends), are illustrated across varying temperatures in plasma simulations with a power density of 1000 W/cm3, considering a 50/50 ratio of CO2/CH4 over a 10 ms residence time[24].

Below 1700 K, CO_2 dissociation primarily occurs through electron impact reactions, and analyzing the electron density and temperature provides insights into this phenomenon. The electron density progressively increases within the studied temperature range, up to 2×10^{13} cm^{-3}, indicating that high electron density is not the primary factor driving CO_2 dissociation via electron impacts (Fig. 6). Conversely, at lower gas temperatures, the elevated electron temperature around 17000 K results in a higher fraction of electrons possessing the energy needed for CO_2 dissociation. This leads to increased reaction rates for electron impact

dissociation, contributing to the overall dissociation process. The shift to lower electron temperatures above 1700 K coincides with increased conversion and the formation of key chemical species like CO, H_2, C_2H_2, and H_2O, related to their larger collisional cross sections and concentrations, leading to greater electron energy loss and lower electron temperatures.

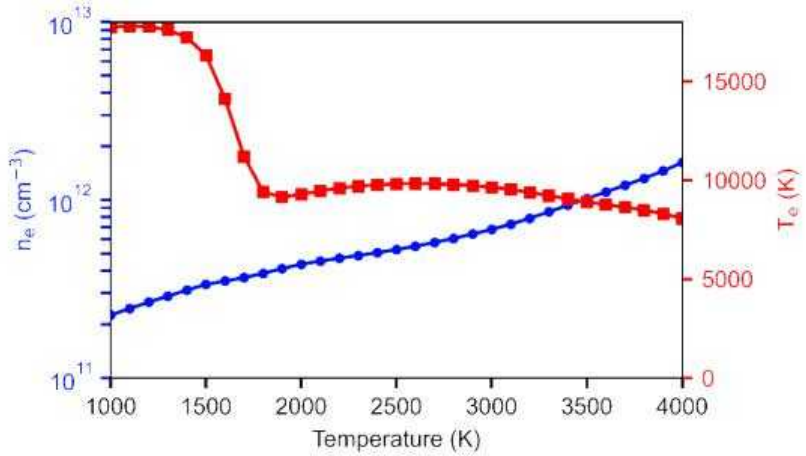

Fig. 6. The electron density (depicted by the blue line) and electron temperature (represented by the red line) were computed for gas temperatures ranging from 1000 to 4000 K, with a 50/50 CO_2/CH_4 ratio under 1000 W/cm^3 plasma conditions, and a residence time of 10 ms[24].

Overall, thermal kinetics dominate above 2000 K, while electron impact reactions play a crucial role in CO_2 dissociation below 1500 K. Variations in power density typical for warm plasmas do not significantly affect the temperature threshold where thermal kinetics become prevalent. It shows that electron impact dissociation involves excitation to highly electronically excited states, requiring more energy compared to direct thermal dissociation. Consequently, warm plasmas, characterized by predominantly thermal conversion processes, exhibit higher energy efficiency than cold or non-thermal plasmas that heavily rely on electron impact dissociation due to minimal thermal chemistry. Experimental findings indicate a lower energy cost for DRM processes in warm plasma sources like GA, MW, APGD, and NPD compared to non-thermal plasmas such as DBD. [1, 4, 9, 13, 23, 24].

Conclusions

Our research focused on investigating plasma-based dissociation of CO_2 by Dry Reforming of Methane Process through batch reactor simulations within a temperature range of 1000 to 4000 K, particularly relevant for warm plasma conditions and various CO_2/CH_4 ratios. By comparing our results with pure thermal conversion and thermodynamic equilibrium calculations, this

study offer valuable insights into the impact of plasma parameters on conversion, product distribution, and potential process enhancements. Significantly, the advanced chemical kinetics scheme provided a comprehensive understanding of plasma-specific chemistry, showcasing how plasma can notably enhance conversion efficiency below 2000 K compared to purely thermal pathways. The electron impact dissociation of CO_2 at lower temperatures facilitates faster conversions by initiating essential reaction steps, which contrasts with the slower molecular collision-based dissociation observed in purely thermal processes. The importance of residence time in targeting specific products and the transition to thermal reactions dominating kinetics above 2000 K were highlighted, emphasizing the energy efficiency of warm plasmas compared to cold plasmas relying on electron impact dissociation.

This study also delved into the influence of CO_2/CH_4 ratios on conversion, product distribution, and syngas ratio, revealing insights on optimal conditions for maximizing H_2 production and syngas yields. Mixtures with excess CO_2 showed limitations in conversion and product distribution, favoring H_2O production over H_2 generation. Conversely, mixtures with excess CH_4 facilitated full conversion and higher H_2 concentrations, with predictions pointing to achieving optimal syngas ratios with specific gas mixtures within varying temperature ranges. The comprehensive model predictions offer valuable insights into DRM chemical kinetics across diverse conditions, independent of reactor designs, and serve as a useful tool for designing and optimizing experimental reactors to enhance DRM processes efficiently.

Acknowledgements

The authors gratefully acknowledge *Emam Reza Innovation Center* and *Plasmant Research Group (University of Antwerp)* for providing financial support and access to state-of-the-art facilities which significantly enhanced the quality and scope of this research.

References

[1] Snoeckx, R., & Bogaerts, A. (2017). Plasma technology–a novel solution for CO_2 conversion?. Chemical Society Reviews, 46(19), 5805-5863.

[2] Cuéllar-Franca, R. M., & Azapagic, A. (2015). Carbon capture, storage and utilisation technologies: A critical analysis and comparison of their life cycle environmental impacts. Journal of CO_2 utilization, 9, 82-102.

[3] Bogaerts, A., & Neyts, E. C. (2018). Plasma technology: an emerging technology for energy storage. ACS Energy Letters, 3(4), 1013-1027.

[4] Vadikkeettil, Y., Subramaniam, Y., Murugan, R., Ananthapadmanabhan, P. V., Mostaghimi, J., Pershin, L., ... & Kobayashi, Y. (2022). Plasma assisted decomposition and reforming of greenhouse gases: A review of current status and emerging trends. Renewable and Sustainable Energy Reviews, 161, 112343.

[5] Scapinello, M., Martini, L. M., Dilecce, G., & Tosi, P. (2016). Conversion of CH_4/CO_2 by a nanosecond repetitively pulsed discharge. Journal of Physics D: Applied Physics, 49(7), 075602.

[6] Ramakers, M., Trenchev, G., Heijkers, S., Wang, W., & Bogaerts, A. (2017). Gliding arc plasmatron: providing an alternative method for carbon dioxide conversion. ChemSusChem, 10(12), 2642-2652.

[7] Zhang, H., Wang, W., Li, X., Han, L., Yan, M., Zhong, Y., & Tu, X. (2018). Plasma activation of methane for hydrogen production in a N2 rotating gliding arc warm plasma: a chemical kinetics study. Chemical Engineering Journal, 345, 67-78.

[8] Raja, R. B., Halageri, A. C., Sankar, R., Sarathi, R., & Vinu, R. (2023). Dry Reforming of Methane Using a Swirl-Induced Plasma Discharge Reactor. *Energies*, *16*(4), 1823.

[9] Kwon, H., Kim, T., & Song, S. (2023). Dry reforming of methane in a rotating gliding arc plasma: Improving efficiency and syngas cost by quenching product gas. Journal of CO_2 Utilization, 70, 102448.

[10] Khoja, A. H., Tahir, M., & Amin, N. A. S. (2017). Dry reforming of methane using different dielectric materials and DBD plasma reactor configurations. Energy Conversion and Management, 144, 262-274.

[11] Tu, X., & Whitehead, J. C. (2012). Plasma-catalytic dry reforming of methane in an atmospheric dielectric barrier discharge: Understanding the synergistic effect at low temperature. Applied Catalysis B: Environmental, 125, 439-448.

[12] Uytdenhouwen, Y., Bal, K. M., Neyts, E. C., Meynen, V., Cool, P., & Bogaerts, A. (2021). On the kinetics and equilibria of plasma-based dry reforming of methane. Chemical Engineering Journal, 405, 126630.

[13] Cleiren, E., Heijkers, S., Ramakers, M., & Bogaerts, A. (2017). Dry reforming of methane in a gliding arc plasmatron: towards a better understanding of the plasma chemistry. ChemSusChem, 10(20), 4025-4036.

[14] Wanten, B., Maerivoet, S., Vantomme, C., Slaets, J., Trenchev, G., & Bogaerts, A. (2022). Dry reforming of methane in an atmospheric pressure glow discharge: Confining the plasma to expand the performance. Journal of CO_2 utilization, 56, 101869.

[15] Liu, J. L., Xue, Z. W., Zhang, Z. Y., Sun, B., & Zhu, A. M. (2023). Mechanism study on gliding arc (GA) plasma reforming: Unraveling the decisive role of CH_4/CO_2 ratio in the dry reforming reaction. Plasma Processes and Polymers, 20(4), 2200175.

[16] Slaets, J., Aghaei, M., Ceulemans, S., Van Alphen, S., & Bogaerts, A. (2020). CO_2 and CH_4 conversion in "real" gas mixtures in a gliding arc plasmatron: how do N_2 and O_2 affect the performance?. *Green chemistry*, *22*(4), 1366-1377.

[17] Wang, W., Snoeckx, R., Zhang, X., Cha, M. S., & Bogaerts, A. (2018). Modeling plasma-based CO_2 and CH_4 conversion in mixtures with N_2, O_2, and H_2O: the bigger plasma chemistry picture. The Journal of Physical Chemistry C, 122(16), 8704-8723.

[18] Van Alphen, S., Slaets, J., Ceulemans, S., Aghaei, M., Snyders, R., & Bogaerts, A. (2021). Effect of N2 on CO_2-CH_4 conversion in a gliding arc plasmatron: Can this major component in industrial emissions improve the energy efficiency?. Journal of CO_2 utilization, 54, 101767.

[19] Snoeckx, R., Aerts, R., Tu, X., & Bogaerts, A. (2013). Plasma-based dry reforming: a computational study ranging from the nanoseconds to seconds time scale. *The Journal of Physical Chemistry C*, *117*(10), 4957-4970.

[20] De Bie, C., Van Dijk, J., & Bogaerts, A. (2015). The dominant pathways for the conversion of methane into oxygenates and syngas in an atmospheric pressure dielectric barrier discharge. *The Journal of Physical Chemistry C*, *119*(39), 22331-22350.

[21] Pancheshnyi S, Eismann B, Hagelaar GJM, Pitchford LC. (2008), Computer code ZDPlasKin,
http://www.zdplaskin.laplace.univ-tlse.fr (University of Toulouse, LAPLACE, CNRS-UPSINP, Toulouse, France, 2008).

[22] Hagelaar, G. J. M., & Pitchford, L. C. (2005). Solving the Boltzmann equation to obtain electron transport coefficients and rate coefficients for fluid models. *Plasma sources science and technology*, *14*(4), 722.

[23] Abiev, R. S., Sladkovskiy, D. A., Semikin, K. V., Murzin, D. Y., & Rebrov, E. V. (2020). Non-thermal plasma for process and energy intensification in dry reforming of methane. *Catalysts*, *10*(11), 1358.

[24] Slaets, J., Loenders, B., & Bogaerts, A. (2024). Plasma-based dry reforming of CH4: Plasma effects vs. thermal conversion. Fuel, 360, 130650.

ICNST 2024
International Conference on Nuclear Science and Technology
6- 8 MAY 2024 | Isfahan, Iran

Role of Nuclear Science in Addressing Environmental Challenges (Paper ID : 1600)

Karimi Sabet J. Co-Author[1], Zamani F. Co-Author[2]

[1]*Nuclear Science and Technology Research Institute, Tehran, Iran*

[2]*Nuclear engineering, shahid Beheshti University, Tehran, Iran*

Abstract

Nowadays, developed or developing countries are facing many environmental challenges that are considered a serious threat to the sustainable development of societies. The four super challenges of today's human societies are climate change, plastic pollution, environmental pollution, and finally the water crisis. Nuclear sciences and techniques, along with other modern sciences, have a special role in protecting the environment and sustainable development of countries, which cannot be replaced by other sciences.

In this review article, we will discuss the basic challenges of the environment and then the role of nuclear science and technology in protecting the environment, and as a case study examine the role of the Bushehr nuclear power plant in environmental protection.

Keywords: climate change - environmental protection - Nuclear sciences and techniques - environmental challenges

1 . Introduction

The term "environment" refers to the sum total of all external conditions, factors, and influences that affect an organism or a system, including physical, biological, social, and cultural elements, as well as their interactions and nuclear science and technology is an interdisciplinary field of study that encompasses the scientific understanding, development, and practical applications of nuclear processes and radiation. It involves the study of atomic and subatomic phenomena, nuclear reactions, the behavior of atomic nuclei and the applications of this field are Power Generation, Hydrogen Production, Ship Propulsion, Nuclear Medicine & Healthcare, Nuclear Agriculture, Nuclear Industry Applications, District and Process Heat, Space Missions, Synthetic Fuels, Water desalination, Archaeology, Synthetic Fuels and The Environment.

As a result, according to the application of nuclear science and technology in environmental protection, in this article, firstly, in section 2, we will express the super-challenges in the environment, and in section 3, we will express the nuclear solutions related to them. Then, in section 4, we will discuss the case study of Bushehr power plant, and in the last section, we will present the results.[1]

2 . The Main Environmental Challenges

They are four critical environmental challenges from the point of view of the International Atomic Energy Agency

2 . 1 . Climate Change

Climate change is one of the biggest environmental challenges affecting humanity today, causing a dangerous rise in sea levels and disturbances to the water cycle and leading to more frequent extreme weather events. The IAEA helps Member States combat climate change on a variety of fronts: mitigating the production and release of greenhouse gases (GHGs) and monitoring and adapting to their negative effects that we will discuss more in section 3.

Atmospheric levels of GHGs have fluctuated for billions of years, primarily due to natural orbital, solar and volcanic activities. Since the middle of the eighteenth century, anthropogenic factors have steadily increased the concentration of CO2 in the Earth's atmosphere, from approximately 278 parts per million to over 400 parts per million as of 2016. This is in addition to substantial increases in the concentration of other potent GHGs, including methane and nitrous oxide.[2]

2 . 2 . Plastic Pollution

Plastic pollution is a pressing global environmental issue, with projections of more plastic than fish in the ocean by 2050. Nuclear technology can play a crucial role in turning plastic waste into valuable raw materials. Several countries, including the Philippines, are conducting pre-feasibility studies for pilot- scale plastic recycling plants using radiation technology.[3] 63 countries monitor marine microplastics, and 30 develop recycling tech with nuclear science support.

2 . 3 . Environmental Pollution

Various human activities release pollutants into the environment, affecting air, water, and soil, and becoming integrated into biological, geological, and chemical cycles.[4]

Nuclear and isotopic tools are utilized to monitor heavy metals, greenhouse gases, and radioactive gases and particles in the atmosphere, allowing scientists to trace their sources and movements.

2 . 4 . Water Crisis

Potable water is in short supply in many parts of the world. Lack of it is set to become a constraint on development in some areas. A 2015 World Economic Forum report highlighted freshwater scarcity as a major global threat in the next decade.

Nuclear energy is already being used for desalination, and has the potential for much greater use. Nuclear desalination is generally very cost-competitive with using fossil fuels. "Only nuclear reactors are capable of delivering the copious quantities of energy required for large-scale desalination projects" in the future (IAEA 2015).[5]

As well as desalination of brackish or sea water, treatment of urban waste water is increasingly undertaken. Electrically-driven desalination can benefit from base-load power generation by operating mainly during off-peak times and potentially load-shedding during peak demand.

3. The Role of Nuclear Science And Technology In Solving Environmental Challenges

Nuclear science and technology offers three types of solutions in relation to existing environmental challenges: Mitigation, Monitoring and Adaptation.

3 . 1 . Mitigation

Mitigating climate change requires reducing greenhouse gas concentrations. Over 40% of energy-related carbon dioxide (CO2) emissions are due to the burning of fossil fuels for electricity generation.

All electricity generation technologies emit greenhouse gases at some point in their life-cycle but nuclear fission does not produce any CO2. For both nuclear and renewable generation, emissions are produced indirectly, for example during plant construction. Over its life-cycle,

nuclear produces about the same amount of CO2-equivalent emissions per unit of electricity as wind, and about one-third that of solar.[6] Nuclear power, currently being generated in 30 countries, is already reducing carbon dioxide emissions by about two Gigatonnes per year. That is the equivalent of taking more than 400 million cars off the road every year.

As you can see in Figure 1. globally we see that coal, followed by gas, is the largest source of electricity production.

Of the low-carbon sources, hydropower and nuclear make the largest contribution; although wind and solar are growing quickly.

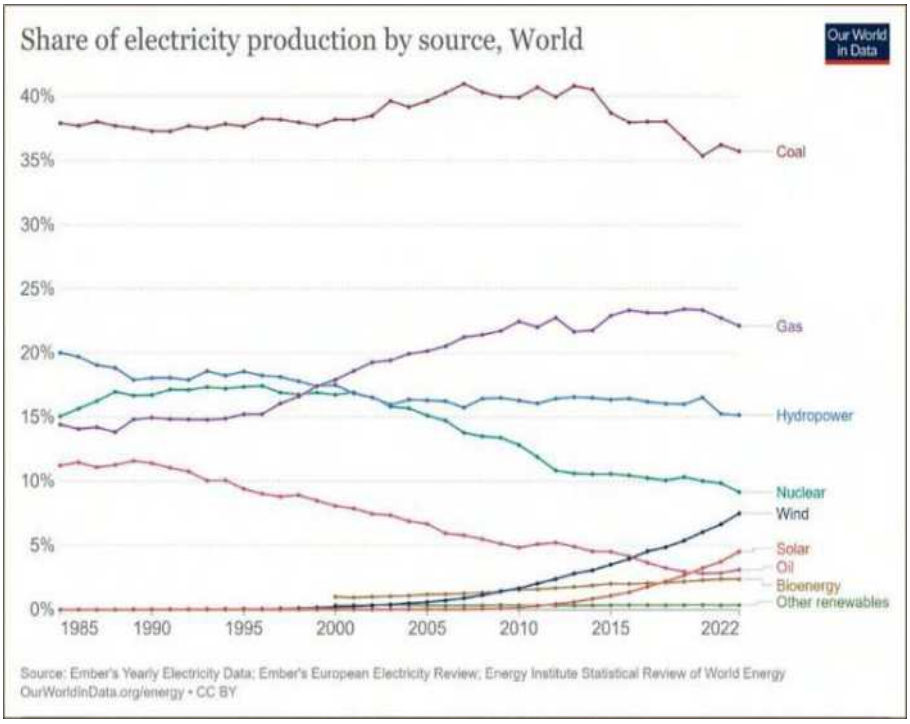

Figure 1. Share of electricity production by source, world

Another way to reduce greenhouse gas emissions is in agriculture with the help of nuclear techniques. In this field, nuclear science and technology will help by using radiation techniques, tracking and analysis by activation method. Applying these techniques will have positive consequences including controlling insects by sterilizing them, production of vaccines from radiation-attenuated parasites, determining the persistence time of the poison in the plant (residues of the poison in the plant or soil), investigating the movement and accumulation of used fertilizer in the soil and plants. All of these cases lead to reducing the water consumption pattern, increasing productivity, reducing the loss of agricultural products, reducing the use of poisons and chemical fertilizers, and as a result, protecting the environment.[7]

3 . 2 . Monitoring

Nuclear science provides valuable data for a better understanding of climate change. The International Atomic Energy Agency (IAEA) employs nuclear techniques, primarily isotopic, to identify and monitor GHG emissions and associated risks. And also policymakers can use nuclear and isotopic data to create, evaluate, and refine policies aimed at achieving long-term sustainability.

Reliable data on how GHGs impact land, oceans, and the atmosphere are crucial for addressing climate change. The IAEA shares data with Member States to support research and sustainable climate policy formulation.

By using isotope hydrology we can study rainfall patterns and manage groundwater sustainably in the face of climate change. Isotopic techniques help record the "memory" of water, allowing scientists to understand past climate events and improve future meteorological event planning. Also, special nuclear derived techniques capture isotopic fingerprints of extreme weather events, enabling predictions of future events.[8]

As an example, By measuring the difference in isotopic proportions, scientists can estimate the origin of different water sources, such as lakes, rivers, and aquifers (figure 2.).

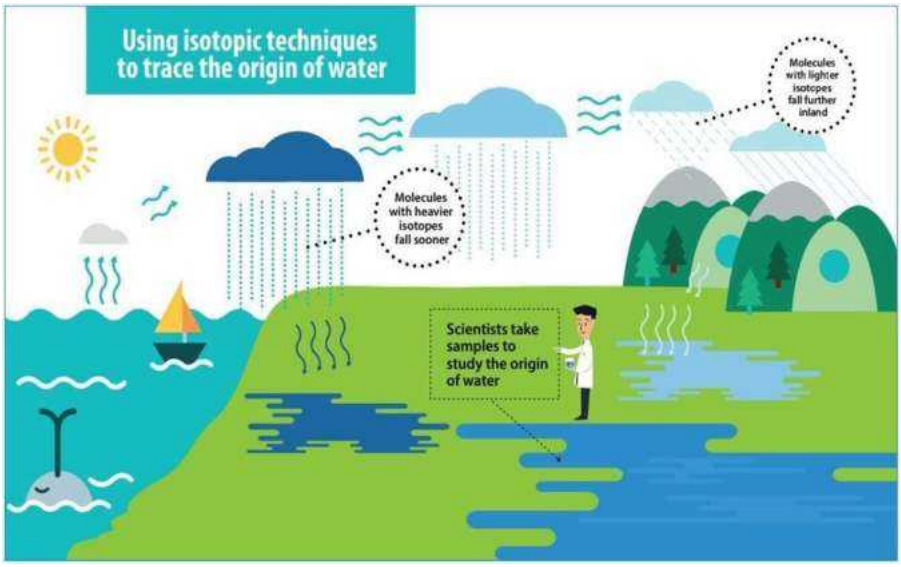

Figure 2. using isotope techniques to trace the water origin (IAEA)

Another way for monitoring is "Neutron Detection". As you can see in figure 3. , the cosmic ray neutron sensor detects and counts neutrons in the soil and the air just above it. Scientists use this data to determine soil moisture levels. Neutrons are generated by high energy cosmic rays, primarily protons, from outside the solar system. Cosmic rays collide with nitrogen and oxygen

atoms in the Earth's upper atmosphere, producing subatomic particles including protons and neutrons. These neutrons fall through the atmosphere, continually colliding with other atoms and gaining energy. As neutrons reach the Earth's surface, they are fast moving and their energy is absorbed by atoms in the environment, primarily hydrogen atoms.

Most terrestrial hydrogen is found in water in the soil, making it a key absorber of neutron energy. Scientists count fast neutrons in and around the soil to estimate water content. Dry soil has more fast-moving neutrons, while wet soil has fewer, as more hydrogen from water is available to absorb energy.

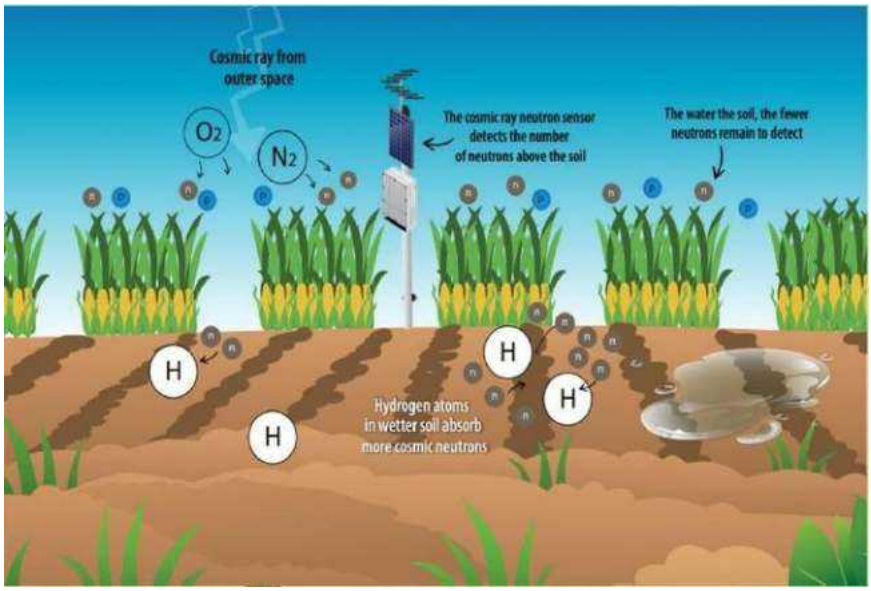

Figure 3. How the cosmic ray neutron sensor works

3 . 3 . Adaptation

Adaptation to the consequences of climate change is crucial alongside mitigation efforts. This is especially important given the immediate impact of climate change-related challenges. Because climate change has acute effects such as global increase in water shortage, food shortage, loss of biodiversity and most of the natural disasters are caused by climate change.

In this regard IAEA supports adaptation efforts like plant breeding, soil and crop management, livestock production, and insect pest control. And performs some activities in this field such as support sustainable management of freshwater resources and agriculture systems, advise on and develop climate-smart agriculture methods including for soil, crop and water management, research and provide expertise on ecosystems and how to counter biodiversity loss, Study and

provide guidance on ways to reduce the impact of climate-related severe weather on energy systems.

4 . The role of Bushehr nuclear power plant in environmental protection

Bushehr nuclear power plant is designed for the construction and operation of three nuclear reactor units. Currently, the 1st unit of this power plant is in operation with a power of 1000 MW, and its 2nd and 3rd units, each with a power of 1057 MW, are being designed and built. Unit 1 of Bushehr Nuclear Power Plant has produced 61,118 MWh of electricity and 55,658 MWh were delivered to the national electricity network in the years of its launch from 2011 and commercial operation from October 2013 to the end of the first six months of 2023. It should be mentioned that from the beginning of 2013 to the end of 2023, Unit 1 of Bushehr Nuclear Power Plant produced about 3108 million kilowatt hours of electricity and delivered 2824 MWh of electricity to the national electricity network.

Bushehr nuclear power plant from 2011 to 2023 with a total electricity production of 51.96 TWh will reduce more than 623,520 tons of CO2 in total and prevent the emission of 72,096 tons of CO2 almost every year, which is in line with achieving the goal of the Paris Climate Agreement. It is based on limiting the increase in global temperature to below two degrees Celsius and fulfilling part of Iran's commitments in the Paris Climate Agreement.

The amount of emission of polluting gases as well as the amount of savings in the consumption of fossil fuels, including natural gas and crude oil, are given below, respectively.

Figure 4. The amount of non-emission of polluting gases in the chemical unit of Bushehr nuclear power plant

Year	Periodic non-release rate (thousand tons)	Cumulative non-emission rate (thousand tons)
2011	563	2270
2012	1707	3977
2013	4194	8171
2014	4124	12295
2015	2686	14981
2016	6103	21084
2017	6868	27952
2018	6123	34075
2019	5574	39649
2020	6579	46228
2021	5211	51439
2022	7032	58471
(until Sept) 2023	3701	62172

Figure 5. The amount of savings in fossil fuel equivalent consumption resulting from electricity production in the first unit of Bushehr Nuclear Power Plant (in million cubic meters of natural gas)

Year	Periodic gas consumption (million cubic meters of natural gas)	Cumulative amount of savings (million cubic meters of natural gas)
2011	125	620
2012	495	1115
2013	1216	2331
2014	1196	3527
2015	780	4307
2016	1772	6079
2017	1995	8074
2018	1913	9987
2019	1784	11771
2020	1459	13230
2021	1156	14386
2022	1559	15945
(until Sept) 2023	780	16725

Figure 6. The graph of the amount of savings in the equivalent consumption of fossil fuels resulting from electricity generation Unit 1 of Bushehr Nuclear Power Plant (in barrels of crude oil equivalent)

Year	Periodic savings (million barrels of crude oil)	Cumulative savings (million barrels of crude oil)
2011	0.7	3.6
2012	2.9	6.5
2013	7.2	13.7
2014	7.1	20.8
2015	4.6	25.4
2016	10.5	35.9
2017	11.7	47.6
2018	11.4	59
2019	10.7	69.7
2020	8.7	78.4
2021	6.9	85.3
2022	9.7	95
(until Sept) 2023	5.1	100.1

5. Conclusion

The environment is strongly affected by the risks of climate change. Nuclear science and techniques, along with other modern sciences, can be an important part of solving the four basic

challenges of climate change, plastic pollution, environmental pollution, and the water crisis. According to the experience of countries and the reports of the International Atomic Energy Agency, the role of nuclear science and technology is divided into three parts: reduction, monitoring, and adaptation. The International Atomic Energy Agency is responsible for supporting all countries in taking the necessary measures to deal with climate change in all areas of mitigation, monitoring, and adaptation.

Iran is also aiming to increase the share of its nuclear power portfolio from its power generation portfolio to produce clean electricity to reduce fossil fuels and also reduce the amount of greenhouse gas emissions because of its successful experience from the first phase of the Bushehr nuclear power plant.

References

[1]. Correia, A. M., & Lopes, L. F. (2023). Revisiting Biodiversity and Ecosystem Functioning through the Lens of Complex Adaptive Systems. Diversity, 15(8), 895.

[2]. Udalova, A. A. (2020). Nonpower applications of nuclear technology. [3]. Nonpower applications of nuclear technology. Alla A. Udalova

[4]. Nuclear Power and the Environment. R.E. HESTER AND R.M. HARRISON 2011.

[5]. Non-electric applications of nuclear power: seawater desalination, hydrogen production, and other industrial applications, Proceedings of an International Conference. Oarai, Japan, 16–19 April 2007, IAEA, Vienna, 2009. 604 pp.

[6]. IAEA, Market Potential for Non-Electric Applications of Nuclear Energy, 2002. Vienna, Technical Reports Series no. 410. 252.

[7]. Industrial Applications of Nuclear Energy, IAEA, Vienna, 2017. IAEA Nuclear Energy Series no. NP-T-4.3. 96 pp.

[8]. Food Irradiation. A Technique for Preserving and Improving the Safety of Food, WHO, Geneva, 1988. 87 pp.